

Juan Carlos Jauregui *Editor*

Nonlinear Structural Dynamics and Damping

Mechanisms and Machine Science

Volume 69

Series Editor

Marco Cecarelli
LARM; Laboratory of Robotics and Mechatronics
DICeM; University of Cassino and South Latium
Cassino, Frosinone, Italy

Editorial Board Member

Alfonso Hernandez
Mechanical Engineering, University of the Basque Country, Bilbao, Vizcaya, Spain
Tian Huang
Department of Mechatronical Engineering, Tianjin University, Tianjin, China
Yukio Takeda
Mechanical Engineering, Tokyo Institute of Technology, Tokyo, Japan
Burkhard Corves
Institute of Mechanism Theory, Machine Dynamics and Robotics, RWTH Aachen
University, Aachen, Nordrhein-Westfalen, Germany
Sunil Agrawal
Department of Mechanical Engineering, Columbia University,
New York, NY, USA

This book series establishes a well defined forum for monographs, edited Books, and proceedings on mechanical engineering with particular emphasis on MMS (Mechanism and Machine Science). The final goal is the publication of research that shows the development of mechanical engineering and particularly MMS in all technical aspects, even in very recent assessments. Published works share an approach by which technical details and formulation are discussed, and discuss modern formalisms with the aim to circulate research and technical achievements for use in professional, research, academic, and teaching activities. This technical approach is an essential characteristic of the series. By discussing technical details and formulations in terms of modern formalisms, the possibility is created not only to show technical developments but also to explain achievements for technical teaching and research activity today and for the future. The book series is intended to collect technical views on developments of the broad field of MMS in a unique frame that can be seen in its totality as an Encyclopaedia of MMS but with the additional purpose of archiving and teaching MMS achievements. Therefore the book series will be of use not only for researchers and teachers in Mechanical Engineering but also for professionals and students for their formation and future work. Indexed in SCOPUS, Ei Compendex, EBSCO Discovery Service, OCLC, ProQuest Summon, Google Scholar and SpringerLink.

More information about this series at <http://www.springer.com/series/8779>

Juan Carlos Jauregui
Editor

Nonlinear Structural Dynamics and Damping



Springer

@Seismicisolation

Editor

Juan Carlos Jauregui
Faculty of Engineering
Autonomous University of Queretaro
Querétaro, Mexico

ISSN 2211-0984

ISSN 2211-0992 (electronic)

Mechanisms and Machine Science

ISBN 978-3-030-13316-0

ISBN 978-3-030-13317-7 (eBook)

<https://doi.org/10.1007/978-3-030-13317-7>

Library of Congress Control Number: 2019931517

© Springer Nature Switzerland AG 2019

This work is subject to copyright. All rights are reserved by the Publisher, whether the whole or part of the material is concerned, specifically the rights of translation, reprinting, reuse of illustrations, recitation, broadcasting, reproduction on microfilms or in any other physical way, and transmission or information storage and retrieval, electronic adaptation, computer software, or by similar or dissimilar methodology now known or hereafter developed.

The use of general descriptive names, registered names, trademarks, service marks, etc. in this publication does not imply, even in the absence of a specific statement, that such names are exempt from the relevant protective laws and regulations and therefore free for general use.

The publisher, the authors and the editors are safe to assume that the advice and information in this book are believed to be true and accurate at the date of publication. Neither the publisher nor the authors or the editors give a warranty, express or implied, with respect to the material contained herein or for any errors or omissions that may have been made. The publisher remains neutral with regard to jurisdictional claims in published maps and institutional affiliations.

This Springer imprint is published by the registered company Springer Nature Switzerland AG
The registered company address is: Gewerbestrasse 11, 6330 Cham, Switzerland

@Seismicisolation

Preface

I want to thank all the contributors to this book for their patience and hard work. This book compiles some of the newest research work of the members of IFToMM that are part of the Technical Committee for Vibrations (TC-Vibrations). This book came out as a joint effort to disseminate and share theoretical and experimental research in the field of vibrations and to promote the work done by different groups around the world. This book is a sample of various topics that the TC-Vibrations group are working on, and every chapter presents an in-depth analysis of the current methods for modeling Nonlinear Structural Dynamics and Damping.

The mission of IFToMM is to promote research and development in the field of machines and mechanisms, both theoretically and experimentally, and this book aims to spread the knowledge and experience of the TC-Vibration members. Thus, this book aims to present relevant topics on dynamics and vibrations that are of the interest of the community and could help in the solution of practical applications. The chapters of this book also present questions for further research and opportunity areas for future improvements in modeling and validating our current understanding of Nonlinear Dynamics.

The chapters are related to the modeling of nonlinear structures and nonlinear vibrations, presenting techniques for identifying nonlinear responses, the application of nonparametric methods for analyzing nonlinear mechanical systems and structures, and the analysis of synchronization in complex mechanical systems.

Friction and damping are fundamental parameters in the analysis of nonlinear structures; therefore, this book includes contributions related to the development and analysis of damping models.

Reviewing the table of contents will let you know that this book brings together the results of research topics of current interest that are fully explained. Authors that have a great experience in the matter, and are willing to share their knowledge with the scientific and engineering community present every chapter.

I want to thank the Publisher and Editorial staff of Springer for helping the publication of this book.

Querétaro, Mexico
November 2018

Juan Carlos Jauregui

Contents

1	Introduction to Scientific Computing Technologies for Global Analysis of Multidimensional Nonlinear Dynamical Systems	1
	Nemanja Andonovski, Franco Moglie and Stefano Lenci	
2	Review of Synchronization in Mechanical Systems	45
	Mihir Sen and Carlos S. López Cajún	
3	Research on Vibration Suppression of Nonlinear Energy Sink Under Dual-Frequency Excitation	71
	B. Sun and Z. Q. Wu	
4	Identification of Nonlinearities in Mechanical Systems Using Recurrence Plots	83
	J. C. Jauregui-Correa	
5	Passive Vibration Control Using Viscoelastic Materials	119
	D. A. Rade, J.-F. Deü, D. A. Castello, A. M. G. de Lima and L. Rouleau	
6	Dry-Friction Damping in Vibrating Systems, Theory and Application to the Bladed Disc Assembly	169
	Ludek Pesek, Ladislav Pust, Pavel Snabl, Vitezslav Bula, Michal Hajzman and Miroslav Byrtus	
7	Bifurcation-Based Shimmy Analysis of Landing Gears Using Flexible Multibody Models	261
	C. J. J. Beckers, A. E. Öngüt, G. Verbeek, R. H. B. Fey, Y. Lemmens and N. van de Wouw	
8	Spectral Analysis of Nonlinear Vibration Effects Produced by Worn Gears and Damaged Bearing in Electromechanical Systems: A Condition Monitoring Approach	293
	J. J. Saucedo-Dorantes, M. Delgado-Prieto, R. A. Osornio-Rios and R. J. Romero-Troncoso	

Chapter 1

Introduction to Scientific Computing Technologies for Global Analysis of Multidimensional Nonlinear Dynamical Systems



Nemanja Andonovski, Franco Moglie and Stefano Lenci

Abstract To determine global behaviour of a dynamical system, one must find invariant sets (attractors) and their respective basins of attraction. Since this cannot be made extensively with analytical methods, the numerical global analysis is currently the subject of intensive research, especially for strongly nonlinear, multidimensional dynamical systems. Numerical analysis in dimensions higher than four present a challenge, since it requires significant computing resources. Numerical methods used in global analysis that can benefit from high-power computing are those that can parallelize either data or task elaboration on a large scale. Mass parallelization comes with large number of difficulties, restrictions and programming hazards. When not implemented in compliance with hardware organization, data and instruction management can lead to severe loss of parallel algorithm performance. Systematic and methodical approach to design parallel programs is, therefore, critical to get the most from expensive high-power computing systems and to avoid unrealistic speed-up expectation. Considering these difficulties, the goal of this chapter is to introduce readers to the world of high-power computing systems for science and global analysis of strongly nonlinear, multidimensional dynamical systems. Topic covered are classification and performance of hardware and software, classes of computing problems and methodical design of programs. Two major hardware platforms used for scientific computing, clusters and systems with computational GPU are considered. Functionality of widely utilized software solutions (OpenMP, MPI, CUDA and OpenCL) for high-power computing systems is described. Performance of individual computer components are addressed so that the reader can understand advantages, disadvantages, efficiency and limits of each hardware platform. With

N. Andonovski (✉) · F. Moglie · S. Lenci
Polytechnic University of Marche, Ancona, Italy
e-mail: n.andonovski@pm.univpm.it

F. Moglie
e-mail: f.moglie@univpm.it

S. Lenci
e-mail: lenci@univpm.it

this knowledge users can judge if their computation problem is suitable for mass parallelization. If this is the case, which hardware and software platforms to use. To avoid many traps of parallel programming, one of the methodical design approaches is covered. Topic is closed with example applications in science and global analysis.

1.1 Introduction

Well explored analytical methods for linear phenomena is not viable to fully determine dynamics of systems that model real life application. Lack of analytical methods have led to development of various numerical methods for global analysis of nonlinear dynamical systems. Numerical methods offer possibility to solve problems that do not have analytical solution in closed form, sacrificing generality of solution—any change in system parameters require new computations. To determine global behaviour of nonlinear systems, the amount of computations increases dramatically and require large computing resources, especially in higher dimensions [1, 2].

Historical roots of numerical computations are found in rudimentary mechanical calculating devices that over long number of years have evolved to contemporary electrical supercomputers. Major point of calculating machines remains the same—to aid people in solving various, mostly mathematical, problems. Precursors of electrical computers are mechanical tools like simple adding devices, abacus, mechanisms for drawing integrals of graphical functions or mechanical machines that integrate differential equations [3].

Transition from various mechanical computers to electrical ones were made with implementation of concept machine capable to compute anything that is computable (Turing machine). First electrical, vacuum tube computer, EINIAAC (Electronic Numerical Integrator and Calculator), marks beginning of new era that will lead to computational capacity that surpasses anything ever imagined. Technology evolved to such scale that functionality of mechanical calculating machines are reproduced with integrated circuits, approx. 10 nm in size each [3–5].

High complexity of massively parallel computing systems used in science and engineering often cause difficulties during program design, particularly for those not educated in information technologies. In this chapter we aim to introduce readers to the capabilities of modern day computer systems and systematically explain all concepts needed to start making efficient program for large-scale numerical computing of global behaviour for high-dimensional nonlinear dynamical systems. Before tackling problems of high-power computing, it is necessary to analyse performance of basic computer components from which supercomputers are made of. Organization of components are described through architectures that act as logical concepts capable to deal with various computational problems. Families of problems that benefit from mass parallelization are explained along with architectures and computer implementations able to efficiently compute related tasks. Systematic design method is crucial to avoid dangers of parallel execution that do not exist in sequential approach. First step is to decide which hardware platform is most efficient for com-

puting of the problem to be addressed. Following steps of design methodology focus on how to make program that exploits optimally or almost optimally the computer resources. Brief introduction is offered also for most common software platforms used in scientific applications.

Topic is closed with examples massively parallel computations in global analysis and science. For in-depth understanding and functionality of software and hardware platforms or global analysis methods, readers are referred to abundant resources provided by scientific literature, manufacturers and user community.

For clarity and brevity, number of definitions and formulas are omitted and principles are explained as concisely as possible. Readers that find certain topic useful for their analysis should refer quoted literature for more details and further hints on practical implementations.

1.2 Analysis of Dynamical Systems

Mathematical description of dynamics is not limited to a mechanical systems. Biological, economics, psychological and many other non-mechanical systems evolve dynamically, and their evolution is governed by systems of various equations [1]. Continuous-time systems are represented through ordinary differential equations and discrete with difference equations. Other representations such as cellular automata, lattice maps and other are also often used, especially partial differential equations where system evolution is dependent from both spatial organization and time [6]. The mathematical notion of dynamical systems express fact that the motions are determined by some rules or laws. Thus, this deterministic approach allows to form space of states (phase space) and to acquire system state at any time given the initial (and boundary when required) condition [6].

1.2.1 Linear Analysis

Traditionally, the analysis starts from linear approximation of nonlinear systems. Having a general solution in closed form gives a formal way to explore linear systems [6]. Family of linear systems gives qualitatively same response for all values of system parameters, making parameter analysis straightforward. With analytical methods it is fairly easy (from computational point of view) to determine stable and unstable behaviour of the solution. For these systems the attractor, if present, is unique, and thus the long term solution is “easy”. No multi-stability occurs, and thus basins of attraction are meaningless.

1.2.2 Nonlinear Analysis

Majority of natural systems are in fact nonlinear [6], but an initial clue of overall dynamics can be obtained by analyzing corresponding linear system. Similarities between linear and nonlinear system depend on the magnitude of nonlinearities, where higher nonlinearity produce more diverse collection of behaviours, such as multi-stability, quasi-periodicity, deterministic chaos, solitons, fractals, riddled basins or pattern formation. In order to determine which of those diverse behaviors are present in the system, analysis combines analytical approximation, numerical calculations and experimental data. An important part of analysis is observation of system behavior during the change of some system parameters, since in many cases it can lead to change in topology of the system (qualitative change), especially when the system is nonlinear.

Two classes of nonlinear systems that are in most cases subjected to analysis are those that can be represented through systems of partial differential equations or with the systems of ordinary differential equations. For global analysis most interesting are dynamical systems which can be reduced to a system of ordinary differential equations of first order [7]. Most important family are systems of second order differential equations, modelled from Second Newton's Law of motion, that can easily be reduced to the first order systems. Dimension of resulting system (not to be confused with degrees of freedom) is equal to the number of first order differential equations. Each dimension in this case corresponds either to the coordinate or velocity that appears in the system. This representation gives possibility to use well developed numerical techniques [8]. Solutions then can be analysed as trajectories in multi-dimensional state space.

1.2.3 Global Analysis

Nonlinear systems may have arbitrary number of steady motions, some stable some not. If trajectories converge towards certain steady state, it is called attractor and repellor if trajectories are diverging away from it. Basin of an attractor consists of the all initial conditions that converge to associated attractor in forward time. Goal of global analysis is to get a global behaviour of system, expressed in terms of attractors and their respective basins. It is usually conducted together with time series, frequency response and parameter variation (bifurcations) [1].

Resulting behaviour can be very colorful. Beside geometrically regular shapes as points or limit cycles and torus, attractors that may occur in nonlinear dynamics can be of a fractal structure (strange attractors) [6]. Fractal curves [9] are not smooth, but geometrically irregular or an uneven shape of non-integer dimension, repeated over all magnifications (from large to infinitesimally small). Attractors with fractal structure are usually associated with chaotic motion, but also strange nonchaotic attractors exist. In cases where multiple attractors coexist basins can be separated

by smooth or fractal curves. Numerically, fractal boundaries can only be assumed up to the computer precision. Another possibility is that basins may be riddled [9]. It means that border between basins is not a curve (neither smooth nor fractal) and points in infinitesimally small hyper-sphere around certain initial condition do not necessarily converge to same attractor.

Although behaviour may be complex, the numerical procedures used at global analysis are able to compute fairly accurate results [10]. Difficulty comes with increase in system dimension, as number of required computations increases exponentially. Therefore, to numerically analyse dynamical systems with large dimension it is necessary to resort on powerful computational computer systems, which heavily rely on mass parallelization of computation. Currently, multidimensional global analysis is focused at building basins in more than four dimensions. Six-dimensional systems are being examined contemporary while eight-dimensional present a challenge for both computation and visualization.

1.2.4 Numerical Computing Integration

Numerical integration schemes [8], used to overcome the limits of analytical methods are broadly classified as either explicit or implicit. In explicit schemes the governing equation is written at time for which all the solution variables are already known, and the difference equation is then solved for the solution at the next time step. Explicit methods are generally preferred for solution of problems where the interesting part of the solution is changing rapidly in time like in wave propagation problems or crash analyses. In implicit schemes, the governing equation is written at time $t + \Delta t$, while the solution is known for time t . Implicit methods are better suited for problems where the solution variation over time is less rapid, and relatively larger time steps can adequately resolve the problem.

Commonly used numerical methods (i.e. adaptive step Runge-Kutta of 4th order) can be already found within libraries and freely used for scientific computing without need to implement the whole numerical procedures in programming language.

1.3 Computer Architectures

Functionality of a computer or sub-system, without concern of actual implementation, is defined by the *architecture* [5, 11, 12]. Architectures are classified according certain properties of hardware (parallelism type, memory organization, etc.) and every computer system is synthesis of various architectures.

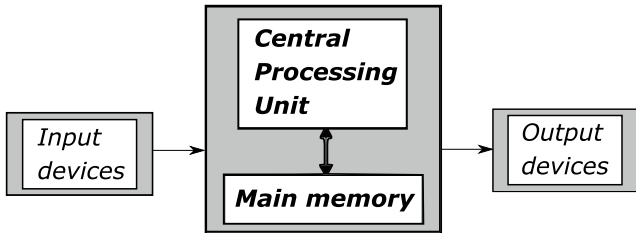


Fig. 1.1 Von Neumann concept of computer

1.3.1 Von Neumann Architecture

Basic logical concept of computers is presented through Von Neumann model [5, 11, 12] on Fig. 1.1. It consists of a processing unit (*processor*), memory and data pathways (buses). Processor interprets and executes programs which are combination of instructions and data. Processor fetches instructions and data and execute them sequentially one after another. Every instruction refers to memory address where next instruction and data are stored, meaning that flow of program is driven by instructions.

Complexity of real computer system is significantly higher than in Von Neumann model, as consequence of adding various complements to compensate restrictions of low-performing components. Concepts of high-power computing are based on combining multiple logical units in various ways [12, 13] resulting in numerous computer systems dealing with problems in science, engineering, economy, etc.

1.3.2 Parallel Architectures Parallelization Classification

As current manufacturing technology reached peak where fabrication process is getting increasingly difficult to improve, performance increase is achieved by parallelizing the computations. Performance is enhanced by parallelizing processing elements (i.e. multiprocessors, neural networks) or instructions inside processing element (pipeline, vector processing) [5, 11–13].

Pipelining and vector processing are already implemented inside modern processors and are not widely used as stand-alone parallelization concepts. For scientific computing most relevant are multiprocessor architectures, as being most performant parallelization concept. Other existing parallel architectures are rarely used because they are efficient only for problem-specific applications. It is notable to mention data flow computing, systolic processing and neural networks as concepts utilized in science, that are not instruction driven as majority of architectures based on von Neumann model.

1.3.2.1 Pipeline, Superscalar and Very Long Instruction Word (VLIW) Processors

Processor have multiple stages of executing one instruction. Main segments are instruction fetching, decoding, execution and result store. All segments can be further fragmented, resulting that processor have to do multiple steps in order to fully execute one instruction. Pipeline parallelization is achieved by simultaneously executing different segments of successive instructions. Pipeline technique is also exploited in architectures where instructions are pipelined with multiple processors.

VLIW are instructions combined from several shorter, that allow processors to have a deeper pipeline. Superscalar processors exploit pipelining concept by adding more hardware circuits, so processor can do arithmetic, logic or floating-point operations of several separate instructions parallelly.

1.3.2.2 Vector Processors

As pipelined computers execute multiple instructions simultaneously, vector computers can process entire vector of data in one instruction [5]. Fetching of data is done for whole vector not for just one piece of data. Multiple arithmetic circuits then can manipulate entire vector during one instruction period instead of processing each vector element as successive instruction. Each vector element is manipulated with same instruction.

1.3.2.3 Systolic Architecture

In systolic array [5], processing units are organized in a network, so that at each cycle part of data is calculated and forwarded to the subsequent processing elements in grid. After initial latency (number of cycles until all computing elements receive first block of data) system can efficiently compute repetitive task (matrix transformation, sorting, Fourier transform, etc.). Implementations of this architecture is effective for specialized computations, making it efficient, compact and economically convenient but inflexible.

1.3.2.4 Data Flow Architecture

In dataflow computing [5], the order of execution is managed by data availability, not by order of instructions. An instruction executes when required data arrives, as result of program flow being driven by data dependencies. Each instruction reference to next instruction, contrary to instruction ruled architectures where instructions reference to memory location of next instruction. This architecture found successful implementation only in several areas (telemetry, digital signal processing, etc.).

1.3.2.5 Neural Networks

An attempt to mimic structure and function of biological neural networks [5] is implemented by parallelly interconnecting large number of simple processing elements. Artificial neural networks can derive solutions in dynamic situations from incomplete or probabilistic data. To be able to adapt, the learning algorithm of neural network requires training multiple running of program with correct input data and known solutions. Difficulties come from possibility that network is adapting its behaviour from incorrect previous information. Great complexity of artificial neural networks limits its usage at scientific computing, although the promising potential uses.

1.3.2.6 Multiprocessors

Strict definition of multiprocessors [5, 12, 13] is not well established due to variety of implementations. General idea is to connect multiple computing entities into network that act as single system, which can run one or more programs that are divided into numerous parallel tasks. Concepts and implementations of multiprocessor computers often match the requirements necessary to compute most problems encountered in scientific and engineering applications. Remainder of this chapter is therefore, dedicated to multiprocessor architectures, implementations and design methodology.

1.3.3 Stream Concurrency Architecture Classification

Flynn's taxonomy [5, 11–13] classifies computer architectures according to number of parallel streams. Instruction stream (program) is sequence of commands/instructions executed by processors. The flow of data that is being manipulated by commands from instruction stream is called data stream. Flow of instructions goes from memory to processing unit, while data flow is bi-directional. Flynn's taxonomy is most often used for classifying multiprocessors, since logical concepts of taxonomy reflect multiprocessor organization.

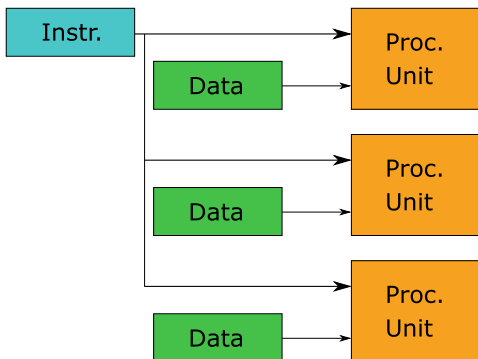
1.3.3.1 Single Instruction Stream, Single Data Stream (SISD)

Conventional serial computers with one processor, built according to the von Neumann model, work on SISD principle. Processor is able to sequentially process one stream of instructions and operate over single data set. Flow scheme of SISD architecture is depicted in Fig. 1.2.

Fig. 1.2 SISD execution model



Fig. 1.3 SIMD execution model



1.3.3.2 Single Instruction Stream, Multiple Data Streams (SIMD)

Concept of multiprocessor computer that parallelly execute single instruction stream on multiple data streams. This means that each processing unit will execute same sequence of instructions, but with distinct data stream, as on Fig. 1.3. Execution is lock-stepped, which means that processing units are synchronized and all tasks will start and finish in same time. Examples are graphical coprocessors and array computers where multiple processing units work under control of single control unit.

1.3.3.3 Multiple Instruction Streams, Single Data Stream (MISD)

In MISD architecture each processing unit handles own (distinctive) instruction stream, operating over single data stream. This architecture, shown in Fig. 1.4, is

Fig. 1.4 MISD execution model

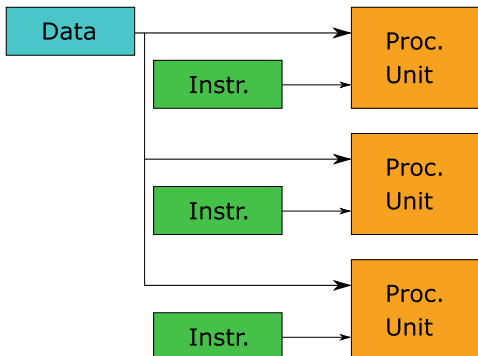
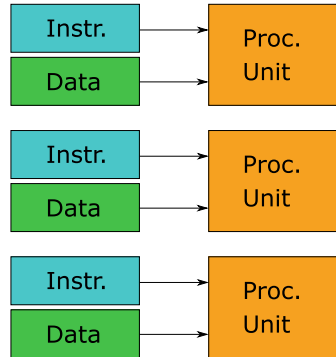


Fig. 1.5 MIMD execution model



rarely used, mostly for fault tolerance, as system must agree on the result from all instruction streams. Space shuttle flight control computer is an example.

1.3.3.4 Multiple Instruction Streams, Multiple Data Streams (MIMD)

Computer system where multiple autonomous processing units simultaneously execute distinct instruction streams over separate data streams is shown on Fig. 1.5. Tasks in MIMD architecture are asynchronous and execution can start and finish at any time independently on other processing unit tasks. Almost all modern systems are built according to MIMD architecture, from computers with one multi-core processor to clusters and cloud super-computers.

1.3.4 Memory Access Level Classification

To achieve massive performance increase, multiple processors are connected into single system (networking). Coupling between processors in network might be implemented on various ways, resulting in computer systems spanned from single case to geographically dispersed systems [11, 14, 15]. Programs that are run on high-power computing systems are divided into numerous parallel *tasks*. Common name for parallelly executing tasks in shared memory systems are *threads* and on distributed memory systems—*processes*.

1.3.4.1 Shared Memory Architecture

Memory hierarchy of shared memory systems [11, 14, 15] allows all processors to access central system memory. Memory that is shared between tightly coupled processors is called *local memory*. High performance of shared memory systems

comes from availability to access data directly. If synchronization of instructions and data management are not handled carefully, it can lead to various errors.

1.3.4.2 Distributed Memory Architecture

In distributed memory systems [11, 14, 15] every processor has its own local memory. Systems architecturally organized like these are loosely coupled and processors can operate independently. Local memory of one processor is inaccessible by remote processors and data is exchanged through communication channels. Part of system consisting of a processor and its local memory is named *node*. Theoretically there is no limit in how many nodes can be connected to form distributed memory high power computing system. Data coherency is automatically maintained since remote memory is not directly accessible in any case. Drawback is that node interconnections transfer data at much lower rates than bus connections on shared memory systems.

1.3.4.3 Hybrid Memory Access Architectures

Actual implementations are not restricted to strictly shared or distributed architecture. Reality rather correspond to MIMD architectures [13, 15]. In fact, many of the high-power systems are combination of multiple coupled sub-systems. Hybrid architectures have interconnected nodes where each node may be architecturally different from others. For example, node might consist of several processors or can be GPU accelerated.

1.3.5 Other Architecture Classifications

To avoid over encumbering reader with unnecessary information for scientific computing other classifications of parallel designs are not considered. For curiosity reader may refer to literature [11–14] for classifications based on instruction set architecture, network organization, degree of parallelization, pipelining level, etc.

1.4 Hardware Components

Basic computer components are building blocks for personal computers and supercomputers as well. In this section readers are introduced to functionality and performance of relevant components, required to efficiently design parallel software for scientific purposes. High level of attention must be paid to the performance of all components to avoid *bottlenecks*—limited capacity of computer caused by single low-performing component [11, 16].

Actual physical parts of computer are various combinations of electrical circuits [11, 12, 16]. Electrical elements (transistors, capacitors, resistors, diodes, inductors, etc.) are integrated in chipsets that perform designated operations. Chipsets can be digital that operate only on binary data (0 and 1 values) or analogue which can manipulate variable continuous signals.

Personal computers are relatively small sets, while high-power computing systems are created from considerably larger number of components, combined to operate as coordinated system. To grasp how complex systems behave it is necessary to understand functionality and performance of each of the individual components. To interact with user, computers need input/output devices (keyboard, mouse, monitor, printer, etc.). Modern computers also cannot be imagined without a Graphical Processing Unit (GPU) that enhance visual output of computers. Other numerous components and devices such as TV cards, sound reproduction systems or gaming controllers do not play role in scientific applications and although are regular parts of modern computers, are not considered.

1.4.1 *Central Processing Unit (CPU)*

The set of electronic components that operate and manage data is integrated on one chip called *central processing unit* or *processor* [11, 12, 16]. It fetches instructions from main memory, decodes them and perform indicated operations over correct data set. *Datapath* is part of processor that execute instructions and manipulate data. It is a network of arithmetic and logic units connected to internal memory. Logical circuits can perform i.e. bitwise logical operations, while arithmetic circuitry can add, subtract, increment, etc. Modern processors have also floating-point units, the circuitry specialized to perform arithmetic operations over floating-point numbers faster than arithmetical can. The control unit is part of processor that manages scheduling of instructions, data transfer from/to memory and coordinates other components. Multi-core processor is one integrated chip consisting of two or more independent processors named *cores* in this case.

System clock [5, 11, 12] is part of processor that regulate update time of internal components. At every *cycle* (tick of clock) states of components are changed. Cycle length must be long enough to allow the propagation of state change through all processor components. To execute one instruction, processor in most cases requires multiple cycles.

With combination of large number of integrated circuits processor can perform diverse range of operations at extremely high rate. Current high-end technology enables billions of transistors to be integrated on a single chip. For example, Qualcomm Centriq 2400® processor (one processor with 8 cores) have about 18 000 000 000 integrated circuits on chip with 398 mm² area [4].

1.4.2 Main Memory

Instructions and data of currently running programs are stored in *main memory* [11, 12, 16]. Every time processor is ready to execute some part of the program, it has to make an access to main memory to retrieve required information. Fetching process is slow in comparison to execution time of processor, creating frequent bottlenecks. *Memory Wall* is the name for performance restriction imposed by low performance of main memory.

Main memory can be either read-only (ROM) or read and write (random access memory—RAM). Data residing on ROM is permanently stored and mostly used to keep hardware management programs hidden from users. On the other side, RAM is volatile type of memory where all user applications are loaded on runtime. When speaking about memory in following sections, it will be referred to main memory (RAM). When mentioned, other memories will be addressed by their type—registers, cache or storage.

1.4.3 Internal Memory

Major mechanism to overcome restrictions of main memory is to use small amounts of high-speed memory integrated on processor chip. Two types of internal memories, that considerably reduce data access time, are *registers* and *cache* [5, 11, 12].

Registers, that are located directly near processing circuits, are very low latency memory with access time from one to few clock cycles. Other memory types that are located far away, require additional access control and pathways that considerably increase fetching time. Despite the high performance, processors are fabricated with low amount of register memory due to high manufacturing costs (per storage capacity) and large spatial occupancy on processor chip.

Cache memory serves as a buffer between registers and main memory. When some piece of data is processed, it is highly probable that nearby data will also be needed in near future. Therefore, processor transfers entire block from main memory to cache, instead of only data needed at the exact moment of access. Cache is organized into levels, where lower levels, closer to processor cores are faster but with lesser capacity. Levels 1 and 2 are commonly dedicated to each core and are not shared, while higher levels of cache are accessible to all processor cores. Highest level of cache sometimes can be allocated as part of main memory, while lower levels are always integrated on processor chip.

1.4.4 Mass Storage Memory

Storage (or secondary) memory [5, 12] is a component or external device where data and programs are permanently kept when computer is not powered. Examples are Hard Disk Drive, DVD disks, Flash memory or online cloud storages. It has high capacity and low manufacturing cost per storage unit. Access time is considerably slower compared to execution time of processor operations. Storage memory does not actively participate in computations, but for task with large data sets, writing and reading of information can create performance drops due to low speed of mass storage devices.

1.4.5 Data Transfer

Internal transfer of information between processor and other components is done by *bus* [11, 12, 16], a combination of wires acting as data highway. It can be a point-to-point pathway, connecting two specific components or shared (multi-point) connection between several components. Speed of the bus is affected by its length as well as by the number of devices sharing it. Bus clock manages the time interval of its state update. Bus cycle is longer than processors which makes it inefficient to supply information directly from main memory.

Computer systems created by joining multiple computing entities can exchange information over Local Area Network (LAN) or Wide Area Network (WAN) [16]. Various protocols manage how data is sent and received in network. Internet and Ethernet are protocols with low and medium data transfer performances used in loosely coupled systems. Tightly coupled systems use high-performance network protocols (i.e. InfiniBand®) to communicate information on higher rates.

Actual links that represent communication channels can be wired (collection of digital or analogue wires, coaxial cables, Ethernet cables or optical wires) or wireless (radio signals or optical communications). Connections other than bus have considerably lower transfer capacity, causing low utilization of resources on systems that have to communicate large quantities of information.

1.4.6 Graphical Processing Unit

Graphical image processing is data intensive operation and accelerator graphic coprocessors are intensively developed to aid processor to visualize graphic content [13, 17]. When processor encounters graphically intensive part of program it forwards data and instructions to Graphical Processing Unit (*GPU*, coprocessor or accelerator for short) that have electronic circuits optimized for efficient image processing. Price

for being specialized for certain tasks is that GPU is highly inflexible and unable to function on its own.

Special branch is computational GPUs (or General-Purpose GPUs) that utilize high number of simple cores (stream processors, shaders) which are able to conduct general computations, while retaining high performance in data intensive applications [13, 18]. Graphical coprocessors are fabricated on separate (graphic) card connected to processor by bus. High-performance RAM is located on the coprocessor card due to high demand for data.

In this chapter, when mentioning GPU, we will refer to the general purpose graphical coprocessors only, since computations are major concern, not the image processing acceleration.

1.4.7 ASIC and FPGA

Application-Specific Integrated Circuit (ASIC) is an integrated chip intended for specific use, while field-programmable gate arrays (FPGAs) are designed to be configured by user after manufacturing [11, 17]. Either design offers excellent efficiency when developed for specific use. To formulate functionality of both designs elevated expertise in information technologies is required, thus not covered in this chapter.

1.4.8 Performance of Computer Components

Principal matter for high-power computing systems is how well extensive tasks can be accomplished. Performances of individual components reflect the overall ability of computer system to complete required tasks. Knowing the performance of data operations and transfer helps in understanding why various components exist and why are implemented in certain ways. From efficiency perspective, performance issues of particular components must be considered during design of parallel algorithms.

Depending from context, performance can be measured as amount of jobs done per unit of time (throughput) or amount of time required for some task to complete (execution time, latency, response time, access time or delay) [11, 17].

1.4.8.1 CPU Performance

When comparing performance of processors, usually their speed is a relevant factor. Unfortunately, term speed of processor does not have a determinate meaning. It may refer to several measures that quantify some of the processor characteristics. Reason for this is rich complexity of micro-architectures that differ even between processors

of same manufacturer and family. Current technologies of manufacturing processors with multiple cores, additionally complicates comparison of different processors.

Number of instructions per second (*IPS*) [11, 17] is one of the measures used, but for processors with complex instruction set it is not an accurate measurement. Instructions have unequal size, resulting in variable execution time for each instruction. More common and precise speed measure is number of system state updates per second, namely *clock speed* or *frequency* (GHz) [11, 17]. Clock speed also does not give definite comparison quantities, since some processors may finish certain actions in fewer clock cycles than others. Thus, even equal clock speeds of different processors do not guarantee that they will do equal amount of work.

Benchmark programs are used to get somewhat accurate comparison of performances for various systems or components. They may test performance of overall systems or a single component in various workload situations. In this way processors can be compared on how well they perform at certain task. For scientific computing where data is mainly floating-point numbers, measure how well system (or single component) perform is represented through floating-point operations per second (*FLOPS*) [11, 14, 17].

1.4.8.2 GPU Performance

Graphical coprocessors are highly specialized hardware and their high performance limits the flexibility. Metrics for GPU performance are same as for processors, but direct comparison of processors versus general-purpose GPUs is vague because each is designed to be efficient at different type of tasks [17, 18]. However, certain applications are not focused on computation, such as the matrix transpose. In those cases, metric relevant to indicate throughput of GPU tasks is MBPS (megabytes per second).

GPU use extensive amounts of electrical energy for computations, that often causes necessity to measure also the power consumption [19]. *Energy* is a measure of how much electrical energy the system consumes in total, *power* is energy consumption per time unit and *power efficiency* quantifies arbitrary performance measure per power consumption.

1.4.8.3 Data Transfer Performance

Performance of data transfer is governed by two factors, *latency* and *channel width* [11, 16]. Latency is time in seconds that takes to access the data. Width is the amount of information that can be transferred at once. Combined, is a measure called *bandwidth* that quantifies transfer capacity by the amount of data that can be transferred per unit of time. Drops of overall computer performance is often caused by data transfer bottlenecks, where data is not supplied fast enough or in low quantities required for high percent of utilization of computing resources.

Table 1.1 Memory hierarchy

Mem. type	Approx. cap.	Latency
Registers	200 ps	4 kB
Cache L1	64 kB	1 ns
Cache L2	256 kB	3–10 ns
Cache L3	16–64 MB	10–20 ns
RAM	up to 256 GB	50–100 ns
HDD	up to 64 TB	5–10 ms
Flash	up to 16 TB	100–200 ms

1.4.8.4 Memory Hierarchy and Performance

Memory can be hierarchically classified based on capacity and response time [5, 12]. Table 1.1 shows performance and capacities of various memories that can be effectively manufactured with current technologies [20]. At top levels of hierarchy are internal memories with fast access speed and low capacity. Main memory is in middle, with average access time and significantly higher capacity than internal memory. Low levels of hierarchy are occupied by massive storage devices with slow response time.

1.4.8.5 Overall System Performance

Overall system performance depends on combination of components and type of task being computed. Systems with fast and numerous processors cannot work efficiently if memory and data interconnections cannot keep up with performance of processors. Drops of performance is even more evident with GPUs where efficiency is highly influenced on both hardware factors and how tasks are scheduled. Optimization of hardware according to one component is bad practice and each platform should be designed to efficiently utilize all resources. Also, to maximize performance of hardware platform it is equally important to use an appropriate programming model [11, 13–15].

Supercomputers that exist today are often combination of multiple processors and GPUs. List of current (scientific) supercomputers compared to their floating-point operation power can be found at The Top500 web-site [21]. Lately, for ecological and economic purposes another measure is often used in scientific computing—FLOPS/Watt, which measures the amount of work done per energy consumption. Supercomputers sorted by their energy efficiency are found at The Green500 List [22].

1.5 Massively Parallel Designs

Systems with large number of processing units are named massively parallel designs for high-power computing [17]. Those systems use numerous processors, connected computers or GPUs to achieve coordinated execution of program in parallel [11–13]. Depending on the interconnection implementation and centralization level, computers might be developed as mainframes or connected in clusters, grids or clouds. Other types of computer designs are available, such as fog or peer-to-peer computing. Some of the nodes in network might have computational GPU, which does not change type of computer system, only the performance of the node.

Topic of massively parallel computers is too large to be covered in one chapter, also unnecessary because two designs mostly used in scientific and engineering computing are clusters and computers with computational GPU. Functionality of cluster and GPU accelerated computers (nodes) will, therefore, be explained in detail while other implementations are only listed according to [11, 13, 17].

1.5.1 *Classification of High-Power Computing Platforms*

Workstation is historically broad term, firstly used for hubs where the operating person would interact with large sized computers. Nowadays it is referred to personal computers or computers from which bigger systems are managed. Importance of PC workstation is that whole design process is done on it and finished programs are executed on more expensive platforms. But, if supplied with computational GPU, regular workstation becomes a high-power computing platform.

1.5.1.1 Mainframe

Mainframe computers contain multiple processors connected at the bus level. Mostly used in business applications for transaction processing. Since the metrics used to measure performance of mainframes is set of certain tasks (update of database, disk I/O, etc.), it is not useful for science and engineering applications where large number of floating point operations are required.

1.5.1.2 Clusters

Clusters are formed by connecting nodes into network that act as a single unit, computing single task (program/application). Cluster nodes are often closely centralized and connected with local high-speed interconnections.

1.5.1.3 Grid Computers

Resemble clusters, usually larger, more geographically dispersed and are not dedicated to run only one task.

1.5.1.4 Clouds

Cloud computers are systems whose organization is hidden from end user. Primarily developed to provide application services to commercial purposes without need from user to know organization of nodes or to have expertise in information technologies. Recently cloud services are as well available to scientific computing, usually as virtual machines representing clusters.

1.5.1.5 GPU Computing

Contrary to mass parallelization done by adding more processors or nodes to the system, any computer can become high-power computing platform by adding a general-purpose graphic card. When installed, GPU cards significantly increase capabilities in data intensive tasks of any computer (or node).

1.5.2 *Clusters and General-Purpose Graphic Cards*

Programming models mostly used in science are based on SIMD and MIMD architectures [13, 14, 17] for HPC computing. To have efficient computations, the programming models must be efficiently mapped to hardware. SIMD type problems efficiently exploit the inherit (hardware level) parallelism of GPUs, while clusters reflect MIMD architectures.

1.5.2.1 Clusters

Clusters computers are networks of computing entities (nodes) [13, 17, 18]. Nodes are commonly stand-alone computers, typically connected in LAN, with one of the high-speed protocols. Property of clusters, that distinguish them from other networked computers is that clusters operate as single system performing single task (program).

Considering that nodes are separate computers, memory of each node is not shared, making clusters a distributed memory system. Nodes communicate data by passing messages to each other. Transferring time of messages between nodes that are not directly connected can be considerably longer than between directly connected nodes.

To avoid communication overheads, it is advisable to know network topology of the cluster (line, ring, tree, mesh, hypercube, fully connected, star or bus).

Clusters are often implemented on master/slave dogma. Master process manages existence and work of numerous slave processes that carry out actual computations. MIMD problems that are instruction intensive and do not require large amount of data communication are highly suitable for cluster computations.

1.5.2.2 GPU Computing

Development of processors through history was focused on increase in number of successive instructions it can perform per unit of time. Graphical processing as SIMD operation had low benefit from increased clock speed. It required large number of equal operations to be carried out simultaneously. Graphical coprocessors evolved from being capable only to perform graphical computations to devices that can achieve remarkable speed-up in data intensive applications [13, 17, 18].

A GPU consists of several stream processors, each one having dozens of simple computing cores (CUDA cores). For example, GPU card based on NVIDIA Fermi® architecture can have up to 16 stream processors with 32 cores each [23].

1.5.2.3 GPU Cluster Combination

To expand capabilities of clusters, GPUs are added to some of the nodes. This mixed implementation is not surprising and it is good practice since it combines computational power of both MIMD and SIMD environments [24].

1.5.3 *Classification of High-Power Computing Problems*

Parallelization aim to speed-up the serial execution by either dividing instructions or data between concurrent processing units. To efficiently carry out parallelization process, it is necessary to determine what type of parallelization can be achieved.

1.5.3.1 Task Parallelism

Task parallelism [14, 17] occurs in cases where sequence of instructions can be divided into multiple, parallel and independent tasks. Task may run same or different code over same or different data, communicate information during execution and start and stop at arbitrary time unless explicitly specified otherwise.

1.5.3.2 Data Parallelism

Data intensive computations are those where large number of data elements have to be processed in the same way [14, 17]. One sequence of instruction is executed over multiple parallel data elements as in SIMD architecture. In comparison with task parallelism where instruction set is split over multiple tasks, in data parallelism data set is distributed between parallel processing elements.

1.5.3.3 Combining of Data and Task Parallelism

At various degrees, majority of actual programs and computation problems are not strictly data or task parallel. Problems described with MIMD architecture often combine parallelization on both data and instruction levels [25]. Certain problems, such as Fast Fourier transform or some sorting procedures, also benefit from possibility that algorithm can switch between data and task parallel execution models during computations.

1.5.4 *Classification of High-Power Computing Paradigms*

1.5.4.1 High-Performance Computing (HPC)

Tasks that require large amount of computational power during short time periods (one day or less) are characterized as *high-performance computing* [26]. Measure of computational power in HPC jobs is FLOPS. HPC systems tend to focus on tightly coupled parallel tasks, and as such they must execute within a particular site with low-latency interconnects, mainly clusters or mainframes. Presuming that majority of scientific computing is done over floating-point data, HPC is in most cases appropriate computing paradigm for scientific applications.

1.5.4.2 High-Throughput Computing (HTC)

When task at hand is far larger than require months or years to compute it is not important how fast, but how many jobs can be finished per unit of time (in HTC terms—jobs per month or year) [26]. HTC systems deal with sequential jobs that can be individually scheduled (loosely-coupled tasks) on many different computing resources, such as grids or clouds.

1.5.4.3 Many-Task Computing (MTC)

Many applications are not computing extremes as HPC and HTC [26]. Paradigm that offer middle ground is MTC, where both tightly coupled and independent task can be executed, no matter if tasks are instruction or data intensive, large or small.

1.6 Performance of Parallel Designs

For high performance of computing systems, it is not enough to have parallelization on massive scale [11, 13–15, 18, 20, 27–29]. Utilization of resources depends on both hardware and software factors and each computing problem should be computed on appropriate platform. Algorithm type, programming issues and hardware or communication restrictions downgrade performance when are not addressed properly.

As many factors are involved in science and engineering, it is substantial to decide what performance metric is relevant. Performance models serve to compare how efficiently different algorithms perform specific requirements. Analysis of performance models can discover many inefficiency causes. Often when not planned in advance, program hits performance wall, in which case code re-factoring must be done. To achieve optimal performance of parallel designs it is necessary to balance software and hardware factors and in many cases, programming effort and costs also must be considered. To evaluate performance of parallel programs, number of models are proposed [15, 20, 28] to address different performance issues.

Performance measures and issues of parallel designs are addressed in advance, so that during design methodology section reader can comprehend importance of each step.

1.6.1 Scalability

Property of computer system or computing problem that describe how well it cope with resource improvement is called *scalability* [11, 14, 15, 17, 28]. *Overheads* are the segments of program code that do not benefit from improved resources since must be executed serially on one processor. Problem or computer that can manage well the increase of resources is called *scalable*. Effect of overheads is that for fixed size problems efficiency drops by increasing the number of parallel processing units. To maintain efficiency at decent levels, solution is to proportionally increase also the problem size. Basically, scalability is a measure or a property of code and system sensitivity to resource improvement. Code and computer system that are scalable will not lose efficiency with increased number of processors. Term *strong scaling* defines how solution time varies for fixed total size problem during increase of resource power. *Weak scaling* measures variation of problem solution time with resource improvement for fixed size problem per processor. Highly scalable problems, that do

not have overhead are being called *embarrassingly parallel* [14]. This is in practice often rare.

Beside overheads, other hardware and programming factors reduce parallelization benefits. Actual speed-up during parallelization is less than theoretical, since the performance values are calculated only by processor utilization time, ignoring constraints of hardware components, interconnections effects, technology cost and performance or algorithm structure. Factors that affect scalability are number of processing units, variable clock speeds of components, problem size, execution time, data input/output demand, memory capacity, communication overheads, programming and hardware costs. To achieve computational objectives, some parameters may be fixed while optimizing other factors. *Scalability analysis* is engineering procedure that helps to systematically identify critical factors of any algorithm performance [15, 28].

1.6.2 Parallelization Degree

The degree of parallelism [15] reflects how much software parallelism matches hardware parallelism. During execution, parallel program can use variable number of processing units over different time periods. Number of processors utilized at each time period is defined as the *degree of parallelization*. *Parallelism profile* is the plot of parallelism degree versus time.

1.6.2.1 Average Parallelism

In systems with multiple processors (of equal computing capacity) that during computation use various degrees of parallelism it is possible to calculate total amount of work done over some time period. *Average parallelism* [15] is total amount of work done expressed as single constant degree of parallelism (during this time period).

1.6.2.2 Available Parallelism

Parallelism degree is directly tied to type of problem. *Available parallelism* [15] characterize what degree is possible to achieve with certain problem. It is reported that data-intensive applications may have degree of parallelism from 500 to 3500, in an idealized environment, while at the instruction-level parallelism is rarely higher 7. However, the degree of parallelism may be extended to thousands in some scientific algorithms where it is possible to parallelize instructions inside basic blocks (sequence of instructions with has a single entry and exit).

1.6.3 Parallelization Speed-Up

Main goal of parallelization is to speed-up the computing process by dividing computational load over multiple processors [11, 15, 17, 28, 30]. Ideally, speed-up is equal to the number of processors that share workload. In reality, this does not happen because of negative hardware and algorithmic effects of parallelization and often, some of the program code that must remain sequential. As performance depends on multiple factors, it is not easy to formulate unified speed-up measure for all problems. To evaluate speed-up number of techniques are proposed, neither fully standardized nor agreed upon, but all serve purpose to quantitatively demonstrate efficiency of parallel designs under certain conditions.

1.6.3.1 Amdahl's Law and Gustafson's Law

Amdahl and Gustafson gave formulas to calculate theoretical speed-up of parallel program versus to sequential one. Speed-up according to Amdahl is quantified as percentage of sequential processing time for one processor, versus overall parallel execution time for fixed size of computing problem, while Gustafson's law describes theoretical speed-up in cases with increased workload. As described in [30] those two laws are related and in fact are equivalent. Often it is hard or impossible to determine required serial percentage and those laws do not reflect real speed-up achieved by parallelization. Furthermore, those laws can give misleading speed-up for algorithms that change structure when parallelized.

1.6.3.2 Memory-Bounded Speed-Up

Many scientific and engineering computations are often bound by memory capacity rather than performance of processing units. *Memory-bounded speed-up model* [31] generalizes Amdahl's law and Gustafson's law by maximizing the use of both processing and memory capacities. The idea behind this model is to solve the largest possible problem, limited only by the capacity of available memory. To achieve scalable performance, this model may result in an increased execution time.

1.6.4 Efficiency, Utilization and Quality of Parallelism

To enlarge scope of measuring performance, efficiency, utilization and quality of parallelism is measured by overall execution times instead of using the time percent. Balance between following several parameters are often good practice to achieve efficient parallel computations.

1.6.4.1 Efficiency

The speed-up factor of parallel computer system that does fixed amount of work, is expressed as execution time ratio between single-processor system and multiprocessor system. *Efficiency* [15] is for this case speed-up divided by number of processors running on parallel computer. Calculated this way, efficiency gives the degree of speed-up in comparison to theoretical (maximum) values.

1.6.4.2 Utilization and Redundancy

Redundancy [15] of system expresses the matching degree between hardware and software parallelism. Value is calculated by dividing amount of operations done by multiprocessors system with the value for single-processor system. When efficiency is multiplied by redundancy, result is overall *utilization* [15] of resources used during execution of program.

1.6.4.3 Quality

Parallelism *quality* [15] is single value used to validate speed-up of increased resources. Expression combines previous factors and is directly proportional to the speed-up and efficiency and inversely related to the redundancy.

1.6.4.4 Mean Performance

Arithmetic and *harmonic mean* performance measures [15] are used for parallel computers that execute multiple programs and in various parallelization modes (multiprocessing, vector processing, pipelining, etc.). Scientific computations are mostly organized as multiprocessor system running single programs, rendering those measures rarely significant.

1.6.5 Performance Summary

As it can be seen from previous parts of this section, models and measures that try to generalize performance of parallel computations often do not give an accurate image. To adjust performance representation to certain problems, many different approaches have been proposed. Extensive quantitative approach to performance analysis of various problems is treated in [20, 32].

At certain point scientific programmer have to make a trade-off between evaluating performance and working on actual computations. Performance models that are less accurate, but easy to examine, can often give an enough clear picture if parallelized problem computes with acceptable performance.

1.7 Efficiency Issues of Massively Parallel Designs

Parallelization consequences, hardware restrictions and programming approaches influence performance and correctness of results and program propagation. Certain issues manifest only on shared memory systems, other on distributed and some are system independent. Typical issues are overheads, dependencies and bottlenecks, caused by either hardware or algorithm.

This section classifies at what conditions common issues may occur. To achieve scalable performance, attention must be paid to avoid or resolve those problems.

1.7.1 General Issues

1.7.1.1 Overheads

Overhead [13, 17, 28] is common name for conditions that avert processor from actual computations. Algorithmic overheads or excess computations are parts of program that are difficult to or cannot be parallelized at all. In those cases, parallel algorithm can be either much more complex than sequential or it must be run sequentially on only one processor. Communication overhead (interprocess interaction) is time that processors spend on data transfer instead of computations. It includes reading, writing and waiting for data.

Idling is state of processing elements at which no useful computations are done. Reasons for idle time of processors might be synchronization requirements, overheads or load imbalance.

1.7.1.2 Bottlenecks

As seen from previous sections, data transfer often downgrades processor performance. In multiprocessor environments, memory bandwidth is aggregated with adding more nodes, but for multi-core it is harder to achieve desired level of scalability. Situation where processor speed gets limited as result of insufficient increase of memory bandwidth is called *memory wall* [17]. Computations where performance is constrained by transfer rates of memory are referred as *memory bound* [28].

Techniques to overcome memory performance problems are named latency hiding, tolerating or reducing mechanisms. Those techniques and mechanisms [15] (memory consistency, cache coherence, prefetching, cache and coherence misses and other) are actually very important, but are concern only to engineers who build multiprocessor systems. In general, (scientific) programmer should properly balance computations with data transfer and not be occupied with low-level implementation and issues.

In multiprocessor systems bottlenecks [11, 14] can also be caused by poor load balance, where whole system waits idle for one processor to finish computations.

1.7.1.3 Dependencies

Often for certain computations to advance, data from previous iterations is required. Such cases are called data dependent [14, 15]. Parallelization is interrupted by task that must wait for data to continue. Other types of dependencies exist, but are not significant from scientific programmer perspective.

1.7.2 *Issues on Shared Memory Systems*

1.7.2.1 Result Preservation

In parallel program, order of execution is changed in comparison to sequential one [29]. Some operations that are sequentially executed one after another, now may be executed parallelly. Order of execution can cause change of accuracy on some systems due to number truncation or rounding off on different places in program. To avoid such errors, it is required to check if results are consistent during change in order of execution.

1.7.2.2 Synchronization Errors

Very common errors manifest on shared memory systems when threads are not time synchronized [29]. Program executes correctly, since there is no actual bug, but results may be incorrect. Timing of threads impacts if those errors happen or not, even in cases when synchronization is not explicitly imposed.

First type of incorrect results may occur when one thread starts to work on data from another thread that have not yet finished with computations. A barrier can be instructed to ensure that the thread will wait for another one to finish.

Result inconsistency can also happen when a thread is scheduled to work on part of data already processed by another thread. To avoid this issue, programmer can explicitly protect access to data of another thread.

Race condition is a conflicting state when multiple threads try to simultaneously update same variable. Without access synchronization variable update may not be as it is intended. To resolve race conditions, reading and writing to a shared variable should be enclosed in critical section that permit only one thread at time to manipulate data. Critical sections are implemented as *atomic instructions*. One atomic instruction is sequence of instructions that manipulate shared variable. At any given time, only one atomic instruction is allowed to be executed by whole computer system and it must be executed entirely before any other instruction.

1.7.2.3 Variable Scope Issues

Certain variables may be declared to be shared between all threads or private to each thread. If declared incorrectly shared variable may not be updated when necessary and private may be updated by wrong thread [29].

1.7.3 *Issues on Distributed Memory Systems*

1.7.3.1 Deadlocks

Situation when two or more processes keep waiting for resource from each other and none of them can make any progress [13, 14, 18]. Resource in those cases can be message send/receive operation, synchronization instructions or access to remote device or memory. Conditions under which deadlocks happen are when resource is mutually exclusive (only one process may use it), when process that use a resource requests another resource (hold and wait condition), in cases when resource cannot be released without process action (no pre-emption condition) and when multiple processes in circular chain wait a message from another one.

Deadlock detection [33] is analysis conducted to reveal if deadlock conditions apply to set of resources and processes. Prevention and avoidance ensure that deadlock conditions do not hold and will not occur upon resource utilization. To prevent mutual exclusion, resource should be available to multiple processes. Hold and wait condition may be eliminated by forcing the process to release all resources upon request for another or to acquire all resources with single operation. No pre-emption is eliminated by allowing a resource to be released from process. Circular chain waiting is prevented by imposing an order of resource employment.

1.7.3.2 Livelocks

Similar situation to deadlock, where two or more processes fail to progress because all keep responding to each other request indefinitely [17, 33]. It is resolved by giving respond priority to one of the process.

1.7.3.3 Busy Waiting

Occurrence when one process sends a message to another process that continuously denies it or when process constantly tests if a condition is satisfied [33]. The first process keeps resending the message or checking the condition state and cannot continue with useful work.

1.7.3.4 Starvation

In cases where processes are scheduled by another entity, starved process [17, 33] is one that is ready to continue, but scheduler ignores it.

1.8 Parallel Program Design

In multi-core environments there is no certainty that some parallel operations will be executed at exactly same time or in exactly specified order without losing parallelization or introducing idle waiting time. For example, in parallel program one core might supply certain data to another core too late or too early. The program code does not report any error (since there is none), yet it produces incorrect output due to loss of data coherency or processors stay unnecessary idle. De-bug difficulty presents that on certain runtime program will work and on another runtime, it will go into a dead-lock even with same data, depending how threads are scheduled by operating system [13, 14, 17, 18, 27]. Step-by-step debugging and data tracing is therefore not feasible solution for checking errors and flow of a parallel program. Much more attention must be invested in methodical design to prevent dead-locks, incoherent data operations and other dangers of parallelization. Design methodology will be described in order to minimize parallel program flaws and bugs due to common bad practice during programming while maintaining decent level of simplicity and efficiency [18, 27]. More detailed approach to design of parallel algorithms may be found in [13, 14, 20]

1.8.1 *Parallel Program/Algorithm Properties*

1.8.1.1 Concurrency Versus Parallelism

Often confused for same, but fundamentally different procedures of instructing commands [17, 18, 27]. Concurrency enables several different threads to be open for execution by single processor. This means that while one thread is executed (sequentially), other threads stay idle and processor can arbitrary switch between execution of threads.

In parallelism, every thread is executed on dedicated processor in the same time, resulting that (ideally) there is no idle time for any thread.

1.8.1.2 Locality

Ratio of local memory accesses to remote memory accesses is defined by locality of program [27]. It is one of the major properties of parallel programs which can lead to efficiency loss due to communication constraints.

1.8.1.3 Modularity

Property of program (and in some cases hardware) to be composed of number of smaller, independent units (modules) is in general good practice in software engineering, both sequential and parallel [11, 27].

1.8.2 Design Methodology

To get from problem specification to effective parallel algorithm it is crucially important to rely on design methodology than on pure creativity of programmer. Anyway, creativity is of great importance even when following methodical approach. It allows to increase range of considered options, distinguish bad from good alternatives and to minimize backtracking from bad choices. Design flaws easily compromise parallel program performance. As most of problems have multiple parallelization possibilities, methodical design helps to characterize most favourable solution [13, 14, 18, 27, 28].

1.8.2.1 Partitioning (Problem Decomposition)

First step before starting to design a parallel program, is to determine if problem is inherently parallel by its nature or it may or may not be parallelized [14, 27, 28]. To be parallelizable an algorithm must satisfy certain conditions. Detecting methods serve to discover if some algorithm is parallel when it might not be obvious.

Partitioning serve to recognize parallelization opportunities in the problem. Data and operations are decomposed into smaller (independent when possible) tasks. If decomposed tasks are not independent, they have to communicate data according to dependencies. *Domain decomposition* is technique where data set of problem is divided into independent pieces. Next step is to associate tasks to partitioned data set. Complementary technique, the *functional decomposition*, focuses on dividing the computations into smaller disjoint tasks. In case when decomposed tasks correspond to partitioned data, decomposition is complete. By nature of many problems this is not possible. In those cases, replication of data or task set must be considered. Even when it is not necessary, it might be worth to replicate data or instructions to reduce communication. Several guidelines should be considered before proceeding to next steps of parallelization, to ensure that there are no obvious design flaws:

1. to increase flexibility in following design stages, there should be at least one order of magnitude more tasks than processors in the system and
2. consider both decomposition techniques and identify alternative options,
3. scalability can be compromised with larger problems if there are redundant computations or data input/output after partitioning,
4. it is hard to allocate equal amount of load to each processor if tasks are not comparable in size,
5. to properly scale, with increase in problem size, number of task should grow, rather than size of individual task.

1.8.2.2 Communication Design

Flow of data is specified in communication stage [27] of design. In general, tasks can execute parallelly, but it is rare that they are independent. Proper communication structures are required to efficiently exchange data between parallel tasks. Goal of communication design process is to allow efficient parallel execution, by acknowledging what communication channels and operations are required and eliminating those which are not necessary. Communication channels for parallel algorithms obtained by functional decomposition correspond to the data flow between tasks. For domain decomposed algorithms, data flow is not always straightforward, since some operations might require data from several tasks.

Local communication structures are used when task communicate only with small number of neighbouring tasks. Global communication protocols are more efficient when many tasks communicate with each other. Communication networks can be structured, where tasks form a regular composition and unstructured where task are arbitrarily arranged. If identity of communication pairs varies during program execution, communication is dynamic and for unchangeable identities, it is static. In synchronous communication information exchange is coordinated, but for asynchronous communication structures, data is transferred with no mutual cooperation.

The following check-list is proposed to avoid overheads and scalability issues arising from inefficient communication layout:

1. for scalable algorithm, all tasks should perform similar number of communication operations,
2. when possible, arrange task so that global communication can be encapsulated in local communication structure,
3. evaluate if communication operations are able to proceed parallelly,
4. evaluate if tasks can execute parallelly and does communication prevents any of the tasks to proceed.

1.8.2.3 Agglomeration

One of the principal requisites for efficient execution is level of matching between hardware and software. In agglomeration stage [27] algorithm from previous phases is adapted to be homologous to the computer system used for computation. It is known that it is useful to combine (agglomerate) large number of small tasks into fewer task larger in size or to replicate either data or computation. Reduced number of tasks or replication can substantially reduce communication overheads.

Revision of parallel algorithm attained by decomposition and communication design phase can be optimized by following agglomeration procedure:

1. reduce communication cost by increasing task locality,
2. verify that benefits outweigh the costs of replication or limit scalability,
3. task created by agglomeration should have similar communication costs as single smaller task,
4. evaluate if agglomerated algorithm with less parallel opportunities execute more efficiently than highly parallel algorithm with large communication costs,
5. check if granularity (size of tasks) can be increased even further, since fewer large task are often simpler and less costly,
6. evaluate modification costs of parallelization and strive to increase possibilities of code reuse.

1.8.2.4 Mapping

Final stage of design is to decide how to map task execution on processors [27]. Since there is no universal mechanism to assign set of tasks and required communications to certain processors, two strategies are used to minimize execution time. First option is to map tasks to different processors in order to increase parallelization level. Other option that increase locality, is to map tasks that communicate often to the same processor. Those strategies are conflicting and a trade-off must be made to achieve optimal performance. Favoured strategy is problem specific and use of task-scheduling or load balancing algorithms can be used to dynamically manage task execution.

1.8.3 Design Evaluation

Before starting to write actual code, parallel design should be evaluated according to few criterion. Some simple performance analysis should be conducted to verify that parallel algorithm meets performance requirements and that is the best choice among available alternatives. Also, to be considered are the economic costs of implementing and possibilities for future code reuse or integration into larger system [27, 28].

1.9 Software Solutions

Software solutions are the connection between hardware platforms and computing problems. Various libraries, frameworks and APIs (application programming interfaces) are added to backbone programming languages like C/C++ or Fortran. Functionality of parallelization software is developed to be independent from backbone languages. To exploit parallel resources, programmer only need to call (parallelization) sub-routines from one of the supported programming language [13, 18].

This section explains principal functionality (concepts) of major software solutions for science applications. Logic behind those software platforms is clarified and for actual coding tutorials readers are invited to use specialized programming literature.

1.9.1 *OpenMP*

OpenMP (Open Multi-Processing) [13, 18, 34] is an API that supports programming on shared memory computers in C, C++ and Fortran languages. It offers intuitive, multi-threading method of parallelization, where one main thread (master) forks when parallelizable part of code is encountered. Work is then divided among number of secondary (slave) threads. There can also be multiple levels of forking. Threads of same level execute same code over designated portion of total data. It is usually used in combination with other parallel software when is possible to parallelize work inside nodes.

1.9.2 *Message Passing Interface (MPI)*

MPI [13, 18, 35] is a standard that defines syntax and semantics of library routines used for writing message-passing programs in C, C++ and Fortran. It operates on variety of parallel architectures, but is major standard for programming of distributed memory systems, such as clusters. Message passing with MPI is not so intuitive approach to parallel programming and requires more attention than multi-threading approach with OpenMP.

Parallelization is achieved by creating one master and numerous slave tasks (*ranks*) at program runtime. Each rank runs own instance of MPI program. Within code it is specified what parts are executed or skipped by certain ranks. In this way, each rank has own instance of data structures that are not shared with other ranks (although the structures are declared under the same name). To access some remote data, rank have to explicitly request it.

Core of MPI is based on communication by passing messages between ranks. The simplest form of information exchange is by send/receive operations. One rank would request some data, other rank has to acknowledge this request and send required

data back. First rank then has to appropriately receive the message containing the requested information.

Beside point-to-point communications as send/receive, there are collective class of communication operations. When large number of ranks have to exchange data it is much more efficient to use collective message passing.

Synchronization of execution can be explicitly imposed by instructing barriers or implicitly by using blocking communication. Neither rank is allowed to proceed until all ranks execute the explicit barrier instruction. Blocking communication prevents receiving rank to continue until message is received. Asynchronous communication can be achieved by using non-blocking message passing or by using probe instructions. With probe instructions, ranks check if there is pending message. When message is there, probing rank receives it, when not, rank continues with execution.

Communicator is a structure that defines communication privileges. It is used to specify what ranks will participate in certain communication operations.

Functionality of message passing makes it appropriate for programming of MIMD problems in HPC. Technique often used is *hybrid programming*, where MPI and OpenMP are used together.

1.9.3 CUDA and OpenCL

Compute Unified Device Architecture (CUDA) [13, 18, 23] is programming environment developed to efficiently map data parallel task to GPU structure. GPU program is separated in parts run by CPU (*host*) and data intensive functions (*kernels*) that are executed on GPU (*device*).

Beside memory allocation that hold transfer of data between CPU and GPU memories, programmer has to specify how threads are organized inside kernel. Kernel *grid* is organized in two levels. Top level is organization of thread *blocks* within the grid. On second level threads are arranged inside block. Each block of same grid has same number and structure of threads. Latest GPUs support three-dimensional organization of threads within block.

Execution configuration of kernel is further divided into smaller units *wraps*, that are collection of threads which executes at once. Mechanism called thread *scheduler* decided which wrap will be executed. This execution model efficiently exploits memory and core organization of GPU even in cases when programmer poorly organize kernel grid and memory allocation.

Kernel execution requires large amounts of data and access to it is very time-expensive. *Memory coalescing* is a technique that combines neighbouring data and copies it together from slow global to fast shared register memory. To exploit memory coalescing, programmer should organize data so that neighbouring threads in wrap use equally organized data in memory (consecutive threads should use consecutive memory locations). Technique that help to methodically arrange data according to thread execution schedule is called *tiling*. It enables also to efficiently reuse data or pre-load piece of data for faster access.

Open Computing Language (OpenCL) [13, 18, 36] is cross-platform programming environment that provide standardized support for computers with multiple processors, GPUs and other computing units. It provides methods to efficiently assign tasks and exploit all resources of heterogeneous computing platforms. Execution model of OpenCL programs are slightly more complex, but very similar to CUDA.

1.9.4 Other HPC and Scientific Software

The above mentioned software are not only solutions available on market, but are widely used and supported by user community. Other software such as job schedulers, node installation and management, integrated stacks and monitoring programs are more concern of system administrators than to programmers. For larger jobs it might be useful also to get familiar with load balancing, task scheduling and management [32].

Most HPC platforms are never dedicated to only one computing job. Resources (HPC time) are shared/distributed between large number of scientific and industry projects. It is worth to mention that large amount of HPC time is dedicated to *Computational Fluid Dynamics*. Although it is a nonlinear phenomena, it is not focused on global analysis but on modeling the motion of specific problems, such as interaction of fluids with a solid surface. Reference [37] presents an example of scientific applications available at one of the supercomputers from Top500 list.

1.10 HPC in Global Analysis

It is assumed that reader is familiar with the basic of nonlinear dynamics and is looking to parallelize his/her own computations. This section is thus, dedicated to introduction to some of main methods of global analysis, to present possible parallelization options and to provide examples of how it may be accomplished.

1.10.1 Numerical Global Analysis Methods

As computers are able to manipulate and store numbers with limited number of digits, numerical methods operate with somehow discretized continuous state space. There are two types of methods, classified according to discretization methodology. First class are methods that treat state space as collection of points. Second class of methods divide state space into number of hyper-cubes (*cells*).

1.10.1.1 Point Integration

Straightforward method to get a basin of attraction is to take a cross-section of continuous state space and approximate it with set of points. To determine basin, every point is evolved by integrating forward in time. It is assumed that orbit converges if, after certain amount of time, distance from it to one of the one of the attractors is within some small predefined tolerance [10]. This method often requires integration of trajectories for extensive amount of time, that depends on the length of the transient motion [38].

1.10.1.2 Point Mapping

Instead of looking for the continuous time history of a motion of the system, it is also possible to track the system state at a sequence of discrete time instants. Methods how to approximate continuous trajectories with point mapping depend on the type of system and nature of analysis. Result of discretization is mapping function where discrete trajectory is formed by iterating the map, starting from an initial state [1].

1.10.1.3 Basins of Attraction

Theory of point mapping allows to determine equilibrium points, periodic motions and strange attractors, associated with continuous counterpart. To determine basins for stable sets there are several methods. Direct approach investigates where each initial condition maps after certain number of iterations. Time saving method consists of starting from small known region around an attractor and then expand the boundary. For certain two-dimensional maps it is possible to separate basins by using stable manifolds of saddle points.

1.10.1.4 Grid of Starts

Integration of grid of points (or grid of starts) [39] is a method related to the point integration. Basins are determined in the same manner, by integration from initial condition to the attractor. The initial condition in this case is a cell, commonly its center point. In other words, all states residing inside the cell are approximated as single cell entity. Although this method give fairly accurate results, the drawback is high computational requirements [40] because of the long integration time needed to overcome transient.

1.10.1.5 Cell Mappings

Closely related to the point mapping, cell mapping methods also approximate continuous trajectories by a discrete map. Starting from state space discretized as in Sect. 1.10.1.4, each cell is enumerated with a positive integer number. Initial conditions are then integrated over small time period to obtain the mapping. An image (or image cell) is a cell where the initial cell is mapped after one step of a map. It is possible to use methods analogue to point mapping to determine attractors and corresponding basins. As cell mapping is less computing intensive than fore-mentioned methods, and over the years, various cell mapping methods were developed, each with its advantages and drawbacks.

The *Simple cell mapping (SCM)* method [1] assumes that each cell can have only one image cell. If a cell maps to itself, it is considered to be a periodic cell. When certain cell maps to itself after multiple map steps, all cells in the sequence form a periodic motion. Basin of attraction is then a collection of cells that after arbitrary number of map steps get mapped to some periodic cell or motion. With SCM it is not possible to accurately approximate chaotic attractors or fractal basin boundaries, but it can give a hint if those are present in the dynamical system. E.g. a chaotic attractor in SCM can be recognized as a several periodic motions with a very long period. Advanced cell mapping methods can be used to overcome obstacles of SCM, but at certain computational costs.

The *Generalized cell mapping (GCM)* method [1] improves SCM by incorporating more information on system dynamics inside the map. Function that governs the map evolution is based on probability of each cell to map into one of the possible image cells. Such formulation of GCM mapping leads to the finite Markov chains for which well developed theory enables identifying the dynamics of the system. GCM is effective for discovering occurrence of chaos in the system.

The *Interpolated cell mapping (ICM)* [39] is a method developed to combine good characteristics of SCM and GCM. In SCM trajectory endpoint is rarely in the center of image cell. ICM records beside image cell also the actual location of endpoint inside image cell. Next iteration is calculated by taking the relative position of terminal point in respect to four surrounding cells. The end point of this iteration is obtained by interpolating between endpoints of the trajectories emerging from fore-mentioned four surrounding cells. In comparison to SCM and GCM, this method gives more accurate trajectories, but requires additional computational costs for computing new terminal positions.

Cell mapping methods are particularly suitable for systems with a periodic excitation. In this case the map is the stroboscopic one, sampled at the period of the excitation.

1.10.2 Multi-dimensional and Parallelized Numerical Global Analysis Methods

Before-mentioned methods work well in lower dimensions, but do not scale so well with increase in system dimension. To overcome dimensionality restrictions in [41] the authors developed a multi-degree of freedom (MDOF) extension to cell mapping methods. Beside dimensionality, another, difficult task is to overcome inner seriality of those methods. Survey of successful attempts to parallelize global analysis methods follows.

In [42] MDOF cell mapping algorithm is restructured to exploit most time consuming part of global analysis – the system integration. In a series of papers [43–45] the authors examined parallelization of grid of starts method on cluster computers. Successfully computed basins of attraction in both previous cases are used to determine integrity measures of dynamical systems.

To exploit massive parallelization capabilities of GPU, in [46] the authors refined the SCM method with subdivision techniques, in order to solve problems in multi-objective optimization. Another GPU parallelization approach on global analysis is tackled in [47] that combined several cell mapping methods (SCM, GCM and ICM). This combined method gives fast and resource efficient method to discover attractors, but require additional computations to determine basins. Authors provide example applications to impact model, plasma model and six-dimensional Lorenz system.

1.10.3 Example of Global Analysis

To illustrate computing of basins with SCM we used the four-dimensional system of two coupled and driven Duffing-Van der Pol oscillators considered in [48], governed by the equations:

$$\begin{aligned}\dot{x}_0 &= x_1, \\ \dot{x}_1 &= v(1 - x_0^2)x_1 - \omega_1^2x_0 - \epsilon x_0^3 + \beta x_2 + F \sin(t), \\ \dot{x}_2 &= x_3, \\ \dot{x}_3 &= v(1 - x_2^2)x_3 - \omega_2^2x_2 - \epsilon x_2^3 + \beta x_0 + F \sin(t + 0.25),\end{aligned}\quad (1.1)$$

with $\omega_1 = 0.000023216854686$, $\omega_2 = 0.022222854255$, $v = 0.25$, $\beta = 0.01$, $\epsilon = 1$, and $F = 1.4$.

Calculations are carried out with two different resolutions to demonstrate accuracy and performance of the method. For the low resolution the state space region $x_i = (-4, 4)$ is divided into 110 intervals per dimension, totaling 146 410 000 cells and size cell $h_i \approx 0.073$. Significantly higher number of cells, 1 632 240 801 is achieved by dividing each dimension into 201 intervals, here having size cell $h_i \approx 0.039801$.

Initially, the system (1.1) is integrated with a parallelization process on a small cluster using MPI standard implemented in C programming language. Then, the four-dimensional basins of attraction are determined with SCM post-processing algorithm. Low resolution case is calculated on two different computers. On the one with lower performance integration time was approximately 4 h and basin search lasted about 15 min. Then, the same calculations are carried out on computer with four times more processors. Result was that integration stage scaled well reducing computing time to around 1 h, but result of increased communication in post-processing stage increased time to build basins to 30 min.

Bad scaling of post-processing is even more evident in the high resolution case, where integration lasted 6 h and post-processing 12 h. From achieved performance it is obvious that integration stage can be considered as parallelizable, since it scales well. On the other hand, SCM post-processing is highly inadequate to be computed on distributed memory systems where large amount of communication operations drastically degrade performance.

In Figs. 1.6a and 1.7a we report the $x_0 - x_1$ and $x_2 - x_3$ basins cross-sections (other coordinates are fixed to 0) of low resolution and on Figs. 1.6b and 1.7b of high resolution case. To synthetically present usefulness of full-dimensional basins we report in Figs. 1.8 and 1.9 how the $x_0 - x_1$ cross-section of basins changes as the x_3 coordinate is varied.

Although the fastest and least resource consuming method, the drawback of pure SCM computations is that there is the possibility that some basins and attractors are assimilated as a result of the low accuracy of approximated trajectories, especially at low resolutions.

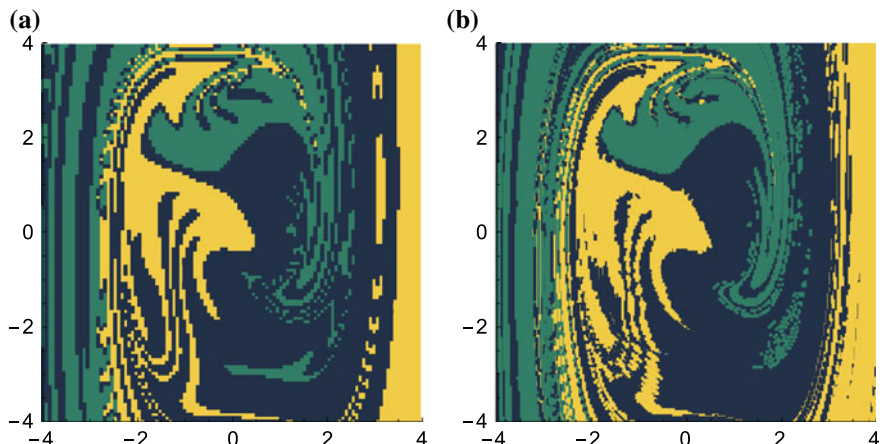


Fig. 1.6 $x_0 - x_1$ basin cross-section of **a** low and **b** high resolution cases

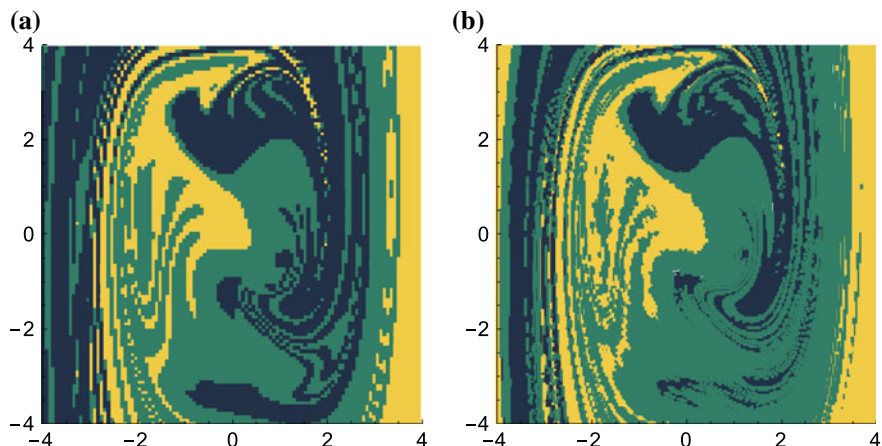


Fig. 1.7 $x_2 - x_3$ basin cross-section of **a** low and **b** high resolution cases

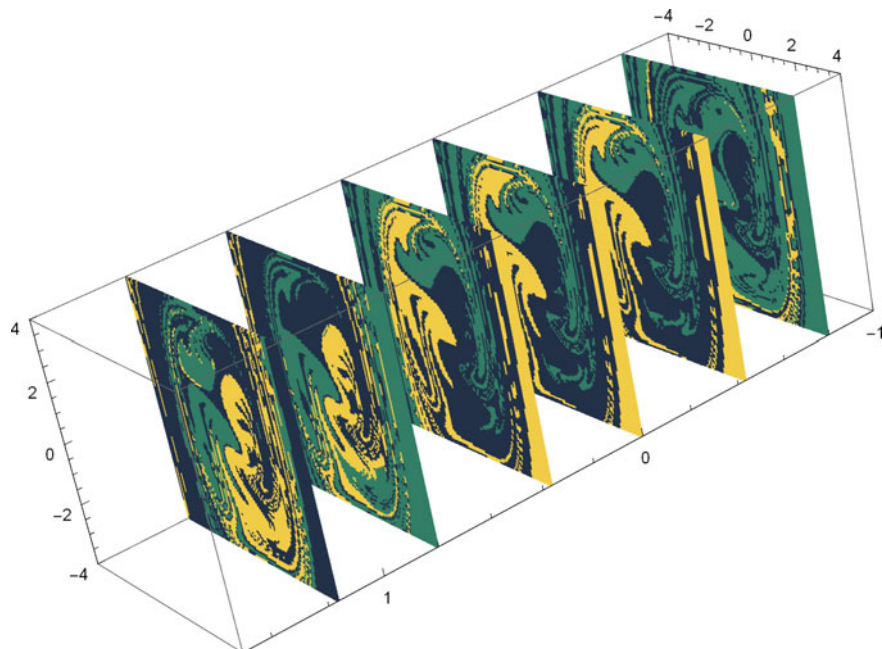


Fig. 1.8 Various $x_0 - x_1$ basin cross-sections of low resolution case

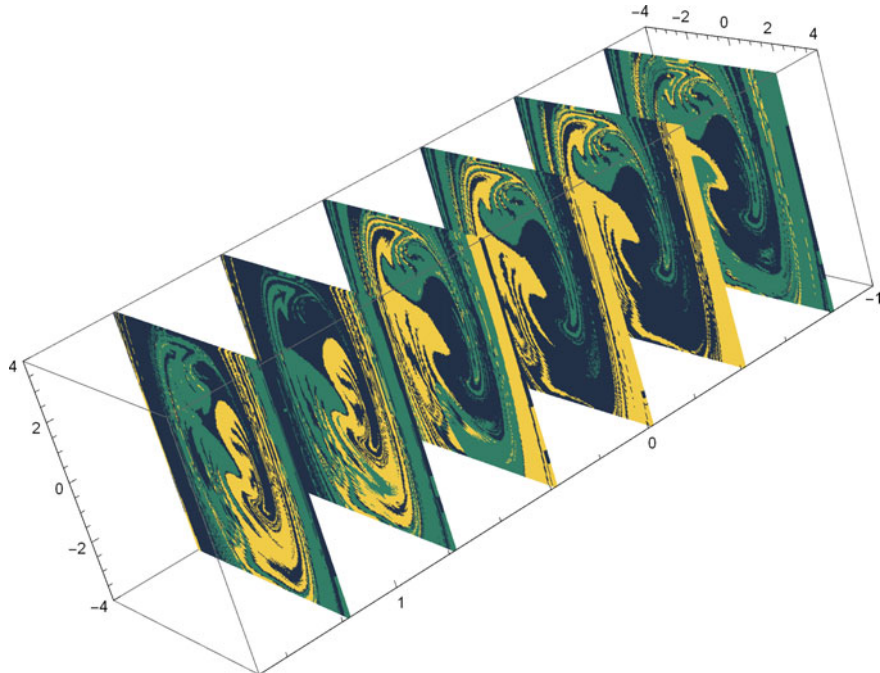


Fig. 1.9 Various $x_0 - x_1$ basin cross-sections of high resolution case

1.11 Conclusion

Vast amount of scattered literature and examples is available and newcomers often get lost. In this chapter we hope to have introduced scientists and engineers to topics of high power-computing in step-by-step fashion to all concepts, implementations and methods required to understand how to efficiently solve large computing problems.

Performance of individual components is explained in enough detail that is required to understand overall system performance. With concepts of hardware organization (architectures) and different implementations readers were introduced to world of massively parallel computing. From mentioned concepts of high-power computing, high performance computing with clusters and GPU is most relevant for science and engineering.

In design process, programmers now understand why should strive to make parallel software scalable, as local as possible and modular. It is possible to achieve this task by methodical development of algorithm through partitioning the problem, optimizing communication structures and agglomeration of communication intensive parts.

Performance issues and parallelization speed-up are discussed to prevent unrealistic expectations from parallel computing. Readers were also introduced to functionality of main software solutions in HPC, OpenMP for shared memory computers,

MPI standard for distributed systems and OpenCL and CUDA for environments with computational GPUs.

Topic is closed by presenting common methods and applications of global analysis. After studying this paper, it is hoped that reader is able to identify type of computing problem, to choose proper hardware/software platform, methodically plan design process and evaluate parallel algorithm by referring to specific literature for deepening on specific topics.

Acknowledgements NA and SL would like to thank Radu Serban and Dan Negruț, University of Wisconsin-Madison, USA, for help with HPC and for the kind hospitality during the visit of NA.

References

1. Hsu, C.S.: Cell-to-Cell Mapping: A Method of Global Analysis for Nonlinear Systems. Springer, New York (1987)
2. Sun, J.-Q., Luo, A.C.J. (eds.): Global Analysis of Nonlinear Dynamics. Springer, New York (2012)
3. Category: History of computing hardware—Wikipedia, the Free Encyclopedia. Accessed 15 Nov 2017
4. Disrupting the datacenter: Qualcomm Centriq™ 2400 processor. Accessed 15 Jan 2018
5. Null, L., Lobur, Julia: The Essentials of Computer Organization and Architecture. Jones and Bartlett Publishers, Sudbury, Mass (2003)
6. Hilborn, R.C.: Chaos and nonlinear dynamics: an introduction for scientists and engineers, 2nd edn. Oxford University Press, Oxford (2000)
7. Strogatz, S.H.: Nonlinear Dynamics and Chaos: With Applications in Physics, Biology, Chemistry, and Engineering. Mass, Wokingham, Addison-Wesley Pub, Reading (1994)
8. Jain, M.K., Iyengar, S.R.K., Jain, R.K.: Numerical Methods for Scientific and Engineering Computation. Wiley Eastern Ltd., New Delhi etc. (1986)
9. Aguirre, J., Viana, R.L., Sanjuán, M.A.F.: Fractal structures in nonlinear dynamics. Rev. Mod. Phys. **81**, 333–386 (2009)
10. Engelina Nusse, H., Hunt, B.R., John Kostelich, E., Yorke, J.A.: Dynamics: numerical explorations. In: Applied Mathematical Sciences, 2nd edn. Springer, New York (1998)
11. Comer, D.: Essentials of Computer Architecture, 2nd edn. Chapman and Hall CRC (2017)
12. Elahi, A.: Computer Systems: Digital Design. Fundamentals of Computer Architecture and Assembly Language. Springer, Cham (2018)
13. Czarnul, Paweł: Parallel Programming for Modern High Performance Computing Systems. CRC Press, Taylor and Francis Group (2018)
14. Aubanel, E.: Elements of Parallel Computing. Chapman and Hall CRC (2016)
15. Hwang, K.: Advanced Computer Architecture: Parallelism, Scalability, Programmability. McGraw-Hill Series in Computer Engineering. McGraw-Hill, New York (1993)
16. Clements, A.: Principles of Computer Hardware, 4th edn. Oxford University Press, Oxford, New York (2006)
17. Padua, D. (ed.): Encyclopedia of Parallel Computing. Springer US (2011)
18. Rauber, T., Rnger, G.: Parallel Programming for Multicore and Cluster Systems, 2nd edn. Springer, Berlin, Heidelberg (2013)
19. Jiao, Y., Lin, H., Balaji, P., Feng, W.: Power and performance characterization of computational kernels on the gpu. In: Green Computing and Communications (GreenCom), 2010 IEEE/ACM International Conference on Cyber, Physical and Social Computing (CPSCom), pp. 221–228, Dec 2010
20. Hennessy, J.L., Patterson, D.A., Asanović, K.: Computer architecture: a quantitative approach, 5th edn. Morgan Kaufmann/Elsevier, Amsterdam, Boston (2012)

21. The Top500 List—November 2017. Accessed 11 Feb 2018
22. The Green500 List—November 2017. Accessed 11 Feb 2018
23. CUDA zone. Accessed 15 Jan 2018
24. Sourouri, M., Langguth, J., Spiga, F., Baden, S.B., Cai, X.: Cpu+gpu programming of stencil computations for resource-efficient use of gpu clusters. In: 2015 IEEE 18th International Conference on Computational Science and Engineering, pp. 17–26, Oct 2015
25. Chakrabarti, S., Demmel, J., Yelick, K.: Modeling the benefits of mixed data and task parallelism. In: Proceedings of the Seventh Annual ACM Symposium on Parallel Algorithms and Architectures, SPAA '95, pp. 74–83. ACM, New York, NY, USA (1995)
26. Raicu, I., Foster, I.T., Zhao, Y.: Many-task computing for grids and supercomputers. In: 2008 Workshop on Many-Task Computing on Grids and Supercomputers, pp. 1–11, Nov 2008
27. Foster, Ian: Designing and Building Parallel Programs: Concepts and Tools for Parallel Software Engineering. Addison-Wesley Longman Publishing Co., Inc, Boston, MA, USA (1995)
28. Grama, A.: Introduction to Parallel Computing, 2nd edn. Addison-Wesley, Harlow, England, New York (2003)
29. Solihin, Y.: Fundamentals of Parallel Multicore Architecture, 1st edn. Chapman-Hall, CRC (2015)
30. Shi, Y.: Reevaluating Amdahl's law and Gustafson's law (1996)
31. Sun, X.-H., Ni, L.M.: Institute for computer applications in science, and engineering. In: Scalable Problems and Memory-Bounded Speedup. ICASE Report. Institute for Computer Applications in Science and Engineering, NASA Langley Research Center, Hampton, Va. (1992)
32. Pllana, S., Xhafa, F. (eds.) Programming Multi-core and Many-core Computing Systems, 1st edn. Wiley Publishing (2014)
33. Stallings, W., Paul, G.: Operating Systems: Internals and Design Principles, 7th international edn. Pearson, Boston, Mass, London (2012)
34. The OpenMP API specification for parallel programming. Accessed 15 Jan 2018
35. Message Passing Interface (MPI) Forum. Accessed 15 Jan 2018
36. The OpenCL™ specification. Accessed 15 Jan 2018
37. Cineca SCAI application software for science. Accessed 01 June 2018
38. Medio, A., Lines, M.: Nonlinear Dynamics: A Primer. Cambridge University Press (2001)
39. Tongue, B.-H., Gu, K.: Interpolated cell mapping of dynamical systems. *J. Appl. Mech.* **55**(2), 461–466 (1988)
40. Ge, Z.-M., Lee, S.-C.: A modified interpolated cell mapping method. *J. Sound Vib.* **199**(2), 189–206 (1997)
41. Spek, J.A.W., van der, D.H. Campen, V., Kraker de, A.: Cell mapping for multi degrees of freedom systems. In: Bajaj, A.K. (ed.) Nonlinear and Stochastic Dynamics: Presented at 1994 International Mechanical Engineering Congress and Exhibition, Nov 6–11, 1994, pp. 151–159. Chicago, Illinois, AMD, ASME (1994)
42. Eason, R.P., Dick, A.J.: A parallelized multi-degrees-of-freedom cell mapping method. *Nonlinear Dyn.* **77**(3), 467–479 (2014)
43. Belardinelli, P., Lenci, S.: A first parallel programming approach in basins of attraction computation. *Int. J. Non-Linear Mech. Dyn. Stab. Control Flexible Struct.* **80**, 76–81 (2016)
44. Belardinelli, P., Lenci, S.: An efficient parallel implementation of cell mapping methods for mdof systems. *Nonlinear Dyn.* **86**(4), 2279–2290 (2016)
45. Belardinelli, P., Lenci, S.: Improving the global analysis of mechanical systems via parallel computation of basins of attraction. In: Procedia IUTAM, IUTAM Symposium on Nonlinear and Delayed Dynamics of Mechatronic Systems, vol. 22, pp. 192–199 (2017)
46. Fernández, J., Schtze, O., Hernández, C., Sun, J.-Q., Xiong, Fu-Rui: Parallel simple cell mapping for multi-objective optimization. *Eng. Opt.* **48**(11), 1845–1868 (2016)
47. Xiong, F., Qin, Z.-C., Ding, Q., Castellanos, C.H., Fernandez, J., Schetze, O., Sun, J.Q.: Parallel cell mapping method for global analysis of high-dimensional nonlinear dynamical systems, vol. 82 (2015)
48. Battelino, P.M., Grebogi, C., Ott, E., Yorke, J.A., Yorke, E.D.: Multiple coexisting attractors, basin boundaries and basic sets. *Phys. D* **32**(2), 296–305 (1988)

Chapter 2

Review of Synchronization in Mechanical Systems



Mihir Sen and Carlos S. López Cajún

Abstract Synchronization of coupled sub-systems in both natural and engineered systems is a commonplace occurrence, but its existence and analysis in mechanical systems has received much less attention. This is a review, written for mechanical engineers, of some of the work done on complex machines that are in common use. Theoretical characteristics of the phenomena that are present are indicated by solutions to models based on self-excited oscillations. A variety of experiments on synchronization that have been carried out are reported, including work done by the authors on vibrations of rotor blades due to airflow and of automobile parts. A large number of references on the subject has been included so that a researcher who is new to synchronization in complex machinery can use this as a starting point.

2.1 Introduction

2.1.1 Complex Systems

Although complexity and complex systems, and the subject of synchronization in complex systems, are very broad subjects [1], here we will restrict ourselves only to *mechanical systems*, especially their subset that transmit energy that we will call *machines*. There are few comprehensive reviews of the subject, though there are specific exceptions [2, 3], and this is directed to mechanical engineers. To begin with, it is important to define the terms that will be used, to provide a framework for the discussion and, for reasons of space, to limit the scope of this review. A *system*,

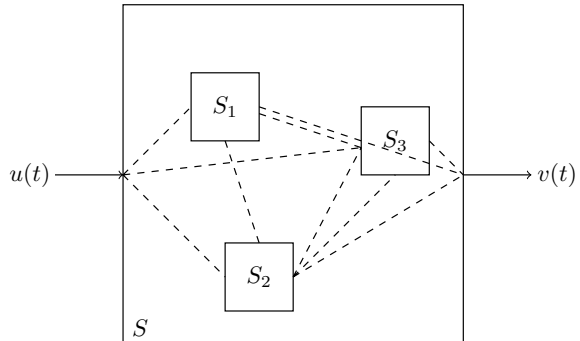
M. Sen

Department of Aerospace and Mechanical Engineering, University of Notre Dame,
Notre Dame, IN 46556, USA
e-mail: Mihir.Sen.1@nd.edu

C. S. López Cajún (✉)

División de Investigación y Posgrado, Facultad de Ingeniería, Departamento de Ingeniería
Mecánica, Universidad Autónoma de Querétaro, 76010 Querétaro, QRO, Mexico
e-mail: hectorcslc1948@gmail.com

Fig. 2.1 Schematic of a complex system S with subsystems S_1 , S_2 and S_3 . $u(t)$ and $v(t)$ are the input and output of S respectively, where t is time. Dashed lines indicate connections involving sub-systems



for our purposes, is a machine that has an input $u(t)$ and an output $v(t)$, where t is time. A *complex* system consists of a number—perhaps a large number—of *sub-systems* that are interconnected in some way. The sub-systems considered here are *mechanical* in the sense that they are components consisting of masses, springs and dampers and the like, though no assumption of linearity is *a priori* made. The masses are in vibratory motion and their *state* is represented by displacements, so the signals $u(t)$ and $v(t)$ may be displacements, their derivatives, or forces.

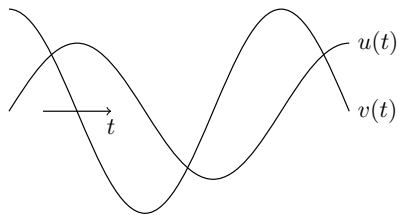
As an example, examine Fig. 2.1; there are three sub-systems, S_1 , S_2 and S_3 , within the system S and each sub-system is in general connected to the others and also to $u(t)$ and $v(t)$. A *connection* between two sub-systems means that the *state* of each one is coupled to that of the other. The connectivity between sub-systems may be represented by a complex network (also called a graph) [4–7] with masses at the junctions (nodes or vertices) and springs and dampers in the branches (edges, arcs, lines).

Practical examples of complex machinery may be washer/dryers, turbines or automobiles. In each case, the complete system consists of a number of sub-systems, each of which is composed of fundamental components such as masses, springs or dampers. Each sub-system is coupled to another or to others through mechanical coupling elements. In special circumstances it is possible to have isolated sub-systems within a machine that are completely disconnected from the rest and which can be safely excluded from the network, at least from the point of view of mechanical response. There are many other characteristics of complex machines that are of interest, such as the interaction between foreground and background components [8, 9], multiple scales [10] and others [11], which will not be explored here.

2.1.2 What is Synchronization?

Synchronization has been variously described as the movement of sub-systems “to develop a uniform rhythm of coexistence in spite of differences in individual rhythms

Fig. 2.2 Two out-of-phase sinusoids



and often extremely weak mutual connections” [11], moving in “unison” [12], or “an adjustment of rhythms of oscillating objects due to their weak interaction” [13]. For instance, take the sinusoids $u(t)$ and $v(t)$ shown in Fig. 2.2. They are at the same frequency but are of different amplitudes and are out of phase. $u(t)$ and $v(t)$ could be different quantities, such as displacement, velocity or acceleration, measured at different points in a complex machine, but in any case through a transducer they end up as electronic signals that can be sampled and stored as a vector in a computer. The fact that they are at the same frequency indicates that the two signals are in synchronization. Mechanical machines are often run by an engine or motor shaft turning at a constant rate. The rest of the machine then follows this frequency but moves or vibrates according to how they are connected to other parts of the system and the laws of mechanics that govern their motion. For simple arrangements, such as a low degree of freedom vibratory system, it may be easy to come up with a mathematical model from the ground up, but this for more complex systems may be harder to do. For the latter, then, an understanding of the system has to be at least partially based on data obtained in situ.

Books on the subject that are good as starting points for this subject are [5, 13–20]. Many of the applications of synchronization are in areas outside the scope of this review, in areas like biology [21] or physics [11, 22], although much can be learned from them about the techniques of analysis that have been used. Recent interest in engineering applications was boosted by the work of Strogatz [23, 24] that has led to a new lease of life in the subject and a search for new applications in engineering.

Generally speaking there are two common situations that are of interest in the dynamics of linear mechanical systems: forced oscillations in response to a periodic input, and relaxation in which the system changes from one constant steady state to another. Synchronization, of course, can only occur in the former. In nonlinear systems, in addition, it is possible to have self-excited oscillations. Thus the necessary conditions for synchronization to exist, though not sufficient, are that there be oscillations due to either internal self-excitations or an external periodic input, and that two or more oscillatory sub-systems have at least a weak coupling between them. Among the elementary characteristics of synchronization are phase-angle difference [13], mode locking [25] and oscillation death [26].

2.2 Historical Outline

The first written reference to the phenomenon of *synchronization*, as understood here, was by Christiaan Huygens (1629–1695). The *Proceedings of the Royal Society* of 1664–5 has a letter from him on the use of pendulum clocks that included the observation that there was “an odd kind of sympathy perceived by him in these watches suspended by the side of each other.” Huygens, at that time, was involved in the study of pendulum clocks and their use at sea [27]. There are more details available on his experiments with two coupled pendulums side by side and his observations of the “sympathy” between them [28, 29]. This problem has also been analyzed intensively in recent years, and there is a good amount of modeling and experimental literature on the synchronization of multi-pendulums [11, 30–40].

Early engineering applications of synchronization have been in biomedical systems [41, 42], micromechanical systems [43], electrical circuits [44], lasers [45], computation [46], communications [47], complex networks [48], and chaotic systems [49], among others. The dynamics of two coupled nonlinear oscillators subject to an external periodic force have been examined by Woaf and collaborators [50]. Examples in thermal engineering are thermally-connected cavities [51–55], thermal-hydraulic networks [56], conduction in plates [57], and candle flames [58]. In relation to technological applications, in the 1940s “at the Institute Mekhanobr, a mechanical ore-handling research and design institute in Leningrad, it was accident[al]ly discovered that two dissimilar induction motors driving unbalanced rotors mounted at different locations on the same vibratory structure tended to operate synchronously. Later it was discovered that in some circumstances the tendency to synchronism was so strong that the power to one of the motors could be turned off without disturbing the synchronization” [59]. This has also been reported by Kuznetsov et al. [60]. Synchronization between multiple shafts is described in [61]. This is a non-linear phenomenon in which two or more unbalanced shafts are located on a common structure. Structural vibrations through the structure can lead to synchronization, and a simple two-shaft model is used to demonstrate it.

2.3 Oscillations

Synchronization, in the end, is based on oscillations in time. There are several types of oscillations possible in a machine and different ways in which they can be modeled.

- *Forced oscillations:* These are due to an external periodic input that is usually a force or a displacement. The system itself may or may not be linear. If linear, the oscillation frequency will be the same as that of the external forcing. For example, the simplest linear oscillator model with forcing is

$$\ddot{v} + \dot{v} + v = u(t),$$

where $v(t)$ is a displacement and the forcing input is $u(t) = A \sin \omega t$. The solution is the output

$$v(t) = a \sin(\omega t + \phi).$$

The amplitude and frequency of the output are a and ω , respectively. Since the system considered is linear, the frequency of input and output are the same. The phase angle ϕ is the angular relation between the sinusoidal input and the sinusoidal output. In fact the input force $u(t)$ and the output displacement $v(t)$ could perhaps be the two curves shown in Fig. 2.2.

- *Self-excited oscillations:* Here external forcing may not be necessary because the nonlinearity of the system makes a steady state unstable and the system responds to this instability by oscillating. There must also be a source of energy. Figure 2.3 shows the solution to one such equation that does this, the van der Pol equation

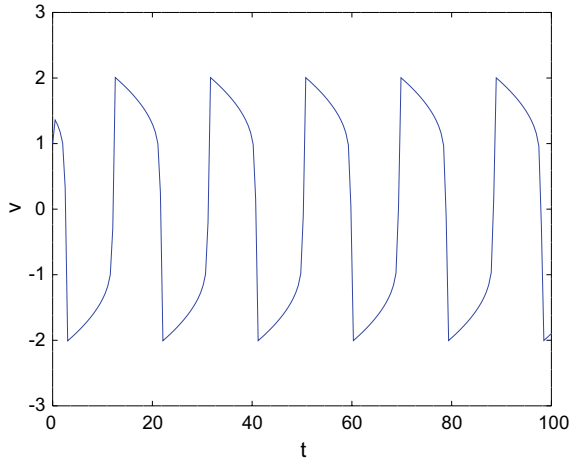
$$\ddot{v} - \mu(1 - v^2)\dot{v} + v = 0. \quad (2.1)$$

If the initial condition is anything other than the critical point of the equation, here $v = \dot{v} = 0$, the solution will oscillate; the oscillations will grow and eventually stabilize to a constant amplitude. Notice that the oscillations in the figure are periodic, have a fixed frequency, but are not sinusoidal. The van der Pol equation is thus often used to represent self-excited oscillations.

- *Mixed:* Of course it is possible, and indeed common, to have systems that have a combination of both. For example, we may have

$$\ddot{v} - \mu(1 - v^2)\dot{v} + v = A \sin \omega t.$$

Fig. 2.3 Solution of Eq. (2.1) for $\mu = 1$



- *Kuramoto model:* This is described in [62–64], and represents the response of a set of oscillators. In one form it can be represented by

$$\dot{\theta}_i = \omega_i + \frac{K}{N} \sum_{j=1}^N \sin(\theta_j - \theta_i), \quad i = 1 \dots N,$$

where N is the number of oscillators, each oscillation has a phase angle θ_i and K is the coupling between them. $\theta_i(t)$ can be plotted as a point moving around the circumference of a circle. Depending on the value of the parameters, the N oscillators can be found to be without phase locking, or partially/fully phase-locked (see also [65]).

2.4 Models of Synchronization in Machines

There are two extreme approaches the modeling of complex systems: from the ground up (*reductionism* or from basic principles) or from the top down (*holism* or data-driven) [66]. Examples of the latter are methods based on artificial neural networks, fuzzy logic or genetic/evolutionary algorithms [67]. For simplicity, in this section we will only consider the former based on self-exitations of the van der Pol oscillator.

2.4.1 Ring of Coupled Van der Pol Oscillators

The dynamics of a ring of oscillators is described in [68]. Consider four masses connected by van der Pol coupling [69, 70]. Thus

$$\underbrace{\ddot{v}_i}_I + \underbrace{A(v_i^2 - 1)\dot{v}_i}_{II} + \underbrace{v_i}_{III} = \underbrace{B(v_{i-1} - 2v_i + v_{i+1})}_{IV},$$

where $v_i(t)$ is the nondimensional displacement of masses $i = 1, \dots, 4$. The terms I , II , and III represent the acceleration, damping force, and spring force, respectively, and IV represents the linear interaction between adjacent masses. First a stability condition is derived in [70] based on linearization around a limit cycle giving a Hill's equation. Then from numerical solutions it is seen that a diversity of phase-shift attractors is present for the coupling constant below a critical value, and for values above this an in-phase attractor is predominant. It is seen that there is synchronization of the oscillations even with non-identical oscillators over a range of parameter values (see also [71]); this has great practical effect on machines in common use since in reality even components that are supposed to be truly identical are not actually so.

2.4.2 Initial Conditions

The effect of initial conditions is reported in [72, 73]. Vinod et al. [74] investigate numerically the dynamics of coupled oscillators in a ring. The coupling between neighboring oscillators is assumed to be through a linear dissipative component. The effect on synchronization of initial conditions is analyzed. The study is for identical oscillators as well for those that are different. The dynamics of the system are analyzed from the perspective of time and frequency plots. The instantaneous dynamics of each oscillator is revealed by a Hilbert transform and the phase equation obtained by asymptotic expansion. Phenomena such as amplitude death, oscillation suppression, oscillation resurrection, frequency locking and beat frequency are observed.

2.4.3 Nonlocal Interactions

These are interactions between parts of the system that are not adjacent to each other. A vibrating system has been studied in [75], impulsively coupled oscillators in [76], rotors in [77] and rotor-pendulum systems in [78]. In [79] the coupling is assumed to be non-local with a scaling exponent that decays with distance between the oscillators. In addition symmetry in an even number ring is broken by the presence of an odd oscillator. The effect of change in initial conditions is also examined. Numerical solutions show interesting dynamics including the shift from anti-phase to in-phase clustering, and resurrection of the oscillators from amplitude death.

2.4.4 Metronomes

A group of metronomes offers a mechanical example of self-excited oscillations that can enter into synchrony [80–83]. Usually the individual metronomes communicate among themselves through a beam or plate on which they are sitting. There are many remarkable movies and videos that have been made of this phenomenon which are easily available on the internet. The individual metronomes are set in motion at different initial phases but ultimately, after a while, enter into a synchrony in which they all oscillate in phase.

The setup in the metronome experiments reported in [80] consisted of two metronomes resting on a light wooden board between two cans. The oscillations were observed to eventually synchronize for small initial frequency differences as long as the metronome worked as such, and after that the oscillations were locked into an almost zero phase difference. Antiphase synchronization, it was found, was unstable and hence was not observed under normal circumstances but only if alterations were made to the setup. Martens et al. [83] looked into the phenomena of chimera states in which the oscillators are synchronous but are separated into two

groups: some are in-phase and the rest are out-of-phase. They devised experiments with different couplings to confirm that these states do exist.

2.4.5 Beams

Continuous media are also susceptible to synchronization. For example, frequency lock-in during vortex-induced vibration of a rotating blade is reported in [84]. Also, as mentioned before, unbalancing in rotatings shafts can lead to vibrations, and vibrations in shafts that are weakly coupled can synchronize [61]. Synchronization has been observed in turbines that are connected to a common structure [61]. The behavior of four self-excited elastic beams with linear coupling between them at the roots of the beams has been modeled in [85], and numerical simulations using finite differences show that the synchronization among them is enhanced as the coupling is increased. Temporal and spatial correlations are used as measure of the degree of synchronization. Additional work on this is reported in [86–91].

2.5 Analysis of Experimental Data

The mathematical models described in Sect. 2.4 do not demonstrate that synchronization *actually* happens in real systems, but only that it is possible. To address this what is needed is that careful laboratory experiments be carried out, instrumented and documented to demonstrate synchronization. Although experiments with multi-pendulums [34, 40] and metronomes [80, 81] certainly demonstrate synchronization, the physical situations seem artificially contrived and the devices are not actual machines that are commonly used in the field.

Working with mathematical models is straightforward in one sense since one only has to analyze the characteristics of the solutions, but it is harder to understand and interpret data obtained from experiments. The information of use may not be directly available but has to be extracted from the measurements in some manner. Experiments with commercial equipment are, however, easier said than done, since reality, of course, is not as clear as analysis would like, and experimental data with this kind of hardware are rarely as sharp as the signals shown in Fig. 2.2. Though several methods of measurement of vibrations are available, such as optical or electromagnetic, the easiest are with accelerometers which are transducers that are sensitive to accelerations. The acceleration may be static such as due to gravity, or dynamic like those in the vibrations of machines. Microelectromechanical system (MEMS) technology has made it possible to have extremely small, low power and accurate devices. Time signals of accelerations can, of course, be converted to velocity or displacement by integration in time. This is not necessary, however, for the present study since, if there is synchronization, all three quantities will be synchronized.

In fact synchronization, when it exists, is embedded within a quantitative cloud that makes the phenomenon difficult to discern. Reasons for this include the presence of “random” vibrations, rolling and rubbing friction, multiple sources of out-of-balance forces, finite tolerances and backlash, measurement errors, low signal to noise ratio, internal resonances, nonlinearities that create new frequencies, and so on. For this reason one has to develop the tools that will be necessary to tease out the phenomenon, and these will be briefly described in this Section. The following are some of the common techniques that are used, but of course there are many others. Further details of the items below are in popular textbooks [92–94] and also outlined in [17].

2.5.1 Spectral Analysis

One of the most common tools for signal analysis of a time signal $u(t)$ is the *Fourier transform*. This is defined by

$$\hat{u}(f) = \int_{-\infty}^{\infty} u(t)e^{-2\pi i t f} dt,$$

where $\hat{u}(f)$ is the transform of $u(t)$. If t is time then f is frequency and, in a simplistic sense, this gives the constituent frequency components in the signal, called the *spectrum*.

2.5.2 Correlations

There are several definitions of correlation available but in general it is a numerical measure of the statistical relationship between two variables. For example, the Pearson correlation coefficient between vectors u and v is

$$\rho = \frac{E[(u - \mu_u)(v - \mu_v)]}{\sigma_u \sigma_v},$$

where $E(\cdot)$ is the expected value, μ is the mean, and σ is the standard deviation. The numerator is the covariance. Two-dimensional maps with this correlation will be used later in Sect. 2.6.1.

2.5.3 Time-Frequency Maps

The time-frequency signal processing tools, such as the continuous wavelet transform, have been used for the analysis of time signals. This is defined by

$$W(a, \tau) = \frac{1}{|a|^{1/2}} \int_{-\infty}^{\infty} y(t) \psi^* \left(\frac{t - \tau}{a} \right) dt$$

where a is the scale factor that determines the time and frequency resolution of the scaled mother wavelet ψ , τ is its shift along the time axis, and $*$ is the complex conjugate. For ψ , the Morlet wavelet function

$$\psi(\eta) = \pi^{1/4} e^{-\eta^2/2} e^{i2\pi f_0 \eta}$$

where f_0 and η are the dimensionless central frequency and the time parameter respectively, is commonly used in the analysis of vibrations. Time-frequency maps can be easily generated from experimental data using MATLAB®.

2.5.4 Kuramoto Order Parameter

To get this the *Hilbert transform*, $\tilde{u}(t)$, of the signal $u(t)$ is first obtained by taking

$$\tilde{u}(t) = \frac{1}{\pi} \int_{-\infty}^{\infty} \frac{u(\tau)}{t - \tau} d\tau,$$

where the integral is a Cauchy principal value. Then a complex *analytic signal*

$$y(t) = u(t) + i\tilde{u}(t)$$

is created. The instantaneous phase angle is

$$\phi(t) = \arctan \frac{\tilde{u}(t)}{u(t)}.$$

For N such signals with phase angles ϕ_j ($j = 1, \dots, N$) the Kuramoto order parameter is

$$r(t) = \frac{1}{N} \left| \sum_{j=1}^N e^{i\phi_j(t)} \right|.$$

The order parameter r is a measure of the degree of synchronization that exists between the N signals, while $s(t) = 1 - r(t)$ is an order-deficit parameter. The value of $r = 1$, corresponding to $s = 0$, indicates perfect synchronization.

2.6 Other Experiments

Some details of two different synchronization experiments are described below. In the first rotor blade-tip synchronization is presented, and in the next synchronization between the dashboard and the door of an automobile is demonstrated.

2.6.1 Synchronization in a Stationary Rotor Blade

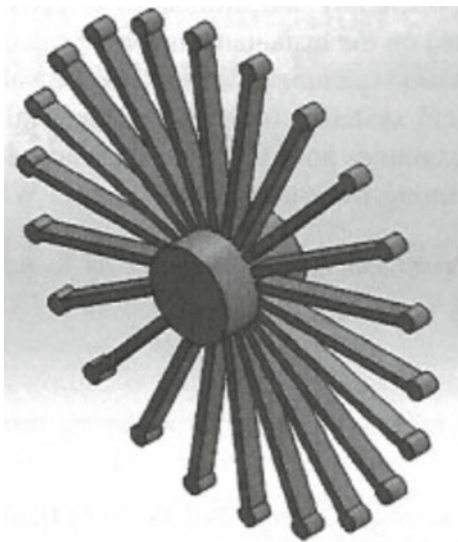
The first experiment, reported in detail in [95], is on the identification of synchronization in the blade-tip vibrations of a stationary rotor with airflow. For this purpose, individual blade-tip vibrations were measured simultaneously under two different conditions. First, the rotor was excited by an impact force and the natural frequencies of the blade-tips were identified. Thereafter the blades were excited by air flow over the rotor and individual blade-tip vibrations were recorded.

The experimental setup is shown in Fig. 2.4. The rotor itself consisted of 24 blades, each of a rectangular cross section as shown in Fig. 2.5. Measurements were made with double-axis MEMS accelerometers attached to the tip of each blade. The 24 accelerometers were calibrated using a vibrometer. They were connected to a data acquisition system, and the acceleration data were recorded simultaneously.



Fig. 2.4 Rotor: setup and laser vibrometer used for calibration

Fig. 2.5 Rotor: 24-blade rotor



2.6.1.1 Impact Test

As examples, the impact time responses of blades 1 and 2 are shown in Fig. 2.6, and blades 8 and 9 in Fig. 2.7 respectively. Although it is clear that some blade-tips vibrate in phase, a statistical procedure of analysis was used to show the relation among all blade-tips. The analysis of the signals was based on the Pearson correlation coefficient (see Sect. 2.5.2) which indicates the linear dependence between two variables. To show the coupling response between any two blade-tips a 24×24 correlation matrix was constructed. This is shown in Fig. 2.8 as a correlation map. In this map the Pearson correlation coefficient is arranged in two dimensions. The x - and y -axes represent two different blade numbers, and the color at that coordinate point represents the

Fig. 2.6 Rotor: time response of blades 1 (blue, larger amplitude oscillation) and 2 (red)

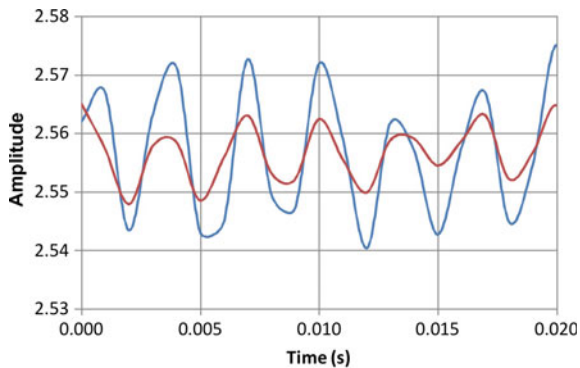


Fig. 2.7 Rotor: time response of blades 8 (blue, larger amplitude oscillation) and 9 (red)

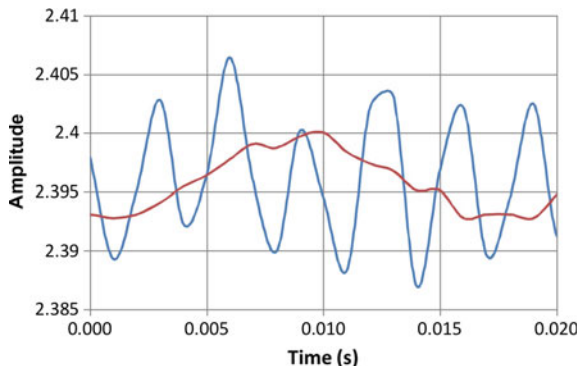
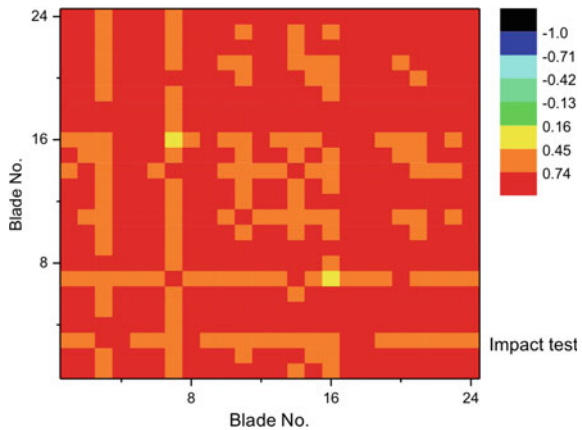


Fig. 2.8 Rotor: correlation map for impact test



Pearson correlation ρ of the response of these two blades. The map thus represents the structural behavior of all blades. The smallest correlation value was 0.43, and the largest phase difference was found to be around 64.5° .

2.6.1.2 Vibrations Due to Airflow

The main experiments were conducted with an air flow from the blower at a constant speed. The blower rotational speed was 800 rpm and it had 4 blades, so that the blade-passing frequency at the blower was around 53 Hz. The air flow was kept on for several hours to get enough information of the dynamic behavior of the blades for this length of time. The sampling frequency was 2 MHz. Because of an insufficient data-storage capacity, all this data was not recorded, but rather the data from each blade was stored in groups of vectors of length 2000 (i.e., 1 s in time) starting at 0, 8, 16, . . . min from the start, i.e. at $8i$ min with $i = 0, 1, 2, \dots$.

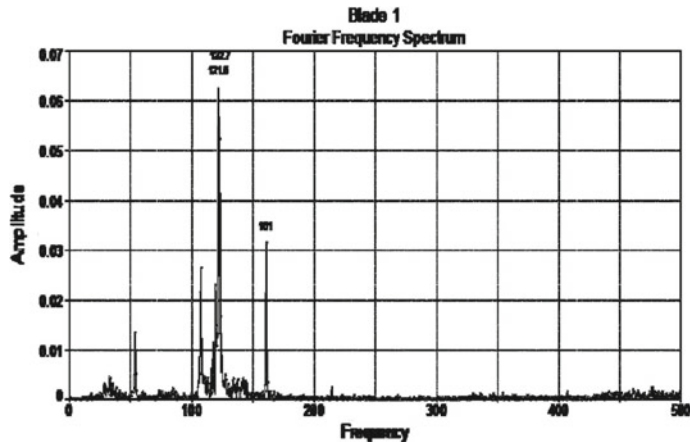


Fig. 2.9 Rotor: frequency spectrum for $i = 0$

The frequency spectrum (see Sect. 2.5.1) for the first interval ($i = 0$) representing measurements taken just after the air starts to flow is shown in Fig. 2.9. From that figure, the blade passing frequency of 53.5 Hz, with two harmonics at 107 and 161 Hz, can be clearly observed. The corresponding correlation map for this interval is shown in Fig. 2.10. The structural pattern remains as in the impact test, but correlation values vary from -0.7 to 0.7 ; there is no synchronization between blade-tips, and the phase angles vary from -45° to 45° . It can also be seen that there are cluster areas around the structural patterns. Figure 2.11 shows the correlation map for $i = 3$. From that figure, it is clear that the blade-tips have synchronized their vibration since most of the correlation values are positive. In this map, clusters around the same structural areas are observed.

Fig. 2.10 Rotor: correlation map for $i = 0$

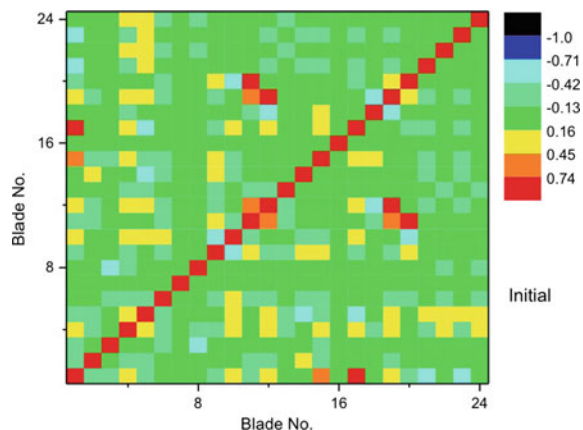


Fig. 2.11 Rotor: correlation map for $i = 3$

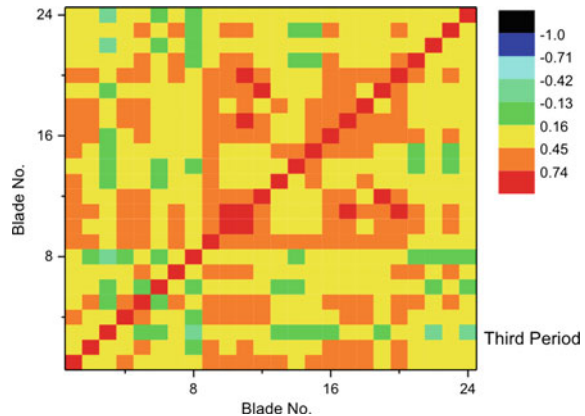
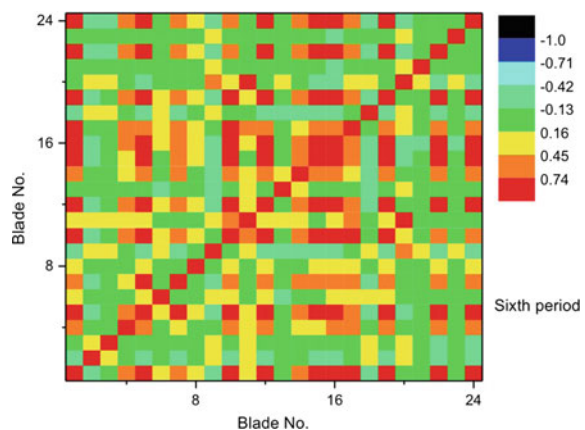


Fig. 2.12 Rotor: correlation map for $i = 6$



For $i = 6$, Fig. 2.12 shows that the correlation map changes its pattern. Indeed, some blade-tips move out of phase and there is less synchronization in the system. Figures 2.13 and 2.14 show measurements taken after a long period of time, and it was noticed that the coefficient maps present oscillations of very long periods. These oscillations are of a very low frequency, which is difficult to measure directly with accelerometers but can be detected from these correlation maps; they may be due to background coupling between components [8]. It is also possible to identify that the structural pattern remains present in every map. Adjacent blades are synchronized, and the pattern along the diagonal is similar in every map.

Fig. 2.13 Rotor: correlation map for $i = 9$

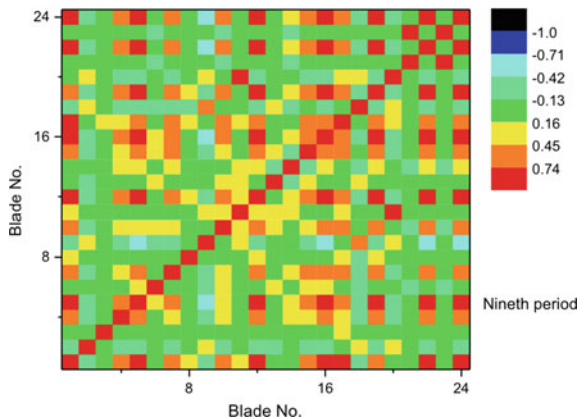
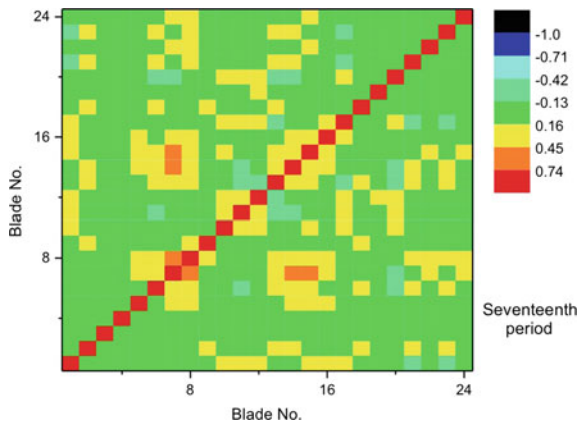


Fig. 2.14 Rotor: correlation map for $i = 17$



2.6.2 Synchronization in an Automobile

For this experiment accelerometers were fixed to two components of a midsized car: one a door and the other the dashboard. The localizations are as shown in Fig. 2.15. The x and y directions are shown for each location.

2.6.2.1 Impact Test

First, separate impact tests on the dashboard and the door were carried out, and their corresponding responses were recorded. The frequency spectra of the impact responses are shown in Figs. 2.16 and 2.17. The corresponding time-frequency maps (see Sect. 2.5.3) are shown in Figs. 2.18 and 2.19.

A plot of amplitude vs. time is shown in Fig. 2.20. This was obtained by sectioning transversally the time-frequency maps of the impact response at the frequencies of

Fig. 2.15 Automobile:
layout of accelerometers, A1
dashboard, A2 door

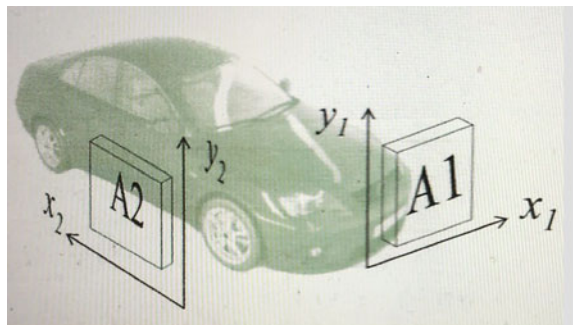


Fig. 2.16 Automobile
experiment: dashboard
response due to impact on
dashboard

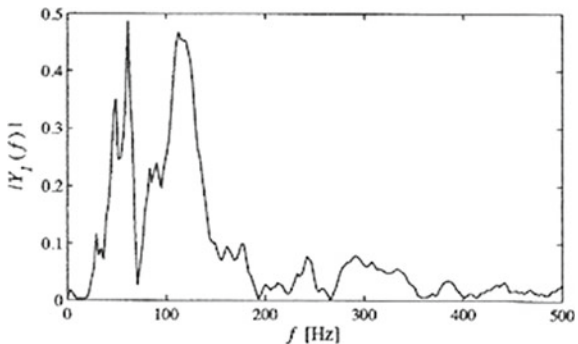
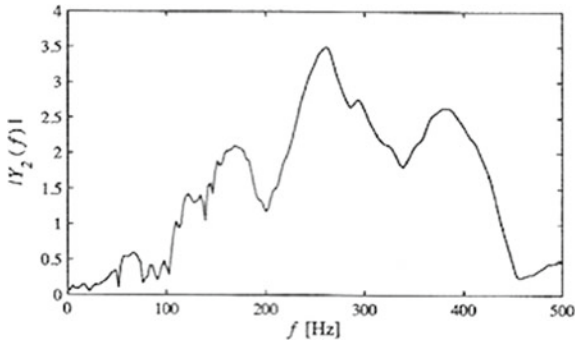


Fig. 2.17 Automobile
experiment: door response
due to impact on door



interest. The natural frequency, $f_2 = 117$ Hz, from the dashboard impact test can be noted in the figure. Several frequency responses were also obtained when the door was struck. From those figures, the frequency response can be approximated as a decaying exponential function, from which the damping coefficient per unit mass c can be estimated. Similarly, the stiffness coefficient per unit mass, k , can also be estimated. All these values are listed in Table 2.1.

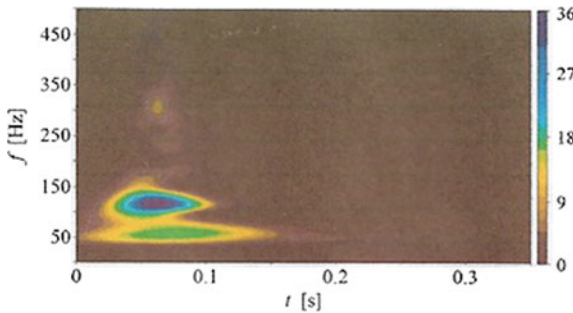


Fig. 2.18 Automobile: dashboard response with impact on dashboard

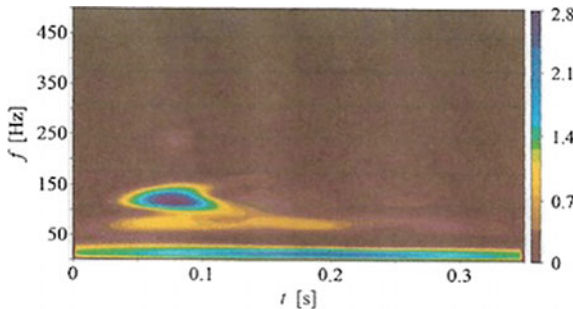


Fig. 2.19 Automobile: door response with impact on dashboard

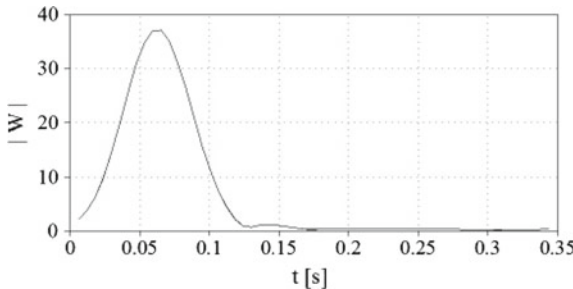


Fig. 2.20 Automobile experiment: dashboard $f_2 = 117$ Hz

Table 2.1 Automobile: dashboard and door parameters from the impact tests

Component	n	f_n (Hz)	k (s^2/kg)	c (s/kg)
Dashboard	1	63	3969	22.9
	2	117	13,619	87.4
Door	3	170	28,900	75.7
	4	256	65,536	113.8

2.6.2.2 Motion Tests

The next experiment was conducted with the automobile at different speeds, namely 60, 70 and 80 km/h. Clearly, when it is in motion, there are several sources of regular and random excitations due, for example, to pavement roughness, the engine, the power transmission subsystem, among others causes. Thus, the recorded signals were filtered, allowing to pass only the frequencies f_1 for dashboard-dashboard effect, f_2 for dashboard-door, f_3 for door-dashboard and f_4 for door-door, where the first component is the one impacted and second is where the response is measured. The four values of f_n are in Table 2.1. From the recorded unfiltered signals, a frequency $f_v = 1.5$ Hz arises due to the first vibration mode of the automobile, and a second one f_w corresponding to the wheel angular velocity. Based on the radius of the wheel and the speed of the automobile, these were $f_w = 8.8, 10.3$, and 11.8 Hz at 60, 70 and 80 km/h, respectively.

2.6.2.3 Cross Correlation

The first stage for identification of the synchronization was the computation of the correlation coefficient between the dashboard and door unfiltered signals. However, the computed values were relatively small though positive, that is the correlation coefficient was unable to separate the high content of signal frequencies. Thus, it was necessary to resort to correlation functions, one of which is shown in Fig. 2.21. From similar plots for the other speeds, the maximum cross correlation between dashboard and door was found to have a delay of 5×10^{-3} s. This delay is possibly associated with the propagation time of an acoustic wave from one component to the other.

Fig. 2.21 Automobile experiment: road speed 60 km/h

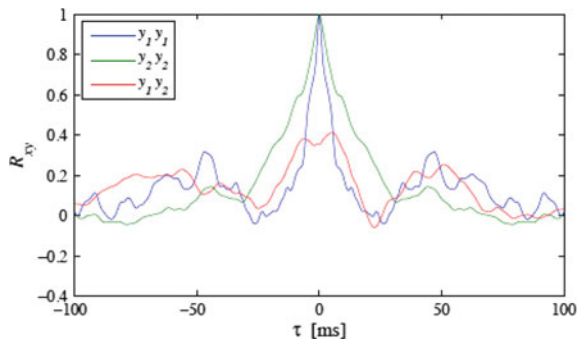


Fig. 2.22 Automobile: time-frequency map of dashboard, road speed 60 km/h

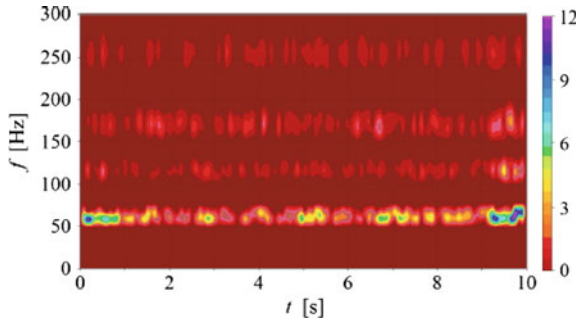
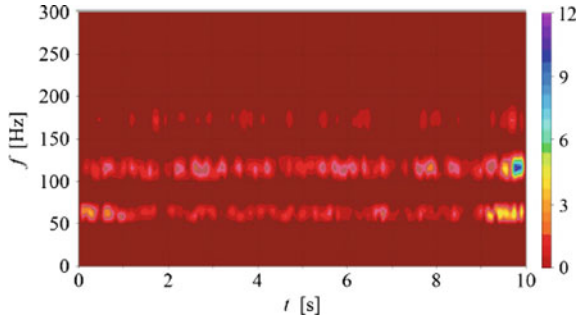


Fig. 2.23 Automobile: time-frequency map of door, road speed 60 km/h



2.6.2.4 Time-Frequency Maps

Time-frequency maps, shown in Figs. 2.22 and 2.23, were generated using the filtered signals. Similarly, maps for the other road speeds were also generated. From these maps, it is seen that the amplitude of all natural frequencies increases with the speed, and the response seems to be sensitive to high frequencies (about 250 Hz). The correlation coefficient was computed from the natural frequency behavior. The values of correlation are higher for the filtered signals.

2.6.2.5 Deficit-Order Parameter

The deficit-order parameter s was introduced in Sect. 2.5.4 to quantify synchronization in complex machines. As an example, the filtered signals for the dashboard and door when the automobile ran at 60 km/h are shown in Fig. 2.24. The deficit-order parameter, s , for those signals is shown in Fig. 2.25. From the latter, it can be seen that s is close to zero most of the time, thus indicating that the components are close to synchronization. Similar analysis was done from filtered signals at 70 and 80 km/h. Table 2.2 shows the statistical analysis of s . The standard deviation was computed from the maximum value of synchronization ($s = 0$). From the results the mean value of s is around 0.2, which means that most of the time the components are synchronized.

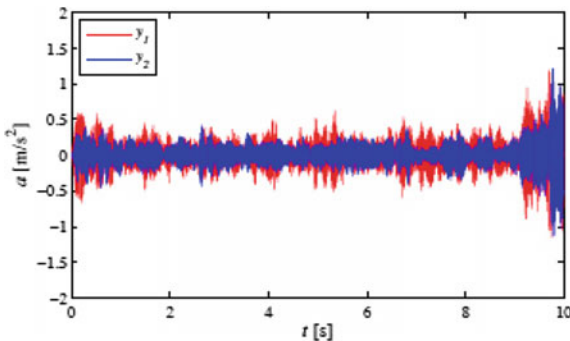


Fig. 2.24 Automobile experiment: acceleration signal, road speed 60 km/h

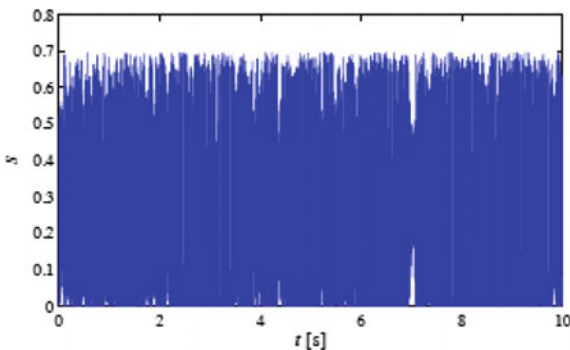


Fig. 2.25 Automobile experiment: deficit parameter, road speed 60 km/h

Table 2.2 Automobile: statistics of the deficit-order parameter

Descriptor	Speed		
	60 (km/h)	70 (km/h)	80 (km/h)
Mean	0.218	0.217	0.226
Standard deviation	0.307	0.307	0.313
Percentage of events with $s \leq 0.2$	0.560	0.563	0.537

2.7 Concluding Remarks

Complex mechanical systems are common in our daily life. In many of these there is a periodic and/or random input which results in shaking or vibrations throughout the machine even during normal operation. As a result it is possible, in many instances, that different parts of the machine that have only weak links with each other enter into synchrony, i.e. their vibrations are mechanically linked to each other. The study of synchronization brings out this relationship. What we have reviewed here is the

synchronization of sub-systems that appear in complex machines. On the one hand we have reviewed the modeling approaches that have been suggested to describe the behavior of these systems, and on the other we have attempted a brief outline of some experiments and the data analysis that have been carried out in this regard.

It is hoped and expected that other complex machinery will be similarly investigated in the future. It is possible that hybrid approaches may be developed that combine both reductionist model-driven and holistic data-driven perspectives. Non-linear interaction, such as with the effect of Coulomb friction, is another area that has to be advanced. It is possible that the study of synchronization and its change over time can lead to useful techniques, such as health monitoring of machines or the diagnoses of defects as they occur, that can be applied to current challenges in mechanical engineering.

Synchronization is but one aspect of complex systems, and mechanical engineers must move beyond that. Though mechanical systems may differ in their details compared to other systems that have been studied in the literature, there are global features that they share. Particularly important are the techniques of experimentation and data analysis that have been developed over the years. Mechanical engineers in this regard are just beginning to appreciate the complexity inherent in the systems that they work with, but there is a long way to go still.

Acknowledgements This is to gratefully acknowledge the participation of Professor Juan Carlos Jáuregui Correa of the *Universidad Autónoma de Querétaro* who has been a co-author in some of the publications on which this review is based.

References

1. Mitchell, M.: Complexity: A Guided Tour. Oxford University Press, Oxford, U.K. (2009)
2. Felippa, C.A., Park, K.C., Farhat, C.: Partitioned analysis of coupled mechanical systems. *Comput. Methods Appl. Mech. Eng.* **190**(24–25), 3247–3270 (2001)
3. Machado, J.A.T., Lopes, A.M.: Editorial: complex systems in mechanical engineering. *Adv. Mech. Eng.* **9**(7), 1–3 (2017)
4. Strogatz, S.H.: Exploring complex networks. *Nature* **410**(6825), 268–276 (2001)
5. Wu, C.W.: Synchronization in Complex Networks of Nonlinear Dynamical Systems. World Scientific, Singapore (2007)
6. Arenas, A., Díaz-Guilera, A., Kurths, J., Moreno, Y.: Synchronization in complex networks. *Phys. Rep.* **469**(3), 93–153 (2008)
7. Latora, V., Nicosia, V., Russo, G.: Complex Networks: Principles, Methods and Applications. Cambridge University Press, Cambridge, U.K. (2017)
8. Sen, M., Jáuregui-Correa, J.C., López, C.S.: Foreground and background components in separable complex systems. *Systems* **4**(3) (2016)
9. Kutz, J.N., Fu, X., Brunton, S.L.: Multiresolution dynamic mode decomposition. *SIAM J. Appl. Dyn. Syst.* **15**(2), 713–735 (2016)
10. Gao, J., Cao, Y., Tung, W., Hu, J.: Multiscale Analysis of Complex Time Series: Integration of Chaos and Random Fractal Theory, and Beyond. Wiley, Hoboken, NJ (2007)
11. Blekhman, I.I.: Synchronization in Science and Technology. ASME Press, New York (1988)
12. Rosenblum, M., Pikovsky, A.: Synchronization: from pendulum clocks to chaotic lasers and chemical oscillators. *Contemp. Phys.* **44**(5), 401–416 (2003)

13. Pikovsky, A., Rosenblum, M., Kurths, J.: *Synchronization: A Universal Concept in Nonlinear Sciences*. Cambridge University Press (2003)
14. Nijmeijer, H., Rodriguez-Angeles, A.: *Synchronization of Mechanical Systems*. World Scientific, Singapore (2003)
15. Pikovsky, A., Maistrenko, Y. (eds.): *Synchronization: Theory and Application*. Kluwer Academic Publishers, Dordrecht (2003)
16. Manrubia, S.C., Mikhailov, A.S., Zanette, D.H.: *Emergence of Dynamical Order Synchronization Phenomena in Complex Systems*. World Scientific, Singapore (2004)
17. González-Miranda, J.M.: *Synchronization and Control of Chaos: An Introduction for Scientists and Engineers*. World Scientific, Singapore (2004)
18. Osipov, G.V., Kurths, J., Zhou, C.: *Synchronization in Oscillatory Networks*. Springer, Berlin (2007)
19. Balanov, A., Janson, N., Postnov, D., Sosovtseva, O.: *Synchronization: From Simple to Complex*. Springer, Berlin (2009)
20. Boccaletti, S., Pisarchik, A.N., del Genio, C.I., Amann, A.: *Synchronization: From Coupled Systems to Complex Networks*. Cambridge University Press, Cambridge, U.K. (2018)
21. Winfree, A.T.: *The Geometry of Biological Time*. Springer, New York (1980)
22. Uchida, A.: *Optical Communication with Chaotic Lasers: Applications of Nonlinear Dynamics and Synchronization*. Wiley-UCH, Weinheim, Germany (2011)
23. Strogatz, S.H., Stewart, I.: Coupled oscillators and biological synchronization. *Sci. Am.* **269**(6), 102–109 (1993)
24. Strogatz, S.: *Sync: How Order Emerges from Chaos in the Universe, Nature, and Daily Life*. Hachette Books (2004)
25. Perlikowski, P., Stefanski, A., Kapitaniak, T.: Mode locking and generalized synchronization in mechanical oscillators. *J. Sound Vib.* **318**, 329–340 (2008)
26. Koseska, A., Volkov, E., Kurths, J.: Oscillation quenching mechanisms: amplitude versus oscillation death. *Phys. Rep. Rev. Sect. Phys. Lett.* **531**(4), 173–199 (2013)
27. Huygens, C.: *The pendulum clock or geometrical demonstrations concerning the motion of pendula as applied to clocks*. Blackwell, R.J. (trans., eds.) Edinburgh Books, Edinburgh, U.K. (1986)
28. C. Huygens. Letter to de Sluse, Letter No. 1333 of February 24, 1665, p. 241. *Oeuvres Complète de Christiaan Huygens. Correspondance* **5**, 1664–1665; Société Hollandaise des Sciences, Martinus Nijhoff, 1893, La Haye, 2002
29. Yang, J., Wang, Y., Yu, Y.Z., Xiao, J.H., Wang, X.G.: Huygens' synchronization experiment revisited: luck or skill? *Eur. J. Phys.* **39**(5), Art. No. 055004 (2018)
30. Ganiev R.F., Fazullin, F.F.: On the non-linear synchronous oscillation and stability of turbine blades. *Trudy Ufimsk aviat. in-ta* **98** (1975)
31. Ganiev, R.F., Balakshin, O.B., Kukharenko, B.G.: On the occurrence of self-synchronization of auto-oscillations of turbo compressor rotor blades (original in Russian in Problemy Mashinostroeniya i Nadezhnosti Mashin, no. 6, pp. 16–23; *J. Mach. Manuf. Reliab.*, **38**(6), 535–541 (2009))
32. Ganiev, R.F., Balakshin, O.B., Kukharenko, B.G.: Flutter synchronization for turbo-compressor rotor blades (original in Russian in Doklady Akademii Nauk, vol. 427, no. 2, pp. 179–182); *Dokl. Phys.* **54**(7), 312–315 (2009)
33. Quinn, D.D., Wang, F.: Synchronization of coupled oscillators through controlled energy transfer. *Int. J. Bifurcat. Chaos* **10**(6), 1521–1535 (2000)
34. Bennett, M., Schatz, M.F., Rockwood, H., Wiesenfeld, K.: Huygens's clocks. *Proc. Roy. Soc. A-Math. Phys. Eng. Sci.* **458**(2019), 563–579 (2002)
35. Balthazar, J.M., Felix, J.L.P., Brasil, R.M.: Some comments on the numerical simulation of self-synchronization of four non-ideal excitors. *Appl. Math. Comput.* **164**(2), 615–625 (2005)
36. Peña Ramirez, J., Fey, R.H.B., Aihara, K., Nijmeijer, H.: An improved model for the classical Huygens' experiment on synchronization of pendulum clocks. *J. Sound Vib.* **333**(26), 7248–7266 (2014)

37. Jaros, P., Borkowski, L., Witkowski, B., Czolczynski, K., Kapitaniak, T.: Multi-headed chimera states in coupled pendula. *Eur. Phys. J. Spec. Top.* **224**(8), 1605–1617 (2015)
38. Oliveira, H.M., Melo, L.V.: Huygens synchronization of two clocks. *Sci. Rep.* **5** (2015)
39. Dudkowski, D., Grabski, J., Wojewoda, J., Perlikowski, P., Maistrenko, Y., Kapitaniak, T.: Experimental multi-stable states for small network of coupled pendula. *Sci. Rep.* **6** (2016)
40. Peña Ramirez, J., Olvera, L.A., Nijmeijer, H., Alvarez, J.: The sympathy of two pendulum clocks: beyond Huygens' observations. *Sci. Rep.* **6** (2016)
41. Bertram, C.D., Sheppard, M.D.: Interactions of pulsatile upstream forcing with flow-induced oscillations of a collapsed tube: mode-locking. *Med. Eng. Phys.* **22**(1), 29–37 (2000)
42. Glass, L.: Synchronization and rhythmic processes in physiology. *Nature* **410**(6825), 277–284 (2001)
43. Hoppensteadt, F.C., Izhikevich, E.M.: Synchronization of MEMS resonators and mechanical neurocomputing. *IEEE Trans. Circ. Syst. I-Regul. Pap.* **48**(2), 133–138 (2001)
44. Woafó, P.: Transitions to chaos and synchronization in a nonlinear emitter-receiver system. *Phys. Lett. A* **267**(1), 31–39 (2000)
45. Wu, S., Smith, S.L., Fork, R.L.: Kerr-lens-mediated dynamics of 2 nonlinearly coupled mode-locked laser-oscillators. *Opt. Lett.* **17**(4), 276–278 (1992)
46. Roychowdhury, J.: Boolean computation using self-sustaining nonlinear oscillators. *Proc. IEEE* **103**(11, SI), 1958–1969 (2015)
47. Ling, F.: Synchronization in Digital Communication Systems. Cambridge University Press, Cambridge, U.K. (2017)
48. Rodrigues, F.A., Peron, T.K.D.M., Ji, P., Kurths, J.: The Kuramoto model in complex networks. *Phys. Rep. Rev. Sect. Phys. Lett.* **610**, 1–98 (2016)
49. Pecora, L.M., Carroll, T.L.: Synchronization of chaotic systems. *Chaos* **25**(9) (2015)
50. Woafó, P., Fotsin, H.B., Chedjou, J.C.: Dynamics of two nonlinearly coupled oscillators. *Phys. Scr.* **57**(2), 195–200 (1998)
51. Thwaites, F.W., Sen, M.: Dynamics of temperatures in thermally-coupled, heated rooms with PI control. In: Proceedings of the ASME IMECE 2007 Pts. A and B, Heat Transfer, Fluid Flows, and Thermal Systems, vol. 8, pp. 585–589 (2008)
52. Cai, W., Sen, M.: Synchronization of thermostatically controlled first-order systems. *Int. J. Heat Mass Transf.* **51**(11–12), 3032–3043 (2008)
53. O'Brien, J., Sen, M.: Temperature synchronization, phase dynamics and oscillation death in a ring of thermally-coupled rooms. In: Proceedings of the ASME IMECE 2011, Pts A and B, pp. 73–82 (2012)
54. Sen, M.: Effect of walls on synchronization of thermostatic room-temperature oscillations. *Ingeniería Mecánica, Tecnología y Desarrollo* **4**(3), 81–88 (2012)
55. Sen, M., Amegashie, I., Cecconi, E., Antsaklis, P.: Dynamics of air and wall temperatures in multiroom buildings. In: Proceedings of the ASME IMECE 2012, vol. 10, pp. 263–272 (2013)
56. Cai, W., Sen, M., Yang, K.T., McClain, R.L.: Synchronization of self-sustained thermostatic oscillations in a thermal-hydraulic network. *Int. J. Mass Transf.* **49**(23–24), 4444–4453 (2006)
57. Barron, M.A., Sen, M.: Synchronization of temperature oscillations in heated plates with hysteretic on-off control. *Appl. Therm. Eng.* **65**(1–2), 337–342 (2014)
58. Kitahata, H., Taguchi, J., Nagayama, M., Sakurai, T., Ikura, Y., Osa, A., Sumino, Y., Tanaka, M., Yokoyama, E., Miike, H.: Oscillation and synchronization in the combustion of candles. *J. Phys. Chem. A* **113**(29), 8164–8168 (2009)
59. Crandall, S.H.: Foreward in [11]
60. Kuznetsov, Y.I., Minakova, I.I., Tshedrina, M.I.: Mutual synchronization mechanisms of 2 resonance coupled oscillators. *Vestnik Moskovskogo Universiteta Seriya 3 Fizika Astronomiya*, **31**(3), 94–96 (1990)
61. Dimentberg, M., Cobb, E., Mensching, J.: Self-synchronization of transient rotations in multiple-shaft systems. *J. Vib. Control* **7**(2), 221–232 (2001)
62. Kuramoto, Y.: Chemical Oscillations, Waves, and Turbulence. Springer, New York (1984)
63. Strogatz, S.H.: From Kuramoto to Crawford: exploring the onset of synchronization in populations of coupled oscillators. *Phys. D* **143**(1–4), 1–20 (2000)

64. Moreno, Y., Pacheco, A.F.: Synchronization of Kuramoto oscillators in scale-free networks. *Europhys. Lett.* **68**(4), 603–609 (2004)
65. Dolmatova, A.V., Goldobin, D.S., Pikovsky, A.: Synchronization of coupled active rotators by common noise. *Phys. Rev. E*, **96**(6) (2017)
66. Bocca, N.: Modeling Complex Systems. Springer, New York (2004)
67. Pacheco-Vega, A., Diaz, G., Sen, M., Yang, K.T.: Applications of artificial neural networks and genetic methods in thermal engineering. In: Chhabra, R. (ed.) The CRC Handbook of Thermal Engineering, pp. 1217–1269, Section 4.27. CRC Press, Boca Raton, FL (2017)
68. Barron, M.A., Sen, M.: Dynamic behavior of a large ring of coupled self-excited oscillators. *J. Comput. Nonlinear Dyn.* **8**(3) (2013)
69. Barron, M.A., Sen, M., Corona, E.: Dynamics of large rings of coupled Van der Pol oscillators. In: Elleithy, K. (ed.) Innovations and Advanced Techniques in Systems, Computing Sciences and Software Engineering, pp. 346–349 (2008); International Conference on Systems, Computing Science and Software Engineering, Electr Network, 03–12 Dec 2007
70. Barron, M.A., Sen, M.: Synchronization of four coupled van der Pol oscillators. *Nonlinear Dyn.* **56**(4), 357–367 (2009)
71. Kuznetsov, A.P., Roman, J.P.: Properties of synchronization in the systems of non-identical coupled van der Pol and van der Pol-Duffing oscillators. Broadband synchronization. *Phys. D-Nonlinear Phenom.* **38**(6), 499–1506 (2009)
72. Kibirkstis, E., Pauliukaitis, D., Miliunas, V., Ragulskis, K.: Synchronization of pneumatic vibroexciters under air cushion operating mode in a self-exciting autovibration regime. *J. Mech. Sci. Technol.* **31**(9), 4137–4144 (2017)
73. Sun, Z., Xiao, R., Yang, X., Xu, W.: Quenching oscillating behaviors in fractional coupled Stuart-Landau oscillators. *Chaos* **28**(3) (2018)
74. Vinod, V., Balaram, B., Narayanan, M.D., Sen, M.: Effect of oscillator and initial condition differences in the dynamics of a ring of dissipative coupled van der Pol oscillators. *J. Mech. Sci. Technol.* **29**(5), 1931–1939 (2015)
75. Zhang, X., Wen, B., Zhao, C.: Theoretical study on synchronization of two excitors in a nonlinear vibrating system with multiple resonant types. *Nonlinear Dyn.* **85**(1), 141–154 (2016)
76. Jiang, H., Liu, Y., Zhang, L., Yu, J.: Anti-phase synchronization and symmetry-breaking bifurcation of impulsively coupled oscillators. *Commun. Nonlinear Sci. Numer. Simul.* **39**, 199–208 (2016)
77. Hou, Y., Fang, P., Nan, Y., Du, M.: Synchronization investigation of vibration system of two co-rotating rotors with energy balance method. *Adv. Mech. Eng.* **8**(1) (2016)
78. Fang, P., Hou, Y.: Synchronization characteristics of a rotor-pendula system in multiple coupling resonant systems. *Proc. Inst. Mech. Eng. Part C-J. Mech. Eng. Sci.* **232**(10), 1802–1822 (2018)
79. Vinod, V., Balaram, B., Narayanan, M.D., Sen, M.: Effect of configuration symmetry on synchronization in a Van der Pol ring with nonlocal interactions. *Nonlinear Dyn.* **89**(3), 2103–2114 (2017)
80. Pantaleone, J.: Synchronization of metronomes. *J. Phys.* **70**, 992 (2002)
81. Oud, W.T.: Design and experimental results of synchronizing metronomes, inspired by Christiaan Huygens. Master's thesis, Eindhoven University of Technology, Eindhoven, Department of Mechanical Engineering (2006)
82. Kuznetsov, N.V., Leonov, G.A., Nijmeijer, H., Pogromsky, A.: Synchronization of two metronomes. *IFAC Proc.* **40**(14), 49–52 (2007)
83. Martens, E.A., Thutupalli, S., Fourriere, A., Hallatschek, O.: Chimera states in mechanical oscillator networks. *Proc. Natl. Acad. Sci. USA* **110**(26), 10563–10567 (2013)
84. Hoskoti, L., Misra, A., Sacheendran, M.M.: Frequency lock-in during vortex induced vibration of a rotating blade. *J. Fluids Struct.* **80**, 145–164 (2018)
85. Barron, M.A., Sen, M.: Synchronization of coupled self-excited elastic beams. *J. Sound Vib.* **324**(1–2), 209–220 (2009)
86. Wang, D., Zhao, C., Yao, H., Wen, B.: Vibration synchronization of a vibrating system driven by two motors. *Adv. Vib. Eng.* **11**(1), 59–73 (2012)

87. Zhang, X.-L., Wen, B.-C., Zhao, C.-Y.: Synchronization of three homodromy coupled exciters in a non-resonant vibrating system of plane motion. *Acta Mech. Sin.* **28**(5), 1424–1435 (2012)
88. Wang, D., Chen, Y., Hao, Z., Cao, Q.: Bifurcation analysis for vibrations of a turbine blade excited by air flows. *Sci. China-Technol. Sci.* **59**(8), 1217–1231 (2016)
89. Wang, D., Chen, Y., Wiercigroch, M., Cao, Q.: Bifurcation and dynamic response analysis of rotating blade excited by upstream vortices. *Appl. Math. Mech.-Eng. Ed.* **37**(9), 1251–1274 (2016)
90. Wang, D., Chen, Y., Wiercigroch, M., Cao, Q.: A three-degree-of-freedom model for vortex-induced vibrations of turbine blades. *Meccanica* **51**(11, SI), 2607–2628 (2016)
91. Wang, D., Hao, Z., Chen, Y., Zhang, Y.: Dynamic and resonance response analysis for a turbine blade with varying rotating speed. *J. Theor. Appl. Mach.* **56**(1), 31–42 (2018)
92. Oppenheim, A.V., Willsky, A.S., Hamid, S.: Signals and Systems. Pearson, 2nd edn. (1996)
93. Haykin, S., Van Veen, B. Signals and Systems. Wiley (2002)
94. Porat, B.: Digital Processing of Random Signals: Theory and Methods. Dover (2008)
95. Jáuregui, J.C., Sen, M., López-Cajún, C.S.: Experimental characterization of synchronous vibration of blades. In: Proceedings of the ASME Turbo Expo 2011, Pts A and B, vol. 6, pp. 821–828 (2012)

Chapter 3

Research on Vibration Suppression of Nonlinear Energy Sink Under Dual-Frequency Excitation



B. Sun and Z. Q. Wu

Abstract Most of modern civil turbofan engines adopt the dual-rotor layout, which introduces the typical dual-frequency excitation into the dynamic models. This work sets a single degree of freedom (SDOF) linear oscillator for the main system, and establishes the dynamic models of that coupled with the SDOF linear dynamic vibration absorber (DVA) and different configurations of nonlinear energy sink (NES). In view of the typical flutter mechanism of wing, the modal frequency of the first-order symmetric twist typical state of wing is introduced into dynamic models. With the wing, low and high characteristic frequency ratio (1:2.67:12.66) for the typical dual-rotor aero-engine in cruise, the fourth-order Runge-Kutta algorithm is employed for analysis. According to the energy criteria for the dynamic vibration absorber optimization, focusing on the effects of the characteristic frequency ratio on the kinetic energy of the primary mass, total system energy etc., numerical simulation results of comparison can indicate that reducing the torsional vibration of wing by NES is feasible, and NES has better vibration suppression effect than the traditional linear DVA with certain set of parameters under the dual-frequency excitation. In addition, the vibration suppression effects of the SDOF, two-DOF serial and parallel NES on the main oscillator system are focused on. Under the condition that the characteristic parameters of the main system and additive total mass of the vibration absorber remain unchanged, results show the two-DOF parallel NES has the best vibration energy suppression effect under dual-frequency excitation.

Keywords NES · Civil aero-engine · Dual-frequency excitation · Vibration suppression optimization

B. Sun · Z. Q. Wu (✉)

Tianjin Key Laboratory of Nonlinear Dynamics and Chaos Control, Department of Mechanics, School of Mechanical Engineering, Tianjin University, Tianjin 300072, People's Republic of China

e-mail: zhiqwu@tju.edu.cn

B. Sun

Department of Aircraft, School of Aeronautical Engineering, Civil Aviation University of China, Tianjin 300300, People's Republic of China

© Springer Nature Switzerland AG 2019

J. C. Jauregui (ed.), *Nonlinear Structural Dynamics and Damping, Mechanisms and Machine Science* 69,

<https://doi.org/10.1007/978-3-030-21777-7>

3.1 Introduction

In aeronautical engineering, vibration suppression design of the modern civil turbofan engine is very important in the engineering practices. However, even for the most advanced civil turbofan aircrafts, the failure problems caused by engine vibration, such as the local structural cracks, pipeline leaks and loosening of fasteners still occur frequently. The dual-rotor layout civil turbofan engine introduces the typical dual-frequency excitation into the wings [1–5], but the research of wing under dual-frequency excitation is very limited, especially the dynamic analysis of vibration suppression of wing under dual-frequency excitation has not been carried out. Moreover, the dual-frequency excitation has also attracted researchers' attention in other engineering fields, for example in deep-sea research [6, 7].

The selection of the efficient vibration suppression method has always been a key issue in many engineering fields. The research on linear dynamic vibration absorber (DVA) is earlier and the basic theory is relatively mature. However, the study of nonlinear energy sink (NES) started late. The influence of nonlinear factors makes the energy transfer and dissipation mechanism of nonlinear systems more complicated. Because NES has the advantages of wide vibration absorption frequency band, high energy dissipation rate and strong robustness, etc., the NES is introduced in order to research its potential on vibration suppression of the nonlinear systems with the typical dual-frequency excitation in this paper.

Various researchers have focused on the theoretical research and applications of NES in the recent years. Gendelman et al. [8, 9] studied the attractor problems of tuned forced linear system with NES, under certain damping and frequency range settings, NES could have better energy absorption effects than the traditional linear DVA with single-frequency excitation, and the parameter optimization design method of NES was proposed. Starosvetsky et al. [10, 11] analyzed the effects of two-DOF linear system NES on the internal resonance problems, studied the response mechanism of the system with NES under 1:1:1 internal resonance quasi-periodic forcing and random excitation, and it was proved that the parameters of NES can be tuned to effectively reduce the vibration caused by quasi-periodic (with closely spaced frequencies) and even random excitation.

The vibration suppression mechanism of NES is target energy transfer (TET), in Refs. [12–16], initial conditions of TET between the nonlinear coupled oscillators in NES were investigated, based on which the typical parameters like cubic stiffness, damping and mass ratio of NES can be designed to obtain better vibration suppression effects. Hubbard et al. [17, 18] designed a single degree of freedom (SDOF) NES on the wingtip for the vibration suppression research by experiment, and provided the design process of NES in detail. Borošon et al. [19] studied the parallel NES optimization design, considered the uncertainty of the NES efficiency caused by the loading conditions or the disturbances of the design parameters and proved the effectiveness of the method through a comparative analysis. For the vibration suppression research of the continuous systems coupled with the NES, Ahmadabadi et al. [20] studied the vibration suppression effect of the grounded and ungrounded NES on

the cantilever beam under shock excitation, and investigated firstly the application of the nonlinear normal modes (NNMs) theory in identifying dynamics of energy pumping in the continuous systems. Kani et al. [21] studied the performance of the NES attached to a beam with different support conditions, by means of the sensitivity analysis and particle swarm optimization, parameters of the NES can be optimized.

NES has been widely applied in engineering vibration suppression in previous researches. However, the vibration suppression effects of different configurations of NES under dual-frequency still remain unknown. The main research aim of this paper is to study the vibration suppression effects of the linear DVA, SDOF NES and two-DOF serial/parallel NES on the main oscillator system using the energy criteria for the DVA optimization. In Sect. 3.1, the dynamic models of different types of DVA under dual-frequency are established. Section 3.2 analyzes the vibration suppression effects of the NES on the main oscillator system. Section 3.3 makes a comparison of vibration suppression effects between NES and the linear DVA. Section 3.4 focuses the configuration optimization of NES, and Sect. 3.5 summarizes the main achievements of this research.

3.2 Description of the Dynamic Models

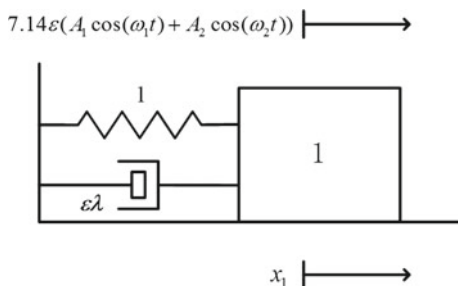
In this section, five dynamic models are presented in order to study the vibration suppression effects of different absorbers.

3.2.1 Dynamic Model of the Main Oscillator System

For the system shown in Fig. 3.1, its dimensionless dynamic equation can be expressed as:

$$\ddot{x}_1 + x_1 + 2.67\varepsilon\lambda_0\dot{x}_1 = 7.14\varepsilon(A_1 \cos(2.67\omega_1 t) + A_2 \cos(2.67\omega_2 t)) \quad (3.1)$$

Fig. 3.1 Schematic diagram of the main oscillator system



x_1 is the displacement of the linear main oscillator, and the mass and natural frequency of linear main oscillator are taken as equal to unity; the damping coefficient is $\varepsilon\lambda = 2.67\varepsilon\lambda_0$. In addition, $7.14\varepsilon A_1$ and $7.14\varepsilon A_2$ are the amplitudes of the dual-frequency excitation, respectively.

ω_1 and ω_2 are two excitation frequencies, and their frequency ratio can be defined as $\gamma = \omega_2/\omega_1$. In order to investigate the vibration suppression of wing under the dual-frequency excitation, related research shows that the wing vibration takes mainly with the first-order torsional mode [22, 23], for instance, a type of aircraft has the wing symmetric first-order torsional natural frequency of 21 Hz, on which the engine's dual rotors rotate respectively at about 57 and 270 Hz in the cruise phase. Therefore, the frequency ratio between the main oscillator system and the two excitations in the dynamic models of this paper is set to 1:2.67:12.66 according to the engineering practice.

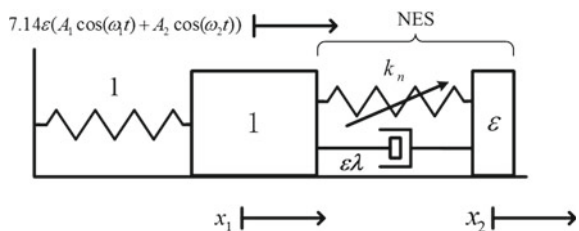
3.2.2 Dynamic Model of the System with SDOF NES

Figure 3.2 shows the single linear main oscillator system coupled with SDOF NES, the basic physical and dynamic model of which can be found in Ref. [8], and here the dynamic modeling process takes into account the defined frequency ratio between the main oscillator system and the two excitations. The dynamic equations after time scale transformation can be expressed as:

$$\begin{cases} \ddot{x}_1 + x_1 + 2.67\varepsilon\lambda_0(\dot{x}_1 - \dot{x}_2) + 7.14k_{n0}(x_1 - x_2)^3 \\ = 7.14\varepsilon(A_1 \cos(\omega_1 t) + A_2 \cos(\omega_2 t)) \\ \varepsilon\ddot{x}_2 + 2.67\varepsilon\lambda_0(\dot{x}_2 - \dot{x}_1) + 7.14k_{n0}(x_2 - x_1)^3 = 0 \end{cases} \quad (3.2)$$

where, x_1 and x_2 are respectively the displacements of the linear main oscillator and NES; ε represents the mass ratio between the NES and the main oscillator being used as the small parameter, and can also scale the coupling between two oscillators, the damping forces and amplitudes of the dual-frequency excitation, here $\varepsilon \ll 1$; the damping coefficient of the NES is $\varepsilon\lambda = 2.67\varepsilon\lambda_0$; To simplify the analysis, the stiffness term [6, 21] of NES k_{n0} equals to $4/3\varepsilon$, means that the nonlinear stiffness is $k_n = 7.14k_{n0}$. And the dual-frequency excitation is the same as in Eq. (3.1).

Fig. 3.2 Schematic diagram of the system coupled with SDOF NES



3.2.3 Dynamic Model of the System with SDOF Linear DVA

One considers the comparison with the traditional linear DVA, to analyze the vibration suppression effects of NES, and the dynamic model of the single linear main oscillator system coupled with SDOF linear DVA is established. A DVA oscillator is used to substitute the NES oscillator in Eq. (3.2), and the related dynamic equations after time scale transformation are:

$$\begin{cases} \ddot{x}_1 + x_1 + 2.67\varepsilon\lambda_0(\dot{x}_1 - \dot{x}_2) + 7.14k_{Lin0}(x_1 - x_2) \\ = 7.14\varepsilon(A_1 \cos(\omega_1 t) + A_2 \cos(\omega_2 t)) \\ \varepsilon\ddot{x}_2 + 2.67\varepsilon\lambda_0(\dot{x}_2 - \dot{x}_1) + 7.14k_{Lin0}(x_2 - x_1) = 0 \end{cases}, \quad (3.3)$$

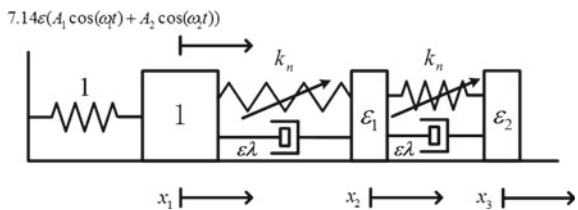
where, $k_{Lin} = 7.14k_{Lin0}$ is the linear stiffness of DVA, and the linear stiffness term k_{Lin0} equals to $4/3\varepsilon$ for comparison; the damping coefficient of the linear DVA is $\varepsilon\lambda = 2.67\varepsilon\lambda_0$, and the other parameters and the dual-frequency excitation are consistent with those in Eq. (3.2).

3.2.4 Dynamic Model of the System with Two-DOF Serial NES

Figure 3.3 shows the single linear main oscillator system coupled with two-DOF serial NES. The dynamic modeling should consider the coupling relationships among the main oscillator and the serial absorbers, and the dynamic equations of which after time scale transformation can be expressed as:

$$\begin{cases} \ddot{x}_1 + x_1 + 2.67\varepsilon\lambda_0(\dot{x}_1 - \dot{x}_2) + 7.14k_{n0}(x_1 - x_2)^3 \\ = 7.14\varepsilon(A_1 \cos(\omega_1 t) + A_2 \cos(\omega_2 t)) \\ \varepsilon_1\ddot{x}_2 + 2.67\varepsilon\lambda_0(\dot{x}_2 - \dot{x}_1) + 2.67\varepsilon\lambda_0(\dot{x}_2 - \dot{x}_3) \\ + 7.14k_{n0}(x_2 - x_1)^3 + 7.14k_{n0}(x_2 - x_3)^3 = 0 \\ \varepsilon_2\ddot{x}_3 + 2.67\varepsilon\lambda_0(\dot{x}_3 - \dot{x}_2) + 7.14k_{n0}(x_3 - x_2)^3 = 0 \end{cases}, \quad (3.4)$$

Fig. 3.3 Schematic diagram of the system coupled with two-DOF serial NES



where, ε_1 and ε_2 are respectively dimensionless mass of two serial NES; x_2 and x_3 are respectively the displacements of two NES, and the other characteristic parameters remain the same as those in the system with SDOF NES.

3.2.5 Dynamic Model of the System with Two-DOF Parallel NES

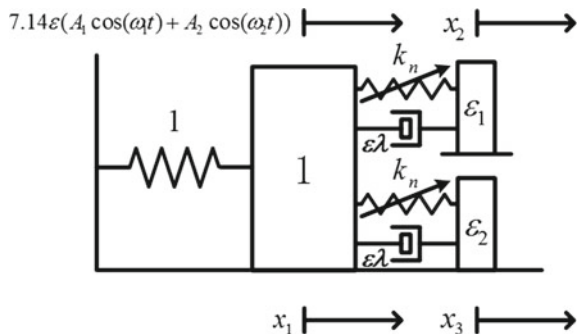
Figure 3.4 shows the single linear main oscillator system coupled with two-DOF parallel NES. The dynamic modeling should consider the coupling relationship between the main oscillator and each parallel absorber, and the dynamic equations of which after time scale transformation can also be expressed as:

$$\begin{cases} \ddot{x}_1 + x_1 + 2.67\varepsilon\lambda_0(\dot{x}_1 - \dot{x}_2) + 7.14k_{n0}(x_1 - x_2)^3 \\ + 2.67\varepsilon\lambda_0(\dot{x}_1 - \dot{x}_3) + 7.14k_{n0}(x_1 - x_3)^3 \\ = 7.14\varepsilon(A_1 \cos(\omega_1 t) + A_2 \cos(\omega_2 t)) \\ \varepsilon_1\ddot{x}_2 + 2.67\varepsilon\lambda_0(\dot{x}_2 - \dot{x}_1) + 7.14k_{n0}(x_2 - x_1)^3 = 0 \\ \varepsilon_2\ddot{x}_3 + 2.67\varepsilon\lambda_0(\dot{x}_3 - \dot{x}_1) + 7.14k_{n0}(x_3 - x_1)^3 = 0 \end{cases}, \quad (3.5)$$

where, ε_1 and ε_2 are respectively dimensionless mass of two parallel NES; x_2 and x_3 are respectively the displacements of two NES, and the other parameters are left the same as those in the system with SDOF NES.

In order to compare the vibration suppression effects of different dynamic systems above, according to the related energy criteria proposed in Ref. [24], the vibration suppression optimization of DVA should mainly consider such factors as the main oscillator kinetic energy, total system energy and total area occupied by the total system energy curve. Here the main oscillator kinetic energy of each system can be set directly as:

Fig. 3.4 Schematic diagram of the system coupled with two-DOF parallel NES



$$E_{kin} = \frac{\dot{x}_1^2}{2} \quad (3.6)$$

Total system energy of the main oscillator system is:

$$E_{tot_Main} = \frac{\dot{x}_1^2}{2} + \frac{x_1^2}{2} \quad (3.7)$$

Total system energy of the system coupled with SDOF linear DVA can be expressed as:

$$E_{tot_Lin} = \frac{\dot{x}_1^2}{2} + \varepsilon \frac{\dot{x}_2^2}{2} + \frac{x_1^2}{2} + k_{Lin} \frac{(x_1 - x_2)^2}{2} \quad (3.8)$$

Meanwhile, total system energy of the system coupled with SDOF NES, two-DOF serial and parallel NES can be obtained similarly as follows:

$$E_{tot_SDOF\,NES} = \frac{\dot{x}_1^2}{2} + \varepsilon \frac{\dot{x}_2^2}{2} + \frac{x_1^2}{2} + k_n \frac{(x_1 - x_2)^4}{4} \quad (3.9)$$

$$\begin{aligned} E_{tot_two-DOF\,serial\,NES} = & \frac{\dot{x}_1^2}{2} + \varepsilon_1 \frac{\dot{x}_2^2}{2} + \varepsilon_2 \frac{\dot{x}_3^2}{2} + \frac{x_1^2}{2} \\ & + k_n \frac{(x_1 - x_2)^4}{4} + k_n \frac{(x_2 - x_3)^4}{4} \end{aligned} \quad (3.10)$$

$$\begin{aligned} E_{tot_two-DOF\,parallel\,NES} = & \frac{\dot{x}_1^2}{2} + \varepsilon_1 \frac{\dot{x}_2^2}{2} + \varepsilon_2 \frac{\dot{x}_3^2}{2} + \frac{x_1^2}{2} \\ & + k_n \frac{(x_1 - x_2)^4}{4} + k_n \frac{(x_1 - x_3)^4}{4} \end{aligned} \quad (3.11)$$

3.3 Comparison with the Main Oscillator System

In Eqs. (3.1) and (3.2), to compare the vibration suppression effects of the systems with SDOF NES and without DVA, we set $\varepsilon = 0.01$, $\lambda_0 = 0.2$, $A_1 = 1.3$, $A_2 = 0.1$ both in these two systems. The stiffness term of NES is $k_{n0} = 4/3\varepsilon$, and the initial displacement and velocity of each oscillator in these two systems are set to 0.

Considering that typical dual-rotor civil turbofan engines are taken as the main engineering background in this paper, and the maximum frequency ratio between two exciters in the cruise phase is usually less than 7. Therefore, when ω_1 is fixed to 2.67 as defined in Sect. 3.1, we increase monotonically the frequency ratio γ from 1 to 8 with the step of 0.01, making the range of which cover the characteristic frequency ratio corresponding to the target aircraft cruise phase ($\gamma = 4.74$). The

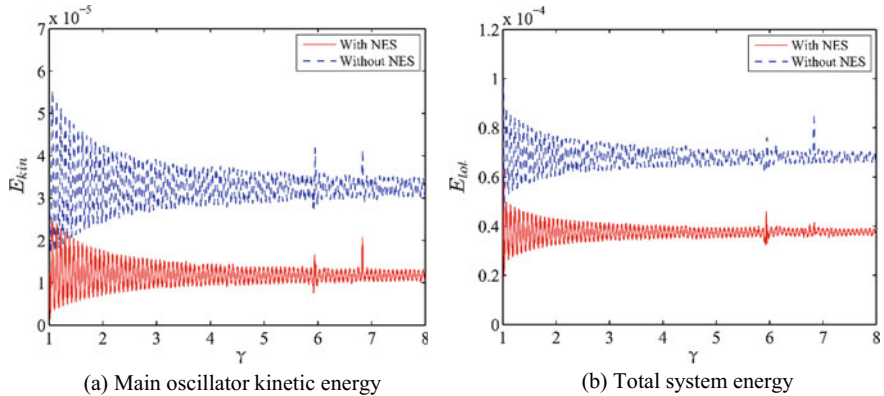


Fig. 3.5 Contrast with the effects of γ on the main oscillator kinetic energy and total system energy of the main oscillator system

comparison results of main oscillator kinetic energy and total system energy curves after numerical simulation are displayed in Fig. 3.5.

From the numeric results above, it is shown that the main oscillator kinetic energy and total system energy of the system coupled with NES are lower, and NES has a significant vibration suppression effect on the main oscillator system. Therefore, NES is promising for the application in civil turbofan engine vibration suppression.

3.4 Comparison with the Case of SDOF Linear DVA

In Eqs. (3.2) and (3.3), in order to compare the vibration suppression effects of the systems with SDOF NES and linear DVA, we set $\varepsilon = 0.01$, $\lambda_0 = 0.2$, $A_1 = 1.3$, $A_1 = 0.1$. The stiffness terms of NES and linear DVA are $k_{n0} = k_{lin0} = 4/3\varepsilon$, and the initial displacement and velocity of each oscillator are likewise set to 0. Here ω_1 is fixed to 2.67, increasing the frequency ratio γ from 1 to 8, and the comparison results of main oscillator kinetic energy and total system energy curves are displayed in Fig. 3.6.

Numerical simulation results in Fig. 3.6 can illustrate that NES has better vibration suppression effects than linear DVA. It is found that comparing with the traditional linear DVA the NES can provide better vibration suppression performance in a wide frequency ratio range.

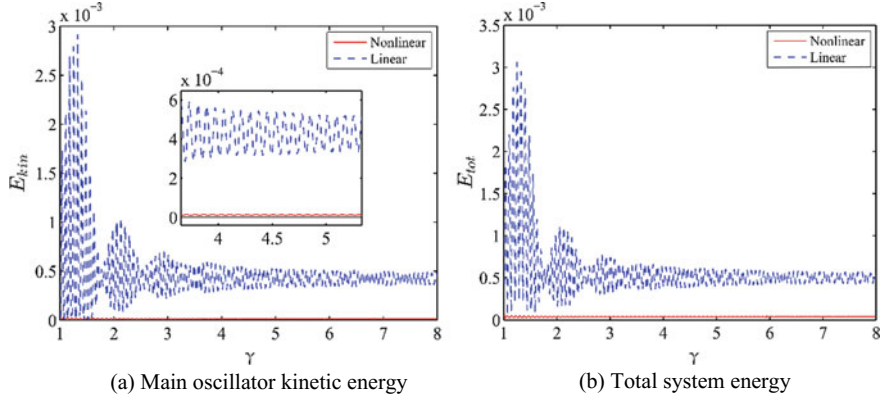


Fig. 3.6 Contrast with the effects of γ on the main oscillator kinetic energy and total system energy of the system coupled with linear DVA

3.5 Comparison with the Case of Two-DOF Serial/Parallel NES

To make the vibration suppression optimization research of NES, the comparisons with the vibration suppression effects of two-DOF serial and parallel NES are carried out. In Eqs. (3.4) and (3.5), ε_1 and ε_2 are respectively set to 0.009 and 0.001; the initial displacement and velocity of each oscillator are 0, and the other characteristic parameters still remain the same as those in Eq. (3.2). Here ω_1 equals to 2.67, and the numerical simulation results can be obtained as shown in Fig. 3.7.

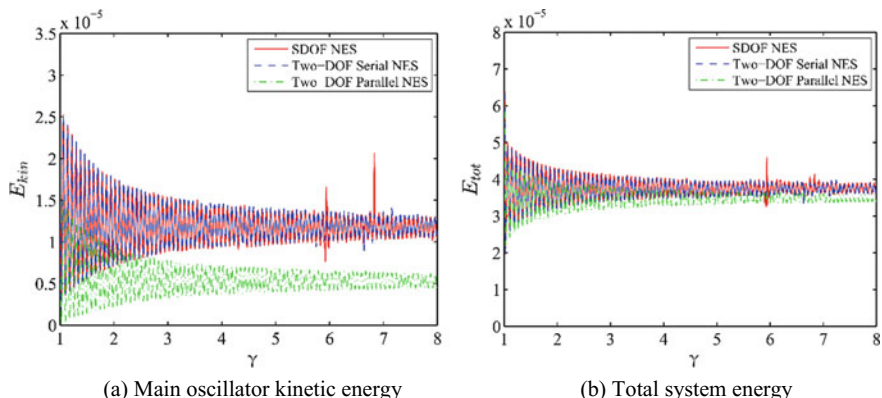


Fig. 3.7 Contrast with the effects of γ on the main oscillator kinetic energy and total system energy of the system coupled with two-DOF Serial/Parallel NES

The comparison in Fig. 3.7 can indicate that when the characteristic parameters of the main oscillator system and additional total mass of the vibration absorber remain unchanged, according to the main factors of the vibration suppression optimization described in Sect. 3.1, the case of two-DOF parallel NES has the best vibration energy suppression effects.

3.6 Concluding Remarks

Based on the characteristic frequency ratio of a typical dual-rotor aero-engine, this paper constructed dynamic models of system coupled with linear DVA and different configurations of NES under the dual-frequency excitation, meanwhile introduced the modal frequency of the first-order symmetric twist typical state of the wing into the dynamic models. The obtained numeric results based on the fourth-order Runge-Kutta algorithm demonstrate that:

- (1) NES has a significant vibration suppression effect on the main oscillator system under the dual-frequency excitation, and it is feasible to use NES to reduce the torsional vibration of wing;
- (2) By comparison with the system coupled with linear DVA, the vibration suppression effects of NES are better in a wide frequency ratio range;
- (3) When the characteristic parameters of the main oscillator system and additional total mass of the vibration absorber remain the same, compared with the system with SDOF and two-DOF serial NES, two-DOF parallel NES has the best vibration energy suppression effects, which can provide data reference for vibration suppression design of the dual-rotor turbofan engine.

Acknowledgements This work was supported by the National Basic Research Program of China (No. 2014CB046805) and the National Natural Science Foundation of China (No. 11372211, No. 11672349).

References

1. Yan, L.T., Wang, D.Y.: Vibration features from rubbing between rotor and casing for a dual-shaft aeroengine. *J. Aerosp. Power* (1998). (in Chinese)
2. Depriest, J.: Aircraft engine attachment and vibration control. *Manufacturing* (2000)
3. Han, J., Gao, D.P., Hu, X., et al.: Research on beat vibration of dual-rotor for aero-engine. *Acta Aeronaut. et Astronaut. Sin.* **28**(6), 1369–1373 (2007). (in Chinese)
4. Chen, Y., He, E.M., Hu, X.Z., et al.: Exploring wing-mounted engine vibration transmission for new generation airplanes with turbofan engines of high bypass ratio. *J. Northwest. Polytechn. Univ.* **30**(3), 384–389 (2012). (in Chinese)
5. Ouyang, Y.F., Ming, Y.: Research on rub-impact fault vibration characteristics of aeroengine dual-rotor system. *Mech. Eng.* **11**, 65–71 (2016). (in Chinese)
6. Xiao, F., Yang, H.Z., Lu, Q.J., et al.: Vortex-induced parametric resonance of top tensioned riser based on bi-frequency excitation. *Ocean. Eng.* **31**(2), 28–34 (2013). (in Chinese)

7. Xiao, F., Yang, H.Z.: Hill stability prediction of deep-sea steel catenary riser. *Shanghai Jiao Tong Univ.* **48**(4), 583–588 (2014). (in Chinese)
8. Gendelman, O.V., Starosvetsky, Y.: FELDMAN M, Attractors of harmonically forced linear oscillator with attached nonlinear energy sink I: Description of response regimes. *Nonlinear Dyn.* **51**(1), 31–46 (2007)
9. Starosvetsky, Y., Gendelman, O.V.: Attractors of harmonically forced linear oscillator with attached nonlinear energy sink II: Optimization of a nonlinear vibration absorber [J]. *Nonlinear Dyn.* **51**(1–2), 47–57 (2008)
10. Starosvetsky, Y., Gendelman, O.V.: Interaction of nonlinear energy sink with a two degrees of freedom linear system Internal resonance. *J. Sound Vib.* **329**(10), 1836–1852 (2010)
11. Starosvetsky, Y., Gendelman, O.V.: Response regimes in forced system with non-linear energy sink: quasi-periodic and random forcing. *Nonlinear Dyn.* **64**(1), 177–195 (2011)
12. Kong, X.R., Zhang, Y.C.: Vibration suppression of a two-degree-of-freedom nonlinear energy sink under harmonic excitation. *Acta Aeronaut. et Astronaut. Sin.* **33**(6), 1020–1029 (2012). (in Chinese)
13. Zhang, Y.C., Kong, X.R.: Initial conditions for targeted energy transfer in coupled nonlinear oscillators. *J. Harbin Inst. Technol.* **44**(07), 21–26 (2012). (in Chinese)
14. Zhang, Y.C.: Dynamics of a nonlinear energy sink used for suppressing two-separated resonance peaks. *Spacecr. Environ. Eng.* **32**(05), 477–483 (2015). (in Chinese)
15. Xiong, H., Kong, X.R., Liu, Y.: Influence of structural damping on a system with nonlinear energy sinks. *J. Vib. Shock* **11**, 116–121 (2015). (in Chinese)
16. Xiong, H., Kong, X.R., Liu, Y.: Energy transfer and dissipation of a class of nonlinear absorber and its parameter design. *J. Vib. Eng.* **28**(5), 785–792 (2015). (in Chinese)
17. Hubbard, S.A., McFarland, D.M., Bergman, L.A., et al.: Targeted energy transfer between a model flexible wing and nonlinear energy sink. *J. Aerogr.* **47**(6), 1918–1931 (2010)
18. Hubbard, S.A., McFarland, D.M., Bergman, L.A., et al.: Targeted energy transfer between a swept wing and winglet-housed nonlinear energy sink. *AIAA J.* **52**(12), 2633–2651 (2014)
19. Boroson, E., Missoum, S., Mattei, P.O., Vergez, C.: Optimization under uncertainty of parallel nonlinear energy sinks. *J. Sound Vib.* **394**, 451–464 (2017)
20. Ahmadabadi, Z.N., Khadem, S.E.: Nonlinear vibration control of a cantilever beam by a nonlinear energy sink. *Mech. Mach. Theory* **50**(50), 134–149 (2012)
21. Kani, M., Khadem, S.E., Pashaei, M.H., et al.: Design and performance analysis of a nonlinear energy sink attached to a beam with different support conditions. *Arch. Proc. Inst. Mech. Eng. Part C J. Mech. Eng. Sci.* **230**(4), 527–542 (2016)
22. Liu, C.Y., Sun, X.H., Ma, X.: Vibration and flutter characteristics analysis of wing finite element model. *Comput. Aided Eng.* **15**(s1), 53–55 (2006). (in Chinese)
23. Zhang, H. B., Zhang, G. G.: Research on flutter characteristics of wing structure with variable parameters. In: Proceedings of the Thirteenth National Conference on Air Elasticity (2013). (in Chinese)
24. Gendelman, O.V.: Targeted energy transfer in systems with external and self-excitation. *Arch. Proc. Inst. Mech. Eng. Part C J. Mech. Eng. Sci.* **225**(9), 2007–2043 (2011)

Chapter 4

Identification of Nonlinearities in Mechanical Systems Using Recurrence Plots



J. C. Jauregui-Correa

Abstract The identification of nonlinear vibrations in mechanical systems is an unsolved problem. The structure of the measured data and waveforms have been studied for many years, and different techniques have been applied. Nevertheless, there is no single technique for identifying the nonlinear parameters. Parameter identification can be conducted either with a parametric approach or with a non-parametric approach. Among parametric approaches many researchers have work with the Hilbert transform, continuous and discrete wavelet transform, nonlinear modal analysis, phase space. Meanwhile, nonparametric procedures include fractal analysis, Hurt factor, and approximate entropy. In this paper, the recurrence plots are applied for the identification of nonlinear parameters. Recurrence plots are constructed from the phase space. To calibrate the method, the recurrence plots were obtained from two theoretical models, a Van der Pol pendulum, and a Duffing mass-lump model. Then, the recurrence plots were constructed from a mechanical gearbox. Recurrence plots are an alternative solution for the identification of nonlinearities in mechanical systems.

Keywords Recurrence plot · Nonlinear systems · Parameter identification

4.1 Introduction

Recurrence plot is an alternative solution for the identification of nonlinearities in mechanical systems [1]. Henri Poincaré introduced the formal concept of recurrences in his seminal work from 1890. In 1987 Eckmann et al. [2] presented the method of Recurrence Plots. They defined the basis for the procedure that will be shown in the following section. After the basic definition, further analysis has been developed. Marwan and Weber [3] summarized the theory behind the application of the recurrence plot. They described how a dynamic system could be represented in the phase

J. C. Jauregui-Correa (✉)

Universidad Autónoma de Querétaro, Santiago de Querétaro, Mexico

e-mail: jc.jauregui@uag.mx

plane (phase space) and the analysis of the trajectories along the phase plane can be quasi-stationary or non-stationary.

Thiel et al. [4] analyzed simulated data that were produced from a Rössler system. They applied the recurrence quantity analysis, and then they quantified the structures generated by recurrence plot. With this method, they were able to identify the effect of embedding on the spurious correlations. To validate their procedure, they applied the embedding method to Gaussian noise, and they found that the embedding method caused the artificial data. Fontaine et al. [5] analyzed the nonlinear dynamics of fibrous materials. They characterized the phase plane using the dimension “d”, the Shannon entropy, the Lyapunov exponent and the diameter of attraction. Faure and Lesne [6] used the Kolmogorov entropy to characterize the dynamics of a system. They explained that Recurrence Plots, based on a trajectory-centered characterization, require a complete reconstruction of the phase diagram; meanwhile, the analysis of the Recurrence Plot with an entropy estimation reduce the amount of analysis and can be applied to continuous and discrete phase diagrams. Their method is based on the application of the Kolmogorov entropy to the phase diagram. Eckmann et al. [2] method is based on the application of the Kolmogorov entropy to the phase diagram. Eckmann et al. [2] used the Recurrence Plot as a new tool for measuring the time constancy of dynamic systems. They distinguished, for the first time, this measuring method from other methods for computing the dynamical parameters of time series, such as information dimension, entropy, Lyapunov exponents or the dimension spectrum. The method is based on the analysis of the phase space (or phase plane), the orbits on the phase plane (q and \dot{q}) are cyclic repeated, and each point in the plane appears several times. They proposed a way of finding time correlations in a signal, and they analyzed experimental and computer-generated time series. They used these results to separate large-scale forms as “typologies” and small-scales as “textures.” The analysis of the typology and the textures is a research topic that will be described in this chapter.

Leonardi [7] also analyzes the information of a Recurrence Plot by applying the entropy of the signal, (Applied to cognitive science with signals without noise). In his work, it is assumed that the embedded multidimensional space matches exactly each period. However, in nonlinear systems or with multiple frequencies response, the Recurrence Plot has different geometric structures rather than simplified straight lines. Kwuimy et al. [8] analyzed bifurcations in a nonlinear pendulum using the recurrence plot. They emphasized in the importance of selecting the tolerance value between two trajectories. Ramdani et al. [9] used the Gaussian distribution to define the path along the phase diagram, and they estimate the probability density function. With it, they compute the probability of occurrence of two points within the Recurrence Plot; their results are applied to unembedded signals. Spiegel et al. [10] presented a summary of the details of the Recurrence Plot and the measurements of its properties.

Sipers et al. [11] proposed a method for reconstructing a signal from a recurrence plot. Its application is limited to embedded signals that are difficult to find in real vibration measurements. Tang et al. [12] reviewed different complexity testing techniques for time series data. They defined three significant areas: Fractal anal-

ysis for self-similarity signals, an attractor in phase plane for nonlinear dynamics, and entropy for identifying the disordered state. Pham and Yan [13] propose the use of sample entropy to measure irregularities in time series. Girault [14] proposed a method for the analysis of symmetry quantifications in time series. The study is based on the Recurrence Plot

Belaire-Franch and Contreras [15] classified the methods for identifying nonlinear time series. They organized those methods that have been applied in econometric packages as metric, dynamical and topological. Metric are those methods that calculate the distances from the attractors of the system. The dynamical relates to those methods that evaluate the orbit variations from a Lyapunov point of view. The topological methods study the organization of the attractors of the system. One of this method is the Recurrence Plot. They decompose the time series into a set of embedded vectors divided by a time delay. The time delay concept cannot be applied to vibration signals, except when the signal response is characterized by one frequency only. Carrión and Miralles [16] defined surrogate techniques and utilized surrogated data to analyze nonlinear time series. They compare the time series with the Recurrence Plot. Le Bot et al. [17] proposed a method for detecting an unknown deterministic signal hidden in white noise. Their approach is based on the Recurrence Plot.

Schultz et al. [18] found that the quantification of structures in a Recurrence Plot requires a tremendous computational effort when analyzing time series, the determinism (DET) been an effective analysis technique. To prove their analysis they assume that the tolerance is zero, but this assumption is unreal since the signal has some variations (The definition of tolerance is explained in the following sections).

Other researchers have applied the Recurrence Plot to specific problems. Feeny and Lin [19, 20], and Feeny and Liang [21], presented a method for extracting all the dynamic parameters of a system from field data. The goal is to reconstruct all the active states in the system form a single sample of data (embedding). They stated that a full reconstruction of the state space is useful for system characterization and nonlinear prediction. Their method is based on the use of fractional derivatives. The proposed method reconstructs the phase plane assuming that the output signal is represented by a discrete vector in which a delay index h , and the delay time is $\tau = h\delta$, where δ is the sampling rate. In this way, the system is represented as a discrete system with finite differences. Their method determined a procedure for calculating the embedding dimension and the delay time. For determining the unstable orbits of a nonlinear system, they proposed the use of the Recurrence Plot.

Viana et al. [22] built a periodicity parameter-space with a Chuac's circuit. They produced experimental data from a nonlinear system. Based on the measurements, they were able to observe self-organized periodic windows. In a similar work, [23] they used the Recurrence Plot to determine synchronization, and they measured DET and LAM (These concepts will be explained in the following sections). In their conclusions, they used the Kuramotos parameter for comparison. Jeeverekha et al. [24] investigated the dynamics of Tamasevicius Namajunas and Cenys (TNC) oscillator with antiparallel diodes. Prakash and Roy [25] studied a four DOF chaotic system. The system has one non-linear term and is represented as a Rössler type chaotic system. They simulated the system with Matlab and with an electrical circuit. Kiss

and Hudson [26] studied the Rössler oscillators, and they found the synchronization using the Recurrence Plot. From the Recurrence Plot, they calculated the probability that the system returns to the same position in the phase plane after a defined period; then, they calculated the cross-correlation from two system (to determine if the two systems are synchronous).

Jana et al. [27] studied the effect of time delay on the dynamics of food chain systems. The system is represented as nonlinear ordinary differential equations, they analyzed the results as chaotic systems, and they applied the Recurrence Plot for identifying the dynamic parameters.

Kwuimy and Kadji [28] and Kwuimy et al. [8, 29, 30], studied the synchronization of oscillators with coexisting attractors. They based the analysis on the Recurrence Plot. They defined the model as two Van der Pol type oscillators couple by a time-delayed spring. This phenomenon is visible also when utilizing the Kuramotos parameter. They measure the synchronization as a ration between the two Recurrence Plots.

Syta and Litak [31] applied the Recurrence Plot and the phase space analysis for identifying the parameters in cutting materials. Elias and Namboothiri [32] analyzed signals form a machining process. They determine the vibrations of machined (chatter) parts produced by turning. They presented scaled recurrence plots, and they found the time delay by using the average mutual information function.

Friction [33] is a multiscale and complex process that involves—among other factors—multiple mechanical forces, chemical interactions, change of surface topology and wear. In this work, they simulated the friction on a disk brake, and analyzed the results with different techniques; it is interesting to notice the application of the Recurrence Plot. Chelidze et al. [34, 35] investigated the synchronization in the stick-slip friction process, and they found the dynamical patterns in seismology using the Recurrence Plot.

Litak et al. [36] built the Recurrence Plot using the time series shift concept. They obtained the dynamic characteristics from the Recurrence Plot and the evolution of air bubbles within a water flow. Other works related to flow measurement are found in [37].

Xiong et al. [38] compared the results obtained with the Recurrence Plot and the Empirical Mode Decomposition, and they applied these techniques to time series derived from traffic flow. Tang et al. [39] studied the traffic flow dynamics to develop an intelligent control for transportation systems. They determined the periodicity and complexity of the time series obtained from traffic flow measurements using the Recurrence Plot [40]. Ukherjee et al. [41] also use the Recurrence Plot and the Recurrence Quantification Analysis for identifying the dynamic behavior of traffic in a mobile wireless network.

There are a vast amount of publications dealing with the application of the Recurrence Plot to the analysis of medical signals [42–44].

Another use of the Recurrence Plot is the identification of DC discharge plasma [45], and Craciunescu and Murari [46] applied the Recurrence plot to identify the geodesic distance on Gaussian manifolds for the identification of chaotic systems.

In this paper, the Recurrence Plots are applied to the analysis of nonlinear parameters. Recurrence Plots are constructed from the phase plane. The method is calibrated with recurrence plots that were obtained from two theoretical models, a Van der Pol pendulum and a Duffing mass-lump model. Then, the recurrence plots were constructed from a mechanical gearbox.

4.2 Phase Plane

The position and momentum of a particle specify a point in a space called the phase space, phase plane, phase diagram [47]. The construction of the phase plane is based on the transformation of a particle trajectory into a two-dimensional energy field (Alternatively, into two-dimensional state variables). A linear system can be represented as a differential equation of the form:

$$\frac{dy}{dt} = Ay(t) \quad (4.1)$$

where A is a $n \times n$ matrix and $y(t)$ is a vector containing the state variables. The dimension of the matrix A is one of the invariants that describes the evolution of the dynamic system, and it is equal to the dimension of the phase plane. From a mechanical point of view, the phase plane is defined using the Hamiltons principle:

$$H(p \cdot q) = \frac{p^2}{2m} + V(q) \quad (4.2)$$

where p is the linear momentum of a particle, $V(q)$ is the potential energy and q is the position of the particle. The equilibrium of the system is obtained when:

$$\dot{q} = \frac{\partial H}{\partial p} \quad (4.3)$$

and

$$\dot{p} = -\frac{\partial H}{\partial q} \quad (4.4)$$

Thus, there is a function $\varphi(p, q)$ such that

$$\frac{d\varphi}{dt} = \frac{\partial\varphi}{\partial q} \frac{\partial H}{\partial p} - \frac{\partial\varphi}{\partial p} \frac{\partial H}{\partial q} \quad (4.5)$$

$\varphi(p, q)$ resembles the dynamic behavior at any time t . Equation (4.4) represents the evolution of the phase plane as a function of time, and it can be used to determine

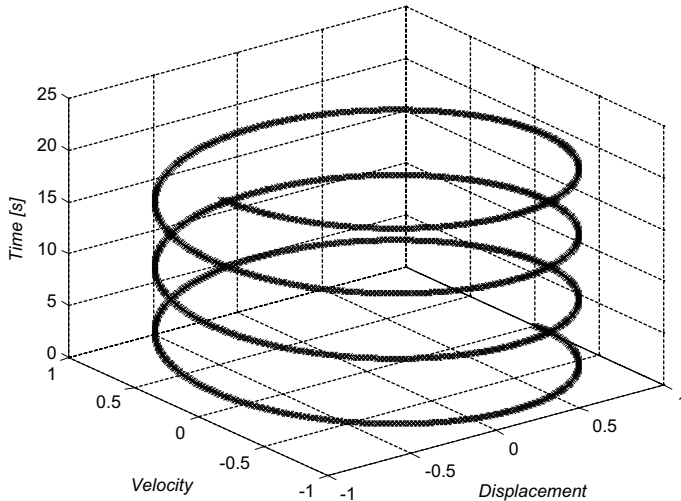


Fig. 4.1 Evolution of the state variables of a linear harmonic system

the dynamic stability of the system. According to Liouville's theorem, the dynamic stability is found when

$$\frac{dH}{dt} = \frac{\partial H}{\partial q}\dot{q} + \frac{\partial H}{\partial p}\dot{p} = 0 \quad (4.6)$$

In other words, this implies that the volume of the phase plane will be preserved in time.

Assuming the linear momentum only depends on the velocity; then the phase plane describes the relation between two state variables (velocity and position). Therefore, the representation of the time evolution of an autonomous system is a trajectory that never crosses with itself. The output signal of a dynamic system contains a sequence of regular and irregular behaviors that can be classified as deterministic and random; deterministic response have a define spectral representation; meanwhile the random response has a random spectrum pattern, for example, a Gaussian noise. Figure 4.1 is an example of a single degree of freedom system with a harmonic response ($\dot{p} + kq = 0$ and $\dot{q} = \frac{p}{m}$). The phase plane is represented in Fig. 4.2. The trajectory of a deterministic system has a predictable and privileged direction, and a nonlinear stationary system has no irregularities. Therefore, a nonlinear system that shows irregular paths will quickly be identified. There are several techniques for evaluating the phase plane. Fountain et al. [5] proposed to use the correlation dimension and false nearest neighbor. This technique is helpful for time-series with a fixed time-delay parameter.

The evaluation of the stability of a system requires the development of analytical techniques such as the Recurrence Plot. The phase plane by itself is unable to predict

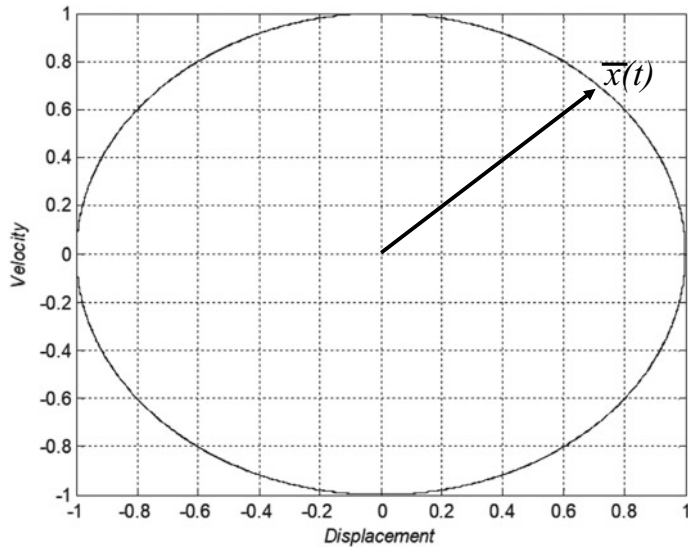


Fig. 4.2 Phase plane of a linear harmonic system

the evolution, and it only defines the shape of the dynamic system, but it cannot provide a quantitative analysis of the dynamics of the system.

Other systems are also analyzed with the phase plane and the Recurrence Plot. In general, they are represented as time series, and the state variables are obtained numerically, the first derivative is estimated by shifting the time series (Takens' theorem).

4.3 Recurrence Plot

The trajectory along the phase plane can be represented as a discrete vector (Fig. 4.2)

$$\bar{x}(t) = [\bar{x}_1, \bar{x}_2, \dots, \bar{x}_n] \quad (4.7)$$

The vector $\bar{x}(t)$ represents a state of the system at time t , and it transforms the phase plane into an abstract mathematical base. Besides, the dynamic behavior of the system is easier analyzed in this new mathematical base; thus, If the system has a steady state harmonic response, and the period is τ , then $\bar{x}_1(t) = \bar{x}_n(t + \tau)$ (one loop in Fig. 4.1).

A system recurs if it returns to a previous state, meaning that a state condition will occur again at a certain period. Such recurrence is a fundamental characteristic of any dynamical systems, and a method for identifying these characteristics is the

Recurrence Plot. In the introduction, it was explained that the Eckmann et al. [2] defined the Recurrence Plot as a graphical representation of a matrix calculated as:

$$R_{ij} = \begin{cases} 1 : \bar{x}_i = \bar{x}_j & i, j = 1, \dots, N \\ 0 : \bar{x}_i \neq \bar{x}_j \end{cases} \quad (4.8)$$

where N is the number of state vectors in the time array. However, due to numerical truncations or measurement deviations, the vectors cannot be identical; thus, the definition is modified as

$$R_{ij} = \begin{cases} 1 : |\bar{x}_i - \bar{x}_j| < \varepsilon, & i, j = 1, \dots, N \\ 0 : |\bar{x}_i - \bar{x}_j| > \varepsilon, \end{cases} \quad (4.9)$$

where ε is a tolerance value. The tolerance should be less than 10% of the mean diameter of the phase plane, or five times larger than the standard deviation of the observational noise.

It has been recognized that recurrences are part of one of three classes of asymptotic invariants: Growth of the number of orbits, types of recurrence, and the asymptotic distribution and statistical behavior of the orbits. The growth of orbits is related to the topology of the entropy of the system, and it describes nonlinearities and chaos.

The Recurrence Plot describes the time-evolution of the system and enables the calculation of future states given a state at a particular moment. In mechanical systems, the phase plane has to be determined from the solution of the differential equations, or measurements of the dynamic response. Whereas, in other systems represented by a single time series, the phase plane can be constructed using the time delay method. One of the significant challenges of the application of the Recurrence Plot is the calculation of the phase plane. Actual data include transients, nonlinear responses, and noise, and, if the data is recorded with an accelerometer, the time series must be integrated numerically because the time delay method produces significant uncertainties. Therefore, the limitation arises from the integration method.

4.3.1 Characteristics of the Recurrence Plot

The Recurrence Plot is always symmetric (due to its definition) and has a main diagonal, which is the identity of each vector. Figure 4.3 shows the recurrence plot of a single degree of freedom system with a harmonic response. In this case, the diagonal has a bandwidth equivalent to the value of the tolerance. The selection of the tolerance is critical because it modifies the topology of the Recurrence Plot, if ε is small, the plot will eliminate almost all of the recurrence and the topology will be almost flat (empty). If ε is too large, the plot will display almost every adjacent point and it will create a topology with artificial figures that are not related to any dynamic characteristic of the system.

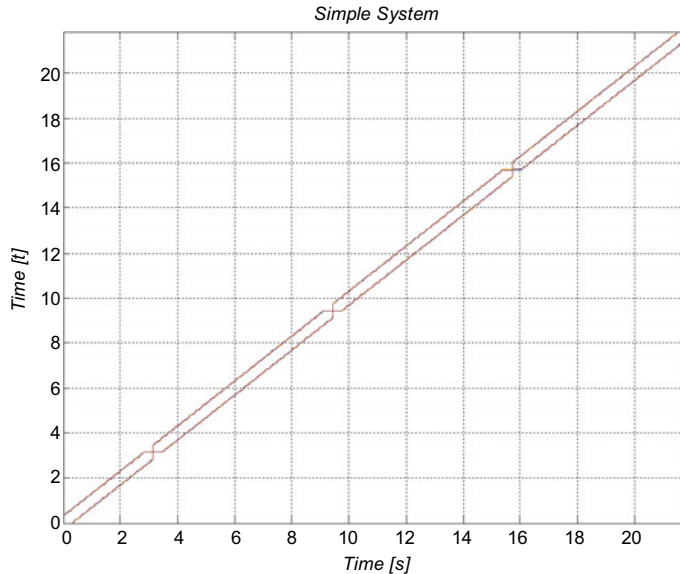


Fig. 4.3 Recurrence plot of a linear harmonic system

The Recurrence Plot provides the basis for analyzing nonlinear dynamic systems. These analyses are classified as Recurrence Quantification Analysis and are computed with different parameters. These parameters are described next:

Recurrence Rate measures the average of recurrence points in the plot

$$RR = \frac{1}{N^2} \sum_{i,j}^N R_{ij} \quad (4.10)$$

Determinism is a measure of the percentage of recurrence point that lay in a diagonal

$$DET = \frac{\sum_{l=1}^N \min_l IP(l)}{\sum_{l=1}^N IP(l)} \quad (4.11)$$

where, l is the index of the corresponding diagonal, $P(l)$ is the histogram of the diagonal. For example, the system of Fig. 4.3 has a $DET = 1$.

(DET) gives information on the deterministic nature of the system. A chaotic system tends to have none or very short diagonals in contrast to periodic or quasi-periodic dynamics which tend to form regular diagonals parallel to the central diagonal along with a mixture of short and long diagonals.

Liminality is the percentage of recurrence points that create a vertical line. The example of Fig. 4.3 has a $LAM = 0$.

$$LAM = \frac{\sum_{v=v}^N \min_{l=1}^N vP(v)}{\sum_{l=1}^N vP(v)} \quad (4.12)$$

where, v is the index of the corresponding vertical line, $P(v)$ is the histogram of the vertical line.

Other two quantities that characterize a Recurrence Plot are the length of the longest diagonal and the length of the longest vertical.

The longest diagonal is calculated as:

$$L_M = \max\{l_i\} \quad (4.13)$$

And the longest vertical line is:

$$V_M = \max\{v_i\} \quad (4.14)$$

The Shannon entropy is a measurement of the disorder in the phase plane. The phase plane of a linear deterministic and periodic system will be smooth; therefore, its Shannon entropy will be almost zero. In the case of a nonlinear deterministic system, the Shannon entropy will be finite. Moreover, a non-deterministic and noisy system, the entropy will be almost infinite. The Shannon entropy is calculated as:

$$E = - \sum_1^N P_i \ln(P_i) \quad (4.15)$$

where $P_i = P(x_j = x_i)$ is the relative frequency, it is calculated as the ratio of diagonal with non-recurrence points divided by the number of recurrent points [48].

Besides the quantification of the distribution of the values within the R_{ij} matrix, the Recurrence Plots have specific topologies and textures that characterize the dynamics of the system.

4.3.2 Topology and Texture

The main characteristic of the Recurrence Plot is its diagonal. The interpretation of diagonals is that the trajectory along the phase plane returns to the same point at regular time intervals (first period). If there are only diagonals in the plot, it means that the system is periodic or quasi-periodic. The amount of time determines the length of each diagonal that a trajectory lays over similar regions of the phase plane. The length of the diagonals is related to the predictability of the dynamic system,

meaning that a particular state the system will be repeated continuously at constant time intervals. The contrary occurs if the system is chaotic. When the diagonal are tilted from the main diagonal, it means that some states are recurrent but at different time intervals. If the distances between the diagonal lines are different, it says that the response has frequency ratios that are irrational.

From the topology of the Recurrence Plot, it is possible to identify the variation of the state variables that describe the dynamics of the system. A summary of the interpretation of the topology is [1].

- A homogeneous Recurrence Plot represents a system that is stationary with short relaxation times.
- Vertical and horizontal lines mean that some states change slowly, have no change during some time, or the system halts or are stuck at a singularity.
- Single and isolated points can occur if states do not persist for any time, if they fluctuate heavily or if they are rare. They also mean that the states vary continuously.
- Adrift is caused by systems with slowly varying parameters, for example, non-stationary systems.
- White represent abrupt changes in the states as well as sudden events or nonstationary conditions. These events can also interrupt the main diagonal, and they can be identified in the time series from the location of the white areas in the Recurrence Plot.
- Drifting systems with slowly varying parameters also cause paling or darkening at the upper or right corners of the Recurrence Plot. Thus, slow changes in the dynamic over time produce lighter areas in the Recurrence Plot.

The Recurrence Plot can be used for reconstructing measuring data and finding the parameters of the system. A method for restoring the state trajectory is finding the time-delay and determining the embedding dimension and the delay parameter τ . Random errors from different paths can be eliminated and the time delay can be estimated using the autocorrelation or the auto covariance function. This method is used in the analysis of systems that can be represented with time series with fixed periods, such as medical signals. Its application in mechanical systems requires the use of other complementary techniques since the time-delay method is not always feasible. In this chapter, the reconstruction of measuring data is not included, only some of the most representative dynamic systems are described next.

4.4 Examples

In this section, the Recurrence Plots of dynamic systems are described. Linear and nonlinear models are included, and experimental data are compared with numerical results. The most simple model was illustrated in Fig. 4.3. A simple one degree of freedom oscillating system has a perfect elliptical phase plane (when normalized the trajectory is circular) and every point recurs at the same period (the specific period),

and the Recurrence Plot only has a single diagonal. This plot is the basis for the following analysis.

4.4.1 Simple Oscillator with Harmonic Excitation

The second example is a system with two excitation frequencies. The mathematical model is:

$$\dot{p} + kq = a_0 \cos(\omega_0 t) \quad (4.16)$$

and

$$\dot{q} = \frac{p}{m} \quad (4.17)$$

where $\sqrt{\frac{k}{m}} \neq \omega_0$.

Figure 4.4 shows the evolution of the two state variables (\dot{q} and q). Fig. 4.5 is the phase plane and Fig. 4.6 is the corresponding Recurrence Plot. There are two diagonals, corresponding to the excitation frequency and the natural frequency; the dots along the plot are the instant when the maximum amplitudes coincide, and the horizontal distance between the diagonals is period of the excitation function.

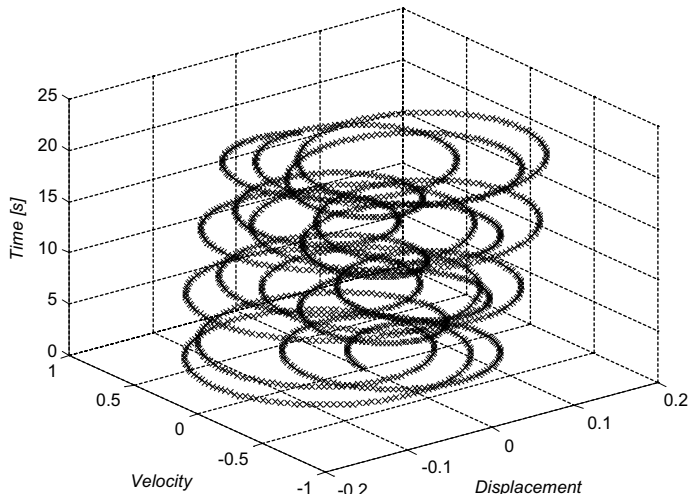


Fig. 4.4 Evolution of the state variable. Simple oscillator with a harmonic excitation

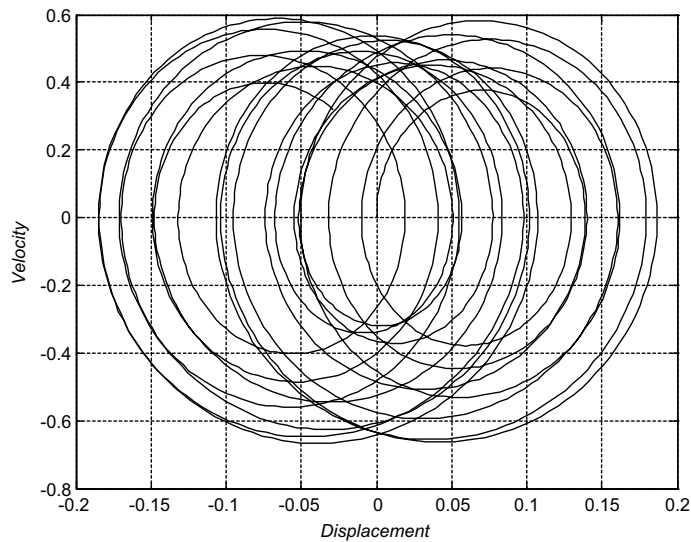


Fig. 4.5 Phase plane of a simple oscillator with a harmonic excitation

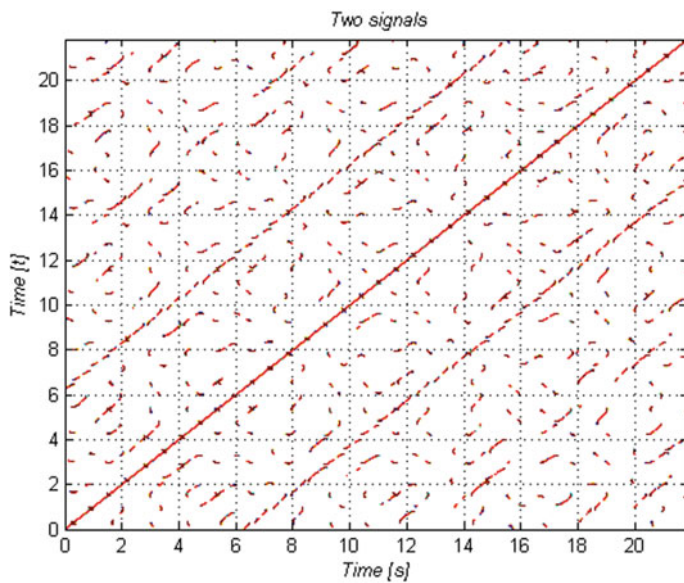


Fig. 4.6 Recurrence plot of a simple oscillator with a harmonic excitation

4.4.2 Nonlinear Pendulum

The next example is the nonlinear pendulum. The dynamic equation is:

$$\ddot{\theta} + \frac{g}{l} \sin(\theta) = 0 \quad (4.18)$$

In this case, the initial condition is close to π and the solution is found numerically. Figure 4.7 shows the evolution of the state variables ($\dot{\theta}$ and θ), although the response is periodic, the function is not harmonic. The phase plane (Fig. 4.8) shows a lemon type shape and the Recurrence Plot shows several characteristics: The main diagonal is not a continuous line, and the square type shapes depend on the ascending or descending position of the pendulum. The vertical lines correspond to the instants when the state variables have a very slow variation; this condition occurs when the pendulum is at the unstable position (Fig. 4.9).

4.4.3 Van der Pol Oscillator

The next example shows the dynamic response of a Van der Pol oscillator. This oscillator is another system that has a nonharmonic periodic response, the dynamic equation is:

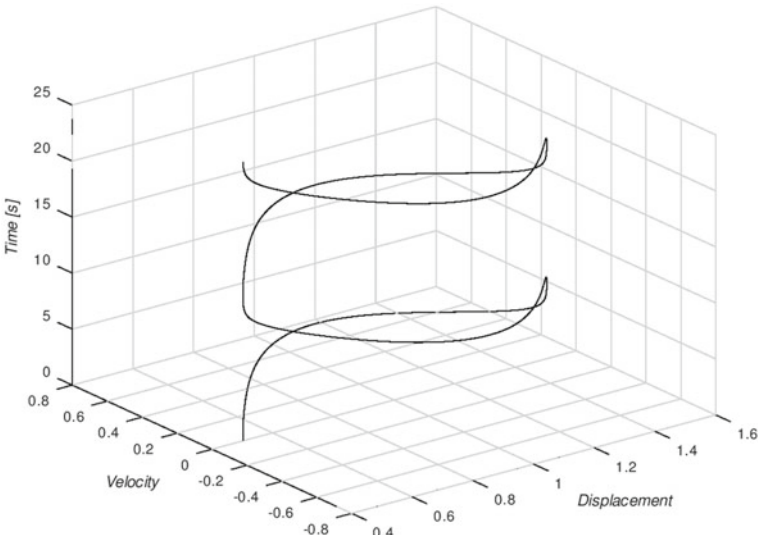


Fig. 4.7 Evolution of the state variables, a nonlinear pendulum

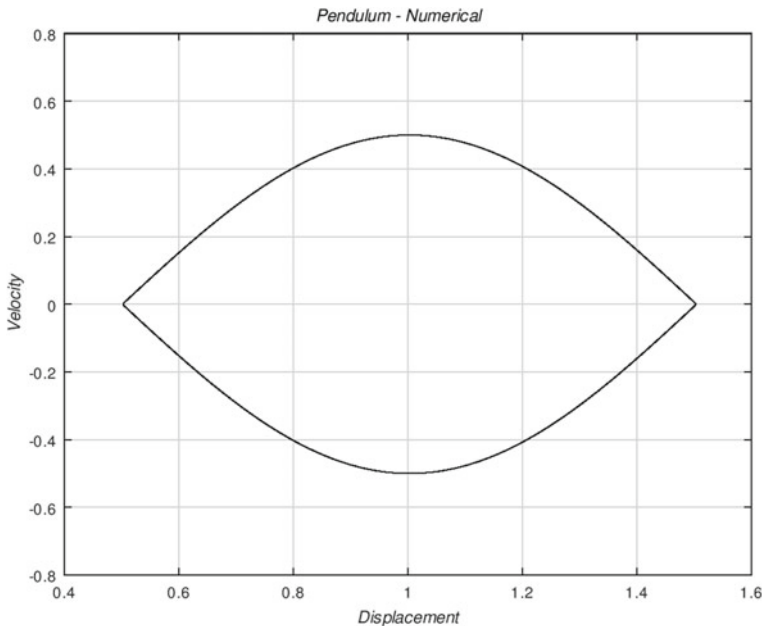


Fig. 4.8 Phase plane of a nonlinear pendulum with initial conditions close to π

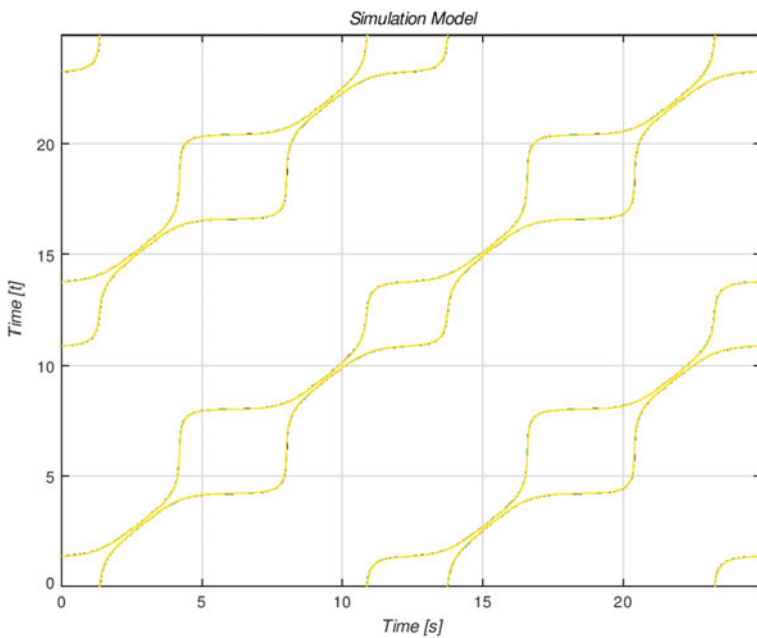


Fig. 4.9 Recurrence plot of a nonlinear pendulum with initial conditions close to π

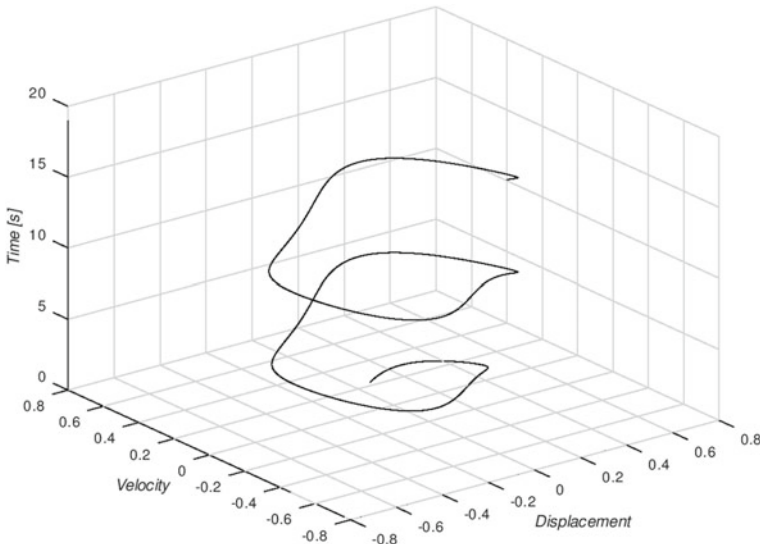


Fig. 4.10 Evolution of the state variables of a Van der Pol oscillator

$$\ddot{x} - \zeta(1 - x^2)\dot{x} + \omega^2 x = 0 \quad (4.19)$$

where ζ and ω are the parameters of the system.

Figure 4.10 describes the evolution of the state variables (\dot{x} and x), and Fig. 4.11 shows the typical phase plane for this oscillator. The Recurrence Plot (Fig. 4.12) displays the nature of the nonlinear response; since the evolution of the state variables follows identical patterns every loop, the Recurrence Plot has dominant diagonals, never the less, the diagonals show periodic discontinuities associated with the changes in the trajectory along the phase plane.

4.4.4 Duffing Oscillator

The Duffing oscillator represents a large number of nonlinear systems that show the jump phenomenon. Several mechanical systems can be approximated using this model. The general equation of motion is (Fig. 4.13):

$$\ddot{x} + \omega_0^2 x + \beta x^3 = f(t) \quad (4.20)$$

The characteristic of this equation is that it has two attractive poles, and the dynamic response jumps from one solution (one pole) to the other. The evolution of the state variables (\dot{x} and x) is presented in Fig. 4.14, and the phase plane in Fig. 4.15.

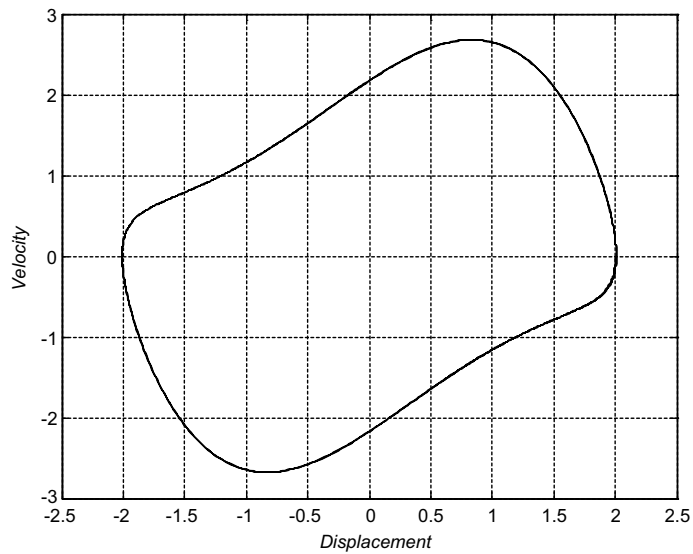


Fig. 4.11 Phase plane of a Van der Pol oscillator

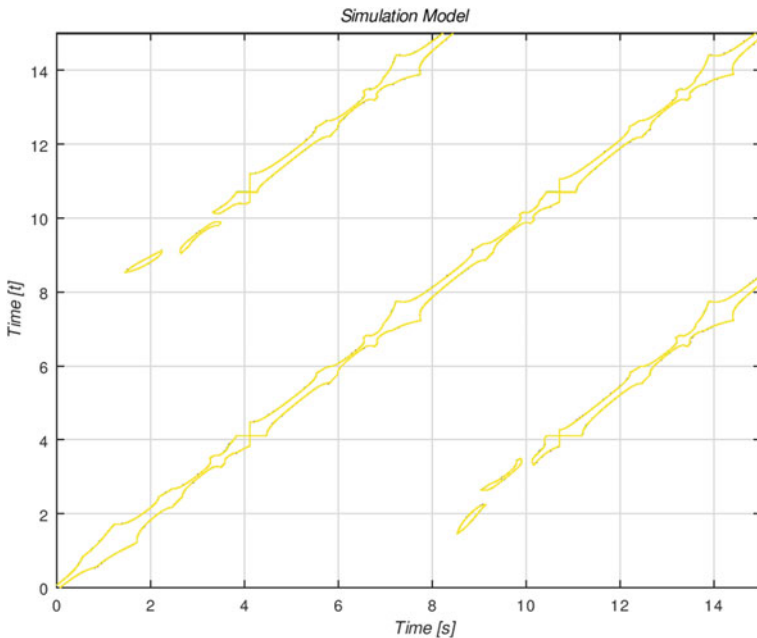


Fig. 4.12 Recurrence plot of a Van der Pol oscillator

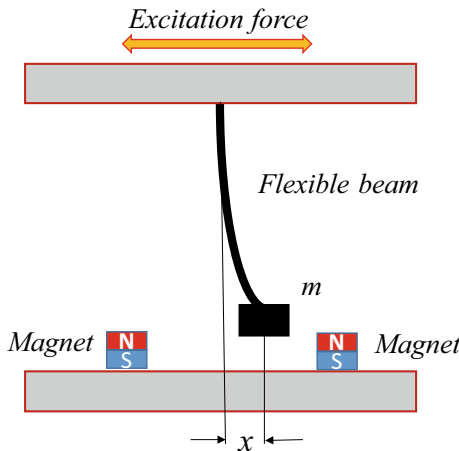


Fig. 4.13 Duffing oscillator

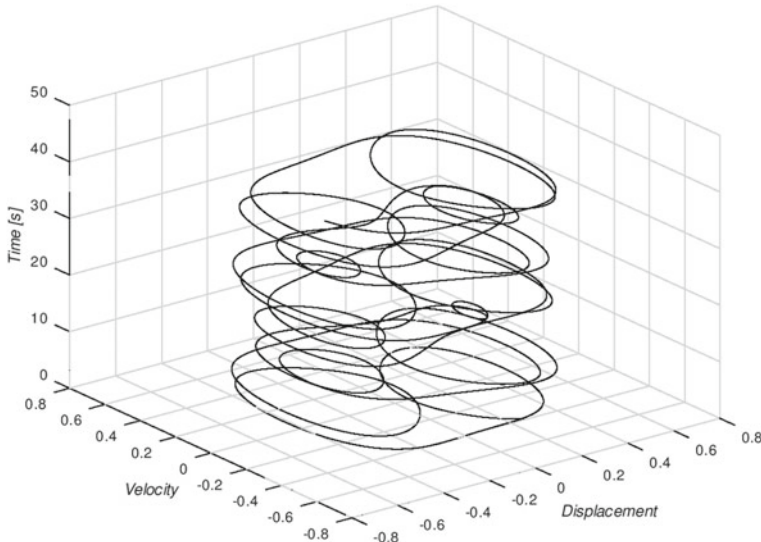


Fig. 4.14 Evolution of the state variables of a Duffing oscillator

The two attractive poles are identified in the phase plane, and they are located at $x = 1.5$ and $x = -1.5$.

The Recurrence Plot (Fig. 4.16) shows events that interrupt the main diagonal and isolated short lines. These patterns represent abrupt changes in the states (jumps) and nonstationary conditions, typical of the Duffing equation.

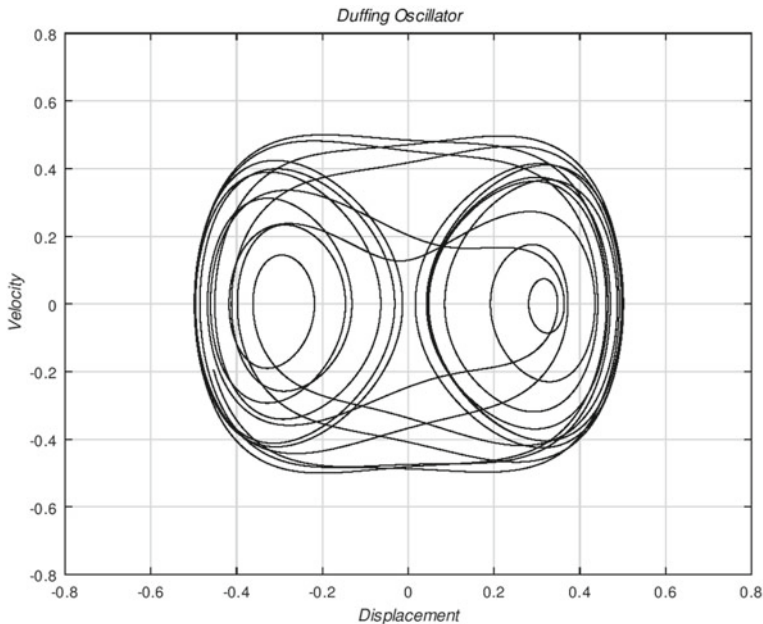


Fig. 4.15 Phase plane of a Duffing equation

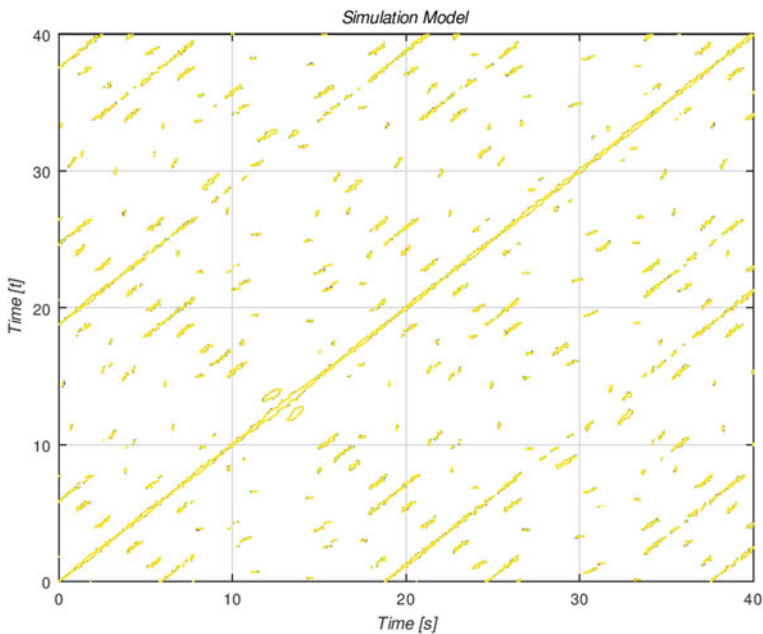


Fig. 4.16 Recurrence plot of a Duffing equation

4.4.5 Cantilever Beam with Large Deformations

Another system that presents a nonlinear behavior is a cantilever beam with large deformations. Figure 4.17 represents a beam and the notation. According to [49], a simplified dynamic equation can describe the nonlinear behavior with a single degree of freedom model.

$$m \frac{\partial^2 w}{\partial t^2} + EI \left(\frac{1485w^5}{385l^7} - \frac{162w^5}{35l^5} + \frac{3w}{l^3} \right) = f(t) \quad (4.21)$$

The numerical solution of this equation gives the evolution of the state variables (\dot{w} and w) as shown in Fig. 4.18. The phase plane is presented in Figs. 4.19 and 4.20 shows the Recurrence Plot. In this figure, it is noticeable the presence of vertical lines, that corresponds to the time when the system has no change or halts. This phenomenon is observed when w reaches displacements similar to the length and stays at that position for a while.

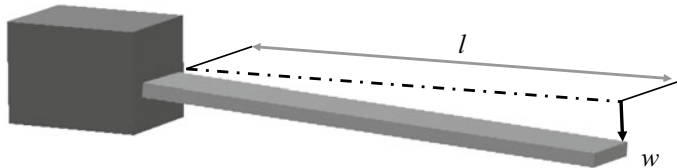


Fig. 4.17 Sketch that represents a cantilever beam

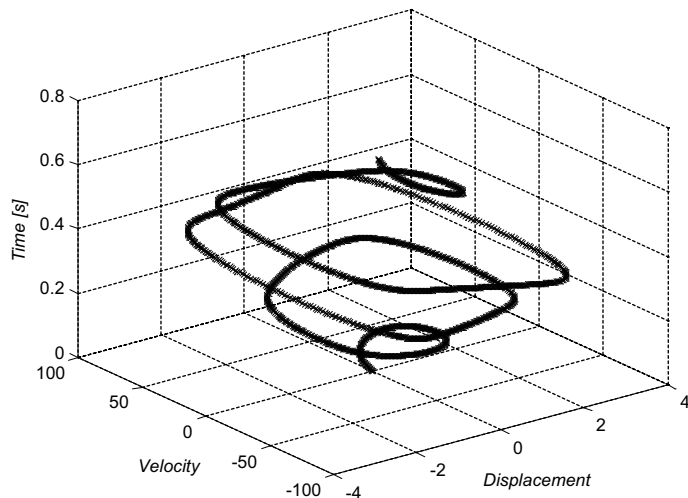


Fig. 4.18 Evolution of the state variables of a cantilever beam with large deformations

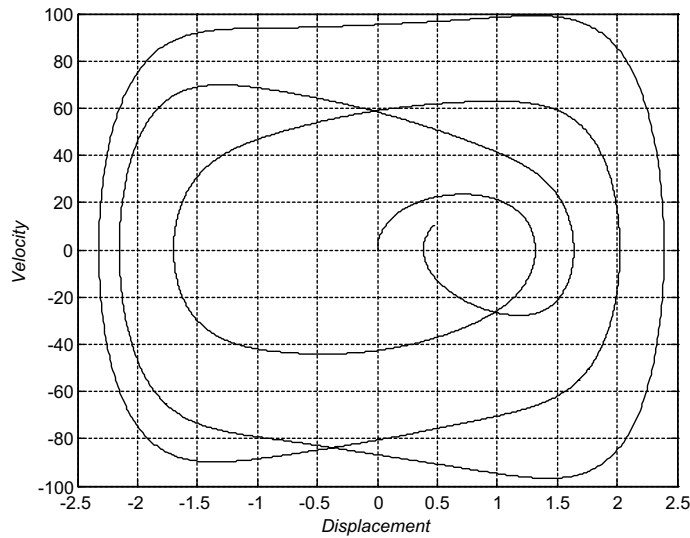


Fig. 4.19 Phase plane of a cantilever beam with large deformations

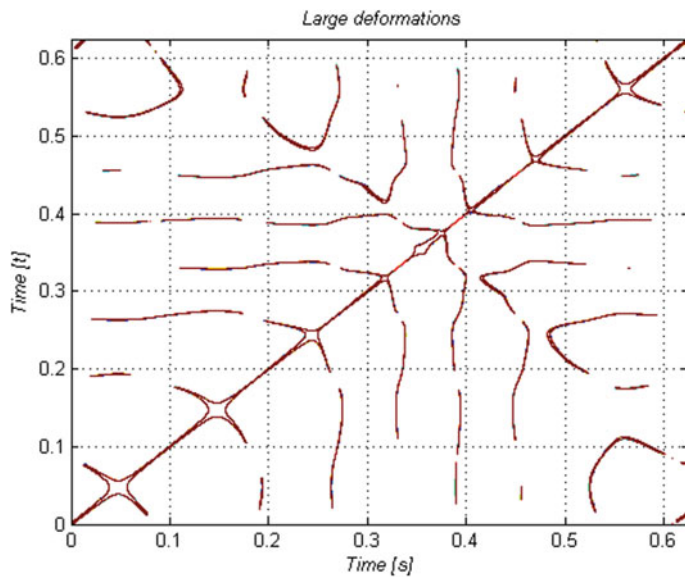
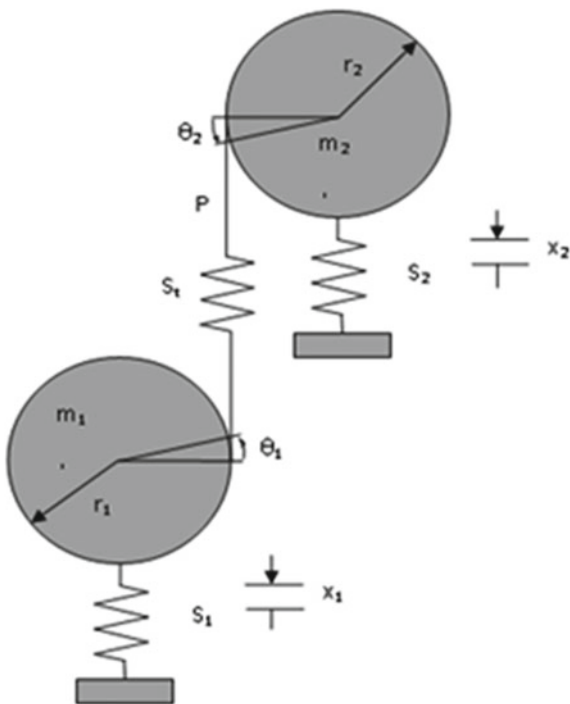


Fig. 4.20 Recurrence plot of a cantilever beam with large deformations

Fig. 4.21 Sketch that represents the dynamic variables of a single stage gearbox



4.4.6 Numerical Analysis of a Gearbox

The following example includes an analytical solution of a single stage gearbox and the study of vibration measurements taken from an experimental transmission. The mathematical model is derived from Fig. 4.21, where the generalized displacements x_1 and x_2 are aligned with the line of action of the gears [50].

$$\begin{aligned} \ddot{x}_1 + \frac{S_1}{m_1}x_1 + \frac{S_t}{m_1}[(x_1 - x_2) + (r_1\theta_1 + r_2\theta_2)] &= \frac{P_1(t)}{m_1} \\ \ddot{x}_2 + \frac{S_2}{m_2}x_2 - \frac{S_t}{m_2}[(x_1 - x_2) + (r_1\theta_1 + r_2\theta_2)] &= \frac{P_2(t)}{m_2} \\ \ddot{\theta}_1 + \frac{S_t r_1}{J_1}[(x_1 - x_2) + (r_1\theta_1 + r_2\theta_2)] &= \frac{r_1 P_e(t)}{J_1} \\ \ddot{\theta}_2 - \frac{S_t r_2}{J_2}[(x_1 - x_2) + (r_1\theta_1 + r_2\theta_2)] &= \frac{-r_2 P_e(t)}{J_2} \end{aligned} \quad (4.22)$$

The first solution that is a baseline for the analysis is obtained when the stiffness of the supports S_1 and S_2 (bearings) and the gears S_t are assumed to be constant. Figure 4.22 shows the evolution of the state variables \dot{x}_1 and x_1 , and the phase plane is presented in Fig. 4.23. From this figure, it is possible to identify the low and high

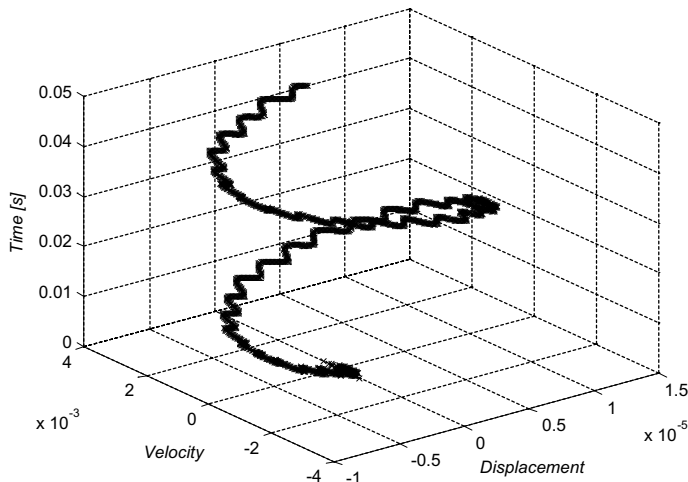


Fig. 4.22 Evolution of the state variables of a gearbox model with constant stiffness

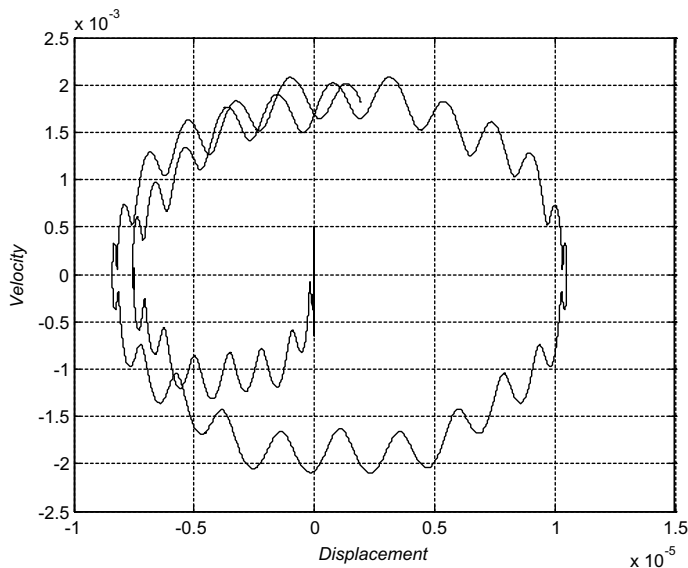


Fig. 4.23 Phase plane of a gearbox model with constant stiffness

frequency that characterized a gearbox. The Recurrence Plot (Fig. 4.24) shows a topology that described systems with high-frequency oscillations.

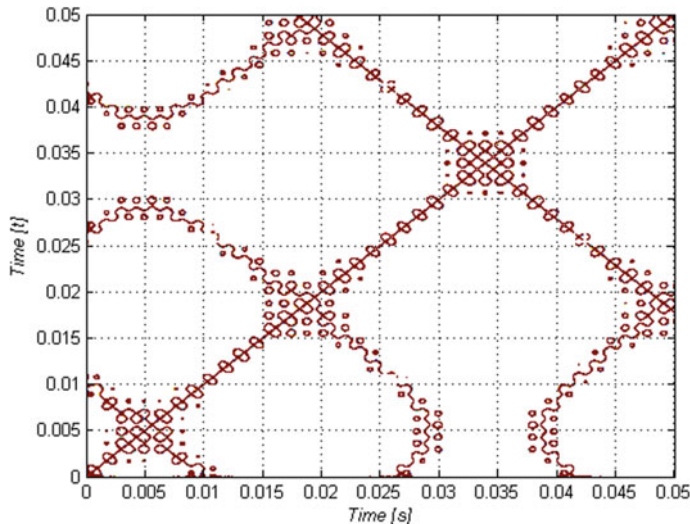


Fig. 4.24 Recurrence plot of a gearbox model with constant stiffness

The second solution corresponds to a gearbox with nonlinear stiffness. The stiffness of the gear mesh (S_t) is estimated as:

$$S_t = \begin{cases} 2Eb\operatorname{tan}\left(\frac{\alpha}{2}\right)^3(n+1), & 0 < \theta < \frac{2\pi}{N}(m_p - n) \\ 2Eb\operatorname{tan}\left(\frac{\alpha}{2}\right)^3(n+1), & \frac{2\pi}{N}(m_p - n) < \theta < \frac{2\pi}{N} \end{cases} \quad (4.23)$$

where E is the elastic modulus, b is the gear width and α is the angle for the maximum point of contact (in general $\alpha = 30^\circ$). m_p is the contact ratio, n is the minimum number of teeth in contact and N is the total number of teeth in the pinion. The analytical solution is found numerically, and the results show a characteristic nonlinear behavior. Figure 4.25 presents the evolution of the state variables \dot{x}_1 and x_1 , and Fig. 4.26 is the phase plane; it is clear that the system has two attracting poles. Figure 4.27 is the Recurrence Plot, the main diagonal shows discontinuities and there are several isolated dots. This behavior is similar to the solution of a Duffing equation.

4.4.7 Analysis of the Experimental Data of a Gearbox

An experimental test rig was built to corroborate the dynamic behavior and the vibrations on the gearbox housing were measured [51]. The acceleration signals were numerically integrated and the state variables were estimated from the experimental data. Numerical integration is an important topic of research since the integration

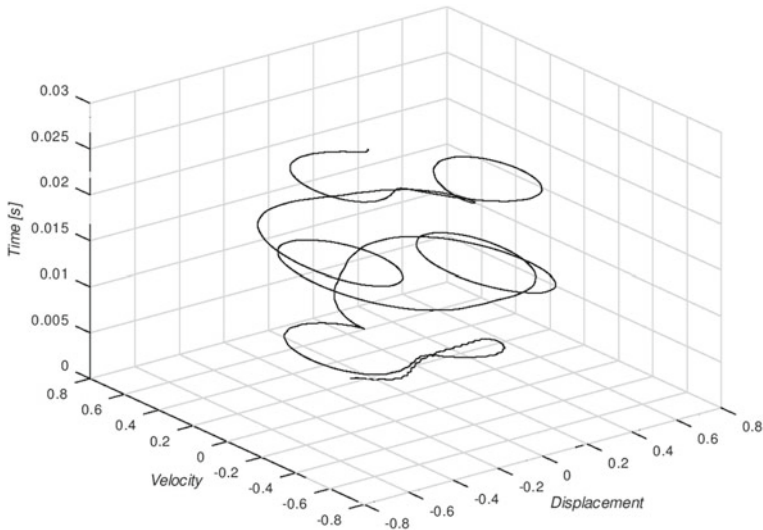


Fig. 4.25 Evolution of the state variables of a gearbox model with nonlinear stiffness

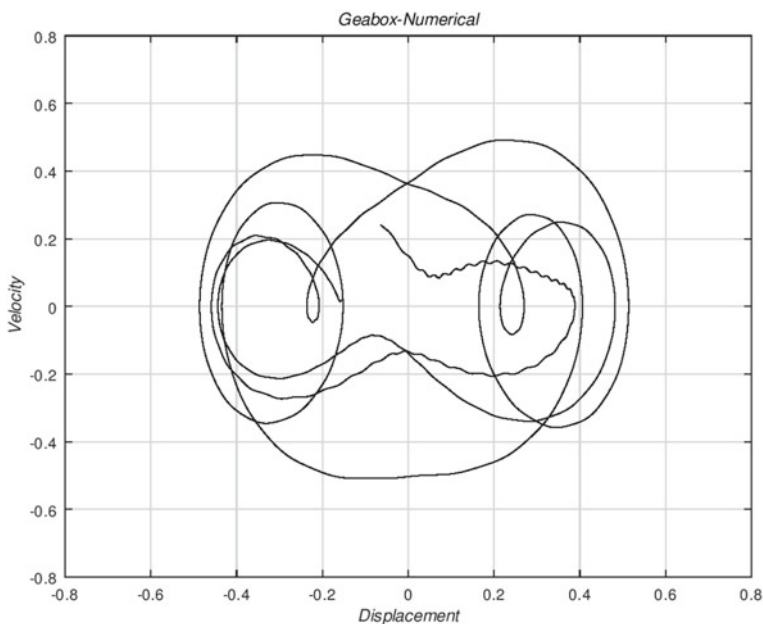


Fig. 4.26 Phase plane of a gearbox model with nonlinear stiffness

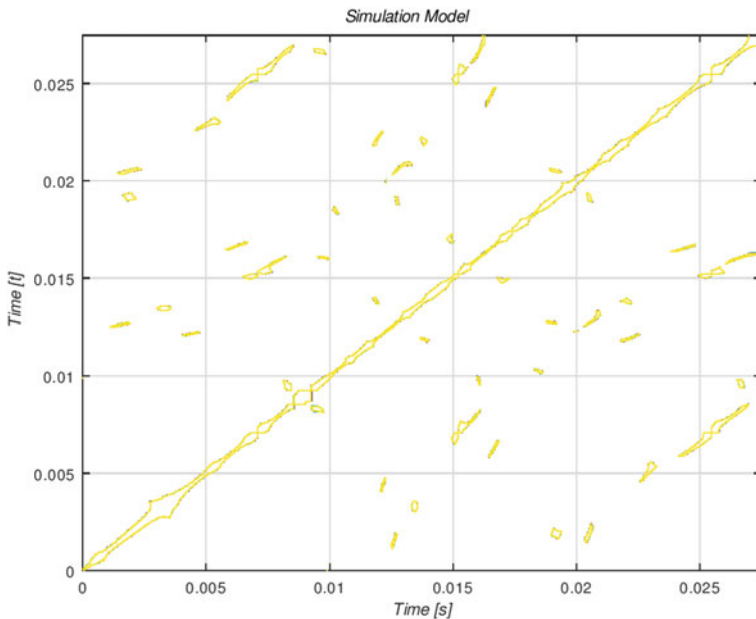


Fig. 4.27 Recurrence plot of a gearbox model with nonlinear stiffness

method is very sensitive to noisy data. The time delay method produced distortions and artificial signals that were absent in the original data. It was found that the most effective method was piece-wise integration. Figure 4.28 shows the evolution of the state variables and Fig. 4.29 presents the phase plane. From this figure, it is clear that the system displays two attractive poles and several high-frequency oscillations. The Recurrence Plot (Fig. 4.30) shows excellent discontinuities along the main diagonal, and a second diagonal that is interrupted, which means that the system has sudden changes or interruptions. Figure 4.30 is an excellent example of the application of the Recurrence Plot for the identification of nonlinear behaviors and the estimation of the system parameters.

4.4.8 Numerical Analysis of a Rotor Rubbing the Housing

The last example is the analysis of a rotor rubbing the housing. The phenomenon is a failure condition frequently found in the operation of turbomachinery. Several researchers have studied this phenomenon, but most of the analytical model cannot predict the actual behavior. The mathematical model presented by Mushinska and Goldman [52, 53] is analyzed with the Recurrence Plot to understand the nature of this failure. The mathematical model is based on the following sketch (Fig. 4.31).

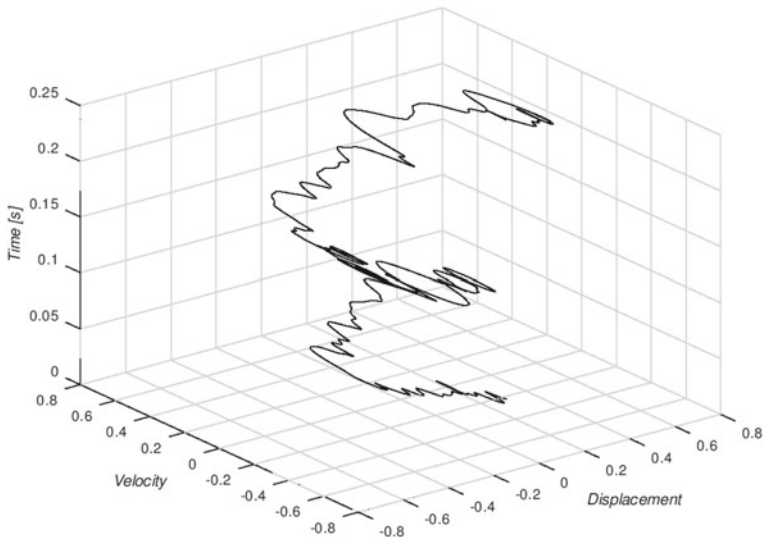


Fig. 4.28 Evolution of the state variables of a gearbox, measured data

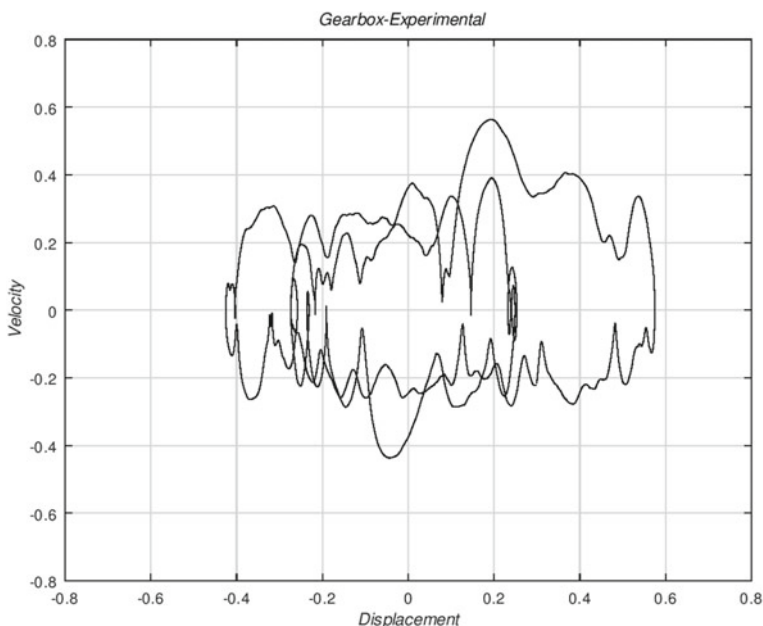


Fig. 4.29 Phase plane of a gearbox, measured data

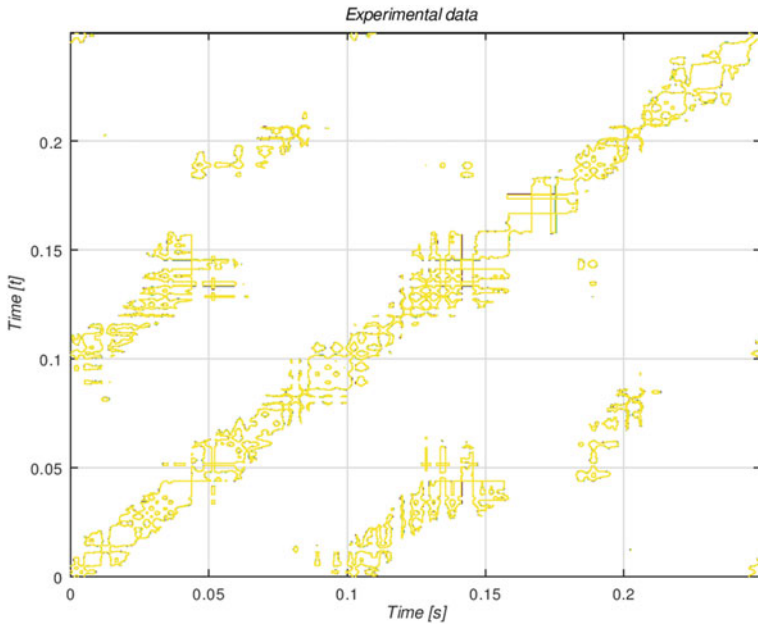


Fig. 4.30 Recurrence plot of a gearbox, measured data

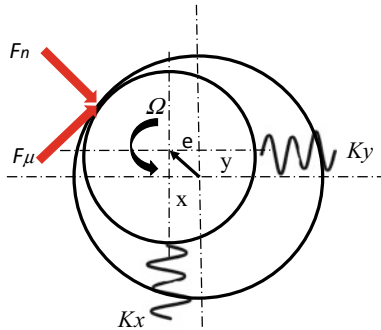


Fig. 4.31 Sketch for the analysis of a rotor rubbing the housing

The model presented by Muszynska [52] is:

$$M\ddot{z} + (D + \delta D_f)\dot{z} + Kz + \delta K_f(z - ce^{j\psi}) + j\delta F_\mu \left(1 + \frac{r}{|z|}\right) e^{j\psi} = ma\omega^2 e^{j(\omega t + \phi)} \quad (4.24)$$

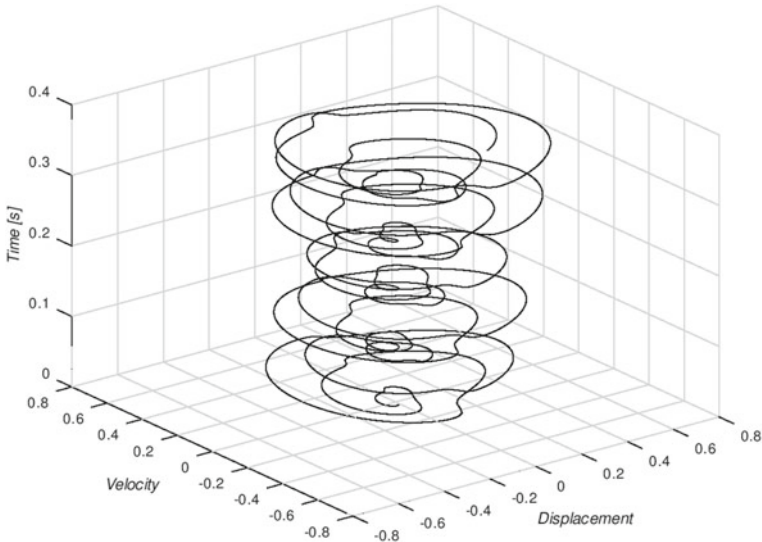


Fig. 4.32 Evolution of the state variables, Muszynska's model for rotor rubbing

where

$$z = x + jy \quad (4.25)$$

$$\tan(\psi) = \frac{y}{x} \quad (4.26)$$

and

$$F_\mu = D_c(\dot{\psi}|z| + \Omega r) + \mu \left[D_f \frac{d|z|}{dt} + K_f(|z| - c) \right] \text{sign}(\dot{\psi}|z| + \Omega r) \quad (4.27)$$

In this model, the stiffness of the system is modified by adding the rigidity of the housing during contact. It is also assumed that the friction force changes the damping of the system. The solution of the model is solved numerically and Fig. 4.32 shows the evolution of the state variables (\dot{x} and x). Figure 4.33 presents the phase plane; it is evident the asymmetry and the sudden changes in the trajectory of the state. The Recurrence Plot (Fig. 4.34) presents diagonals that are interrupted and dots that follow specific patterns that are perpendicular to the main diagonal.

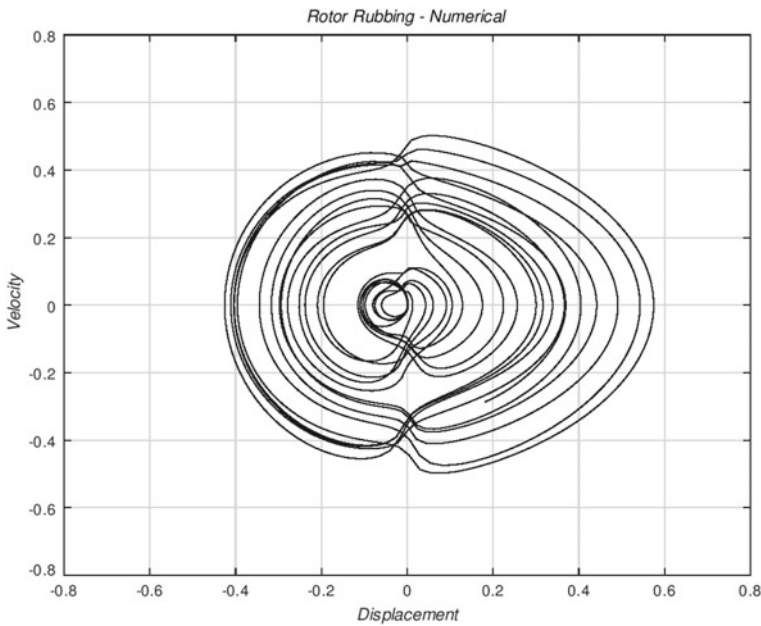


Fig. 4.33 Phase plane, Muszynska's model for rotor rubbing

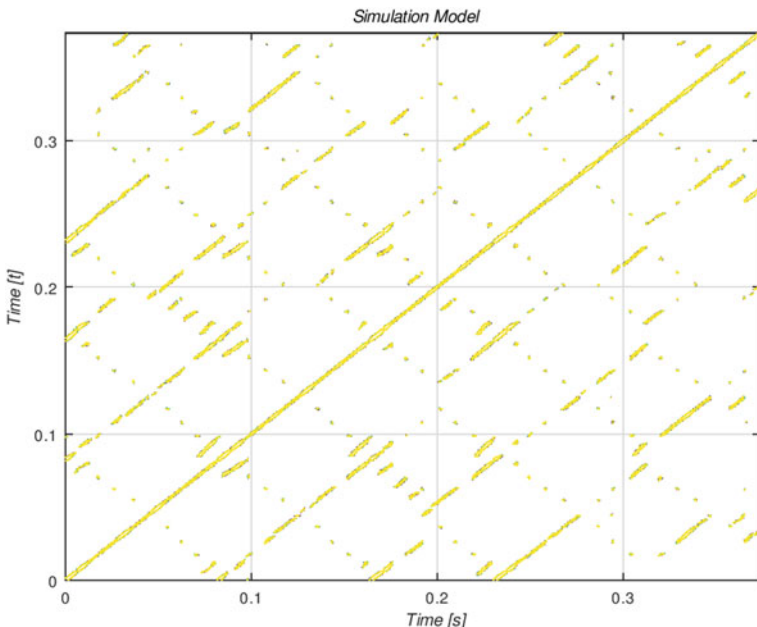


Fig. 4.34 Recurrence plot, Muszynska's model for rotor rubbing

4.4.9 Analysis of the Experimental Data of a Rotor Rubbing the Housing

The rotor rubbing was reproduced in an experimental rig. The rotor with a single unbalanced mass was set in a position that hit a fixed surface. The surface was instrumented with a force sensor, and the bearings were instrumented with two accelerometers. The accelerometer data was recorded, and the state variables were obtained integrating the measurements. The same integration procedure, as in the gearbox example was used. Figure 4.35 shows the evolution of the state variables and Fig. 4.36 shows the phase plane. It is clear that the trajectory of the numerical solution is different from the measured data. The Recurrence Plot (Fig. 4.37) has a single diagonal with many discontinuities and there are two shadows at the corners, which are due to the drifting of the system.

4.4.10 Quantitative Analysis

Previous examples are quantified with the Shannon entropy. The Shannon entropy distinguish the statistical variations among the systems. Table 4.1 describes the model and its Shanon entropy. The table shows that the system with larger disorder, and the numerical analysis gives and estimation of the level of nonlinearity of each system.

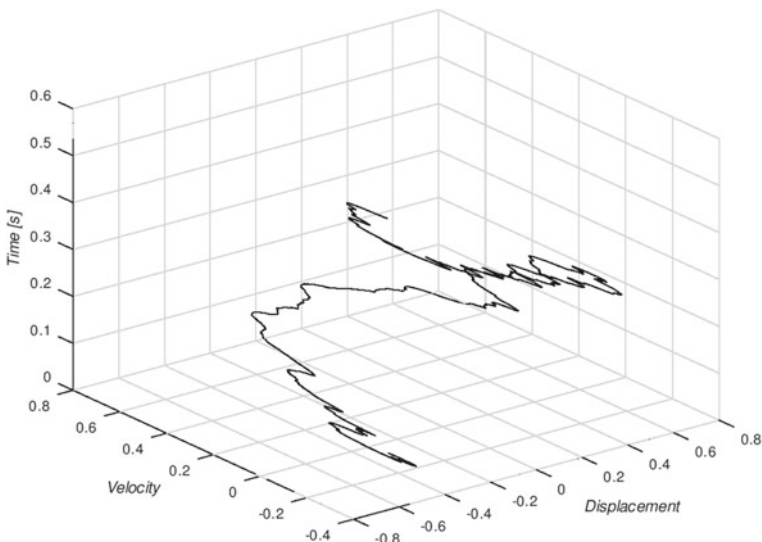


Fig. 4.35 Evolution of the state variables of a rotor rubbing the housing, experimental data

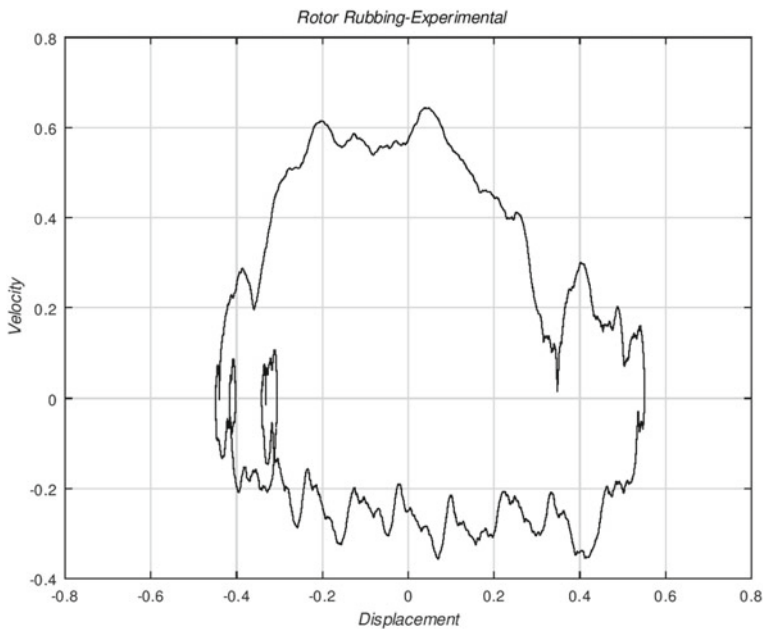


Fig. 4.36 Phase plane of a rotor rubbing the housing, experimental data

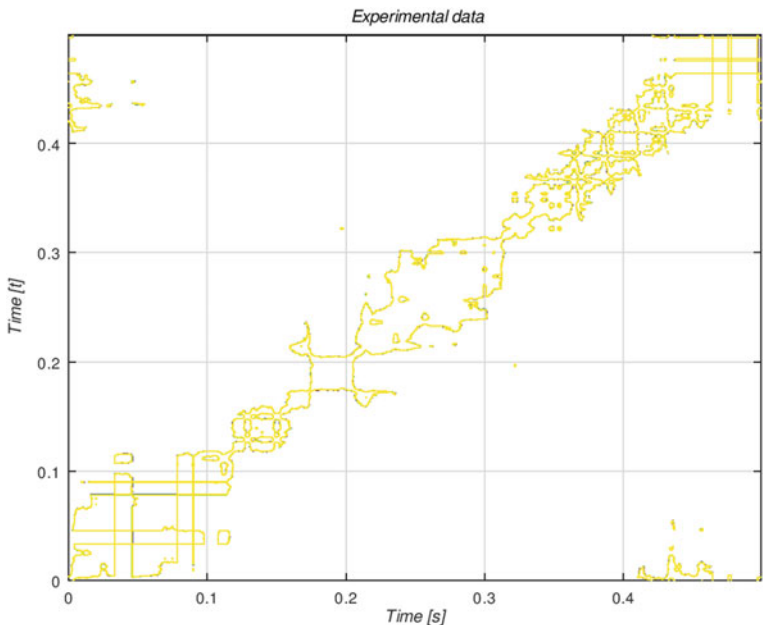


Fig. 4.37 Recurrence plot of a rotor rubbing the housing, experimental data

Table 4.1 Recurrence quantification analysis

Case	Shannon entropy
Simple Harmonic oscillator	0.003138
Duffing Oscillator	0.068420
Van der Pol oscillator	0.13480
Muszinka model	0.06357
Nonlinear Pendulum	0.29268

The evolution of the Shannon entropy is an indication of the changes in the state variables during a specific period, therefore, monitoring the Shannon entropy can be used for predicting failures in mechanical systems.

4.5 Conclusions

Recurrence Plots is a powerful tool for analyzing the dynamic behavior of nonlinear mechanical systems. It comprises the basic concepts of a dynamic system and simplifies the analysis of the energy variations (within the system) since it is based on the phase plane. Recurrence is related to the ability of a system to maintain a state condition along a specific cycle; therefore, the Recurrence Plot produces graphical displays that represent variations of this ability, and it can be used to relate this state changes with the nature of the nonlinear response, thus allowing identifying the parameters of the system. The Recurrence Plot has some limitations, one is the relationship between the topology and the characteristics of the system response, this relationship can be determined only taking previous solutions as a reference, and these solutions are obtained from analytical models. The other problem is the construction of the phase plane from measurement data. Practically, the most common dynamic measurements are obtained with accelerometers, but the structure of the phase plane requires the integration of the data. For this purpose, all the integration methods (numerically or electronically) filter the signal and reduces the resolution of the phase plane. Nevertheless, the Recurrence Plot is a simple technique that has a high potential for analyzing nonlinear systems and predicting unexpected conditions, or changes in the system configuration, such failures on the mechanical components.

Although the analysis of nonlinear, non-stationary systems with the Recurrence Plot has been applied a long time ago, its application to mechanical system is relatively new, and there are specific examples in the literature. Therefore, it is an area of opportunity for practical analysis of a mechanical system, and it could become a new technique for predicting failures in machinery.

The sensitivity and simplicity of the Recurrence Plot were explained, and the mathematical background and quantification tools were described. Analytical and experimental solutions show the goodness of the method, and they helped to illustrate

the relationship between the topology of the Recurrence Plot and the nature of the system.

Future work should look for integrations methods for experimental data and methods for automating the analysis to the topologies, beyond the application of the quantitative tools.

References

1. Webber, C.L., Loana, C., Marwan, N. (eds.): Recurrence Plots and Their Quantifications: Expanding Horizons. In: Proceedings of the 6th International Symposium on Recurrence Plots, June 2015
2. Eckmann, J., Ollifson, S., Ruelle, D.: Recurrence plots of dynamical systems. *Eur. Lett.* **4**(9), 973–977 (1987)
3. Marwan, N., Webber, C.L.: Mathematical and computational foundations of recurrence quantifications. In: Marwan, N., Webber, C.L. (eds.) *Recurrence Quantification Analysis*, pp. 3–43. Springer International Publishing, Switzerland (2015)
4. Thiel, M., Romano, M., Kurths, J.: Spurious structures in recurrence plots induced by embedding. *Nonlinear Dyn.* **44**, 299–305 (2006)
5. Fontaine, S., Dia, S., Renner, M.: Nonlinear friction dynamics on fibrous materials, application to the characterization of surface quality. Part I: Global characterization of phase spaces. 625–646 (2011)
6. Faure, P., Lesne, A.: Estimating Kolmogorov entropy from recurrence plots. In: Webber, C.L., Marwan, N. (eds.) *Recurrence Quantification Analysis*, pp. 45–63. Springer International Publishing, Switzerland (2015)
7. Leonardi, G.: A method for the computation of entropy in the recurrence quantification analysis of categorical time series. *Phys. A* **512**, 824–836 (2018)
8. Kwuimy, C., Samadani, M., Nataraj, C.: Bifurcation analysis of a nonlinear pendulum using recurrence and statistical methods: applications to fault diagnostics. *Nonlinear Dyn.* **76**, 1963–1975 (2014)
9. Ramdani, S., Bouchara, F., Lagarde, J., Lesne, A.: Recurrence plots of discrete-time Gaussian stochastic processes. *Phys. D* **330**, 17–31 (2016)
10. Spiegel, S., Schultz, D., Marwan, N.: Approximate recurrence quantification analysis (aRQA) in code of best practice. In: Schultz, D., Marwan, N. (eds.) *Recurrence Plots and Their Quantification: Expanding Horizons*, pp. 113–135. Springer International Publishing, Switzerland (2016)
11. Sipers, A., Borm, P., Peeters, R.: Robust reconstruction of a signal from its unthresholded recurrence plot subject to disturbances. *Phys. Lett. A* **381**(6), 604–615 (2017)
12. Tang, L., Lv, H., Yang, F., Yu, L.: Complexity testing techniques for time series data: a comprehensive literature review. *Chaos Solitons Fractals* **81**, 117–135 (2015)
13. Pham, T.D., Yan, H.: Spatial-dependence recurrence sample entropy. *Phys. A* **494**, 581–590 (2018)
14. Girault, J.-M.: Recurrence and symmetry of time series: application to transition detection. *Chaos Solitons Fractals* **77**, 11–28 (2015)
15. Belaire-Franch, J., Contreras, D.: Recurrence plots in nonlinear time series analysis: free software. *J. Stat. Softw.* **7**(9), 1–18 (2002)
16. Carrión, A., Miralles, R.: New Insights for testing linearity and complexity with surrogates: a recurrence plot approach. In: Webber, C.L. (ed.) *Recurrence Plots and Their Quantifications: Expanding Horizons*. Springer Proceedings in Physics, pp. 91–112 (2016)
17. Le Bot, O., Mars, J.I., Gervaise, C.: Similarity matrix analysis and divergence measures for statistical detection of unknown deterministic signals hidden in additive noise. *Phys. Lett. A* **379**(40–41), 2597–2609 (2015)

18. Schultz, D., Spiegel, S., Marwan, N., Albayrak, S.: Approximation of diagonal line based measures in recurrence quantification analysis. *Phys. Lett. A* **379**(14–15), 997–1011 (2015)
19. Feeny, B.F., Lin, G.: Fractional derivatives applied to phase-space reconstructions. *Nonlinear Dyn.* **85**–99 (2004)
20. Lin, G., Feeny, B., Das, T.: Fractional derivative reconstruction of forced oscillators. *Nonlinear Dyn.* **55**, 239–250 (2009)
21. Feeny, B.F., Liang, J.W.: Phase-space reconstructions and stick-slip. *Nonlinear Dyn.* **39**–57 (1997)
22. Viana, E., Rubinger, R., Albuquerque, H., Dias, F., Oliveira, A., Ribeiro, G.: Periodicity detection on the parameter-space of a forced Chua's circuit. *Nonlinear Dyn.* 385–392 (2012)
23. Batista, C.A.S., Szezech, J.D., Batista, A.M., Macau, E.E.N., Viana, R.L.: Synchronization of phase oscillators with coupling mediated by a diffusing substance. *Phys. A* **470**, 236–248 (2017)
24. Jeevarekha, A., Sabarathinam, S., Thamilmaran, K., Philominathan, P.: Analysis of 4D autonomous system with volume-expanding phase space. *Nonlinear Dyn.* **84**, 2273–2284 (2016)
25. Prakash, J., Roy, S.B.K.: The simplest 4-D chaotic system with line of equilibria, chaotic 2-torus and 3-torus behaviour. *Nonlinear Dyn.* **89**(3), 1845–1862 (2017)
26. Kiss, Z., Hudson, J.L.: Synchronization analysis of coupled noncoherent oscillators. **2**, 135–149 (2006)
27. Jana, D., Agrawal, R., Kumar, R.: Top-predator interference and gestation delay as determinants of the dynamics of a realistic model food chain. *Chaos Solitons Fractals* **69**, 50–63 (2014)
28. Kuwimy, C.A.K., Kadji, H.G.E.: Recurrence analysis and synchronization of oscillators with coexisting attractors. *Phys. Lett. A* **378**(30–31), 2142–2150 (2014)
29. Kuwimy, C.A.K., Nataraj, C.: Recurrence and Joint Recurrence Analysis of Multiple Attractors Energy Harvesting System (2015)
30. Kuwimy, C.A.K., Nataraj, S.A.A.C.: Characterization of the vibration transmitted in the human arm using selected recurrence quantification parameters. *Nonlinear Dyn.* **88**(4), 2873–2887 (2017)
31. Syta, A., Litak, G.: Vibration Analysis in Cutting Materials, pp. 279–290 (2014)
32. Elias, J., Namboothiri, V.N.N.: Cross-recurrence plot quantification analysis of input and output signals for the detection of chatter in turning. *Nonlinear Dyn.* **76**, 255–261 (2014)
33. Stender, M., Tiedemann, M., Hoffmann, N., Oberst, S.: Impact of an irregular friction formulation on dynamics of a minimal model for brake squeal q. *Mech. Syst. Signal Process.* **107**, 439–451 (2018)
34. Chelidze, T., Lursmanashvili, O., Matcharashvili, N., Zhukova, N., Mepharidze, E.: High-order synchronization of stick-slip process: experiments on spring-slider system. *Nonlinear Dyn.* **59**, 259–275 (2010)
35. Chelidze, T., Matcharashvili, T.: Dynamical Patterns in Seismology, pp. 291–334 (2014)
36. Litak, G., Górska, G., Mosdorff, R., Rysak, A.: Study of dynamics of two-phase flow through a minichannel by means of recurrences. *Mech. Syst. Signal Process.* **89**, 48–57 (2017)
37. Zhai, L., Zong, Y., Wang, H., Yan, C., Gao, Z.: Characterization of flow pattern transitions for horizontal liquid–liquid pipe flows by using multi-scale distribution entropy in coupled 3D phase space. *Phys. A* **469**, 136–147 (2017)
38. Xiong, H., Shang, P., Bian, S.: Detecting intrinsic dynamics of traffic flow with recurrence analysis and empirical mode decomposition. *Phys. A* **474**, 70–84 (2017)
39. Tang, J., Wang, Y., Wang, H., Zhang, S., Liu, F.: Dynamic analysis of traffic time series at different temporal scales: a complex networks approach. *Phys. A* **405**, 303–315 (2014)
40. Vlahogianni, E.I., Karlaftis, M.G.: Comparing traffic flow time-series under fine and adverse weather conditions using recurrence-based complexity measures. *Nonlinear Dyn.* 1949–1963 (2012)
41. Ukherjee, S., Ray, R., Samanta, R., Khondekar, M.: Nonlinearity and chaos in wireless network traffic. *Chaos Solitons and Fractals* **96**, 23–29 (2017)

42. Joelle, E., Bialonski, S., Marwan, N., Kurths, J., Geier, C., Lehnertz, K.: Evaluation of selected recurrence measures in discriminating pre-ictal and inter-ictal periods from epileptic EEG data. *Phys. Lett. A* **380**(16), 1419–1425 (2016)
43. Puthanmadam, N., Hyttinen, J.: Characterization of dynamical systems under noise using recurrence networks: application to simulated and EEG data. *Phys. Lett. A* **378**(46), 3464–3474 (2014)
44. Yan, J., Wang, Y., Ouyang, G., Yu, T., Li, X.: Using max entropy ratio of recurrence plot to measure electrocorticogram changes in epilepsy patients. *Phys. A* **443**, 109–116 (2016)
45. Saha, D., Shaw, P.K., Ghosh, S., Janaki, M.S., Iyengar, A.N.S.: Quantification of scaling exponent with crossover type phenomena for different types of forcing in DC glow discharge plasma. *Phys. A* **490**, 300–310 (2018)
46. Craciunescu, T., Murari, A.: Geodesic distance on Gaussian manifolds for the robust identification of chaotic systems. *Nonlinear Dyn.* **86**(1), 677–693 (2016)
47. Jáuregui, J.C.: Phase diagram analysis for predicting nonlinearities and transient responses. In: Baddour, N. (ed.) *Recent Advances in Vibrations Analysis*, pp. 27–46. InTech (2011)
48. Letellier, C.: Estimating the Shannon entropy: recurrence plots versus symbolic dynamics. *Phys. Rev. Lett.* **96**, 55–60 (2006)
49. Gonzalez-Cruz, C.A., Jauregui-Correa, J.C., Herrera-Ruiz, G.: Nonlinear response of cantilever beams due to large geometric deformations: experimental validation. *Stroj. Vestnik/J. Mech. Eng.* **62**(3), 187–196 (2016)
50. Jauregui-Correa, J.C.: The effect of nonlinear traveling waves on rotating machinery. *Mech. Syst. Signal Process.* **39**(1–2), 129–142 (2013)
51. González-Cruz, C.A., Jáuregui-Correa, J.C., Domínguez-González, A., Lozano-Guzmán, A.: Effect of the coupling strength on the nonlinear synchronization of a single-stage gear transmission. *Nonlinear Dyn.* **85**(1), 123–140 (2016)
52. Muszynska, A.: *Rotordynamics*. CRC Press, Taylor & Francis Group, Boca Raton (2005)
53. Goldman, P., Muszynska, A., Bently, D.E.: Due rotor-to-stator. *6*(2), 91–100 (2000)

Chapter 5

Passive Vibration Control Using Viscoelastic Materials



D. A. Rade, J.-F. Deü, D. A. Castello, A. M. G. de Lima and L. Rouleau

Abstract This chapter is devoted to the use of viscoelastic materials as a strategy intended for passive vibration control in mechanical systems. It provides a review of the theoretical foundations underlying the constitutive modeling of the viscoelastic behavior, and the association of constitutive models with modern numerical resolution procedures, especially the finite element method. This currently enables the accurate prediction of the dynamic behavior of rather complex structural systems featuring viscoelastic dampers, duly accounting for the particular characteristics of the viscoelastic behavior, namely the memory effect and the dependence of stiffness and damping properties on frequency and temperature. Other relevant aspects considered are: (i) model condensation techniques, intended to reduce the computation cost involved in the evaluation of the response of viscoelastic structures using finite element models with large numbers of degrees-of-freedom; (ii) the identification of viscoelastic constitutive models from experimental data. In addition, some applications of viscoelastic materials to structures of engineering interest are presented to illustrate the use of some techniques discussed.

D. A. Rade (✉)

Mechanical Engineering Division, Aeronautics Institute of Technology,
São José dos Campos, Brazil

e-mail: rade@ita.br

J.-F. Deü · L. Rouleau

LMSSC, CNAM, Paris, France
e-mail: jean-francois.deu@cnam.fr

L. Rouleau

e-mail: lucie.rouleau@cnam.fr

D. A. Castello

Department of Mechanical Engineering, Federal University of Rio de Janeiro,
Rio de Janeiro, Brazil
e-mail: castello@mecanica.ufrj.br

A. M. G. de Lima

School of Mechanical Engineering, Federal University of Uberlândia,
Rio de Janeiro, Brazil
e-mail: amglima@ufu.br

5.1 Introduction

Viscoelastic materials have long been used as an efficient means of mitigating vibration and noise. They have been successfully applied, either as surface treatments or discrete devices, in a variety of engineering systems such as industrial equipment, automobiles, airplanes, artificial satellites, household appliances, robotic systems and civil constructions [1, 2].

Despite the considerable maturity of the technology related to the use of viscoelastic materials, challenges still exist and further research is needed to face them. In fact, it is recognized that commercially available viscoelastic materials, most frequently present in the form of soft polymers, exhibit broad ranges of mechanical properties (mainly stiffness and damping), which strongly depend on operational and environmental factors, such as vibration frequency, temperature, pre-stress, aging and moisture [3]. As a result, the variability involved in the performance of viscoelastic devices is expected to be high, and must be properly accounted for both in the design and maintenance planning of viscoelastic dampers.

In addition, the analysis and design of viscoelastically damped structures in the modern scope of computer-aided design, especially using finite element models, requires appropriate procedures to conciliate accuracy of the response predictions and computation effectiveness in terms of memory and time requirements. Hence, in the last decades, a large number of studies have been devoted to the proposition and investigation of the performance of viscoelastic constitutive models capable of representing accurately the viscoelastic behavior in rather complex situations (such as three-dimensional stress states), accounting for the operational and environmental influences mentioned above. Particular interest has been directed towards the association of those constitutive models with finite element discretization [4]. In parallel, much effort has been devoted to the development of efficient computational procedures, especially model condensation techniques, with the objective of alleviating the computational costs involved in computations based on finite element models with large numbers of degrees-of-freedom. High computation costs are frequently prohibitive in applications in which a large number of response evaluations are necessary, such as optimization and uncertainty propagation. Clearly, effective condensation techniques must be capable of dealing with the particular characteristics of viscoelastic materials, especially the dependency of the material properties on frequency, temperature and pre-stress.

Given the technological importance of viscoelastic materials, the large amount of knowledge available in the literature, and the current interest in pursuing developments and applications on this topic, the present chapter, based on the perspectives and previous experience of the authors, provides a review of some important scientific and technological aspects related to passive vibration control in engineering, exploring viscoelastic materials.

The chapter is organized as follows: following this introductory section, Sect. 5.2 is devoted to the fundamentals of linear viscoelasticity. It includes the description and formulation underlying the characterization of the mechanical behavior of vis-

coelastic materials in frequency and time domains, the influence of environmental and operational factors on the viscoelastic behavior, and the constitutive models in both domains. Section 5.3 addresses procedures for parameter identification of viscoelastic models from experimental data. Special emphasis is placed on a Bayesian stochastic approach. Section 5.4 is devoted to the association of viscoelastic constitutive models with finite element resolution procedures. Techniques intended for the condensation of viscoelastic finite element models aiming at alleviating computational costs are also addressed in this section. Section 5.5 presents some examples of modeling and numerical analyses of mechanical systems featuring viscoelastic elements, serving to illustrate many of the concepts previously presented as applied to problems of industrial interest. Finally, Sect. 5.6 brings general conclusions and perspectives.

5.2 Fundamentals of Linear Viscoelasticity

5.2.1 *Mechanical Behavior of Viscoelastic Materials in Time and Frequency Domains*

As the name implies, viscoelastic behavior can be regarded as resulting from the combination of two fundamental types of mechanical behavior, namely: (a) purely elastic behavior, exhibited by Hookean materials, for which, assuming unidimensional loading, the applied stress (either normal or shear) and the observed strain are proportional to each other, i.e., $\sigma(t) = E\varepsilon(t)$, where E denotes the material elastic (Young's) modulus; (b) the purely viscous behavior of Newtonian fluids, for which the time rate of the shear strain and the applied shear stress are proportional to each other, i.e., $\tau(t) = \eta\dot{\gamma}(t)$, where η is the coefficient of viscosity of the fluid.

According to Christensen [5], purely elastic materials can store mechanical energy without any dissipation. On the other hand, a Newtonian fluid in a nonhydrostatic stress state exhibits the capacity of dissipating energy, but not of storing it. In viscoelastic materials, part of the work done to deform them can be recovered. Such materials possess a capacity to both store and dissipate mechanical energy. Another distinguishing feature of viscoelastic materials is that their response at a given time is not only determined by the state of loading at the time, but depends on all past states of loading. This implies that viscoelastic materials exhibit a *memory effect*.

The viscoelastic behavior appears in a variety of natural and synthetic materials, which include amorphous and semicrystalline polymers, biological tissues and metals at very high temperatures. From the perspective of noise and vibration control technology, polymeric viscoelastic materials are certainly the most prominent. For these materials, the damping capacity results from the process of relaxation, and recovery of the molecular chains after deformations. Due to the relation between temperature and molecular motions, the mechanical characteristics of viscoelastic materials are shown to be significantly affected by this parameter. In the current state

of development of polymer science, this category of viscoelastic materials can be manufactured to have a wide variety of mechanical properties, which can fulfill the needs identified in a broad range of applications.

The behavior of viscoelastic materials is usually characterized either in time or frequency domain. In time domain, the response of viscoelastic materials can be represented by exploring the well-known Boltzmann Superposition Principle, which can be stated as follows: (a) the response of a viscoelastic specimen is a function of the entire loading history; (b) each increment of load makes an independent and additive contribution to the total deformation.

The application of the Boltzmann's Superposition Principle, in combination with the usual hypotheses adopted in the linear theory of elasticity (material homogeneity and isotropy, linear stress-strain relations and infinitesimal displacements and strains) leads to constitutive laws that establish links between the stress and strain histories in the form of convolution integrals, as follows [5]:

$$\sigma_{ij}(t) = \mathcal{K}_{ijkl}^g(t)\varepsilon_{kl}(0) + \int_0^t \mathcal{K}_{ijkl}^g(t-\tau) \frac{d\varepsilon_{kl}(\tau)}{d\tau} d\tau \quad (5.1)$$

$$\varepsilon_{ij}(t) = \mathcal{K}_{ijkl}^J(t)\sigma_{kl}(0) + \int_0^t \mathcal{K}_{ijkl}^J(t-\tau) \frac{d\sigma_{kl}(\tau)}{d\tau} d\tau \quad (5.2)$$

where $\sigma_{ij}(t)$ and $\varepsilon_{ij}(t)$ denote the components of the symmetric second-order stress and strain tensors, and $\mathcal{K}_{ijkl}^g(t)$ and $\mathcal{K}_{ijkl}^J(t)$ denote the fourth-order *relaxation tensor function* and *creep tensor function*, respectively. The components of these two tensors fully characterize the mechanical behavior of linear viscoelastic materials in time domain.

Figure 5.1 illustrates typical relaxation and creep functions associated to unidirectional stress and strain states.

To extend the formulation to frequency domain, Fourier transformation is applied to Eq. 5.1, assuming null initial conditions, which leads to:

$$\tilde{\sigma}_{ij}(\omega) = \tilde{\mathcal{C}}_{ijkl}(\omega)\tilde{\varepsilon}_{kl}(\omega) \quad (5.3)$$

where ω stands for the circular frequency of motion.

Invoking the symmetry of the stress and strain tensors, Eq. 5.3 can be rewritten in Voigt notation:

$$\tilde{\sigma}(\omega) = \mathbb{C}^*(\omega)\tilde{\varepsilon}(\omega), \quad (5.4)$$

where the contracted notation for stress and strain is defined by the following equivalences:

$$\begin{aligned} \tilde{\sigma} &= [\sigma_{11}, \sigma_{22}, \sigma_{33}, \sigma_{23}, \sigma_{31}, \sigma_{12}]^T \\ \tilde{\varepsilon} &= [\varepsilon_{11}, \varepsilon_{22}, \varepsilon_{33}, 2\varepsilon_{23}, 2\varepsilon_{31}, 2\varepsilon_{12}]^T \end{aligned} \quad (5.5)$$

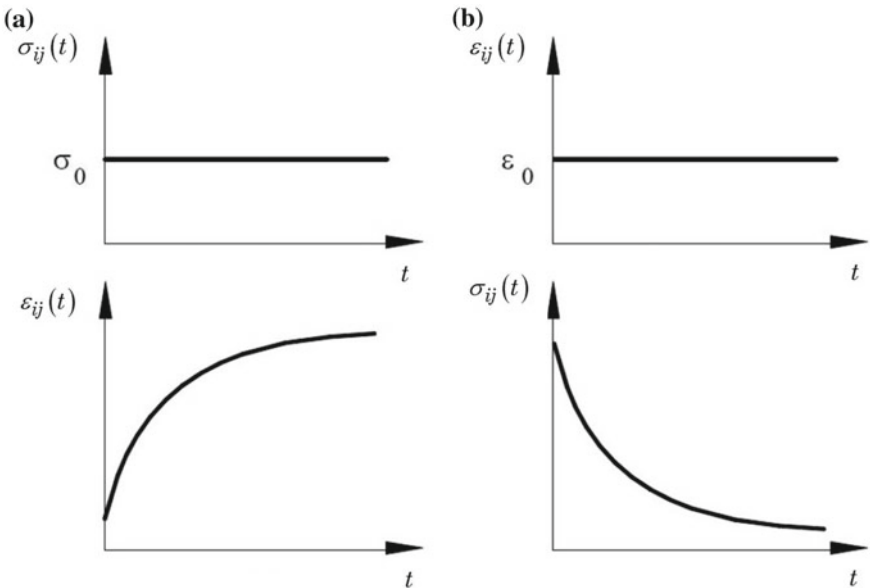


Fig. 5.1 Illustration of a creep function (a) and relaxation function (b)

and $\tilde{\mathbb{C}}$ is a second-order tensor.

In the case of a homogeneous and isotropic material, the stress-strain relation takes on a simple form involving only two independent elastic constants. In the frequency domain, the viscoelastic behaviour can be described by a stiffness tensor whose Lamé coefficients are complex and frequency-dependent¹:

$$\mathbb{C}^*(\omega) = \begin{bmatrix} 2\mu^*(\omega) + \lambda^*(\omega) & \lambda^*(\omega) & \lambda^*(\omega) & 0 & 0 & 0 \\ \lambda^*(\omega) & 2\mu^*(\omega) + \lambda^*(\omega) & \lambda^*(\omega) & 0 & 0 & 0 \\ \lambda^*(\omega) & \lambda^*(\omega) & 2\mu^*(\omega) + \lambda^*(\omega) & 0 & 0 & 0 \\ 0 & 0 & 0 & \mu^*(\omega) & 0 & 0 \\ 0 & 0 & 0 & 0 & \mu^*(\omega) & 0 \\ 0 & 0 & 0 & 0 & 0 & \mu^*(\omega) \end{bmatrix} \quad (5.6)$$

Since the Lamé coefficients are phenomenological constants, it is usually best to express matrix \mathbb{C} as a function of elastic constants which can be directly measured, such as the Young's modulus E , the shear modulus $G (= \mu)$, the bulk modulus K and the Poisson ratio ν . Based on a theoretical study [6], Guillot and Trivett showed that the best pair of elastic constants to measure for complete characterization of a material is (G, K) or (E, K) . In this way, other elastic constants can be computed with maximum accuracy [7]. Using classical conversions between the various elastic parameters and decomposing the strain tensor into a hydrostatic and a deviatoric

¹The Lamé coefficients can depend more generally on various parameters (see Sect. 5.2.1).

parts [8], the stiffness tensor $\mathbb{C}^*(\omega)$ written in terms of shear and bulk moduli is:

$$\mathbb{C}^*(\omega) = K^*(\omega) + G^*(\omega) \begin{bmatrix} 1 & 1 & 1 & 0 & 0 & 0 \\ 1 & 1 & 1 & 0 & 0 & 0 \\ 1 & 1 & 1 & 0 & 0 & 0 \\ 0 & 0 & 0 & 0 & 0 & 0 \\ 0 & 0 & 0 & 0 & 0 & 0 \\ 0 & 0 & 0 & 0 & 0 & 0 \end{bmatrix} \quad (5.7)$$

where $K^*(\omega)$ and $G^*(\omega)$ are the complex and frequency-dependent bulk and shear moduli characterized experimentally (see Sect. 5.2.1). The bulk modulus is related to the hydrostatic part of strain and stress and is associated to changes in volume while the shear modulus is related to the deviatoric part of strain and stress and is associated to changes in shape. In practice, since viscoelastic materials are nearly incompressible materials, the hydrostatic part of the stiffness tensor is often taken as constant. For nearly incompressible materials, assuming a constant bulk modulus usually corresponds to a constant Poisson ratio since the bulk modulus remains several orders of magnitude higher than the shear modulus on a large frequency range [6, 9]. Therefore, the stiffness tensor $\mathbb{C}^*(\omega)$ written in terms of Young's modulus and Poisson ratio becomes:

$$\mathbb{C}^*(\omega) = \frac{E^*(\omega)}{(1+\nu)(1-2\nu)} \begin{bmatrix} (1-\nu) & \nu & \nu & 0 & 0 & 0 \\ \nu & (1-\nu) & \nu & 0 & 0 & 0 \\ \nu & \nu & (1-\nu) & 0 & 0 & 0 \\ 0 & 0 & 0 & \frac{1}{2}-\nu & 0 & 0 \\ 0 & 0 & 0 & 0 & \frac{1}{2}-\nu & 0 \\ 0 & 0 & 0 & 0 & 0 & \frac{1}{2}-\nu \end{bmatrix} \quad (5.8)$$

Assuming a constant bulk modulus also corresponds to shear and Young's moduli having the same frequency-dependence.

The complex modulus $E^*(\omega)$ can be expressed as:

$$E(\omega) = E'(\omega) + iE''(\omega) = E'(\omega) [1 + i\eta(\omega)] \quad (5.9)$$

where $E'(\omega)$ and $E''(\omega)$ are known as the storage modulus and loss modulus, respectively, and $\eta(\omega)$ is the loss factor. The storage modulus is considered as the parameter that quantifies the stiffness of the viscoelastic material, while the loss factor quantifies its damping capacity. Hence, the knowledge of these two properties, as functions of frequency, is necessary for the complete characterization of the mechanical behavior of viscoelastic materials in the frequency domain.

Assuming uniaxial harmonic strain loading (either normal or shear) with frequency ω and amplitude ε_0 , $\varepsilon(t) = \varepsilon_0 e^{i\omega t}$, and steady-state stress response $\sigma(t) =$

$\sigma_0 e^{i\omega t}$, it can be easily demonstrated that the stress-strain relation for any load cycle is represented graphically by an ellipse, as illustrated in Fig. 5.2.

The energy dissipated by the material, mainly under the form of heat, is given by the area confined within the ellipse, which is computed as follows:

$$W_d = \int_0^T \sigma \dot{\varepsilon} dt = E' \eta \varepsilon_0^2 \omega \int_0^{\frac{2\pi}{\omega}} \sin^2 \omega t dt = \pi E' \eta \varepsilon_0^2 = 2\pi \eta W_p \quad (5.10)$$

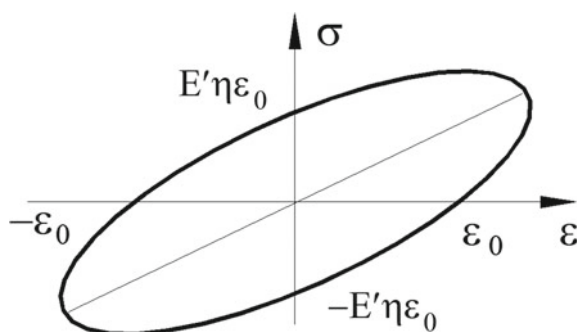
where $W_p = E' \varepsilon_0^2 / 2$ is the maximum strain energy stored in the material during the cycle. Hence, the loss factor can be interpreted as the ratio between the dissipated and stored energies in a cycle, i.e.:

$$\eta = \frac{1}{2\pi} \frac{W_d}{W_p} \quad (5.11)$$

5.2.2 Influence of Environmental and Operational Factors on Viscoelastic Properties

The previous section highlights the memory effect in viscoelastic materials, which is associated to time-dependent or frequency-dependent modulus and loss factor. The representation of both quantities as a function of temperature or frequency (Fig. 5.3) may be considered as consisting of three regions [10]: (i) the glassy state, where the material presents high values of storage modulus and low loss factor, (ii) the glass-rubber transition zone, characterized by a strong variation of the storage modulus and high values of loss factor, (iii) the rubber state, where the loss factor and the storage modulus take low, nearly constant values. The change in state is related to changes in the internal mobility of polymer chains. In practice, viscoelastic materials are selected to operate in the transition or rubberlike phases for optimal damping performance [3].

Fig. 5.2 Typical stress-strain hysteresis loop for viscoelastic materials



From Fig. 5.3, the similarity in the temperature-dependency and the frequency-dependency can be clearly perceived. For amorphous polymers, which constitute a broad class of viscoelastic materials of engineering interest, there is an equivalence between time or frequency effects and temperature effects above T_g , which can be stated as the time-temperature superposition principle [11]. This principle relates

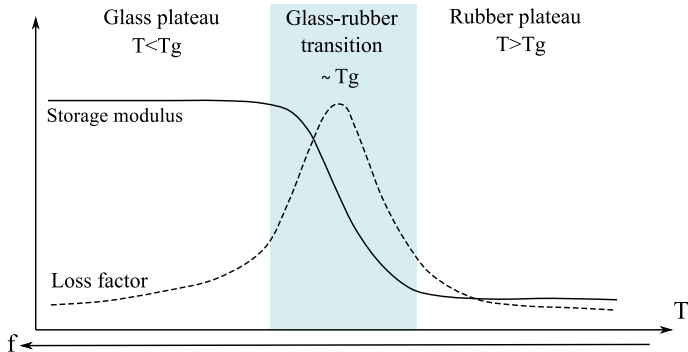


Fig. 5.3 Typical master curves of viscoelastic materials: influence frequency and temperature on the storage modulus and the loss factor

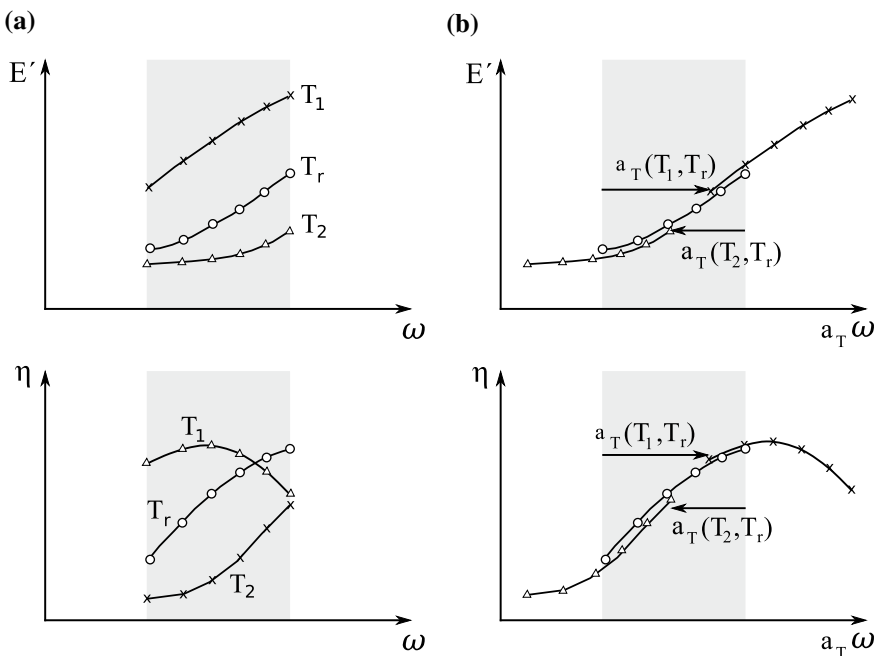


Fig. 5.4 Illustration of the time-temperature superposition principle: **a** isotherms of storage modulus and loss factor at temperatures T_1 , T_2 and T_r ($T_1 > T_r > T_2$), **b** storage modulus and loss factor at the reference temperature of T_r , after application of the shift coefficients

the material response at a given time t (or frequency ω) and a given temperature T to that at a so-called reduced time t_r (or reduced frequency ω_r) and temperature T_r . Expressed in the frequency domain, the frequency-temperature superposition principle can be expressed as follows:

$$\begin{cases} \omega_r = a_T(T, T_r)\omega \\ E'(\omega_r, T_r) = a_T(T, T_r)E'(\omega, T) \\ E''(\omega_r, T_r) = a_T(T, T_r)E''(\omega, T) \end{cases} \quad (5.12)$$

where $a_T(T, T_r)$ are horizontal shift coefficients to be applied to isotherms of storage and loss moduli at a temperature T in order to estimate the material properties at another temperature T_r . As a result, the functions describing the storage modulus and loss factor at various temperatures can be collapsed to form the master curves, as depicted in Fig. 5.4, by applying shifts along the frequency axes.

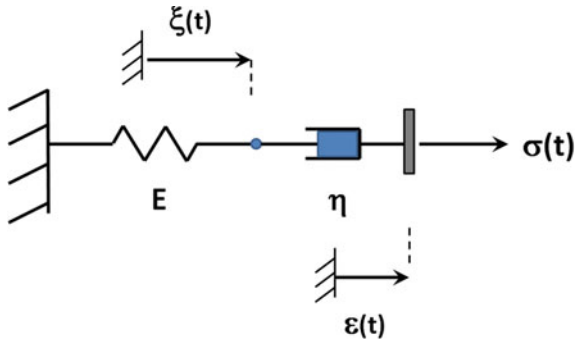
The practical aspects of the frequency-temperature superposition principle is discussed in [10, 12]. Drake and Soovere [13] suggested analytical expressions for the complex shear modulus and shift factors for various commercially available viscoelastic materials as functions of the forcing frequency and temperature. The shift coefficients can be computed in order to respect the causality principle [14].

Other environmental parameters are known to influence the mechanical properties of viscoelastic materials. For instance, the characterization and modeling of the influence of static prestrain on the elastic and dissipative properties of viscoelastic materials have gained increased interest in the past few years [15, 16]. Various experiments indicate an increase of the storage modulus and a decrease of the loss factor with increasing static prestrain. In addition, the static prestrain level is found to affect the frequency-dependency of the loss factor.

The sensitivity of the viscoelastic properties to a variety of parameters proves the importance of defining properly the operating range for viscoelastic damping treatments ahead of the design process.

5.2.3 Viscoelastic Constitutive Models

The use of Eqs. (5.1), (5.2) and (5.3) leads to a quest for relaxation and creep functions which describe the main characteristics observed experimentally for specific viscoelastic materials. Therefore, the process of building mechanical models and the understanding of the role of their parameters in model predictions becomes an important task. One strategy consists in exploiting ideas extracted from phenomenological models called *mechanical analogs*, which are built by the combination of basic mechanical components such as springs and dampers. Next will be presented the Maxwell model, the linear standard solid model, the Generalized Maxwell model and the fractional linear standard solid model.

Fig. 5.5 Maxwell model

5.2.3.1 Maxwell Model

The Maxwell model is comprised of a spring in series with a viscous damper as shown in Fig. 5.5. The constitutive equation based on this model is described as follows

$$\sigma_s(t) = E \xi \quad (5.13)$$

$$\sigma_d(t) = \eta \frac{d}{dt}(\varepsilon - \xi) \quad (5.14)$$

where the subscripts $(\bullet)_s$ and $(\bullet)_d$ denote spring and damper, respectively. As the modeling of the spring and the viscous damper does not take inertia into account, the elastic stress σ_s should be equal to the viscous stress σ_d . Therefore, one gets

$$\sigma(t) = \sigma_d(t) = \sigma_s(t) \quad (5.15)$$

One should highlight that the observable variables in the model shown in Fig. 5.5 are the stress $\sigma(t)$ and the total strain $\varepsilon(t)$. As for the strain $\xi(t)$, it is an internal variable. Therefore, one may reorganize Eqs. (5.13) and (5.14) aiming at writing the constitutive equation in terms of the observable variables $\sigma(t)$ and $\varepsilon(t)$. Firstly, one may reorganize Eq. (5.14) as follows

$$\dot{\sigma}_d(t) = \eta \dot{\varepsilon}(t) - \eta \dot{\xi}(t) \quad (5.16)$$

and replace $\dot{\xi}(t)$ by its value extracted from Eq. (5.13)

$$\sigma(t) = \eta \dot{\varepsilon}(t) - \eta \frac{\dot{\sigma}(t)}{E} \quad (5.17)$$

and finally obtaining the constitutive equation for the Maxwell element as follows

$$\frac{\dot{\sigma}(t)}{E} + \frac{\sigma(t)}{\eta} = \dot{\varepsilon} \quad (5.18)$$

Equation (5.18) is the constitutive equation of the Maxwell model.

One may investigate the predictions provided by the Maxwell model under specific conditions such as creep and stress-relaxation which are of interest when dealing with viscoelastic materials. Concerning creep conditions, one may assume that the stress $\sigma(t)$ is described as follows

$$\sigma(t) = \sigma_0 u(t) \quad (5.19)$$

where $u(t)$ corresponds to the step function defined by

$$u(t) = \begin{cases} 0 & \text{if } t \leq 0 \\ 1 & \text{if } t > 0 \end{cases} \quad (5.20)$$

Applying the Laplace transform to both sides of Eq. (5.18) leads to

$$\frac{s \tilde{\sigma}(s) - \sigma(0)}{E} + \frac{\tilde{\sigma}(s)}{\eta} = s \tilde{\varepsilon}(s) - \varepsilon(0) \quad (5.21)$$

where $\tilde{\sigma}(s)$ denotes the Laplace transform of the function $\sigma(t)$, i.e., $\mathcal{L}\{\sigma(t)\} = \tilde{\sigma}(s)$. Further, assuming that the system is at rest at $t = 0$ with $\sigma(0) = 0$ and $\varepsilon(0) = 0$ and considering that $\mathcal{L}\{u(t)\} = \tilde{U}(s) = \frac{1}{s}$, one may reorganize Eq. (5.21) as shown next

$$\tilde{\varepsilon}(s) = \sigma_0 \left(\frac{1}{s E} + \frac{1}{s^2 \eta} \right) \quad (5.22)$$

Equation (5.22) describes the creep response provided by the Maxwell model written in the Laplace domain. Its time domain representation is obtained by the application of the inverse Laplace Transform to Eq. (5.22), viz.

$$\varepsilon(t) = \sigma_0 \left(\frac{1}{E} + \frac{t}{\eta} \right) u(t) = \sigma_0 \mathcal{K}^J(t) \quad (5.23)$$

where the function $\mathcal{K}^J(t)$ corresponds to the creep kernel associated to the Maxwell model. As for Eq. (5.23) itself, one may highlight some points. The first one concerns the fact that $x(0^+) = \frac{\sigma_0}{E}$ which is the elastic response of the system due to the stress discontinuity at $t = 0$. The second one is that the model predicts a continuous flow of the system at a constant rate $\dot{\varepsilon}(t) = \frac{\sigma_0}{\eta}$ which indicates a fluid-like behavior.

Concerning stress relaxation conditions, one may assume that the strain $\varepsilon(t)$ is described as follows

$$\varepsilon(t) = \varepsilon_0 u(t) \quad (5.24)$$

whose Laplace domain version is $\mathcal{L}\{\varepsilon(t)\} = \tilde{\varepsilon}(s) = \frac{\varepsilon_0}{s}$. Additionally, assuming that the system is in equilibrium at $t = 0$ with $\varepsilon(0) = 0$ and $\sigma(0) = 0$, Eq. (5.21) may be reorganized as follows

$$\tilde{\sigma}(s) = \varepsilon_0 \left(\frac{\eta E}{E + \eta s} \right) \quad (5.25)$$

whose time domain representation is obtained by the application of the inverse Laplace Transform to Eq. (5.25), viz.

$$\sigma(t) = \varepsilon_0 E \exp\left(\frac{-E}{\eta} t\right) u(t) = \varepsilon_0 \mathcal{K}^g(t) \quad (5.26)$$

where the function $\mathcal{K}^g(t)$ corresponds to the stress relaxation kernel associated to the Maxwell model. Equation (5.26) predicts an initial elastic response $\sigma(0^+) = \varepsilon_0 E$ which is the response of the system due to a strain discontinuity at $t = 0$. In addition, the model predicts a stress relaxation behavior of exponential type with a relaxation time $\tau_R = \frac{\eta}{E}$. The fact that the stress relaxation goes to zero indicates a fluid-like behavior.

When one considers general motions or general forces, a natural question is how to compute the system response. Concerning general strain histories $\varepsilon(t)$ for the Maxwell model, the following procedure points a way to make these analyses. Let us come back to Eq. (5.18) and multiply it by an integrating factor $\phi(t)$:

$$\phi(t) \dot{\sigma}(t) + \frac{E}{\eta} \sigma(t) \phi(t) = E \dot{\varepsilon}(t) \phi(t) \quad (5.27)$$

when assuming that the integrating factor is such that $\frac{E}{\eta} \phi(t) = \dot{\phi}(t)$, then one gets $\phi(t) = \exp(E t / \eta)$. Therefore, the following relation holds

$$\frac{d}{dt} (\phi(t) \sigma(t)) = E \phi(t) \dot{\varepsilon}(t) \quad (5.28)$$

whose integration from 0^+ until t leads to

$$\sigma(t) \phi(t) = \phi(0^+) \sigma(0^+) + \int_{0^+}^t E \phi(t') \frac{d\varepsilon(t')}{dt'} dt' \quad (5.29)$$

Considering that $\varepsilon(0^+) = \frac{\sigma(0^+)}{E}$ as in the previous analysis, Eq. (5.29) may be recast as:

$$\sigma(t) = \mathcal{K}^g(t) \varepsilon(0^+) + \int_{0^+}^t \mathcal{K}^g(t - \tau) \frac{d\varepsilon(\tau)}{d\tau} d\tau \quad (5.30)$$

where the operator \mathcal{K}^g is the relaxation kernel associated to this model and which is defined in Eq. (5.26).

As for general stress histories $\sigma(t)$, one may integrate Eq. (5.18) from 0^+ until t :

$$\int_{0^+}^t \frac{d\sigma(\tau)}{d\tau} \frac{1}{E} d\tau + \int_{0^+}^t \frac{\sigma(\tau)}{\eta} d\tau = \varepsilon(t) - \varepsilon(0^+) \quad (5.31)$$

Let us integrate by parts the second integral on the left side of Eq. (5.31) as follows

$$\int_{0^+}^t \frac{\sigma(\tau)}{\eta} d\tau = \frac{(\tau - a')}{\eta} \sigma(\tau) \Big|_{\tau=0^+}^{\tau=t} - \int_{0^+}^t \frac{(\tau - a')}{\eta} \frac{d\sigma(\tau)}{d\tau} d\tau \quad (5.32)$$

where a' does not depend on t . Taking Eq. (5.32) into Eq. (5.31) leads to

$$\varepsilon(t) = \varepsilon(0^+) + \frac{(\tau - a')}{\eta} \sigma(\tau) \Big|_{\tau=0^+}^{\tau=t} + \int_{0^+}^t \left(\frac{1}{E} + \frac{a' - \tau}{\eta} \right) \frac{d\sigma(\tau)}{d\tau} d\tau \quad (5.33)$$

Finally, adopting $a' = t$ and remembering that $\varepsilon(0^+) = \frac{\sigma(0^+)}{E}$ from the previous analysis one may rewrite Eq. (5.32):

$$\varepsilon(t) = \mathcal{K}^J(t)\sigma(0^+) + \int_{0^+}^t \mathcal{K}^J(t-\tau) \frac{d\sigma(\tau)}{d\tau} d\tau \quad (5.34)$$

where $\mathcal{K}^J(t)$ is the creep kernel provided by this model and whose definition is given in Eq. (5.23)

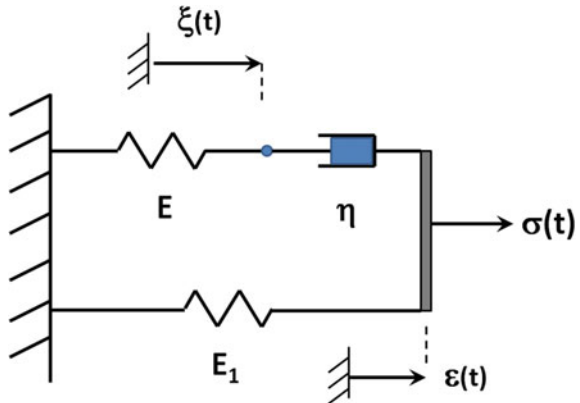
As for the complex modulus $E^*(\omega)$ provided by the Maxwell model, it may be obtained by the Fourier transform of Eq. (5.18) which, after reorganization, provides the following relation

$$E^*(\omega) = \frac{\mathcal{F}\{\sigma(t)\}}{\mathcal{F}\{\varepsilon(t)\}} = \frac{\tilde{\sigma}(\omega)}{\tilde{\varepsilon}(\omega)} = \frac{j\omega}{j\omega \frac{1}{E} + \frac{1}{\eta}} = E \left(\frac{(\omega \tau_R)^2 + (\omega \tau_R) j}{1 + (\omega \tau_R)^2} \right) \quad (5.35)$$

where $\tau_R = \eta/E$ is the relaxation time provided by the Maxwell model.

Equations (5.30) and (5.34) describe, respectively, the stress $\sigma(t)$ for general strain history and describe the strain $\varepsilon(t)$ for general stress history when working with the Maxwell model. The relaxation kernel $\mathcal{K}^g(t)$ and the creep kernel $\mathcal{K}^J(t)$ for the Maxwell model are given in Eqs. (5.23) and (5.26), respectively. The characteristics of the Maxwell model allows one to determine its response analytically for several operational scenarios as shown previously. Nevertheless, when one analyzes its creep and stress relaxation responses one concludes that the model is more appropriate to describe fluid-like behavior. One key aspect is the fact that the user may build proposals for phenomenological models considering different combinations of springs and dampers. Some of these models are well known in the literature such as the Kelvin-Voigt, standard linear solid, generalized Maxwell [17], for example. Next will be described three specific models, namely, the linear standard solid model, the generalized Maxwell model and fractional standard solid model. As this chapter does not aim at presenting all the models in details, readers should refer to the reference books by Winneman and Rajagopal [17] and Lakes [18] in order to obtain detailed information about other models.

Fig. 5.6 Standard linear solid model



5.2.3.2 Three-Parameter Solid or Standard Linear Solid

The standard linear solid or three-parameter solid is described in Fig. 5.6. The upper branch is composed of a spring in series with a damper and it corresponds to the Maxwell model. The lower branch is composed of a linear spring. The observable variables are the strain $\varepsilon(t)$ and the stress $\sigma(t)$, while the variable $\xi(t)$ is an internal variable. The stress $\sigma(t)$ should be equal to the sum of the stress of the upper component and the stress of the lower component of the model, viz.

$$\sigma(t) = E_1 \varepsilon(t) + E \xi(t) \quad (5.36)$$

As the inertial terms are negligible, the elastic and viscous stresses along the upper component are equal and the following relation holds

$$E \xi(t) = \eta (\dot{\varepsilon}(t) - \dot{\xi}(t)) \quad (5.37)$$

As the observable variables $\varepsilon(t)$ and $\sigma(t)$ are the only measurable quantities, one may obtain a constitutive equation with these variables. Firstly, let us derive Eq.(5.36) with respect to time and replace the term $\dot{\xi}(t)$ by its value extracted from Eq.(5.37) as follows

$$\dot{\sigma}(t) = E_1 \dot{\varepsilon}(t) + E \left(-\frac{E}{\eta} \xi(t) + \dot{\varepsilon}(t) \right) \quad (5.38)$$

Finally, replacing $\xi(t)$ from Eq.(5.36) into Eq.(5.38) leads to the constitutive equation of the standard linear solid as shown next

$$\left(\frac{1}{\eta} \right) \sigma(t) + \left(\frac{1}{E} \right) \dot{\sigma}(t) = \left(\frac{E_1}{\eta} \right) \varepsilon(t) + \left(1 + \frac{E_1}{E} \right) \dot{\varepsilon}(t) \quad (5.39)$$

As for the model predictions provided by the standard linear solid model, one may investigate it under the creep and stress relaxation conditions. Firstly, let us consider the conditions under which the strain is prescribed as a step function $\varepsilon(t) = \varepsilon_0 u(t)$ in which $u(t)$ is the unit step function defined as shown in Eq.(5.20). The Laplace transform of Eq.(5.39) is given as follows

$$\left(\frac{1}{\eta}\right)\tilde{\sigma}(s) + \left(\frac{1}{E}\right)(s\tilde{\sigma}(s) - \sigma(0)) = \left(\frac{E_1}{\eta}\right)\tilde{\varepsilon}(s) + \left(1 + \frac{E_1}{E}\right)(s\tilde{\varepsilon}(s) - \varepsilon(0)) \quad (5.40)$$

Let us additionally assume that the system is at rest at $t = 0$. Therefore, as $\tilde{\varepsilon}(s) = \frac{\varepsilon_0}{s}$, one may recast Eq.(5.40) as follows

$$\tilde{\sigma}(s) = \frac{1}{s} \left(\frac{EE_1 + (E + E_1)\eta s}{E + \eta s} \right) \varepsilon_0 \quad (5.41)$$

The time domain response of the system is found by applying the inverse Laplace transform to Eq.(5.41), leading to

$$\sigma(t) = \varepsilon_0 \left(E_1 + E e^{-\frac{E}{\eta}t} \right) u(t) = \varepsilon_0 \mathcal{K}^g(t) \quad (5.42)$$

where the function $\mathcal{K}^g(t)$ in Eq.(5.42) corresponds to the stress relaxation kernel provided by the standard linear solid model. As for Eq.(5.42), one identifies a stress relaxation with a relaxation time $\tau_R = \frac{\eta}{E}$. Further, the elastic response is $\sigma(0^+) = (E_1 + E)\varepsilon(0^+)$ and the equilibrium response is $\sigma(+\infty) = E_1\varepsilon(0^+)$.

As for the creep behavior, one assumes that the system is at rest and that the stress follows a step as follows $\sigma(t) = \sigma_0 u(t)$. Following the same steps that were used to obtain the creep response of the model, one gets

$$\tilde{\varepsilon}(s) = \frac{1}{s} \left(\frac{E + \eta s}{EE_1 + (E + E_1)\eta s} \right) \sigma_0 \quad (5.43)$$

whose time domain version is obtained by the inverse Laplace transform as follows

$$\varepsilon(t) = \sigma_0 \left(\frac{1}{E_1} - \frac{E e^{-t/\tau_c}}{E_1(E + E_1)} \right) u(t) = \sigma_0 \mathcal{K}^J(t) \quad (5.44)$$

where the function $\mathcal{K}^J(t)$ in Eq.(5.44) corresponds to the creep kernel provided by the standard linear solid model and the creep time τ_c is written as:

$$\tau_c = \frac{\eta(E + E_1)}{E_1 E} \quad (5.45)$$

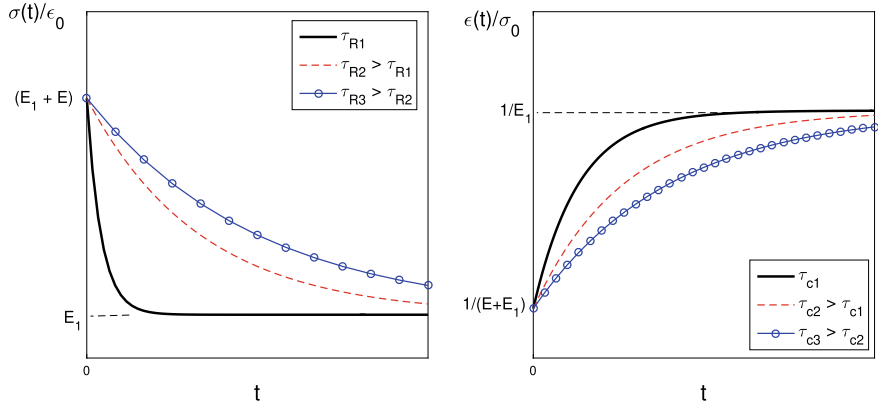


Fig. 5.7 Mechanical behavior provided by the standard solid model. On the left: Stress relaxation. On the right: Creep

From Eq. (5.44) one concludes that creep behavior is described with a creep constant of time $\tau_c = \frac{\eta(E_1+E)}{E_1E}$. Additionally, the elastic response is given by $\varepsilon(0^+) = (E_1 + E)^{-1}\sigma(0^+)$ and the equilibrium response is $\varepsilon(+\infty) = \frac{\sigma(0^+)}{E_1}$.

Figure 5.7 presents the stress relaxation and the creep behavior provided by the standard linear solid model as a function of its models parameters $\{E, E_1, \eta\}$.

Concerning the response provided by this model when the stress or strain is arbitrary, the next lines present a procedure that can be used to determine them. To this end, without loss of generality, let us suppose that the system is at rest at $t = 0$ and let us write the relation between stress and strain in the Laplace domain, viz.

$$\tilde{\sigma}(s) = \left(\frac{EE_1 + (E + E_1)\eta s}{E + \eta s} \right) \tilde{\varepsilon}(s) = \frac{1}{s} \left(\frac{EE_1 + (E + E_1)\eta s}{E + \eta s} \right) \times (s \tilde{\varepsilon}(s)) \quad (5.46)$$

The stress $\tilde{\sigma}(s)$ is a simple product of two functions, therefore $\sigma(t)$ is obtained by the convolution product of the time domain version of these two functions. For instance, using Eqs. (5.41), (5.42) and (5.47), one concludes that Eq. (5.46) may be rewritten as follows

$$\tilde{\sigma}(s) = \tilde{\mathcal{K}}^g(s) \times (s \tilde{\varepsilon}(s)) \quad (5.47)$$

where the function $\tilde{\mathcal{K}}^g(s)$ corresponds to the Laplace transform of the relaxation kernel, as shown in Eqs. (5.41) and (5.42). Therefore the time domain stress $\sigma(t)$ is given by

$$\sigma(t) = \mathcal{L}^{-1}\{\tilde{\mathcal{K}}^g(s)\} * \mathcal{L}^{-1}\{s \tilde{\varepsilon}(s)\} = \int_0^t \mathcal{K}^g(t - \tau) \frac{d\varepsilon(\tau)}{d\tau} d\tau \quad (5.48)$$

where $\cdot * \cdot$ denotes the convolution operator.

The same procedure can be adopted to determine the system response when the stress is arbitrary. This leads to the following relation

$$\varepsilon(t) = \mathcal{L}^{-1}\left\{\frac{1}{s}\left(\frac{E + \eta s}{EE_1 + (E + E_1)\eta s}\right)\right\} * \mathcal{L}^{-1}\{s\tilde{\sigma}(s)\} = \int_0^t \mathcal{K}^J(t - \tau) \frac{d\sigma(\tau)}{d\tau} d\tau \quad (5.49)$$

where the relaxation creep kernel \mathcal{K}^J is given in Eq. (5.44).

As for the complex modulus $E^*(\omega)$ provided by the standard linear solid model, using the relaxation kernel in Eq. (5.42) and the definition of the relaxation time, one obtains:

$$E^*(\omega) = \frac{(EE_1) + \eta(j\omega)(E + E_1)}{E + \eta(j\omega)} = \frac{E_1 + j(\omega\tau_R)(EE_1)}{1 + j(\omega\tau_R)} = \quad (5.50)$$

$$\frac{\mathcal{K}^g(+\infty) + j(\omega\tau_R)\mathcal{K}^g(0)}{1 + j(\omega\tau_R)} \quad (5.51)$$

5.2.3.3 Generalized Maxwell Solid Model

The constitutive equation for the generalized Maxwell model depicted in Fig. 5.8, is described by the equation which equals the stress of the system $\sigma(t)$ with the sum of the stresses along each one of the n horizontal Maxwell components as follows

$$\sigma(t) = \sum_{r=1}^n \sigma_r(t) = \sum_{r=1}^n E_r \xi_r(t) \quad (5.52)$$

and by the set of coupled equations that describe the stress $\sigma_r(t)$ along the r -th subcomponent, viz.

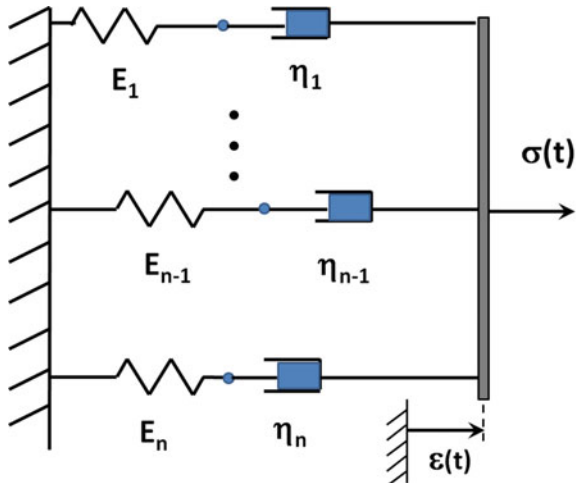
$$\sigma_r(t) = E_r \xi_r(t) = \eta_r(\dot{\varepsilon}(t) - \dot{\xi}_r(t)); \quad r = 1, \dots, n \quad (5.53)$$

This model is described by a set of n internal variables $\xi_r(t)$. In order to write the relation in terms of the observable variables $\sigma(t)$ and $\varepsilon(t)$, one may resort to the analyses of the system in the Laplace domain. The idea consists in transforming Eq. (5.53) to Laplace domain, write $\tilde{\xi}_r(s)$ as a function of $\tilde{\varepsilon}(s)$ and take it to Eq. (5.52). This leads to the following equation

$$\tilde{\sigma}(s) = \left(\sum_{r=1}^n \frac{E_r s}{\frac{E_r}{\eta_r} + s} \right) \tilde{\varepsilon}(s) = \left(\frac{1}{s} \sum_{r=1}^n \frac{E_r s}{\frac{E_r}{\eta_r} + s} \right) \times (s \tilde{\varepsilon}(s)) = \tilde{A}(s) \times (s \tilde{\varepsilon}(s)) \quad (5.54)$$

Therefore, the time history $\sigma(t)$ is given by the convolution integral of $\mathcal{L}^{-1}\{\tilde{A}(s)\}$ with $\mathcal{L}^{-1}\{s\tilde{\varepsilon}(s)\}$, viz.

Fig. 5.8 Generalized Maxwell model



$$\sigma(t) = \mathcal{L}^{-1}\{\tilde{A}(s)\} * \mathcal{L}^{-1}\{s\tilde{\varepsilon}(s)\} = \int_0^t A(t-\tau) \frac{d\varepsilon(\tau)}{d\tau} d\tau \quad (5.55)$$

where one may identify the hereditary integral relating stress and strain and, therefore, the relaxation function $\mathcal{K}^g(t) = A(t)$ is given by

$$\mathcal{K}^g(t) = \mathcal{L}^{-1}\left\{ \frac{1}{s} \sum_{r=1}^n \frac{E_r s}{\frac{E_r}{\eta_r} + s} \right\} = \sum_{r=1}^n E_r e^{-\frac{E_r}{\eta_r} t} \quad (5.56)$$

From Eq. (5.56) one notices that the Maxwell model predicts stress relaxation as a composition of n terms such that each term has its own relaxation time $\tau_R^r = \eta_r/E_r$. The generalized Maxwell model has a spectrum of relaxation times [17], and thus applies to materials whose stress relaxation may not be properly described by a single relaxation time. Another characteristic is that $\mathcal{K}^g(0) = \sum_{r=1}^n E_r$ and that $\mathcal{K}^g(+\infty) = 0$. Further, if the user needs to model some material whose behavior for $\mathcal{K}^g(t)$ does tend to zero as $t \rightarrow +\infty$, then one may assume that $\eta_n \rightarrow +\infty$ in Eq. (5.56) which leads to $\mathcal{K}^g(+\infty) = E_n$.

As for the complex modulus $E^*(\omega)$, it can be obtained by the definition shown in Eq. (5.54) and using Eq. (5.56), as follows:

$$E^*(\omega) = \sum_{r=1}^n \frac{E_r (\omega \tau_R^r) j}{1 + (\omega \tau_R^r) j} \quad (5.57)$$

From previous analyses, it can be concluded that there is a myriad of combinations among springs and dashpots that could have been proposed. The engineer may propose a specific combination aiming at building a model to describe some particular class of materials. Literature provides several analyses considering different models

such as Zener, Anti-Zener, Burger, standard linear solid, generalized Maxwell etc., whose theoretical aspects may be found in the reference books [17, 18]. Among these, there is a specific model class which deserves special attention. It is the class of models based on the concept of fractional derivative operators. This is described in the next subsection.

5.2.3.4 Models Based on Fractional Derivative Operators

Let us consider a mechanical analog whose configuration is similar to the one shown in Fig. 5.6 except for the damping component which is replaced by one based on a fractional operator. More specifically, the fractional damping component has a constitutive equation relating its stress $\sigma_d(t)$ and strain $\varepsilon(t) - \xi(t)$ as follows

$$\sigma_d(t) = \eta \frac{d^\alpha}{dt^\alpha} (\varepsilon(t) - \xi(t)) \quad (5.58)$$

where the time derivative present in Eq. (5.59) is a fractional derivative operator [19] whose definition is presented as follows

$$\frac{d^\alpha g(t)}{dt^\alpha} = \begin{cases} \frac{1}{\Gamma(m-\alpha)} \int_0^t \frac{g(\tau)}{(t-\tau)^{\alpha+1-m}} d\tau & \text{if } m-1 < \alpha < m \\ \frac{d^m g(t)}{dt^m} & \text{if } \alpha = m \end{cases} \quad (5.59)$$

where $\Gamma(m-\alpha)$ is the gamma function [19], α is the order of the fractional derivative and m is a nonzero natural number, i.e., $m \in \{1, 2, \dots\}$.

As for the definitions of the fractional derivative of a function, one may find some definitions such as [20]: (i) Grünwald Letnikov, (ii) Riemann-Liouville and (iii) Caputo. In particular, the one presented in Eq. (5.59) is the Caputo fractional derivative. The definition proposed by Caputo has a quite interesting characteristic for situations in which one is interested in solving initial value problems. This definition allows for the compatibility of initial conditions in a very convenient fashion. Therefore, due to the fact that engineering problems in general involve differential equations, the use of the Caputo definition when building the fractional differential equations is very convenient.

The process of obtaining the constitutive equation for this model follows the procedures used in the previous models. Therefore, the constitutive equation for a fractional version of the standard solid is written as [19]:

$$\left(\frac{1}{E}\right) \frac{d^\alpha \sigma}{dt^\alpha} + \left(\frac{1}{\eta}\right) \sigma = \left(1 + \frac{E_1}{E}\right) \frac{d^\alpha \varepsilon}{dt^\alpha} + \left(\frac{E_1}{\eta}\right) \varepsilon \quad (5.60)$$

The model described in Eq. (5.60) with $0 < \alpha < 1$ presents a continuum *spectrum of relaxation times* instead of a single relaxation time that is provided by the standard linear solid ($\alpha = 1$) or a finite set of n relaxation times as in the generalized Maxwell

models. Therefore, concerning relaxation times, one may say that models based on fractional derivative operators are more parsimonious than models based on classical integer derivatives. It is due to the fact that fractional models are characterized by a number of model parameters that is smaller than the number required by models based on classical integer derivatives [21, 22]. This parsimony characteristic appears under both linear [19] and non-linear operational conditions [23]. Concerning its physical consistency, Lion [24] presented detailed analysis of this model from the perspective of the thermodynamics of irreversible processes.

As for the stress relaxation and creep predictions as well as their respective kernels $\mathcal{K}^g(t)$ and $\mathcal{K}^J(t)$ provided by the fractional standard linear solid model, a detailed analysis may be found in the reference book by Mainardi [19]. Therefore, for the sake of conciseness, instead of presenting the details for the computation of $\mathcal{K}^g(t)$ and $\mathcal{K}^J(t)$, they are presented in their final shape:

$$\mathcal{K}^g(t) = E_1 + E \mathbb{M}_\alpha[-(t/\tau_\sigma)^\alpha]; \quad \tau_\sigma^\alpha = \frac{\eta}{E} \quad (5.61)$$

$$\mathcal{K}^J(t) = \frac{1}{E + E_1} + \left(\frac{E}{E_1(E + E_1)} \right) (1 - \mathbb{M}_\alpha[-(t/\tau_\varepsilon)^\alpha]); \quad \tau_\varepsilon^\alpha = \left(\frac{1}{E_1} + \frac{1}{E} \right) \eta \quad (5.62)$$

where the function $\mathbb{M}_\alpha[z]$ corresponds to the Mittag-Leffler function [19] whose definition is

$$\mathbb{M}_\alpha[z] = \sum_{r=1}^{+\infty} \frac{z^n}{\Gamma(\alpha r + 1)}; \quad \alpha > 0, \quad z \in C \quad (5.63)$$

The Mittag-Leffler function is the generalization of the exponential function. It should be highlighted that when $\alpha = 1$ one obtains $\mathbb{M}_\alpha[z] = e^z$ and for this situation the relaxation and creep kernels in Eqs. (5.61) and (5.62) become the relaxation and creep kernels provided by the standard linear solid shown in Eqs. (5.42) and (5.45).

As for the complex modulus $E^*(\omega)$, the fractional standard linear solid provides the following expression:

$$E^*(\omega) = (E + E_1) \left(\frac{\frac{EE_1}{\eta(E+E_1)} + (j\omega)^\alpha}{\frac{E}{\eta} + (j\omega)^\alpha} \right) \quad (5.64)$$

where $(j\omega)^\alpha$ has the following representation

$$(j\omega)^\alpha = \left(e^{\frac{j\pi}{2}} \omega \right)^\alpha = e^{\frac{j\pi\alpha}{2}} \omega^\alpha = \omega^\alpha \cos\left(\frac{\pi\alpha}{2}\right) + j\omega^\alpha \sin\left(\frac{\pi\alpha}{2}\right) \quad (5.65)$$

5.2.4 Note

Each of the models shown in the previous sections present its own characteristics concerning stress relaxation kernel, creep kernel or complex modulus. The use of a specific constitutive equation to model some material in engineering design demands the complete characterization of the constitutive parameters. Inverse problems [25, 26] may be used to obtain information about model parameters based on a set of measured data. This is the topic of next section.

5.3 Parameter Identification of Viscoelastic Models

Let us consider that one is interested in estimating parameters of a viscoelastic constitutive model. For example, one may be interested in determining the parameters $\{E, E_1, \eta\}$ for the standard linear solid, or the parameters $\{E_1, \eta_1, E_2, \eta_2, \dots, E_n, \eta_n\}$ for the generalized Maxwell model or the parameters $\{E, E_1, \eta, \alpha\}$ for the fractional standard linear solid, to cite a few. For the sake of simplicity, let us consider that once a constitutive model has been chosen, its N_θ parameters are organized in a vector $\boldsymbol{\theta} \in \mathbb{R}^{N_\theta}$. Additionally, let us also suppose that one has access to a set of N_y measured data from the material of interest such as creep, stress relaxation, time domain cyclic data or the complex modulus, for example. Independently of the type of data, let us assume that the measured data is organized in a vector $\mathbf{y} \in \mathbb{R}^{N_y}$. Finally, let us consider that one has a computational model that provides model predictions according to the map $\boldsymbol{\theta} \in \mathbb{R}^{N_\theta} \mapsto \mathbf{A}(\boldsymbol{\theta}) \in \mathbb{R}^{N_y}$. It will be shown next how one may conjugate our current state of knowledge about $\boldsymbol{\theta}$ with information from measured data \mathbf{y} and the model structure given by $\mathbf{A}(\boldsymbol{\theta})$ to obtain information about model parameters $\boldsymbol{\theta}$ using a Bayesian framework.

5.3.1 Bayesian Framework

In the Bayesian framework for inverse problems: (i) all the unknowns and measured data are modeled as random variables [25], (ii) the level of uncertainty of random variables is encoded in their probability density functions (pdf) and (iii) the solution of the inverse problem corresponds to the exploration of the posterior density of model parameters given a set of measured data. Concerning pdfs, the following notation will be used herein: $\pi(x)$ denotes the pdf of the random variable x , $\pi(x, y)$ denotes the joint pdf of the random variables x and y , $\pi(x|y)$ denotes the pdf of x conditioned to y and $\pi(\mathbf{x})$ denotes the pdf of the random vector $\mathbf{x} = \{x_1, \dots, x_{N_x}\}^T$ (Fig. 5.9).

Let us assume that the relation between measured data \mathbf{y} and model predictions $\mathbf{y}^m = \mathbf{A}(\boldsymbol{\theta})$ is described by an additive error model as follows

$$\mathbf{y} = \mathbf{A}(\boldsymbol{\theta}) + \mathbf{e} \quad (5.66)$$

where it is also assumed that the model given by $\mathbf{A}(\boldsymbol{\theta})$ is accurate and that discrepancies between measurements \mathbf{y} and model predictions $\mathbf{y}^m = \mathbf{A}(\boldsymbol{\theta})$ could be tackled by a random variable vector \mathbf{e} which is in charge of describing measurement noise. As \mathbf{y} , $\boldsymbol{\theta}$ and \mathbf{e} are random variables, one may write a relation among them by means of the Bayes rule [25]

$$\pi(\boldsymbol{\theta}|\mathbf{y}) = \frac{\pi(\mathbf{y}|\boldsymbol{\theta}) \pi(\boldsymbol{\theta})}{\pi(\mathbf{y})} \quad (5.67)$$

where $\pi(\mathbf{y}|\boldsymbol{\theta})$ is the likelihood model, $\pi(\boldsymbol{\theta})$ is the prior model for the unknown $\boldsymbol{\theta}$ and $\pi(\mathbf{y})$ is the probability density of measured data. In practice, one would never be able to get information about $\pi(\mathbf{y})$ as this would require a prohibitive number of experiments. Fortunately, $\pi(\mathbf{y})$ acts as a scaling factor and it is of little importance as shown in [25, 27]. $\pi(\boldsymbol{\theta})$ is called *prior density* due to the fact that it describes all the information, expectation and belief about the unknown $\boldsymbol{\theta}$ before measured data \mathbf{y} has been taken. For example, the user may build the prior gathering information from model parameters obtained from previous experiments, from catalogues provided by product manufacturer and also from physical constraints that are associated to model parameters. The likelihood model $\pi(\mathbf{y}|\boldsymbol{\theta})$ expresses the probability of observing the data \mathbf{y} given a set of parameters $\boldsymbol{\theta}$ for the model. $\pi(\boldsymbol{\theta}|\mathbf{y})$ is called the *posterior density* of model parameters $\boldsymbol{\theta}$ given a set of measured data \mathbf{y} . In fact, $\pi(\boldsymbol{\theta}|\mathbf{y})$ corresponds to the updated information about $\boldsymbol{\theta}$ when one conjugates measured data \mathbf{y} and prior information encoded in $\pi(\boldsymbol{\theta})$.

Assuming that the mapping $\boldsymbol{\theta} \mapsto \mathbf{A}(\boldsymbol{\theta})$ provides accurate model predictions one may also assume that the random variables $\boldsymbol{\theta}$ and \mathbf{e} are mutually independent. There-

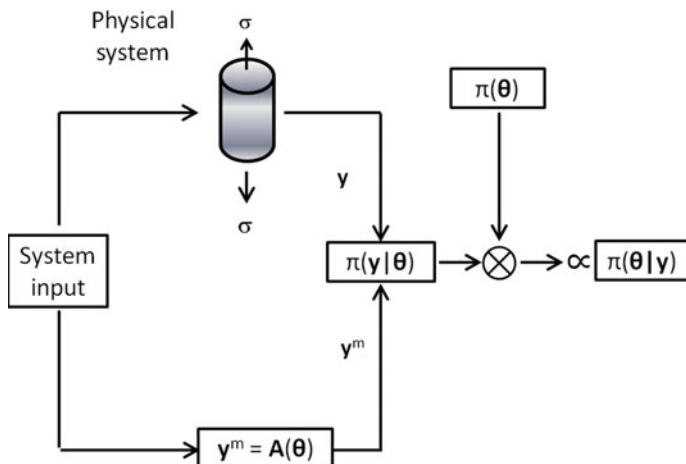


Fig. 5.9 Bayesian inference

fore, in this case the likelihood function casts as follows

$$\pi(\mathbf{y}|\boldsymbol{\theta}) = \pi_e(\mathbf{y} - \mathbf{A}(\boldsymbol{\theta})) \quad (5.68)$$

where $\pi_e(\mathbf{y} - \mathbf{A}(\boldsymbol{\theta}))$ corresponds to the probability density of the additive noise \mathbf{e} when evaluated at the residue $\mathbf{y} - \mathbf{A}(\boldsymbol{\theta})$. It is important to note that the likelihood is a density in \mathbf{y} not in $\boldsymbol{\theta}$ and that is why it is named likelihood function. In particular, let us assume that the random variable in charge of describing the measurement error \mathbf{e} follows a Gaussian distribution

$$\mathbf{e} \sim \mathcal{N}(\mathbf{e}^*, \boldsymbol{\Sigma}_{ee}) \quad (5.69)$$

where \mathbf{e}^* and $\boldsymbol{\Sigma}_{ee}$ correspond to the mean value and the covariance matrix of \mathbf{e} , respectively. When \mathbf{e} is modeled as shown in Eq. (5.69), the likelihood function is expressed as [25]:

$$\begin{aligned} \pi(\mathbf{y}|\boldsymbol{\theta}) &= \pi_e(\mathbf{y} - \mathbf{A}(\boldsymbol{\theta})) \\ &= \frac{1}{(2\pi)^{N_y} |\boldsymbol{\Sigma}_{ee}|^{1/2}} \exp \left\{ -\frac{1}{2} (\mathbf{y} - \mathbf{A}(\boldsymbol{\theta}) - \mathbf{e}^*)^T \boldsymbol{\Sigma}_{ee}^{-1} (\mathbf{y} - \mathbf{A}(\boldsymbol{\theta}) - \mathbf{e}^*) \right\} \end{aligned} \quad (5.70)$$

The complete probabilistic model for the inverse analysis of the viscoelasticity problem is presented by Eq. (5.67). Therefore, one may use $\pi(\boldsymbol{\theta}|\mathbf{y})$ to compute various estimates for $\boldsymbol{\theta}$ as well as a posteriori uncertainties for these estimates. For example, one may be interested in computing the conditional expected value of the model parameters $\mathbb{E}_{\boldsymbol{\theta}|\mathbf{y}}[\boldsymbol{\theta}]$ as follows

$$\mathbb{E}_{\boldsymbol{\theta}|\mathbf{y}}[\boldsymbol{\theta}] = \int \boldsymbol{\theta} \pi(\boldsymbol{\theta}|\mathbf{y}) d\boldsymbol{\theta} \quad (5.71)$$

Another example that is quite common is the interest in using information from $\pi(\boldsymbol{\theta}|\mathbf{y})$ to make some predictive analyses $\mathbf{z} = \mathbf{z}(\boldsymbol{\theta}; \mathcal{S}_p)$ in a scenario \mathcal{S}_p that is different from the scenario used for calibration. This is the case when one needs to make reliability analysis [28], uncertainty quantification analysis [29] and robust optimization, to cite a few. As for \mathbf{z} , it could be the maximum displacement, the maximum stress, etc.. For this situation, the expected value of the quantity \mathbf{z} would be given as follows

$$\mathbb{E}_{\boldsymbol{\theta}|\mathbf{y}}[\mathbf{z}] = \int \mathbf{z}(\boldsymbol{\theta}; \mathcal{S}_p) \pi(\boldsymbol{\theta}|\mathbf{y}) d\boldsymbol{\theta} \quad (5.72)$$

It should be highlighted here that in general the probabilistic model of Eq. (5.67) does not have an analytical solution. Nevertheless, the user may compute some point estimates such as maximum likelihood $\hat{\boldsymbol{\theta}}_{ML}$ and the maximum a posteriori $\hat{\boldsymbol{\theta}}_{MAP}$ [25]. The maximum likelihood point estimate is presented as follows

$$\hat{\boldsymbol{\theta}}_{ML} = \arg \max_{\boldsymbol{\theta} \in \Theta} \pi(\mathbf{y}|\boldsymbol{\theta}) \quad (5.73)$$

which is equivalent to the solution of the following problem

$$\hat{\boldsymbol{\theta}}_{ML} = \arg \min_{\boldsymbol{\theta} \in \Theta} \left\{ \frac{1}{2} (\mathbf{y} - \mathbf{A}(\boldsymbol{\theta}) - \mathbf{e}^*)^T \boldsymbol{\Sigma}_{ee}^{-1} (\mathbf{y} - \mathbf{A}(\boldsymbol{\theta}) - \mathbf{e}^*) \right\} \quad (5.74)$$

where one identifies that it corresponds to the weighted least-squares estimator.

As for the maximum a posteriori estimator, it casts as follows

$$\hat{\boldsymbol{\theta}}_{MAP} = \arg \max_{\boldsymbol{\theta} \in \Theta} \pi(\boldsymbol{\theta}|\mathbf{y}) \quad (5.75)$$

As for the posterior density $\pi(\boldsymbol{\theta}|\mathbf{y})$, although one is hardly able to obtain it analytically, one may explore it by means of sampling based techniques such as Markov Chain Monte Carlo methods [25, 30]

A Markov chain Monte Carlo (MCMC) method produces samples of an ergodic Markov chain $\{\boldsymbol{\theta}^{(1)}, \boldsymbol{\theta}^{(2)}, \dots, \boldsymbol{\theta}^{(N_{mc})}\}$ for the simulation of a target distribution $\bar{\pi}(\boldsymbol{\theta})$ [30]. These methods draw samples in a sequential way such that the density of the sample $\boldsymbol{\theta}^{(r)}$ depends only on the last sample of the chain $\boldsymbol{\theta}^{(r-1)}$. When working with inverse problems in viscoelasticity, one sets the target density as being the posterior density of model parameters, i.e., $\bar{\pi}(\boldsymbol{\theta}) = \pi(\boldsymbol{\theta}|\mathbf{y})$. Therefore, the drawn samples $\{\boldsymbol{\theta}^{(1)}, \boldsymbol{\theta}^{(2)}, \dots, \boldsymbol{\theta}^{(N_{mc})}\}$ can be used to approximate any information associated to $\pi(\boldsymbol{\theta}|\mathbf{y})$ such that, for example, the expected mean value of model parameters in Eq.(5.71) and the expected mean value of model predictions in Eq.(5.72) are approximated by

$$\mathbb{E}_{\boldsymbol{\theta}|\mathbf{y}}[\boldsymbol{\theta}] \approx \mathbb{E}_{\boldsymbol{\theta}|\mathbf{y}}^m[\boldsymbol{\theta}] = \frac{1}{m} \sum_{j=1}^m \boldsymbol{\theta}^{(j+N_b)} \quad (5.76)$$

$$\mathbb{E}_{\boldsymbol{\theta}|\mathbf{y}}[\mathbf{z}] \approx \mathbb{E}_{\boldsymbol{\theta}|\mathbf{y}}^m[\mathbf{z}] = \frac{1}{m} \sum_{j=1}^m \mathbf{z}(\boldsymbol{\theta}^{(j+N_b)}) \quad (5.77)$$

where the sum in Eqs.(5.76) and (5.77) starts at the N_b -th sample in order to discard the *burn-in* period. One should discard the first N_b samples of the chain aiming at eliminating the influence of the first sample of the chain $\boldsymbol{\theta}^{(0)}$.

Generally speaking, a Markov Chain starts at some initial point $\boldsymbol{\theta}^{(0)}$. At the $(j-1)$ -th state, a *candidate* $\boldsymbol{\theta}^{(c)}$ for the j -th state should be drawn from a Transition/Proposal distribution $\mathbb{T}(\boldsymbol{\theta}^{(c)}|\boldsymbol{\theta}^{(j-1)})$ which depends on the previous drawn sample $\boldsymbol{\theta}^{(j-1)}$ [25, 30, 31]. The next step consists in assessing the candidate to check if it will be accepted or rejected according to some probability level.

The reader may find details about MCMC methods in the reference books by Robert and Casellas [30] and by Gamerman and Lopes [31].

5.4 Modeling of Structures with Viscoelastic Materials

In this section, the finite element modeling of structures with viscoelastic materials is described. The coverage is confined to frequency domain analysis. In a first approach, fully three-dimensional models are considered for the modeling of viscoelastic structures (Sect. 5.4.1), as they embrace all practical problems. The matrix equation of motion for a vibrating structure with viscoelastic materials is derived in the frequency domain and involves a frequency dependent stiffness matrix. For some problems, lower-dimensional finite elements such as beams, plates and shells offer more adequate models. The presence of viscoelastic material requires some adaptations of classical theories, which are presented in Sect. 5.4.2.

Dynamic analysis of structures in the frequency domain usually involves the computation of frequency response functions over a broad frequency range. This is often performed through standard direct approaches, where the matrix system is solved at each frequency. For some problems, this approach leads to prohibitive computational times. Many existing reduction techniques aims at enhancing the computational efficiency and it is the goal of Sect. 5.4.3 to describe some of the reduction techniques most adapted to structures with viscoelastic materials.

5.4.1 Finite Element Modeling in the Frequency Domain

For the sake of generality, let us consider a structure Ω to which displacement boundary conditions $\mathbf{u} = \mathbf{0}$ are applied on $\partial_u \Omega$, and subjected to a harmonic excitation \mathbf{F} applied on $\partial_F \Omega$ (Fig. 5.10). The outward-facing unit normal vector to the surface $\partial \Omega$ is denoted \mathbf{n} . In the frequency domain, the equations governing the motion of the structure are:

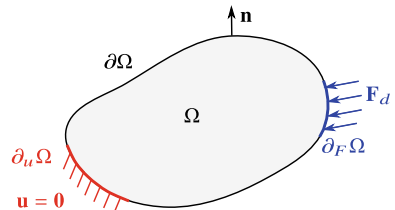
$$\left\{ \begin{array}{l} \operatorname{div} \boldsymbol{\sigma} + \rho \omega^2 \mathbf{u} = 0 \quad \text{dans } \Omega, \\ \mathbf{u} = \mathbf{0} \quad \text{sur } \partial_u \Omega, \end{array} \right. \quad (5.80a)$$

$$\left\{ \begin{array}{l} \mathbf{u} = \mathbf{0} \quad \text{sur } \partial_u \Omega, \\ \boldsymbol{\sigma} \cdot \mathbf{n} = \mathbf{F} \quad \text{sur } \partial_F \Omega, \end{array} \right. \quad (5.80b)$$

$$\left\{ \begin{array}{l} \boldsymbol{\sigma} \cdot \mathbf{n} = \mathbf{F} \quad \text{sur } \partial_F \Omega, \end{array} \right. \quad (5.80c)$$

where ρ is the density of the material and ω is the harmonic pulsation.

Fig. 5.10 Continuous problem



The trial-function method is used to derive the weak formulation of the coupled problem [32]. Multiplying Eq. (5.80a) by any admissible trial function $\delta\mathbf{u}$, applying Green formula and taking Eq. (5.80c) into account leads to:

$$\int_{\Omega} \boldsymbol{\epsilon}(\delta\mathbf{u}) : \boldsymbol{\sigma} dV - \omega^2 \int_{\Omega} \rho \delta\mathbf{u} \cdot \mathbf{u} dV = \int_{\partial_F \Omega} \delta\mathbf{u} \cdot \mathbf{F}_d dS, \quad \forall \delta\mathbf{u}. \quad (5.81)$$

The continuum Ω is divided into n_e finite elements Ω_e . Shape functions N_k are used to interpolate the nodal displacements \mathbf{U}_e to approximate the displacement $\mathbf{u}_e(M)$ of any point M inside the element:

$$\mathbf{u}_e(M) = \mathbb{N}_e(M)\mathbf{U}_e, \quad (5.82)$$

where \mathbb{N}_e is the element shape function matrix:

$$\mathbb{N}_e = \begin{bmatrix} N_1 & \dots & N_{n_N} & 0 & \dots & 0 & 0 & \dots & 0 \\ 0 & \dots & 0 & N_1 & \dots & N_{n_N} & 0 & \dots & 0 \\ 0 & \dots & 0 & 0 & \dots & 0 & N_1 & \dots & N_{n_N} \end{bmatrix}, \quad (5.83)$$

and \mathbf{U}_e is the elementary nodal displacement vector:

$$\mathbf{U}_e = [U_x^1 \dots U_x^{n_N} \ U_y^1 \dots U_y^{n_N} \ U_z^1 \dots U_z^{n_N}]^T, \quad (5.84)$$

where n_N is the number of nodes per element.

The gradient operator \mathbb{D} allows to express element strains $\boldsymbol{\epsilon}_e$ as a function of the displacement \mathbf{u}_e :

$$\boldsymbol{\epsilon}_e = \mathbb{D}\mathbf{u}_e, \quad (5.85)$$

where

$$\mathbb{D} = \begin{bmatrix} \partial/\partial x & 0 & 0 \\ 0 & \partial/\partial y & 0 \\ 0 & 0 & \partial/\partial z \\ 0 & \partial/\partial z & \partial/\partial y \\ \partial/\partial z & 0 & \partial/\partial x \\ \partial/\partial y & \partial/\partial x & 0 \end{bmatrix}. \quad (5.86)$$

By introducing Eq. (5.82) into Eq. (5.85), element strains can be written directly in terms of nodal displacements:

$$\boldsymbol{\epsilon}_e = \mathbb{B}_e \mathbf{U}_e, \quad (5.87)$$

where $\mathbb{B}_e = \mathbb{D}\mathbb{N}_e$. After discretization of each term of Eq. (5.81) by the finite element method, one gets the following matrix system:

$$[\mathbb{K} - \omega^2 \mathbb{M}] \mathbf{U} = \mathbf{F}, \quad (5.88)$$

where \mathbb{K} is the stiffness matrix, \mathbb{M} the mass matrix, \mathbf{F} the harmonic load vector and \mathbf{U} the nodal displacement vector. Global stiffness and mass matrices are computed by assembling individual element matrices:

$$\mathbb{K} = \mathbf{A}_{k=1}^{n_e} \mathbb{K}_e^k \quad \mathbb{M} = \mathbf{A}_{k=1}^{n_e} \mathbb{M}_e^k, \quad (5.89)$$

The element matrices are computed as:

$$\begin{aligned} \mathbb{K}_e &= \int_{\Omega_e} \mathbb{B}_e^T \mathbb{C} \mathbb{B}_e d\Omega_e, \\ \mathbb{M}_e &= \int_{\Omega_e} \mathbb{N}_e^T \rho \mathbb{N}_e d\Omega_e, \end{aligned} \quad (5.90)$$

where \mathbb{C} is the stiffness tensor derived from the material constitutive law.

If the continuum Ω is composed of an elastic media Ω_E and a viscoelastic media Ω_V , two stiffness matrices \mathbb{K}_E and \mathbb{K}_V are computed by considering appropriate stiffness tensors in Eq. (5.90). By considering the stiffness tensor $\mathbb{C}^*(\omega)$ written in terms of Young's modulus and Poisson ratio as per Eq. (5.8), the stiffness matrix corresponding to the viscoelastic media is complex and frequency-dependent:

$$\mathbb{K}_V^*(\omega) = \beta^*(\omega) \mathbb{K}_V^0 \quad (5.91)$$

where $\beta^*(\omega) = \frac{E^*(\omega)}{E^*(\omega=0)}$ and \mathbb{K}_V^0 is a constant stiffness matrix.

The discretized problem associated to the dynamics of a viscoelastic structure in the frequency domain is then formulated as:

$$[\mathbb{K}_E + \beta^*(\omega) \mathbb{K}_V^0 - \omega^2 \mathbb{M}] \mathbf{U}^* = \mathbf{F}, \quad (5.92)$$

The advantage of decomposing the stiffness matrix into an elastic and a viscoelastic part is that the frequency-dependent coefficient $\beta^*(\omega)$ is factored out of a constant matrix. In this way, the matrices do not need to be computed at each frequency during frequency sweep calculations.

The frequency dependency of the Young's modulus can be described by tabular data or by any viscoelastic model (see Sect. 5.2.3).

5.4.2 Finite Element Modeling of Slender Structures

Many structural systems of practical interest, to which viscoelastic materials are applied to attenuate vibration and radiated noise, are slender structures such as beams, plates and shells vibrating mainly in bending motion. These types of structures are frequently encountered in aerospace structural systems, and are typically characterized by low values of natural frequencies.

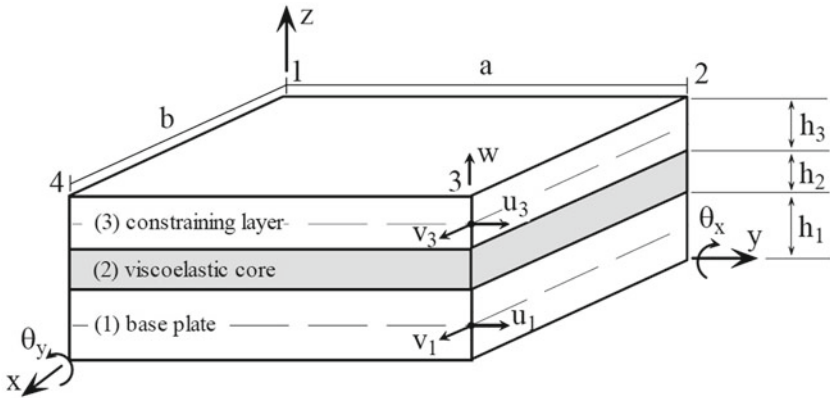


Fig. 5.11 Three-layer plate finite element

Very often, solutions for vibration control of these types of structures consist in the application of viscoelastic surface treatments, which can be of two main variants, namely: (a) *free layers*, which consist in thin viscoelastic layers directly bonded to the surface of the structure. In this case, the damping layer is primarily deformed with normal strains when the structure vibrates in bending; (b) *constrained layers*, which consist of a thin viscoelastic layer inserted between the structure surface and another thin metal or composite (constraining) cover. In spite of the more complex configuration and increased added weight, constrained damping layers are recognized as being more efficient in terms of achievable damping levels, since the confinement of the viscoelastic layer between two more rigid layers enables increased shear strains in the viscoelastic layer.

In this section, the formulation of a thin or moderately thin three-layer sandwich plate FE is summarized, based on the original developments made by Khatua and Cheung [33]. It should be seen as a particular case of the formulation presented in Sect. 5.4.1, accounting for specific stress/strain states and kinematic hypotheses adopted for thin three-layer plates. Many other theories, in particular those adapted to thick plates, can be found described in the literature [34].

Figure 5.11 depicts a rectangular element formed by an elastic base-plate (1), a viscoelastic core (2) and an elastic constraining layer (3). This element contains four nodes and seven DOFs per node, representing the in-plane displacements in the middle plane of the base-plate in directions x and y (denoted by u_1 and v_1 , respectively), the in-plane displacements of the middle plane of the constraining layer in directions x and y (denoted by u_3 and v_3 , respectively), the transverse displacements, w , and the cross-section rotations about x and y , denoted by θ_x and θ_y , respectively.

In the developments that follow, the assumptions adopted are: (i) all the materials involved are homogeneous and isotropic, and exhibit linear mechanical behavior; (ii) normal stresses and strains in direction z are neglected for all the three layers; (iii) the elastic layers (1) and (3) are modeled according to Kirchhoff's theory; (iv) for

the viscoelastic core, Mindlin's theory is adopted (i.e. transverse shear is included); (v) the cross-section rotations θ_x and θ_y are assumed to be the same for the elastic layers; (vi) the transverse displacement w is the same for all the three layers.

These assumptions have been considered by many authors as being adequate for the modeling of thin panels, as is the case of the structures considered here [35].

The strain-displacement relations are used and the resulting strains for elastic layers and for the viscoelastic core are separated, respectively, by uncoupling membrane, bending and shear effects, as follows:

$$\boldsymbol{\epsilon}^{(k)} = \begin{Bmatrix} \frac{\partial u_k}{\partial x} \\ \frac{\partial v_k}{\partial y} \\ \frac{\partial u_k}{\partial y} + \frac{\partial v_k}{\partial x} \end{Bmatrix} + z_k \begin{Bmatrix} \frac{\partial^2 w}{\partial x^2} \\ \frac{\partial^2 w}{\partial y^2} \\ 2 \frac{\partial^2 w}{\partial x \partial y} \end{Bmatrix}, k = 1, 3 \quad (5.93)$$

$$\boldsymbol{\epsilon}^{(2)} = \begin{Bmatrix} \frac{\partial u_2}{\partial x} \\ \frac{\partial v_2}{\partial y} \\ \frac{\partial u_2}{\partial y} + \frac{\partial v_2}{\partial x} \end{Bmatrix} + \frac{z_2}{h_2} \begin{Bmatrix} \frac{\partial u_3}{\partial x} - \frac{\partial u_1}{\partial x} + \frac{d_1}{2} \frac{\partial^2 w}{\partial x^2} \\ \frac{\partial v_3}{\partial y} - \frac{\partial v_1}{\partial y} + \frac{d_1}{2} \frac{\partial^2 w}{\partial y^2} \\ 2 \frac{\partial^2 w}{\partial x \partial y} \\ 0 \\ 0 \end{Bmatrix} + \frac{1}{h_2} \begin{Bmatrix} 0 \\ 0 \\ 0 \\ u_3 - u_1 + \frac{d_1}{2} \frac{\partial w}{\partial x} \\ v_3 - v_1 + \frac{d_1}{2} \frac{\partial w}{\partial y} \end{Bmatrix} \quad (5.94)$$

where $\boldsymbol{\epsilon}^{(k)} = [\varepsilon_x^{(k)} \varepsilon_y^{(k)} \gamma_{xy}^{(k)}]^T$, $\boldsymbol{\epsilon}^{(2)} = [\varepsilon_x^{(2)} \varepsilon_y^{(2)} \gamma_{xy}^{(2)} \gamma_{xz}^{(2)} \gamma_{yz}^{(2)}]^T$, $u_2 = \frac{1}{2} (u_1 + u_3 + \frac{d_2}{2} \frac{\partial w}{\partial x})$, $v_2 = \frac{1}{2} (v_1 + v_3 + \frac{d_2}{2} \frac{\partial w}{\partial y})$, $d_1 = h_1 + h_3$ and $d_2 = h_2 - h_3$.

In the equations above, z_k , $k = 1, 3$ designate the transverse coordinates measured from the lower surface of each layer, and subscripts m , b and s designate membrane, bending and shear effects, respectively.

The discretization of the displacement fields within the element is made by using the following linear and cubic interpolation functions:

$$\begin{aligned} u_1(x, y, t) &= a_1(t) + a_2(t)x + a_3(t)y + a_4(t)xy \\ v_1(x, y, t) &= a_5(t) + a_6(t)x + a_7(t)y + a_8(t)xy \\ u_3(x, y, t) &= a_9(t) + a_{10}(t)x + a_{11}(t)y + a_{12}(t)xy \\ w(x, y) &= b_1(t) + b_2(t)x + b_3(t)y + b_4(t)x^2 + b_5(t)xy \\ &\quad + b_6(t)y^2 + b_7(t)x^3 + b_8(t)x^2y + b_9(t)xy^2 \\ &\quad + b_{10}(t)y^3 + b_{11}(t)x^3y + b_{12}(t)xy^3. \end{aligned}$$

where the coefficients $a_i(t)$, $i = 1$ to 16 and $b_i(t)$, $i = 1$ to 12 are to be expressed in terms of the 28 nodal displacements and rotations that form the vector of element degrees-of-freedom $\boldsymbol{\delta}_e(t)$, in such a way that:

$$\boldsymbol{u}_e(x, y, t) = N_e(x, y)\boldsymbol{\delta}_e(t) \quad (5.95)$$

where $N_e(x, y)$ is the matrix formed by the shape functions.

Based on the kinematic hypotheses and stress states assumed for each layer, the mass and stiffness matrices at element level are expressed as:

$$\mathbb{M}_e = \sum_{k=1}^3 \rho_k h_k \int_x \int_y \mathbf{N}_e^T(x, y) \mathbf{N}_e(x, y) dx dy \quad (5.96)$$

$$\mathbb{K}_e(\omega) = \bar{\mathbb{K}} + \mathbb{K}_v(\omega) \quad (5.97)$$

$$\bar{\mathbb{K}} = \sum_{k=1,3} \int_x \int_y \int_z \mathbf{D}_k^T(x, y, z) \mathbf{C}_k \mathbf{D}_k(x, y, z) dx dy dz \quad (5.98)$$

$$\mathbb{K}_v(\omega) = \int_x \int_y \int_z \mathbf{D}_2^T(x, y, z) \mathbf{C}_2(\omega) \mathbf{D}_2(x, y, z) dx dy dz \quad (5.99)$$

where \mathbb{K} and $\bar{\mathbb{K}}_v$ are, respectively, the contributions of the elastic and viscoelastic parts to the element stiffness matrix. ρ_k is the mass density of the k -th layer and matrices $\mathbf{D}_k(x, y, z)$ are constructed by applying the differential operators appearing in the strain-displacement relations to the matrix of shape functions. In addition, \mathbf{C}_k , $k = 1, 3$ and $\mathbf{C}_2(\omega)$ are, respectively, the matrices of elastic and viscoelastic material properties.

5.4.3 Reduction Methods for Structures with Viscoelastic Materials

We recall here that the discretized equation of motion for a vibrating structure with viscoelastic material in frequency domain is of the form:

$$[\mathbb{K}^*(\omega) - \omega^2 \mathbb{M}] \mathbf{U}^* = \mathbf{F}, \quad (5.100)$$

where $\mathbb{K}^*(\omega)$ is the complex, frequency-dependent stiffness matrix, \mathbb{M} is the mass matrix, \mathbf{F} is the amplitude vector of the harmonic load of angular frequency ω applied to the structure and \mathbf{U}^* is the nodal degrees of freedom vector.

For large-scale systems, the direct resolution of Eq. (5.100) is computationally expensive and performing frequency sweeps with fine frequency steps becomes prohibitive. To alleviate the computational burden, several reduction techniques are proposed in the literature. Most of them can be classified in three main groups of techniques:

- Modal techniques [36, 37]
- Non-modal techniques [38, 39]
- Domain decomposition techniques [40, 41]

The first two groups of methods rely on the concept of subspace projection: a lower-order approximation \mathbf{U}_r^* of the solution \mathbf{U}^* is sought in a subspace of reduced dimension spanned by the columns of a reduction basis \mathbb{T} :

$$\mathbf{U}^* \approx \mathbf{U}_r^* = \mathbb{T}\mathbf{X}^* \quad (5.101)$$

Once projected onto the reduction basis, the discretized system yields a much smaller reduced system so that the approximated solution can be obtained with important computational gain. The methods classified as modal techniques use modal information to form the reduction basis, as opposed to non-modal techniques. It should be noted at this point that traditional modal techniques, such as mode superposition method, are not applicable to systems with frequency-dependent materials. Computational variants of the mode superposition method have been developed [42–48] and are discussed in Sect. 5.4.3.1. Most methods pertaining to the second group which are appropriate for systems with frequency-dependent systems are interpolatory model order reduction methods. They are based on an approximation of \mathbf{U}^* which matches the solution and some of its derivatives at some frequencies ω_p :

$$\mathbf{U}_r^*(\omega_p) = \mathbf{U}^*(\omega_p), \frac{d\mathbf{U}_r^*}{d\omega}(\omega_p) = \frac{d\mathbf{U}^*}{d\omega}(\omega_p), \frac{d^2\mathbf{U}_r^*}{d\omega^2}(\omega_p) = \frac{d^2\mathbf{U}^*}{d\omega^2}(\omega_p), \dots \quad (5.102)$$

One popular approach, described in Sect. 5.4.3.2, that embraces this concept, is to use Padé type approximants.

Finally, domain decomposition techniques, or dynamic substructuring techniques consist in partitioning the structure into substructures, which can be solved independently before being recombined to obtain the global dynamic response. For each substructure, the reduced local system to be solved is of the form:

$$[\mathbb{K}_j^*(\omega) - \omega^2 \mathbb{M}_j] \mathbf{U}_j^* = \mathbf{F}_j, \quad (5.103)$$

where \mathbf{U}_j^* contains the nodal degree of freedom associated to the substructure j . Coupling strategies at the interfaces between substructures ensures continuity of displacements at the interfaces.

5.4.3.1 Modal Techniques

The mode superposition method is the reduction method most extensively used in the industry for efficient computational dynamic analysis, and is implemented in most FEA softwares. This method, initially developed for undamped systems, aims at efficiently computing the solution \mathbf{U} of the undamped equation of motion:

$$[\mathbb{K} - \omega^2 \mathbb{M}] \mathbf{U} = \mathbf{F}, \quad (5.104)$$

where \mathbb{K} and \mathbb{M} are the stiffness and mass matrices of dimensions $N \times N$, where N is the size of the system. The associated generalized eigenvalue problem is:

$$[\mathbb{K} - \omega_k^2 \mathbb{M}] \boldsymbol{\phi}_k = \mathbf{0}, \quad (5.105)$$

where $\boldsymbol{\phi}_k$ and is the eigenvector corresponding to the eigenfrequency ω_k . The basis formed by the eigenvectors $\mathbf{T} = [\boldsymbol{\phi}_1, \boldsymbol{\phi}_2, \dots, \boldsymbol{\phi}_N]$ spans the response space, so that the dynamic response can be expressed as a superposition of modal contributions:

$$\mathbf{U} = \sum_{k=1}^N \boldsymbol{\phi}_k \chi_k = \mathbf{T} \mathbf{X} \quad (5.106)$$

where $\mathbf{X} = [\chi_1, \chi_2, \dots, \chi_N]^T$ is the vector of modal coordinates. Due to the orthogonality properties of eigenvectors, projecting Eq. (5.104) onto the basis of eigenmodes leads to uncoupled equations of motion, represented in modal coordinates as:

$$(\omega^2 - \omega_k^2) \chi_k = \boldsymbol{\phi}^T \mathbf{F} \quad (5.107)$$

To reduce the computational cost, an approximation \mathbf{U}_r^* of the solution is sought in a subspace of reduced dimension spanned the first eigenvectors of the system:

$$\mathbf{U} \approx \mathbf{U}_r^* = \sum_{k=1}^n \boldsymbol{\phi}_k \chi_k \quad (5.108)$$

where $n \ll N$. This truncation is justified by the fact that the low frequency response is generally dominated by the modes of lowest eigenvalues. In practice, as an engineering rule of thumb, the eigenvectors selected in the reduced basis are those with eigenfrequencies up to twice the upper limit of the considered frequency range. A static correction is generally added in the reduced basis to account for the contribution of the truncated modes in the static response [49]. For a vibrating structure with viscoelastic material, the stiffness matrix becomes complex and frequency-dependent (see Eq. 5.100) which leads to a nonlinear eigenvalue problem [50]:

$$[\mathbb{K}^*(\lambda_k^*) + \lambda_k^{2*} \mathbb{M}] \boldsymbol{\phi}_k^* = \mathbf{0}, \quad (5.109)$$

where the eigenfrequency λ_k^* and the eigenvectors $\boldsymbol{\phi}_k^*$ are complex. The main challenge in applying modal reduction techniques to systems with viscoelastic material lies in the resolution of this nonlinear eigenvalue problem. Two major numerical approaches arise from literature review. The first one consists in estimating the complex eigenvectors, either by the asymptotic numerical method [51], either by iterative procedures such as the iterative modal strain energy method [48], the iterative complex eigensolution method [46] or the modified modal strain energy method [44]. The second approach consists in solving a linear eigenvalue problem and enrich the modal basis by adding corrective terms. This approach is based on the modal strain energy method [45] which approximates the eigenvectors of Eq. (5.109) by the eigenvectors of the following linear eigenproblem:

$$[\mathbb{K}_0 - \omega_k^2 \mathbb{M}] \boldsymbol{\phi}_k = \mathbf{0}, \quad (5.110)$$

where $\mathbb{K}_0 = \Re(K^*(\omega = \omega_p))$ is the real part of the complex stiffness matrix evaluated at a given frequency ω_p , and the eigenvectors $\boldsymbol{\phi}_k$ are referred to as pseudo-normal modes. While providing good results for lightly damped structures, this method can lead to significant errors for highly damped structures. To improve the accuracy of the approximated solution, a variety of corrective terms can be added into the reduction basis: pseudo-normal modes computed with a stiffness matrix evaluated at a different frequency (so-called multi-modal projection method) [42, 52], viscoelastic damping forces [47, 53], displacement residuals [43, 53]. Another approach based on the enrichment of the modal basis is presented in Subsection 5.5.3.1.

An overview and a quantitative comparison of the various modal techniques based on modal projection for structures with frequency-dependent damping is given in [36]. Figure 5.12 compares modal techniques in terms of mean displacement error and relative computational time, when computing the frequency response of a cantilever sandwich beam. For each method, an increasing number of modes (or pseudo-modes) is included in the reduction basis. The reader can refer to [36] for more details on the implementation of those modal techniques and their application to a more challenging structure.

5.4.3.2 An Example of Non-modal Techniques: Padé-Based Methods

A class of non-modal reduction techniques which allows the computation of an approximated solution based on the characterization of the solution \mathbf{U}^* and its derivatives at sampling points ω_p (see Eq. (5.102)). Several approaches have been proposed in the literature for constructing an interpolatory approximation of the solution [38, 39]. Among them, Padé approximation offers a good representation of a function containing poles, as it is the case for structural frequency responses.

Padé-based methods consist in approximating a function $u(\omega)$ around a point ω_p by a rational function of the type:

$$u(\omega_p + \Delta\omega) \approx \frac{\sum_{k=0}^L p_k (\Delta\omega)^k}{\sum_{k=0}^M q_k (\Delta\omega)^k} = \frac{P_L(\Delta\omega)}{Q_M(\Delta\omega)} \quad (5.111)$$

where $\Delta\omega = \omega - \omega_p$, $P_L(\Delta\omega)$ and $Q_M(\Delta\omega)$ are two power series in the variable $\Delta\omega$, to the orders L and M respectively. When they exist, the Padé coefficients p_k and q_k are unique [54]. By setting $q_0 = 1$, the $L + M + 1$ remaining coefficients can be determined by requiring that when the rational function is expanded in a Taylor series around ω_p , the first $L + M + 1$ coefficients match those of the Taylor expansion of $u(\omega)$:

$$A_{L+M}(\Delta\omega) = \frac{P_L(\Delta\omega)}{Q_M(\Delta\omega)} \quad (5.112)$$

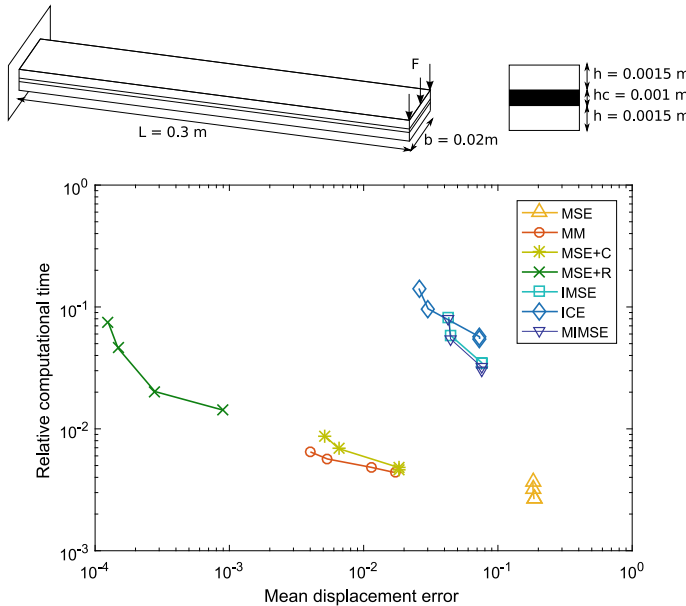
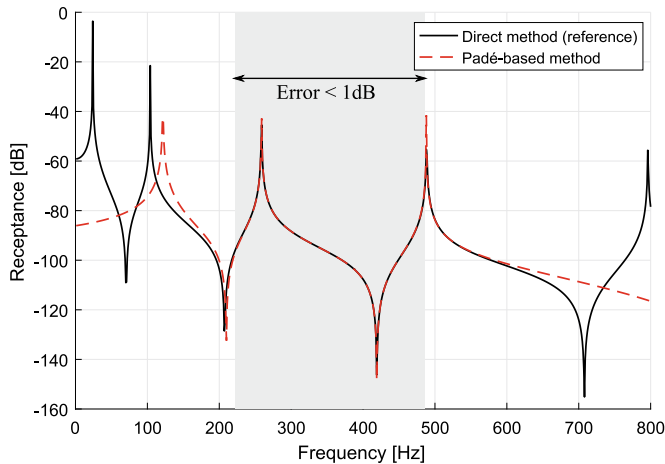
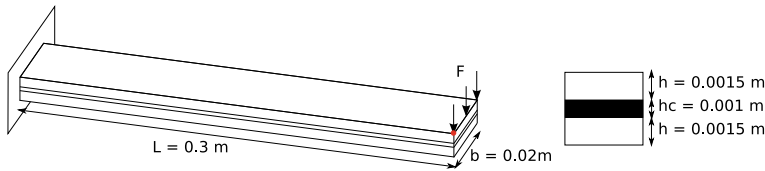


Fig. 5.12 Relative computational time of the frequency response of the sandwich beam using: the modal strain energy method (MSE) [45], the multi-model method (MM) [42, 52], the MSE technique enriched with viscoelastic damping forces (MSE+C) [47, 53] or displacement residuals (MSE+R) [43, 53], the iterative MSE method (IMSE) [48], the iterative complex eigensolution method (ICE) [46] and the modified MSE method (MMSE) [44]

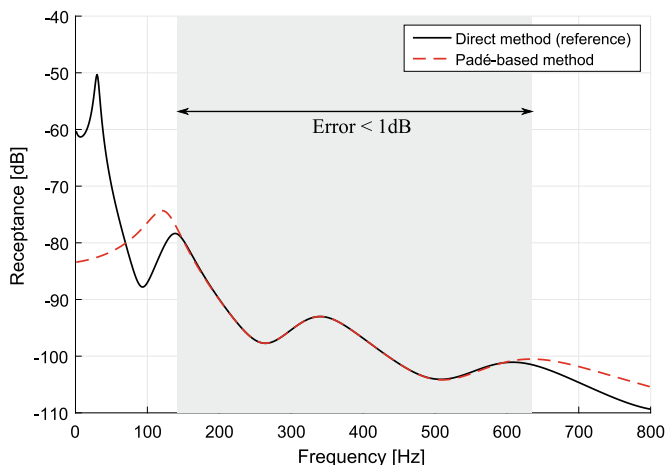
where $A_{L+M}(\Delta\omega) = \sum_{k=0}^{L+M} \frac{u^{(k)}(\omega_p)}{k!} (\Delta\omega)^k$. In this way, the Padé coefficients are obtained by solving a small system of $(L + M + 1)$ linear equations. In [54], the Padé coefficients are calculated by a two-step procedure, to limit the numerical conditioning problem that may arise. When the reconstruction of $u(\omega)$ is based on the solution at one point $u(\omega_p)$, the method is referred to as a single-point Padé approximation, but it can be extended to multi-point Padé approximations [55] for better accuracy and efficiency.

The Padé-based method, previously introduced for a unidimensional function, can be applied to solve Eq. (5.100) by using Padé approximants for each dof solution function $U_i^*(\omega)$. As implied by Eq. (5.112), the computation of the $(L + M + 1)$ Padé approximants requires the determination of the $(L + M)$ first derivatives of the solution vector $\mathbf{U}^*(\omega)$ around ω_p : $\mathbf{U}^{*(k)}(\omega_p)$. They can be obtained from differentiating Eq. (5.100) at the order k :

$$\sum_{j=0}^k \binom{k}{j} \mathbb{Z}^{(k-j)}(\omega_p) \mathbf{U}^{*(j)}(\omega_p) = \mathbf{F}^{(k)}(\omega_p) \quad (5.113)$$



(a) Undamped problem



(b) Damped problem

Fig. 5.13 Approximation of the frequency response of the cantilever sandwich beam around 340 Hz using Padé-based method (considering $L = 3$ and $M = 4$ in the truncated power series), for an undamped (a) and a damped (b) problem

where $\mathbb{Z}(\omega) = \mathbb{K}^*(\omega) - \omega^2 \mathbb{M}$. In the case of constant harmonic excitations, the right-hand term is null for $k > 0$.

The k th derivative of the solution $\mathbf{U}^{*(k)}(\omega_p)$ can be computed in a recursive way, in terms of its lower-order derivatives, by solving the following system of equations, of dimension N :

$$\mathbb{Z}(\omega_p) \mathbf{U}^{*(k)}(\omega_p) = \mathbf{F}^{(k)}(\omega_p) - \sum_{j=0}^{k-1} \binom{k}{j} \mathbb{Z}^{(k-j)}(\omega_p) \mathbf{U}^{*(j)}(\omega_p) \quad (5.114)$$

Padé-based methods are particularly interesting for the reconstruction of frequency response of structures damped by viscoelastic materials for two main reasons:

- Contrary to most reduction methods, Padé-based methods are not limited to constant non-proportional damping. In the formulation, the frequency dependence is represented by scalar functions multiplying a constant matrix, so that the successive derivatives of \mathbb{Z} can be determined analytically for a given viscoelastic model [56].
- Applications of this method to vibro-acoustic problems indicate that Padé-based methods are more efficient for highly damped structures since the smoothness of damped responses increases the range of convergence of the approximation [57].

An illustration of the Padé-based method, applied to the reconstruction of the frequency response of a sandwich cantilever beam, is given in Fig. 5.13. It shows the efficiency of this approach to approximate damped responses.

5.5 Examples

This section describes additional examples of applications of viscoelastic materials to problems of industrial interest, exploring many of the aspects addressed previously in this chapter.

5.5.1 Automotive Application

Often regarded as significantly quieter than thermal motors, electric motors are becoming more widely used in the automotive industry. Nevertheless, since a vehicle's NVH characteristics are an important quality criterion, the reduction of noise and vibration in electric alternators is a competitive issue [58]. There are three main sources of noise and vibrations in such systems: aerodynamic, mechanical and electromagnetic. The noise generated by electromagnetic excitations usually predominates at low frequencies (below 10 kHz). Therefore it is important to understand this phenomenon, and correct it as early as possible during the design process.

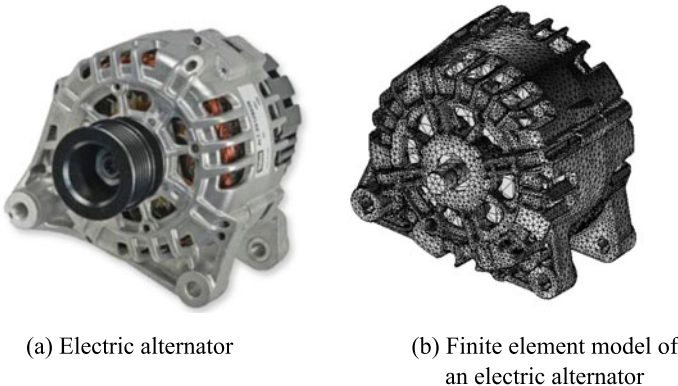


Fig. 5.14 Finite element model of an electric alternator (≈ 1.3 million degrees of freedom)

An electric alternator converts mechanical power, transmitted through a driving shaft to the rotor, into electric power. Most common electric alternators (see Fig. 5.14a) are composed of a moving rotor, which acts as a spinning electromagnet, and a fixed stator surrounding the rotor core which contains a set of conductive coils. Both are integrated into a housing, the rotor shaft being supported by bearings connected to the housing and the stator being fixed between the front and the rear housing. Rotation of the rotor creates a constantly rotating electromagnetic field around the stator, which induces voltage in the stator windings. The rotating electromagnetic forces between the rotor and the stator act as a dynamic excitation which causes the structure to vibrate and radiate noise.

One way of mitigating electromagnetic noise and vibrations is to reduce the structural response of the alternator by applying damping treatments. In [59], prestrained elastomer buffers are placed between the housing and the stator, as indicated in Fig. 5.15. Electric alternators operate over a large temperature range, typically from -20 to 200°C , which can modify significantly the damping performance of the elastomer buffers due to viscoelastic effects. Moreover, the elastomer buffers are prestrained up to 30% when assembling the stator into the housing. Prestrain is an additional parameter on which the mechanical properties of viscoelastic materials depend. The goal of this study is to evaluate the influence of temperature and prestrain on the dynamic response of the alternator.

The finite element model of the electric alternator contains about 1.3 million degrees of freedom (Fig. 5.14b). The alternator is maintained in position by constraining the four mounting screw holes. The structural dynamic response of this system to a harmonic excitation applied on the stator winding is sought in the frequency range [0–2000] Hz. As the elastomer buffers evidence viscoelastic behavior, this frequency sweep problem is described by Eq. (5.100).

Due to the size of the model, a direct evaluation of the dynamic response at a single frequency takes about 30' on a work station with 8 logical processors and 64 Go bRAM. Therefore, reduction method should be applied to reduce the computational

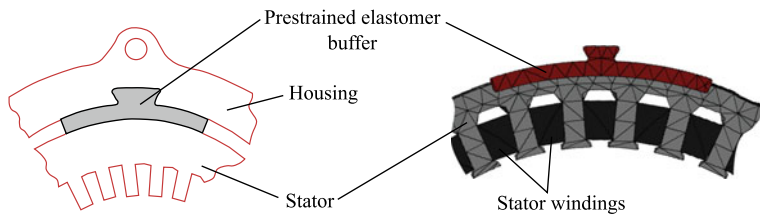


Fig. 5.15 Presence of viscoelastic materials to reduce structural vibrations and as a consequence reduce radiated noise [ref to patent]

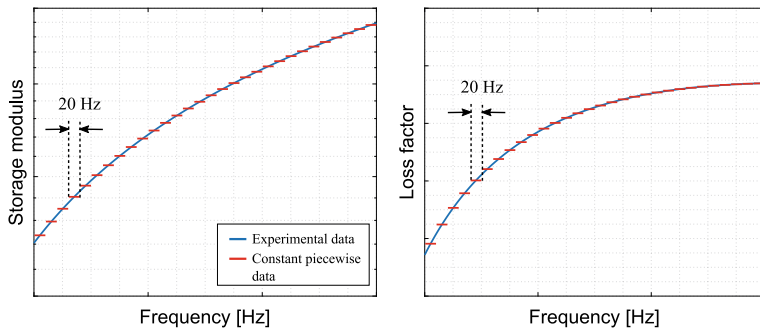


Fig. 5.16 Definition of constant piecewise viscoelastic properties

time. However, the range of reduction methods provided by most industrial FE software is rather limited. The classical mode superposition method is generally available in any industrial FE software, but cannot take into account the frequency-dependent properties of viscoelastic materials. An alternative technique is to consider constant piecewise viscoelastic properties, and to apply the modal strain energy method on each frequency subrange. In this study, the frequency band under study is divided into subranges of 20 Hz (see Fig. 5.16). The dynamic response of the alternator is computed on each frequency subrange $[f_k, f_{k+1}]$ by considering constant viscoelastic properties for the elastomer buffers:

$$\bar{E}_k^* = \frac{1}{f_{k+1} - f_k} \int_{f_k}^{f_{k+1}} E^*(\omega) d\omega$$

where \bar{E}_k^* is the average Young's modulus of the elastomer buffer on the frequency subrange k .

Considering a frequency step of 1 Hz, the estimated time to compute the dynamic response on the frequency range [0–2000] Hz using a direct method would be about 40 days. Using the proposed method allows a drastic reduction in the computational time:

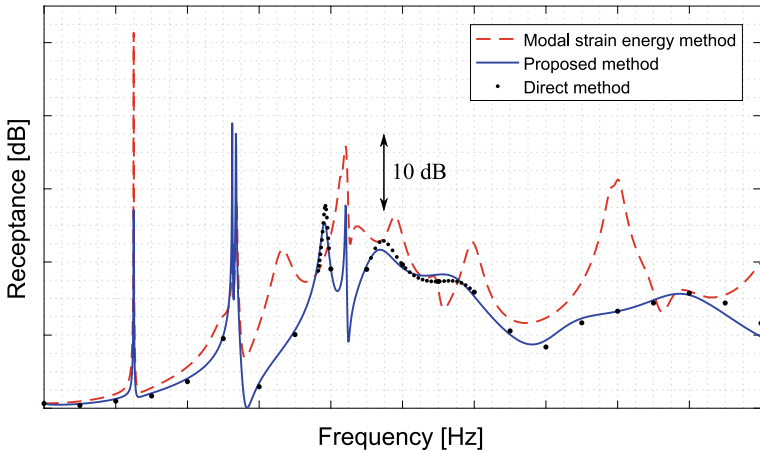


Fig. 5.17 Frequency response of the alternator at 20 °C without prestrain, using the direct method, the modal strain energy method and the proposed methodology

28 h instead of 40 days. Figure 5.17 compares the structural dynamic response computed by the proposed method, the modal strain energy method (considering constant viscoelastic properties on the whole frequency range) and the direct method for some sampled frequencies. The proposed method produces a good approximation of the dynamic response, at a reasonable cost, and can be used to study the influence of temperature and prestrain on the dynamic response.

The frequency response of the alternator is computed for three operating temperatures: -20, 20 and 200 °C, without prestrain in the elastomer buffers. Figure 5.18 evidences a strong influence of temperature on the structural dynamic response. Only the vibration modes of the rotor are little affected by a variation in temperature. Since the elastomer buffers are placed between the stator and the housing, they strongly modify the dynamic response when stator modes are excited.

To study the influence of prestrain in the elastomers buffers, the dynamic response of the alternator is computed at 20 °C considering viscoelastic properties measured at 30% compression prestrain. Figure 5.19 shows that prestrain also affects the dynamic response of the alternator, but to a lesser extent than temperature.

This study shows the importance of applying adequate model order reduction techniques when computing the frequency response of a structure integrating viscoelastic materials. It also emphasizes the impact of temperature and prestrain on the dynamic response of the damped structure.

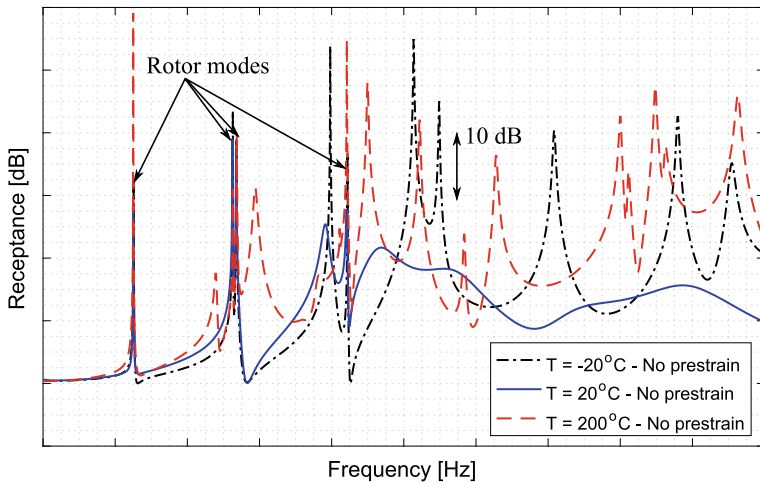


Fig. 5.18 Influence of temperature on the frequency response of the alternator

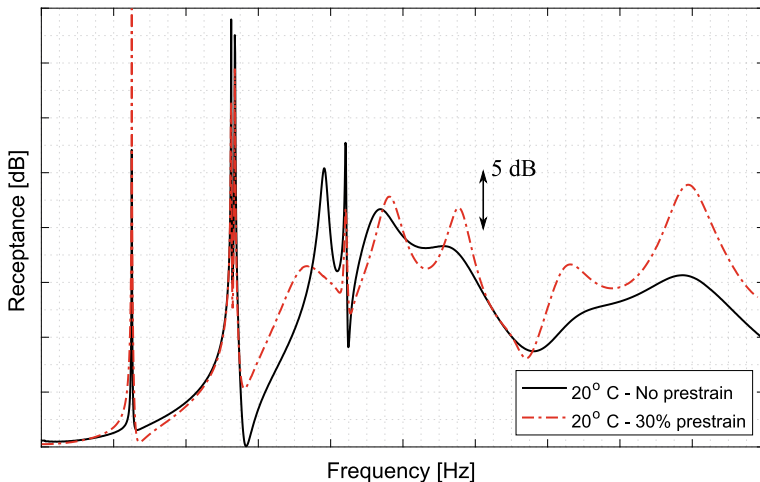


Fig. 5.19 Influence of prestrain on the dynamic response of the alternator

5.5.2 Stochastic Parameter Identification

In order to use computational models for predictive analyses and mechanical design one should properly calibrate them. It is the case when the computational model contains a viscoelastic structure as one of its sub-components.

As for the calibration of viscoelastic constitutive models, it is quite usual to consider frequency domain data and calibration mechanical prototypes specifically designed for that purpose [60–63].

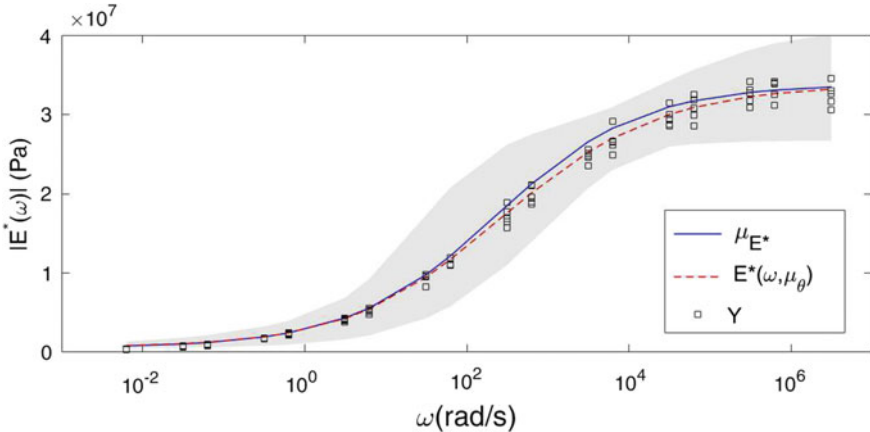


Fig. 5.20 Complex modulus. $\mu_{E*} = |\mathbb{E}[E^*(\omega, \theta)]|$: corresponds to the expected value of model response. $E^*(\omega, \mu_\theta) = |E^*(\omega, \mathbb{E}[\theta])|$: corresponds to the model prediction evaluated at the mean value of model parameters $\mathbb{E}[\theta]$. Y: corresponds to synthetic data used for model calibration. Gray area: corresponds to the 99% credibility interval of model predictions

Here we present an example of model calibration when the constitutive model of interest is the fractional standard linear solid presented in Eq. (5.60). The example considers synthetic data that is polluted with numerical noise. The ideal data \mathbf{y}^I corresponds to the complex modulus $E^*(\omega, \boldsymbol{\theta})$ generated with a certain vector of model parameters $\boldsymbol{\theta} = \{E, E_1, \eta, \alpha\}^T$. The reference model used here has the following parameters: $E = 3.32 \times 10^7$ Pa, $E_1 = 5.96 \times 10^5$ Pa, $\eta = 2.51 \times 10^6$ Pas $^\alpha$ and $\alpha = 0.45$. The synthetic data \mathbf{y} is generated from the ideal data \mathbf{y}^I as follows, $\mathbf{y} = \mathbf{y}^I + \mathbf{v}$, where \mathbf{v} is a vector of numerically simulated noise. It is considered that measurements are taken at 18 frequencies ω_r encompassing several decades. The set of synthetic data used for model calibration is presented in Fig. 5.20 by black squares.

Information about model parameters were obtained by means of Bayesian inference using the Metropolis-Hastings algorithm [25, 27, 29, 30, 64]. Figure 5.20 presents the expected mean of model response $|\mathbb{E}[E^*(\omega, \theta)]|$, the model response evaluated at the mean value of model parameters $|E^*(\omega, \mathbb{E}[\theta])|$ and the 99% credibility interval provided by the calibrated model. It should be emphasized that the model is stochastic inasmuch as its parameters are random variables. The samples $\{\boldsymbol{\theta}^{(1)}, \boldsymbol{\theta}^{(2)}, \dots, \boldsymbol{\theta}^{(mc)}\}$ obtained from the posterior density $\pi(\boldsymbol{\theta}|\mathbf{y})$ are used to obtain statistics of model parameters $\boldsymbol{\theta}$. As an example, Fig. 5.21 presents the histograms of each of the model parameters. Detailed analyses concerning Bayesian model calibration may be found in the works by Zhang et al. [63] and by Hernández et al. [60].

This illustrates the identification of the parameters of a particular viscoelastic model in a stochastic framework, but can certainly be extended to other constitutive models as well.

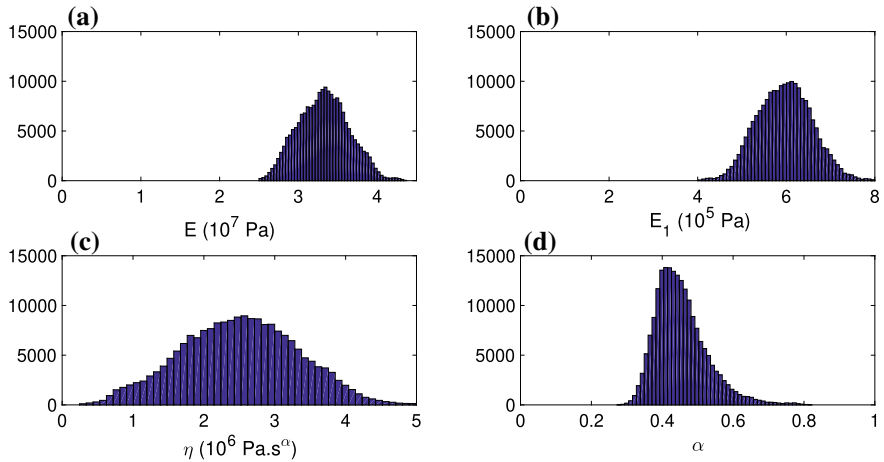


Fig. 5.21 Histogram of model parameters $\theta = \{E, E_1, \eta, \alpha\}^T$

5.5.3 Aeroelastic Application

This section presents an application of viscoelastic material in the form of constrained layer to increase the dynamic aeroelastic stability of a curved panel under supersonic flow.

According to [65] “aeroelasticity is the subject that describes the interaction of aerodynamic, inertia and elastic forces for a flexible structure and the phenomena that can result”. One of the most notorious and relevant aeroelastic phenomena in the scope of aerospace engineering, known as *flutter*, involves the onset of dynamic instability when the relative velocity between the air flow and the structure achieves a certain value. As this condition can have catastrophic consequences, flutter must be accounted for and avoided in the early design phases or by means of corrective actions. As a result, many strategies have been devised to control flutter instability. A comprehensive historic and scientific survey of a large number of research programs devoted to aeroelastic control up to 2004 is provided in Ref. [66]. Among the various strategies, the use of viscoelastic materials as a passive means of mitigating aeroelastic phenomena, especially by increasing stability margins, has been investigated by many authors [67–70]

The emphasis here is placed on the use of an efficient model condensation technique developed in [71] to alleviate the computational cost involved in aeroelastic predictions.

5.5.3.1 An Iterative Model Reduction Method for General Aeroviscoelastic Systems

It is presented here an efficient and accurate iterative enriched Ritz method (IERM) [71] used to obtain reduced-order aeroelastic models with viscoelastic damping.

For aeroelastic systems with viscoelastic damping (named herein *aeroviscoelastic systems*), discretized by finite elements (see Sect. 5.4) the flutter stability analysis is carried-out by solving an eigenvalue problem of the type [71]:

$$[\mathbf{K}_e + G(\omega_j) \bar{\mathbf{K}}_v + \lambda \mathbf{A} - \omega_j^2 \mathbf{M}] \boldsymbol{\phi}_j = \mathbf{0} \quad (5.115)$$

where $\boldsymbol{\phi}_j$, $j = 1, 2, \dots$ are the complex eigenvalues and frequency, respectively, \mathbf{A} is the aerodynamic matrix, $\lambda = \rho_\infty U_\infty^2 / \sqrt{M_\infty^2 - 1}$ is the dynamic pressure, ρ_∞ and U_∞ designate the air density and free-stream velocity, respectively, and M_∞ is the free-stream Mach number.

In this case, one could use the enriched reduction method (ERM) proposed in [72] to reduce the aeroviscoelastic system (5.115), where the reduction basis \mathbf{T} is formed by the eigenmodes of the associated conservative viscoelastic system (5.116), $\boldsymbol{\phi}^0 = [\boldsymbol{\phi}_1^0, \dots, \boldsymbol{\phi}_{NR}^0]$, which are further enriched by first-order static residues associated to the excitations, $\mathbf{R} = \mathbf{K}_0^{-1} \mathbf{b}$, and the viscoelastic forces, $\mathbf{R}_v^0 = \mathbf{K}_0^{-1} \bar{\mathbf{K}}_v \boldsymbol{\phi}^0$.

$$[\mathbf{K}_e + G_0 \bar{\mathbf{K}}_v - (\omega_k^0)^2 \mathbf{M}] \boldsymbol{\phi}_k^0 = \mathbf{0} \quad (5.116)$$

A further enrichment of the reduction basis is performed to account for the first static residues associated to the aerodynamic forces, $\mathbf{R}_A^0 = \mathbf{K}_0^{-1} \mathbf{A} \boldsymbol{\phi}^0$, resulting in the following enriched reduction basis for aeroviscoelastic systems:

$$\mathbf{T}_{ERM} = [\boldsymbol{\phi}_0 \quad \mathbf{R} \quad \mathbf{R}_v^0 \quad \mathbf{R}_A^0] \quad (5.117)$$

However, as will be shown later the basis \mathbf{T}_{ERM} is not capable of predicting the aerodynamic modifications associated to the supersonic airflow. Thus, it is clearly the necessity of a more accurate enriched reduction basis.

The IERM method presented here is a variant of the iterative strategy suggested in [73] to construct a constant modal projection basis in order to account for the aerodynamic modifications provoked by the flow, besides the frequency-dependent behavior of the viscoelastic material.

Starting from the nominal basis vectors $\boldsymbol{\phi}_k^0$ and frequency ω_k^0 , $k = 1, \dots, NR$, obtained by solving the eigenproblem (5.116), the following steps are followed iteratively, starting from the definition of the initial IERM basis $\boldsymbol{\phi}^0$, a tolerance tol and the temperature of the viscoelastic material:

Step 1: the complex dynamic stiffness matrix of the full finite element model is computed for ω_k^0 and λ_k :

$$\mathbf{Z}(\omega_k^0, T) = \mathbf{K}_e + G(\omega_k^0, T) \bar{\mathbf{K}}_v + \lambda_k \mathbf{A} - (\omega_k^0)^2 \mathbf{M} \quad (5.118)$$

where the pressure interval $\lambda_{min} \leq \lambda_k \leq \lambda_{max}$ is chosen to account for the number of eigenmodes $k = 1$ to NR considered in the basis ϕ^0 , where $\lambda_{min} = \lambda_1$ and $\lambda_{max} = \lambda_{NR}$ belong to the ordered series of pressure levels $\lambda_1 < \lambda_2 < \dots < \lambda_{NR}$ used to perform the flutter analysis. The following substeps are performed until the convergence criterion $\varepsilon_k < tol$ is satisfied, where ε_k is the error and tol is a specified tolerance:

Substep 1.1: the reduced dynamic stiffness matrix is computed as:

$$\mathbf{Z}(\omega_k^0, T) = \mathbf{T}_{IERM}^T [\mathbf{K}_e + G(\omega_k^0, T) \bar{\mathbf{K}}_v + \lambda_k \mathbf{A} - (\omega_k^0)^2 \mathbf{M}] \mathbf{T}_{IERM} \quad (5.119)$$

Substep 1.2: residuals associated to the external excitations for the reduced responses given by $\mathbf{Q}_R(\omega_k^0, T) = \mathbf{Z}(\omega_k^0, T)^{-1} \mathbf{T}_{IERM}^T \mathbf{b}$ are obtained as follows:

$$\mathbf{R}_f(\omega_k^0, T) = [\mathbf{K}_e + G(\omega_k^0, T) \bar{\mathbf{K}}_v + \lambda_k \mathbf{A} - (\omega_k^0)^2 \mathbf{M}] \mathbf{Q}_R(\omega_k^0, T) - \mathbf{b} \quad (5.120)$$

Substep 1.3: the displacement residuals are computed as:

$$\mathbf{R}_d(\omega_k^0, T) = [\mathbf{K}_e + G_0 \bar{\mathbf{K}}_v]^{-1} \mathbf{R}_f(\omega_k^0, T) \quad (5.121)$$

Substep 1.4: enrichment of the basis \mathbf{T}_{IERM}^k to generate the new reduction basis:

$$\mathbf{T}_{IERM}^{(k+1)} = \begin{bmatrix} \mathbf{T}_{IERM}^{(k)} & \Re(\mathbf{R}_d(\omega_k^0, T)) & \Im(\mathbf{R}_d(\omega_k^0, T)) \end{bmatrix} \quad (5.122)$$

Substep 1.5: computation of error indicator as:

$$\varepsilon_k = \frac{\mathbf{R}_d(\omega_k^0, T)^T [\mathbf{K}_e + G_0 \bar{\mathbf{K}}_v] \mathbf{R}_d(\omega_k^0, T)}{\mathbf{T}_{IERM}^{(k+1)}^T \mathbf{Q}_R(\omega_k^0, T) [\mathbf{K}_e + G_0 \bar{\mathbf{K}}_v] \mathbf{Q}_R(\omega_k^0, T) \mathbf{T}_{IERM}^{(k+1)}} \quad (5.123)$$

It is expected that the size of the IERM basis (5.122) increases at each substep. However, it improves significantly the accuracy of the predictions. Additionally, due to the small influence of the residuals associated to the aerodynamic forces on the accuracy of the flutter predictions, it is not necessary to consider them in the basis.

In the application that follows, the interest is to demonstrate the efficiency and accuracy of the IERM reduction method to deal with a relatively complex aeroelastic system containing constrained viscoelastic layers for flutter suppression. It is considered a curved cylindrical stiffened panel found in aeronautical applications, shown in Fig. 5.22. The FE model is formed by 768 thin shell elements and 160 three-layer sandwich shell elements, according to the formulation presented in Sect. 5.4.2. The positions of the viscoelastic treatments are indicated in green in the same figure. The resulting aeroviscoelastic system, having a total of 5928 degrees-of-freedom, is subjected to a supersonic airflow with airspeed indicated by U_∞ , along direction x .

The dimensions of the curved panel are: internal radius: 938 mm; arc length: 680 mm; length: 720 mm; thicknesses of the base-plate and stringers: 1.2 mm; height of the stringers: 30 mm. The constraining and viscoelastic layers have the same

thickness of 0.5 mm. The mechanical properties of the elastic layers and stringers are: elastic modulus $E = 70 \times 10^9 \text{ N/m}^2$, density $\rho = 2700 \text{ kg/m}^3$, Poisson ratio $\nu = 0.34$. For the viscoelastic core, it is used the well-known TM3M ISD112, whose properties are provided in [13].

First it is verified the accuracy of the IERM method in predicting the frequency response functions (FRFs) of the aeroviscoelastic model subjected to supersonic flow. In this case, $\mathbf{H}(\omega, \lambda, T)$ represents the FRF related to the transverse displacement of the panel at point P , due to an external excitation applied at point I , both points being indicated in Fig. 5.22. The frequency range is [0–1000 Hz], for an arbitrarily airspeed of 500 m/s, and temperature 15 °C.

For a reduction basis $\mathbf{T}_{IERM} = [\phi^o(50) \quad \mathbf{R}_d(104)]$ composed by 50 eigenmodes of the associated conservative system ϕ^o and 124 displacement residuals \mathbf{R}_d for the airflow interval [480–2500 m/s] the dynamic responses of full and reduced-order FE models have been generated, as depicted in Fig. 5.23. It can be clearly perceived that the reduced-order model approximates quite well the FRFs of the full FE model in the bandwidth [0–500 Hz] containing the first two modes of vibration.

Now, the efficiency of the IERM method in approximating the critical flutter speed of the curved panel is demonstrated. For this purpose, the V-g plots are constructed

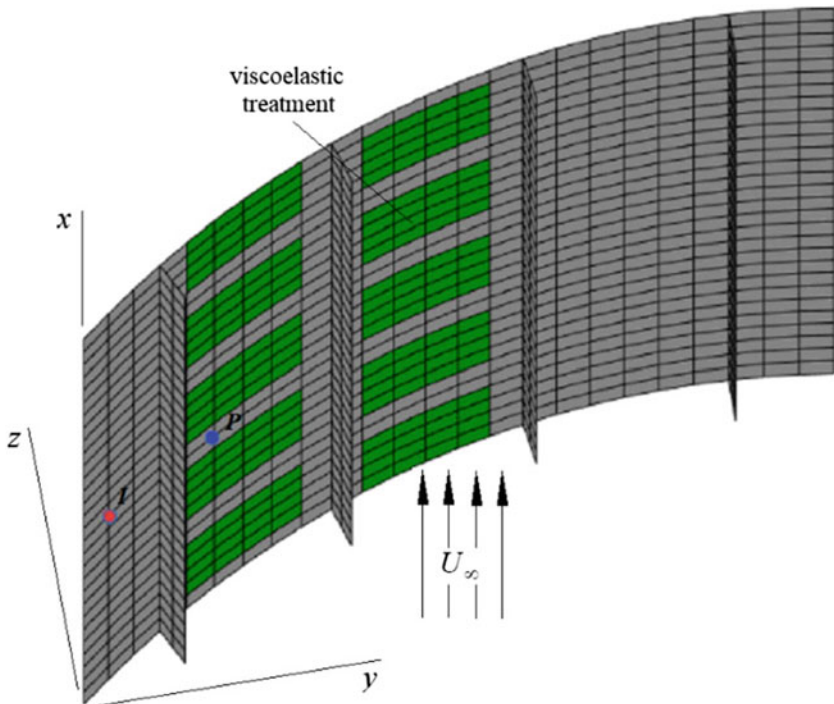


Fig. 5.22 Illustration of a curved stiffened panel in supersonic flow partially treated with viscoelastic constrained layers (indicated in green)

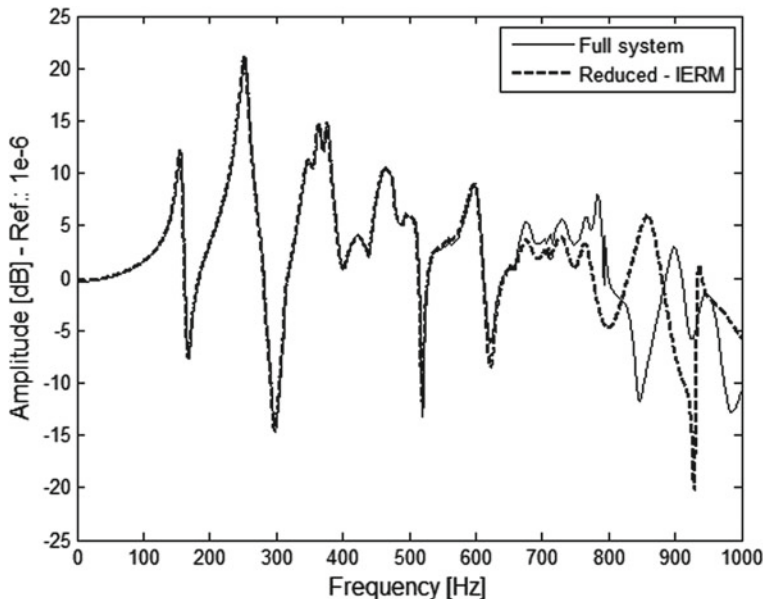


Fig. 5.23 FRFs amplitudes of the full and reduced models of the curved panel

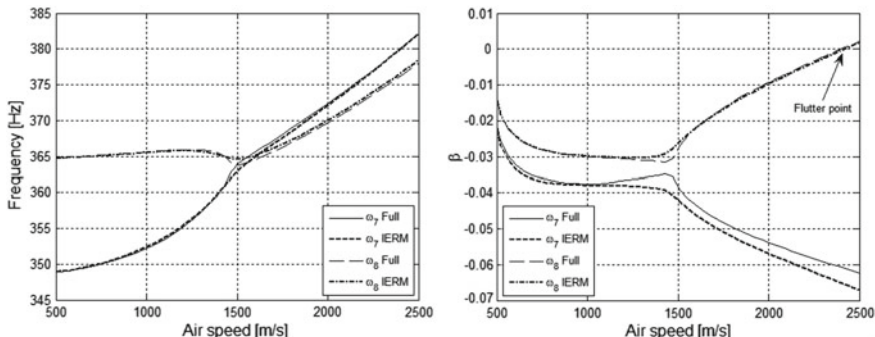


Fig. 5.24 Evolution of natural frequencies and modal damping factors for the full and IERM reduced models of the curved panel

for the airflow speed range of [500–2500 m/s] and for a given operation temperature of 15 °C. Figure 5.24 shows the evolution of the natural frequencies and damping factors with respect to the airspeed for the full and reduced-order aeroviscoelastic models. It is evident that the critical flutter speed predicted by the reduced model agrees very well with the corresponding obtained by the full model, with a critical flutter speed of 2413 m/s. As for computation times involved, Table 5.1 enables to confirm the efficiency of the IERM method in terms of the required computation time.

Table 5.1 Computation times for the flutter predictions of the full and reduced models

FE model	Basis construction	Flutter analysis	Total
Full	–	49 days	49 days
IERM (min)	38	15	53

This example illustrates the use of viscoelastic material to increase the aeroelastic stability margin of aerospace structures, and confirm the interest in using reduction techniques to alleviate the computation cost involved.

5.6 Conclusion

In this chapter some of the most important theoretical and practical aspects related to viscoelastic materials as applied to vibration control have been addressed. It provides the reader with the basic knowledge about the phenomenology of the viscoelastic behavior and the constitutive modeling of viscoelastic materials accounting for frequency and temperature dependence. In addition, it provides the formulation underlying the identification of parameters appearing in viscoelastic constitutive models in an stochastic framework and the association of viscoelastic constitutive models with two- or three-dimensional finite element structural models. The applications presented enable to assess the current capabilities for performing numerical dynamic analysis of rather complex structural systems featuring viscoelastic components.

In the authors' opinion, in spite of the high degree of maturity achieved, research is still needed to increase the range of application of viscoelastic materials to engineering problems, which can be done by, among other actions: (a) developing new high-performance viscoelastic materials, in the scope of polymer science; (b) applying advanced numerical analysis to the design of structural systems containing viscoelastic elements, including: stochastic modeling to account for uncertainties, reliability assessment and structural optimization.

References

1. Rao, M.D.: Recent applications of viscoelastic damping for noise control in automobiles and commercial airplanes. In: USA Symposium on Emerging Trends in Vibration and Noise Engineering, India (2001)
2. Zhou, X.Q., Yu, D.Y., Shao, X.Y., Zhang, S.Q., Wang, S.: Research and applications of viscoelastic vibration damping materials: a review. Compos. Struct. **136**, 460–480 (2016)
3. Nashif, A.D., Jones, D.I.G., Henderson, J.P.: Vibration Damping, p. 1985. Wiley, New York (1985)
4. Bobillot, A., Balmès, E.: Analysis and design tools for structures damped by viscoelastic materials. In: International Modal Analysis Conference—IMAC, Los Angeles (2002)

5. Christensen, R.M.: Theory of Viscoelasticity. Dover Publications, New York, NY (2003)
6. Guillot, F.M., Trivett, D.H.: Complete elastic characterization of viscoelastic materials by dynamic measurements of the complex bulk and Young's moduli as a function of temperature and hydrostatic pressure. *J. Sound Vib.* **330**, 3334–3351 (2011)
7. Pritz, T.: Measurement methods of complex Poisson's ratio of viscoelastic materials. *Appl. Acoust.* **60**, 279–292 (2000)
8. Kaliske, M., Rothert, H.: Formulation and implementation of three-dimensional viscoelasticity at small and finite strains. *Comput. Mech.* **19**, 228–239 (1997)
9. Pritz, T.: Frequency dependences of complex moduli and complex Poisson's ratio of real solid materials. *J. Sound Vib.* **214**, 83–104 (1998)
10. Ferry, J.D.: Viscoelastic properties of polymers. John Wiley & Sons (1980)
11. Emri, I.: Rheology of solid polymers. *Rheol. Rev.* **3**, 49–100 (2005)
12. Dealy, J., Plazek, D.: Time-temperature superposition - a users guide. *Rheol. Bull.* **78**, 16–31 (2009)
13. Soovere J, Drake ML (1984) Aerospace structures technology damping design guide. Technology review, Technical report, DTIC Document, aFWAL-TR-84-3089, vol. I
14. Rouleau, L., Detu, J.-F., Legay, A., Le Lay, F.: Application of Kramers-Kronig relations to time-temperature superposition for viscoelastic materials. *Mech. Mat.* **65**, 66–75 (2013)
15. Thorin, A., Azoug, A., Constantinescu, A.: Influence of prestrain on mechanical properties of highly-filled elastomers: measurements and modeling. *Polym. Testing* **31**, 978–986 (2012)
16. Martinez-Agirre, M., Illescas, S., Elejabarrieta, M.J.: Characterisation and modelling of prestrained viscoelastic films. *Int. J. Adh. Adhes.* **50**, 183–190 (2014)
17. Wineman, A.S., Rajagopal, K.R.: Mechanical Response of Polymers. Cambridge University Press, Cambridge (2000)
18. Lakes, R.S.: Viscoelastic Solids. CRC Press (1998)
19. Mainardi, F.: Fractional Calculus and Waves in Linear Viscoelasticity. Imperial College, London (2005)
20. Podlubny, I.: Fractional Differential Equations. Academic Press (1999)
21. Yin, D., Duan, X., Zhou, X., Li, Y.: Time-based fractional longitudinal-transverse strain model for viscoelastic solids. *Mech. Time-Depend. Mater.* **18**, 329–337 (2014)
22. Zhang, G., Yang, H., Xu, Y.: A surrogate-model-based identification of fractional viscoelastic constitutive parameters. *Mech. Time-Depend. Mater.* **1**, 1–19 (2015)
23. Ghoreishy, M.H.R., Firouzbakht, M., Naderi, G.: Parameter determination and experimental verification of Bergström-Boyce hysteresis model for rubber compounds reinforced by carbon black blends. *Mater. Design* **53**, 457–465 (2014)
24. Lion, A.: On the thermodynamics of fractional damping elements. *Contin. Mech. Thermodyn.* **9**, 83–96 (1997)
25. Kaipio, J., Somersalo, E.: Statistical and Computational Inverse Problems, 1st edn. Springer, New York, NY (2005)
26. Aster, R.C., Borchers, C., Thurber, C.H.: Parameter Estimation and Inverse Problems, 2nd edn. Academic Press (2013)
27. Gelman, A., Carlin, J.B., Stern, H.S., Rubin, D.B.: Bayesian Data Analysis, 2nd edn. Chapman & Hall/CRC, Boca Raton, Florida (2004)
28. Melchers, R.E., Beck, A.T.: Structural Reliability Analysis and Prediction, 3rd edn. Wiley (2018)
29. Smith, R.C.: Uncertainty Quantification: Theory, Implementation, and Applications. SIAM, Computational Science and Engineering (2013)
30. Robert, C.P., Casella, G.: Monte Carlo Statistical Methods, 2nd edn. Springer, New York, NY (2010)
31. Gamermann, D., Lopes, H.F.: Markov Chain Monte Carlo: Stochastic Simulation for Bayesian Inference, 2nd edn. Chapman and Hall/CRC (2006)
32. Hughes, T.J.R.: The Finite Element Method—Linear Static and Dynamic Finite Element Analysis. Prentice Hall Inc., Englewood Cliffs, N.J. (1987)

33. Khatua, T.P., Cheung, Y.K.: Bending and vibration of multilayer sandwich beams and plates. *Int. J. Numer. Methods Eng.* **6**, 11–24 (1973)
34. Carrera, E.: Historical review of Zig-Zag theories for multilayered plates and shells. *Appl. Mech. Rev.* **56**(3), 287–308 (2003)
35. Austin, E.M.: Variations on modeling of constrained-layer damping treatments. *Shock Vib. Digest* **31**(4), 275–280 (1999)
36. Rouleau, L., Detu, J.-F., Legay, A.: A comparison of model reduction techniques based on modal projection for structures with frequency-dependent damping. *Mech. Syst. Signal Pr.* **90**, 110–125 (2017)
37. Vasques, C., Moreira, R., Rodrigues, J.: Viscoelastic damping technologies—Part I: Modeling and finite element implementation. *J. Adv. Res. Mech. Eng.* **1**, 76–95 (2010)
38. Antoulas, A.C.: Approximation of Large-Scale Dynamical Systems. Advances in Design and Control. SIAM, Philadelphia, PA, USA (2005)
39. Hetmaniuk, U., Tezaur, R., Farhat, C.: Review and assessment of interpolatory model order reduction methods for frequency response structural dynamics and acoustics problems. *Int. J. Numer. Methods Eng.* **90**, 1636–1662 (2012)
40. Craig, R.R., Chang, C.-J.: A review of substructure coupling methods for dynamic analysis. *Adv. Eng. Sci.* **2**, 393–408 (1976)
41. de Klerk, D., Rixen, D.J., Voormeeren, S.N.: General framework for dynamic substructuring: history, review and classification of techniques. *AIAA J.* (2008)
42. Balmès, E.: Parametric families of reduced finite element models. *Mech. Syst. Signal Pr.* **10**, 381–394 (1996)
43. Balmès, E., Bobillot, A.: Analysis and design tool for structures damped by viscoelastic materials. In: Proceedings of the 21st ISMA Conference, Leuven, Belgium (2002)
44. Hu, B.-G., Dokaishi, M., Mansour, W.: A modified MSE method for viscoelastic systems: a weighted stiffness matrix approach. *Trans. ASME J. Appl. Mech.* **117**, 226–231 (1995)
45. Johnson, C., Kienholz, D., Rogers, L.: Finite element prediction of damping in beams with constrained viscoelastic layers. *Shock Vib.* **1**, 71–81 (1980)
46. Lin, R., Lim, M.: Complex eigensensitivity-based characterization of structures with viscoelastic damping. *J. Acoust. Soc. Am.* **100**, 3182–3191 (1996)
47. Plouin, A.-S., Balmès, E.: Pseudo-modal representations of large models with viscoelastic behavior. In: Proceedings of the 16th ISMA Conference, Leuven, Belgium (1998)
48. Zhang, S., Chen, H.: A study on the damping characteristics of laminated composites with integral viscoelastic layers. *Compos. Struct.* **74**, 63–69 (2006)
49. Dickens, J., Nakagawa, J., Wittbrodt, M.: A critique of mode acceleration and modal truncation augmentation methods for modal response analysis. *Comput. Struct.* (1997)
50. Tisseur, F., Meerbergen, K.: The quadratic eigenvalue problem. *SIAM Rev.* **43**, 235–286 (2001)
51. Daya, E., Potier-Ferry, M.: A numerical method for nonlinear eigenvalue problems application to vibrations of viscoelastic structures. *Comput. Struct.* **79** (2001)
52. Tran, G., Ouisse, M., Bouhaddi, N.: A robust component mode synthesis method for stochastic damped vibroacoustics. *Mech. Syst. Signal Pr.* **24**, 164–181 (2010)
53. de Lima, A., da Silva, A., Rade, D., Bouhaddi, N.: Component mode synthesis combining robust enriched Ritz approach for viscoelastically damped structures. *Eng. Struct.* (2010)
54. Baker, G.J., Graves-Moris, P.: Padé Approximants. Cambridge University Press (1996)
55. Avery, P., Farhat, C., Reese, G.: Fast frequency sweep computations using a multi-point Padé-based reconstruction method and an efficient iterative solver. *Int. J. Numer. Methods Eng.* **69**, 2848–2875 (2007)
56. Chazot, J.-D., Nennig, B., Chettah, A.: Harmonic response computation of viscoelastic multi-layered structures using a ZPST shell element. *J. Sound Vib.* **89**, 2522–2530 (2011)
57. Rumpf, R., Göransson, P.: An assessment of two popular Padé-based approaches for fast frequency sweeps of time-harmonic finite element problems. In: Proceedings of Acoustics'17, Boston, USA (2017)
58. Millithaler, P., Dupont, J.-B., Ouisse, M., Sadoulet-Reboul, E., Bouhaddi, N.: Viscoelastic property tuning for reducing noise radiated by switched-reluctance machines. *J. Sound Vib.* **407**, 191–208 (2017)

59. Hirsou, D., Le Quere, E., Magnier, M., Selosse, D.: Rotary electric machine, and in particular motor vehicle alternator, comprising a stator elastically mounted in a heat-conductive resin. European patent EP1249064B1 (2002)
60. Hernández, W.P., Castello, D.A., Roitman, N., Magluta, C.: Thermorheologically simple materials: a Bayesian framework for model calibration and validation. *J. Sound Vib.* **402**(18), 14–30 (2017)
61. Borges, F.C.L., Castello, D.A., Magluta, C., Rochinha, F.A., Roitman, N.: An experimental assessment of internal variables constitutive models for viscoelastic materials. *Mech. Syst. Signal Process.* **50–51**, 27–40 (2015)
62. Castello, D.A., Rochinha, F.A., Roitman, N., Magluta, C.: Constitutive parameter estimation of a viscoelastic model with internal variables. *Mech. Syst. Signal Process.* **22**(8), 1840–1857 (2008)
63. Zhang, E., Chazot, J.D., Antoni, J., Hamdia, M.: Bayesian characterization of Young's modulus of viscoelastic materials in laminated structures. *J. Sound Vib.* **332**(16), 3654–3666 (2013)
64. Faming, L., Liu, C., Carroll, R.J.: Advanced Markov Chain Monte Carlo Methods—Learning from Past Samples. Wiley, Chichester, Wester Sussex (2010)
65. Wright, J.R., Cooper, J.E.: Introduction to Aeroelasticity and Loads, 2nd edn. Wiley (2015)
66. NASA: Control of Aeroelastic Response: Taming the Threats. NASA Historical Series 100 (2004)
67. Lacarbonara, W., Cetra, M.: Flutter control of a lifting surface via visco-hysteretic vibration absorbers. *Int. J. Aeronaut. Space Sci.* **12**, 331–345 (2011)
68. Merrett, C.G., Hilton, H.H.: Elastic and viscoelastic panel flutter in incompressible, subsonic and supersonic flows. *J. Aeroelast. Struct. Dyn.* **2**(2010), 53–80 (2010)
69. Cunha-Filho de Lima, A.M.G., Donadon, M.V., Leão, L.S.: Flutter suppression of plates using passive constrained viscoelastic layers. *Mech. Syst. Signal Process.* **79**, 99–111 (2016)
70. Martins, P.C.O., DA Guimarães, Pereira, Marques, F.D., Rade, D.A.: Numerical and experimental investigation of aeroviscoelastic systems. *Mech. Syst. Signal Process.* **85**, 680–697 (2017)
71. Cunha-Filho, A.G., Briand, Y.P.J., Lima, A.M.G., Donadon, M.V.: An efficient iterative model reduction method for aeroviscoelastic panel flutter analysis in the supersonic regime. *Mech. Syst. Signal Process.* 575–588 (2018)
72. de Lima, A.M.G., da Silva, A.R., Rade, D.A., Bouhaddi, N.: Component mode synthesis combining robust enriched Ritz approach for viscoelastically damped structures. *Eng. Struct.* **32**, 1479–1488 (2010)
73. Bobillot, A., Balmés, A.: Iterative techniques for eigenvalue solutions of damped structures coupled with fluids. *AIAA J.* **32**, 2002–1391 (2002)

Chapter 6

Dry-Friction Damping in Vibrating Systems, Theory and Application to the Bladed Disc Assembly



Ludek Pesek, Ladislav Pust, Pavel Snabl, Vitezslav Bula, Michal Hajzman and Miroslav Byrtus

Abstract The chapter deals with a dry friction damping in the dynamics of model blade systems. The main emphasis is to the solution of damping effects of dry friction contacts in tie-bosses and shrouds. Friction is considered herein from phenomenological view. The variety of modified dry-friction models and results of their equivalent linearization are presented at the beginning. Then numerical models, i.e. discrete analytical, reduced and full finite element, used in our research of non-linear dynamic behavior of the blade cascades and bladed wheel with dry friction contacts are discussed. Dynamics states, such as resonant vibration, free attenuation, self-excitation, are considered. The detailed dynamic analysis of non-linear behavior of these systems due to dry-friction contacts is presented for discrete analytical model with the stick-slip friction contact. Furthermore, the solution of the blade bundle dynamics with the tie-boss coupling by the 3D FE model with surface to surface contacts is described. Because of the rotary periodicity, the bladed wheels bring special resonant vibration mode, i.e. travelling wave mode, in dependence on a type of wheel excitation, the dynamic responses of the wheel to nozzle excitation and self-excitation are studied, too. For validation purposes, we describe the experiments and their results on blade bundles with two types of dry friction coupling. The comparisons with the numerical results show that in spite of simplifications in the modelling of the dry-friction contacts, the used numerical models can deliver very useful information about additional stiffness, damping and stabilization effect.

L. Pesek (✉) · L. Pust · P. Snabl · V. Bula

Institute of Thermomechanics AS CR, v.v.i., Dolejskova 5, Prague, Czech Republic

e-mail: pesek@it.cas.cz

L. Pust

e-mail: pust@it.cas.cz

V. Bula

e-mail: bula@it.cas.cz

M. Hajzman · M. Byrtus

University of West Bohemia, Univerzitni 8, Pilsen, Czech Republic

e-mail: mhajzman@kme.czu.cz

M. Byrtus

e-mail: mbyrtus@kme.czu.cz

© Springer Nature Switzerland AG 2019

J. C. Jauregui (ed.), *Nonlinear Structural Dynamics and Damping*,
Mechanisms and Machine Science 69,

<https://doi.org/10.1007/978-3-030-21777-7>

6.1 Introduction

The trend in the development of power turbines and jet engines is to continuously improve performance and energy efficiency. Modern turbines are designed for higher operating temperatures and flow rates. The rotating turbine blades are, apart from the considerable centrifugal forces, subject to aerodynamic forces from the flowing medium. However, the trend of producing ever-longer and ever-thinner blades leads to lower dynamic stiffness. Therefore, dynamic stiffness and structural damping must be increased by additional structural elements, e.g. tie-bosses, shroud connections, with minimal impact on blade weight and aerodynamic loss (Fig. 6.1).

The research of these physical phenomena is based on modern computational methods and experimental studies on the dynamics of rotating blade wheels and the unsteady flow in blade cascades.

Although the turbines and their bladings can be carefully designed, it is not possible to omit resonant vibration leading to a high-cycle fatigue risk. The resonance phenomena arise from two different mechanisms depending on whether it is forced response vibration or self-excited vibration. The former case leads to so-called synchronous vibration that is caused by unbalances or by circumferential periodical pressure field known as nozzle excitation. Then, blade vibration frequencies are integer multiple of shaft rotation frequencies that coincide with some eigenfrequencies of a bladed disk. In the latter case, the vibration is caused by aeroelastic coupling between blades and a flow field. According to distortions of flow and its volumetric rate around blade airfoil, the different types of self-excited vibration occur synchronously or non-synchronously with respect to the rotation frequency. These states in full operational range are more difficult to predict. The bladed wheel with sufficient dissipation of mechanical energy is the protection against this case. Since the material damping of the blades that is mostly of metal is very low, it is necessary to increase the damping by additional construction damping. Dry-friction damping in bladed discs in combination with their mistuning or at travelling wave deformation modes was studied in eighties of the last century (e.g. [25–27]) and later (e.g. [3, 9, 22]). From that time many publications dealt with dry friction damping as blade to blade or blade to ground with couplings in roots (e.g. [41]), shrouds (e.g. [2, 15, 37, 54]) or platforms (e.g. [7, 14, 42, 43, 65, 30]) and its introduction into the turbine design (e.g. [50]). Besides very positive effect of higher damping on the self-excited vibration, it decreases

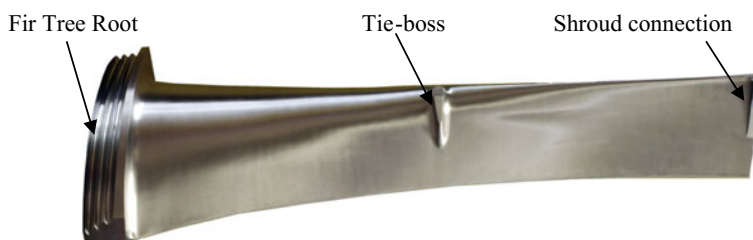


Fig. 6.1 Real turbine blade (courtesy of Doosan Škoda Power)

forced response vibration level, too. Therefore the friction damping and snubbing mechanism is still studied for reduction of turbine blade vibration. The influence of the friction damping on the dynamic behavior of the blading is, however, a complex non-linear problem of continuum mechanics as to the dynamic behavior of spatial distorted blades coupled by disk and time-variant boundary conditions at contacts with friction [55]. It leads to multipoint contacts influenced by production accuracy and roughness of the contact surfaces, thermo-mechanical coupling etc. [1].

As to the contact problems of elastic bodies, Hertz's pioneering work [17] on this topic is the basis for analytical solutions of contact problems till today. Analytical solution techniques for more complex geometries with linear elastic contacts and contacts with friction came much later (e.g. [6, 19, 20, 24]). First papers on finite element methods applied to contact problems appeared in seventies of the last century (e.g. [13, 18]). Then abundant amount of literature on linear and complex non-linear contact scenarios within the FEM have appeared afterwards (e.g. [28, 56, 60]).

Nowadays there are many approaches that allow solving this problem from analytical models with few degrees of freedom (e.g. [2, 29, 33, 32]) to numerical spatial 3D finite element models (e.g. [4, 11, 34, 35, 38, 61]). Friction is herein described from phenomenological view. The general Coulomb law, where friction coefficient is a function of a relative velocity and quality of surfaces, is mostly used for the description of friction forces in contacts. The contact model with friction can be simplified for stationary harmonic vibration by linearization of the non-linear contact forces by the harmonic balance method (HBM) [23]. The HBM is very well theoretically developed and very popular in the bladed disc dynamics with friction contacts (e.g. [5, 12, 39, 40, 44, 52, 53, 57, 58, 63, 64]). This simplified approach of solution is very computational efficient. The next methods of computational contact mechanics based on finite element technology is still under investigation. The contact forces are here computed by e.g. Penalty, Lagrangian or Augmented Lagrangian methods. These methods are usable for general dynamic excitation with smooth and non-smooth contact surfaces since the bladed disc dynamics with non-holonomic contact constrains are solved as discretized fully coupled non-linear problem in time-domain. This solution leads, however, to high performance computations (HPC). Due to possible space and time discretization inaccuracies and numerical errors, an experimental validation is still needed. The last bunch of methods for solution of dynamics of bladed discs with dry friction contacts are based on the reduced models, where the linear blades and discs are reduced, e.g. by modal condensation, to small number of DOFs and the non-linearity remains only in contacts [31, 62]. Then the time-integration of the reduced model is computationally more efficient than for the full FE model and it enables to respect the non-linear contact constrains.

In this chapter we present the methods and results of our research of dry friction damping in bladed disc assembly. Section 6.2 describes the main types of dry friction analytical models. The solution of dynamical contacts with friction in bladed cascade is a complex problem concerning a coupled problem of dynamical systems with non-holonomic couplings in normal and tangential directions. To solve this problem semi-analytically it is necessary to simplify this problem by reducing the number of DOFs, reducing contact "surface to surface" to one-point contact that moves on

the contact surface, estimation of normal contact stiffness from benchmark tests, method of solution that consider just one mode of vibration. Therefore, in practice, this problem is simplified by reducing the number of DOFs, reducing contact “surface to surface” to one-point contact that moves on the contact surface, linearization or by the method of harmonic balance with the decomposition of a non-linear solution for harmonic excitation to the Fourier series of harmonic functions. The linearization leads to the calculation of equivalent damping and stiffness that are suitable for qualitative assessment of the non-linear effect of friction couplings on the dynamic behavior of the systems at different excitation amplitudes. Therefore, in Sect. 6.2, equivalent quantities of selected friction models for different parameters are evaluated and discussed, too. To describe the nonlinear influence of friction couplings on dynamic behavior of blades, Sect. 6.3 deals with the analysis of two types of friction couplings in bladed bundle, namely the effect of tie-boss couplings on the blade triple and the effect of the friction element placed between the pair of blades. At the beginning of each study case experimental results are described and further results of the numerical solution obtained by discrete analytical or reduced FE model of the bladed bundle with one-point friction contacts. In case of tie-boss couplings, the numerical solution of the non-reduced 3D FE model with surface to surface contact by the Augmented Lagrangian method is also described. This approach shows the possible temporal and spatial variability of contacts during one period of oscillation which is neglected under simplified approaches. This phenomenon is caused by variable relative movements of contact surfaces of geometrical complex structure of blades. Part of the study cases was ascertained by HPCs. However, solving a full FE model with a large number of nonlinear coupling conditions in discretized contact surfaces is still computationally challenging due to many iterations in each integration time step. Therefore, in Sect. 6.4, the dynamics of a bladed disc with tie-boss couplings is solved by two simplified approaches, i.e. an analytical discretized model and a reduced FE model. The time responses and damping effect of dry-friction couplings are shown herein for three types of dynamic load: (a) free attenuation from the prescribed initial conditions, (b) forced resonant vibration of the wheel at the sweep nozzle excitation when passing critical speed, (c) aeroelastic self-excitation of the wheel modelled by van der Pol.

6.2 Analytical Models of Dry-Friction at Solid and Elastic Bodies

Friction is the physical phenomenon, which occurs in all mechanical processes in the world and has huge numbers of forms of manifestation—internal friction in solids, viscosity in fluids, friction between solids, rolling friction, etc. This contribution is oriented only on one seemingly narrow kind of friction—dry-friction between solids and its mathematical description.

The dry-friction forces are present in all machine structures and mechanisms, where they strongly influence both the energy dissipations and also the dynamic behaviour of the entire systems. The oscillations of systems with dry-friction belong to the so called non-smooth strongly non-linear phenomena, where jumps in friction forces occur during motion. At certain conditions, the dry friction can cause instability and dangerous self-excited vibrations.

Characteristics of dry-friction defined as “force–relative motion” relationships have been intensively investigated for more than two centuries both experimentally and analytically. The mathematical description of friction characteristics is of primary importance for analytical and numerical solutions and it often determines the quality of mathematical model of the whole investigated system and its ability to express the real mechanical structure properties.

The simple Coulomb dry-friction law cannot describe a huge variety of real frictional phenomena. Therefore, many articles and books related to theoretical and experimental approaches to friction properties have been published. Let us shortly mention some overviews of friction problems solved very often in connection with non-linear oscillations. From the basic contact theory [17] it last a half century to expand the simple dry-friction theory and its application in technical vibration theory into very detailed mathematical methods enabling sufficiently exact solution of non-linear systems ([6, 20, 24], etc.). Applications of these methods facilitate to solve nearly all important problems, e.g. [1, 8, 16, 19, 50, 55, 59].

6.2.1 Description of Main Types of Dry-Friction Model

This section presents several main types of dry friction characteristics (see also [31, 33, 47]), which enable to describe and to calculate frequently occurred friction connections in dynamic mechanical systems.

6.2.1.1 Characteristics of Dry-Friction Contacts

The simplest and also very frequently used description of dry-friction force arising between two contacting and mutually moving surfaces of solid bodies is called Coulomb law (see Fig. 6.2):

$$\begin{aligned} F_t &= f F_N v / |v|, \quad \text{for } v \neq 0, \\ F_t &\in \langle -f F_N, f F_N \rangle, \quad \text{for } v = 0, \end{aligned} \quad (6.2.1a)$$

where f [1] is coefficient of dry-friction, F_N [N] normal force, v [m/s] relative velocity, F_t [N] friction force positive in the sense of velocity.

The first row of Eq. (6.2.1a, 6.2.1b) expresses the force-velocity relationship in the slip phase of motion; the second row gives the interval of force, in which the relative

velocity of bodies is zero—stick phase of contact. The graph of Coulomb law, where both phases of contact are drawn is in Fig. 6.2. Because the frictional drag of contact in the stick phase of loading before the beginning of motion is usually greater than during the slip phase with non-zero velocity, the Coulomb law is frequently modified by the addition of another second row in (6.2.1a)

$$F_t \in \langle -f_s F_N, f_s F_N \rangle, \quad \text{for } v = 0, \quad (6.2.1b)$$

where the static friction coefficient f_s is greater than the dynamic friction coefficient f ; $f_s > f$. Graphical presentation of such characteristic is in Fig. 6.3.

However, more important is the dependence of slip friction force at the non-zero velocity v . In the majority of technical systems, the friction force changes its magnitude with increasing velocity v . Then it is important to modify the Coulomb law by introducing a variable friction coefficient $f(v)$ into the Eq. (6.2.1a). Such a description of general friction characteristic in the slip phase is

$$F_t = f(v)F_N v / |v|, \quad v \neq 0, \quad (6.2.2a)$$

where the friction coefficient function $f(v)$ is continuous and can be expressed e.g. by a power series:

Fig. 6.2 Coulomb dry-friction

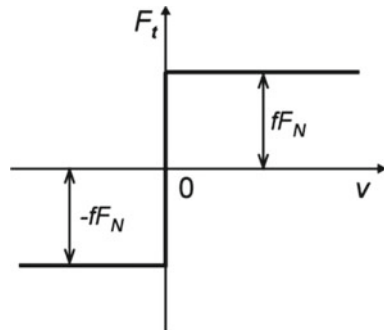


Fig. 6.3 Different friction coefficients

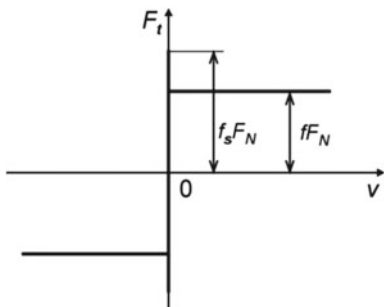


Fig. 6.4 Dry-friction with linear damping

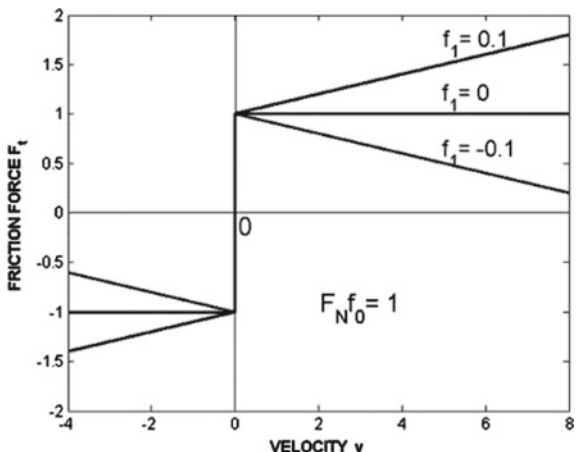
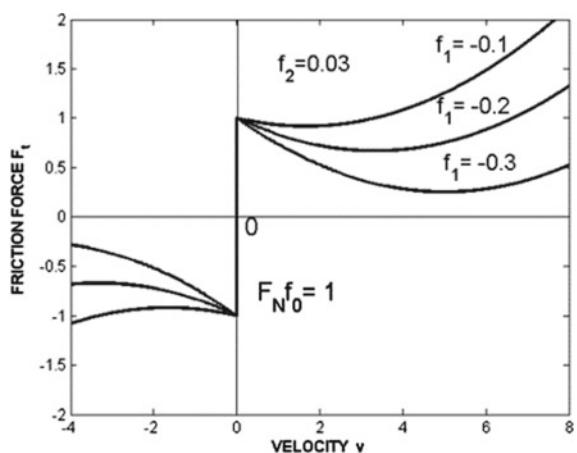


Fig. 6.5 Dry and non-linear damping



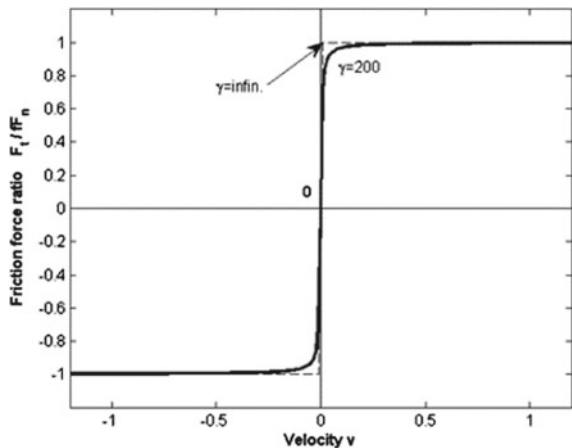
$$f(v) = f_0 + \sum_{n=1}^N f_n |v^{n-1}| v, \quad (6.2.2b)$$

where $N = 0$ corresponds to the classical Coulomb law. Friction coefficient at higher value of N can describe increasing, decreasing or general course of friction forces. The friction characteristics for $N = 1$ and $f_1 = -0.1, 0, 0.1$ are plotted in Fig. 6.4. The case of the friction characteristic, when the sum in (6.2.2b) contains also the quadratic term $f_2|v|v$, is depicted in Fig. 6.5.

Friction coefficient can sometimes depend also on the intensity of normal force F_N . Expressions (6.2.1a) can also be used in this case, but the function f has to be replaced by a more complicated one: $f = f(v) \rightarrow f(v, F_N)$.

Friction functions F_t in previous equations have break and jumps at zero velocity. However, the pressure distribution in the real contact surfaces differs very often

Fig. 6.6 Smooth dry-friction



from constant, the transitions from stick to slip aren't simultaneous in all points and therefore, and also for simplified computing, this non-smooth characteristic can be replaced by the continuous one. It is realized by using continuous function “ $\arctg(\gamma v)2/\pi$ ” with sufficiently high parameter γ instead of “ $\text{sign}(v)$ ” or “ $v/|v|$ ”. The Coulomb law (Fig. 6.2, Eq. (6.2.1a)) can be replaced by a continuous function

$$F_t = f F_N \arctg(\gamma v)2/\pi \quad (6.2.3)$$

and for $\gamma = 200$ graphically presented by a thick full line in Fig. 6.6. The thin dashed line corresponding to the Fig. 6.2 and Eq. (6.2.1a) is there plotted for comparison.

This “ \arctg ” modification of Coulomb dry-friction law can be applied also for the case when the friction coefficient f exponentially decreases from static value f_s to dynamics value f_d valid for large velocities as seen in Fig. 6.7. The passage between the both states of friction is smooth without any break. Mathematical description of this characteristic with exponential transition between stick and slip phase is

$$F_t/f_s F_N = [1 + f_d/f_s(-1 + \exp(-\beta|v|))] \arctg(\gamma v)2/\pi. \quad (6.2.4)$$

The slope of slip dry-friction declination is determined by the decrease parameter β .

All kinds of friction are connected with loss of energy. The energy loss at vibration can be pictured in form of hysteresis loop i.e. dependence of friction force on relative displacements in contact area. Hysteresis loop of exact Coulomb “stick-slip” damping element ($f_d = f_s = f$) at simple cosine excitation motion $x_1(t) = a \cos(\omega t)$ has rectangular form and contains four break points in one cycle. This form is shown in Fig. 6.8 for 2 amplitudes $a = 0.5, 1$ and it is drawn in thin dashed lines. The similar hysteresis loops but for the “arctan friction Coulomb law” ($\gamma = 30$) are drawn in the same diagram by full thick lines.

Fig. 6.7 Dry-friction and exponential damping

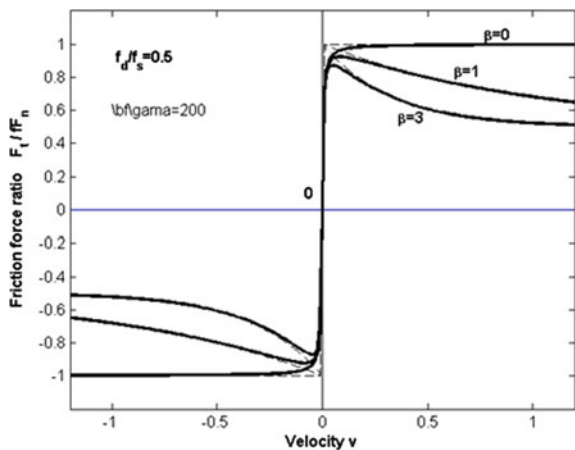
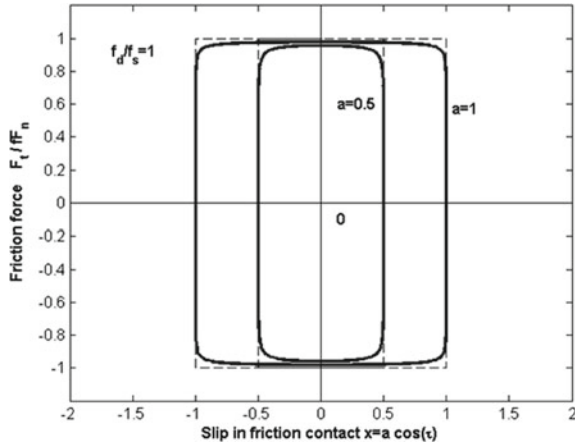


Fig. 6.8 Hysteresis loops of smooth dry-friction



If in the slip phase of motion the dynamic slip frictions coefficient f_d exponentially decreases, then the friction characteristics are shown in Fig. 6.6 and the corresponding hysteresis loops are shown in Fig. 6.9 again for three values of decease parameter $\beta = 0, 1, 3$.

Micro-deformations in the friction surfaces are caused mostly by partial micro-slips in several points of the contact area, where owing to non-uniform distribution of contact pressure a part of the area is less loaded or even without contact.

Processes which happen during the stick period near the zero relative velocity are therefore always related to friction motions and are also highly influenced by wear, geometric precision, etc. Their mathematical model is therefore very uncertain and it is often modelled approximately by a inclined line, as seen in Fig. 6.10, where the so-called modified Coulomb diagram is shown.

Fig. 6.9 Hysteresis loops of smooth dry-friction with exponential damping

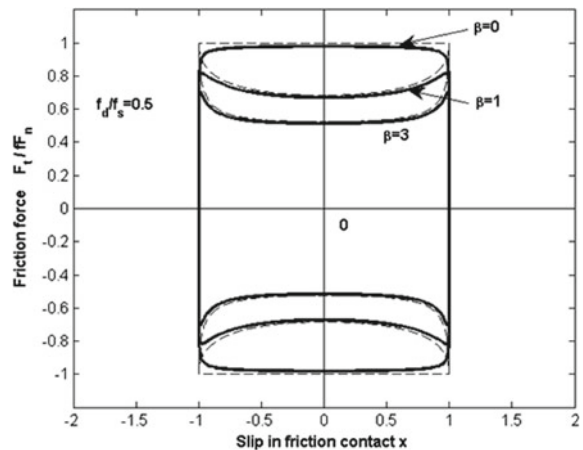
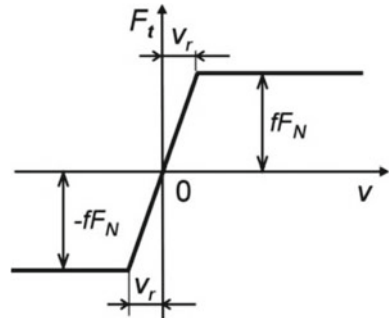


Fig. 6.10 Dry-friction with micro-slip



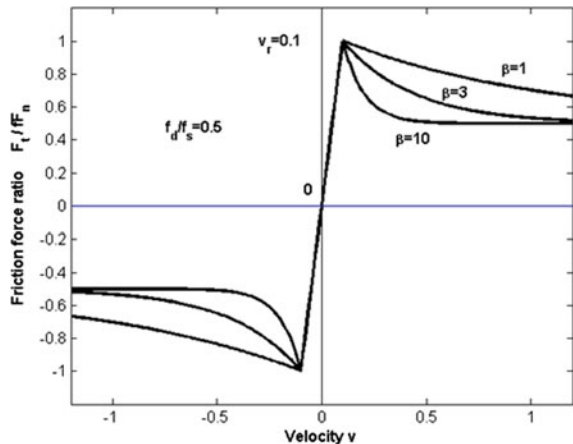
The linear “contact stick-slip” process is limited by the threshold velocity v_r . The full slip between contacting surfaces begins at $|v| > v_r$ and in the whole slip phases of motion the friction force is $F_t = fF_N \frac{v}{|v|}$. This modified Coulomb law presented in Fig. 6.10 is described by Eq. (6.2.5), where two version, either with Heaviside function H or with function sign are used

$$\begin{aligned} F_t &= fF_N \left(\frac{v}{v_r} (1 - H(|v| - v_r)) + \frac{v}{|v|} H(|v| - v_r) \right) \\ &= fF_N / 2 \left(\frac{v}{v_r} (1 - \text{sign}(|v| - v_r)) + \text{sign}(v) (1 + \text{sign}(|v| - v_r)) \right) \end{aligned} \quad (6.2.5)$$

Similarly as in the classical Coulomb law (see Eqs. (6.2.1a) and (6.2.2a)), also here the friction in slip motion can vary with velocity v due to the variable dynamic friction coefficient $f_d(v)$

$$F_t = F_N \left(f_s \frac{v}{v_r} (1 - H(|v| - v_r)) + f_d(v) \frac{v}{|v|} H(|v| - v_r) \right) \quad (6.2.6)$$

Fig. 6.11 Micro-slip and exponential damping



Very often can be the friction forces in the slip region described by the exponential function:

$$F_t/f_s F_N = \left(\frac{v}{v_r} (1 - H(|v| - v_r)) + (1 + \alpha \exp(-\beta(|v| - v_r))) \frac{v}{|v|} H(|v| - v_r) \right), \quad (6.2.7)$$

where coefficient $\alpha = f_d/f_s$ gives the ratio of dynamic to static friction coefficient and $\beta[\text{s}/\text{m}]$ characterizes the steepness of decrease in the beginning of slip motion. The graphical form of Eq. (6.2.7) is for $\alpha = f_d/f_s = 0.5$ and three decrease parameters $\beta = 1, 3, 10$ shown in the Fig. 6.11.

6.2.1.2 Dry-Friction Contact on Elastic Body

Applications of dry-friction characteristics described by a comparatively simple 2D “force-velocity” expression are useful in the ranges of great relative velocities or in the couple of very stiff bodies. However, if the friction surfaces are placed on some relative compliant parts of moving bodies,—see e.g. Figure 6.12a—it is necessary to use more sophisticated computational model, (Fig. 6.12b). This case is significant especially at vibrations with small amplitudes. The motion of bodies is usually defined by motion $x_I(t)$ of center of gravity I, which can be far from the friction contact II, where the relative displacement $x(t)$ is slightly different. Also at experimental investigation of dynamic systems, the position of motion- or force-transducer III is usually at a certain distance from the friction area.

Part of the body between the points I and II is elastically deformed by the forces F_N, F_t . Due to this deformations, the relative motion of solid body $x_I(t)$ slightly differs from the motion $x(t)$ in the friction area. Therefore it is possible to model such a contact according to the computing “stick-slip” model shown in Fig. 6.13.

Fig. 6.12 **a** Real physical friction contact.
b Mathematical model of friction contact

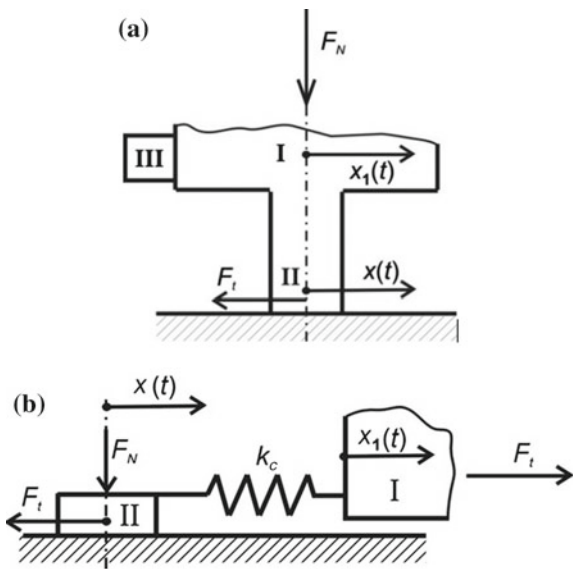
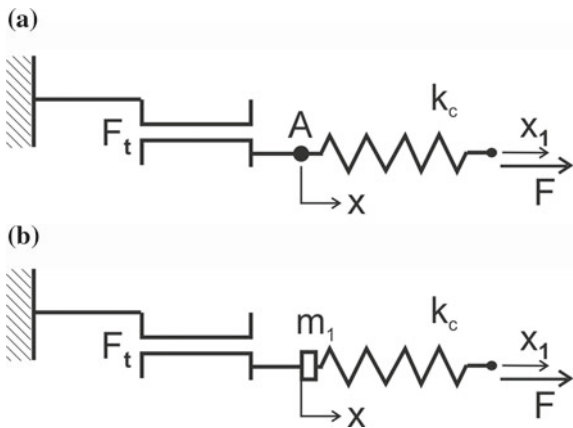


Fig. 6.13 Two possibilities of stick-slip modeling



Point A of spring and damper connection can be supposed either weightless (Fig. 6.13a) or with a very small mass m_1 , which models the mass of elastically deformed parts II of contacting bodies near to the friction surface (Fig. 6.13b).

Hysteresis loop of this slip-stick element can be obtained by a stepwise solution for simple harmonic excitation $x_1 = a \cos(\omega t)$. Coulomb dry-friction force is there modeled by means of two relations describing two different types of dry-friction surfaces connection

- (a) Motionless one $\dot{x} = 0$, when $-F_{t0} \leq F_t \leq F_{t0}$.
- (b) Relative slip $\dot{x} \neq 0$, when $F_t = F_{t0} \operatorname{sign} \dot{x}$.

Motion of friction contact is non-harmonic with non-smooth velocity. Course of displacement $x(t)$ is given by

$$\begin{aligned}x &= a - fF_N/k_c, \quad t \in (0, t_r), \\x &= a \cos \omega t + fF_N/k_c, \quad t \in (t_r, T/2), \\x &= -a + fF_N/k_c, \quad t \in (T/2, T/2+t_r), \\x &= a \cos \omega t - fF_N/k_c, \quad t \in (T/2+t_r, T),\end{aligned}\tag{6.2.9a}$$

where $T = 2\pi/\omega$, model spring stiffness k_c includes both contact stiffness in the friction surface and the stiffness of contacting bodies. The threshold time t_r between contact stick phase and slip phase is:

$$\omega t_r = \arccos(1 - 2fF_N/(k_t a)).\tag{6.2.9b}$$

Time histories of motions $x(t)$, $x_1(t)$ are shown in Fig. 6.14a. Corresponding force course of this “contact stick-slip” element is shown in Fig. 6.14b where is $\tau = \omega t$, $\tau_r = \omega t_r$ and the deformation of spring in slip motion Δx evident as the difference $|x - x_1|$ is:

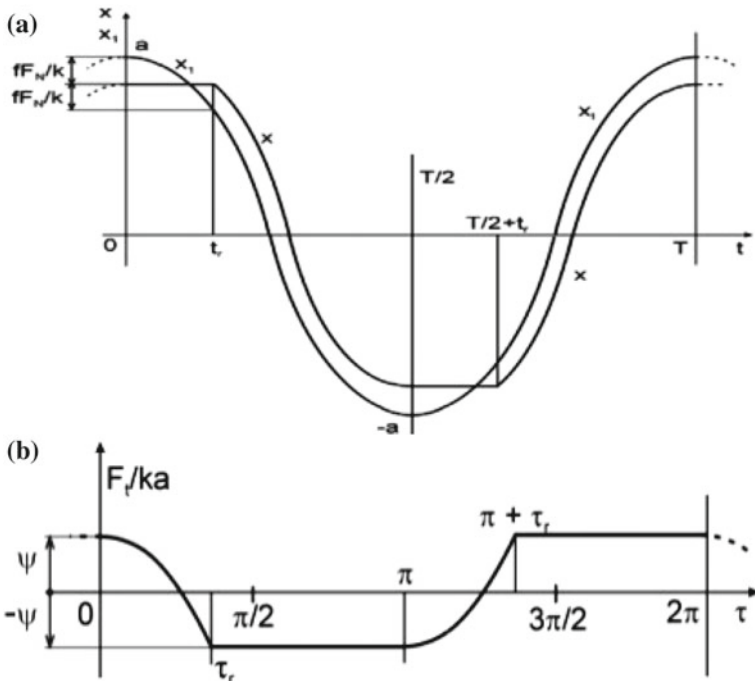
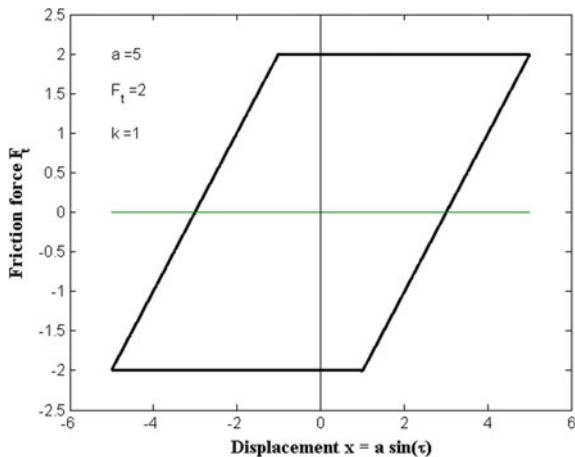


Fig. 6.14 Time histories of stick-slip dry-friction contact at harmonic excitation

Fig. 6.15 Hysteresis loop of dry-friction on elastic body



$$\Delta x = f F_N / k_c. \quad (6.2.9c)$$

Hysteresis loop—friction force versus displacement—is in Fig. 6.15. Its rhomboid-form contains four breaks for simple cosine excitation motion $x_1(t)$.

An attempt to bypass this exact piece-wise method by continuous direct numerical solution of ordinary differential equation can sometimes run in difficulties with inverting function *sign* in friction characteristic. This complication can be removed by expressing the Coulomb law by means of continuous “arctg” function. The slope of smooth transition from positive to negative values of friction force can be set using multiplication of velocity $v = \dot{x}$ by appropriate value of parameter γ

$$F_t = F_{t0} \frac{2}{\pi} \operatorname{arctg}(\gamma \dot{x}). \quad (6.2.10)$$

Effect of multiplicative parameter α is shown in Fig. 6.16.

This property enables to transfer a set of differential equations describing motion of multi-body system containing non-linear stick-slip elements of dry-friction into a set of first order differential equations and then apply routine calculation method for its solution.

Examples of such time histories of body motions $x_1(t)$ (full lines) and contact motion $x(t)$ (dashed lines) are plotted in Fig. 6.17a for three amplitudes $a = 2, 1.5, 1$ and for $\gamma = 25$. Corresponding hysteresis loops are shown in Fig. 6.17b, where parameters of spring and dry-friction element (see Fig. 6.17a) are $k_c = 1, F_{t0} = 1$. The width of hysteresis loop decreases with decreasing amplitude a and its form for smaller than $a < 1$ passes from rhomboid into narrow ellipse. This property matches to the experimental experience at vibrations with very small amplitudes.

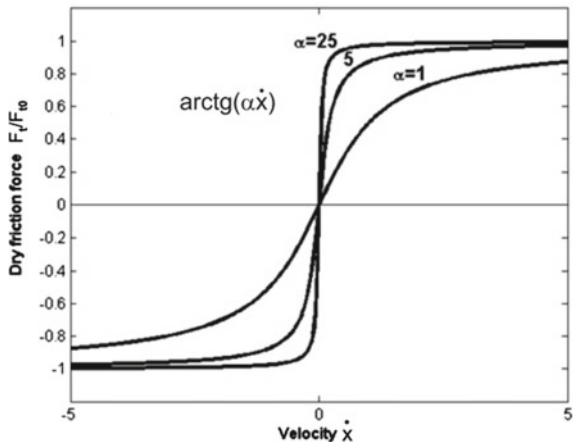


Fig. 6.16 Continuous description of dry-friction characteristic

6.2.2 Equivalent Stiffness and Damping of Dry-Friction Models

Importance of equivalent linearization method is supported by the fact that in the last decades a lot of commercial program packets based on solutions of linear differential equations have been more and more employed. If one applies a method of equivalent linearization to the non-linear element, the whole system can be treated as linear, which simplifies the solution. The method of equivalent linear was derived by Krylov and Bogoljubov [20] to replace the differential equation of a weakly non-linear system (e.g. $m\ddot{x} + kx + \varepsilon f(x, \dot{x}) = 0$) by a linear differential equation with such coefficients that solutions of both systems coincident in the first approximation, i.e. for ε^0 and ε^1 in the solution obtained in the form of power row of ε . This method can be effectively applied also for strongly non-linear systems [10, 24]. Similar results can be obtained also using the harmonic balance method [12].

Therefore it is advantageous also in the case of “spring—dry-friction” system to replace strongly non-linear friction characteristic by means of equivalent linear functions. Let us suppose system of spring with coulomb dry-friction contact that is excited by harmonic oscillations $x = a \sin \omega t$ with velocity $\dot{x} = v = a\omega \cos \omega t$.

When replacing a non-linear force function F_t by the equivalent linear expressions we must respect the stiffness and frictional components of spring-dry friction system and replace it with an equivalent linear damping $b_e(a, \omega)$ and also with equivalent stiffness $k_e(a)$:

$$F_t = b_e(a, \omega)\dot{x}_1 + k_e(a)x_1. \quad (6.2.11)$$

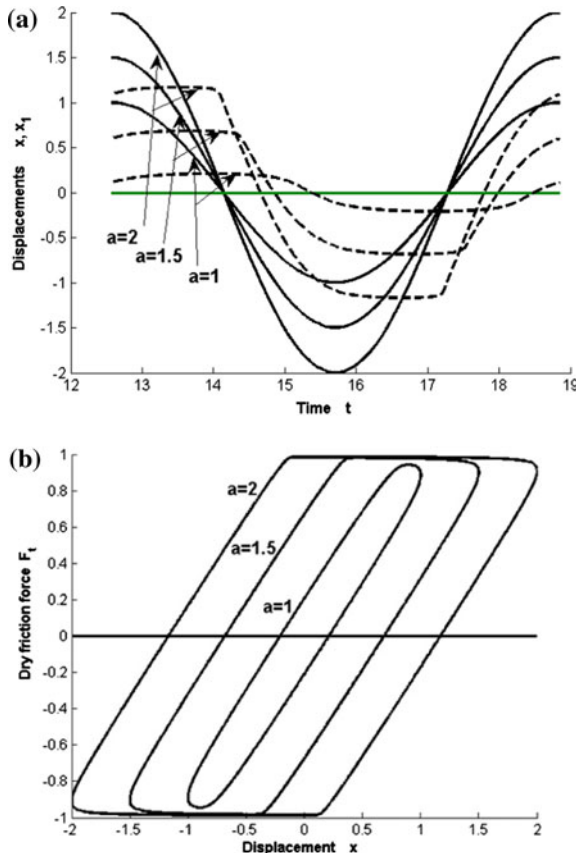


Fig. 6.17 Stick-slip dry-friction \arctg element at harmonic excitation: **a** time history, **b** hysteresis loops

Let us suppose system of spring with Coulomb dry-friction contact excited by harmonic oscillations. Equivalent linear damping coefficient $b_e(a\omega)$ [46, 20] is then

$$b_e(a\omega) = \frac{1}{\pi a\omega} \int_0^{2\pi} F_t(a\omega \cos \tau) \cos \tau d\tau = \frac{2}{\pi a\omega} \int_0^\pi F_t(a\omega \cos \tau) \cos \tau d\tau, \quad (6.2.12a)$$

and equivalent stiffness for the harmonic vibration is given by

$$k_e(a) = \frac{1}{\pi a} \int_0^{2\pi} F_t(a\omega \cos \tau) \sin \tau d\tau = \frac{2}{\pi a} \int_0^\pi F_t(a\omega \cos \tau) \sin \tau d\tau. \quad (6.2.12b)$$

Here we exploit the symmetry of functions at $\tau = \pi$.

6.2.2.1 Example of Pure Friction

This linearization procedure let us shown on an example of friction element described by Coulomb's law and connected with linear damping. Corresponding characteristics are drawn in Fig. 6.18, where the friction force

$$F_t = F_{t0} \frac{v}{v_r} [1 - H(|v| - v_r)] + [F_{t0} \text{sign}(v) + b_1(v - v_r \text{sign}(v))] H(|v| - v_r) \quad (6.2.13)$$

contains parameter b_1 ascertaining linear increase of damping in the slip state.

Equivalent linear damping coefficient is realized by substituting $v = v_0 \cos \tau$ ($v_0 = a\omega$) into (6.2.13) and (6.2.11) with view of (6.2.12a, 6.2.12b):

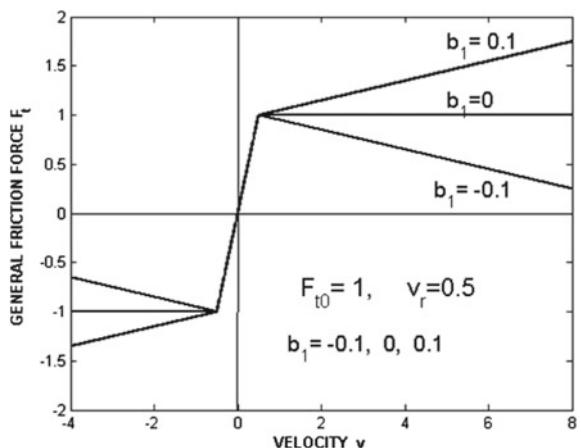
$$b_e(a\omega) = \frac{2}{\pi a\omega} \int_0^\pi \left\{ F_{t0} \frac{v}{v_r} [1 - H(|v| - v_r)] + [F_{t0} \frac{v}{|v|} + b_1(v - v_r \frac{v}{|v|})] H(|v| - v_r), \right\} \cos \tau d\tau. \quad (6.2.14a)$$

Equivalent linear stiffness coefficient is

$$k_e(a) = \frac{2}{\pi a} \int_0^\pi \left\{ F_{t0} \frac{v}{v_r} [1 - H(|v| - v_r)] + [F_{t0} \frac{v}{|v|} + b_1(v - v_r \frac{v}{|v|})] H(|v| - v_r), \right\} \sin \tau d\tau \quad (6.2.14b)$$

Due to the discontinuities of functions H and sign it is necessary to solve this integral by parts with the time boundary τ_r .

Fig. 6.18 Three dry-friction characteristics



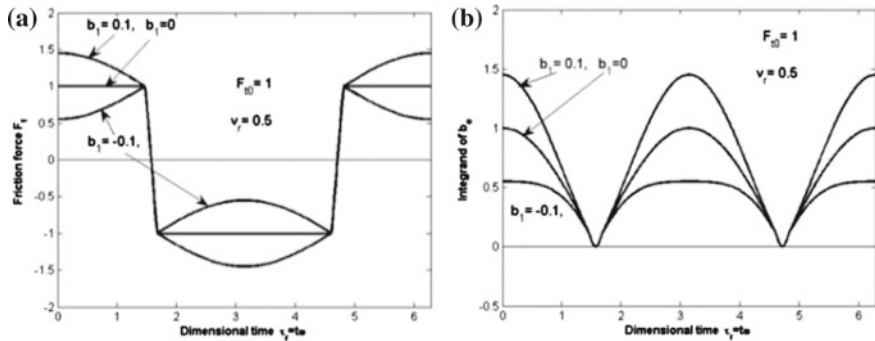


Fig. 6.19 **a** Friction force. **b** Integrand of b_e

The course of one period of friction force according to Eq. (6.2.13) is in the dimensionless time history $F_t(\tau)$ shown in Fig. 6.19a for amplitudes of $v_0 = 5$, $F_{t0} = 1$ and again for three values of viscous damping coefficient b_1 . Multiplying this expression by $\cos \tau$ gives integrand of formula for $b_e(a\omega)$ in Eq. (6.2.14a), which is shown in Fig. 6.19b.

After evaluating the formula for damping characteristic Eq. 6.2.14a, we get the equation of equivalent damping for variable amplitudes of relative velocity in the contact area. As it is seen from Fig. 6.19b, it suffices to integrate in range $0 - \pi/2$. Then we get

$$b_e = \frac{4}{\pi v_0} \left[\int_0^{\pi/2-\tau_r} F_{t0} \frac{v_0 \cos^2(\tau)}{v_r} d\tau + \int_{\pi/2-\tau_r}^{\pi/2} (F_{t0} + b_1(v_0 \cos(\tau) - v_r) \cos(\tau)) d\tau \right] \quad (6.2.15a)$$

and after integration

$$b_e = \frac{4F_{t0}}{\pi v_r} \left[\pi/4 - \tau_r/2 + \frac{\sin(2\tau_r)}{4} \right] + \frac{4(F_{t0} - b_1 v_r)}{\pi v_0} (1 - \cos \tau_r) - \frac{4b_1}{\pi} \sin(2\tau_r) \quad (6.2.15b)$$

Dependence of equivalent damping coefficient $b_e(a\omega)$ on maximum velocity amplitude $v_0 = a\omega$ is seen in Fig. 6.20, where two cases with velocities $v_0 = 0.5, 1.5$ are depicted. Equivalent stiffness $k_e(a)$ is in this case zero.

6.2.2.2 “Spring-Dry-Friction” System

As the second example let us ascertain equivalent linear coefficients $b_e(a\omega)$, $k_e(a)$ by means of which the dynamic properties of a “spring-dry-friction” system from

Fig. 6.20 Equivalent damping coefficient $b_e(v_0)$

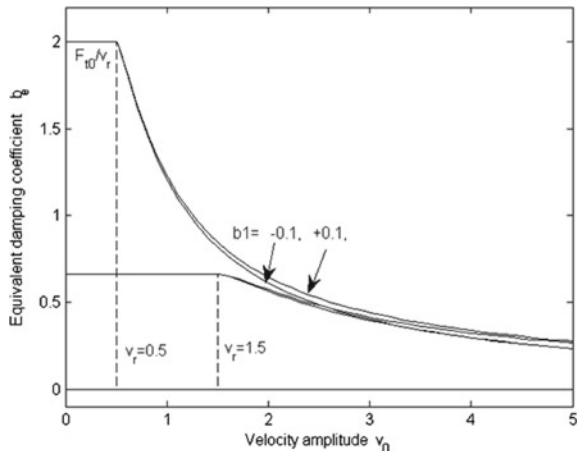


Fig. 6.21 Motion of “spring—dry-friction”

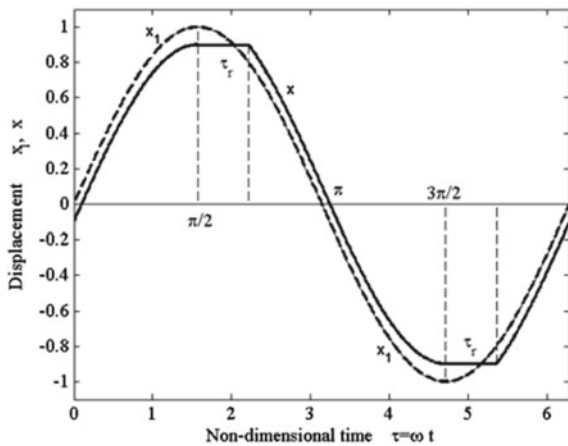
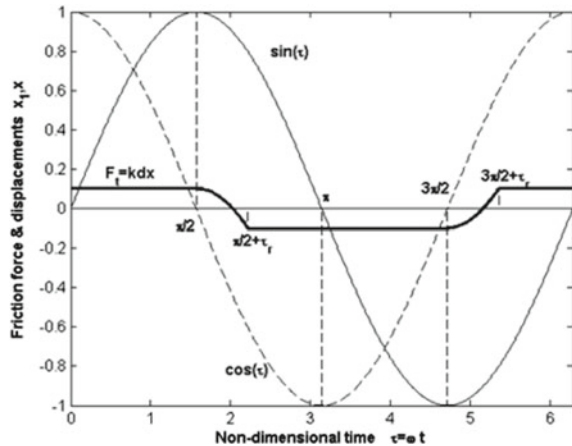


Fig. 6.12a, which is modelled by Fig. 6.13a, can be approximately described. This stick-slip model contains two parameters: Coulomb friction force $F_t = f F_N$ and spring stiffness k_c describing both contact stiffness in contact surface and stiffness of deformable parts of contacting bodies.

If the exciting motion is harmonic $x_1 = a \sin(\omega t)$, $v_1 = \dot{x}_1 = a\omega \cos(\omega t)$, then the slip motion x in the contact surface has more general form. It is seen from Fig. 6.21, where both time dependences are drawn in non-dimensional time $\tau = \omega t$ for an amplitude $a = 1$ and $f F_N = 0.3$, $k_t = 3$, $dx = 0.1$.

The spring of this system at slip motion is deformed by the force

$$F = k_t(x_1 - x) = F_t, \quad (6.2.16)$$

Fig. 6.22 Friction force F_t 

which is identical with the friction force F_t in contact surface and which time behaviour is displayed in Fig. 6.22 and is described by

$$\begin{aligned}
 F_t &= f F_N, && \text{for } 0 \leq \tau < \pi/2, \\
 F_t &= f F_N(\sin \tau - 1 + \Delta x/a) && \text{for } \pi/2 \leq \tau < \pi/2 + \tau_r, \\
 F_t &= -f F_N, && \text{for } \pi/2 + \tau_r \leq \tau < 3\pi/2, \\
 F_t &= f F_N(\sin \tau - 1 + \Delta x/a) && \text{for } 3\pi/2 \leq \tau < 3\pi/2 + \tau_r, \\
 F_t &= f F_N, && \text{for } 3\pi/2 + \tau_r \leq \tau < 2\pi,
 \end{aligned} \tag{6.2.17}$$

where $\Delta x = f F_N/k_c$ and $\cos(\tau_r) = 1 - 2\Delta x/a$, $\tau_r = \arccos(1 - 2\Delta x/a)$.

The course of friction force F_t in this figure corresponds to the ratio of $\Delta x/a = 0.1$ and $a = 0.1 \rightarrow 5$. This form changes at decreasing amplitude a , as seen from Fig. 6.23. If the amplitude a of vibration goes down the value Δx , no damping force exists.

Exact friction force can be approximately replaced by equivalent linearized formulas (6.2.12a, 6.2.12b) derived e.g. in [20, 24, 46]. First of all let us draw the integrands of formulas (6.2.12a), (6.2.12b) with friction force F_t of investigated system for the case $a = 5$. As it is seen from Fig. 6.24, the both integrands consist of two identical parts and therefore the computing can be simplified in this case also on shorter time interval $\tau = \omega t = \langle 0, \pi \rangle$.

The formula for computing equivalent damping coefficient b_e is

$$\begin{aligned}
 b_e = 2f F_N/(\pi a \omega) &\left(\int_0^{\pi/2} \cos(\tau) d\tau + \int_{\pi/2}^{\pi/2 + \tau_r} (\sin(\tau) - 1 + \Delta x/a) \cos(\tau) d\tau + \right. \\
 &- \left. \int_{\pi/2 + \tau_r}^{\pi} \cos(\tau) d\tau \right)
 \end{aligned}$$

Fig. 6.23 Variation of friction force with amplitude a

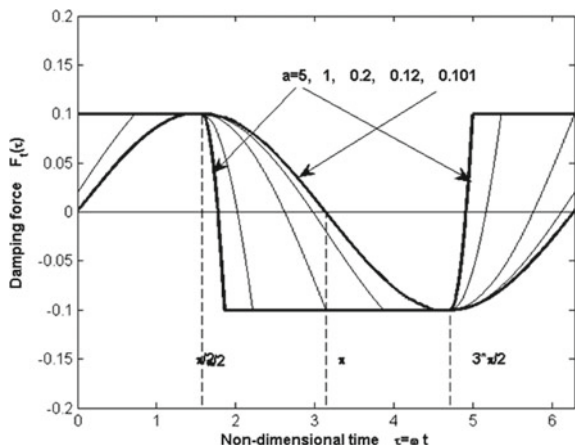
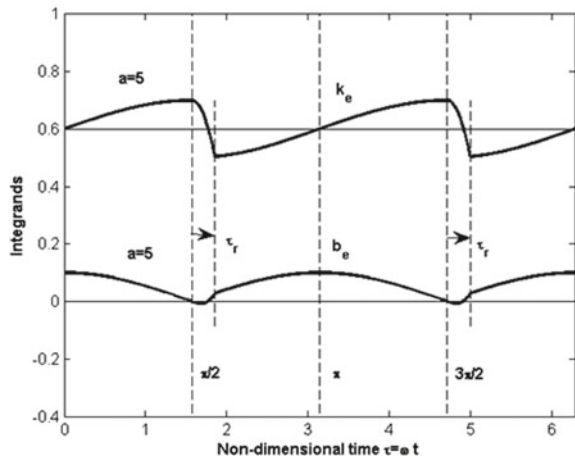


Fig. 6.24 Integrands of formulas for linearization



$$\begin{aligned} &= 2fF_N/(\pi a\omega)[1 + ((\cos \tau_r)^2 - 1)/2 + (-1 + \Delta x/a)(\cos \tau_r - 1) - \cos \tau_r] \\ &= 2fF_N/(\pi a\omega)[2 + ((\cos \tau_r)^2 - 1)/2 + \Delta x/a](\cos \tau_r - 1). \end{aligned} \quad (6.2.18)$$

After using (6.2.17) and replacing $\cos(\tau_r)$ by expression containing Δx , the equivalent damping coefficient b_e can be simplified on

$$b_e = 4k_t/(\pi\omega)[-(\Delta x/a)^2 + \Delta x/a],$$

or in dimensionless form

$$b_e\omega/k_t = 4/\pi[-(\Delta x/a)^2 + \Delta x/a], \quad \text{for } \Delta x/a > 1, \quad (6.2.19)$$

and

$$b_e = 0, \quad \text{or} \quad b_e \omega / k_c = 0 \quad \text{for} \quad \Delta x / a \leq 1.$$

It is very simple to determine the equivalent damping coefficient b_e for amplitude a and for angular velocity ω .

The equivalent linear stiffness $k_e(a)$ can be derived by simple way. Introducing friction force (6.2.17) into (6.2.12b) it gives

$$\begin{aligned} k_e &= 2f F_N / (\pi a) \left(\int_0^{\pi/2} \sin(\tau) d\tau + \int_{\pi/2}^{\pi/2+\tau_r} (\sin(\tau) - 1 + \Delta x/a) \sin(\tau) d\tau - \int_{\pi/2+\tau_r}^{\pi} \sin(\tau) d\tau \right) \\ &= 2f F_N / (\pi a) [\tau_r/2 + \sin 2\tau_r/2 + (\Delta x/a) \sin \tau_r]. \end{aligned} \quad (6.2.20)$$

And again after using (6.2.17) and replacing $\sin \tau_r$ by expression containing Δx , the equivalent stiffness k_e can be described as a function of deflection $\Delta x = f F_N / k_c$

$$k_e = 4f F_N / (\pi a) \left[\arccos(1 - 2\Delta x/a)/4 + (1 - \Delta x/a) \sqrt{\Delta x/a(1 - (\Delta x/a))} \right]. \quad (6.2.21a)$$

or in dimensionless form

$$k_e/k_c = 4/\pi * \Delta x/a \left[\arccos(1 - 2\Delta x/a)/4 + (1 - \Delta x/a) \sqrt{\Delta x/a(1 - (\Delta x/a))} \right]. \quad (6.2.21b)$$

Dependences of dimensionless equivalent linear damping (6.2.19) and stiffness (6.2.21b) on amplitude a are drawn in Fig. 6.25 and Fig. 6.26, respectively.

Fig. 6.25 Dimensionless equivalent linear damping $b_e \omega / k_c$

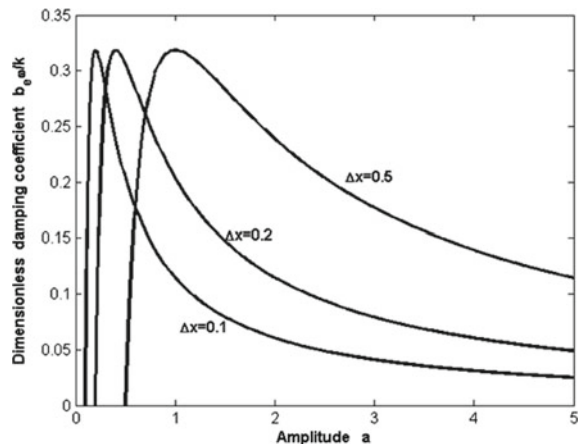
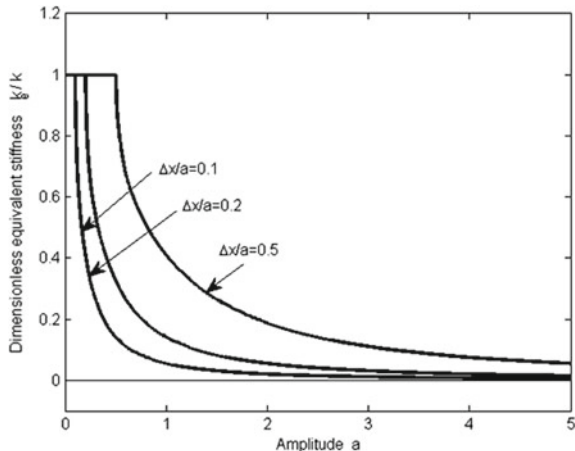


Fig. 6.26 Dimensionless equivalent linear stiffness k_e/k_t



The derived functions (6.2.19) and (6.2.21b) enables to compute easy the equivalent linear damping and stiffness coefficients $b_e(a\omega)$, $k_e(a)$ of each “spring—dry-friction damper” system for arbitrary given parameters: k_c , f , F_N , a , ω .

6.3 Dry-Friction Contacts of Bladed Bundles

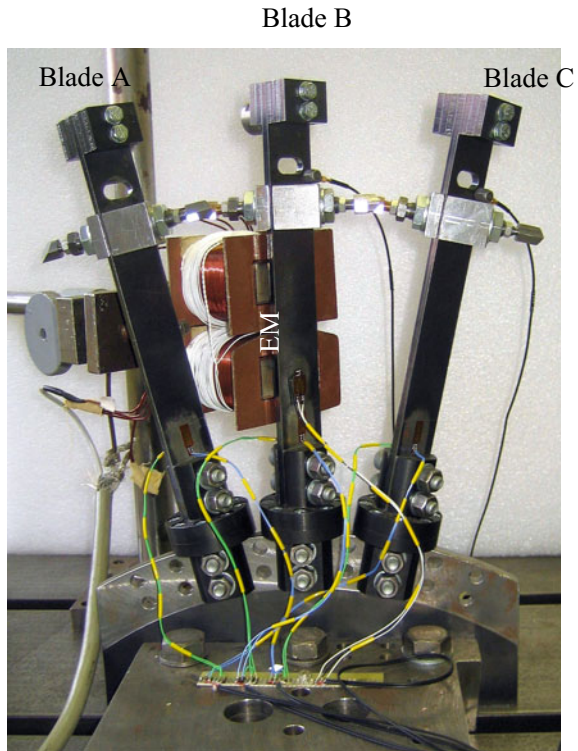
6.3.1 Three-Blade-Bundle with Contacts in Tie-Bosses

The bladed wheel model with “tie-boss” couplings was designed and fabricated for numerical and experimental investigation of the dry-friction damping and the stiffening effect (Sect. 6.4) [35, 36]. Modal analysis of the full bladed disk for two contact limit states, i.e. (I) bonded contacts and (II) open contacts, shows large dynamic stiffening effect for bonded contacts with respect to the open contact wheel case. Bonded contacts arise when high pre-stress and adhesive forces in contacts prevent a complete slip motion in contacts because dynamic excitation is not sufficiently high. Then only a stick-slip state (microslips) in contacts appears. To deal with these phenomena in more detail, we fabricated also three blades bundle and we use it for evaluation of influence of excitation amplitude level and the pre-stress in contacts on its dynamics. The numerical solutions of this system based on different numerical models are presented afterwards.

6.3.1.1 Experimental Study

The experimental setup of the three-blade-bundle is shown in Fig. 6.27. This bundle is constructed to correspond to the section of the designed bladed disk. The mea-

Fig. 6.27 Picture of experimental set-up of the three-blade-bundle



surement set-up is shown in Fig. 6.28. Blades A, B and C are clamped by the fixing console into the steel block by bolts. Because of the smooth friction, one tie-boss end is made of brass and the second of steel in each contact pair. The contact surfaces were polished by compound of the second degree. The normal contact forces were measured by the direct level of strain-gauge signals. The excitation was performed by electromagnet (EM) acting to the blade B.

For stiffening and friction coupling analysis a short block of harmonic excitation with resonant flexural frequency either 47.9 Hz (high excitation force level) or 69 Hz (low excitation force level) by electromagnet was performed. These excitation frequencies were ascertained for different excitation levels experimentally by attuning the resonant conditions. These frequencies fit very good to eigenvalues that were obtained experimentally (Table 6.1). The bonded contacts were achieved by high pre-stress in contacts of the triple.

The time length of excitation was chosen to achieve a stationary resonant vibration. Then the excitation was switched-off. The damping effect was evaluated from vibration amplitude decay of blades after switching-off the excitation. Damping ratios were identified from amplitude logarithmic decrement by Hilbert's transformation.

Each blade displacements u_A , u_B resp. u_C were picked up by strain-gauges and at the same time velocities v_B of the tie-boss end of blade B and v_C of tie-boss

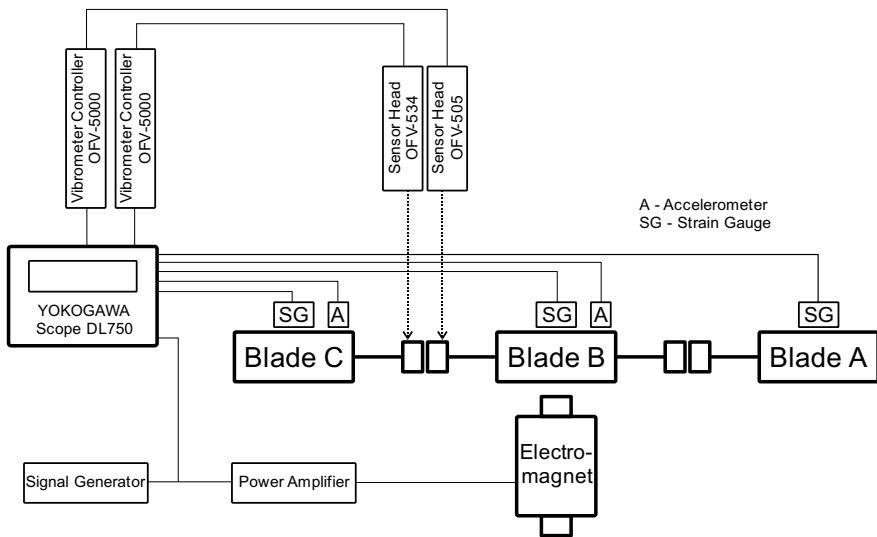


Fig. 6.28 Schema of the measurement set up of the three-blade-bundle

Table 6.1 Eigenfrequencies f_1 and damping ratios b_r of three blades model

		b_r (%)	f_1 (Hz)
Single blade		0.11	46.3
Blade triple	Open contacts	0.15	47.8
	Bonded contacts	0.2	69.1

of blade C by POLYTEC laser vibrometers. Electromagnet was supplied by LDS power amplifier and controlled by signal of generator HP 33120A. Time characteristics of generator signal, blades and two tie-boss heads responses were registered in Scope Recorder YOKOGAWA DL750 for different force levels and three contact pre-stresses, i.e. 3.25, 4.5 and 9 N.

The value of damping ratios of the blade B vibration was designated for estimation of the friction damping effect in the tie-bosses' contacts. The graph (Fig. 6.29) shows the dependence of identified damping ratios on amplitudes of forced responses of the blade B for excitation frequency 47 Hz and macroslips in contacts. The typical results of the blade B vibration are shown in the Figs. 6.31, 6.32 and 6.33 for different excitation frequencies 47 Hz (Fig. 6.31), 69 Hz (Fig. 6.32) and different level of forced amplitudes of the blade B. The top graphs of these figures depict the displacement of the blade B with evaluated damping ratios at the attenuation after switch off of the electromagnet current supply. Bottom graphs show relative displacement of tie-boss ends of the blade B and C (contact BC). The relative displacement was evaluated from the difference of measured velocities v_B and v_C after their integrations. From practical reasons, the linear amplitude decay that is typical for Coulomb's friction law is approximated here by the logarithmic decrement. The analytical and

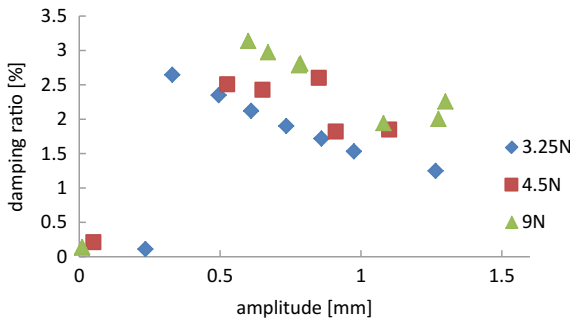


Fig. 6.29 Macroslip damping ratios for different resonant amplitudes of forced response

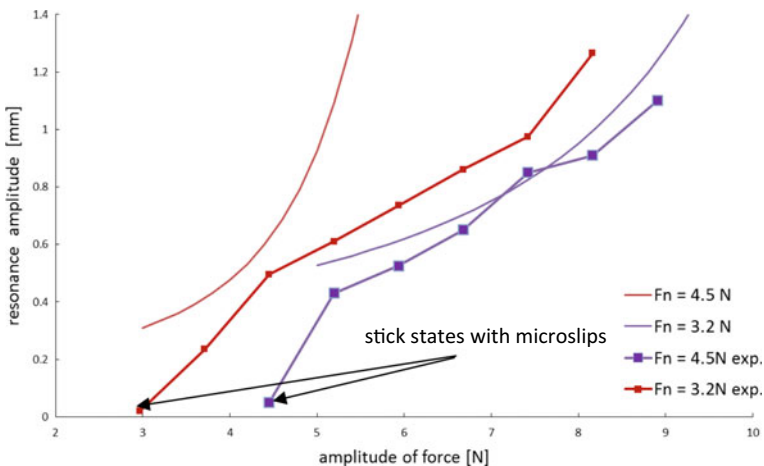


Fig. 6.30 Analytical and experimental dependences of resonance amplitudes on excitation amplitudes at the harmonic excitation for two contact normal forces (exp.—experimental results)

experimental dependences of resonance amplitudes on excitation amplitudes at the harmonic excitation for two contact forces, i.e. 3.2 and 4.5 N are shown in Fig. 6.30. Analytical results were obtained by the same model and parameters described in the Sect. 6.3.1.2 for $F_t = 1.6$ N and 2.25 N that for friction coefficient 0.5 correspond to contact normal forces 3.2 N and 4.5, respectively. Despite the very simplified analytical model we get reasonable agreement.

From the Fig. 6.31 up to 8 we can draw these observations:

- At higher excitation force of the blade B and higher response of the blade B and excitation frequency 47 Hz, the adhesion forces in contacts are exceeded, the contacts get into the slip and damping ratios are in range 1.2–3% (Fig. 6.31), the size of damping ratio drops with increase of forced amplitudes. The blades vibrate on the same frequency as excitation frequency that corresponds to eigen-

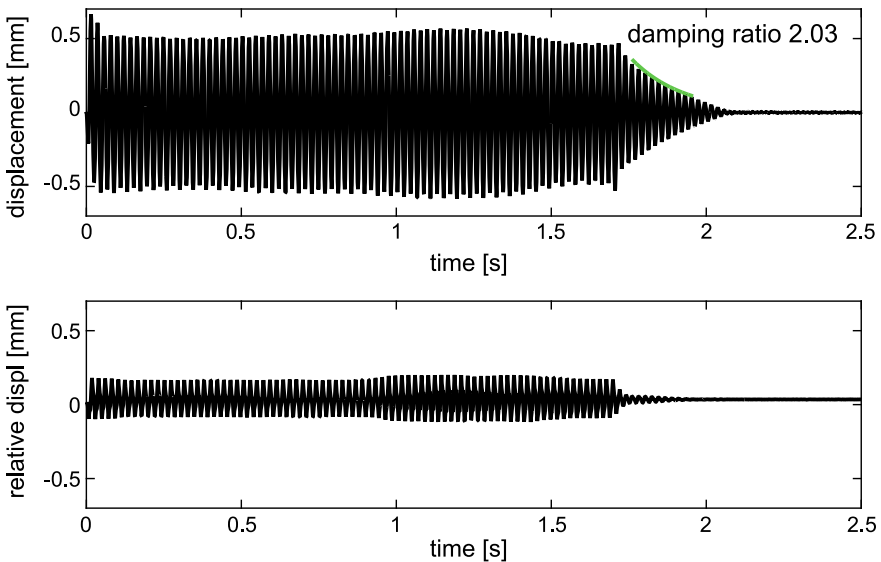


Fig. 6.31 Measured signals of blade B displacement (top) and relative displacement in contact BC (bottom) during the harmonic excitation with frequency 47 Hz and maximal amplitude 0.6 mm—contact pre-stress 3.25 N

frequency of the single contact-free blade. It means that there is no stiffening but only damping effect of the contact with the rest of the bundle.

- (b) At low excitation force of the blade B and excitation frequency 47 Hz, the adhesion forces in contacts are not exceeded, the contacts are in the stick phase with microslips (relative motions $\approx 1e-3$ mm, Fig. 6.32) and damping ratios are low around 0.14%. Yet the excitation is 47 Hz, the vibration frequency 69 Hz prevails at the vibration attenuation when amplitudes decay. The combination of two frequencies in the response causes amplitude modulation. This frequency approaches to the eigen-frequency of the blade triple with bond contacts (76.4 Hz). It means that there is stiffening but damping effect is low.
- (c) At lower excitation force of the blade B and excitation frequency 69 Hz, the adhesion forces in contacts are not exceeded, the contacts are in the microslips (relative motion $\approx 1e-3$ mm) and damping is low (Fig. 6.33). By a certain increase of the force the adhesion is exceeded abruptly and the vibration level is decreased and though the excitation was 69 Hz, the vibration attenuation is modulated by frequency 47 Hz (Fig. 6.34). It means that at the slips the decrease of amplitudes is caused not only by damping but mainly by over tuning the system that changes its eigen-frequency to 47 Hz due to slips (Fig. 6.35).

As to the terminology of three contact phases which will be introduced for the stick-slip friction contact model, i.e. stick, stick-slip and slip (Sect. 6.3.1.2), we use here just two phases, i.e. stick phase with microslips and slip. The stick phase in

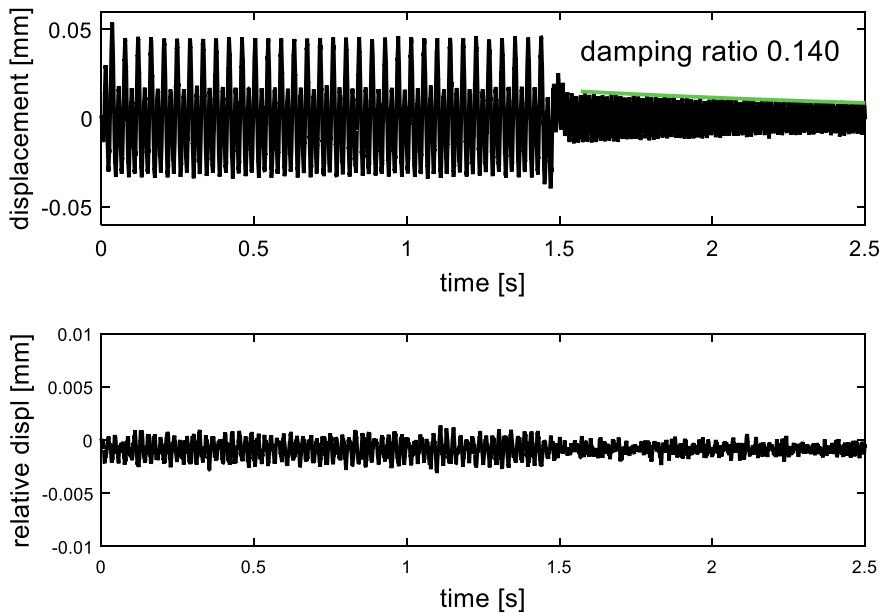


Fig. 6.32 Measured signals of blade B displacement (top) and relative displacement in contact BC (bottom) during the harmonic excitation with frequency 47 Hz and maximal amplitude 0.05 mm—contact pre-stress 9 N

the contacts is in a reality accompanied by microslips on the contact boundaries and therefore it is sometimes called stick-slip phase. So phases stick and stick-slip of analytical model are merged together in one phase of stick with microslips. It is general feature that the transition from the stick state with microslips to slips and a change of dynamical behavior of the system comes very abruptly by achievement of the critical excitation amplitudes (Fig. 6.30).

6.3.1.2 Numerical Simulations of Nonlinear Behavior on Discrete Analytical Model

(a) Model Description

Discrete analytical model of three blades bundle was used to describe the general non-linear effects, such as stiffening and damping, of tie-boss couplings in a bladed wheel dynamic behavior. The dry friction is modeled here by classical Coulomb friction law. Scheme of the model can be seen on Fig. 6.35.

The model consist of three blades modelled as 1 DOF elements with mass m connected to the frame by springs with stiffness k and by viscous dampers with damping b . The viscous dampers describe structural and material damping (STRUD) of blades without dry-friction contact damping (CONTD). The dry-friction contacts

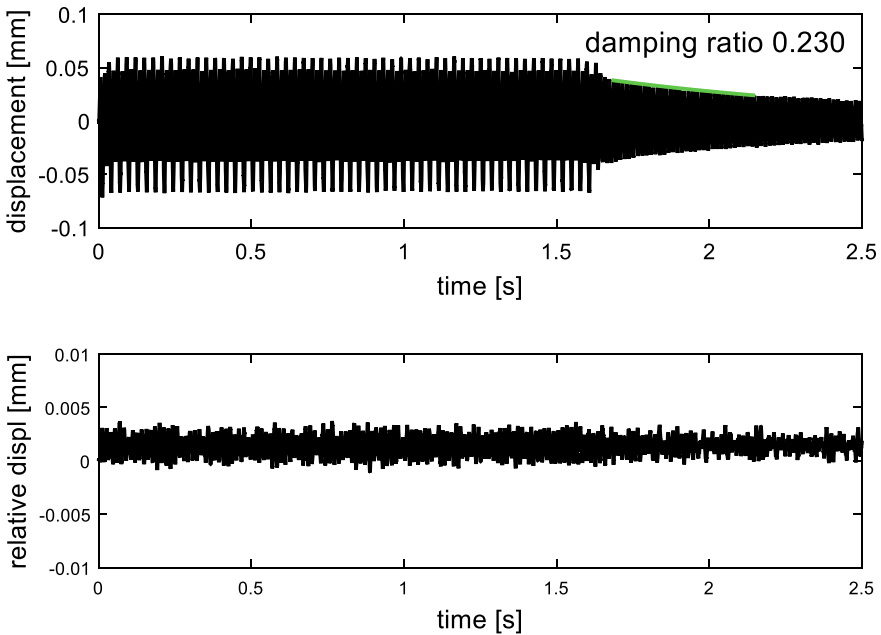


Fig. 6.33 Measured signals of blade B displacement (top) and relative displacement in contact BC (bottom) during the harmonic excitation with frequency 69 Hz and maximal amplitude 0.06 mm—contact pre-stress 9 N

are modelled by the stick-slip model (Fig. 6.13a) using two parameters, friction force $F_{t0} = f F_n$ and spring stiffness k_c . The stiffness k_c describes both contact stiffness and stiffness of deformable part of the tie boss arms. The mechanical system of the model is described by equations of motion (6.3.1):

$$\begin{bmatrix} m & 0 & 0 \\ 0 & m & 0 \\ 0 & 0 & m \end{bmatrix} \cdot \begin{bmatrix} \ddot{y}_A \\ \ddot{y}_B \\ \ddot{y}_C \end{bmatrix} + \begin{bmatrix} b & 0 & 0 \\ 0 & b & 0 \\ 0 & 0 & b \end{bmatrix} \cdot \begin{bmatrix} \dot{y}_A \\ \dot{y}_B \\ \dot{y}_C \end{bmatrix} + \begin{bmatrix} k & 0 & 0 \\ 0 & k & 0 \\ 0 & 0 & k \end{bmatrix} \cdot \begin{bmatrix} y_A \\ y_B \\ y_C \end{bmatrix} + \begin{bmatrix} -F_{cAB}(y_B - y_A, \dot{y}_B - \dot{y}_A) \\ F_{cAB}(y_B - y_A, \dot{y}_B - \dot{y}_A) + F_{cCB}(y_B - y_C, \dot{y}_B - \dot{y}_C) \\ -F_{cCB}(y_B - y_C, \dot{y}_B - \dot{y}_C) \end{bmatrix} = \begin{bmatrix} F_A \cos(\omega t) \\ F_B \cos(\omega t) \\ F_C \cos(\omega t) \end{bmatrix}. \quad (6.3.1)$$

that can be rewritten in matrix notation as

$$\mathbf{M}\ddot{\mathbf{y}} + \mathbf{B}\dot{\mathbf{y}} + \mathbf{K}\mathbf{y} + \mathbf{F}_t(\mathbf{y}, \dot{\mathbf{y}}) = \mathbf{F} \cos(\omega t) \quad (6.3.2)$$

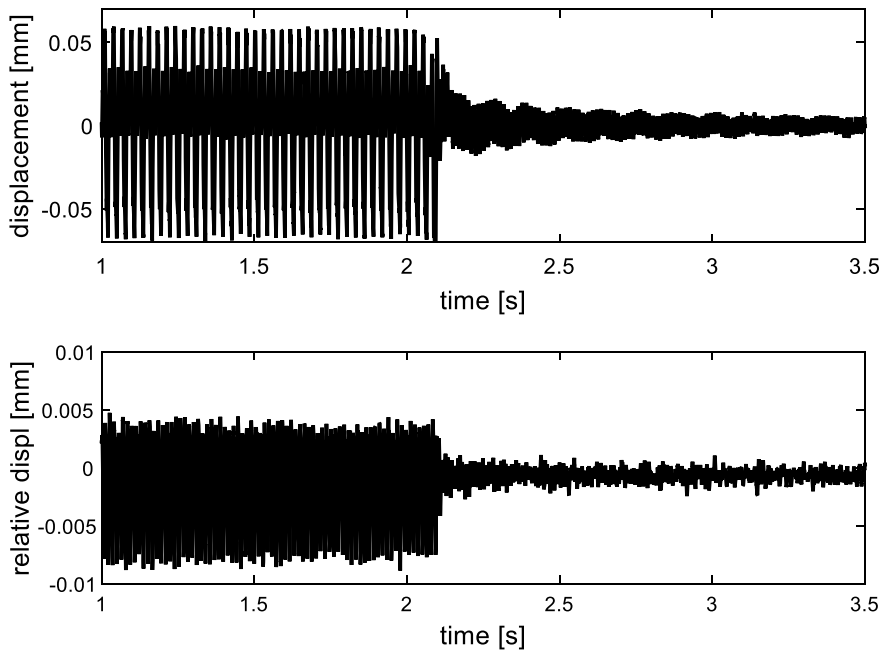


Fig. 6.34 Measured signals of blade B displacement (top) and relative displacement in contact BC (bottom) during the harmonic excitation with frequency 69 Hz and maximal amplitude 0.05 mm—contact pre-stress 9 N

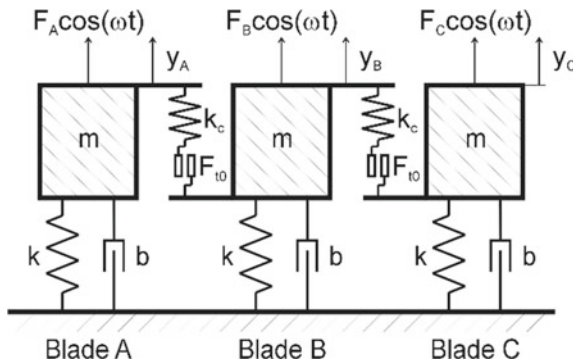


Fig. 6.35 Scheme of three blades bundle with dry-friction contacts

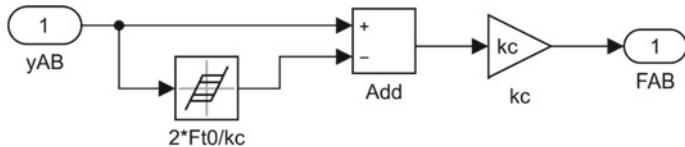


Fig. 6.36 Simulink block scheme of dry friction contact model

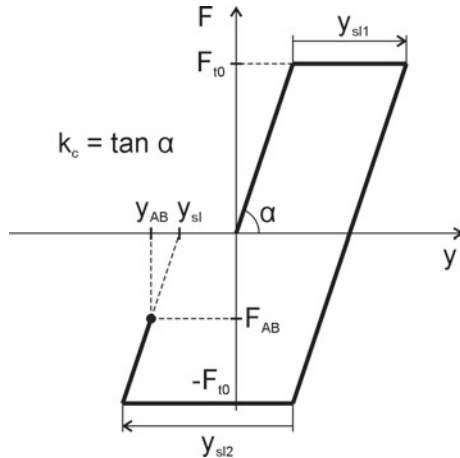


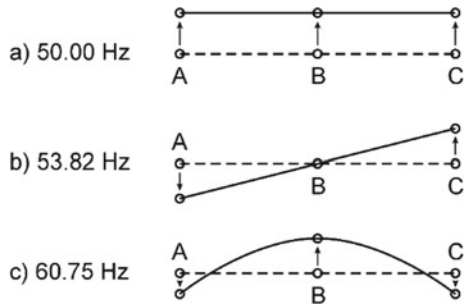
Fig. 6.37 Coulomb friction model behavior

The term $\mathbf{F}_c(\mathbf{y}, \dot{\mathbf{y}})$ covers the non-linear contact forces F_{cAB} and F_{cCB} which are dependent generally on relative displacement and relative velocity between blade pairs.

The proposed system was modelled and solved in Simulink programming environment. The stick-slip contact is described by the block scheme (Fig. 6.28) where the Coulomb friction is modelled by the backlash block ($2 * F_{t0}/k_c$) from Simulink library (Fig. 6.28).

Deformation curve of the contact model to the cyclic deformation is shown in Fig. 6.36. The output of the block scheme of contact between blades A and B is a contact force $F_{AB} = k_c \cdot (y_{AB} - y_{sl})$, where $y_{AB} = y_B - y_A$ is a total, i.e. stick and slip, relative displacement between blades A and B, $y_{sl} = \sum_i y_{sl,i}$ is sum of all slip displacements during dynamic loading (Fig. 6.37). The slip output y_{sl} of the backlash block remains constant in a stick phase and only elastic contact force arises. When the relative displacement y_{AB} reaches the backlash bounds $y_{sl} - F_{t0}/k_c$ at downstroke of the contact spring or $y_{sl} + F_{t0}/k_c$ at upstroke of the contact spring, slip occurs and backlash block output stepwise changes to $y_{sl} = y_{AB} + F_{t0}/k_c$ or $y_{sl} = y_{AB} - F_{t0}/k_c$, respectively. Then during the slip motion $F_{AB} = -F_{t0}$ or $F_{AB} = +F_{t0}$, respectively. When relative displacement y_{AB} falls down the updated backlash bounds the slip motion returns to stick elastic motion and the slip remains constant.

Fig. 6.38 Mode shapes and eigenfrequencies of three blades bundle with bonded contacts

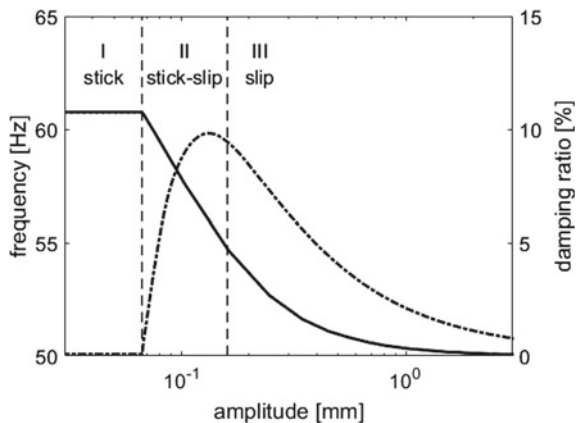


For testing of the model, parameters shown in Table 6.2 were set in accordance with experiment. Stiffness of the blade k was measured on the experimental set-up (Fig. 6.27) where the tip displacement of a single blade was measured under defined static load. Then mass $m = k\omega^2$ was calculated for eigenfrequency value $\omega/2\pi = 50$ Hz that is experimental eigenfrequency of a single blade detached from the disk. Damping ratios were set to 0.1 %. The nominal values of friction force F_{t0} and the contact stiffness k_c for comparison with experimental results was estimated as 1 N and $1 \cdot 10^4$ Nm $^{-1}$. The first three eigenfrequencies and corresponding mode shapes of the bundle model with bonded contacts in tie-bosses are shown in Fig. 6.38. First resonant frequency equals to resonant frequency of a single blade. The value of the contact stiffness influences the size of the next eigenfrequencies and can be tuned to their experimental counterparts. The difference between the third and first eigenfrequencies helps clearly distinguish the transition from the slip to stick contact state of the bundle at the attenuation period from the resonant vibration at third mode as described in the next Section.

(b) Numerical simulations of vibration attenuations

The dynamic behavior, i.e. resonant frequency and damping ratio, of the system changes due to changing contact slip phases during amplitude decay and therefore the attenuation characteristics give a good picture of the system dynamics. Vibration attenuation of three blades bundle is described by homogenous form of equations Eq. 6.3.1. Since the attenuation from a resonant vibration oscillating by the third mode shape (Fig. 6.38) was chosen to study the effect of friction contacts on system resonant frequency and damping, the initial condition as $\mathbf{y}^T = [-1.5, 3, -1.5]$ proportional to the mode shape and zeros velocities $\dot{\mathbf{y}}^T = [0, 0, 0]$ were prescribed to the solution. The non-linear effect of dry-friction damping in the bundle was studied for both one contact stiffness k_c and varying friction force F_{t0} or vice versa. Results of the simulations can be seen on Figs. 6.40 up to 6.47. General characteristics of resonant frequency and damping ratio of the three blades bundle with dry-friction contacts (Fig. 6.39) describe qualitative non-linear effect of the dry-friction on vibration amplitudes. The graph is divided to three phases: (I) stick—no relative motions in contacts during whole period of vibration, (II) stick-slip—combination of no and small relative motion in contacts during a period of vibration and (III) slip—large

Fig. 6.39 General characteristics of resonant frequency and damping ratio for the three blades bundle with dry-friction contacts



relative motion in contacts during most of a time of vibration period. Each phase of the characteristics brings a different dynamic behavior of the system. It can be seen a constant resonant frequency that corresponds to eigenfrequency of the linear case of blades bundle with bonded contacts in a phase I. Then a fast exponential decrease of resonant frequency (phase II) transits to slow approaching to limit frequency that corresponds to eigenfrequency of the linear case of blades bundle with open contacts. As to the damping the COND damping is zero in phase I, ascertains it's maximum in phase II and gradually decrease in phase III. Despite damping decrease with respect to its maximum at higher amplitudes the value of COND damping remarkably tops the STRUD damping of the system.

Amplitude envelopes of blade B for various friction forces and $k_c = 1e^4 \text{ Nm}^{-1}$ are shown in Fig. 6.40 and for various stiffness k_c and $F_{t0} = 1 \text{ N}$ in Fig. 6.41. The fast linear decrease of amplitudes caused by a slip dry-friction damping is seen at the first period of attenuation. Then a slope of amplitude envelopes dramatically decreases because of the transition of slip motion into stick state in the contacts. The stick state in contacts remains during a whole period of vibration. Therefore, the slow amplitude decrease is caused only by the original STRUD damping of the system. The higher friction force the faster decrease of amplitude. Increase of contact stiffness for the given value of friction force results only in slight decrease of amplitude.

Figures 6.42 and 6.43 show the resonant frequency changes for the same cases. At the beginning of attenuation the resonant frequency is close to the eigenfrequency of a single blade, i.e. 50 Hz, since slip state occur and the stiffness couplings in contacts are weak. When the amplitudes of the bundle, however, fall down, the contacts get locked and the resonant frequency passes over to eigenfrequency of the bundle with bonded contacts, i.e. 60.75 Hz. The resonant frequencies at the beginning and at the end are not dependent on friction force. It can be seen that changing friction force only shifts the increase of the frequency in time. On the other hand, change of stiffness of the contact spring leads to higher increase of the stick state resonant frequencies because the resonant frequency of the bundle with stuck contacts increases due to

Fig. 6.40 Amplitude envelope of vibration of blade B for various friction forces and $k_c = 10,000 \text{ Nm}^{-1}$

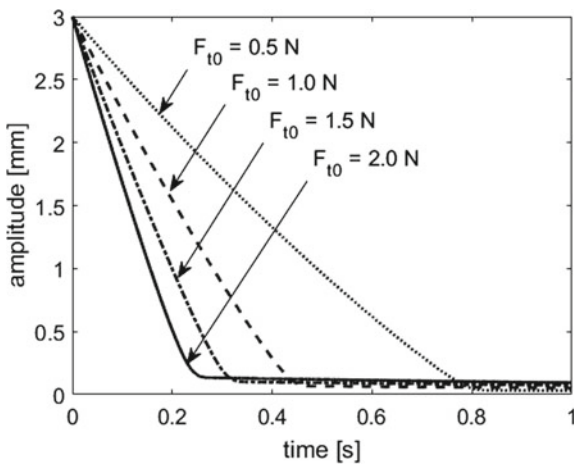
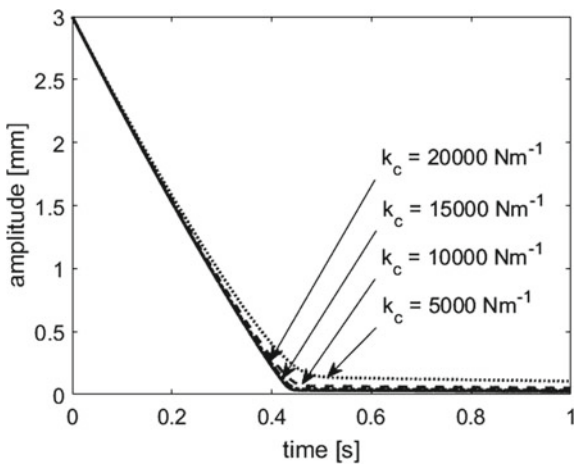


Fig. 6.41 Amplitude envelope of vibration of blade B for various stiffness k_c and $F_{t0} = 1 \text{ N}$



increasing the contact stiffness. The resonant frequency as a function of amplitude for the same cases is shown in Figs. 6.44 and 6.45.

Damping as a function of amplitude was evaluated according to Eqs. (6.3.3) and (6.3.4). Let a time function $a = a(t)$ be an envelope of maximal amplitudes, $f(a)$ a frequency as a function of amplitude decay of the attenuation blade responses. Then logarithmic decrement of amplitude can be written as function of amplitude

$$\delta(a) = \ln \frac{a}{a + \frac{da}{dt} \cdot \frac{1}{f(a)}}, \quad (6.3.3)$$

Then the damping ratio can be expressed as

Fig. 6.42 Frequency-time characteristics of vibration of blade B for various friction forces and $k_c = 10,000 \text{ Nm}^{-1}$

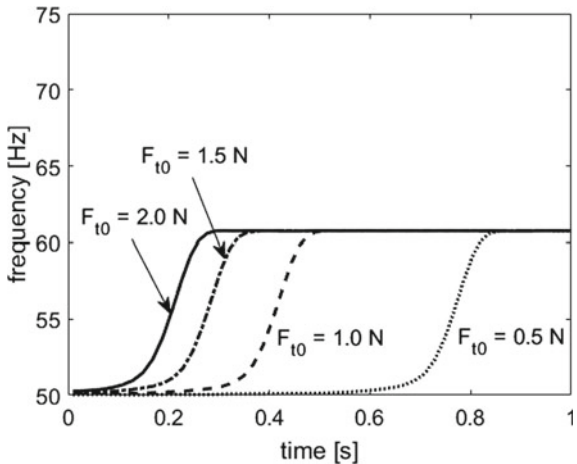
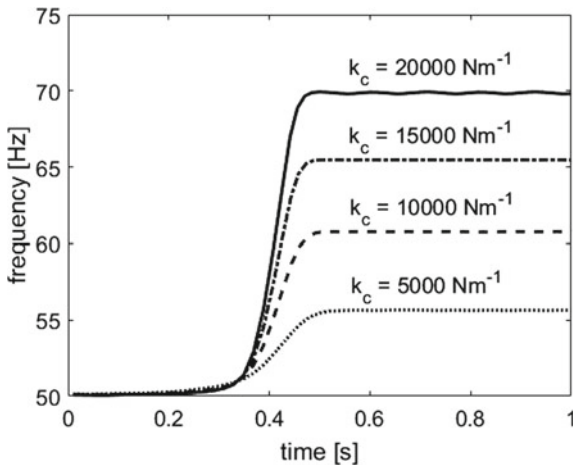


Fig. 6.43 Frequency-time characteristic of vibration of blade B for various stiffness k_c and $F_{t0} = 1 \text{ N}$



$$b_r(a) = \frac{\delta(a)}{2 \cdot \pi}. \quad (6.3.4)$$

Results of damping ratios for various friction forces and contact stiffnesses are shown in Figs. 6.46 and 6.47, respectively. It can be seen that increase of friction force leads to increase of damping ratio for higher amplitudes of vibration. The maximal values for different friction forces, however, are the same and are just shifted to higher amplitudes with increasing friction forces. On the other hand, increase of contact stiffness does not change the damping ratio for higher amplitudes, but for the amplitudes close to the point where transition from stick-slip to stick state occurs, there is a rapid increase of damping ratio which corresponds to quicker slope change of envelope in Fig. 6.41.

Fig. 6.44 Frequency-amplitude characteristics of vibration of blade B for various friction forces and $k_c = 10,000 \text{ Nm}^{-1}$ as a function of amplitude

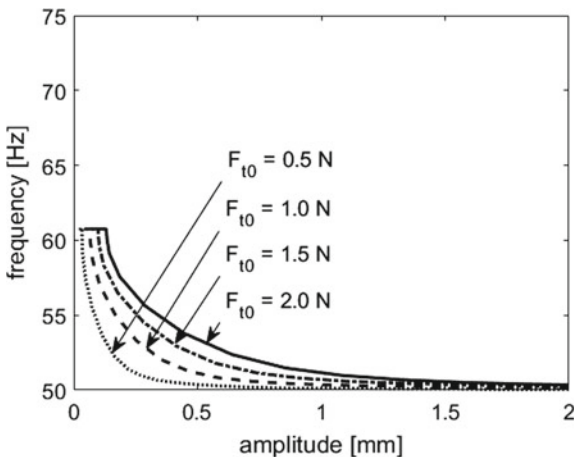
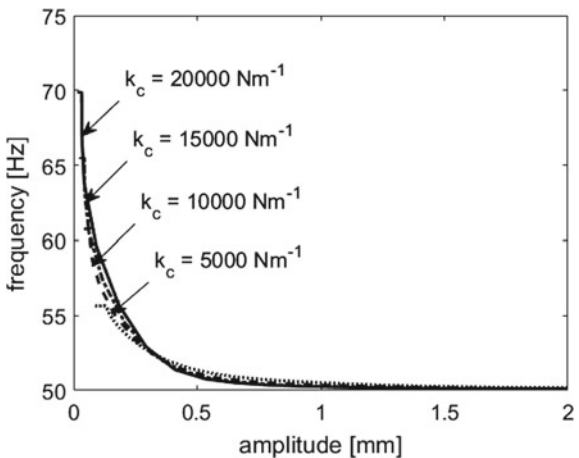


Fig. 6.45 Frequency-amplitude characteristics of vibration of blade B for various stiffness k_c and $F_{t0} = 1 \text{ N}$ as a function of amplitude



As we will see in Sect. 6.4 the characteristics of the three blades bundle with dry-friction couplings are very similar to the characteristics of the whole wheel and can help to predict and to understand its dynamic behavior.

(c) Numerical simulations of system response to sweep excitation

To describe dynamics of non-linear systems besides the attenuation regime the amplitude frequency characteristics of the system is very often used, too. To get this characteristic of our three blades bundle with dry friction couplings we solved Eq. 6.3.1 with continuous change, so called sweep, of excitation angular frequency ω within an interval $\langle \omega_1, \omega_2 \rangle$. The distribution of force amplitudes were set affinity to the third mode of vibration, namely $F_B = F_b$ and $F_A = F_C = -0.5 \cdot F_b$, where different values of F_b were set for each sweep simulation. The sweep excitation was linear

Fig. 6.46 Damping ratio-amplitude characteristics for various friction forces and $k_c = 10,000 \text{ Nm}^{-1}$ as a function of amplitude

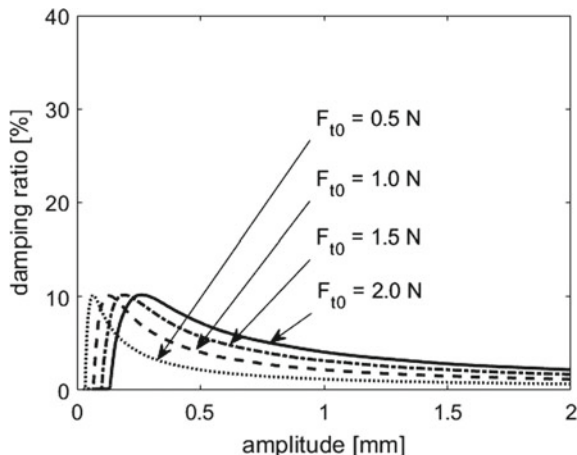


Fig. 6.47 Damping ratio-amplitude characteristics for various stiffness k_c and $F_{t0} = 1 \text{ N}$ as a function of amplitude

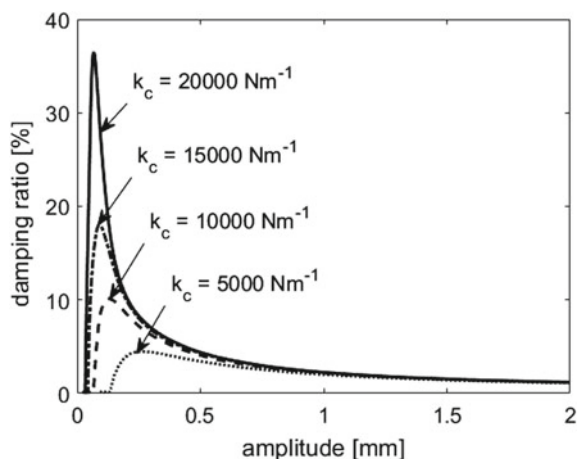


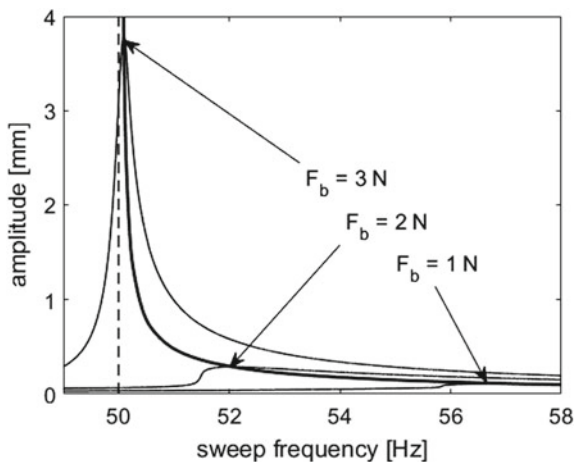
Table 6.2 Parameters of three blade bundle model

Parameter	Value	Unit
m	0.6383	kg
k	$6.3 \cdot 10^4$	Nm^{-1}
b	0.4	kg s^{-1}
k_c	$1 \cdot 10^4$	Nm^{-1}
F_{t0}	1	N

from frequencies 48 to 58 Hz in period 30 s. Model parameters were set same as in previous Section (Table 6.2).

Figure 6.48 shows envelopes of oscillations of blade B which are maximal amplitudes of the three blade bundle system in dependency on sweep frequency for three

Fig. 6.48 Amplitude-frequency characteristics at frequency sweep excitation for three force amplitudes (1, 2 and 3 N)



force amplitudes $F_b = 1, 2. Shift of the resonance peaks for higher excitation forces is clearly visible. It is caused by slip motion in friction contacts that are more dominant for higher excitation forces. During the slip motion, the couplings of blades are weak and therefore their resonant frequency is close to the eigenfrequency 50 Hz of a single blade.$

Maximal resonant amplitudes in dependence on excitation force F_b for various friction forces F_{t0} are in Fig. 6.49 and their corresponding resonant frequencies in Fig. 6.50. It is shown in Fig. 6.49 that by increasing friction forces the maximal amplitudes curves moves right that means the higher excitation force is required to keep the same maximal amplitudes as at lower friction forces. Furthermore, it is obvious from Fig. 6.49 that an increase of friction force in contacts widens stick-slip phase and shifts a transition from stick-slip to slip phase to higher excitation forces where resonant frequency approaches the eigenfrequency of a single blade.

6.3.1.3 Non-linear 3D FE Model with Dry Friction Contacts

Computational contact mechanics based on finite element technology is nowadays very good theoretically established and implemented in many commercial engineering software packages as ANSYS, ABAQUS etc. It enables to use them in very different areas of application, such as biomechanics, crash tests, molding, rail-wheel dynamics and latest dynamics in bladed wheels (e.g. [11, 34, 35, 38, 62]). The advantage is that these models are usable for general dynamic excitation with smooth and non-smooth contact surfaces since the bladed disc dynamics with non-holonomic contact constrains are solved as discretized fully coupled non-linear problem in time-domain. This solution leads, however, to high performance computations. Even the high performance supercomputers with many processors (e.g. 24 processors per 5 nodes) a length of computation of dynamic response of the full bladed wheel with

Fig. 6.49 Maximal resonance amplitude characteristics of blade B dependent on excitation force for various friction forces

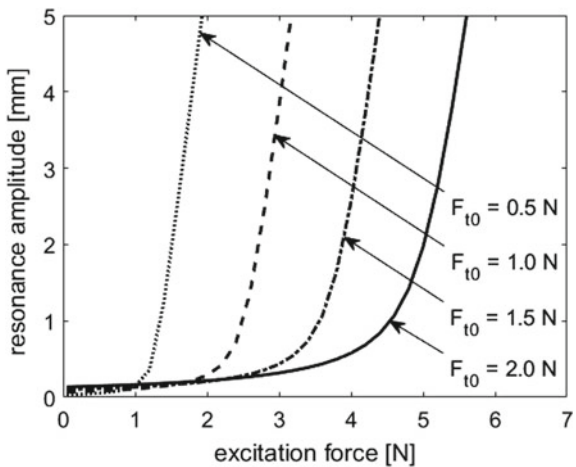
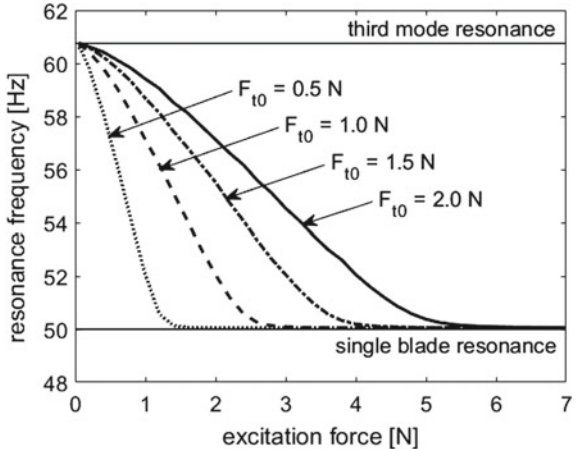


Fig. 6.50 Resonant frequency dependences on excitation force for various friction forces



many inter-blade and blade-to-disc contacts can be expected in order of many days. The long computational time is caused especially by number of iterations in each integration time step (for a solution convergence must be very short) in a large number of non-linear couplings between discretized contact surfaces. So, the development of very efficient parallel algorithms for the contact problem solution is still needed. Due to possible space and time discretization inaccuracies and numerical errors, an experimental validation is needed, too. Because of long computational times of the full bladed wheel solution we decided for the blades with friction contacts in tie-bosses first to aim at a three blade bundle and compare the results with an experiment.

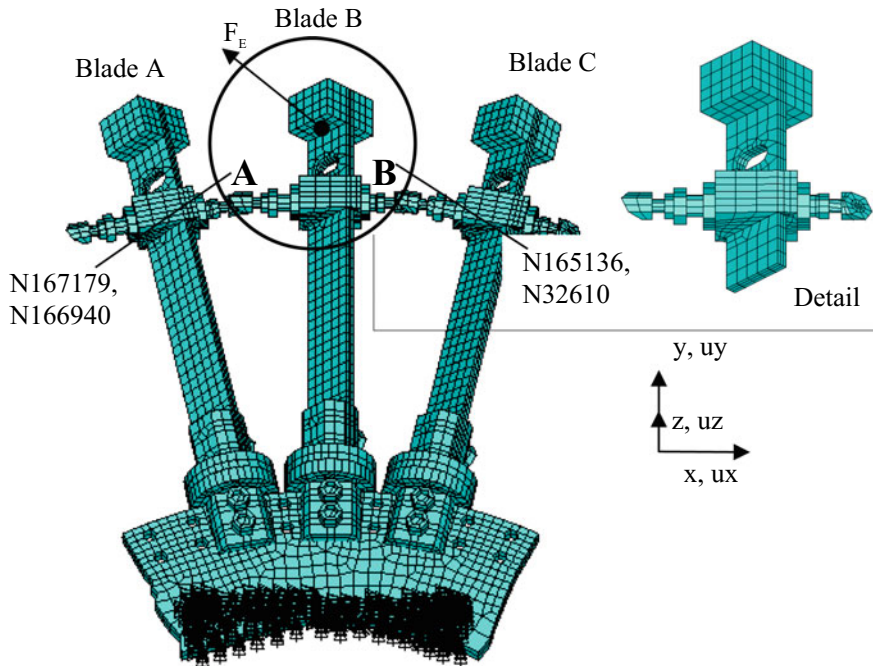


Fig. 6.51 FE mesh of triple blade model with excitation force F_E

(a) Model description

Three-dimensional FE model of the blade triple with tie-bosses (Fig. 6.51) was developed in the program ANSYS 15.0. The detail of the mesh of the blade B in the vicinity of its head and the contact surface is depicted in the figure, too.

The hexahedral eight-nodes elements were chosen for blade and friction element models. Contacts between the blade heads were modeled by a so-called “surface-to-surface” method using a couple of contact surface elements TARGET170 and CONTACT174 placed against each other on contact lateral ends of the tie-bosses. To detect contact points, the “pinball” search algorithm was used. The displacements of nodes located at centers of associated target and contact surfaces of the contacts A (i.e. N167179 and N166940), B (i.e. N165136 and N32610) (see Fig. 6.51) were used for evaluation of the relative motions of the surfaces.

The Augmented Lagrangian method was used to compute contact normal pressures and friction stresses. Contact surface behavior is modelled as standard unilateral contact, i.e. the normal pressure equals to zero if separation occurs. The friction coupling was modeled by the Isotropic Coulomb’s law. If the friction stress τ does not exceed the limit friction stress $\tau < \tau_{\text{lim}}$ in the contact surface where $\tau_{\text{lim}} = fp$ and p is a normal pressure then the contact is in a state of “sticking”. In this state there is zero sliding between the contact surfaces and only elastic deformations x_t occur. The contact stiffness k_c is automatically calculated according to the local stiffness

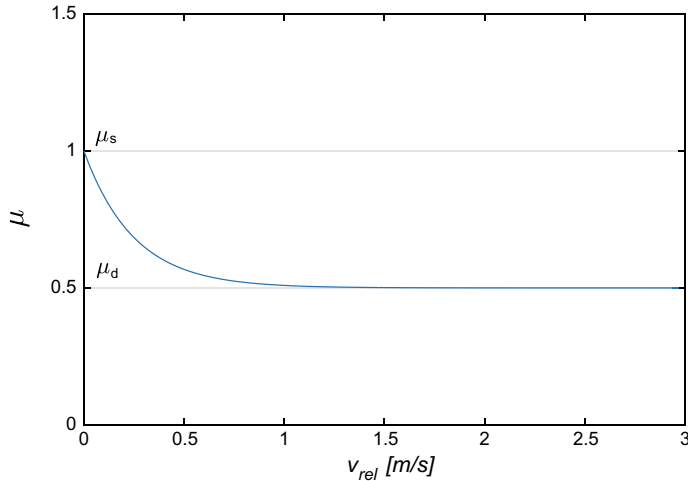


Fig. 6.52 Dependence of friction coefficient on the relative velocity

of the contact areas by the program. After the friction stress exceeds the limit by the equivalent friction stress, “sliding” of contact surfaces appears. The size and direction of sliding are evaluated by the sliding rule using a so-called potential of friction flow.

For a description of the friction coefficient f , the following dependence on relative velocity v_{rel} is considered:

$$f = f_d [1 + ((FACT - 1)e^{-DCv_{rel}})], \quad (6.3.5)$$

where $FACT = f_s/f_d$, f_s static and f_d dynamic friction coefficients, DC decay coefficient. The graph of the friction coefficient for values $f_s = 1$, $f_d = 0.5$, $DC = 4$ that were used for the computation of the dynamics of the triple blades is in Fig. 6.36. For $FACT = 1$ we get Coulomb’s friction model and for $FACT 1$ its modified version (Fig. 6.52).

A full solver for unsymmetrical task solved the transient responses with the Newmark integration method and time step $5e-6$ s. The Newmark parameter $\gamma = 0.5$ was set for numeric stabilization reasons. The damping ratio 0.1% was imposed as the steel material and other construction damping.

Excitation forces are described:

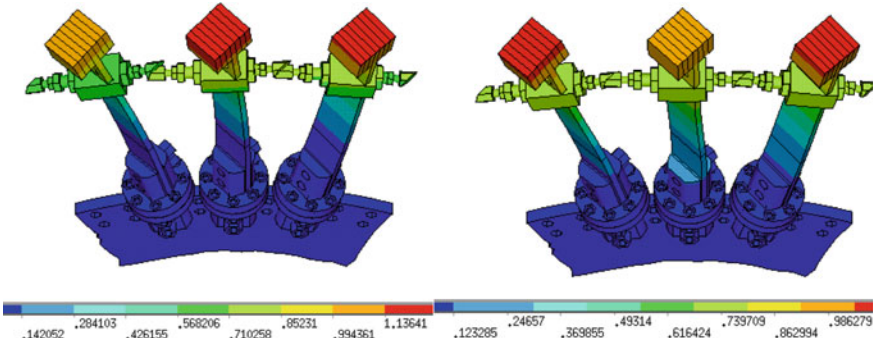
$$F_E = F_b \sin(2\pi f_E t) \quad (6.3.6)$$

where F_b [N] is amplitude, f_E [Hz] is the frequency of excitation. The force was applied perpendicular to the middle blade of the triple at its end (Fig. 6.51).

The pre-stress in contacts was modeled by contact surface offset $2e-5$ m. The resulting static normal pre-stress in contacts was evaluated 4.9 N.

Table 6.3 Computed eigenfrequencies of the first bending mode of FE model

Mode number i	Eigenfrequency	Open contacts	Bonded contacts
1	f_i (Hz)	47.9	78.8
2		48.7	134.1
3		49.1	162.8

**Fig. 6.53** First bending eigenmodes of blade triple with open contacts (left), and bonded (right) contacts in tie-bosse

The first three eigenfrequencies of modal analysis of the FE triple blade model both with open and bonded contacts are summarized in the Table 6.3. The first eigenmodes for both states of contacts are depicted in the Fig. 6.53.

Hence, resonance frequencies of the first flexural eigen-mode of the blade triple for open and bonded contact cases resulted 47.9 Hz and 78.8 Hz, respectively. Contrary to the open contact triple where first three eigenfrequencies belong to the different relative motions of first bending mode of single blades, at the bonded contact state the second eigenfrequency belong to the first torsional and the third to the first lateral mode of the triple. From the differences of the first bending eigenfrequencies it can be seen the large stiffening effect in the triple due to changing boundary conditions in the contacts. Then finally a transient non-linear analysis of blade triple with friction contacts was performed for loading cases: force amplitude $F_b = 28.2$ N, excitation frequency $f_E = 47.9$ Hz corresponding to the eigen-frequency of the first flexural mode of the open contact blade triple.

(b) Numerical simulations of vibration attenuations

The computed contour map of the total displacements and a detail of the contact states (sliding-sticking) at contacts A, B are depicted in the Fig. 6.54 for a static pre-stressed state by offset $2e-5$ m in both contacts. It can be seen that due to static pre-stress the middle blade twists and the contacts are localized not in the middle of the contact surfaces but on the edges.

To study friction contact influence on the blade triple dynamic responses, as to the maximum amplitude, amplitude decay and excited frequencies, the four different

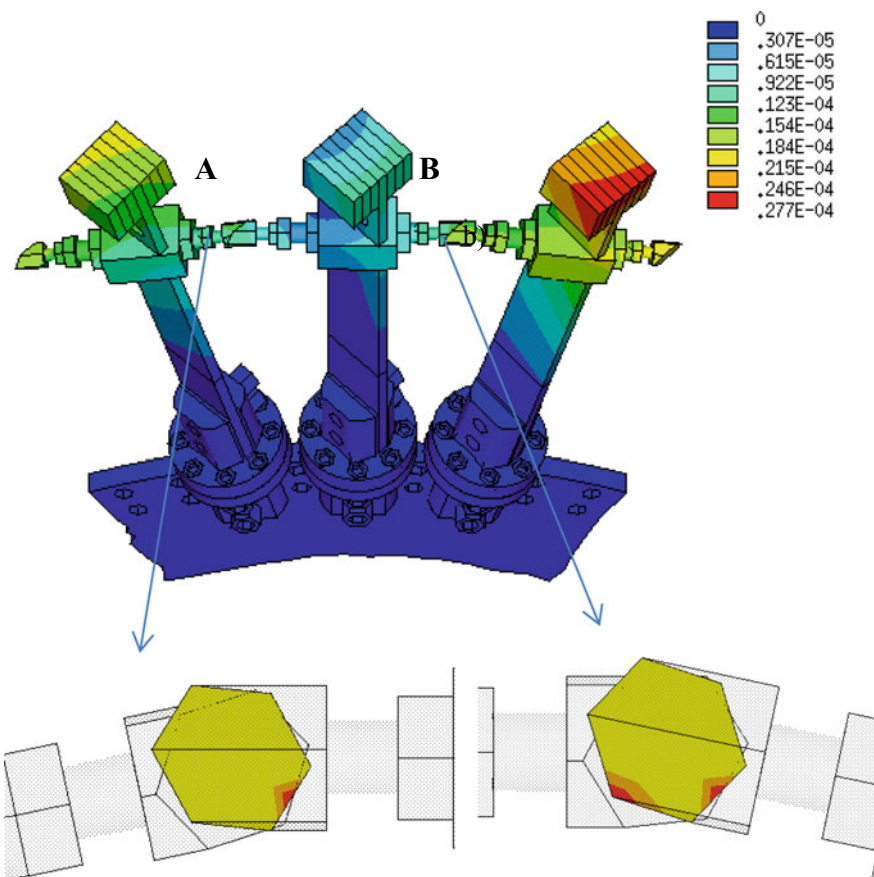


Fig. 6.54 Computed contour maps of total displacement [m] and details of contact status (sliding, sticking) at pre-stressed contacts A, B by offset $2\text{e-}5 \text{ m}$

levels of force amplitude F_b were chosen: (a) 1.41, (b) 4.25 and (c) 7.07 N. The blade B was excited by frequency equal to the eigenfrequency of open contact of blade triple. After four periods the force excitation is switched off. The damping ratios and vibration frequencies were evaluated from the amplitude attenuation.

Results are shown for each load case in several graphical forms, i.e. Figures 6.55, 6.56, 6.57 and 6.58 for case (a), Figs. 6.59, 6.60 and 6.61 for case (b), Figs. 6.62, 6.63, 6.64 and 6.65 for case (c). To show the deformation shapes of the triple and variety of contact states, displacement contours and contact states in three different time steps during one period of vibration is presented (Figs. 6.55 and 6.62). Then time characteristics of directional displacements u_x , u_y , u_z of the blades A, B and C are plotted for comparison of the size of displacements of single blades (Figs. 6.56, 6.59 and 6.63). Furthermore there are depicted relative motions of contact surfaces (Figs. 6.57, 6.60 and 6.65). The relative motions are evaluated from the differences

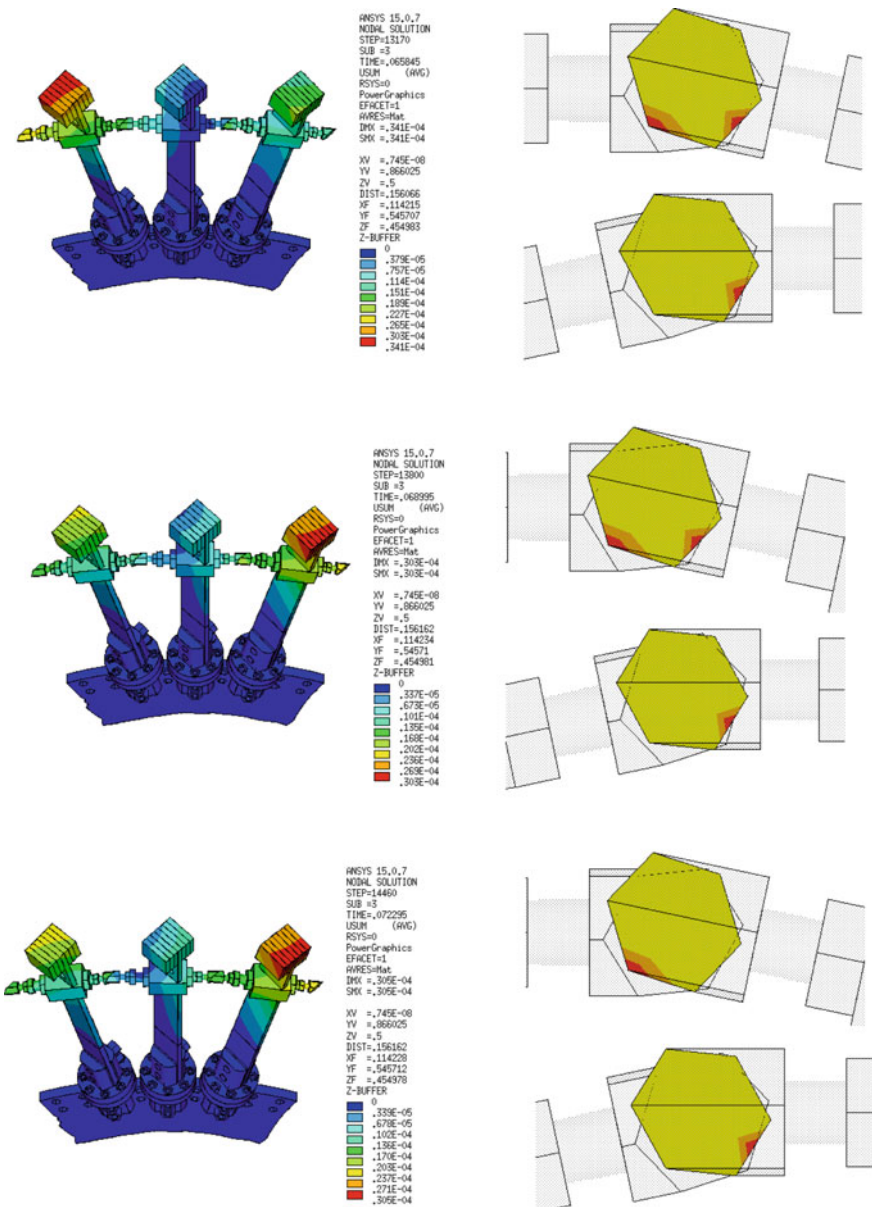


Fig. 6.55 Contours of displacements and contact states in the blade triple at 3 selected times (0.065845, 0.068995, 0.072295 s) of one period for excitation amplitude 1.41 N

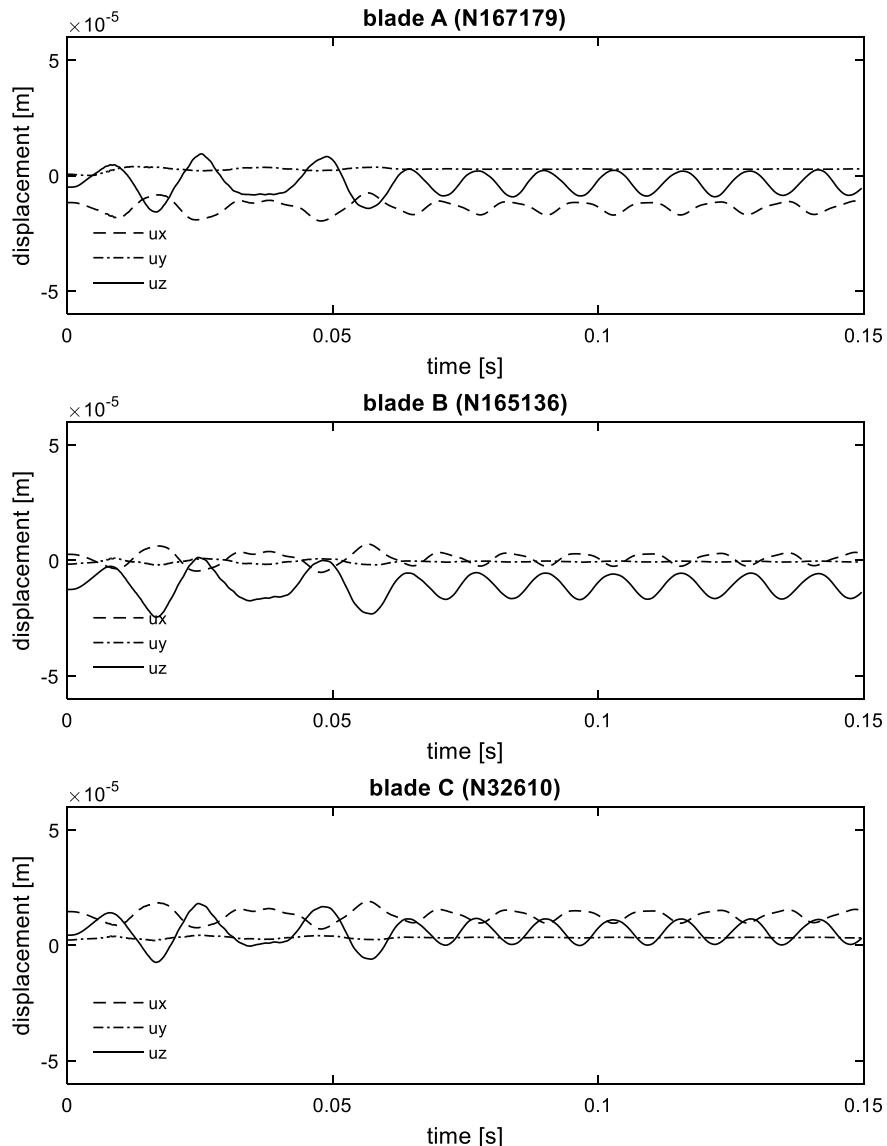


Fig. 6.56 Time characteristics of directional displacements ux , uy , uz of the blades A, B and C for excitation amplitude 1.41 N

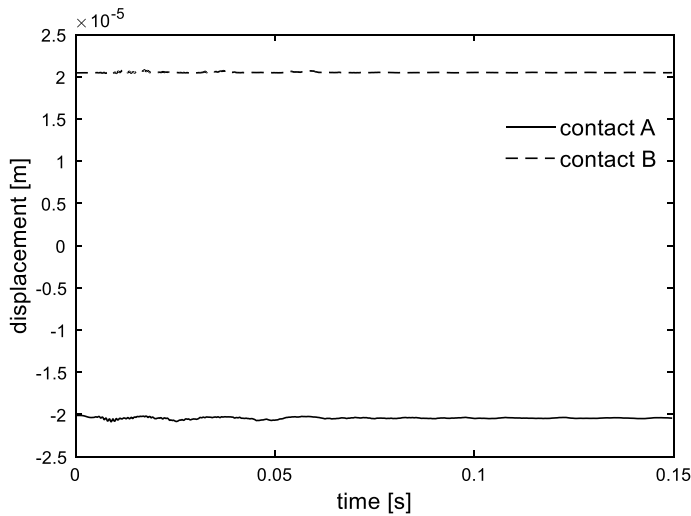


Fig. 6.57 Time characteristics of relative displacements in contact A and B of the blade triple for excitation amplitude 1.41 N

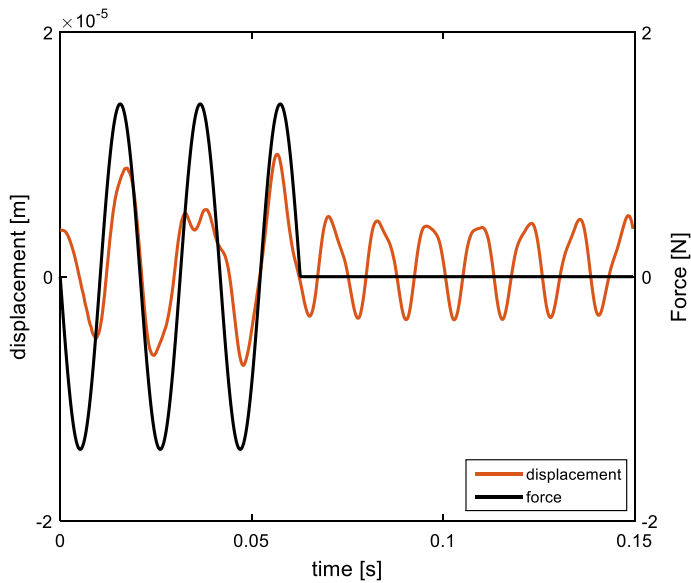


Fig. 6.58 Time characteristics of vector sum of **a** displacements (red line) of the blade B; **b** excitation force (black line) with amplitude 1.41 N

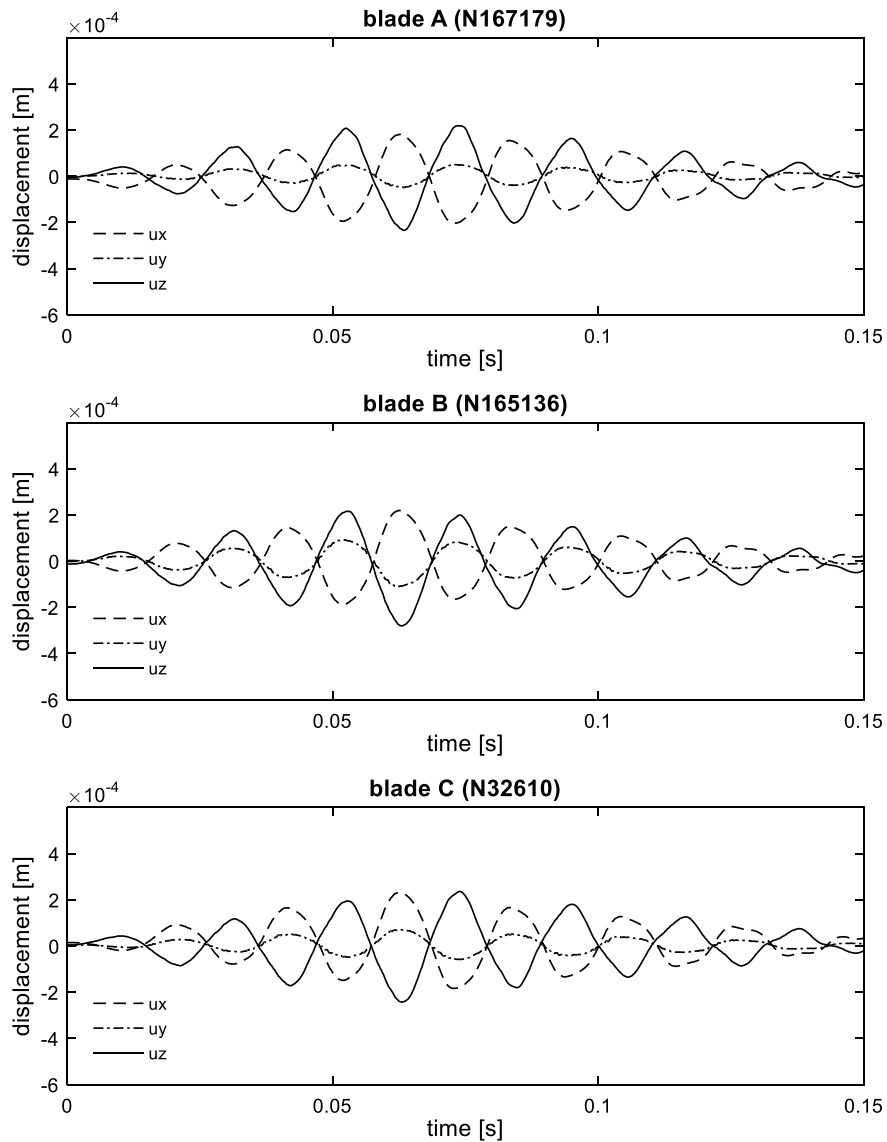


Fig. 6.59 Time characteristics of directional displacements ux , uy , uz of the blades A, B and C for excitation amplitude 4.25 N

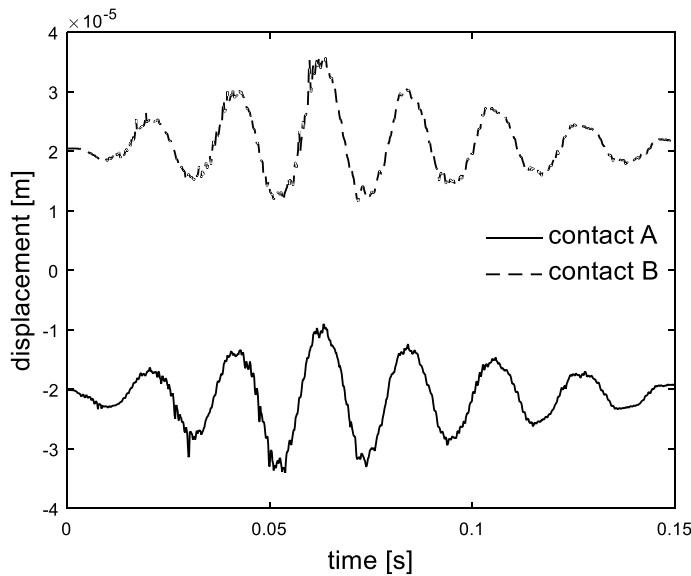


Fig. 6.60 Time characteristics of relative displacements in contact A and B of the blade triple for excitation amplitude 4.25 N

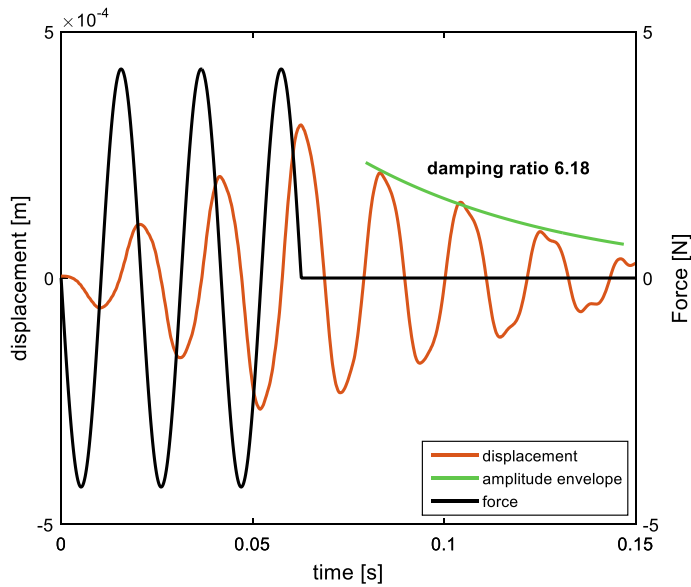


Fig. 6.61 Time characteristics of vector sum of **a** displacements (red line) of the blade B; **b** excitation force (black line) with amplitude 4.25 N

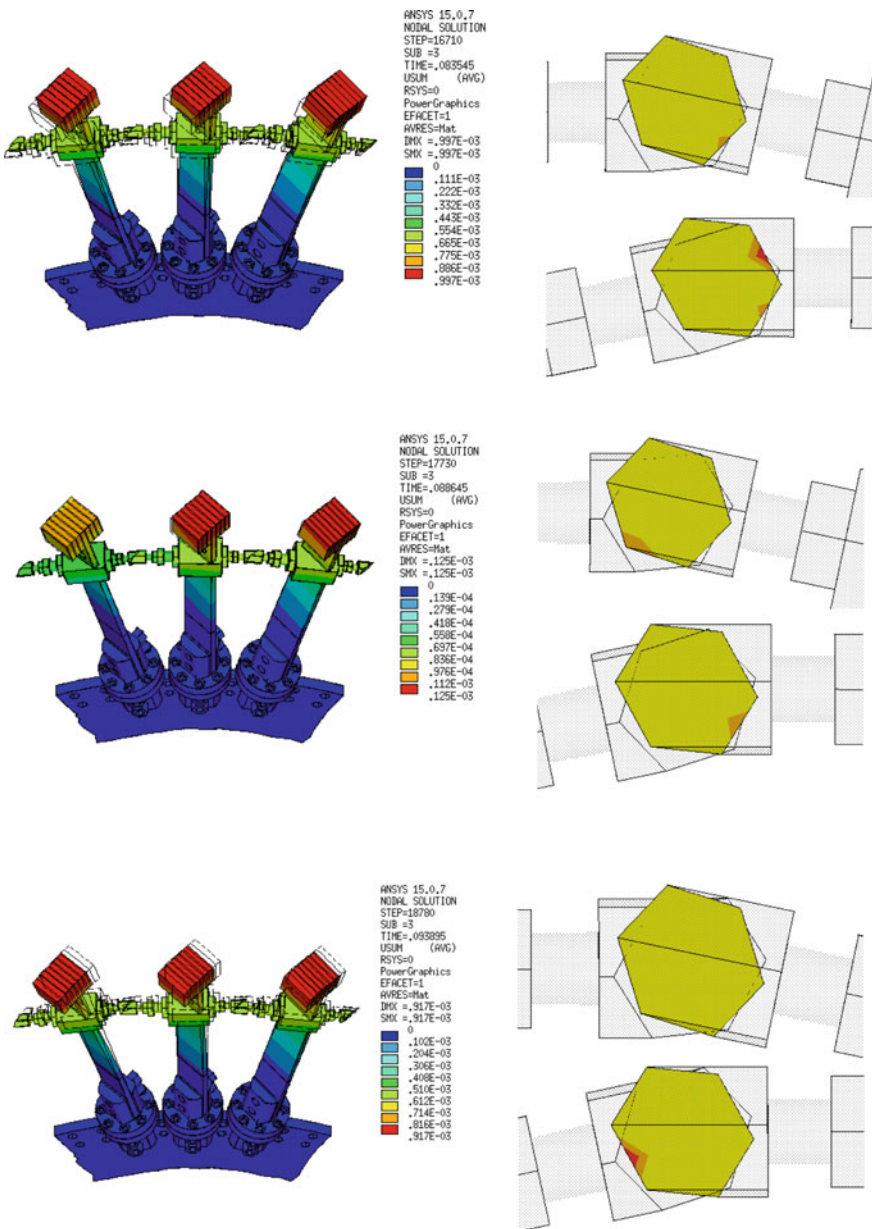


Fig. 6.62 Contours of displacements and contact states in the blade triple at 3 selected times (0.083545, 0.088645, 0.093895 s) of one period for excitation amplitude 7.07 N

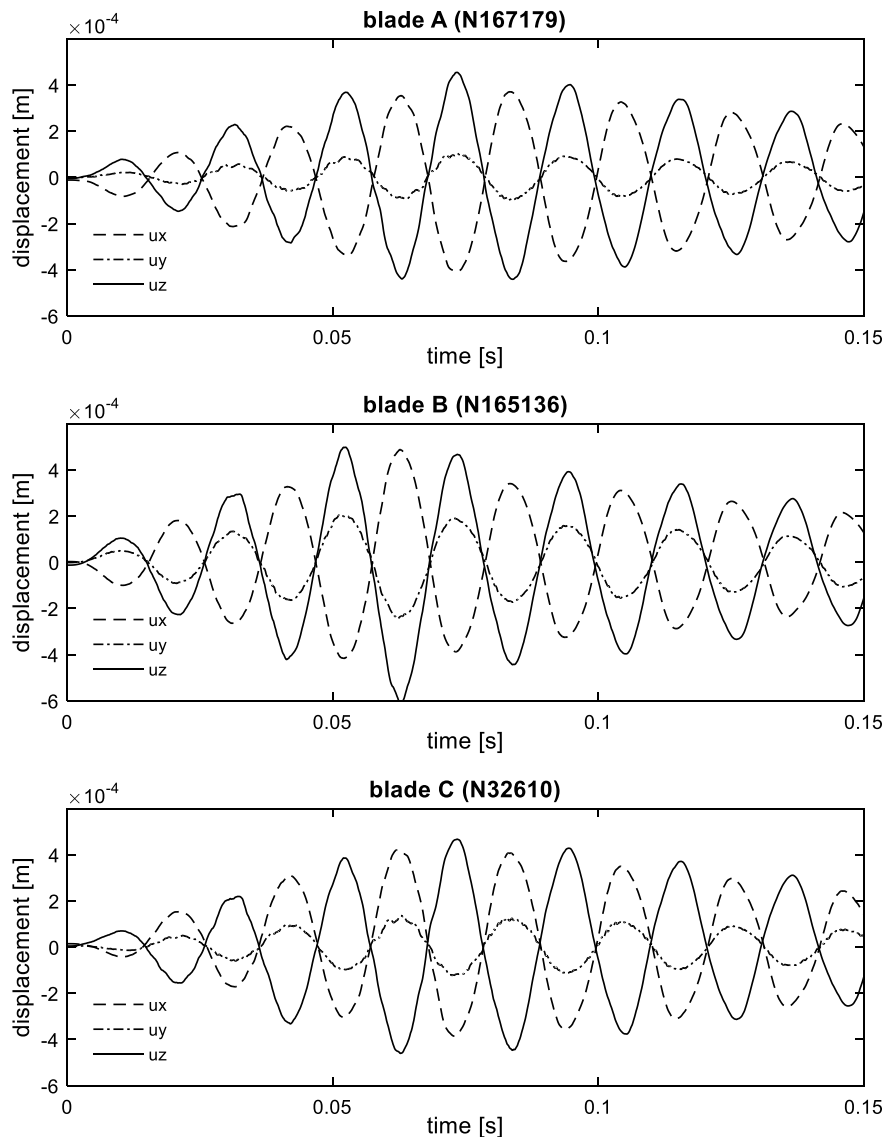


Fig. 6.63 Time characteristics of directional displacements ux , uy , uz of the blades A, B and C for excitation amplitude 7.07 N

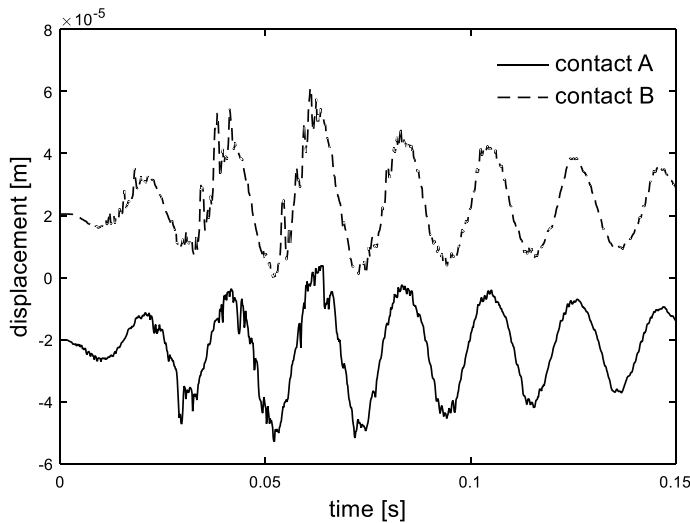


Fig. 6.64 Time characteristics of relative displacements in contact A and B of the blade triple for excitation amplitude 7.07 N

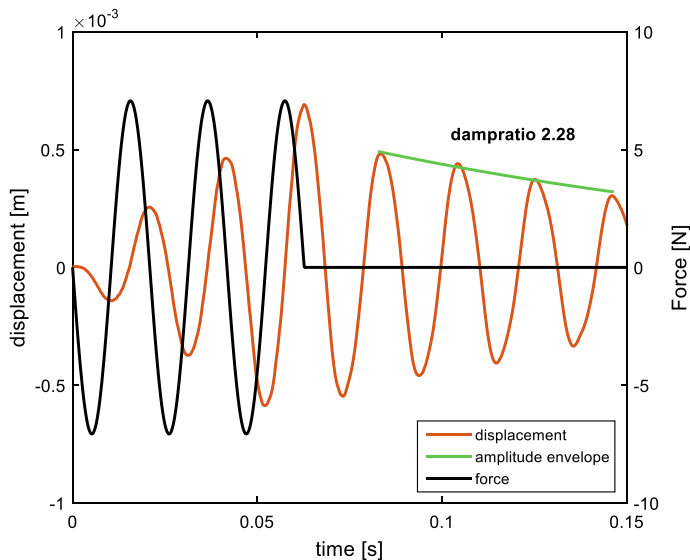


Fig. 6.65 Time characteristics of vector sum of **a** displacements (red line) of the blade B; **b** excitation force (black line) with amplitude 7.07 N

of associated node couples, mentioned earlier, of contacts A and B. In addition to compare them with the experiment we make projection of the relative displacements to the direction perpendicular to the blade. The last form of graphical output is time characteristic of vector sum displacement of the blade B at its end (node N166200) together with the excitation force (Figs. 6.58, 6.61 and 6.65). In some of these graphs are also depicted amplitude envelopes (green line) at the vibration attenuation from which the damping ratio was evaluated by the envelope method.

The first load case corresponds to the stick phase with microslip motions in contacts of the blade triple, the second case shows the transition phase from slips to microslips and the third case slip motion in contacts. For the first case it can be seen that the contacts vary small as to the area and state in a lower load case. The contact areas do not change much with respect to static pre-stressed case. Opposite signs of relative displacement at the time 0 is caused by torsional deformation of the blade B by static pre-stress by contact offset. Since the contacts remain in prevailing stick state the eigenfrequency of the triple is very different (see Table 6.3) than the excitation frequency and we get off-resonant vibration with small amplitudes. In higher load cases large amplitudes are excited so that the adhesion in contact surfaces of the blades is exceeded and the surfaces got first into stick-slip and then into slip motion. Due to excitation frequency equal to the eigenfrequency of open contact of blade triple, the blade B gets into resonant start up vibration when the blade movement reaches the 90° phase angle lag to the time characteristics of the force F_E . Thanks to the resonant excitation we get much higher amplitudes of vibration of the blade B than by low force amplitude of the first load case. The contacts vary markedly both in time as it can be seen from contact states in Fig. 6.46. The contact state changes from stick-slip to slip and in some instants even contacts open. In most times, however, the contact is in a sliding state due to higher vibrational amplitudes. The existence of slips can be also observed from the relative motions.

Blade displacements ux is the same but opposite to uz which means that a plane of vibration of the blade B lies perpendicular to the plane of the blade. The displacements of blades A and C are mutually very similar. It means that relative motion in the contacts between blade pair A, B and B, C and the motion of blades A, C to the blade B is almost symmetric.

As to the damping ratio we can see in the second and third cases fast decrease of amplitudes with high damping ratios 6.18 and 2.28% is achieved, respectively. The high value of damping of the second case is caused by transition of slips into microslips in the vibration attenuation period with polyharmonic character. So it influences faster decrease of amplitude envelope. At the third case the attenuation is almost harmonic with frequency equal to eigenfrequency of the first flexural mode of the blade triple with the open contacts and evaluated damping ratio fits very well to the experimental damping estimation.

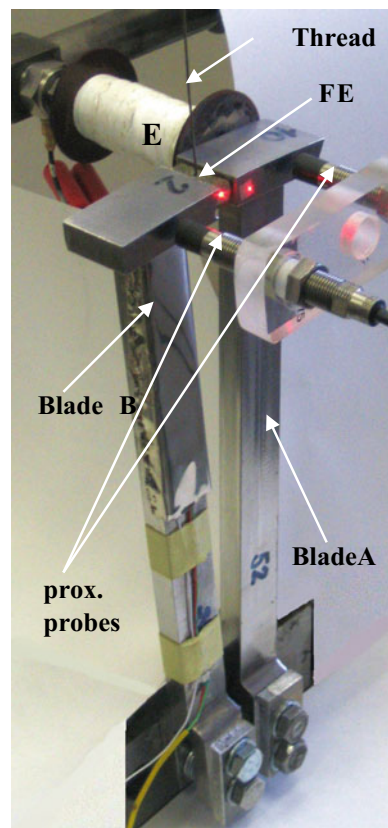
6.3.2 Blade Couple with Dry-Friction Element

6.3.2.1 Experimental Study

For evaluation of how the inter-blade dry-friction elements influences the bladed disk vibrational damping the experiments of the blade couple with friction element made of steel or composite material ARAMID were performed in steady non-rotating state (Fig. 6.66). Blades A and B (prismatic part: width \times thickness 0.02×0.01 m, length 0.2 m, total length 0.25 m) were clamped in the lower ends into the steel block by bolts (Fig. 6.66). The friction element (FE) placed in the slot between the blade ends (height 0.01 m, mass 0.078 kg) was radially extruded by the thread prestressed by the static force F_r . The radial force was set in range up to 5 N.

Dynamic force acted to the blade A was electromagnetic. For description of the damping effect of the dry friction contacts, the excitation were performed by short blocks (several seconds in length) of harmonic excitation with resonant first flexural frequency of the blade fixed on the disk for different static radial F_r and excitation

Fig. 6.66 Picture of measurement set-up (small light spots—target laser points)



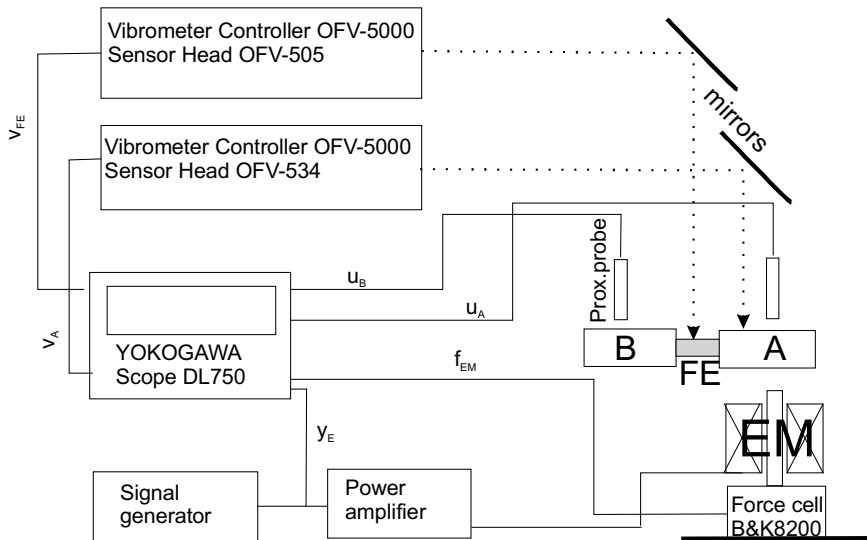


Fig. 6.67 Block scheme of measurement set-up

amplitude F_a . The damping effect was evaluated from vibration amplitude decay of blades after the abrupt switching-off the excitation; damping ratios is identified from amplitude logarithmic decrement by Hilbert's transformation.

Each blade displacement u_A resp. u_B was picked up by proximity probes Schenck IN-081 and at the same time velocities v_A of blade A and v_{FE} of friction element by POLYTEC laser vibrometers (Fig. 6.67). Electromagnet EM or shaker LDS-V406 was supplied by LDS power amplifier and controlled by signal of generator HP 33120A. Dynamic force was measured by force transducer B&K8200. Time characteristics of force, blade and friction element responses, generator signal were registered in Scope Recorder YOKOGAWA DL750.

The typical results of the two blades vibration with the friction element are shown in the Figs. 6.68, 6.70 and 6.72 for three combinations (I–III) of the radial force F_r and excitation amplitude F_a values, i.e. $F_r = 0.5 \text{ N}$, $F_a = 1.6 \text{ N}$ (I); $F_r = 1 \text{ N}$, $F_a = 0.8 \text{ N}$ (II); $F_r = 1 \text{ N}$, $F_a = 1.8 \text{ N}$ (III), respectively. The graphs of the Fig. 6.68 depict the measured signals, i.e. displacements of blades A, B, relative displacement of the friction element with respect to the blade A and electromagnet force F_{EM} . The relative displacement was evaluated from the difference of velocities v_A and v_{ET} after their integrations. The graphs of the Figs. 6.69, 6.71 and 6.73 depict the displacement of the blade A with evaluated damping ratios at the attenuation after switch off of the electromagnet current supply.

Non-linear effect of dry friction is mostly pronounced for the case I. The time characteristics of displacements of blade A, B, relative displacements between the friction element and blade A and excitation force are in Fig. 6.68. The relative displacement of friction element shows higher motion (slip phase) at the first stage

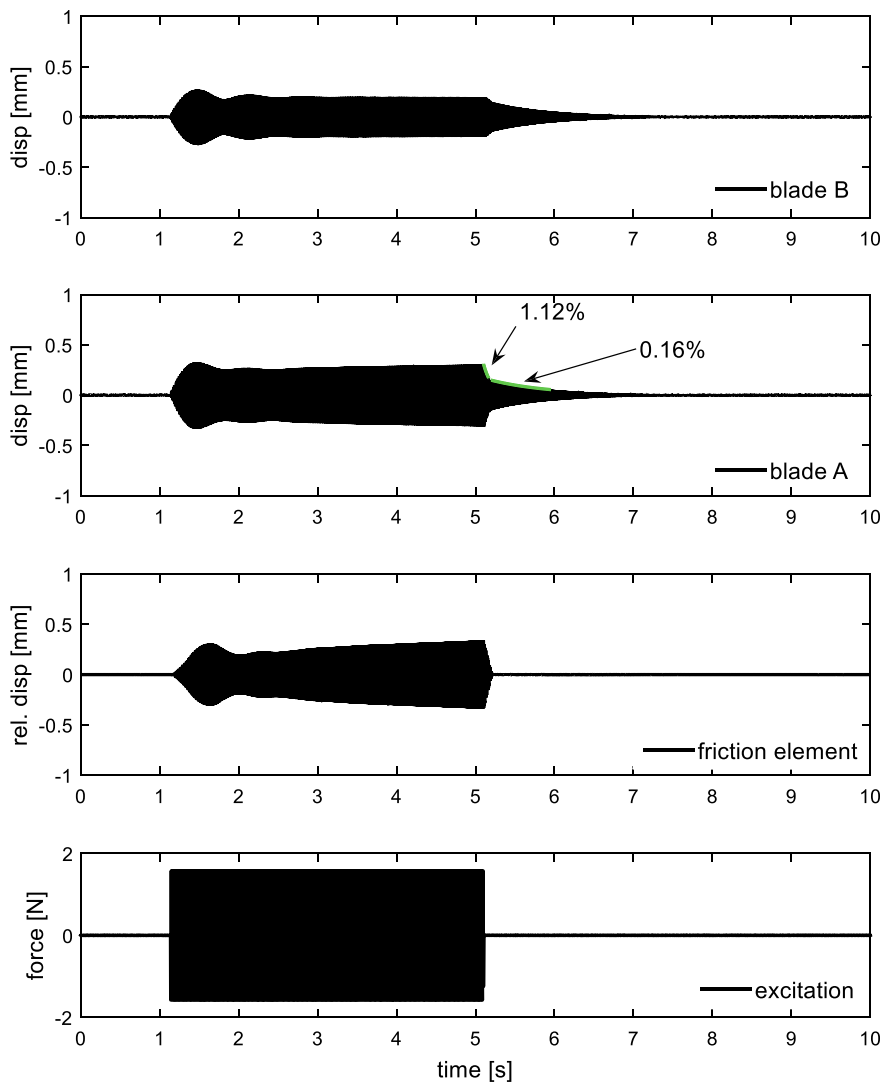


Fig. 6.68 Displacements of the blades B and A, relative displacement of the friction element and electromagnet force—case I

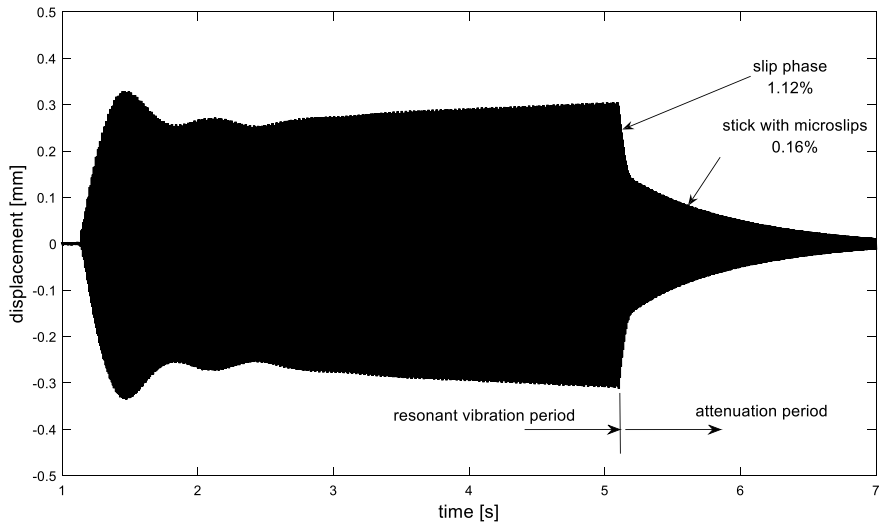


Fig. 6.69 Displacement of the blade A with designation of macroslip and microslip stages in attenuation period—case I

of attenuation and very small (stick with microslips) at the last stage. The zoomed time response of the blade A is in Fig. 6.69 where the contact phases are described. It can be seen that due to slip motions the vibration amplitudes of blades fall down with high damping ratio 1.12%. When the slip motion transfers into stick with microslips the damping ratio drops down to 0.16%.

The weak effect of the stick phase with microslips on damping behavior of the blade couple can be observed in case II (Figs. 6.70 and 6.71). The relative displacement of the friction element is in the range cca $\pm 1e-5$ m and the damping ratio is 0.2%. The attenuation is almost exponential in the whole time.

With the same radial force and higher excitation force (case III, Figs. 6.72 and 6.73) we get higher amplitudes of blade vibration, higher relative displacement of the friction element and slightly higher damping ratio (0.3%) of the attenuation.

Due to higher damping ratio in case I (Fig. 6.68), the vibration amplitudes of blades A, B are approximately half then their amplitudes in the case II (Fig. 6.71) where the relative motion of the friction element is smaller due to higher radial force and higher adhesion forces between the friction element and the blades.

6.3.2.2 Numerical Simulations of Vibration Attenuation on Discrete Analytical Model

Experimental research gives important results useful for design and development of new machines, but it is usually encumbered with a lot of marginal influences and

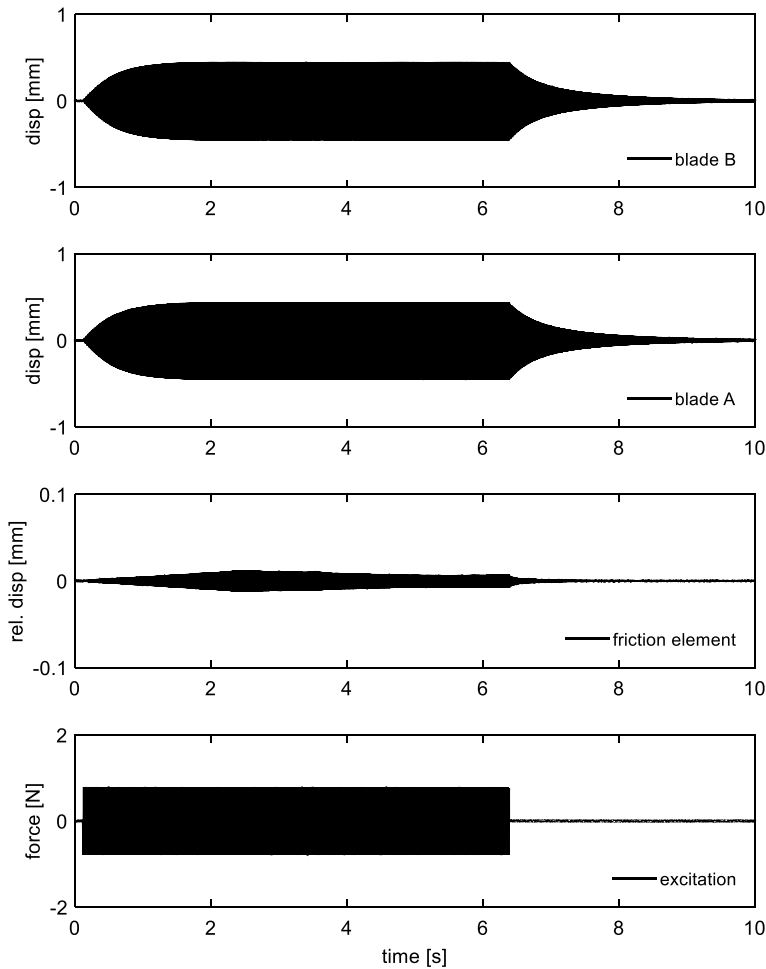


Fig. 6.70 Displacements of the blades B and A, relative displacement of the friction element and electromagnet force—case II

uncertainties. In this investigated case it is e.g. very difficult to measure motion of friction element, dry friction forces and friction coefficient during operation, etc.

Therefore the additional analytical and numerical solution of simplified mathematical model with exact parameters is very useful and enables to completed knowledge of dynamic behaviour of studied system by the new information. Experimental system can be modelled by a simple three masses system shown in Fig. 6.74, where the blades are replaced by 1 DOF systems. For simplicity, the excitation is supposed to be simply harmonic, acting on one blade.

Damping of both blades is in Fig. 6.74 modelled by small viscous damping with coefficients $b_1 = b_2 = 0.1 \text{ N s/m}$. For elimination of gravitational force, the friction

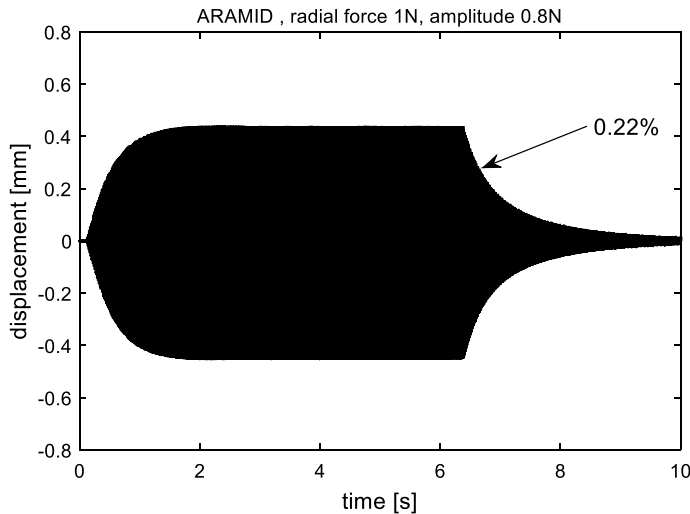


Fig. 6.71 Time characteristic of displacement of the blade A—case II

element $m_3 = 0.01$ kg was hanged on a very weak spring with stiffness $k_3 = 1000$ N/m. Differential equations of motion are then

$$\begin{aligned} m_1 \ddot{y}_1 + b_1 \dot{y}_1 + k_1 y_1 + g_1(y_1 - y_3, \dot{y}_1 - \dot{y}_3) &= F_0 \cos \omega t \\ m_2 \ddot{y}_2 + b_2 \dot{y}_2 + k_2 y_2 + g_2(y_2 - y_3, \dot{y}_2 - \dot{y}_3) &= 0 \\ m_3 \ddot{y}_3 + k_3 y_3 + g_1(y_1 - y_3, \dot{y}_1 - \dot{y}_3) - g_2(y_2 - y_3, \dot{y}_2 - \dot{y}_3) &= 0, \end{aligned} \quad (6.3.7)$$

where the excitation frequency of force $F_0 \cos \omega t$ varies near to the eigenfrequencies of the main subsystems

$$\omega \approx \sqrt{k_1/m_1} = \sqrt{k_2/m_2}.$$

Nonlinear functions g_1, g_2 consist of linear elastic forces modelling the tangential stiffness in the contact surfaces (stick deformation) and nonlinear Coulomb dry friction damping forces (slip motion) and mathematically can be described by expressions (6.2.5–6.2.8) given in Sect. 6.2. Motion of the investigated system is further solved by direct numerical solution of Eq. (6.3.7), with using the Runge-Kutta integration methods.

Damping properties of investigated system can be evaluated from vibration amplitude decay of blades, which are excited into a resonance state, when the forced mode of vibration is very close to the eigenmode and then this excitation is suddenly switched-off. Damping ratios are identified from the logarithmic decrement of the amplitude decay. The qualitative analysis is sometimes sufficient for the information of damping properties with variable amplitudes. Because experiments carried out in

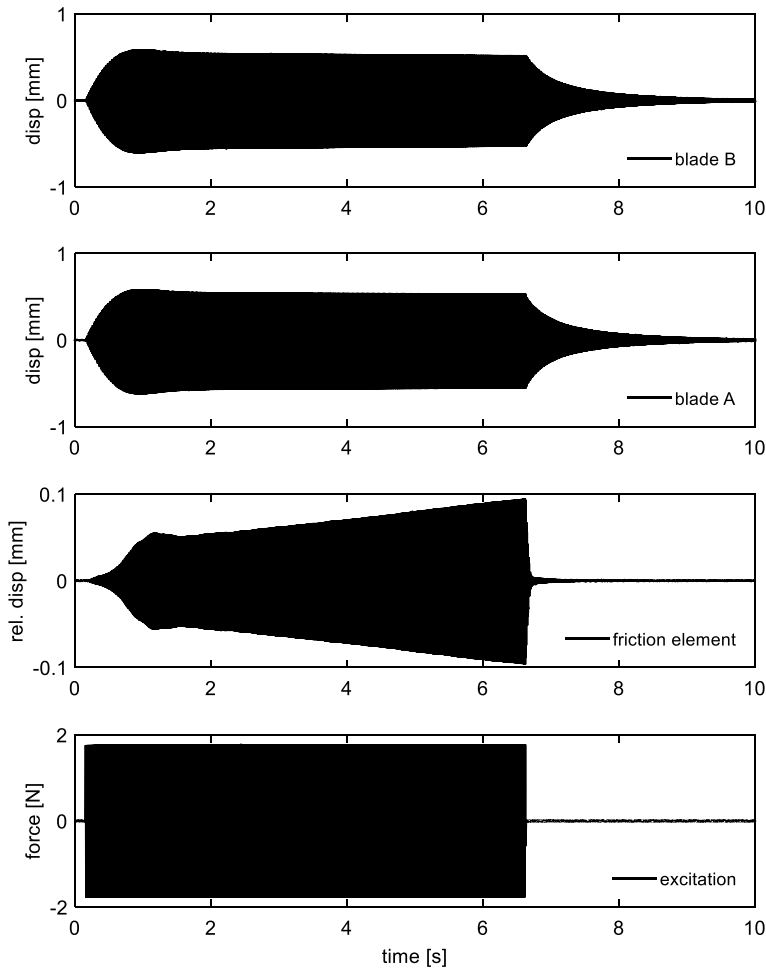


Fig. 6.72 Displacements of the blades B and A, relative displacement of the friction element and electromagnet force—case III

laboratory IT ASCR were oriented also on the application of special composite material ARAMID, having good friction properties, wear and heat resistance, for damping material e.g. in LP steam turbines, the theoretical analysis of this system has been realized as well. Friction elements made of ARAMID are more compliant in comparison with steel, which play important role at small amplitude vibration. Therefore the slip-stick model of friction characteristic has to be used. Friction element mass was $m_3 = 0.01$ kg and its slip-stick characteristic has rheologic parameters: $F_{t0} = 1.25$ N, $k_1 = 30,000$ N/m.

The detail analysis of attenuation processes is better to realize from the records of envelope curves, where all three dependences can be clearly seen. The quick first part

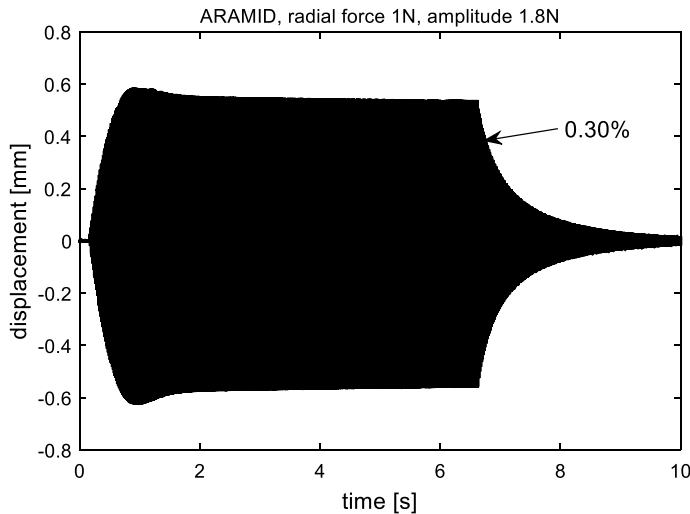
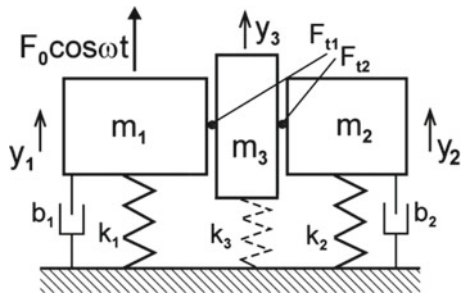


Fig. 6.73 Time characteristic of displacement of the blade A—case III

Fig. 6.74 Mathematical 3DOF model



of decay corresponds to the high damping caused by the energy loss at dry friction slip, the envelope break indicates the end of slip period and beginning of stick period, when no friction losses exist and only losses of deformation energy in blades and element material influence the decay. The influence of individual parameters of stick-slip characteristic (spring stiffness k_1 , dry friction force F_t) on the entire process can be investigated.

Influence of the magnitude of dry friction force F_t at constant value of spring stiffness $k_1 = 50,000$ N/m is seen from comparison of Figs. 6.75, 6.76 and 6.77.

The amplitude a_1 of the excited mass m_1 during the excitation period (Time 0–2 s) decreases very weakly at decreasing of friction force $F_t = 1.5, 1, 0.5$ N, as seen from the highest full curves. However, amplitude a_2 of the non-excited mass m_2 (dashed curve) during the excitation period decreases proportional to the friction force. Differences between both these curves increase. Motion of the inserted friction element copy approximately motion of mass m_2 , but its motion is mildly distorted by a random signal.

Fig. 6.75 Blade responses at $k_1 = 50,000 \text{ N/m}$; $F_t = 1.5 \text{ N}$

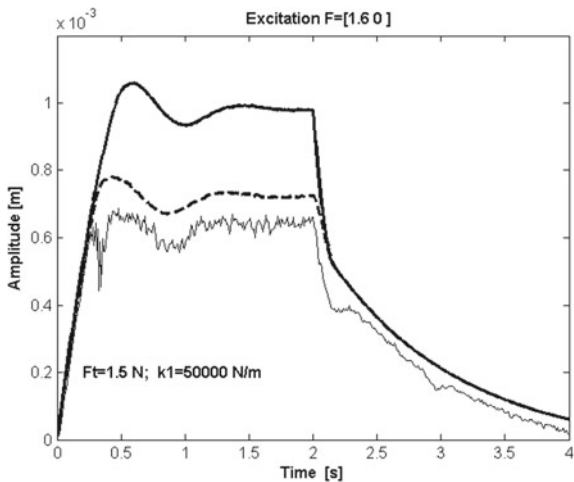
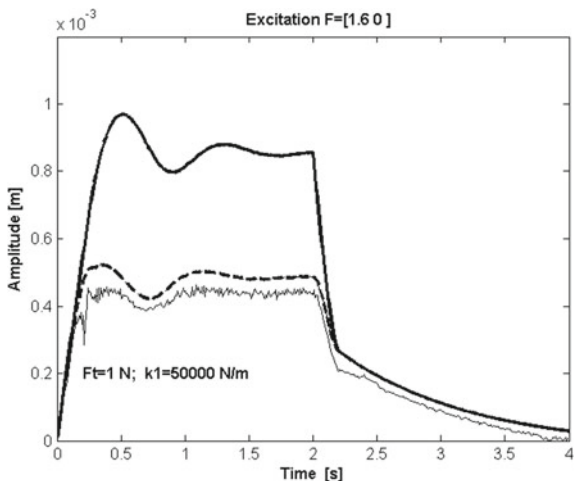


Fig. 6.76 Blade responses at $k_1 = 50,000 \text{ N/m}$; $F_t = 1 \text{ N}$



Sudden jumps of all amplitudes occur after switch-off of excitation force (period 2–4 s). The height of jumps of the amplitude a_1 slightly increases with friction force decrease; jumps of the amplitude a_2 have roughly the same height. After the jump, the all three masses join together and the mild decrease follow. Amplitudes of this attenuation process are high at high friction force and decrease more than proportional with the decreasing friction force.

Similar analysis can be done also about the influence of stick stiffness k_1 . The decrease of stick stiffness $k_1 = 50,000 \text{ N/m}$ (grey lines in Fig. 6.78) on the tenth value $k_1 = 5000 \text{ N/m}$ (black lines) at friction force $F_t = 1.5 \text{ N}$ causes comparatively small shifts of blades amplitudes a_1, a_2 , but the motion of friction elements is more sensitive on the lowering of contact stiffness.

Fig. 6.77 Blade responses at $k_1 = 50,000 \text{ N/m}$; $F_t = 0.5 \text{ N}$

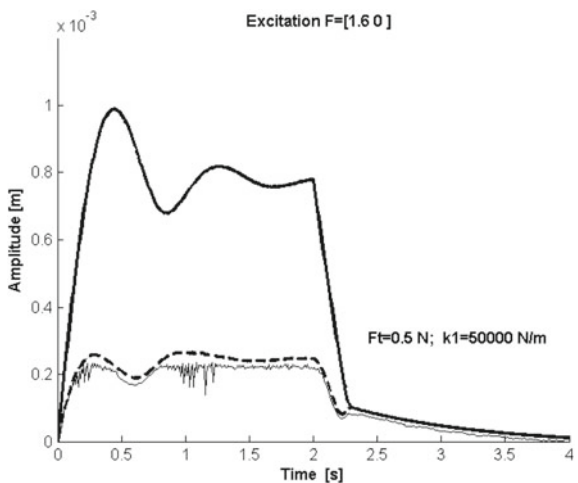
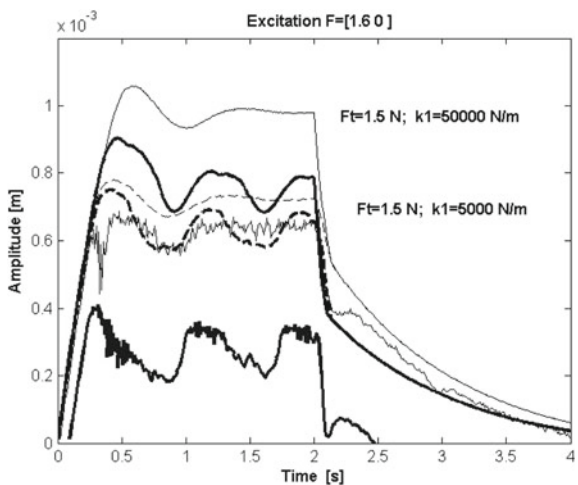


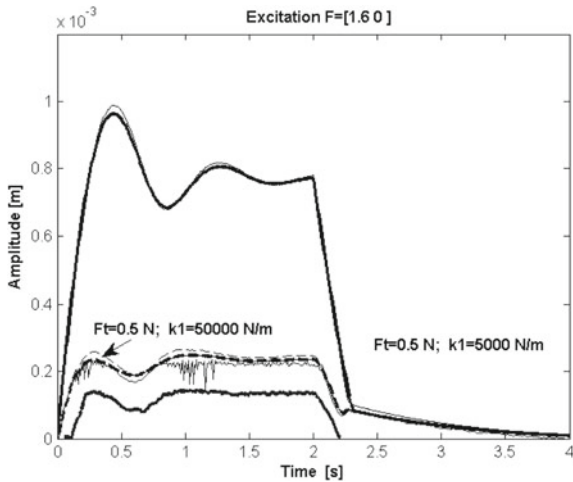
Fig. 6.78 Blade responses at $k_1 = 5000 \text{ N/m}$ (bold), $k_1 = 50,000 \text{ N/m}$ (thin); $F_t = 1.5 \text{ N}$



The blade bundle properties presented in Fig. 6.78 can be generalized only with the great caution, as the investigated system containing two strongly nonlinear connections is for the prediction of exact dynamic behavior dangerous case. An example of such properties is given in the Fig. 6.79, where the same jump in contact stiffness $k_1 = 50,000 \text{ N/m}$ on tenth value $k_1 = 5000 \text{ N/m}$ at the small friction force $F_t = 0.5 \text{ N}$ has practically no influence on the courses of envelopes of both blades amplitudes. The only changes are seen in the dry friction element motion.

By means of several examples it has been shown that the serial combination of Coulomb friction and spring stiffness (stick-slip model) can be successfully applied for computational modeling of vibration amplitude decay processes that are used for evaluation of damping properties experimentally investigated dynamic systems.

Fig. 6.79 Responses at $k_1 = 5000 \text{ N/m}$ (bold), $k_1 = 50,000 \text{ N/m}$ (thin); at $F_t = 0.5 \text{ N}$



The comparison of time histories gained experimentally with the numerical solution enables to ascertain the friction and contact stiffness characteristics. As to the damping effect, it can be concluded similarly to the case of three blades bundle that the higher damping appears when the slips appear in the contacts. When the displacements of the blades decrease, the slips transit into the stick phase and the magnitude of damping decreases rapidly.

6.3.2.3 Numerical Simulations of Nonlinear Dynamic Behavior on Beam Models

The usage of simplified (reduced) mathematical models described in previous sections can be advantageous in case of basic problems concerning the structural complexity and complexity of excitation. The more complex model (Fig. 6.75) utilizable for more structurally complex cases will be shown in this section. More-over, the complex blade couple model will be derived considering all effects of a disk rotation for sake of later usage in the general problems of bladed disk dynamics. The review of various modelling methodologies for rotating blade dynamics can be found, e.g. in [21].

As a simplification, the contacts of the friction element and the blade shrouds (Fig. 6.80) are concentrated to the rectangular effective area with geometric center in point B (in plane b defined by axes $\varepsilon_B \eta_B$), and to the rectangular effective area with geometric center in point A (in plane a defined by axes $\varepsilon_A \eta_A$), respectively. The blades are modelled as 1D continuum discretized by beam finite elements with uniformly distributed nodes at axes of the blades. The first nodes of the blades are fixed to the rigid frame rotating with angular velocity ω . End nodes C_1 and C_2 of the blades are fixed to the blade shrouds modelled as rigid bodies because the shrouds are

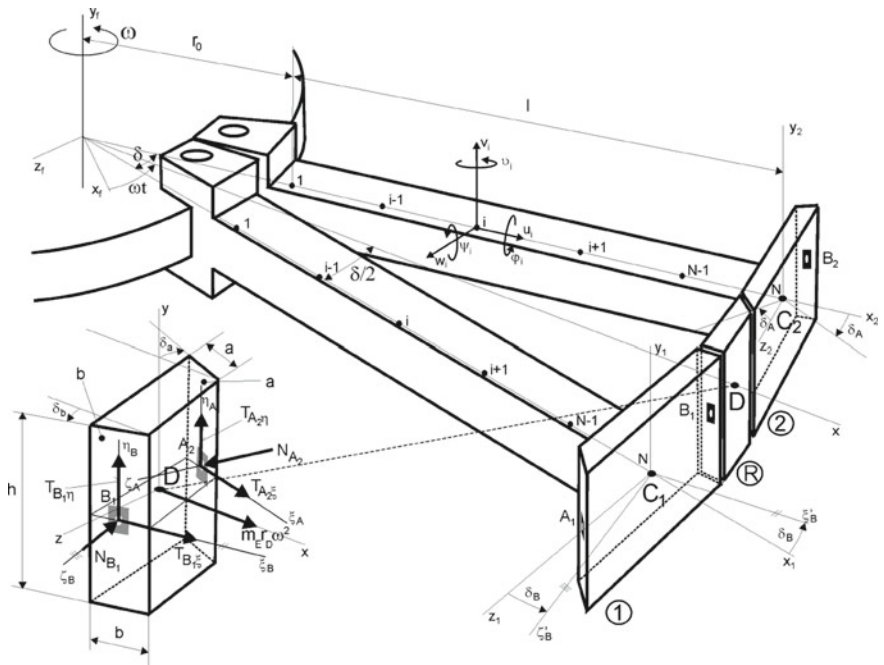


Fig. 6.80 Scheme of the couple of blades with the friction element and its detail

obviously stiffer than the blades. The spatial motion of all blade nodes as well as the friction element is characterized by six degrees of freedom. As the blades rotate, the centrifugal force $m_E r_D \omega^2$ pushes the friction element towards contact surfaces a and b of the adjacent blade shroud. In case of numerical simulation of the experimental measurement, the centrifugal force will be substituted by the proper constant force.

The friction element acts on the blades by contact normal forces N_X and contact torques $M_{\xi X}$, $M_{\eta X}$, $X = A, B$ and by friction forces $\vec{T}_X(T_{X\xi}, T_{X\eta})$ and friction torques $M_{\zeta X}$, $X = A, B$ in contact surfaces.

The real excitation in turbines can be defined as harmonic forces with the nozzle passing frequency (i.e. the first engine order times number of nozzles) acting in tangential (F_t) and axial (F_{ax} parallel to axis of rotation) direction. Excitation forces can be uniformly concentrated in nodes along the blades. The choice of excitation type is general, and it does not influence the modelling approach. However, the excitation forces in this paper will be limited to the single force in y -direction in order to simulate the same conditions as in the experimental set-up.

Equations of motion of the blades with the shroud and the friction element can be expressed in rotating local coordinate systems x_j, y_j, z_j , $j = 1, 2$ (the blades) and x_D, y_D, z_D (the friction element), where axes x_j are the axes of the blades, and axis x_D corresponds to the radial direction from the disk center to the friction element.

Axes y_j, y_D are parallel to the fixed axis of disk rotation y_f (see Fig. 6.80). The vectors of nodal blade generalized coordinates

$$\mathbf{q}_j = [\dots u_i, v_i, w_i, \varphi_i, \vartheta_i, \psi_i, \dots]_j^T, \quad j = 1, 2 \quad (6.3.8)$$

are expressed by translational displacements and rotational displacement in nodes $i = 1, \dots, N$ of the blade j . The equations of motions of two blades with shroud and without shroud the friction element are of the form

$$\mathbf{M}_B \ddot{\mathbf{q}}_j + (\omega \mathbf{G}_B + \mathbf{B}_B) \dot{\mathbf{q}}_j + (\mathbf{K}_{s,B} - \omega^2 \mathbf{K}_{d,B} + \omega^2 \mathbf{K}_{\omega,B}) \mathbf{q}_j = \mathbf{f}_{\omega,B} + \mathbf{f}_{Bj}(t), \quad (6.3.9)$$

where symmetric matrices of order $6N$ $\mathbf{M}_B, \mathbf{B}_B, \mathbf{K}_{s,B}, \mathbf{K}_{d,B}, \mathbf{K}_{\omega,B}$ are mass, material damping, static stiffness, softening under rotation and bending stiffening under rotation, respectively. The symmetrical matrix $\omega \mathbf{G}_B$ considers gyroscopic effects. Constant centrifugal forces are expressed by vector $\mathbf{f}_{\omega,B}$ and general time-dependent forces are expressed by vector $\mathbf{f}_{Bj}(t)$.

The spatial motion of the rigid friction element is described in rotating coordinate system x_D, y_D, z_D by generalized coordinates $\mathbf{q}_E = [u, v, w, \varphi, \vartheta, \psi]^T$ and the equations of motion of still isolated rigid friction element can be written in matrix form analogous to the blade model

$$\mathbf{M}_E \ddot{\mathbf{q}}_E + \omega \mathbf{G}_E \dot{\mathbf{q}}_E - \omega^2 \mathbf{K}_{d,E} \mathbf{q}_E = \mathbf{f}_{\omega,E}. \quad (6.3.10)$$

After placing the friction element in between the blade shroud, acting of contact elastic and friction forces is concentrated into contact points A and B .

Using configuration space of generalized coordinates defined by vector

$$\mathbf{q} = [\mathbf{q}_1^T, \mathbf{q}_E^T, \mathbf{q}_2^T]^T, \quad (6.3.11)$$

equation of motion of the whole system is written in the form

$$\mathbf{M} \ddot{\mathbf{q}} + (\omega \mathbf{G} + \mathbf{B} + \mathbf{B}_C) \dot{\mathbf{q}} + (\mathbf{K}_s - \omega^2 \mathbf{K}_d + \omega^2 \mathbf{K}_\omega + \mathbf{K}_C) \mathbf{q} = \mathbf{h}(\dot{\mathbf{q}}, \mathbf{q}) + \mathbf{f}(t). \quad (6.3.12)$$

In accordance with the equations of motion (6.3.10) and (6.3.12), the matrices stated below have block-diagonal structure

$$\begin{aligned} \mathbf{M} &= \text{diag}(\mathbf{M}_B, \mathbf{M}_E, \mathbf{M}_B), \\ \mathbf{G} &= \text{diag}(\mathbf{G}_B, \mathbf{G}_E, \mathbf{G}_B), \\ \mathbf{B} &= \text{diag}(\mathbf{B}_B, \mathbf{0}, \mathbf{B}_B), \\ \mathbf{K}_s &= \text{diag}(\mathbf{K}_{s,B}, \mathbf{0}, \mathbf{K}_{s,B}), \\ \mathbf{K}_d &= \text{diag}(\mathbf{K}_{d,B}, \mathbf{K}_{d,E}, \mathbf{K}_{d,B}), \\ \mathbf{K}_\omega &= \text{diag}(\mathbf{K}_{\omega,B}, \mathbf{0}, \mathbf{K}_{\omega,B}). \end{aligned} \quad (6.3.13)$$

The influence of contact viscous-elastic and friction forces in (6.3.12) is represented by stiffness coupling matrix \mathbf{K}_C and damping matrix \mathbf{B}_C comprising the influence of contact damping in contact surfaces and by vector $\mathbf{h}(\dot{\mathbf{q}}, \mathbf{q})$ which expresses nonlinear friction forces in friction couplings between the shroud of blade 1 and 2 and the friction element, respectively. Vector $\mathbf{h}(\dot{\mathbf{q}}, \mathbf{q})$ of nonlinear friction forces and torques can be expressed as

$$\mathbf{h}(\dot{\mathbf{q}}, \mathbf{q}) = \begin{bmatrix} \mathbf{0} \\ \vdots \\ \mathbf{0} \\ \mathbf{f}_1 \\ \mathbf{m}_1^F + \mathbf{m}_1 \\ \mathbf{f}_a + \mathbf{f}_b \\ \mathbf{m}_a^F + \mathbf{m}_b^F + \mathbf{m}_b + \mathbf{m}_a \\ \mathbf{0} \\ \vdots \\ \mathbf{0} \\ \mathbf{f}_2 \\ \mathbf{m}_2^F + \mathbf{m}_2 \end{bmatrix} \quad (6.3.14)$$

where nonzero forces and torque vectors are on the positions corresponding to the generalized coordinates of the blade shrouds and to the generalized coordinates of the friction element. For example, vector

$$\mathbf{f}_1 = [-T_{B\xi} \sin \delta_B, -T_{B\eta}, T_{B\xi} \cos \delta_B]^T \quad (6.3.15)$$

and vector \mathbf{m}_1^F express the effects of friction forces between the friction element and the shrouds on motion of the shroud of the first blade (see Fig. 6.80). Vector \mathbf{m}_1 expresses the effect of friction torque in case of relative rotation of two surfaces in contact. It is analogous for other vectors.

The contact stiffness matrix \mathbf{K}_C can be linearized for constant normal forces $N_{X,0}$ ($X = A, B$). These forces are calculated from static equilibrium condition of friction element

$$N_{X,0} = F_r \frac{\cos \delta_X}{\sin(\delta_a + \delta_b)}, \quad X = A, B, \quad (6.3.16)$$

where $F_r = m_E r_E \omega^2$ in case of rotation or F_r can be chosen according to the experimental set-up. Angles of contact surfaces skewing between blade and shroud and friction element are displayed in Fig. 6.80. The contact stiffness matrix \mathbf{K}_C connecting the blades with friction element can be calculated based on the coupling (deformation) energy

$$E_C = \frac{1}{2} \sum_{\substack{X=A,B \\ i=1,2}} \mathbf{d}_{X,C_i}^T \mathbf{K}_X \mathbf{d}_{X,C_i}, \quad (6.3.17)$$

$$\mathbf{d}_{X,C_i} = \mathbf{T}_{X,C_i} \mathbf{q}_{C_i} - \mathbf{T}_{X,E} \mathbf{q}_E, \quad (6.3.18)$$

where \mathbf{q}_{C_i} , $i = 1, 2$ are vectors of generalized displacements in the last nodes C_i of blades, and \mathbf{q}_E is the vector of friction element displacement. Matrices \mathbf{T}_{X,C_i} and $\mathbf{T}_{X,E}$ transform the vectors of displacement of contact points A, B on corresponding body in coordinate system ξ_X, η_X, ζ_X . Diagonal local contact stiffness matrix

$$\mathbf{K}_X = \text{diag}(0 \ 0 \ k_{\zeta_X} \ k_{\xi_X \xi_X} \ k_{\eta_X \eta_X} \ 0), \quad X = A, B \quad (6.3.19)$$

in coordinate system $\xi_X, \eta_X, \zeta_X (X = A, B)$ is defined by contact stiffness k_{ζ_X} in normal direction ζ_X to contact area and two rotational (flexural) stiffnesses $k_{\xi_X \xi_X}$, $k_{\eta_X \eta_X}$ with respect to axes ξ_X and η_X .

The contact normal stiffnesses can be linearized for contact normal forces (6.3.16) according to

$$k_{\xi_X} = \frac{N_{X,0}}{\gamma_X}, \quad \gamma_X = c\sigma_X^p, \quad \sigma_X = \frac{N_{X,0}}{A_{ef,X}}, \quad X = A, B, \quad (6.3.20)$$

where γ_X designates contact normal deformation, σ_X average contact pressure acting on effective area $A_{ef,X}$. Contact deformation coefficient c and contact exponent p were estimated using data published in [51]. The rotational stiffnesses were calculated based on the assumption of identical area contact stiffness $k_{\xi_X}/A_{ef,X}$ in arbitrary point of effective contact area.

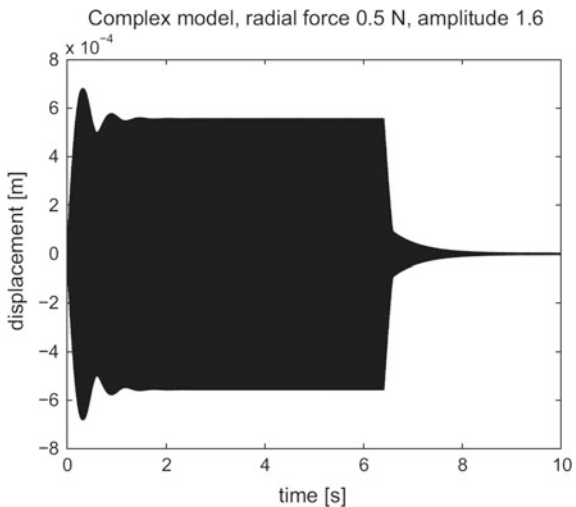
Contact stiffness matrix \mathbf{K}_C was derived using identity

$$\frac{\partial E_C}{\partial \mathbf{q}} = \mathbf{K}_C \mathbf{q} \quad (6.3.21)$$

and contact damping matrix \mathbf{B}_C was considered to be proportional $\mathbf{B}_C = \beta \mathbf{K}_C$. Model (6.3.12) can be solved by various mathematical methods with respect to the character of expected results. The most direct one is a numerical integration of nonlinear equations of motion, which will be used in the next. The resulting variables are obtained for particular case in the form of time series, while all types of nonlinearities including complex excitation can be considered. Nevertheless, other valuable results can be obtained from an analysis based on more qualitative comparisons, which is, e.g. eigenvalue analysis or steady state harmonic analysis, etc.

The above introduced mathematical model of the blade couple with friction element was implemented in MATLAB system. The values of model parameters were set in accordance with the experimental set-up (see Sect. 6.3.2.1). Material damping of the blades was considered 0.2% for all eigenmodes in all simulated cases—the results are shown for three typical combinations (I–III) of the radial force F_r and excitation amplitude F_a . Case I: $F_r = 0.5$ N, $F_a = 1.6$ N, case II:

Fig. 6.81 Displacement of the blade A calculated using the numerical model (case I)



$F_r = 1\text{ N}$, $F_a = 0.8\text{ N}$ and case III: $F_r = 1\text{ N}$, $F_a = 1.8\text{ N}$. The particular values of the friction model parameters were estimated on the basis of previous experimental results ($f_s = 0.6$, $f_d = 0.3$, $d = 2$, $c_k = 10^{-3}\text{ ms}^{-1}$).

The displacements of the blade A calculated the model are shown in Figs. 6.81, 6.82, 6.83. The summary of evaluated damping ratios for all cases is compared in Table 6.4. The damping ratios for both experimental and numerical results were calculated from the particular parts of time history by means of an amplitude logarithmic decrement by Hilbert's transform. The course of time histories in case I compared to case II and III is characterized by macroslip movements in the first stage of the vibration attenuation and by microslip movements in the second stage of the attenuation. It was an expected result since the amplitude value of the harmonic excitation force was relatively high, and the radial force value was lower comparing to other cases. Thus, the adhesion forces in the contact were exceeded, and the macroslip movements were induced.

The computed displacement amplitudes are about twice higher compared to the experiment, see Sect. 6.3.2.1. It is caused by the slight different eigenfrequencies of the real mechanical system and the numerical model of the system. The first bending frequency was calculated by the numerical model, and this value was used for the definition of the excitation frequency. If the same excitation frequency is used for the loading of the real mechanical system with slightly different bending eigenfrequency, the response will not be the same, i.e. the exact resonance is not achieved. The difference in the computed and measured amplitudes can be also caused by the fact that the excitation force has an ideal harmonic character in case of calculation but this is not true for the real force generated by the electromagnet. Therefore, the larger resonance is obtained during the numerical simulation than during the experiment.

Fig. 6.82 Displacement of the blade A calculated using the numerical model (case II)

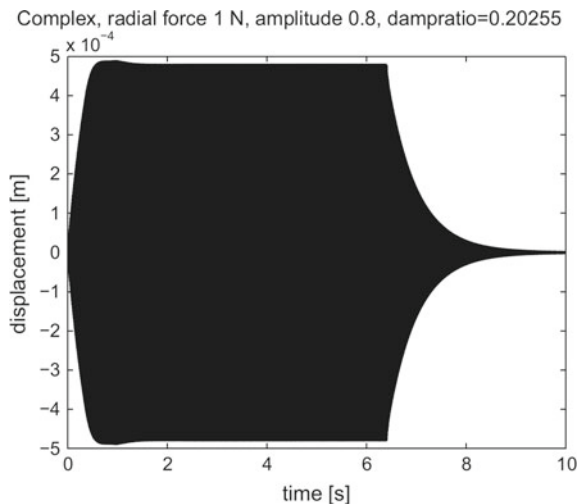


Fig. 6.83 Displacement of the blade A calculated using the numerical model (case III)

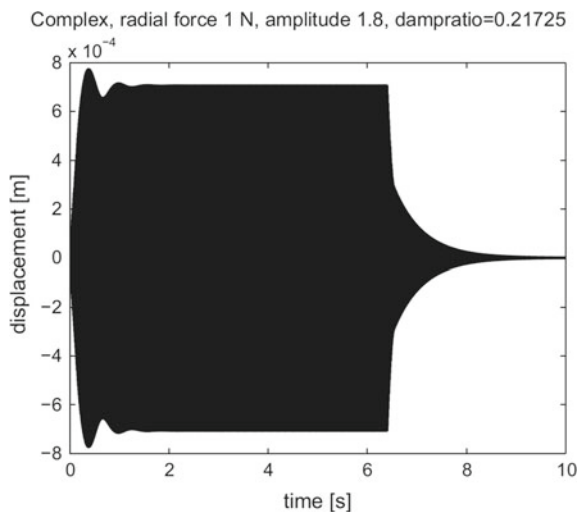


Table 6.4 Evaluated damping ratios (%) for the experiment and numerical model

	Case I	Case II	Case III
Experiment	1.120/0.160	0.220	0.300
Numerical model	1.019/0.224	0.203	0.217

The course of the time history in case II (Fig. 6.82) is characterized by microslip movements in the whole attenuation region. It is caused by the small amplitude value of the electromagnet excitation force with respect to the radial extruding force. It should be noted that the situation is the same as in a real turbine in case of a low dynamic excitation of blades, which are locked for higher angular velocities (i.e. higher centrifugal forces acting on the friction element). The positive effect of the friction element placed in shrouding should occur in case of higher undesirable excitation (and successive higher vibration amplitudes of blades).

The accordance of the results obtained for case III (Fig. 6.83) is not so good as in the two previous cases. The measured course of the displacement time history for the blade A (see Sect. 6.3.2.1) does not show a substantial transition between macroslip and microslip movements. It is rather characterized by certain average switching between these two types of movements. On the other hand, the comparable numerical results show the standard macroslip movements in the first stage of the vibration attenuation and the microslip movements in the second stage of the attenuation (the damping ratios written in Table 6.4 are identified for the second stage). The inconsistency of the measured and calculated results in this limit case could be explained by insufficient friction model parameters, which are not suitable for the particular combination of the radial and transverse excitation forces.

6.4 Bladed Wheel with Friction Contact in Tie-Boss Couplings

In this section we deal with the bladed wheel model with tie-boss couplings that was designed for research of friction contact effect on dynamics of the wheels. Therefore both physical and numerical models of the wheel with tie-boss couplings were built. In the first part of the section the designed model and experimental set-up for its testing are described. Then its numerical and experimental modal analysis is presented. In the last part both discrete analytical and reduced numerical models are described and the results of calculations for several dynamic excitations are discussed.

6.4.1 Physical Model Description

The testing disk is equipped with thirty prismatic blades. Picture of a design of bladed wheels with so-called “tie-boss” couplings and additional weights is shown in Fig. 6.84. The tie-bosses are shoulders of blades whose ends are in a contact with shoulders of the neighboring blades. The ends of the shoulders are cut so that its areas, i.e. contact areas, are parallel to a direction of the flexural vibration of a single blade.

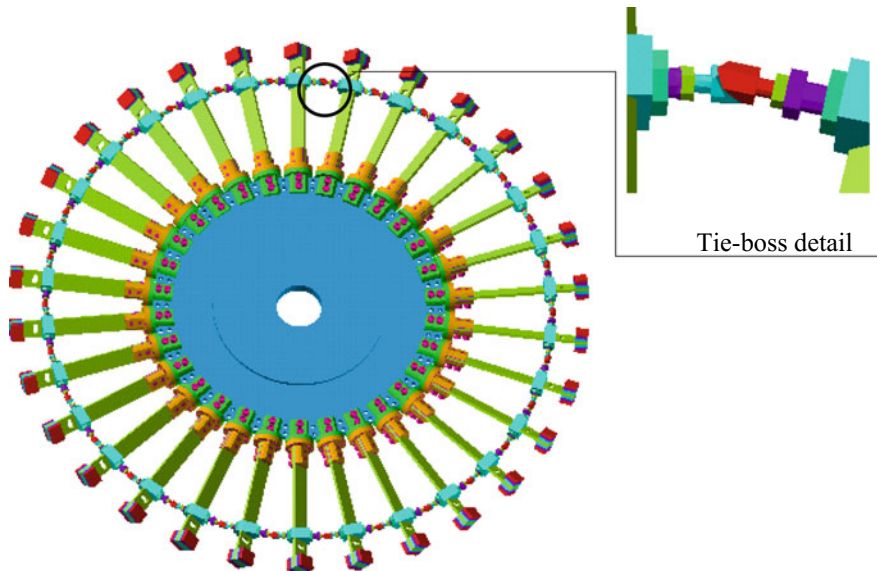


Fig. 6.84 Bladed wheel model with inter-blade tie-boss couplings

Because of setting up the pre-stress in the contacts between the tie-bosses of the neighboring blades, the tie-bosses consist of extensible shoulders screwed with left (right side) and right (left side shoulder) winding into the suspension bolt that was fixed to the blade by two nuts. By screwing the bolt in the nuts the shoulders extend simultaneously on both sides. The detail of the tie-boss structure is in Fig. 6.84, too. Each blade is fixed to the disk by the system of two small finger consoles. Bottom console is bolted down to the disk and upper console is bolted to the blade. The consoles are bolted together and their mutual position is set by angle 45° before their bolting together. At the end of the blades an additional mass is bolted to lower its first flexural eigen-frequency. Experimental set-up of rotary test rig of the designed bladed wheel with denotation of the particular components is in the Fig. 6.85.

6.4.2 Modal Analysis of Full Bladed Disk

Modal analysis of the numerical bladed disk were computed for two contact limit states, i.e. (I) bonded contacts (i.e. contact surfaces stuck together) and (II) open contacts (i.e. no coupling between contact surfaces) between tie-bosses. The dependences of the eigen-frequencies of flexural eigen-modes on number of nodal diameters (ND) are depicted for both contact cases in Fig. 6.88 as so-called SAFE diagram. The open contact model approximates the “eigen-frequency” of the wheel at large relative displacements (slips) in contacts. The eigen-frequencies of the open contact

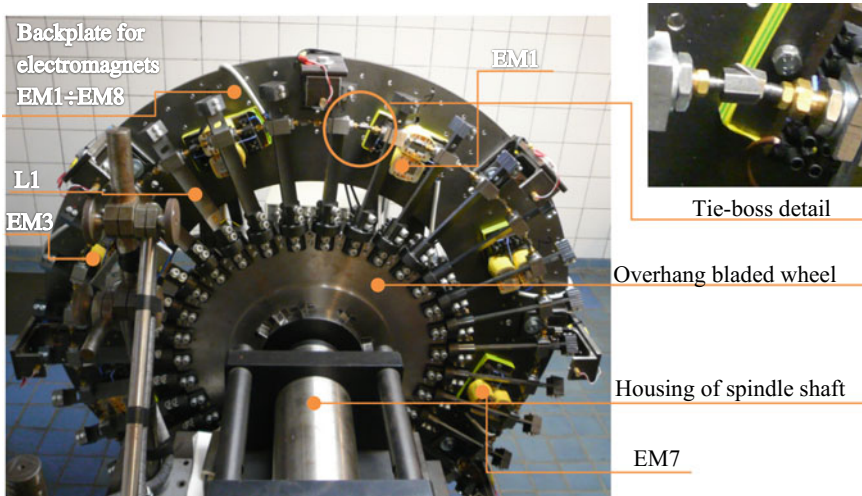


Fig. 6.85 Experimental set-up of the bladed wheel and test rig

model monotonously increase with a number of ND and its value converges to a limit 50.3 Hz that is defined by the first flexural mode of a clamped blade. The highest possible number of ND for 30 blades is 15. At this case the inter-blade angle reaches 180°. The model with bonded contacts served for mapping of modal behavior of the wheel under high pre-stress in contacts and low amplitudes of excitation when only a stick state with microslips in contacts appears. For this case it can be seen large stiffening effect at modes with a higher number of ND.

To attune the numerical model of the bladed wheel to the experiment an experimental modal analysis (Table 6.5) was performed both for (A) open contacts and (B) pre-stress contact states between tie-bosses. As it can be seen, the couples of very close eigenfrequencies for each eigenmode with nonzero ND modal analysis appear in the Table 6.5. It corresponds to the split double eigenfrequencies of the eigenmodes of the rotational bodies with lightly disturbed symmetry.

The pre-stresses in contacts between the tie-bosses were set manually by extending a length of their arms. The values of the pre-stresses were evaluated indirectly after releasing the pre-stresses by the magnetic torque sensor Active-3 Lite that enabled to register the torque moment of each blade. The normal forces in the contacts were ascertained from the torque moments. Normal forces were relatively high, i.e. about 50 N with a slight variation along the circumference. Excitation of the bladed wheel was electromagnetic. The electromagnet placed against the top of the blade L1 (see Fig. 6.85) was excited by the high power pulse in case A and by harmonic frequency sweep function in case B.

The wheel model with open contacts (A) was tuned to the experimental results of modal analysis. The results (Fig. 6.86) of both numerical and experimental modal analysis show good agreement. Furthermore, the results of the numerical analysis

Table 6.5 Results of modal analysis of the bladed wheel for cases: (A) open contacts (FEM, experiment) and (B) bonded contacts (FEM) and (C) pre-stress states (experiment) between tie-bosses

ND	Open contacts FEM	Open contacts EXP		Bonded contacts FEM	Contact prestress EXP	
		freq. (Hz)	freq. (Hz)		freq. (Hz)	freq. (Hz)
0	43.32	—	—	57.17	—	—
1	43.37	37.34	0.32	60.24	43.66	1.29
1	43.47	37.71	0.28	60.35	46.85	1.73
2	44.32	43.51	0.15	65.88	62.51	0.51
2	44.39	—	—	65.99	66.92	0.85
3	46.14	45.43	0.18	79.36	78.58	1.04
3	46.20	45.65	0.12	79.44	80.63	0.24
4	47.37	46.59	0.08	94.48	94.98	1.57
4	47.42	—	—	94.53	98.56	0.28
5	48.10	47.08	0.06	109.65	109.11	0.50
5	48.22	47.67	0.08	109.74	116.38	0.21

with bonded couplings between tie-bosses (C) and of the experimental analysis of the wheel with pre-stresses between tie-bosses (B) are depicted in the Fig. 6.86, too. The figure clearly shows that the eigen-frequencies of case B are placed between the eigen-frequencies of two contact limit cases A and C. The position of each eigen-frequency within the limit eigen-frequencies are given by the level of pre-stress and level of excitation that define rate of stick state with microslips and slips during the vibration. Since the open contact model approximates the blade “eigen-frequency” at slips it means the closer is the pre-stressed state to the open contact model eigen-frequency the higher relative displacements are excited. Since the experimental eigen-frequencies are close to bonded contacts it shows that the pre-stresses in contacts were relatively high with respect to a force excitation capacity and stick state with microslips aroused only in contacts. The differences of 1ND mode measured eigen-frequencies from the numerical counterparts are caused by differences in boundary conditions (bearing of the wheel hub) of physical and numerical model. The influence of the bearing diminishes for higher number of ND.

6.4.3 Discrete Analytical Model

(a) Model Description

Discrete analytical model of bladed wheel with 30 blades (Fig. 6.87) was created analogically as blade triple model described in 6.87a). Each blade is represented by one DOF. In addition the blades model is extended by a disc that is divided to

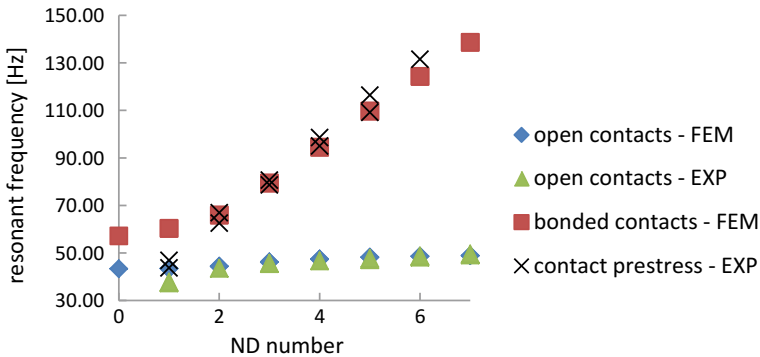
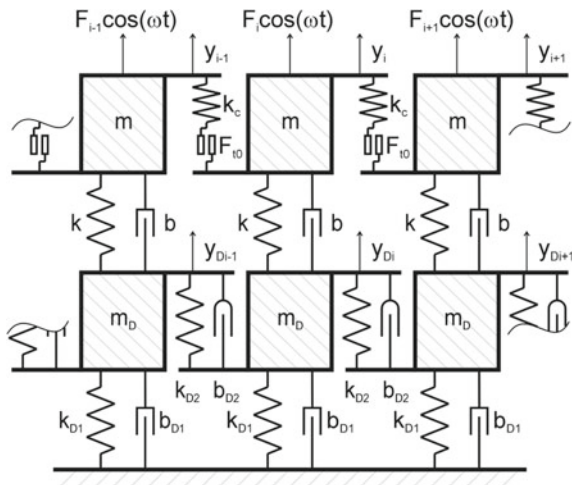


Fig. 6.86 Eigen-frequencies versus number of nodal diameters for the wheel with (I) bonded and (II) open contacts—FEM model tuned to the experiment

Fig. 6.87 Schematic picture of bladed wheel model with disc



masses m_D associated with each blade. Masses m_D are connected to the main frame with springs with stiffness k_{D1} and viscous dampers with damping coefficient b_{D1} . Between masses m_D there are springs with stiffness k_{D2} and viscous dampers with damping coefficient b_{D2} . Hence, the model has 60 DOFs with two DOFs per each blade segment.

Bladed wheel model is described by equations of motion:

$$\begin{aligned}
 & m \cdot \ddot{y}_i + b \cdot (\dot{y}_i - \dot{y}_{Di}) + k \cdot (y_i - y_{Di}) + F_{i-1,i}(y_i - y_{i-1}, \dot{y}_i - \dot{y}_{i-1}) \\
 & - F_{i+1,i}(y_i - y_{i+1}, \dot{y}_i - \dot{y}_{i+1}) + G_i = F_i \cos(\omega t), \\
 & m_D \cdot \ddot{y}_{Di} + b_{D1} \cdot \dot{y}_{Di} + b_{D2} \cdot (2 \cdot \dot{y}_{Di} - \dot{y}_{Di-1} - \dot{y}_{Di+1}) + b \cdot (\dot{y}_{Di} - \dot{y}_i) \\
 & + k_{D1} \cdot y_{Di} + k_{D2} \cdot (2 \cdot y_{Di} - y_{Di-1} - y_{Di+1}) + \dots
 \end{aligned}$$

Table 6.6 Parameters of the detached disc

Parameter	Value	Unit
m_D	0.7	kg
k_{D1}	$1.77 \cdot 10^5$	Nm ⁻¹
k_{D2}	$4.275 \cdot 10^6$	Nm ⁻¹
b_{D1}	0.44	N s/m
b_{D2}	0.44	N s/m ¹

Table 6.7 Disc eigenfrequencies of FEM and SIMULINK models

ND	FEM model	Simulink model
0	177.65	93.19
1	172.02	124.28
2	188.23	188.23
3	251.08	260.33
4	333.20	333.25

$$+ k \cdot (y_{Di} - y_i) = 0, \quad \text{where } i = 1, 2, \dots, 30, \quad (6.4.1)$$

which can be rewritten into a matrix form as

$$\mathbf{M}\ddot{\mathbf{y}} + \mathbf{B}\dot{\mathbf{y}} + \mathbf{K}\mathbf{y} + \mathbf{F}_c(\mathbf{y}, \dot{\mathbf{y}}) = \mathbf{F} \cos(\omega t), \\ \text{where } \mathbf{y}^T = [\mathbf{y}^T, \dot{\mathbf{y}}^T]. \quad (6.4.2)$$

The first equation (6.4.1) describes motion of 30 blades with nonlinear terms for contact force. The second equation describes the disc consisting of 30 parts. Furthermore, the term G_i appears in the Eq. 6.4.1 that expresses an aerodynamic force acting on blade i and is described in the last section of this chapter.

Numerical model of the discrete bladed wheel with friction contacts was built in the same way as in case of three blades bundle (Sect. 3.1.2), i.e. by Simulink block scheme with the stick-slip model (Fig. 6.28). Parameters of the blades and friction contact were used according to Table 6.1. Disc parameters (Table 6.6) were obtained by tuning eigenfrequencies of eigenmodes with 2ND and 4 ND of the detached disk to the 3D FEM model.

Comparison of eigenfrequencies of the detached disc (free without blades) obtained from Simulink model and FEM model are shown in Table 6.7 where the eigenfrequencies (ND = 2, 4) used for a model matching are highlighted. Eigenfrequencies of both models with 0 and 1 ND do not match because these modes are differently sensitive to boundary conditions of the disk clamping.

Eigenfrequencies f_{ND} of the whole bladed wheel both for open and bonded contacts in tie-bosses are in Table 6.8 and Fig. 6.88. As seen from differences of eigenfrequencies of eigenmodes with higher number of ND ($ND > 3$), bonded contacts have stiffening effect on the dynamics of the wheel.

Table 6.8 Eigenfrequencies f_{ND} of bladed wheel with open and bonded contacts

ND	Open contacts	Bonded contacts
0	41.06	41.06
1	45.54	45.72
2	48.25	48.95
3	49.12	50.64
4	49.47	52.06

Fig. 6.88 Dependences of eigenfrequencies on number of ND of the analytical bladed wheel with **a** open and **b** bonded contacts

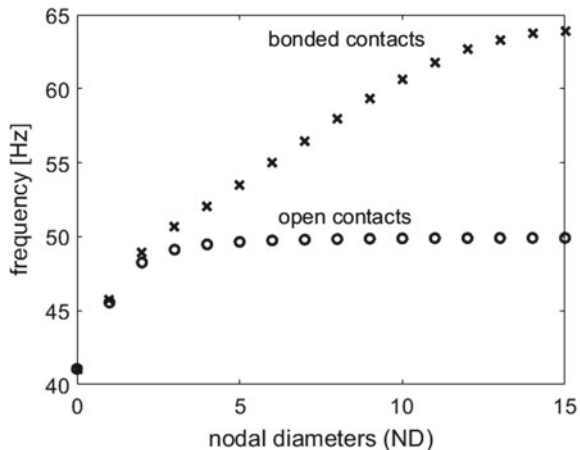
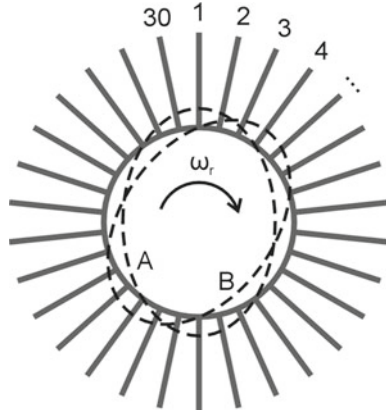


Fig. 6.89 Scheme of bladed wheel with 30 blades and 2ND vibration modes A and B (dashed lines)

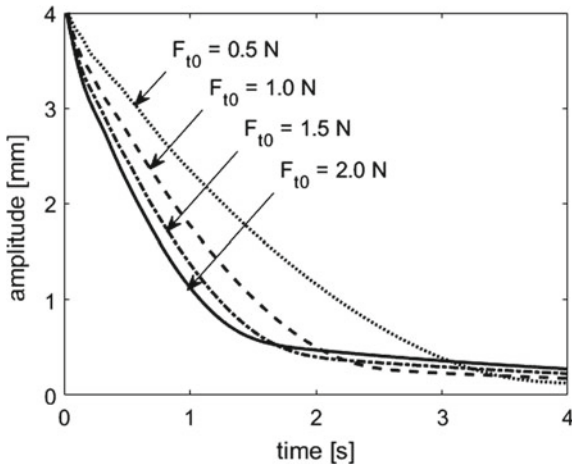


From the numerical modal analysis we get couples of very close eigenfrequencies for each eigenmode with nonzero ND. It corresponds to the theoretical assumption of multiple (double) eigenfrequencies of the eigenmodes of the rotational symmetric wheel. By splitting of multiple eigenfrequencies we get two orthogonal eigenmodes. The locations of the calculated 2 ND eigenmodes A, B with respect to numbering of the blades and positive direction of revolution are depicted in Fig. 6.89.

Table 6.9 Constants of initial vector

y_{10}	y_{20}	y_{30}	y_{40}	y_{50}	y_{60}	y_{70}
0.131	0.24	0.307	0.321	0.279	0.189	0.067

Fig. 6.90 Envelope of maximal vibration peaks of bladed wheel for various adhesion forces and $k_c = 10,000 \text{ N/m}$ and mode shape with 2 ND



(b) Numerical Simulations of Vibration Attenuation

Vibration attenuation from a resonant vibration by the affinity mode to eigenmode B (Fig. 6.88) was chosen, similarly as in Sect. 6.3.1.2b, to study the effects of friction contacts on system resonant frequency and damping. Therefore initial displacement vector for the bladed wheel was set proportional to this mode:

$$\mathbf{y}_0 = \mathbf{y}_{amp} [\mathbf{y}_{10}, \mathbf{y}_{10}, a_1 \mathbf{y}_{10}, a_1 \mathbf{y}_{10}], \quad (6.4.3)$$

where coefficients $y_{amp} = 0.013$, $a_1 = 0.069$ and vector \mathbf{y}_{10} is

$$\mathbf{y}_{10} = [y_{10}, y_{20}, y_{30}, y_{40}, y_{50}, y_{60}, y_{70}, -y_{70}, -y_{60}, -y_{50}, -y_{40}, -y_{30}, -y_{20}, -y_{10}, 0], \quad (6.4.4)$$

whose constants of initial vector are presented in Table 6.9.

Figures 6.90 and 6.91 show envelopes of maximal amplitude that is reached in blade no. 4 since there is prescribed maximal initial displacement (Fig. 6.88). Similarly as for three blades bundle, increase of friction force leads to quicker attenuation and smaller amplitudes in slip phase in contacts. Increase of contact stiffness k_c leads to lower amplitudes in stick mode. In contradiction to the three blades bundle, however, maximal amplitude decay is no longer linear but more exponential.

The damping is due to changeable amplitudes of vibration mode around the wheel ununiformly distributed. For mode 2ND, amplitude attenuations and damping ratios for different blades along quarter of the wheel is shown in Fig. 6.92 and Fig. 6.93, respectively.

Fig. 6.91 Envelope of maximal vibration peaks of bladed wheel for various contact stiffness and $F_{t0} = 1$ N and mode shape with 2 ND

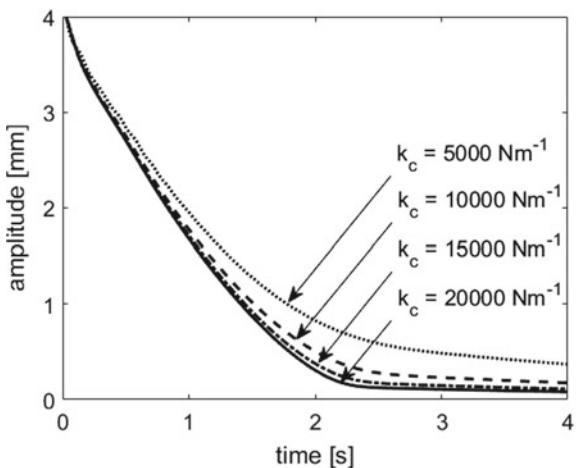
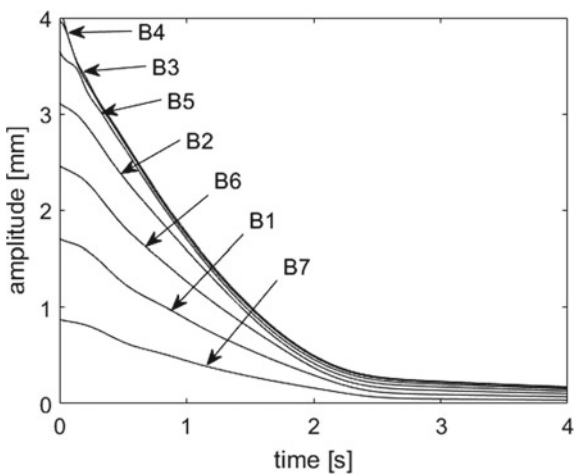


Fig. 6.92 Vibration attenuations of blades no. 1-7 for 2 ND mode



Figures 6.94 and 6.95 show the resonant frequency changes of blade no. 4 for the same simulations as shown in Figs. 6.90 and 6.91. The character of the curves is qualitatively very similar to the case of three blades bundle discussed in Sect. 6.3.1.2. At the beginning of attenuation the resonant frequency is close to the eigenfrequency f_2 of a wheel with open contacts, i.e. 48.25 Hz, since slip state occur and the stiffness couplings in contacts are weak. When the amplitudes of the blades, however, fall down, the contacts get locked and the resonant frequency passes over to eigenfrequency of the wheel with bonded contacts, i.e. 48.95 Hz. The resonant frequencies at the beginning and at the end are not dependent on friction force. It can be seen that changing friction force only shifts the increase of the frequency in time. On the other hand, change of stiffness of the contact spring leads to higher increase of the stick state resonant frequencies because the resonant frequency of the wheel with stuck

Fig. 6.93 Damping ratio of blades no. 1-7 for 2 ND mode

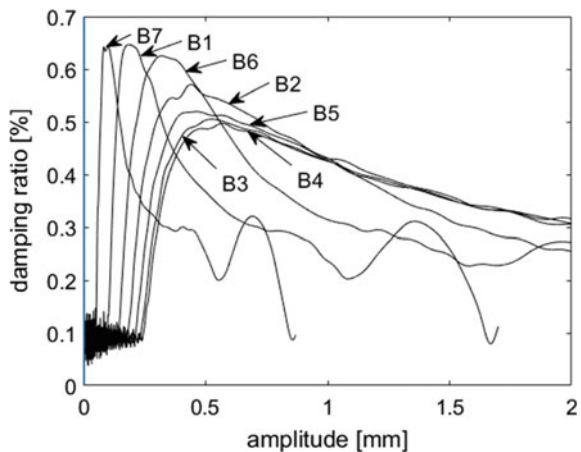
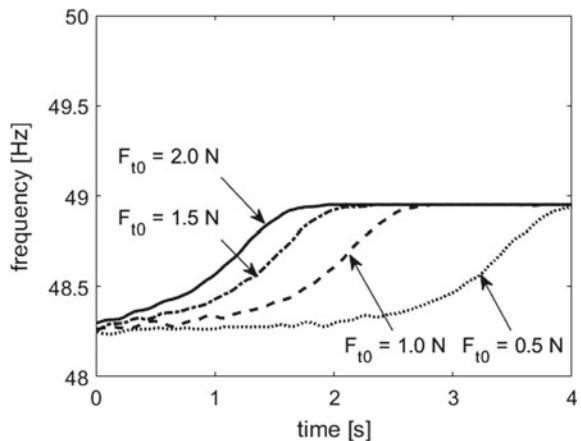


Fig. 6.94 Frequency of vibration of bladed wheel for various adhesion forces and $k_c = 10,000$ N/m and mode shape with 2 ND



contacts increases due to increasing the contact stiffness. The resonant frequency as a function of amplitude for the same cases is shown in Figs. 6.96 and 6.97.

Results of damping ratios for various friction forces and contact stiffnesses are shown in Figs. 6.98 and 6.99, respectively. It can be seen that increase of friction force leads to increase of damping ratio for higher amplitudes of vibration. The maximal values for different friction forces, however, are the same and are just shifted to higher amplitudes with increasing friction forces. On the other hand, increase of contact stiffness does not change the damping ratio for higher amplitudes, but for the amplitudes close to the point where transition from stick-slip to stick state occurs, there is a rapid increase of damping ratio which corresponds to quicker slope change of envelope in Fig. 6.90.

Fig. 6.95 Frequency of vibration of bladed wheel for various contact stiffness and $F_{t0} = 1$ N and mode shape with 2 ND

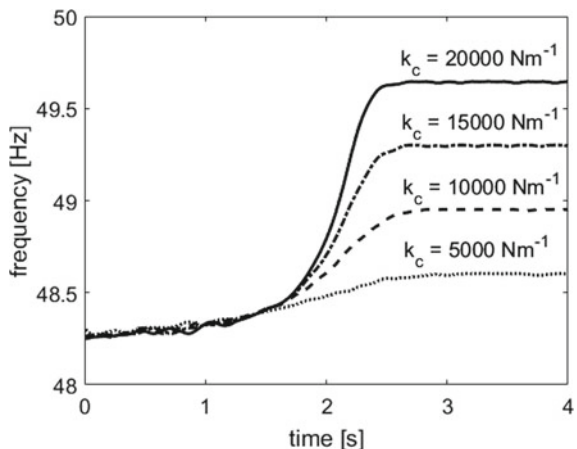


Fig. 6.96 Frequency of vibration of bladed wheel for various adhesion forces and $k_c = 10,000$ N/m and mode shape with 2 ND as a function of amplitude

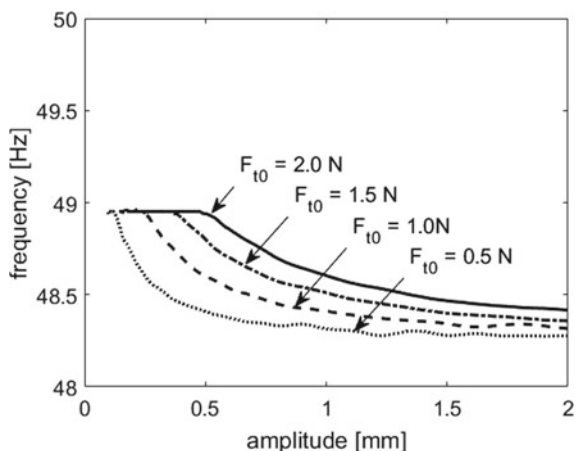


Fig. 6.97 Frequency of vibration of bladed wheel for various contact stiffness and $F_{t0} = 1$ N and mode shape with 2 ND as a function of amplitude

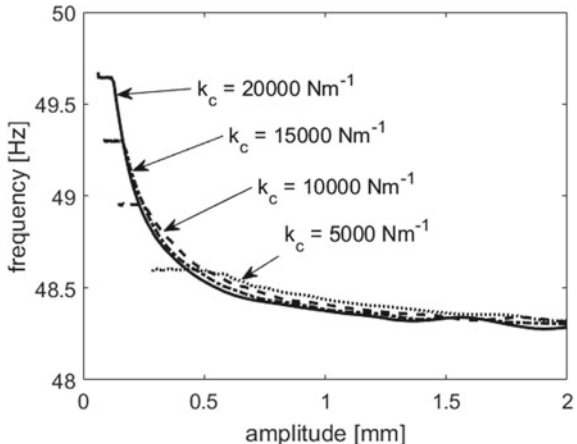


Fig. 6.98 Damping ratio for various adhesion forces and $k_c = 10,000 \text{ N/m}$ and mode shape with 2 ND as a function of amplitude

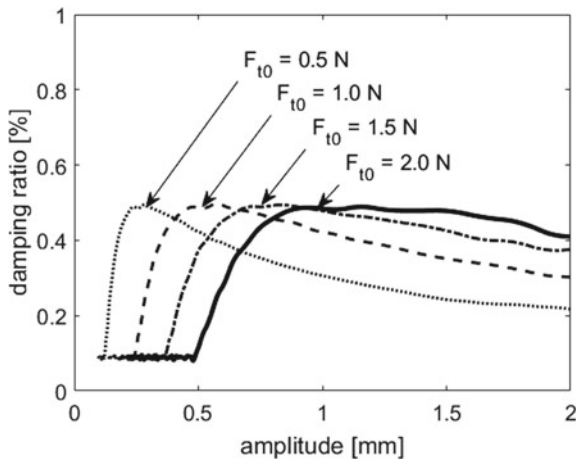
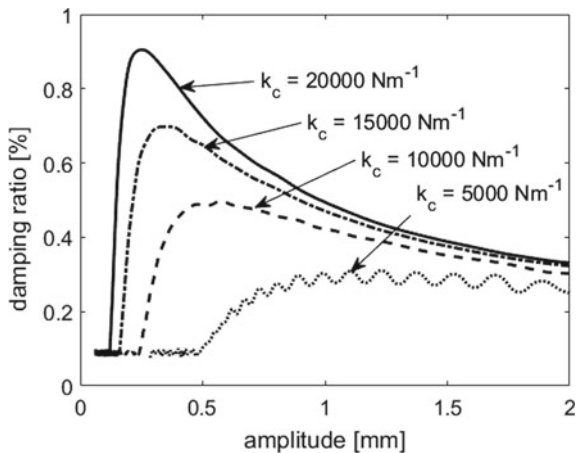


Fig. 6.99 Damping ratio for various contact stiffness and $F_{t0} = 1 \text{ N}$ and mode shape with 2 ND as a function of amplitude



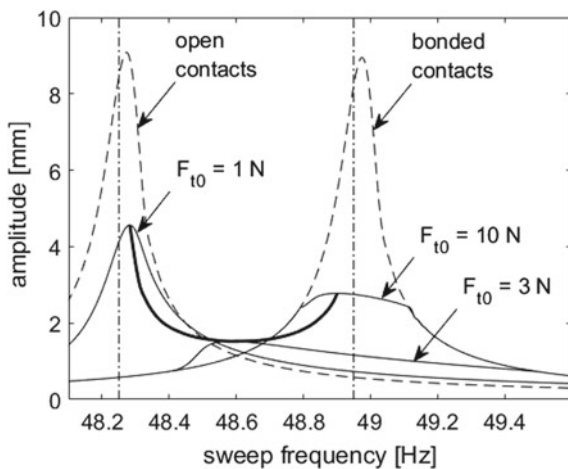
(c) Numerical simulations of sweep nozzle excitation

The sweep nozzle excitation of the bladed wheel by stator blades is used here to simulate passing the resonant frequency of the wheel during the run-up. Number of stator blades is usually opted lower than number of rotor blades and their difference equals to a number of ND of the excited mode [48], which is excited. In our simulations were used 28 stator blades to excite wheel vibrations with 2 ND respectively. Excitation force for each blade is described by Eq. (6.4.5):

$$F_i = F_b \cos\left(\omega_r t - 2\pi\left(1 - \frac{R}{S}\right)i\right), \quad i = 1, 2, \dots, 30, \quad (6.4.5)$$

where F_b is force amplitude, R number of rotor blades, S number of stator blades and ω_r angular frequency of revolutions.

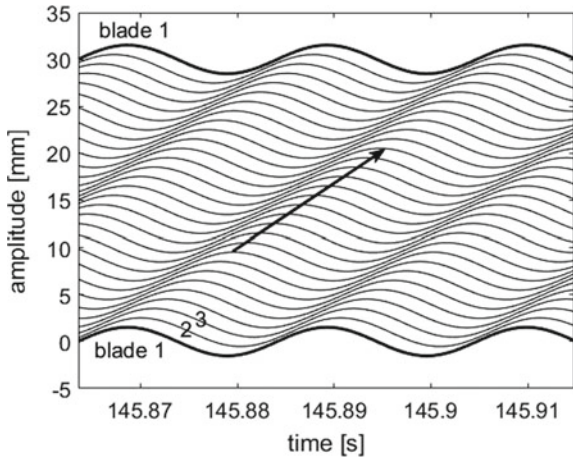
Fig. 6.100 The amplitude-frequency characteristics at sweep nozzle excitation for different friction force F_{t0}



For evaluating dry friction effect on the resonant passage of 2ND mode of the wheel, we choose slow sweep rate $1/15\text{ Hz s}^{-1}$ of revolution frequency, force amplitude $F_b = 1\text{ N}$ and various adhesion forces $F_{t0} = 1, 2, \dots, 10$. The amplitude-frequency characteristics for $F_{t0} = 1, 3$ and 10 (solid lines) are shown in Fig. 6.100. The amplitude-frequency dependences evaluated at sweep nozzle excitation for open and bonded contacts are depicted by dashed lines. Vertical dash-dotted lines show values of eigenfrequencies of the wheel corresponding to open 48.25 Hz and to bonded 48.95 Hz contacts. Small frequency shifts between resonance peaks and calculated eigenfrequencies of the limit contact states are caused mainly by the transient effect of sweep excitation. Envelope of resonant peaks of the characteristics calculated for different F_{t0} in range from 1 to 10 is drawn by a bold line. At low friction forces contacts are in slip phase during vibration and the resonant frequency approaches to the eigenfrequency of the open contacts and at high friction forces due to stick phase they approaches to eigenfrequency of the bonded contacts. The important fact is that there is optimum of the friction force, i.e. $F_{t0} = 3\text{ N}$, for given parameters of the simulation where the wheel resonant amplitude reaches lowest value during the resonant passage.

The zoomed time characteristics of all 30 blade displacement responses on sweep nozzle excitation at excitation amplitude $F_b = 1\text{ N}$, friction forces $F_{t0} = 3\text{ N}$ and revolution frequency $f_r = \omega_r/2\pi = 48.58\text{ Hz}$ where the amplitude-frequency characteristic reaches its maximum are drawn in Fig. 6.101. The bold lines on the top and bottom of the graphs belong to the blade no. 1 that encloses whole circumference of the wheel given by angle 2π . The arrow shows the direction of a movement of the deformation wave. As shown in Fig. 6.101, the wave needs time of two vibration periods ($2T$) for travelling over one circumference of the wheel. Hence the velocity of the wave is $2\pi/2T$ what is equal to $f_2/2$ as corresponds to the analytical assumption for eigenmode with 2ND. Since the deformation wave moves in the direction of rotation (Fig. 6.101) we call it forward traveling wave.

Fig. 6.101 Time characteristics of wheel blades at resonant excitation ($F_b = 1 \text{ N}$, $Ft0 = 3 \text{ N}$, $f_r = 48.58 \text{ Hz}$)



(d) Numerical simulations of nozzle excitation with self-excitation

The flowing gas can cause in addition to the periodic wakes exciting forces also instability and increase of self-excited oscillations. Mathematical model of this aero-elastic phenomenon is very complicated and this effect is intensively investigated to this day. Therefore in the first approximation of solution of running waves and interaction of delayed forced and self-excited oscillation the Van der Pol model of excitation forces acting on individual blades (similar as on the airplane wing) will be applied [49]. The Van der Pol non-linear damping force is often used in electronic engineering and in theory of non-linear oscillations and is described by

$$G_i = -\mu(1 - (x_i/r)^2)\dot{x}_i, \quad (6.4.6)$$

where G_i [N] is the aerodynamic force acting on blade i , x_i , \dot{x}_i [m, m/s] are displacement and velocity of blade i , r [m] is the displacement of blade at which the negative aerodynamic force changes into positive one, μ [Ns/m] is a scalar parameter indicating the intensity of this non-linear damping.

Advantage of this non-linear model is the conversion of negative damping into positive one after the amplitudes of self-excited oscillations exceed prescribed limit $x_i = r$. Amplitudes are therefore also in the unstable regions limited, which enables investigating of system behavior even in these cases. This property is very useful also in numerical solution, when it prevent from overflowing and destroying computing procedure. The dependence of aerodynamic force G_i on the intensity self-excitation coefficient μ for given value of $r = 1 \text{ mm}$ is in Fig. 6.102. The value of parameter r determines a blade displacement at which the aerodynamic force changes its sign from negative into positive one. The increase of dangerous flutter vibration happens, if the intensity self-excitation coefficient μ (Eq. 6.4.6) is greater than the blade damping coefficient b of the blade (Table 6.1).

Fig. 6.102 The dependence of aerodynamic force on the intensity self-excitation coefficient

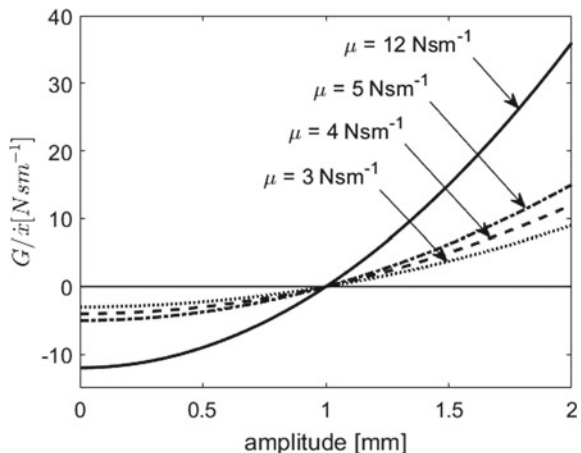
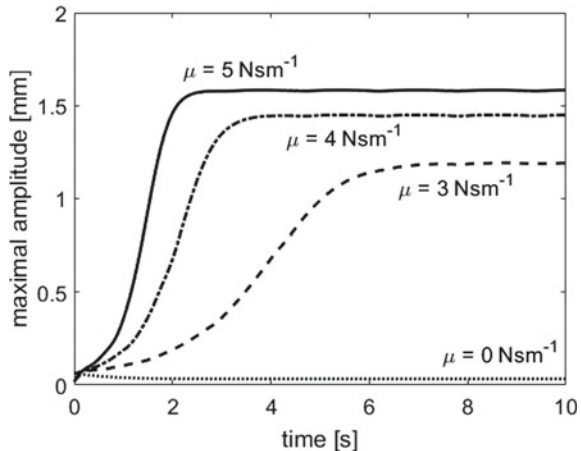
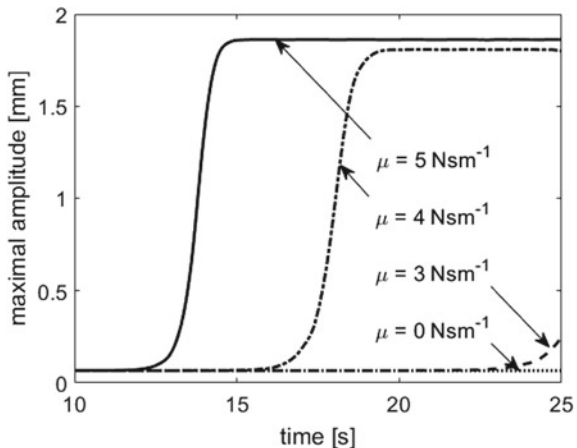


Fig. 6.103 The time characteristics of maximal amplitudes of the wheel with zero friction force and at self-excitation by van der Pol model with different intensity coefficients



This enormous increase of amplitude is very dangerous for reliability and service life of blade cascade. One of the possible arrangements for suppression of these dangerous amplitudes is the increase of total damping. The effect of tie-boss friction contact between neighboring blades on stabilization of one vibration mode will be shown on the next example. We choose the nozzle excitation (Eq. 6.4.5) with number of stator blades $S = 15$ and $f_r = \omega_r/2\pi = 70 \text{ Hz}$ that makes out-of-resonant vibration since the eigen-frequency of the wheel mode with ND = 15 and bonded contacts is 63.9 Hz. The force amplitude was $F_b = 2 \text{ N}$, friction forces in contacts was $F_{t0} = fF_n = 1 \text{ N}$. The time characteristics of maximal amplitudes of the wheel for zero value $F_{t0} = 0$ and various values of μ are shown in Fig. 6.103 and the same characteristics of the wheel with additional dry friction forces are drawn in Fig. 6.104.

Fig. 6.104 The time characteristics of maximal amplitudes of the wheel with $F_t = 1 \text{ N}$ and at self-excitation by van der Pol model with different intensity coefficients



It can be seen for the case of zero friction force (Fig. 6.103) that the maximal amplitudes increase almost from the beginning of the excitation and faster with intensity self-excitation coefficient increase. Then the self-excited vibration transits into a stable phase of vibration due to the Van der Pol model. The mode of the stable phase has 15 ND (Fig. 6.105) as expected to excitation of the wheel with 30 rotor blades by 15 nozzles. By introducing the friction force $F_{t0} = 1 \text{ N}$, the system is stabilized for some time, but afterward the self-excitation occur as well. And, the origin of instability in the system with friction is prolonged the more the lower intensity coefficient of self-excitation is. And again we can see the transition into the stable phase of vibration. From the shapes of the vibration amplitudes (Figs. 6.102, 6.103 and 6.104) in selected times of the stable phase, however, it is evident that due to dry friction, the original mode with 15ND is suppressed and another vibration mode with lower number of ND is excited. Type of this stable vibration mode is dependent on the magnitude of the instability coefficient μ and force amplitude F_b . For our study case, when $\mu = 4 \text{ N s m}^{-1}$ the umbrella mode (Fig. 6.102), when $\mu = 12 \text{ N s m}^{-1}$ a backward traveling mode with 1ND (Fig. 6.103) and when $\mu = 100 \text{ N s m}^{-1}$ a forward traveling mode with 3ND (Fig. 6.104) are excited (Figs. 6.105, 6.106, 6.107 and 6.108).

These results show very complex non-linear behavior of bladed wheels at consideration of dry-friction damping and self-excitation and therefore numerical modeling and experimental validation of fluid-structure interaction by different approaches are still under our investigation (e.g. [45]).

Fig. 6.105 Mode of self-excited vibration of the wheel with zeros friction force and intensity coefficient 4 N s m^{-1} at time 4 s

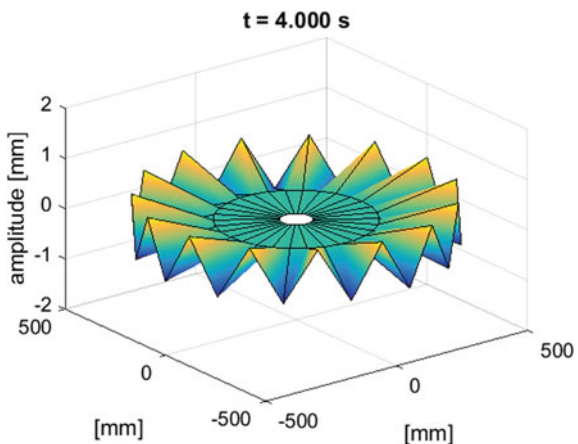


Fig. 6.106 Mode of self-excited vibration of the wheel with friction forces 1 N and intensity coefficient 4 N s m^{-1} at time 20.002 s

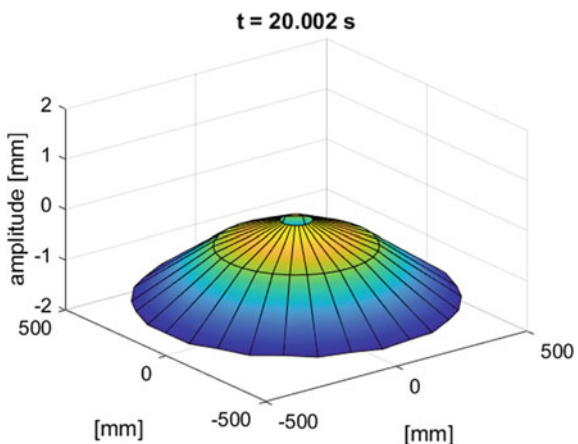


Fig. 6.107 Mode of self-excited vibration of the wheel with friction force 1 N and intensity coefficient 12 N s m^{-1} at time 20.018 s

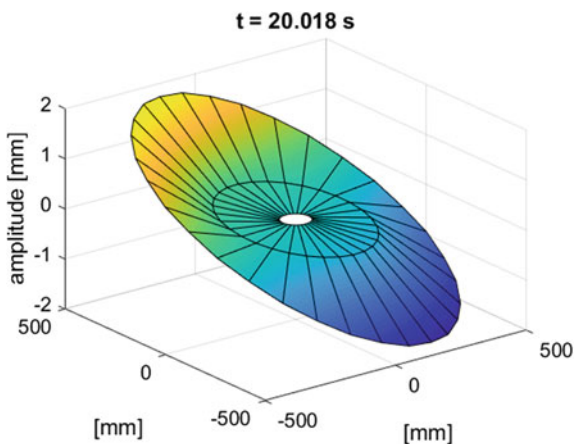
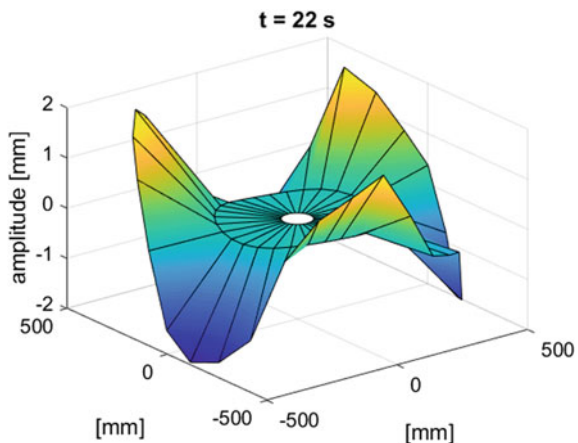


Fig. 6.108 Mode of self-excited vibration of the wheel with friction force 1 N and intensity coefficient 100 N s m^{-1} at time 22 s



6.5 Conclusion

The variety of modified dry-friction models and results of their equivalent linearization were presented at the Sect. 6.2. Friction is considered from phenomenological view within the whole Chapter. Numerical models, i.e. discrete analytical, reduced and full finite element, used in our research of non-linear dynamic behavior, of the blade cascades and bladed wheel with dry friction contacts were described in Sects. 6.3 and 6.4, respectively. Dynamics states, such as resonant vibration, free attenuation, self-excitation, were considered. The detail dynamic analysis of non-linear behavior of these systems due to dry-friction contacts were presented for discrete analytical model with the stick-slip friction contact. The results show that the general characteristics of dry-friction damping dependences on contact stiffness and friction force of the blades bundle are similar to whole bladed wheel. What is different and much rich is, however, structural dynamics of the bladed wheels because of their periodic structure with rotational symmetry. It brings different resonant modes of vibration in dependence on a type of wheel excitation. In Sect. 6.4 the responses of the wheel to nozzle excitation and self-excitation were studied, too. To assess the agreement of numerical results with experiment, the experimental set-ups, results of measurement and their analysis for blades bundles with dry friction coupling, i.e. by tie-boss contacts or by imposed friction element, were described. The comparisons show that in spite of simplifications in the modelling of the dry-friction contacts, the used numerical models can deliver very useful information about additional stiffness, damping and stabilization effect due to the contact couplings between blades. Despite plentiful publications on this topic as seen in the Introduction, a high interest of scientists about it continues till today. Our latest research is mainly aimed at the experimental testing of the bladed wheel with tie-bosses described in Sect. 6.4 for validation of our numerical models. As was shown on case of tie-boss couplings of three blades bundle, the computation of the non-reduced 3E FE model with surface

to surface contact was performed. The results of dynamics responses, stiffening and damping estimation were very promising and therefore we would like to overcome to computation of the whole wheel mode.

Acknowledgements This work was supported by the research project of the Czech Science Foundation No. 16-04546S “Aero-elastic couplings and dynamic behavior of rotational periodic bodies”. The HPC calculations was supported by The Czech Ministry of Education, Youth and Sports from the Large Infrastructures for Research, Experimental Development and Innovations project “IT4 Innovations National Supercomputing Center—LM2015070”.

References

1. Awrejcewicz, J., Pyr'yev, Y.: Nonsmooth Dynamics of Contacting Thermoelastic Bodies. Springer, Berlin (2009)
2. Bachschmid, N., Bistolfi, S., Ferrante, M., Pennacchi, P., Pesatori, E., Sanvito, M.: An investigation on the dynamic behaviour of blades coupled by shroud contacts. In: Proceedings of SIRM 2011, Darmstadt, Germany (2011)
3. Bachschmid, N., Pennacchi, P., Lurati, M.: Combining mistuning and snubbing in bladed disks of turbomachinery. In: Proceedings of ISMA 2008, vol. 1–8, pp. 1009–1022, KU Leuven (2008)
4. Bachschmid, N., Bistolfi, S., Ferrante, M., Pennacchi, P.: An investigation on the dynamic behavior of blades coupled by shroud contacts. In: Proceedings of SIRM 2011, pp. 1–10, Darmstadt, Germany (2011)
5. Barboteu, M., Danan, D.: Analysis of a dynamic viscoelastic contact problem with normal compliance, normal damped response, and nonmonotone slip rate dependent friction. *Adv. Math. Phys.* (2016). Article Number: 1562509. <https://doi.org/10.1155/2016/1562509>
6. Bogolyubov, N.N., Mitropolski, J.A.: Asymptotic Methods in Theory of Nonlinear Oscillations. GITTL, Moscow (1955). (in Russia)
7. Botto, D., Zucca, S., Pavone, S., Gola, M.M.: Parametric study of the kinematic behaviour of the underplatform damper and correlation with experimental data. In: Proceedings of ISMA 2008, vol. 1–8, pp. 1039–1053, KU Leuven
8. Brepta, R., Püst, L., Turek, F.: Mechanical oscillations, TP 71. Sobotales, Prague (1994). (in Czech)
9. Chen, J.J., Zang, C.P., Zhou, B.A., Petrov, E.P.: Analysis of micro-slip properties for models of bladed disc friction joints. In: Proceedings of the ASME Turbo Expo, vol. 7B (2017). Article Number: V07BT35A021
10. Dinca, F., Theodosin, C.: Nonlinear and Random Vibrations. Academic press, Bucuresti (1973)
11. Drozdowski, R., Volker, L., Hafele, D., Vogt D.M.: Experimental and numerical investigation of the nonlinear vibrational behavior of steam turbine last stage blades with friction bolt damping elements. In: Proceedings of the ASME Turbo Expo 2015, vol. 8, Canada (2015)
12. Ferri, A.A., Dowell, E.H.: Frequency domain solutions to multi-degree-of-freedom, dry friction damped systems. *J. Sound Vib.* **124**(2), 207–224 (1998). ISSN 0022460X
13. Francavilla, A., Zienkiewicz, O.C.: A note on numerical computation of elastic contact problems. *Int. J. Numer. Methods Eng.* **9**, 913–924 (1975)
14. Gola, M.M., Liu, T.: A direct experimental–numerical method for investigations of a laboratory under-platform damper behavior. *Int. J. Solids* **51**, 4245–4259 (2014). ISSN 00207683. <https://doi.org/10.1016/j.ijsolstr.2014.08.011>
15. Gu, W., Xu, Z., Liu, Y.: A method to predict the non-linear vibratory response of bladed disc system with shrouded dampers. In: Proceedings of the Institution of Mechanical Engineers Part C-Journal of Mechanical Engineering Science, vol. 226, pp 1620–1632 (2012). <https://doi.org/10.1177/0954406211424671>

16. Guran, A., Pfeiffer, F., Popp, K.: Dynamics with Friction, Modeling, Analysis and Experiments, Part II, Singapore, World Scientific, eBook (2001). ISBN 9789810229542
17. Hertz, H.: Über die Berührung fester elastischer Körper (On the contact of elastic solids). *J. reine und angewandte Mathematik* **92**, 156–171 (1882)
18. Hughes, T.J.R., Taylor, R.L., Sackman, J.L., Curnier, A., Kanoknukulchai, W.: A finite element method for a class of contact-impact problems. *Comput. Methods Appl. Mech. Eng.* **8**, 249–276 (1976)
19. Johnson, K.L.: Contact Mechanics. Cambridge University Press, UK (1985). ISBN 0-521-34796-3
20. Krylov, N.M., Bogoljubov, N.N.: Introduction in Nonlinear Mechanics. Kiew, Iz-AN-USSR (1937) (in Russia)
21. Laccaronara, W., Arvin, H., Bakhtiari-Nejad, F.: A geometrically exact approach to the overall dynamics of elastic rotating blades-part I: linear modal properties. *J. Nonlinear Dyn.* **70**(1), 659–675 (2012)
22. Larin, O.O.: Forced vibrations of bladings with the random technological mistuning. In: Proceedings of the ASME Turbo Expo 2010, vol. 6, pp. 667–672 (2010)
23. Magnus, K., Popp, K.: Schwingungen. Teubner Studienbücher Mechanik, 5 Auflage, Stuttgart (1997)
24. Minorski, N.: Nonlinear oscillations. Princeton, D. van Nostrand Comp. (1962)
25. Muszynska, A., Jones, D.I.G.: On tuned bladed disk dynamics: some aspects of friction related mistuning. *J. Sound Vib.* **86**(1), 107–128 (1983)
26. Muszynska, A., Jones, D.I.G.: Bladed disk dynamics investigated by a discrete model: effects of traveling wave excitation, friction and mistuning. In: Proceedings of the Machine Vibration Monitoring and Analysis Meeting, Oak Brook, Illinois (1982)
27. Muszynska, A., Jones, D.I.G.: A parametric study of dynamic response of a discrete model of turbomachinery bladed disk. *ASME J. Vib. Acoust. Stress Reliab. Des.* **105**, 434–443 (1983)
28. Nacivet, S., Pierre, C., Thouverez, F., Jezequel, L.: A dynamic Lagrangian frequency–time method for the vibration of dry-friction-damped systems. *J. Sound Vib.* **265**(1), pp. 201–219 (2003). ISSN 0022460X. [https://doi.org/10.1016/s0022-460x\(02\)01447-5](https://doi.org/10.1016/s0022-460x(02)01447-5)
29. Pennacchi, P., Chatterton, S., Bachschmid, N., Pesatori, E., Turozzi, G.: A model to study the reduction of turbine blade vibration using the snubbing mechanism. *Mech. Syst. Signal Process.* **25**(4), 1260–1275 (2011)
30. Pesaresi, L., Salles, L., Jones, A., Green, J.S., Schwingshakl, C.W.: Modelling the nonlinear behaviour of an underplatform damper test rig for turbine applications. *Mech. Syst. Signal Process.* **85**, 662–679 (2017). <https://doi.org/10.1016/j.ymssp.2016.09.007>
31. Pešek, L., Hajžman, M., Půst, L., Zeman, V., Byrtus, M., Brůha, J.: Experimental and numerical investigation of friction element dissipative effects in blade shrouding. *J. Nonlinear Dyn.* **79**(3), 1711–1726 (2015)
32. Pešek, L., Půst, L.: Mathematical model of a blade couple connected by damping element. In: Proceedings of 8th EURODYN2011, pp. 2006–2011, KU Leuven, Belgium (2011)
33. Pešek, L., Půst, L.: Blade couple connected by damping element with dry friction contacts. *J. Theor. Appl. Mech.* **52**(3), 815–826 (2014)
34. Pešek, L., Půst, L., Bula, V., Cibulka, J.: Investigation of dry friction effect of shroud damping wire on model test bladed wheel. In: Proceedings of ASME IDETC/CIE 2013, Portland, USA, pages 7 (2013). Article number DETC2013-12851
35. Pešek, L., Půst, L., Bula, V., Cibulka, J.: Numerical analysis of dry friction damping effect of tie-boss couplings on three blade bundle. In: Proceedings of ASME IDETC/CIE 2017, Cleveland, USA, pages 7 (2017)
36. Pešek, L., Půst, L., Šulc, P., Bula, V.: Stiffening effect and dry-fiction damping of bladed wheel model with tie-boss couplings. In: Springer book Mechanisms and Machine Science, 62, pp. 148–162 (2019). https://doi.org/10.1007/978-3-319-99270-9_11
37. Pešek, L., Půst, L., Vaněk, F., Veselý, J., Cibulka, J.: Dynamics of model bladed disc with friction elements for vibration suppression. In: Proceedings of 8th IFTOMM Rotordynamics, pp. 332–339 (2010)

38. Pešek, L., Püst, L., Vaněk, F., Bula, V., Cibulka, J.: Inter-slip damping of twisted blades in opposed bundles under rotation. In: Proceedings of 10th VIRM, Institution of Mechanical Engineers, London, UK, Woodhead Publishing, pages 10 (2012)
39. Petrov, E.P.: Method for direct parametric analysis of non-linear forced response of bladed disks with friction contact interfaces. ASME J. Turbomach. **126**, 654–662 (2004)
40. Petrov, E.P.: Method for sensitivity analysis of resonance forced response of bladed disks with nonlinear contact interfaces. J. Eng. Gas Turbines Power Trans. ASME **131**(2) (2009). <https://doi.org/10.1115/1.2969094>. Article Number 022510
41. Petrov, E.P., Ewins, D.J.: State-of-the-art dynamic analysis for non-linear gas turbine structures. In: Proceedings of the Institution of Mechanical Engineers Part G-Journal of Aerospace Engineering, vol. 218, no. G3, pp. 199–211 (2004). <https://doi.org/10.1243/0954410041872906>
42. Petrov, E.P., Ewins, D.J.: Effects of damping and varying contact area at blade-disk joints in forced response analysis of bladed disk assemblies. J. Turbomach. Trans. ASME **128**(2), 403–410 (2006). <https://doi.org/10.1115/1.2181998>
43. Petrov, E.P., Ewins, D.J.: Advanced modelling of underplatform friction dampers for analysis of bladed disc vibration. In: Proceedings of the ASME TURBO EXPO 2006, vol. 5, pp. 769–778 (2006)
44. Pierre, C., Ferri, A.A., Dowell, E.H.: Multi-harmonic analysis of dry friction damped systems using an incremental harmonic-balance method. J. Appl. Mech. Trans. ASME **52**(4), 958–964 (1985). <https://doi.org/10.1115/1.3169175>
45. Prasad, C.S., Pešek, L.: Analysis of classical flutter in steam turbine blades using reduced order aeroelastic model. In: MATEC Web of Conferences, 211 (2018). <https://doi.org/10.1051/matecconf/201821115001>. Article number 15001
46. Püst, L., Tondl, A.: Introduction into theory of nonlinear and quasiharmonic vibrations of mechanical systems. NCSAV, Prague (1956) (in Czech)
47. Püst, L., Pešek, L., Radolfova, A.: Various types of dry friction characteristics for vibration damping. Eng. Mech. **18**(3), 203–224 (2011)
48. Püst, L., Pešek, L.: Running flutter waves in blades cascades. In: Proceedings of the Engineering Mechanics 2017, Svatka, Czech Republic (2017)
49. Püst, L., Pešek, L.: Blades force vibration under aero-elastic excitation modeled by Van der Pol. Int. J. Bifurc. Chaos **27**(11), (12 pages) (2017)
50. Rao, J.S.: Turbomachine Blade Vibration. Wiley Eastern Limited, New Delhi (1991)
51. Rivin, E.I.: Stiffness and Damping in Mechanical Design. Marcel Dekker, New York (1989)
52. Rizvi, A., Smith, C.W., Rajasekaran, R., Evans, K.E.: Dynamics of dry friction damping in gas turbines: literature survey. J. Vib. Control **22**(1), 296–305 (2016). <https://doi.org/10.1177/1077546313513051>
53. Sanliturk, K.Y., Imregun, M., Ewins, D.J.: Harmonic balance vibration analysis of turbine blades with friction dampers. J. Vib. Acoust. **119**(1), 96–103 (2014). <https://doi.org/10.1115/1.2889693>
54. Santhosh, B., Narayanan, S., Padmanabhan, A.C.: Nonlinear dynamics of shrouded turbine blade system with impact and friction. Appl. Mech. Mater. **706**, 81–92 (2014). ISSN 16609336. <http://dx.doi.org/10.4028/www.scientific.net/AMM.706.81>
55. Sextro, W.: Dynamical Contact Problems with Friction. Springer, Berlin (2007)
56. Simo, J.C., Laursen, T.A.: An augmented lagrangian treatment of contact problems involving friction. Comput. Struct. **42**(1), 97–116 (1992)
57. Suss, D., Jerschl, M., Willner, K.: Adaptive harmonic balance analysis of dry friction damped systems. J. Nonlinear Dyn. **1**. 34TH IMAC Book Series: Conference Proceedings of the Society for Experimental Mechanics Series, pp. 405–414 (2016). https://doi.org/10.1007/978-3-319-29739-2_36
58. Voldřich, J., Lazar J., Polach P., Morávká Š.: Finding the stiffnesses of interface contact elements for the computational model of steam turbine blading. In: Proceedings of ASME IDETC/CIE 2017, Cleveland, USA, pages 12 (2017)
59. Wiercigroch, M., de Kraker, B.: Applied Nonlinear Dynamics and Chaos in Mechanical Systems with Discontinuities, World Scientific Series, vol. 28, London (2000)

60. Wriggers, P., Van Vu, T., Stein, E.: Finite element formulation of large deformation impact contact problems with friction. *Comput. Struct.* **37**, 319–331 (1990)
61. Yamashita, Y., Shiohata, K., Kudo, T., Yoda, H.: Vibration characteristics of a continuous cover blade structure with friction contact surfaces of a steam turbine. In: Proceedings of 10th VIRM, pp. 323–332, London, UK (2012)
62. Zeman, V., Byrtus, M., Hajžman, M.: Harmonic forced vibration of two rotating blades with friction damping. *Eng. Mech.* **17**(3/4), 187–200 (2010)
63. Zmitrowicz, A.: A vibration analysis of a turbine blade system damped by dry friction forces. *Int. J. Mech. Sci.* **23**(12), 741–761 (1981). [https://doi.org/10.1016/0020-7403\(81\)90012-6](https://doi.org/10.1016/0020-7403(81)90012-6)
64. Zucca, S., Firrone, C.M., Muzio, A., Gola, M.: Numerical assessment of friction damping at turbine blade root joints by simultaneous calculation of the static and dynamic contact loads. *J. Nonlinear Dyn.* **67**(3), 1943–1955 (2012). ISSN 0924-090X. <http://dx.doi.org/10.1007/s11071-011-0119-y>
65. Zucca, S., Firrone, C.M.: Nonlinear dynamics of mechanical systems with friction contacts: coupled static and dynamic multi-harmonic balance method and multiple solutions. *J. Sound Vib.* **333**(3), 916–926 (2014). <https://doi.org/10.1016/j.jsv.2013.09.032>

Chapter 7

Bifurcation-Based Shimmy Analysis of Landing Gears Using Flexible Multibody Models



C. J. J. Beckers, A. E. Öngüt, G. Verbeek, R. H. B. Fey, Y. Lemmens
and N. van de Wouw

Abstract Shimmy oscillations are undesired vibrations in aircraft landing gears. In this chapter, the onset of shimmy vibrations, marked by Hopf bifurcations, is investigated in the parameter space of high-fidelity, flexible multibody landing gear models. Such a bifurcation analysis is performed by combining the Virtual.Lab Motion multibody solver with the numerical continuation software AUTO. The resulting quasi-2-parameter bifurcation diagrams, involving aircraft velocity and normal load, are verified using conventional time-simulation methods and are shown to be computationally more efficient. A sensitivity study reveals the influence of design parameters, such as the shimmy damping coefficient, mechanical trail, and steering actuator stiffness, on the occurrence of shimmy.

Keywords Bifurcation analysis · Flexible multibody dynamics · Shimmy · Landing gear dynamics

C. J. J. Beckers · R. H. B. Fey (✉) · N. van de Wouw

Dynamics and Control Group, Department of Mechanical Engineering, Eindhoven University of Technology, Eindhoven, The Netherlands

e-mail: R.H.B.Fey@tue.nl

N. van de Wouw

Department of Civil, Environmental and Geo-Engineering, University of Minnesota, Minneapolis, USA

N. van de Wouw

Delft Center for Systems and Control, Delft University of Technology, Delft, The Netherlands

A. E. Öngüt · Y. Lemmens

Siemens PLM Software, Leuven, Belgium

G. Verbeek

Fokker Landing Gear, Helmond, The Netherlands

© Springer Nature Switzerland AG 2019

J. C. Jauregui (ed.), *Nonlinear Structural Dynamics and Damping, Mechanisms and Machine Science* 69,

<https://doi.org/10.1007/978-3-030-11777-7>

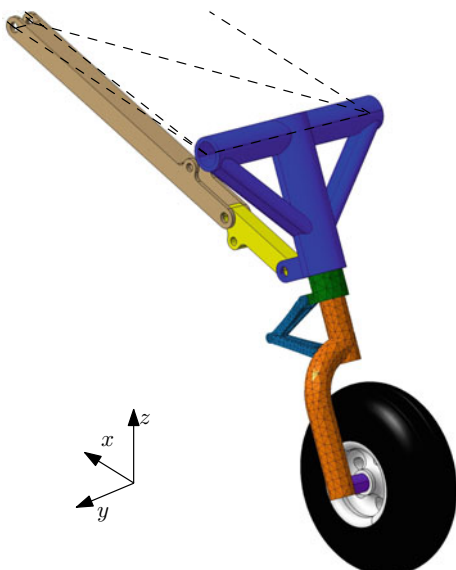
7.1 Introduction

Shimmy is a self-excited lateral-yaw oscillation of landing gear wheels that can occur during take-off, landing, or taxiing of an aircraft. In severe forms, it can cause discomfort for the pilot/passengers or even damage the safety-critical landing gear structure. Therefore, it is essential to assess the susceptibility of landing gears to shimmy early in the design process, preferably through model-based analysis.

Numerical continuation methods are often employed to analyse the Hopf bifurcations that mark the occurrence of shimmy in the parameter space of analytical models, such as in [7] and [13]. However, these models are often of limited complexity and represent significant simplifications of the complex landing gear structures. In contrast, the landing gear industry adopts time integration procedures for flexible multibody models, which can be highly complex and often include several types of nonlinearities and dynamic effects, such as mechanical free-play, flexible structures with large rotations/deformations, nonlinear dampers, contacts, and tires [9]. These multibody models form accurate representations of the actual landing gear dynamics, but the simulations are computationally expensive and only result in the stability properties of the landing gear at discrete points in the parameter space.

This study aims to bridge the gap between these analysis approaches and model types, by analyzing the shimmy stability properties of a complex, high-fidelity, flexible multibody landing gear model, as shown in Fig. 7.1, using numerical continuation software. The simulation framework developed in [11] is adapted to enable the analysis of larger, more complex models. With respect to this previous study, which analysed multibody models with up to 9 discrete degrees of freedom (DOFs), the

Fig. 7.1 Isometric view of the multibody landing gear model used in this study



model in Fig. 7.1 represents both the geometry and the dynamics of a real-world landing gear more accurately. The model is more complex, containing more bodies, some of which are considered flexible to account for the compliance of the landing gear structure. Modelling this compliance with flexible bodies, instead of using discrete rotational DOFs with a lumped stiffness, results in more realistic motions of the landing gear.

In this chapter, Sect. 7.2 summarizes the required preliminary theory for the description of the flexible multibody model, which also includes tire dynamics. In Sect. 7.3, the multibody landing gear model is explained, detailing the specific dynamics that are modeled, after which Sect. 7.4 provides an overview of the used simulation framework. The results of the analysis are discussed in Sect. 7.5 and the conclusions are summarized in Sect. 7.6. This work is an extended version of a conference paper [2], which focuses more on the applied simulation framework.

7.2 Preliminaries on Multibody Dynamics

The dynamics of a multibody system can be described by a system of differential-algebraic equations (DAE's) according to [6, p. 224]

$$\left\{ \begin{bmatrix} \underline{M}(\underline{q}) & \underline{\Phi}_{,\underline{q}}^T(\underline{q}, t) \\ \underline{\Phi}_{,\underline{q}}(\underline{q}, t) & 0 \end{bmatrix} \begin{bmatrix} \ddot{\underline{q}} \\ \underline{\lambda} \end{bmatrix} = \begin{bmatrix} \underline{Q}^A(\underline{q}, \dot{\underline{q}}) + \underline{Q}^E(\dot{\underline{q}}, \underline{q}, t) \\ \underline{\gamma}(\dot{\underline{q}}, \underline{q}, t) \end{bmatrix}, \right. \\ \left. \begin{aligned} \underline{\Phi}_{,\underline{q}}(\underline{q}, t)\dot{\underline{q}} &= -\frac{\partial \underline{\Phi}(\underline{q}, t)}{\partial t}, \\ \underline{\Phi}(\underline{q}, t) &= \underline{0}, \end{aligned} \right. \quad (7.1)$$

where \underline{M} is the mass matrix, which is a function of the column of generalized coordinates \underline{q} , $\underline{\Phi}_{,\underline{q}}$ is the constraint Jacobian, where $_{,\underline{q}}$ denotes the partial derivative with respect to \underline{q} , and $\underline{\Phi}$ reflects the holonomic constraints, $\underline{\lambda}$ is the associated column of Lagrange multipliers, and \underline{Q}^A denotes the column of generalized applied forces. Additionally, in the Virtual.Lab Motion software [10], the column \underline{Q}^E includes applied forces supplied by external sources, such as an external control system. The column $\underline{\gamma}$ defines the acceleration-level constraint equations, according to

$$\underline{\Phi}_{,\underline{q}}(\underline{q}, t)\ddot{\underline{q}} = - \left[\frac{\partial (\underline{\Phi}_{,\underline{q}}(\underline{q}, t)\dot{\underline{q}})}{\partial \underline{q}} + 2\frac{\partial \underline{\Phi}_{,\underline{q}}(\underline{q}, t)}{\partial t} \right] \dot{\underline{q}} - \frac{\partial^2 \underline{\Phi}(\underline{q}, t)}{\partial t^2} =: \underline{\gamma}(\dot{\underline{q}}, \underline{q}, t). \quad (7.2)$$

The second and third equalities in (7.1) represent the constraint equations on velocity and position level, respectively.

The generalized coordinates \underline{q} consist of both dependent- and independent generalized coordinates, respectively \underline{q}_D and \underline{q}_I , which are related through the constraint equations $\underline{\Phi}(\underline{q}, t) = \underline{0}$. The multibody solver of Virtual.Lab Motion, previously known as the DADS solver, and hereafter named the Motion solver,

applies the so-called augmented formulation, i.e., rather than eliminating all redundant equations from the system before solving, the equations of motion are integrated in time with the redundant generalized coordinates and Lagrange multipliers included [8, p. 118]. Before integration, the second-order differential equations in (7.1) are transformed into a first-order form by introducing the state variable $\underline{x} = [\underline{x}_1^T \underline{x}_2^T]^T := [\underline{q}^T \dot{\underline{q}}^T]^T$. The dynamics in (7.1) can now be described in terms of the states \underline{x}_1 , \underline{x}_2 , $\underline{\lambda}$, and $\underline{\chi}$ as

$$\begin{bmatrix} I & 0 & 0 & 0 \\ 0 & M(x_1) & \underline{\Phi}_{x_1}^T(x_1, t) & 0 \\ 0 & \underline{\Phi}_{x_1}(x_1, t) & 0 & 0 \\ 0 & 0 & 0 & I \end{bmatrix} \begin{bmatrix} \dot{\underline{x}}_1 \\ \dot{\underline{x}}_2 \\ \underline{\lambda} \\ \dot{\underline{\chi}} \end{bmatrix} = \begin{bmatrix} \underline{Q}^A(x_1, x_2) + \underline{Q}^E(x_1, x_2, t) \\ \underline{\gamma}(x_1, x_2, t) \\ g(x_1, x_2, \underline{\lambda}, \underline{\chi}) \end{bmatrix}, \quad (7.3)$$

which, in case of time-simulation, is integrated directly using one of the available numerical integration schemes [6, pp. 259–276]. The additional states $\underline{\chi}$ in (7.3) represent the dynamics of the system that are not directly a part of the multibody dynamics, e.g., the tire dynamics. The states in \underline{x} corresponding to the positions and velocities of the independent generalized coordinates are indicated as x_I .

7.2.1 Including Structural Compliance

The rigid multibody model can be extended by taking the structural flexibility of the bodies into account. A model derivation is provided below. A reference to [8, pp. 185–221], [14], and [15] is made for the full details.

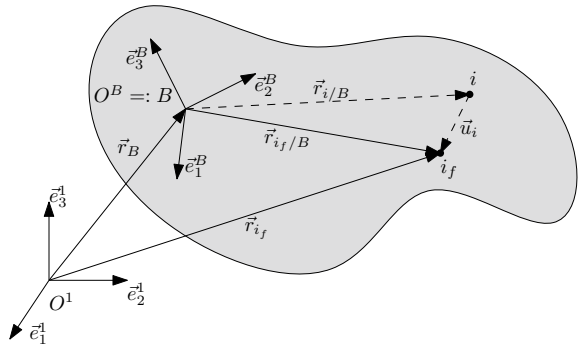
7.2.1.1 Floating Frame of Reference Formulation

The floating frame of reference formulation is used. This implies that the displacements due to the elastic deformation of the flexible body are described with respect to a body-fixed reference frame, as shown in Fig. 7.2. Figure 7.2 shows an inertial reference frame $\{O^1, \vec{e}^1\}$ and a flexible body B , which has a body-fixed reference frame $\{B, \vec{e}^B\}$. The body reference frame position is defined by \vec{r}_B and its orientation by a column of four Euler parameters $\underline{\theta}_B$, which defines the orientation of \vec{e}^B with respect to \vec{e}^1 .

The contribution of elastic deformation to the position of an arbitrary point i on the body, is given by

$$\vec{u}_i = \underline{u}_i^T \vec{e}^B = [u_1 \ u_2 \ u_3]_i \begin{bmatrix} \vec{e}_1^B \\ \vec{e}_2^B \\ \vec{e}_3^B \end{bmatrix}, \quad (7.4)$$

Fig. 7.2 Deformable body vector definitions



where \underline{u}_i is the column with coordinates that defines \vec{u}_i in the body reference frame. The position of point i in the deformed situation, point i_f , with respect to the origin of the body reference frame, is given by

$$\vec{r}_{i_f}/B = \vec{r}_{i/B} + \vec{u}_i , \quad (7.5)$$

where $\vec{r}_{i/B}$ is the position of point i with respect to B in the undeformed situation. The position of point i_f can also be expressed with respect to the inertial reference frame by

$$\begin{aligned} \vec{r}_{i_f} &= \vec{r}_B + \vec{r}_{i/B} + \vec{u}_i \\ &= \underline{\vec{e}}^{1^T} r_B + \underline{\vec{e}}^{B^T} (\underline{r}_{i/B} + \underline{u}_i) \\ &= \underline{\vec{e}}^{1^T} (r_B + \underline{A}^{1B} (\underline{r}_{i/B} + \underline{u}_i)) = \underline{\vec{e}}^{1^T} r_{i_f} , \end{aligned} \quad (7.6)$$

where \underline{A}^{1B} is the direction cosine matrix that defines the rotation from $\underline{\vec{e}}^B$ to $\underline{\vec{e}}^1$, according to

$$\underline{\vec{e}}^1 = \underline{A}^{1B} \underline{\vec{e}}^B . \quad (7.7)$$

This matrix is a function of the four Euler parameters: $A^{1B} = A^{1B}(\theta_B)$.

The lumped mass formulation is used to describe the deformation of the flexible body. This implies that the body is approximated by a finite number of grid points. The mass of the body is lumped into the point masses of the grid points, or nodes. This approach enables us to express the deformation of one of the points, for instance point i , as function of a set of shape vectors Ψ that describe the effect of the deformation on the position of the selected point. Therefore, the deformation coordinates in (7.4) can be described by

$$\underline{u}_i = \Psi_i \underline{\eta}_B , \quad (7.8)$$

where Ψ_i is the $3 \times n_\eta$ matrix containing the modal displacements of point i , and $\underline{\eta}_B$ is the column containing the n_η modal coordinates used to describe the deformation

of body B . Matrix $\underline{\Psi}_i$ is a row partition of the modal matrix $\underline{\Psi}$. This modal matrix describes the reduced elastic modes of all point on the body and is a result of modal reduction that will be described in Sect. 7.2.1.3.

By applying (7.8), the global coordinates of point i_f can be expressed as

$$\underline{r}_{i_f} = \underline{r}_B + \underline{A}^{1B}(\underline{\theta}_B) \left(\underline{r}_{i/B} + \underline{\Psi}_i \underline{\eta}_B \right). \quad (7.9)$$

The global position of point i_f is now fully defined as function of the generalized coordinates of the body

$$\underline{q}_B = \begin{bmatrix} \underline{r}_B \\ \underline{\theta}_B \\ \underline{\eta}_B \end{bmatrix}, \quad (7.10)$$

which comprises the reference coordinates \underline{r}_B and $\underline{\theta}_B$ and the modal coordinates $\underline{\eta}_B$. It is of importance that the modal coordinates $\underline{\eta}_B$ do not include the rigid body modes of the system, because these are already described by the reference coordinates.

The velocity of point i_f can be derived by differentiating (7.9) with respect to time and applying the chain rule

$$\dot{\underline{r}}_{i_f} = \dot{\underline{r}}_B + \dot{\underline{A}}^{1B} \left(\underline{r}_{i/B} + \underline{\Psi}_i \underline{\eta}_B \right) + \underline{A}^{1B} \underline{\Psi}_i \dot{\underline{\eta}}_B, \quad (7.11)$$

where the relation $\dot{\underline{r}}_{i/B} = 0$ has been used. In general, it is possible to rewrite the central term on the right hand side of (7.11) as

$$\dot{\underline{A}}^{1B} \left(\underline{r}_{i/B} + \underline{\Psi}_i \underline{\eta}_B \right) = \dot{\underline{A}}^{1B} \underline{r}_{i_f/B} = \underline{P}_i \dot{\underline{\theta}}_B, \quad (7.12)$$

where $\underline{P}_i = \underline{P}_i(\underline{\theta}_B, \underline{\eta}_B)$ is defined as

$$\underline{P}_i = \begin{bmatrix} \frac{\partial}{\partial \theta_1} (\underline{A}^{1B} \underline{r}_{i_f/B}) & \dots & \frac{\partial}{\partial \theta_4} (\underline{A}^{1B} \underline{r}_{i_f/B}) \end{bmatrix}, \quad (7.13)$$

which is a 3×4 matrix. Full details on how to assemble \underline{P}_i in the particular situation that Euler parameters are used as rotational coordinates are stated in [14, p. 110]. Substituting (7.12) into (7.11) results in

$$\dot{\underline{r}}_{i_f} = [\underline{I} \ \underline{P}_i \ \underline{A}^{1B} \underline{\Psi}_i] \begin{bmatrix} \dot{\underline{r}}_B \\ \dot{\underline{\theta}}_B \\ \dot{\underline{\eta}}_B \end{bmatrix}. \quad (7.14)$$

7.2.1.2 Flexible Equations of Motion

Once the global position and velocity coordinates are known for all points in the body, the kinetic energy of the individual points can be summed to obtain the total kinetic energy of the body, according to

$$\begin{aligned} T_B &= \frac{1}{2} \sum_{i=1}^{n_n} m_i \begin{bmatrix} \dot{\underline{r}}_B \\ \dot{\underline{\theta}}_B \\ \dot{\underline{\eta}}_B \end{bmatrix}^T \begin{bmatrix} I & \underline{P}_i & \underline{A}^{1B} \underline{\Psi}_i \\ sym. & \underline{P}_i^T \underline{P}_i & \underline{P}_i^T \underline{A}^{1B} \underline{\Psi}_i \\ & \underline{\Psi}_i^T \underline{\Psi}_i & \end{bmatrix} \begin{bmatrix} \dot{\underline{r}}_B \\ \dot{\underline{\theta}}_B \\ \dot{\underline{\eta}}_B \end{bmatrix} \\ &=: \frac{1}{2} \begin{bmatrix} \dot{\underline{r}}_B \\ \dot{\underline{\theta}}_B \\ \dot{\underline{\eta}}_B \end{bmatrix}^T \underline{M}_B(\underline{\theta}_B, \underline{\eta}_B) \begin{bmatrix} \dot{\underline{r}}_B \\ \dot{\underline{\theta}}_B \\ \dot{\underline{\eta}}_B \end{bmatrix}, \end{aligned} \quad (7.15)$$

where n_n is the total number of nodes of the body, m_i are the nodal masses, and \underline{M}_B is the resulting mass matrix of the body. This mass matrix is a function of the rotational coordinates $\underline{\theta}_B$ and the modal coordinates $\underline{\eta}_B$.

The elastic strain energy of the body can be expressed as

$$U_B = \frac{1}{2} \begin{bmatrix} \underline{r}_B \\ \underline{\theta}_B \\ \underline{\eta}_B \end{bmatrix}^T \begin{bmatrix} 0 & 0 & 0 \\ 0 & 0 & 0 \\ 0 & 0 & \underline{K}^{red} \end{bmatrix} \begin{bmatrix} \underline{r}_B \\ \underline{\theta}_B \\ \underline{\eta}_B \end{bmatrix}, \quad (7.16)$$

where $\underline{K}^{red} = \underline{\Psi}^T \underline{K} \underline{\Psi}$ is the modal stiffness matrix and \underline{K} is the structural stiffness matrix.

In case $\vec{F}_i = \underline{F}_i^T \underline{e}^1$ is defined to be the net external force acting on node i of the body, the virtual work of all forces acting on the body can be written as

$$\delta W_B = \sum_{i=1}^{n_n} \underline{F}_i^T \delta \underline{r}_{i_f}. \quad (7.17)$$

Given the found relation for $\dot{\underline{r}}_{i_f}$ from (7.14), it can be concluded that

$$\delta \underline{r}_{i_f} = [\underline{I} \ \underline{P}_i \ \underline{A}^{1B} \underline{\Psi}_i] \begin{bmatrix} \delta \underline{r}_B \\ \delta \underline{\theta}_B \\ \delta \underline{\eta}_B \end{bmatrix}. \quad (7.18)$$

Substituting (7.18) into (7.17) results the virtual work

$$\begin{aligned} \delta W &= [\sum_{i=1}^{n_n} \underline{F}_i^T \ \sum_{i=1}^{n_n} \underline{F}_i^T \underline{P}_i \ \sum_{i=1}^{n_n} \underline{F}_i^T \underline{A}^{1B} \underline{\Psi}_i] \begin{bmatrix} \delta \underline{r}_B \\ \delta \underline{\theta}_B \\ \delta \underline{\eta}_B \end{bmatrix} \\ &=: \left[(\underline{Q}_B^e)_r^T \ (\underline{Q}_B^e)_\theta^T \ (\underline{Q}_B^e)_\eta^T \right] \begin{bmatrix} \delta \underline{r}_B \\ \delta \underline{\theta}_B \\ \delta \underline{\eta}_B \end{bmatrix} =: (\underline{Q}_B^e)^T \delta \underline{q}_B, \end{aligned} \quad (7.19)$$

where \underline{Q}_B^e is defined as the generalized forces acting on the body B for the three types of generalized coordinates. These typically include all forces due to spring, damper, and actuator elements.

Together with the obtained definitions for the kinetic energy T_B , the elastic strain energy U_B , and the generalized applied forces \underline{Q}_B^e , the use of Lagrange's equation results in the equations of motion of a single flexible body B , without constraint equations [14]:

$$\begin{bmatrix} \underline{m}_{rr} & \underline{m}_{r\theta} & \underline{m}_{r\eta} \\ \underline{m}_{\theta r} & \underline{m}_{\theta\theta} & \underline{m}_{\theta\eta} \\ sym. & \underline{m}_{\eta r} & \underline{m}_{\eta\eta} \end{bmatrix} \begin{bmatrix} \ddot{\underline{r}}_B \\ \ddot{\underline{\theta}}_B \\ \ddot{\underline{\eta}}_B \end{bmatrix} + \begin{bmatrix} 0 & 0 & 0 \\ 0 & 0 & 0 \\ 0 & 0 & \underline{K}^{red} \end{bmatrix} \begin{bmatrix} \underline{r}_B \\ \underline{\theta}_B \\ \underline{\eta}_B \end{bmatrix} = \begin{bmatrix} (\underline{Q}_B^e)_{r_B} \\ (\underline{Q}_B^e)_{\theta_B} \\ (\underline{Q}_B^e)_{\eta_B} \end{bmatrix} + \begin{bmatrix} (\underline{Q}_B^v)_{r_B} \\ (\underline{Q}_B^v)_{\theta_B} \\ (\underline{Q}_B^v)_{\eta_B} \end{bmatrix}, \quad (7.20)$$

where \underline{m}_{ij} with $i, j \in \theta, r, \eta$, are submatrices of \underline{M}_B , \underline{Q}_B^e are the externally applied generalized forces, and \underline{Q}_B^v are the quadratic velocity vectors resulting from the differentiation of the kinetic energy with respect to the body coordinates and with respect to time. These describe the gyroscopic and Coriolis force components [8, p. 221].

The equations of motion of the total system, as described by (7.1), can be obtained by combining the equations of motion of the individual n_B bodies, together with constraint equations of the Euler parameters and the kinematic constraints between the bodies. This system of equations can be systematically assembled from (7.20). For a complete derivation of these equations, a reference is made to [10, 14, 15].

7.2.1.3 Modal Reduction: Craig-Bampton

As described in Sect. 7.2.1.1, a modal representation of each flexible body is required to incorporate its non-rigid body dynamics in the equations of motion of the multi-body system. By introducing modal deformation coordinates $\underline{\eta}$ instead of nodal displacements and rotations \underline{u} in (7.8), the total number of generalized coordinates \underline{q} required to describe the dynamics can be reduced. The challenge arises to select a set of modes that in a linear combination can accurately represent the local deformations of the body.

An often used reduction method is the one developed by Craig and Bampton [1]. Assuming that a lumped mass finite-element model and mesh are defined for the flexible body, the dynamic response of the undamped flexible body can be described by the differential equations

$$\underline{M} \ddot{\underline{u}}(t) + \underline{K}\underline{u}(t) = \underline{F}(t), \quad (7.21)$$

where \underline{M} and \underline{K} are respectively the $(n_u \times n_u)$ mass and stiffness matrices, \underline{F} is the $(n_u \times 1)$ column of applied loads, and \underline{u} is a $(n_u \times 1)$ column with n_u displacement DOFs of the model.

In the applied Craig-Bampton method, the DOFs \underline{u} are separated in n_{bo} boundary, or interface, DOFs \underline{u}_b and n_{in} internal DOFs \underline{u}_i :

$$\underline{u} = \begin{bmatrix} \underline{u}_b \\ \underline{u}_i \end{bmatrix}. \quad (7.22)$$

The boundary DOFs are defined to be the DOFs that are connected to other bodies in the multibody simulation through joint or force elements.

Static constraint modes are used to exactly represent the static deformation of the body due to force elements and joint reaction forces at the boundary DOFs. After partitioning (7.21) according to (7.22), resulting in

$$\begin{bmatrix} \underline{M}_{bb} & \underline{M}_{bi} \\ \underline{M}_{ib} & \underline{M}_{ii} \end{bmatrix} \begin{bmatrix} \ddot{\underline{u}}_b \\ \ddot{\underline{u}}_i \end{bmatrix} + \begin{bmatrix} \underline{K}_{bb} & \underline{K}_{bi} \\ \underline{K}_{ib} & \underline{K}_{ii} \end{bmatrix} \begin{bmatrix} \underline{u}_b \\ \underline{u}_i \end{bmatrix} = \begin{bmatrix} \underline{F}_b \\ \underline{F}_i \end{bmatrix}, \quad (7.23)$$

the internal DOFs can be expressed as function of the boundary DOFs according to

$$\underline{u}_i = -\underline{K}_{ii}^{-1} \underline{K}_{ib} \underline{u}_b. \quad (7.24)$$

The static deformations, expressed as \underline{u}^s , due to loads on the boundary DOFs can now be expressed in terms of the boundary DOFs \underline{u}_b only

$$\underline{u}^s = \begin{bmatrix} \underline{u}_b \\ \underline{u}_i \end{bmatrix} = \begin{bmatrix} \underline{I}_{bb} \\ \underline{T}_{ib} \end{bmatrix} \underline{u}_b = \underline{T}_{nb} \underline{u}_b; \quad \underline{T}_{ib} = -\underline{K}_{ii}^{-1} \underline{K}_{ib}, \quad (7.25)$$

where \underline{I}_{bb} represents the $(n_{bo} \times n_{bo})$ unity matrix. The n_{bo} columns of \underline{T}_{nb} are referred to as the static constraint modes.

The static constraint modes are supplemented with fixed-interface normal modes. These modes are the eigenmodes as calculated from the undamped, free-vibrating body with all boundary DOFs constrained and can be obtained by solving the eigenvalue problem

$$\left[-\omega_j^2 \underline{M}_{ii} + \underline{K}_{ii} \right] \hat{\underline{\psi}}_j = \underline{0}, \quad j = 1, 2, \dots, n_{in} \quad (7.26)$$

where the resulting n_{in} angular eigenfrequencies and fixed-interface normal modes are stored in the matrices

$$\underline{\Omega}_{ii} = \begin{bmatrix} \omega_1 & & & \\ & \omega_2 & & \\ & & \ddots & \\ & & & \omega_{n_{in}} \end{bmatrix}, \quad \underline{\Psi}_{ii} = \begin{bmatrix} \hat{\underline{\psi}}_1 & \hat{\underline{\psi}}_2 & \hat{\underline{\psi}}_3 & \dots & \hat{\underline{\psi}}_{n_{in}} \end{bmatrix}. \quad (7.27)$$

In order to sufficiently reduce the number of coordinates describing the deformation of the body, usually a limited set of normal modes $\hat{\underline{\psi}}_j$ is taken into account. The

matrix containing the selected kept fixed-interface normal modes is indicated with $\underline{\Psi}_{ik}$. This subset of n_k kept normal modes is used to define the dynamic part of the deformation according to

$$\underline{u}^d = \begin{bmatrix} \underline{u}_b \\ \underline{u}_i \end{bmatrix} = \begin{bmatrix} \underline{O}_{bk} \\ \underline{\Psi}_{ik} \end{bmatrix} \underline{\zeta}_k , \quad (7.28)$$

where \underline{O}_{bk} is the $(n_{bo} \times n_k)$ zero-matrix, corresponding to the fixed boundary DOFs, and $\underline{\zeta}_k$ are the modal coordinates corresponding to the kept fixed-interface normal modes.

Combining the static constraint modes and the kept fixed-interface normal modes, the deformation of the body is approximated by

$$\underline{u} = \underline{u}^s + \underline{u}^d = \begin{bmatrix} \underline{I}_{bb} \\ \underline{T}_{ib} \end{bmatrix} \underline{u}_b + \begin{bmatrix} \underline{O}_{bk} \\ \underline{\Psi}_{ik} \end{bmatrix} \underline{\zeta}_k = \begin{bmatrix} \underline{I}_{bb} & \underline{O}_{bk} \\ \underline{T}_{ib} & \underline{\Psi}_{ik} \end{bmatrix} \begin{bmatrix} \underline{u}_b \\ \underline{\zeta}_k \end{bmatrix} = \underline{\Psi}_{CB} \underline{\eta}_{CB} , \quad (7.29)$$

where $\underline{\eta}_{CB} = [\underline{u}_b^T \underline{\zeta}_k^T]^T$ and $\underline{\Psi}_{CB}$ is the Craig-Bampton reduction matrix. In order to obtain a significant reduction it is required that $n_{bo} + n_k \ll n_u$. By substituting (7.29) in (7.21) and premultiplying with $\underline{\Psi}_{CB}^T$, the equations of motion can be reduced to

$$\underline{M}^{CB} \ddot{\underline{\eta}}(t) + \underline{K}^{CB} \underline{\eta}(t) = \underline{F}^{CB}(t) , \quad (7.30)$$

where $\underline{M}^{CB} = \underline{\Psi}_{CB}^T \underline{M} \underline{\Psi}_{CB}$, $\underline{K}^{CB} = \underline{\Psi}_{CB}^T \underline{K} \underline{\Psi}_{CB}$, and $\underline{F}^{CB} = \underline{\Psi}_{CB}^T \underline{F}$.

The eigenmodes of (7.30) are orthogonalized with respect to \underline{M}^{CB} and \underline{K}^{CB} before integrating them in the equations of motion of the multibody system [10]. This both improves the numerical performance of multibody solver and enables the identification of possible rigid body modes, which are to be excluded from the set of modal coordinates, since the rigid body motion in the multibody formulation is already defined by the reference coordinates \underline{r}_B and $\underline{\theta}_B$.

In order to obtain the orthogonalized mode set, the generalized eigenvalue problem

$$[-\hat{\omega}_j^2 \underline{M}^{CB} + \underline{K}^{CB}] \underline{\xi}_j = \underline{0}, \quad j = 1, 2, \dots, (n_{bo} + n_k) , \quad (7.31)$$

is solved, where $\hat{\omega}_j$ are the undamped angular eigenfrequencies and $\underline{\xi}_j$ the corresponding eigenvectors. The eigenvectors are gathered in the columns of the matrix

$$\underline{\Xi} = \begin{bmatrix} \underline{\Xi}_{rb} & \underline{\Xi}_{fl} \end{bmatrix} , \quad (7.32)$$

which is partitioned in possible rigid body modes $\underline{\Xi}_{rb}$ and the flexible modes $\underline{\Xi}_{fl}$. The rigid body modes are identified by their eigenfrequencies $\hat{\omega}_j$ being (almost) zero. To avoid a redundant description of the rigid body modes in the multibody formulation, the set $\underline{\Xi}_{rb}$ is not used. The modes $\underline{\Xi}_{fl}$ linearly transform the modes $\underline{\Psi}_{CB}$ into the new, orthogonalized mode set

$$\underline{\Psi} = \underline{\Psi}_{CB} \underline{\Xi}_{fl} , \quad (7.33)$$

which is used in the multibody formulation and couples the final generalized DOFs $\underline{\eta}$ to the original set of physical DOFs \underline{u} according to

$$\underline{u} = \underline{\Psi} \underline{\eta} . \quad (7.34)$$

The final reduced version of (7.21) becomes

$$\underline{\Psi}^T \underline{M} \underline{\Psi} \ddot{\underline{\eta}} + \underline{\Psi}^T \underline{K} \underline{\Psi} \dot{\underline{\eta}} = \underline{\Psi}^T \underline{F} , \quad (7.35)$$

where $\underline{\Psi}^T \underline{K} \underline{\Psi} = K^{red}$ is the reduced stiffness matrix and $\underline{\Psi}^T \underline{M} \underline{\Psi} = m_{\eta\eta}$ is the component of the mass matrix corresponding to the modal coordinates in (7.20).

7.2.2 Tire Dynamics

Tire dynamics form an essential part in accurately describing the wheel shimmy phenomenon. A tire model, featured in the Virtual.Lab software [10], describes the dynamics between the tire body and the runway. Based on the position and velocity of the tire with respect to the runway, the resulting normal force F_n , lateral force F_y , longitudinal force F_x , and self-aligning moment around the vertical axis M_z from the road to the tire are determined.

Of these forces, F_y and M_z have the largest influence on the shimmy oscillations, because the oscillations are characterized most by lateral and yaw motion of the tire. The lateral force F_y is a function of the side slip angle α . This angle is defined as the acute angle between the longitudinal tire direction, associated with a longitudinal velocity vector \vec{V}_x , and the velocity vector \vec{V}_{BP} of the bottom point of the tire. These vectors are visualised in Fig. 7.3a. The side slip angle is calculated as

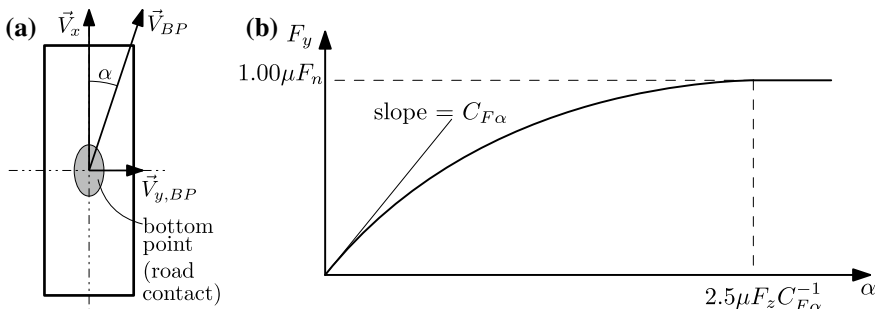


Fig. 7.3 a Top view of a tire with velocity and side slip angle definitions. b Tire lateral force as function of the side slip angle [10]

$$\alpha = \tan^{-1} \left(\frac{|\vec{V}_{y,BP}|}{|\vec{V}_x|} \right) . \quad (7.36)$$

The instantaneous lateral force F_y is defined as a third-order polynomial function of α for $0 < \alpha < 2.5\mu F_n C_{F\alpha}^{-1}$ [10], as shown in Fig. 7.3b. The boundary conditions of $F_y(\alpha)$ are defined as

$$F_y(0) = 0; \quad \frac{dF_y}{d\alpha}(0) = C_{F\alpha}; \quad F_y(2.5\mu F_n C_{F\alpha}^{-1}) = \mu F_n; \quad \frac{dF_y}{d\alpha}(2.5\mu F_n C_{F\alpha}^{-1}) = 0 , \quad (7.37)$$

where $C_{F\alpha}$ is a user-supplied constant indicating the cornering stiffness of the tire and μ is the static friction coefficient between the tire and the road. For small slip angles, this cornering stiffness dictates the lateral force characteristic of the tire. For larger slip angles, the force F_y reaches a maximum of μF_n and stays constant for $\alpha > 2.5\mu F_n C_{F\alpha}^{-1}$.

In reality, the lateral force does not act exactly on the bottom point of the tire, but rather just behind it. Therefore, the self-aligning moment is introduced and defined by

$$M_z = -r_p F_y , \quad (7.38)$$

where r_p is the pneumatic trail, which is assumed to be constant.

7.2.2.1 Relaxation Behavior

The response of the lateral force to side slip is not instantaneous. There is a phase lag between the side slip angle α and the developed lateral force F_y . This relaxation behavior of the tire is characterised by the relaxation length σ . This is the distance a tire has to roll in order to generate 63% of the steady-state lateral force, assuming α is constant.

In this particular tire model, the relaxation behavior of the tire is modeled by introducing a relaxation time t_σ for the lateral force and self-aligning moment:

$$\dot{\tilde{F}}_y = \frac{1}{t_\sigma} (F_y - \tilde{F}_y) , \quad \dot{\tilde{M}}_z = \frac{1}{t_\sigma} (M_z - \tilde{M}_z) , \quad (7.39)$$

where the relaxation time is derived from the relaxation length according to

$$t_\sigma = \frac{\sigma}{|\vec{V}_x|} . \quad (7.40)$$

In (7.39), \tilde{F}_y and \tilde{M}_z are the lateral force and self-aligning moment that include the relaxation behavior. The two differential equations in (7.39) are added to the system of DAE that are analysed by the Motion solver. Therefore, \tilde{F}_y and \tilde{M}_z appear as additional states \underline{x} in (7.3).

Before the calculated forces and moments (F_n , F_x , \tilde{F}_y , and \tilde{M}_z) are applied to the tire body in the multibody system, the friction limit is taken into account. This implies that the vector sum of the lateral and longitudinal forces is reduced in case it exceeds the maximum friction force generated by the tire, according to

$$\sqrt{F_x^2 + \tilde{F}_y^2} \leq \mu F_n . \quad (7.41)$$

7.3 Multibody Model of a Nose Landing Gear

A dedicated multibody model is created to conduct a shimmy study. This model is referred to as the ‘bifurcation study model’, or simply the ‘study model’. The functionalities of a parameterized CAD model of a landing gear, supplied by Fokker LG, are employed to generate the CAD geometry of the multibody study model. The study model contains many of the complexities that are normally present in multibody landing gear models used in the landing gear industry.

7.3.1 Landing Gear Model for Bifurcation Study

A side view of the study model is shown in Fig. 7.4. The figure shows the landing gear structure, the runway, and the airframe. Global coordinate directions are included in all figures. Standard aircraft industry coordinate definitions are used, with the x -axis directed rearward in the longitudinal direction and the z -axis directed vertically upwards.

The airframe, which is represented by dashed lines, is a rigid frame representing the fuselage of the aircraft to which the landing gear is attached. It has a mass that induces the nominal vertical force on the landing gear structure. The airframe is constrained to move only vertically with respect to the fixed global axis system, so

Fig. 7.4 Side view of the study model

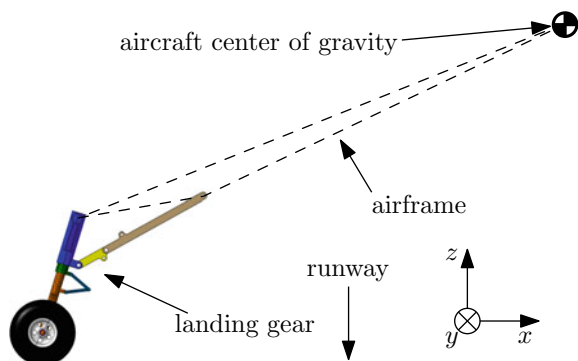
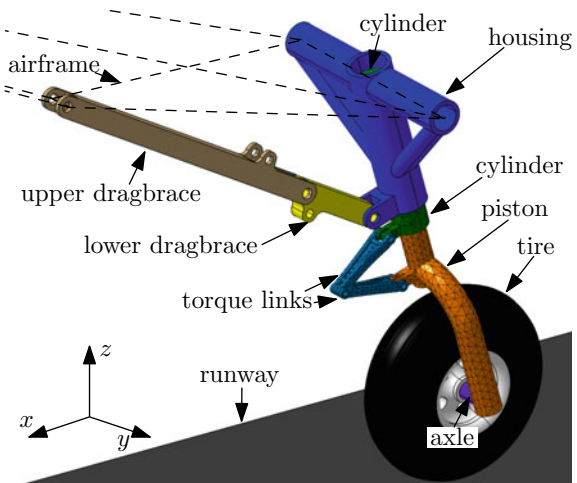


Fig. 7.5 Isometric view of the rear side of the study model, including the names of the individual bodies



the landing gear can drop down onto the runway. The runway is moved backwards relative to the landing gear to simulate a forward motion of the aircraft.

A more detailed, isometric view of the landing gear is shown in Fig. 7.5. All bodies are colored separately and their names are indicated using labels. Again, the airframe is represented by dashed lines. Connected to the airframe are the housing and the upper drag brace. The two are connected through the lower drag brace. These three rigid bodies are constrained such that these cannot move with respect to the airframe or to each other. Therefore, the airframe, upper- and lower drag brace, and the housing move as one rigid body. The bodies are constrained in a statically determined way, as to not introduce any redundant constraints.

The housing takes up a cylindrical part named the cylinder. Between these two bodies, only rotation about their co-axial axis is allowed. During taxiing, this DOF enables the steering of the nose landing gear. During landing or take off, the steering actuator is turned off. In that case, hydraulic shimmy damping is supplied to this DOF by the same actuator. A quadratic damping curve is used to model the hydraulic damping. The used nonlinear relation for the damping moment is displayed in Fig. 7.6a, and is similar to the characteristics of a shimmy damper used in the industry. In case the steering actuator is turned on, linear rotational stiffness and damping are applied on this DOF instead.

The piston can move axially with respect to the cylinder, as well as rotate about their co-axial axis. In reality, this motion is enabled by two bearings that guide the sliding and rotating motion of the piston with respect to the cylinder. In the multibody model, flexible-point-curve-joint constraints [10] are used to simulate these bearings and constrain the two flexible bodies together. This particular landing gear has an asymmetric piston, with a half-forked design, see Fig. 7.5. The piston also forms the bottom of the shock absorber. A vertical shock absorber force acts between the cylinder and the piston. The static shock absorber force is modeled by a non-linear,

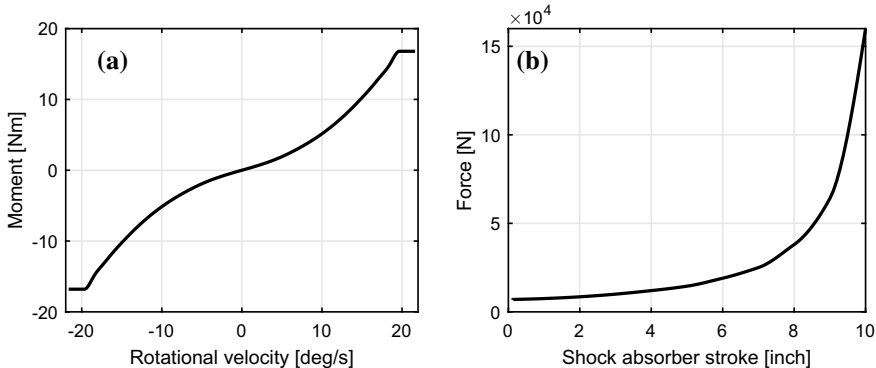


Fig. 7.6 **a** Nonlinear damping moment curve of the shimmy damper. **b** Nonlinear shock absorber force

progressive spring, closely resembling the static shock absorber forces as experienced in industry models. The force is detailed as a function of shock absorber stroke in Fig. 7.6b.

The torque links are two bars that are hinged together. These restrict the rotation of the piston relative to the cylinder, without constraining the shock absorber stroke. Therefore, the torque links determine to a large extent the yaw-stiffness of the landing gear structure. The design of the two torque links is identical.

A rigid axle connects the tire to the piston. The tire is simulated by a rigid body, which is only used to characterize the tire mass and rotational inertia. The forces exerted on the tire by the runway are calculated using the tire model described in Sect. 7.2.2. This model is featured in the Virtual.Lab Motion software and is also used in the landing gear industry.

7.3.1.1 Structural Flexibility—Modal Reduction

For the bodies described in Sect. 7.3.1, the structural compliance of the cylinder, the piston, and the two torque links is taken into account. By default, the Virtual.Lab software only supports Component Mode Synthesis (CMS) as a method to model the flexibility of bodies. Therefore, Craig-Bampton mode sets are used. To this end, a finite element mesh is created for each body, and the interface DOFs are determined, based on the joints and actuators attached to each body. According to the theory described in Sect. 7.2.1.3, static constraint modes are determined for each body, along with fixed-interface normal modes. Material properties of steel are used for all flexible bodies, with a mass density of 7860 kg/m^3 , a Young's modulus of $2 \times 10^{11} \text{ N/m}^2$, and a Poisson ratio of 0.226.

Due to the various joints and force-elements connected to the flexible bodies, 53 static constraint modes are required to represent the static stiffness of the four flexible bodies: 10 for each torque link, 18 for the piston, and 15 for the cylinder. In

order to reduce the model complexity sufficiently to stay within the limitations of the simulation framework, no normal modes are included in the mode sets for the flexible bodies: i.e., $n_k = 0$, in (7.28). Therefore, the total number of modal coordinates n_η is given by the number of static constraint modes minus the 4×6 rigid body modes. This results in 29 modal coordinates.

In order to verify whether the applied reduction has a significant effect on the dynamics of the system, the reduced study model is compared to an unreduced model. As use of CMS is required, a model with larger Craig-Bampton mode sets is assumed to approximate the unreduced model sufficiently accurately. For this ‘unreduced’ model, Craig-Bampton mode sets with $n_k = 10$ kept fixed-interface normal modes per flexible body are used.

The eigenfrequencies and dimensionless damping ratios of the two linearized landing gear models are compared. A simulation is performed on each of the models, where the landing gear is suspended stationary in the air, without tire-road contact. The shock absorber stroke is fixed at 5 in., which is midway between fully compressed and fully extended. By computing the linearized system matrix in this equilibrium situation, the eigenmodes, eigenfrequencies, and dimensionless damping ratios can be determined. The latter two quantities are calculated from the eigenvalues of the system λ_i , according to $\omega_{u,i} = \sqrt{Re(\lambda_i)^2 + Im(\lambda_i)^2}$, where $\omega_{u,i}$ indicates the i^{th} undamped angular eigenfrequency, and $\zeta_i = \frac{-Re(\lambda_i)}{\omega_{u,i}}$, where ζ_i is the corresponding dimensionless damping ratio. Even though the multibody system is generally viscously damped, the dimensionless damping ratios (which in principle only can be used in the proportionally damped case) characterize the damping of the modes, assuming these are only weakly damped. The lowest six eigenfrequencies of both models, including damping factors, are listed in Table 7.1. Visualisations of these eigenmodes are shown in Fig. 7.7a, b.

The results show that there are 2 rigid body modes present in the model, if there is no tire road contact. These are the unobstructed rotation of the tire body and the yaw motion of the entire ‘tire-axle-piston-torque links-cylinder’ sub-structure with respect to the housing. The latter is caused by the steering DOF between the cylinder

Table 7.1 The lowest six eigenfrequencies and the corresponding damping factors of the unreduced study model and the reduced study model

Mode shape	Unreduced study model		Reduced study model	
	ω_u (Hz)	ζ (-)	ω_u (Hz)	ζ (-)
Rigid body wheel	0.01		0.03	
Rigid body yaw	0.02		0.03	
Longitudinal bending	43.0	0.037	46.5	0.034
Lateral bending	47.0	0.038	47.0	0.038
Yaw, torsional	95.8	0.10	95.8	0.10
Lateral bending (2nd)	179.2	0.059	178.8	0.061
...	>300	...	>300	...

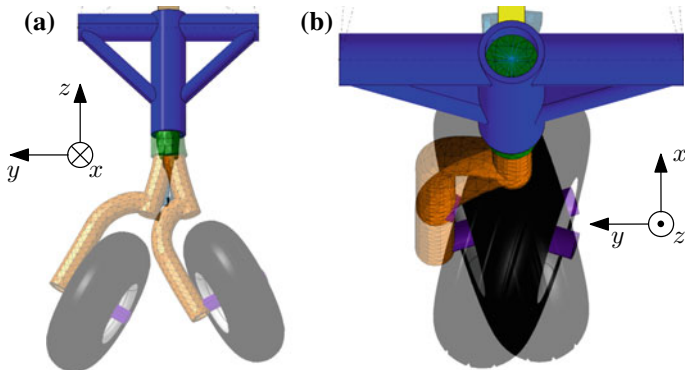


Fig. 7.7 **a** Visualisation of the first lateral bending mode of the study model. **b** Visualisation of the first torsional mode of the study model

and the housing, because the steering actuator, when turned off, does not include any stiffness.

The two most relevant eigenmodes for the shimmy phenomenon are the first lateral bending mode and the first torsional mode. The results show that these remain virtually unchanged by the modal reduction. There is a notable difference in the eigenfrequency of the longitudinal bending mode: roughly 8% between the reduced and the unreduced model. However, in a single-wheeled landing gear, such as presented here, the longitudinal structural dynamics have a relatively small effect on shimmy. Therefore, it can be concluded that the applied modal reduction is sufficiently accurate for the purpose of a shimmy analysis.

7.3.1.2 Model Dimension of the Study Model

The total multibody model contains 16 bodies. These also include weightless dummy-bodies that do not affect the dynamics and are mostly used for modeling convenience. The rigid body motion of all the bodies is described by $7 \times 16 = 112$ generalized coordinates. Furthermore, the structural flexibility of four of the bodies is described by 29 modal coordinates in total, as described in Sect. 7.3.1.1. Each of the two flexible-point-curve-joints introduces 1 dependent generalized coordinate. Lastly, for the Motion solver, torsional springs introduce additional redundant generalized coordinates, which represent the rotational displacement of the respective spring. There are 3 of these torsional springs present in the model, bringing the total count to 146 generalized coordinates in \underline{q} .

Together with the 16 Euler parameter constraints, the joints and drivers in the model introduce a total of 114 constraint equations. By subtracting this number from the total number of generalized coordinates, the total number of independent generalized coordinates can be determined, which is 32. Therefore, the total first

Fig. 7.8 Calculation resulting in the number of independent states in the first-order equation of motion (7.3) for the study model

Bodies	$16 \times 7 =$	112
Modal coordinates	$4 + 4 + 12 + 9 =$	29
flex-point-curve-joints	$2 \times 1 =$	2
Torsional springs	$3 \times 1 =$	3 +
Generalized coordinates in \underline{q}	146	
Euler parameter constraints	$16 \times 1 =$	16
Joint/driver constraints		98 -
Indep. generalized coord. \underline{q}_I	32 × 2	
Indep. states \underline{x}_I	64	
Tire states χ		2 +
Independent states in (3)		66

order representation of the equations of motion, as described by (7.3), contains 66 independent states, as there are also two tire states χ added, as described in Sect. 7.2.2.1. This calculation is summarized in Fig. 7.8.

7.3.2 Comparison to an Industry Model

The study model, as presented above, is based on the nose landing gear of a typical fighter aircraft. In order to verify if the dynamic behavior of the study model is indeed realistic for such a landing gear, it is compared to the dynamic behavior of the original multibody model made by Fokker Landing Gear, which represents a nose landing gear of a typical fighter aircraft. The latter model is referred to as the ‘industry model’.

7.3.2.1 The Industry Model

Before the two models are compared, the industry model is simplified to a certain extent, to ensure that both models include the same dynamic effects. This implies that the following features are removed from the industry model before analysis:

- The **airframe stiffness** is normally taken into account in Fokker models. For purposes of this study, the airframe stiffness is removed from the industry model and the assumption is made that the airframe is completely rigid.
- Standard multibody models from Fokker include **free-play**. This can for instance be lateral free-play between the landing gear structure and the airframe, as well as free-play in the torque links, which affects the yaw motion of the tire. These types of free-play can result in small-amplitude limit cycle oscillations of the landing

gear at all forward velocities. These are too small to be considered as shimmy, but are periodic solutions of the system nonetheless. Even though continuation of periodic solutions is possible using AUTO, it is computationally more expensive than continuation of (quasi-)static solutions and is not considered here. Therefore, the free-play is not taken into consideration and is removed from the industry model. All the connections that are originally governed by free-play are considered close fits.

- In the original Fokker model, the rotational **friction** of the bearings between the piston and the cylinder is taken into account. In the industry model discussed here, all friction is neglected. In a shimmy analysis, friction tends to hide shimmy behavior, as it dissipates energy from the system. Therefore, neglecting friction can be considered to be a worst-case assumption with respect to the emergence of shimmy.

These simplifications imply that the dynamic behavior of the model indicated here as ‘industry model’ will be slightly different from those used in reality. However, the main effects that influence shimmy behavior, such as the tire dynamics and viscous shimmy damper properties, remain unchanged.

Even though the industry model is simplified to some extent, it still exceeds the study model in terms of complexity. In this case, the industry model contains 26 bodies, of which 6 bodies are flexible. This results in an industry model having more than 400 independent states in the first-order form of the equations of motion. As a model of this size still imposes computational challenges for the current bifurcation analysis framework, the study model, with 66 independent states, is used to conduct the bifurcation analysis.

7.3.2.2 Structural Compliance Comparison

Since both models now contain the same dynamic effects, a comparison is pursued. The comparison focuses on the dynamic properties of the landing gear structure, because these are influenced most by the geometry of the bodies, which is slightly different for both models.

The static stiffness is determined by performing time-simulations of both models where a unit force/moment is applied to the axle, in a situation where the airframe is fixed in space while there is no tire-road contact. For this particular analysis, the rotation between the piston and the cylinder is suppressed. The resulting lateral stiffness and yaw stiffness of the landing gear are shown in Fig. 7.9a and Fig. 7.9b, respectively. These are known to have the largest influence on the shimmy behavior compared to stiffnesses in other directions.

Figure 7.9a, b show the stiffness as function of the shock absorber stroke, where 0 in. corresponds to a fully extended shock absorber and 10 in. to a fully compressed shock absorber. In both models, the stiffness increases with increasing shock absorber stroke. In the lateral direction, as seen in Fig. 7.9a, this increase can partially be explained by the fact that the arm at which the lateral force acts on the structure

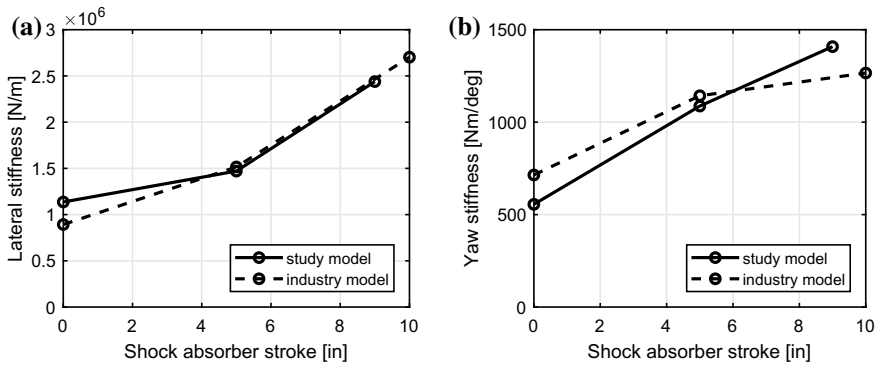


Fig. 7.9 **a** Lateral stiffness of the landing gear structure of the study model, compared to the industry model. **b** Yaw stiffness of the landing gear structure of the study model, compared to the industry model

is a function of the shock absorber stroke. Secondly, a larger part of the piston is inserted in the cylinder if the shock absorber is compressed, thereby also increasing the lateral stiffness. In the yaw direction, shown in Fig. 7.9b, the stiffness is affected the most by the relative angle of the two torque links, which directly depends on the shock absorber stroke. This greatly effects the yaw stiffness.

When comparing the structural stiffness of the two models, it can be seen that both models are in agreement, even though the study model contains less flexible components. It can thus be concluded that the four flexible components of the study model approximate the compliance of much larger industry model accurately.

7.3.2.3 Eigenvalue Analysis

The study model and the industry model are also compared by analyzing eigenfrequencies and modal damping factors of the linearized systems. The same method as described in Sect. 7.3.1.1 is employed: the system is linearized around a static equilibrium situation, where there is no tire-road contact. The relevant resulting eigenfrequencies, and modal damping factors of the two models are shown in Table 7.2.

The results show that the eigenfrequencies of both models are largely in accordance. Most relevant are the eigenfrequencies of the lateral bending mode and the torsional mode in the yaw direction. The lateral bending eigenfrequency compares well, as there is only 2% difference between the eigenfrequencies. The difference between the eigenfrequencies in the yaw direction is with 12% slightly larger. This might be caused by a different mass distribution between the two models.

Furthermore, the damping factors of the lateral and longitudinal modes differ by roughly one order of magnitude between the models. This might be a consequence of the additional flexible bodies in the industry model. The damping factor in yaw-direction is in accordance.

Table 7.2 Relevant Eigenfrequencies and damping factors of the study model and the industry model

Mode shape	Study model		Industry model	
	ω_u (Hz)	$\zeta (-)$	ω_u (Hz)	$\zeta (-)$
Longitudinal bending	46.5	0.034	47.6	0.0025
Lateral bending	47.0	0.038	46.1	0.0035
Yaw, torsional	95.8	0.10	109.4	0.099

7.4 Continuation Analysis of a Multibody System

A recently developed simulation framework by Tartaruga et al. [11] is adapted to perform 1-parameter bifurcation analyses on the study model as described in Sect. 7.3.1. The continuation software AUTO [5] is coupled to the VirtualLab Motion multibody solver through MATLAB. A custom version of the Motion solver is used that includes a MATLAB interface. This interface makes all the states \underline{x} of the first-order equations of motion, (7.3), and the bifurcation parameters of a model available in the MATLAB-workspace.

The bifurcation analysis has to be started from a (quasi-)static stable equilibrium solution of the system. This solution is obtained by integrating the equations of motion, (7.3), in time, from an initial configuration, until the transient dynamics have damped out and the time derivatives of all states are below a small tolerance value. The solution is then assumed to be close enough to the final (quasi-)static solution and the values of all the independent states are stored for use in the next step of the analysis.

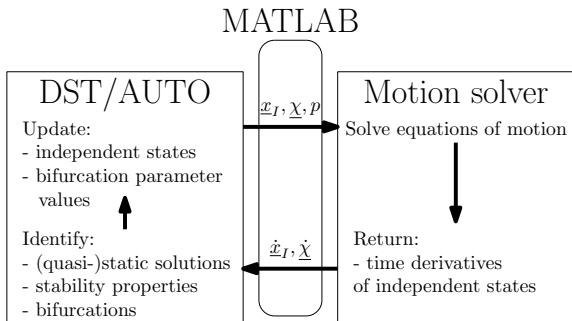
From this initial solution, the challenge is to find subsequent (quasi-)static solutions for varying values of the bifurcation parameter. For this, the Dynamical Systems Toolbox (DST) is employed [3]. The DST is an open source MATLAB-toolbox that encapsulates all the functionalities of the bifurcation software AUTO. The original FORTRAN-code of AUTO is integrated in the toolbox via ‘MATLAB-executable’-files, or MEX-files. The toolbox is normally used to compute branches of solutions of analytical nonlinear systems by evaluating the time derivatives of the states as function of the states and a bifurcation parameter p , according to

$$\dot{\underline{y}} = f(\underline{y}, p) . \quad (7.42)$$

By coupling the DST to the Motion solver and performing a co-simulation, one can impose that $\underline{y} = \{\underline{x}_I, \underline{\chi}\}$, and the multibody system can be evaluated by the DST using the same techniques. This co-simulation workflow is visualised in Fig. 7.10.

Figure 7.10 shows that, given a viable set of inputs $\{\underline{x}_I, \underline{\chi}, p\}$, the Motion solver is able to algebraically solve the first-order equations of motion, (7.3), which results in the time derivatives of the states: $\dot{\underline{x}}_I$ and $\dot{\underline{\chi}}$. These are used by the DST, and the underlying AUTO software, to identify (quasi-)static solutions, stability properties

Fig. 7.10 Schematic of the coupling between the dynamical systems toolbox (DST) and the motion solver through MATLAB



and bifurcation points. This is an iterative process, where the DST constantly updates and applies perturbations the states of the model.

During this continuation analysis, the stability properties of the solutions are determined by analyzing the eigenvalues of the system Jacobian around the solution, which is determined through a finite-difference method. These eigenvalues are also used to detect possible Hopf bifurcations, which are defined by a complex conjugate pair of eigenvalues transversely crossing the imaginary axis [12, pp. 200–201]. By monitoring the number of eigenvalues of the Jacobian in the left-half complex plane together with the real part of the eigenvalue closest to the imaginary axis [4], the AUTO software can detect and locate Hopf bifurcations.

The operation of the simulation framework is discussed in more detail in [2]. Furthermore, as described in [11], this simulation framework also allows for the continuation of periodic solutions of small multibody systems. However, because this requires increasing computational effort for larger models, these type of analyses are not considered here.

7.5 Landing Gear Shimmy Analysis Using Bifurcation Methods

The simulation framework presented in Sect. 7.4 is used to analyse the possible occurrence of shimmy in the flexible landing gear multibody model presented in Sect. 7.3. The relevant (and safety critical) case of a leaking shimmy damper is considered. To emulate the loss of damping in the shimmy damper, the damping moment curve, applied by the hydraulic shimmy damper and shown in Fig. 7.6a, is reduced by a factor d_{damper} . Initially d_{damper} is chosen to be 0.03. This corresponds to a damping moment of only 3% of the original value. As will be shown, this will lead to shimmy within the operational parameter space.

A 1-parameter bifurcation analysis is performed on the landing gear model. The relative velocity of the runway with respect to the landing gear V is chosen to be the primary bifurcation parameter as the velocity has a large influence on the occurrence

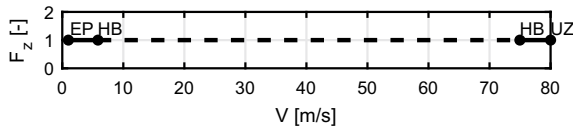
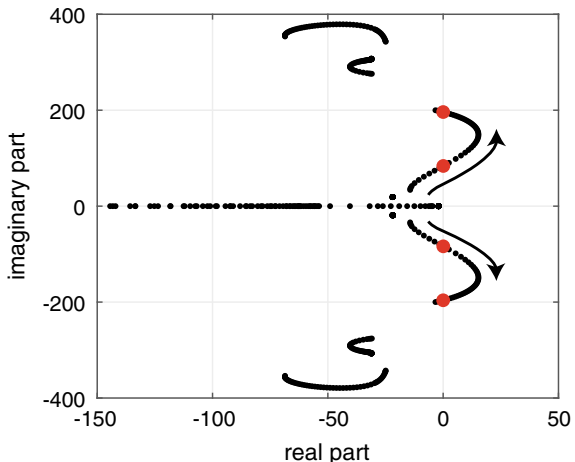


Fig. 7.11 1-Parameter bifurcation diagram. ‘EP’ and ‘UZ’ indicate the start and end of the solution branch respectively. HB indicates a supercritical Hopf bifurcation

Fig. 7.12 Eigenvalues of the system Jacobian for the solutions presented in Fig. 7.11. Arrows indicate the trace of the eigenvalues for increasing velocity V . Only the eigenvalues closest to the imaginary axis are shown. The critical eigenvalue pairs are indicated with larger dots



of shimmy and it can vary significantly during landing and take-off events. The result of this 1-parameter bifurcation analysis is shown in Fig. 7.11. Solid lines indicate (quasi-)static *stable* solutions, while dashed lines indicate (quasi-)static *unstable* solutions.

The figure shows the bifurcation diagram as function of the velocity, at a constant vertical force F_z . The vertical force is normalized at 20 kN. The continuation analysis is started at a velocity of $V = 1$ m/s. This (quasi-)static starting solution, which is determined using conventional time simulation, is marked with ‘EP’. From this point, the (quasi-)static solution is continued for increasing velocities up to 80 m/s, where the end point of the branch is marked by ‘UZ’. This is the maximum landing/take-off velocity for this type of landing gear. Along the solution branch, two supercritical Hopf bifurcations are encountered at 5.8 and 75 m/s, both marked by ‘HB’. These indicate the edges of a domain where the stationary (quasi-)static solution becomes unstable and a coexisting stable oscillatory solution emerges. This is the velocity range where the landing gear model shows shimmy.

The eigenvalues of the system Jacobian are presented in Fig. 7.12 as function of the landing gear velocity V . The results show that as the velocity V changes, the system dynamics, and thus the eigenvalues of the linearized system, change. One pair of complex conjugate eigenvalues can be observed crossing the imaginary axis to the right-half complex plain and back again. These two crossings represent the

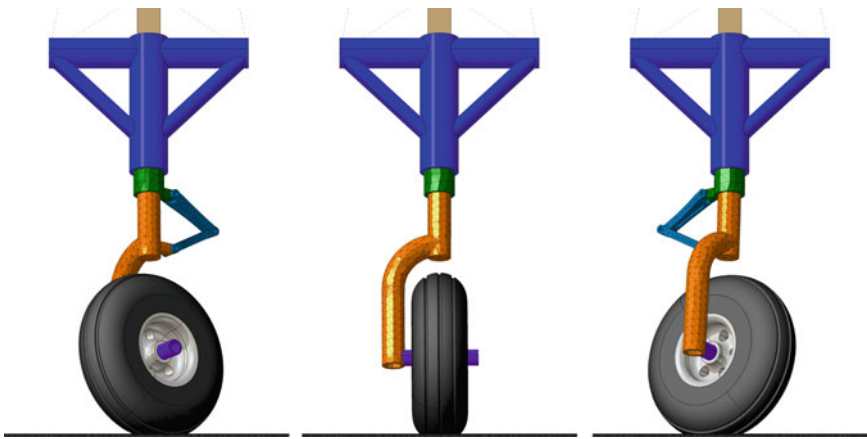


Fig. 7.13 The equilibrium solution at the Hopf bifurcation of $V = 5.8 \text{ m/s}$ (center) and the visualisation of the eigenmode corresponding to the critical eigenvalue pair (left and right)

Hopf-bifurcations at $V = 5.8 \text{ m/s}$ and $V = 75 \text{ m/s}$, respectively, and are marked by larger dots in the figure.

The eigenvectors of the linearized system corresponding to the critical eigenvalue pair can be visualized. The center figure of Fig. 7.13 shows the equilibrium solution of the system at the Hopf bifurcation of $V = 5.8 \text{ m/s}$. Adding or subtracting the real part of the critical eigenvector, which is dominant compared to the negligibly small imaginary part, to this equilibrium solution results in the visualisations shown on the left and right side of Fig. 7.13, respectively. These figures therefore indicate the shape of the landing gear corresponding to the initial oscillation that originates from the Hopf bifurcation. Figure 7.13 shows that the discrete steering DOF, where the shimmy damper acts, is dominant in the oscillating motion. Furthermore, the lateral bending of the piston also plays a significant role.

The (quasi-)static equilibrium solutions of the branch can further be analysed as a function of the bifurcation parameter V . Figure 7.14a, b show the yaw angle and lateral position of the tire as a function of the runway velocity, respectively. The tire has a static yaw angle deflection to the right, due to the asymmetric design of the piston. This static yaw angle is smaller at higher velocities. Figure 7.14b shows that the tire has a small, roughly constant lateral deflection, enabled by the compliance of the flexible piston. The unstable (quasi-)static solutions shown here cannot be determined using time simulation, as these will diverge to a co-existing limit cycle oscillation.

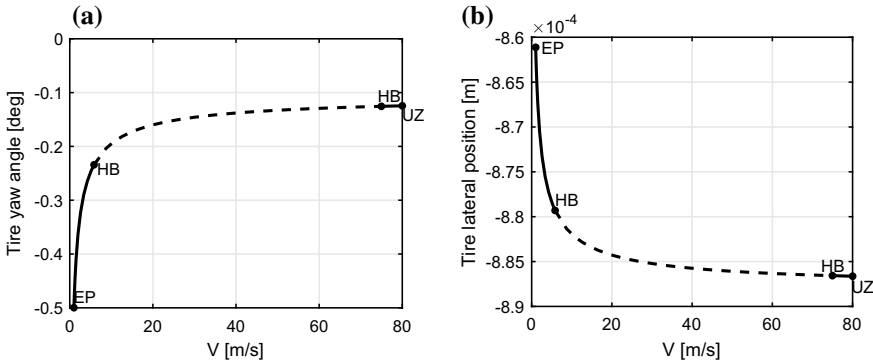


Fig. 7.14 **a** The tire yaw angle of the equilibrium solutions, as function of the bifurcation parameter V at $F_z(\text{norm.}) = 1$. Solid lines are stable solutions, while dashed lines are unstable. **b** The tire lateral position of the equilibrium solutions, as function of the bifurcation parameter V at $F_z(\text{norm.}) = 1$. Solid lines are stable solutions, while dashed lines are unstable

7.5.1 Quasi-2-Parameter Bifurcation Diagrams

The 1-parameter bifurcation analysis can be repeated for different values of the normal force on the landing gear F_z . By doing so, the stability of the landing gear is evaluated in the 2-parameter space (V, F_z) . The results of this quasi-2-parameter bifurcation study are visualized in Fig. 7.15a. Individual 1-parameter bifurcation analyses show the stability of the equilibrium solutions at constant values for F_z . By connecting the Hopf bifurcation points for multiple values of F_z , the stability boundary in the 2-parameter plane can be visualised, as indicated by the black line in Fig. 7.15b. In this figure, the unstable parameter domain is shaded.

The results of the bifurcation analysis are verified through a comparison with standard time simulations of the same multibody model. An aircraft landing is simulated by gradually lowering the landing gear on the moving runway under the influence of gravity and the applied vertical force F_z . After the transient behavior has damped out, the stability properties of the steady-state solution of the model are assessed. This process is repeated for various parameters V and F_z . The results are shown in Fig. 7.15b with black letters, indicating a stable (quasi-)static solution with ‘s’ and an unstable solution with ‘u’. In case of the marker ‘m’, the solution is considered to be marginally stable, as small limit cycle oscillations were found that may only damp out for very long simulation times.

The comparison with 30 of these conventional time-simulations, as displayed in Fig. 7.15b, reveals that the two methods are in accordance. Furthermore, for the results shown here, both methods require a similar amount of computational time. However, the grid of found solutions in the (V, F_z) -parameter space of the bifurcation analysis is much denser and even reveals the exact location of 20 Hopf points on the stability boundary. Achieving the same kind of accuracy with the conventional

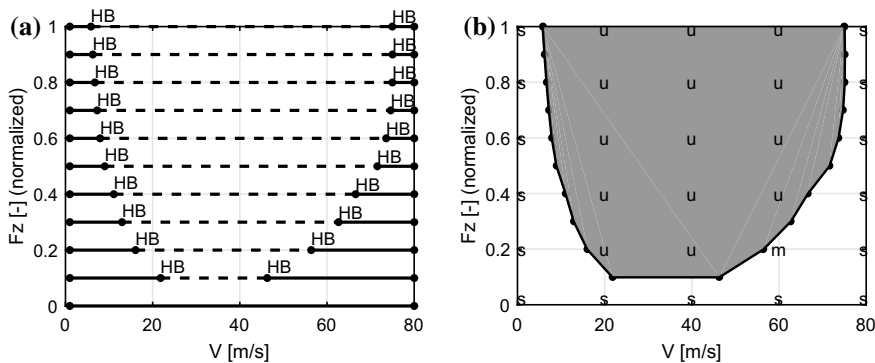


Fig. 7.15 **a** Results of multiple 1-parameter bifurcation analyses, where ‘HB’ indicates the supercritical Hopf bifurcations. Solid lines indicate locally stable solutions, while dashed lines mark local instability of the (quasi-)static solutions. **b** The same stability boundary as in Fig. 7.15a is indicated by a black line and the results of 30 time-domain simulations are indicated by markers: ‘s’ is stable, ‘u’ is unstable, and ‘m’ is marginally stable. The unstable domain is colored gray

time-simulation method would require a multiplication of the performed simulations, and thus of the computational time needed.

When studying the shape of the unstable domain as displayed in Fig. 7.15b, it can be recognized that the range of unstable velocities is smaller at lower vertical loads. The results in Sect. 7.3.2.2 already showed that the lateral and yaw stiffness of the landing gear structure are significantly lower in this region, because the shock absorber is extended. Additionally, tire dynamics will be affected by the decreased vertical force, lowering the ability of the tire to generate lateral force, resulting in less shimmy. Probably, both these effects are responsible for the variation in shimmy behavior as function of the vertical load.

7.5.2 Sensitivity Studies

Using the bifurcation analysis framework, sensitivity studies are performed on the study model. Several design parameters, that are known to have a large influence on the shimmy behavior of the landing gear, are varied and their influence is quantified by generating new quasi-2-parameter bifurcation diagrams, with F_z and V as the bifurcation parameters. Design parameters of interest are the previously discussed reduction factor for the shimmy damper d_{damper} , the mechanical trail, and the steering stiffness.

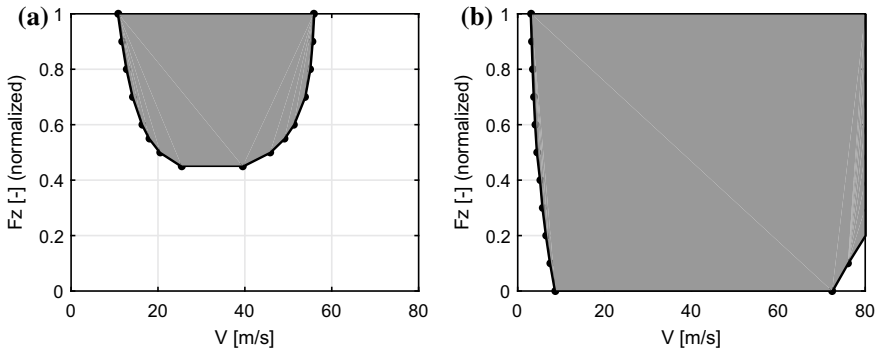


Fig. 7.16 **a** Unstable domain in the (V, F_z) -parameter space for $d_{damper} = 0.04$. The unstable domain is colored gray. **b** Unstable domain in the (V, F_z) -parameter space for $d_{damper} = 0.02$. The unstable domain is colored gray

7.5.2.1 Shimmy Damping Sensitivity Study

The effects of changing the reduction factor d_{damper} of the shimmy damper moment curve are investigated first. The stability boundary is determined using the bifurcation analysis framework, for various values of d_{damper} . The landing gear is found to be stable over the entire considered parameter space, in case $d_{damper} = 1$. From there on, the damping factor is gradually decreased to determine how much shimmy damper malfunction is required for the landing gear stability to be severely compromised.

Results show that even for a reduction factor of $d_{damper} = 0.05$ this landing gear is stable over the entire considered (V, F_z) -space. However, when the damping coefficient of the shimmy damper is reduced further, to $d_{damper} = 0.04$, there emerges an unstable domain for higher vertical loads, as shown in Fig. 7.16a. Further reduction of the damping properties to $d_{damper} = 0.03$, leads to the increase of the size of this unstable domain, as was already shown in Fig. 7.15b. Eventually, when the shimmy damper force is reduced to only 2% of its original value, almost all equilibrium solutions in the operational parameter space are unstable, as is displayed in Fig. 7.16b. In this situation, the shimmy damper is no longer strong enough to prevent shimmy oscillations.

From these results, it can be concluded that the shimmy damper has a significant effect on the stability of the landing gear. Proper damping in the yaw direction is essential to prevent shimmy. Furthermore, it is shown that only after severe failure, i.e., leakage, of the shimmy damper, below $d_{damper} = 0.05$, will shimmy occur within the operational parameter space.

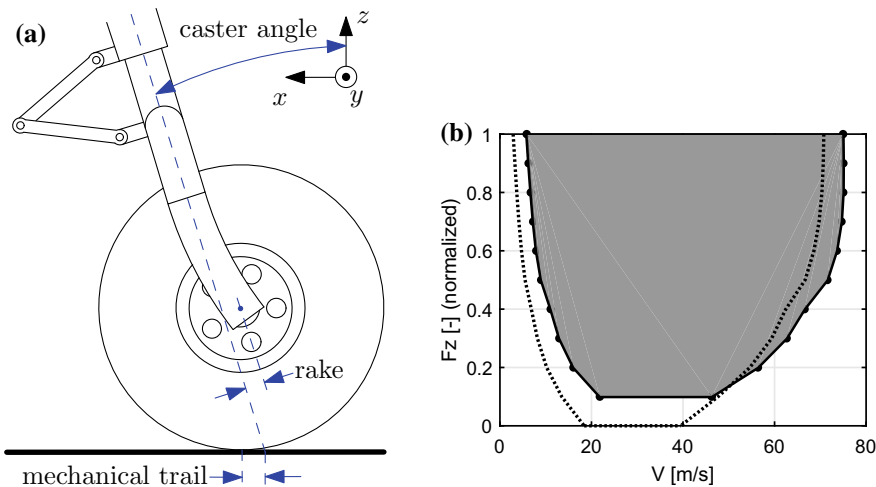


Fig. 7.17 **a** Schematic side view of the bottom part of the nose landing gear, showing the definitions for caster angle, rake, and mechanical trail. **b** Stability boundary for two different rake values. The solid line is 0 mm rake, while dotted line is 15 mm rake. $d_{damper} = 0.03$ in both situations

7.5.2.2 Mechanical Trail Sensitivity Study

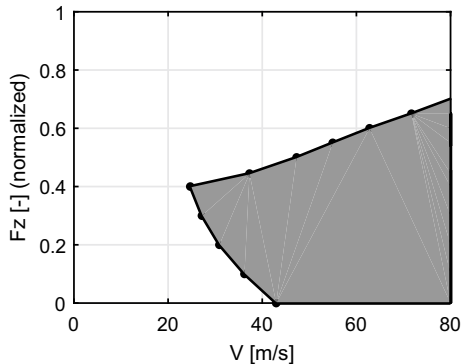
Other design parameters that are at the disposal of the landing gear designer, and that can change the shimmy characteristics of a landing gear, are the rake and the caster angle. As indicated in Fig. 7.17a, the rake is defined to be the offset of the wheel center with respect to the steering axis. Both the rake and the caster angle influence the mechanical trail, which is the distance between the point where the steering axis meets the road and the tire-road contact point, and is known to have a large effect on shimmy behavior.

The study model, as analysed so far and as shown in Fig. 7.5, has a rake of 0 mm. This implies that the piston fork is straight. Together with the caster angle of 17° , this results in a mechanical trail of 67 mm. The bifurcation analysis is repeated with an identical landing gear study model, except for the fact that a rake of 15 mm is implemented, by curving the piston fork forward. This changes both the flexible piston stiffness slightly and results in a reduced mechanical trail of 52 mm.

A bifurcation analysis is performed on the model with a rake of 15 mm and the results are compared to those of the 0 mm rake model, which were already shown in Fig. 7.15b. Both results are combined in Fig. 7.17b. In this figure, the unstable domain of the 0 mm rake model is indicated by the shaded surface and the stability boundary of the 15 mm-rake model is indicated by the dotted line.

The results show that, with respect to the original stability domain, the model with an increased rake has an unstable domain that is roughly the same size. However, the unstable domain shifts to slightly lower velocities.

Fig. 7.18 Unstable domain, in gray, of a landing gear with the steering actuator enabled



7.5.2.3 Steering Actuator Enabled

In all the analysed situations above, the steering actuator of the landing gear is assumed to be off, as it would be during landing or take-off. In the next situation, the steering actuator is assumed to be on, as it would be during a taxi event at low velocities. In that case, the actuator can be modeled as a linear rotational spring-damper with stiffness 10^4 Nm/rad and damping $5 \times 10^3 \text{ Nm s/rad}$. Opposed to the passive shimmy damping results discussed above, the functionality of the steering actuator has not been reduced, i.e., the actuator is assumed to be fully operational. For this situation, the results of a quasi-2-parameter bifurcation analysis are displayed in Fig. 7.18.

The results show that, even with a fully operational steering actuator, the landing gear shows shimmy. The shape of the unstable domain is drastically different from the parabola-like shape encountered in the previous bifurcation analysis results. In this case, the landing gear only experiences shimmy at higher velocities and lower vertical loads. At a normalized vertical force of 0.4, shimmy already starts to occur at a velocity of 25 m/s. However, this will probably not result in any practical problems, because aircraft velocities during taxiing are on average 10 m/s. Time simulations show that, also in this case, where the dynamics are significantly altered with respect to a situation with a disengaged steering actuator, the critical oscillation starts as a yaw oscillation of the landing gear.

7.6 Conclusions

In this chapter, first a complex, high-fidelity, flexible multibody model of a typical industrial nose landing gear is presented. The model contains many of the modeling elements normally encountered in multibody models used in industry, such as complex tire dynamics, complex geometry, non-linear spring/damper elements, and flexible bodies. Reduced Craig-Bampton mode sets are used to approximate

flexible body dynamics. The model is shown to be comparable to a multibody landing gear model used in industry, but with significantly less degrees of freedom, thereby opening possibilities for a bifurcation-based shimmy analysis.

A recently developed simulation framework, that combines AUTO and the Virtual.Lab Motion solver through use of a custom interface with MATLAB, is adapted to perform bifurcation analyses on the landing gear study model. The framework enables the continuation of a branch of (quasi)-static solutions of the multibody model, as function of the horizontal velocity V . By repeating the analysis and varying a second parameter, the vertical normal force F_z , quasi-2-parameter bifurcation diagrams are created.

The practically relevant and safety-critical case of a leaking shimmy damper is considered. The unstable domain, as revealed by a quasi-2-parameter bifurcation analysis, is verified using 30 conventional time simulations. Time-domain steady-state response results are shown to be in accordance with the obtained bifurcation diagram. It is thus shown that it is possible to use the bifurcation analysis framework to analyse the shimmy behavior of complex, high-fidelity multibody models.

A comparison of the computation time reveals that the bifurcation analysis gives a far more detailed view of the stability properties of the model at comparable computational costs, as 20 exact points of the stability boundary are determined. Trying to capture the stability boundary with a comparable accuracy using time-domain simulations would be much more computationally expensive and would be prohibitive in sensitivity studies needed in the context of landing gear design.

Such sensitivity studies are performed to investigate the influence of several design parameters on the bifurcation boundary in the (V, F_z) -parameter space. It is shown that only after severe reduction of the shimmy damper functionality, to less than 5% of its original value, the landing gear will show shimmy within the operational parameter space. Shimmy is more present at higher vertical loads and expands quickly in the (V, F_z) -parameter space if the shimmy damper coefficient is reduced further, indicating the importance of proper shimmy damper operation. Secondly, it is shown that for a model with a decreased mechanical trail, the unstable domain shifts to slightly lower velocities, while its shape and size in the parameter space remain roughly the same. Lastly, in a situation where the steering actuator of the landing gear is turned on, as it would be during taxiing, the additional stiffness in yaw direction leads to drastically different shimmy behavior, mainly present at higher velocities and lower vertical loads.

Acknowledgements The work in this chapter was supported by Siemens PLM Software and Fokker Landing Gear. Their cooperation is gratefully acknowledged.

References

1. Bampton, M.C.C., Craig Jr., R.R.: Coupling of substructures for dynamic analyses. *AIAA J.* **6**(7), 1313–1319 (1968). <https://doi.org/10.2514/3.4741>
2. Beckers, C.J.J., Ongüt, A.E., Verbeek, B., Fey, R.H.B., Lemmens, Y., van de Wouw, N.: Bifurcation analysis of landing gear shimmy using flexible multibody models. In: Ambrósio, J. (ed.) 5th Joint International Conference on Multibody Systems and Dynamics (IMSD), 46, Portugal, June, 24–28 Lisboa (2018). http://imsd2018.tecnico.ulisboa.pt/Web_Abstracts_IMSD2018/pdf/WEB_PAPERS/IMSD2018_Full_Paper_46.pdf
3. Coetzee, E., Thota, P., Rankin, J.: Dynamical Systems Toolbox. <https://nl.mathworks.com/matlabcentral/fileexchange/32210-dynamical-systems-toolbox> (2011). Accessed 14 June 2018
4. Doedel, E., Keller, H.B., Kernevez, J.P.: Numerical analysis and control of bifurcation problems (I): bifurcation in finite dimensions. *Int. J. Bifurc. Chaos* **01**(03), 493–520 (1991). <https://doi.org/10.1142/S0218127491000397>
5. Doedel, E.J., Oldeman, B.E.: AUTO-07P: Continuation and bifurcation software for ordinary differential equations. Technical Report, Concordia University, Montreal. <http://indy.cs.concordia.ca/auto> (2012). Accessed 14 June 2018
6. Haug, E.J.: Computer Aided Kinematics and Dynamics of Mechanical Systems, 1st edn. Allyn and Bacon, 160 Gould Street, Needham Heights, Massachusetts 02194 (1989)
7. Howcroft, C., Lowenberg, M.H., Neild, S., Krauskopf, B., Coetzee, E.: Shimmy of an aircraft main landing gear with geometric coupling and mechanical freeplay. *J. Comput. Nonlinear Dyn.* **10**(5), 051,011 (2015)
8. Shabana, A.A.: Dynamics of Multibody Systems, 4th edn. Cambridge University Press, Cambridge (2013)
9. Siemens Product Lifecycle Management Software Inc.: Case study—GKN Aerospace Fokker Landing Gear. <https://www.plm.automation.siemens.com/pub/case-studies/64181?resourceId=64181> (2017). Accessed 6 Apr 2018
10. Siemens Product Lifecycle Management Software Inc.: LMS Virtual.Lab Motion Online Help (documentation) (2017)
11. Tartaruga, I., Lowenberg, M.H., Cooper, J.E., Sartor, P., Lemmens, Y.: Bifurcation analysis of a nose landing gear system. In: 15th Dynamics Spectral Conference, American Institute of Aeronautics and Astronautics, San Diego, California, USA, AIAA SciTech Forum (2016). <https://doi.org/10.2514/6.2016-1572>
12. Thomsen, J.J.: Vibrations and Stability, 2nd edn. Springer, Berlin, Heidelberg, <https://doi.org/10.1007/978-3-662-10793-5> (2003)
13. Thota, P., Krauskopf, B., Lowenberg, M.H.: Interaction of torsion and lateral bending in aircraft nose landing gear shimmy. *Nonlinear Dyn.* **57**(3), 455–467 (2009). <https://doi.org/10.1007/s11071-008-9455-y>
14. Yoo, W.S., Haug, E.J.: Dynamics of articulated structures. Part I. Theory. *J. Struct. Mech.* **14**(1), 105–126 (1986). <https://doi.org/10.1080/03601218608907512>
15. Yoo, W.S., Haug, E.J.: Dynamics of flexible mechanical systems using vibration and static correction modes. *J. Mech. Trans. Autom.* **108**(3), 315–322 (1986b). <https://doi.org/10.1115/1.3258733>

Chapter 8

Spectral Analysis of Nonlinear Vibration Effects Produced by Worn Gears and Damaged Bearing in Electromechanical Systems: A Condition Monitoring Approach



J. J. Saucedo-Dorantes, M. Delgado-Prieto, R. A. Osornio-Rios
and R. J. Romero-Troncoso

Abstract Condition monitoring and fault identification have become important aspects to ensure the proper operating condition of rotating machinery in industrial applications. In this sense, gearbox transmission systems and induction motors are important rotating elements due to they are probably the most used in industrial sites. Thus, from an industrial perspective, the occurrence of vibrations is inherent to the working condition in any rotating machine. To overcome this issue, condition monitoring strategies have to be developed aiming to avoid unnecessary cost and downtimes; thereby, condition-based maintenance based on vibration analysis has become as the most reliable approach with condition monitoring and fault identification purposes. In this regard, this work proposes a spectral analysis of the nonlinear vibration effects produced by worn gears and damaged bearings during the condition monitoring and fault assessment in an electromechanical system. The analysis is based on the spectral estimation from the available vibration and stator current signals; furthermore, the theoretical fault-related frequency components are estimated for being located in such estimated spectra. Consequently, the identification of different levels of uniform wear is performed by comparing the amplitude increase of those theoretical frequency components. Finally, through time-frequency maps is proved that an incipient fault, such as wear in gears and damage in bearings, may produce nonlinear frequency components that affect the proper operating condition of the electromechanical system. The proposed analysis is validated under a complete experimentally dataset acquired from a real laboratory electromechanical system.

J. J. Saucedo-Dorantes (✉) · R. A. Osornio-Rios · R. J. Romero-Troncoso
HSPdigital CA-Mecatronica, Engineering Faculty, Autonomous University of Queretaro, 76806
San Juan del Rio, Mexico
e-mail: jsaucedo@hspdigital.org

M. Delgado-Prieto
Department of Electronic Engineering, Motion Control and Industrial Applications (MCIA)
Research Center, Technical University of Catalonia, 08034 Barcelona, Spain

Keywords Condition monitoring · Nonlinear vibrations · Gearbox wear · Damaged bearing · Electromechanical systems

8.1 Introduction

Condition monitoring strategies are essential to assess and to ensure the proper operating condition of industrial machinery in different applications. Indeed, most of the industrial applications are related with the use of electrical and mechanical rotating machines [1–3]. In this sense, it should be mentioned that gearboxes and induction motors (IM) have been widely implemented in industrial processes due to its reliability and effectiveness; however, despite of its reliability, these rotating elements are subjected to the appearance of unexpected faults. Indeed, gearbox transmission systems and IM are composed by rotating mechanical elements, such as bearings, rotors and couplings, that are considered as a nonlinear elements; and under the fault influence several damages may be produced [4–6]. Therefore, it is well-known that there exist different configurations of electromechanical systems to perform specific industrial tasks. In this regard, IM and gearboxes are the most common rotating machines that have been widely used to compose such electromechanical systems; consequently, its proper operating working condition must be safeguarded [7, 8].

From a real industrial perspective, most of the implemented applications are subjected to abnormal operating conditions, such as fluctuating loads, that may produce the appearance of unexpected faults that causes the machinery downtime [9, 10]. Accordingly, it has been proved that the possibility of fault appearance in an IM is around 41%, where bearings are the most susceptible elements for the incidence of faults. Whereas, the possibility for the incidence of faults in gearboxes is around 26%; although the probability for fault appearance in gearboxes is lower, the appearance of incipient faults should not be despised due to several consequences may be produce [11, 12]. Indeed, in an electromechanical system, the sudden appearance of an unexpected fault may conduce to severe damages that can compromise the proper operating condition of the whole elements of the machinery and its availability [13]. Therefore, condition monitoring and fault identification strategies may consider the occurrence of multiple faults in order to avoid major damages.

Consequently, it can be assumed that electromechanical systems composed by rotating machinery, such as gearboxes and IM, may produce responses described by nonlinear behaviors; even, such nonlinear response is highlighted if the electromechanical system is subjected to fluctuating loads during its working condition [14–16]. In this regard, the condition monitoring assessment and fault identification could represent a challenge under this assumption; thereby, condition monitoring strategies must be capable to overcome these issues in order to perform accurate outcomes. On the other hand, most of the proposed condition monitoring strategies have been based on the use of different physical magnitudes, such as mechanical vibrations, stator current signatures, sound, among others [17, 18]. However, vibrations analysis and stator current signature analysis remain as the most well-known,

reliable and accepted approaches included for the condition monitoring and fault identification in rotating machinery. Furthermore, the occurrence of vibrations is inherent to the working condition of any rotating machine, thus, the characteristic vibrational pattern of a rotating machine will change whether a fault in an early or advanced stage appears [19, 20].

Different signal processing techniques have been considered to process the available physical magnitudes; in this sense, time domain, frequency domain and time-frequency domain are the most usually signal processing techniques used in condition monitoring strategies [13, 17, 21]. Although time domain analysis which is mainly based on the calculation of statistical-time domain features may help to analyze tendencies in signals, frequency and time-frequency domain analysis represent suitable techniques used for the signal processing due to specific fault-related frequency components may be located and analyzed in the estimated frequency spectra.

In this regard, the Fast Fourier Transform (FFT) and the Continuous Wavelet Transform (CWT) are the most well-known techniques used for frequency domain and time-frequency domain analysis. For instance, the FFT is the most preferred technique to perform analysis over stationary signals with the advantage of obtaining high-performance results with a low computational burden. On the other hand, the consideration of CWT may differ of different aspects where the most important is the selection of the mother wave for performing the analysis. In this sense, the Morlet-Wavelet function has been successfully applied to perform signal processing analysis of signals that describe the nonlinear response of electromechanical systems [22–25]. Therefore, spectrograms and time-frequency maps may be obtained by analyzing signals through these well-known approaches. The advantage of these approaches is that the condition monitoring and fault identification may be carried out by analyzing specific bandwidth frequency components in such estimated spectrograms or time-frequency maps. Moreover, the nonstationary effects produced by nonlinear behaviors can be also analyzed through the propped application of time-frequency domain analysis [26].

Therefore, in this work is performed an spectral analysis of the nonlinear vibration effects produced by worn gears and damaged bearings during the condition monitoring and fault assessment in an electromechanical system. The analysis is performed by estimating the theoretical fault-related frequency components produced by incipient faults in gears and bearing; specifically, uniform wear in gears and damage in the outer raceway in bearings. Consequently, the available vibration signals from the perpendicular plane of the rotating axis of the gearbox and the stator current signals of the IM are continuously acquired. Then, the characteristic fault-related frequency components are analyzed by comparing its amplitude increase in the vibration frequency spectrum estimated through the FFT. Additionally, the vibrations effects are also addressed by performing an analysis of the stator current spectrum. Thereby, the assessment of different faulty condition is carried out by means of the spectral analysis of two different signals. Consequently, the nonlinear effects are detected by the monotonical behavior produced in the amplitude of the theoretical fault-related frequency components. Indeed, the nonlinear effects are also analyzed by means of time-frequency maps resulting from the analysis through the Morlet-Wavelet trans-

form. The obtained results show that incipient faults in gears and bearings produce nonlinear vibration responses, however, the fault identification and assessment may be performed by analyzing fault-related frequency components associated to those damaged elements.

The proposed analysis is performed under a complete experimentally dataset acquired from a real laboratory electromechanical system where four different condition on uniform wear in gear and a condition of damaged bearing are evaluated, the performed results make the proposed analysis suitable to be applied for the condition monitoring and fault assessment in industrial applications.

8.2 Theoretical Background

8.2.1 Vibration Response in Rotating Machines Composed by Gears

From an industrial point of view, in most of its processes and applications the occurrence of mechanical vibrations is inherent to the working condition of the rotating machines that are involved; indeed, in new rotating machines vibrations are also produced just for the sake of working. In this regard, machines and machinery composed of gears are not an exception where the appearance of vibrations does not occur [27]. Otherwise, for an ideal pair of gears, the occurrence of vibrations could be avoided only if the teeth profiles in gears have a perfect involute shape and only if the teeth are considered as a not deformable elements. Therefore, due to there not exist an ideal procedure of gearing for any gearbox power transmission system, vibrations are mainly produced by the existence of backlash and by the excitation of the dynamic forces that are induced when the teeth of a gear enter in contact others of a different gear [13, 22].

Theoretically, for a single-stage gearbox transmission system that comprises a pair of gears, an impact frequency is produced as a result of the teeth meshing in gearbox transmission systems. Thus, under this consideration, its characteristic vibration response is described by such impact frequency that is also defined as the mesh frequency (f_m). Specifically, the f_m may be theoretically estimated through the product of the teeth number (N) and its rotating frequency (f_r), as is described by Eq. (8.1).

$$f_m = N \cdot f_r \quad (8.1)$$

Consequently, a unique component of the f_m . is produced in a single-stage gearbox transmission system; whereas in a multi-stage gearbox transmission systems, the number of components of the f_m is associated to the number of pair of gears that are involved; for example, in a two-stage gearbox there are two different f_m components.

Furthermore, in a gearbox vibration spectrum, it is also expected that two frequency components related to the rotating speeds of the pair of gears appear; that is, one of these components depicts the rotating speed of the driver gear and the other one the rotating speed of the driven gear. Indeed, in a classic gearbox vibration spectrum, the f_m component tend to appear accompanied with sideband components ($f_{\text{sidebands}}$); where such components may be located aside the f_m separated by rotating frequency (f_r), as Eq. (8.2) describes. Certainly, these $f_{\text{sidebands}}$ are very important during the assessment of the gearbox, since through these sidebands is possible to determinate the condition of either of both gears (driver gear or driven gear).

$$f_{\text{sidebands}} = f_m \pm f_r \quad (8.2)$$

Theoretically, such $f_{\text{sidebands}}$ components commonly appear in the vibrational response produced by gears; this is due to the modulation effect that the rotating frequency produces in the tooth meshing waveform. Hence, theoretically it can be assumed that the f_m and $f_{\text{sidebands}}$ will produce low vibration amplitudes when the pair of gears are in a good condition as well as concentric; otherwise, an amplitude increase will be presented in these frequency components and their corresponding harmonics. In this regard, in Fig. 8.1a, b are shown the theoretical vibration spectra when a gearbox is in the healthy condition and under a faulty condition, respectively.

The theoretical spectra from Fig. 8.1a, b belong to an ideal pair of gears, however, as aforementioned, gearbox transmission systems are considered as a complex rotating machines. This assumption may be assert due to nonlinear effects, combined with unexpected frequency components, tend to appear in a real vibration spectrum obtained from an industrial application; indeed, most of the real processes are subjected to adverse conditions such as load oscillations. Additionally, the inclusion of nonlinear effects in the gearbox vibration response is also in function of several factors such as operating frequency, materials and the elements that are linked inside of the gearbox like bearings. Thereby, the analysis of theoretical approximations focused on the mechanical modeling of gearboxes may help to understand the behavior and response of such nonlinear effects produced by a gearbox transmission system. Although the modeling of the nonlinear behavior of mechanical system represents a complex task, it is possible to obtained useful approximations that aim to predict the nonlinear response. In this sense, several approximations have been developed and addressed aiming to model the gearbox response. However, this performed analysis does not include the development of a gearbox model, but, it is important to highlight some theoretical aspects that are considered to perform the proposed analysis; which is focused to determinate how the nonlinear vibrational effects may have influence for assessing the working condition of a gearbox transmission system.

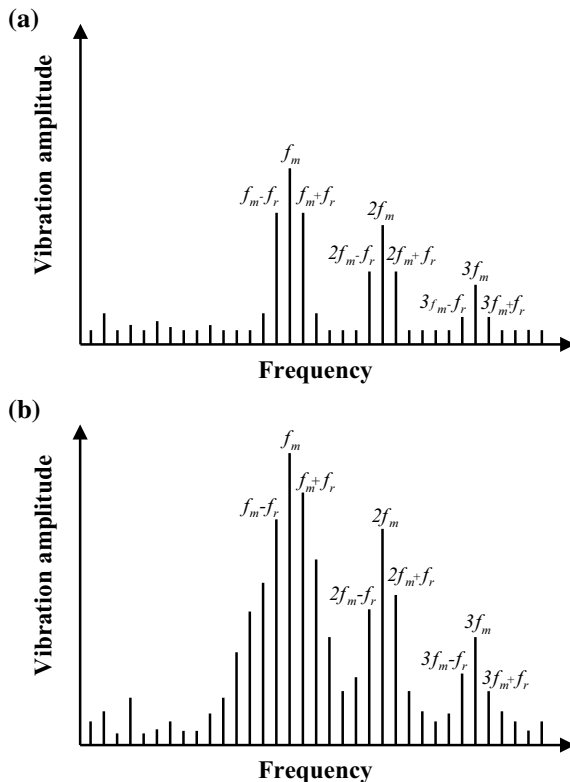


Fig. 8.1 Theoretical vibration spectrum of a gearbox in **a** the healthy condition and **b** under faulty condition

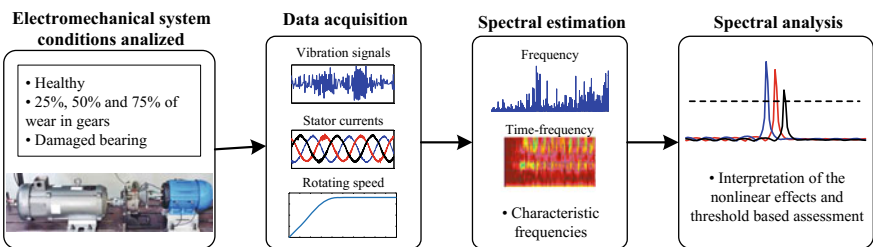


Fig. 8.2 Flow chart of the proposed spectral analysis of nonlinear effects produced by worn wears and damaged bearing in electromechanical systems during the condition monitoring assessment

8.2.2 *Vibration Response Produced by Bearing Elements*

A great deal of rotating machines involve the use of bearing elements, indeed, these elements allows the rotary movement of all the machinery used in different applications. Consequently, due to these elements are subjected to continuous working conditions, the appearance of different damages is commonly presented in bearings. In this sense, there are several factors such as load, rotating speed, temperature, lubrication, among others, that may influence the occurrence of damages.

Thus, as above mentioned, vibrations are inherent to the operating condition of rotating machines; and, similar to rotating mechanical systems with gears, bearings also have their own characteristic vibration frequencies. In this regard, some researches have been focused their studies in the analysis of the effects that different causes tend to produce in the fault-related frequencies of bearings [8, 15]. These characteristic fault-related frequencies produced by the appearance of damage or defects in bearings are theoretically well-known. Yet, although, there exist different variants, their calculation is in function of the rotating frequency and also in function of the geometrical parameters of the analyzed bearing.

Therefore, such frequencies may be referred to specific faults in different parts of the bearing; that is, the inner race, the outer race, the cage and the rolling elements. Thus, these frequencies are specifically defined as follows: the inner and outer race frequency (f_{BPIF} , f_{BPOF}) are also known as the ball pass inner/outer frequencies, the cage frequency (f_{FTF}) refers to the fundamental train frequency and the rolling elements frequency (f_{BSF}) is related to the ball spin frequency. Their theoretical equations are the following [15]:

$$f_{BPIF} = \frac{f_r}{2} N_b \left(1 + \frac{D_b}{D_c} \cos \varphi \right) \quad (8.3)$$

$$f_{BPOF} = \frac{f_r}{2} N_b \left(1 - \frac{D_b}{D_c} \cos \varphi \right) \quad (8.4)$$

$$f_{FTF} = \frac{f_r}{2} \left(1 - \frac{D_b}{D_c} \cos \varphi \right) \quad (8.5)$$

$$f_{BSF} = \frac{D_c}{2D_b} f_r \left(1 + \left(\frac{D_b}{D_c} \right)^2 (\cos \varphi)^2 \right) \quad (8.6)$$

where f_r is the rotating frequency of the shaft on which the inner race of the bearing is mounted, D_c denotes the cage diameter measured from opposites ball centers, D_b describes the diameter of the balls, N_b is the number of balls in the bearing, and φ is denominated the contact angle that exist between the bearing surfaces.

In this sense, for a condition monitoring approach, the theoretical calculation of such frequency components may facilitate the detection of malfunctions in bearing elements; even more when the condition monitoring and fault identification is performed through techniques based on the frequency domain and time-frequency analysis. Indeed, the main source of noise and vibrations that a damaged bearing

produce in a rotating machine is due to the bearing races are mechanically impacted by the rolling elements. Thus, regardless of whether the bearing damage is detected in the inner or outer race, mechanical impulses are produced each time that a rolling element contacts the inner or outer race with damage; consequently, the modulation effects may be commonly produced in the vibration response of bearings. In addition, the modulation effects are also produced by several causes such as fluctuating loads, flexural bearing modes among others.

Although the occurrence of vibrations is the main effect produced by mechanical failures such as damage in bearings, the sudden appearance of mechanical faults may also produce affectations that have influence in the working condition of rotating machinery. Besides the occurrence of mechanical vibrations, the stator current consumption is another physical magnitude that a damaged bearing tend to modify; indeed, several condition monitoring schemes based on motor current signature analysis (MCSA) have been proposed to analyze effects produced by failures in bearings. Thus, bearing defects also produce characteristic fault-related frequencies in a stator current spectra; these characteristic frequencies are related to those characteristic fault-frequencies performed through vibrations analysis (f_{BPIF} , f_{BPOF} , f_{FTF} , f_{BSF}) and are also related to the electrical supply frequency (f_s) [17]. Thereby, for this proposed study, only the outer race defect is analyzed; the following equation describes the relation between the frequency component of the stator current and its corresponding vibration component.

$$f_{BE} = f_s \pm kf_{BPOF} \quad (8.7)$$

where $k = 1, 2, 3, \dots$

8.3 Condition Monitoring Approach for Gearbox Wear Identification and Bearing Damage Identification

The proposed study is performed aiming to analyze the nonlinear effects that malfunction conditions, such as wear in gears and damage in bearing, produce in the mechanical vibration response and the stator current consumption in an electromechanical systems; besides, this study is also performed with condition monitoring and fault identification purposes. Thus, the proposed method for carrying out this analysis consist of four stages as the flow chart of Fig. 8.2 depicts.

First, different experiments are carried out and each considered conditions is iteratively tested in the electromechanical system; that is, three worn gears are experimentally tested in a gearbox, a damaged bearing is tested in the IM and the blending of each different wear level with the damaged bearing are also tested.

Second, in the data acquisition, different physical magnitudes are continuously monitored and acquired during the performance of each experiment; thus, the acquired information include the occurrence of vibrations in the perpendicular plane

of the gearbox rotating axis (radial axis). In this regard, due to the amount of useful information that vibration signals contain, its occurrence in the perpendicular plane of the rotating axis of the machinery represent one of the most reliable information that have been successfully included in most of the reported condition monitoring strategies. Moreover, one stator current is also acquired aiming to have another meaningful measurement able to describe the working condition of the electromechanical system; additionally, the output rotating speed produced by the electromechanical system is also acquired.

Next, third, the spectral estimation is carried out through techniques based on frequency and time-frequency domain analysis; in this sense, both time-domain signals (vibrations and stator currents) are first processed by applying a Hanning time window. Thus, such time-domain signals are first windowed for reducing the spectral leakage that may be induced by the variable frequency driver (VFD). Then, the FFT and the Wavelet transform are separately applied to the windowed signals in order to obtain the vibration and stator current spectra in both domain analysis (frequency and time-frequency). On the other hand, the theoretical characteristic fault-related frequencies are computed by averaging the rotating output speed acquired by the optical encoder and by using this averaged speed in Eqs. (8.1), (8.2), (8.4) and (8.7).

Fourth, subsequently, the spectral analysis is accomplished by searching, in specific bandwidths, those theoretical fault-related frequency components. In this sense, those spectra obtained from vibration and stator current signals acquired during the test of the healthy condition are considered as the reference spectra; thus, it is expected the amplitude increase of the fault-related frequency components when the worn gears and the damaged bearing are experimentally tested. Thereby, the condition assessment of the electromechanical system, and the nonlinear effects produced by the considered faults, is performed by comparing the amplitude increase of the theoretical fault-related frequency components. In this regard, the nonlinear effects are analyzed by means of time-frequency maps computed by applying the Wavelet transform to the acquired signals; specifically, the Morlet-wave function is used as the mother-wave for obtaining such time-frequency maps.

8.4 Experimental Setup

8.4.1 Test Bench

The proposed study has been addressed by performing a vibration spectra analysis of an experimentally database acquired from a real laboratory electromechanical system; the experimental test bench is mainly composed by an induction motor (IM), a gearbox and a DC generator. In Fig. 8.3 is shown a picture of the experimental test bench used for the validation of this proposed research.

Specifically, the considered IM is a 1492-W three-phase induction motor (model WEG00236ET3E145T-W22), the rotational speed of the IM is controlled by means

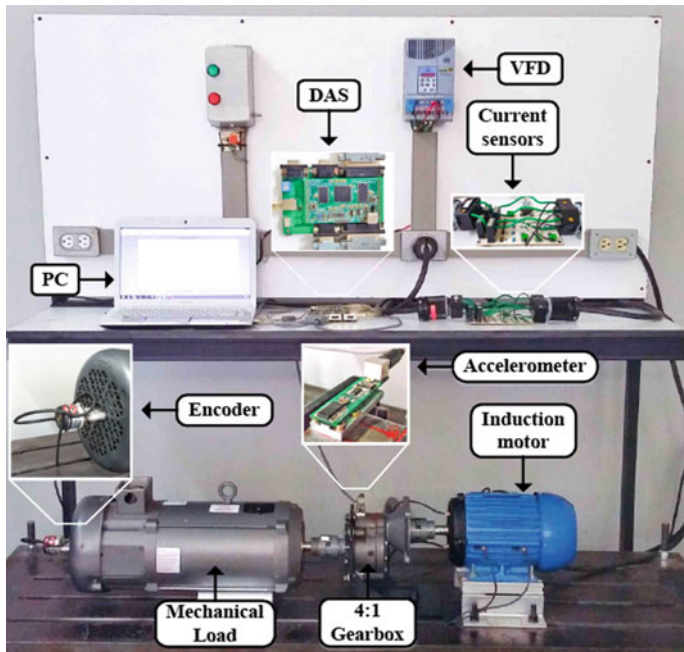


Fig. 8.3 Experimental test bench used to validate the proposed multi-fault diagnosis methodology

of a variable frequency driver (VFD) that controls the supply frequency. Then, the input shaft of the 4:1 ratio gearbox (model BALDOR GCF4X01AA) is mechanically coupled to the IM which drives it; in turn, the DC generator (model BALDOR-CDP3604) is coupled to the output shaft of the gearbox. The DC generator is used as a mechanical load which comprises around 20% of the nominal load during the normal working condition of the electromechanical system.

Different physical magnitudes have been considered to be continuously acquired, thus, a tri-axial accelerometer (model LIS3L02AS4) mounted on the top of the gearbox is used to measure the vibration signatures. Although three different vibration measurements are acquired, only the vibration signals that belongs to the perpendicular plane of the rotating axis of the IM has been analyzed. Thus, the occurrence of vibration in the radial direction has been analyzed. Besides that, an IM stator current phase is acquired by means of a Hall-effect current sensor (model L08P050D15) from Tamura Corporation. Thereby, for this proposal, a stator current phase is also considered in order to perform its spectral analysis and to demonstrate that mechanical faults, such as wear in gears and damage in bearings, may induce nonlinear affects in the IM current consumption. Additionally, the output rotational speed is measured through a digital encoder which is coupled to the DC generator shaft of its free end.

The installed sensors used to measure the vibration response and the stator current consumption are individually mounted on a board with its corresponding signal conditioning and its antialiasing filtering. The data acquisition is performed by means of a data acquisition system (DAS) that uses two 12-bit 4-channel serial-output sampling analog-to-digital converters (model ADS7841) from Texas Instruments. Such DAS is proprietary low-cost design based on field programmable gate array technology. The sampling frequencies considered during the acquisition of vibrations, stator current and rotational speed are set to 3, 4 and 4 kHz, respectively. In this regard, the DAS is programmed to automatically control the IM start-up and to acquire 100 s of the continuous working condition during the steady-state regime of the electromechanical system; therefore, 300, 400 and 400 kS are acquired and stored in a personal computer for its posterior processing.

8.4.2 *Description of the Considered Faults*

As it has been mentioned, a set of worn gears and a damaged bearing are the analyzed conditions. First, the worn gear condition is considered due to is one of the most common faults that occur in power transmission systems with gearboxes. Indeed, the analyzed gearbox wear consists of a uniform wear which is similar to that produced in gearboxes after a long useful life in real industrial applications.

Accordingly, three different levels of wear in gears are evaluated to analyze the nonlinear effects that a typical fault in gears produce in the vibration response and in the stator current consumption. The 4:1 ratio gearbox consists of two gears, the driver gear has 18 teeth and the driven gear has 72 teeth; thus, the wear has been artificially induced uniformly by a gear factory in all teeth of three similar driven gears. From Fig. 8.4a–d are shown the set worn gears analyzed in this proposal: healthy and 25, 50 and 75% of uniform wear, respectively.

In regard with the damaged bearing, the IM uses a bearing model 6205-2ZNR that is located in rotor on the output shaft side; thus, a similar bearing element has been also artificially damaged by means of drilling a through-hole on its outer race with a tungsten drill bit of 1.191 mm diameter to produce the bearing with damage. In Fig. 8.5 is shown a picture of the damaged bearing used to perform the proposed analysis. This faulty condition is analyzed due to most of the rotating machinery involves the use of bearing elements, and their sudden malfunctioning tend to introduce nonlinear effects in the whole elements that are indirectly linked to bearings with damage.

During the experimentation, two different operating frequencies are set in the VDF to drive the IM, that is, 15 and 50 Hz. Such operating frequencies produce an averaging output rotating speed of 889 rpm and 2984 rpm, respectively. Despite the nominal rotating frequency is 60 Hz, low frequencies such as 50, and 15 Hz are considered in order to avoid the addition of noise in the vibration and stator current signature produced by high-speed operating conditions. Moreover, the consideration of different operating frequencies is also in order to analyze the behavior of the

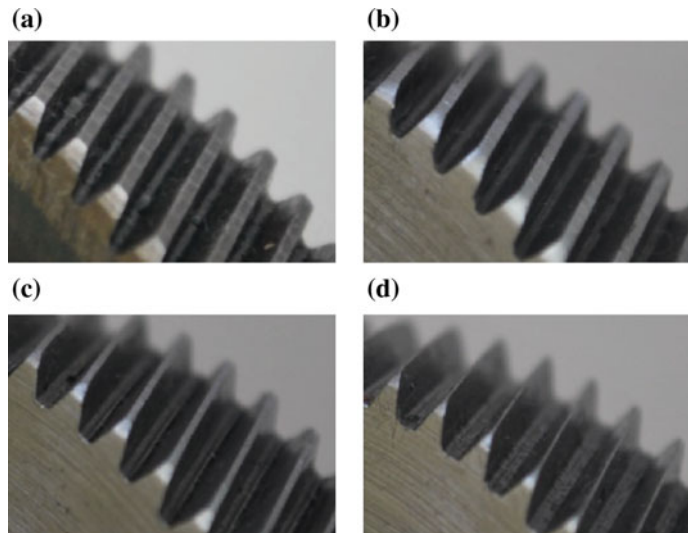


Fig. 8.4 Set of worn gears considered for this proposed analysis. **a** Healthy and **b** 25%, **c** 50% and **d** 75% of uniform wear



Fig. 8.5 Bering element with artificial damage in the outer race

nonlinear produced by the operating frequencies. The experimentation is carried out by the iterative replacement of the damaged elements (worn gears and damaged bearing) by the healthy elements, additionally, the combination of each worn wear with the damaged bearing is also experimented.

8.5 Results and Discussions

The proposed analysis and the final diagnosis outcome is performed under Matlab which is a dedicated software that may be used for signal processing in different engineering applications. As aforementioned, different experiments are carried out by iteratively replacing the worn gears with the healthy gear, also by replacing the damaged bearing with the healthy one and by combining the damaged bearing with each different worn wear condition. Thus, the continuous data acquisition of the vibration occurrence, stator current consumption and rotational speed is performed during each experiment.

In this regard, for each experiment, the rotating speed achieved in the electromechanical system during the steady-state regime is calculated by averaging the speed signal acquired by the digital encoder. Subsequently, this rotating speed is used to compute the characteristic fault-related component frequencies provided by the theory. Thereby, the theoretical frequency components are estimated through equations presented in previous Sect. 8.2, the obtained values are summarized in Table 8.1.

Despite specific frequencies are set in the VFD to feed the IM (15 and 50 Hz), the resulting output rotational speed produced in the electromechanical system presents slight variations that are below to the expected speed; this effect is commonly produced in most of the IM by the slip of the rotor. Thus, as it can be seen in Table 8.1, the output rotating speed is affected an average of 2% compared to the expected rotating speed. Indeed, these speed variations may lead to produce load discontinuities during the working condition; thus, such discontinuities may be the cause of nonlinear response of the vibration pattern in a rotating machine. In this regard, this proposal is performed aiming to analyze the nonlinear effects produced by worn gears and damaged bearings during the condition monitoring and the fault assessment in an electromechanical system. Thus, as aforementioned, the analysis is carried out by obtaining the frequency spectra from the available physical magnitudes, vibrations and stator current, and by locating in the frequency spectra the characteristic fault-related frequencies predicted by the theory. Specifically, the fault assessment is performed by comparing the amplitude increase of such theoretical frequency components.

Previous to the spectral analysis, the time-domain signals are analyzed in order to highlight nonlinear characteristics that may be found in such signals. Therefore, in Fig. 8.6a, b are shown segments, that comprise 0.1 s, of the acquired vibration signals

Table 8.1 Obtained values of the characteristic fault-related frequency components of the studied conditions

Averaged rotating speed (rpm)	Theoretical frequency components (Hz)					
	f_r	f_m	$2f_m$	f_{BPOF}	$2f_{BPOF}$	f_{BE}
2983.19	49.72	894.96	1789.91	178.00	356.00	227.72
888.33	14.81	266.50	533.00	53.00	106.00	67.81

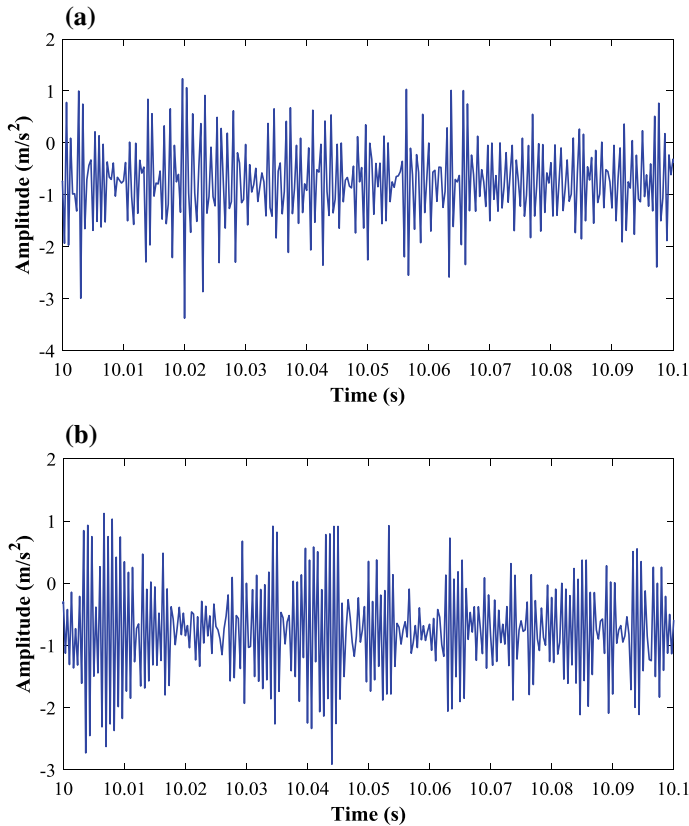


Fig. 8.6 Vibration response produced during the working condition of the considered electromechanical system and when in the gearbox is tested the: **a** Healthy gear and **b** the gear with 75% of uniform wear

during the working condition of the electromechanical system when the healthy gear and the gear with 75% of uniform wear are tested, respectively. In this sense, there are some aspects that must be mentioned from these signal segments; first, although Fig. 8.6a belongs to the vibration response when the healthy gear is tested, it is possible to appreciate that the acquired signal does not follow a specific pattern. Indeed, it can be assumed that this produced response is due to the whole rotating elements involved in the electromechanical system (gearbox, bearings, couplings, among others) are subjected to shock impulses during the working condition.

On the other hand, it is possible to appreciate from Fig. 8.6b that the vibration response when the gear with 75% of uniform wear tend to highlight and to include nonlinear effects in the acquired signal. These nonlinearities are induced due to the existence of backlash that excites the dynamic forces induced when the teeth of a driver gear enter in contact the teeth of a driven gear. Thereby, from these acquired signals it can be supposed that the vibration response produced during the condition

monitoring and the gearbox fault assessment generates a nonlinear response, even when the healthy gear is assessed. Moreover, through these time-domain signals is proved that mechanical systems with gears produce nonlinear responses, as it has been mentioned in several research works [14].

Subsequently, regarding the spectral analysis, for each considered condition tested at different operating frequency, the vibration signal is analyzed by means of applying the FFT and the stator current signal is analyzed by performing the power spectral density (PSD). Yet, although, it is well-known that the FFT has some disadvantages during the signal processing when there exist nonstationary frequencies; all the analyzed signals are acquired during the steady-state regime of the working condition of the electromechanical system. However, on the other hand, the performance of the spectra obtained through FFT may be affected if load oscillations are produced during the working condition. In this sense, by taking into account the acquired vibration signals, most of the reported research have been concluded that better results are obtained from the analysis of those vibration signals that are acquired from the perpendicular plane of the machinery rotating shaft. This assert is due to considered faults such as damaged bearings, unbalances, misalignments, among others, tend to produce radial forces that lead to the appearance of vibrations in the perpendicular plane.

Accordingly, in Fig. 8.7a, b are shown the vibration spectra obtained by the application of the FFT to the vibration signals acquired when the healthy gear and the gear with 50% of uniform wear are experimentally tested at 15 Hz as supply frequency. From these spectra it is possible to identify significant frequency components such as the rotating frequency (f_r), the mesh frequency with its corresponding harmonics (f_m and $2f_m$), and the outer race frequency with its second harmonic (f_{BPOF} and $2f_{BPOF}$). Moreover, from the obtained vibration spectra it is also possible to notice an amplitude increase in the region of the f_m component and its corresponding harmonic ($2f_m$). Specifically, these frequency components, f_m and $2f_m$, present a low amplitude in the spectrum of Fig. 8.7a around the bandwidth frequencies of 266.50 and 533.00 Hz, respectively. Whereas in Fig. 8.7b it is shown an abrupt amplitude increase around the characteristic frequency components related to the gear condition (f_m and $2f_m$). Despite the characteristic frequency components of f_{BPOF} and $2f_{BPOF}$ have been also located in the spectra, their localization result difficult due to all the noise induced by the operating condition of the gearbox. In this regard, as the theory describes, it is expected that an amplitude increase in the characteristic frequencies of a vibration spectrum describe the appearance of unexpected faults, such as uniform wear, in gears. Nevertheless, the inevitable addition of undesirable frequency components may complicate the assessment of other fault-related frequency components produced by a different source, such as a damaged bearing.

Although the amplitude increase in the f_m and $2f_m$ frequency components may lead to distinguish whether the presence of fault exist or not, the appearance of unexpected frequency components in the obtained spectra cannot be avoided. In this regard, the inclusion of unexpected and undesirable frequency components is due to the nonlinearities that are inherent to the working condition of the electromechanical system. For that reason both frequency spectra are full of additional frequency com-

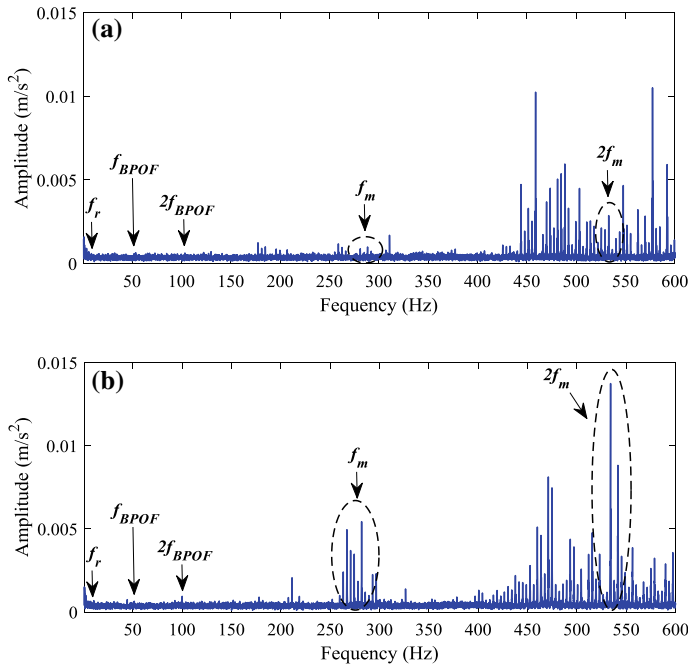


Fig. 8.7 Vibration spectra obtained by applying the FFT to the vibration signals acquired during the experimental test of the: **a** the healthy gear and **b** the gear with 50% of uniform wear when the IM is driven at 15 Hz

ponents in the right and left sidebands of the $2f_m$ component, as spectra of Fig. 8.7a, b shown.

On the other hand, the vibration spectrum of Fig. 8.8a belong to the obtained spectrum when only the damaged bearing is tested in the IM. Whereas, the vibration spectrum of Fig. 8.8b is obtained when the damaged bearing blended with the gear with 75% of uniform wear are tested in the electromechanical system with a supply frequency of 15 Hz. From these spectra it is also possible to identify important frequency components such as the outer race frequency with its harmonic ($f_{BPOF} = 52.41$ Hz and $2f_{BPOF} = 103.8$ Hz), the mesh frequency with its harmonic ($f_m = 267$ Hz and $2f_m = 534$ Hz), and the rotating frequency ($f_r = 14.83$ Hz).

Therefore, for the spectrum of Fig. 8.7a that depicts the healthy condition, the fault-related frequencies present low amplitudes in comparison with the spectrum of Fig. 8.8a obtained when only the damaged bearing is tested in the IM. Although, the frequency components related to the damaged bearing are not totally detectable, the appearance of unexpected frequency components around the gearbox frequency components is inevitable due to the influence of the damaged bearing. In this regard, the nonlinear working condition of the gearbox does not allow to identify problems when only the bearing element is damaged. Indeed, this problem may be due to the accelerometer sensor is placed on the top of the gearbox. However, on the other

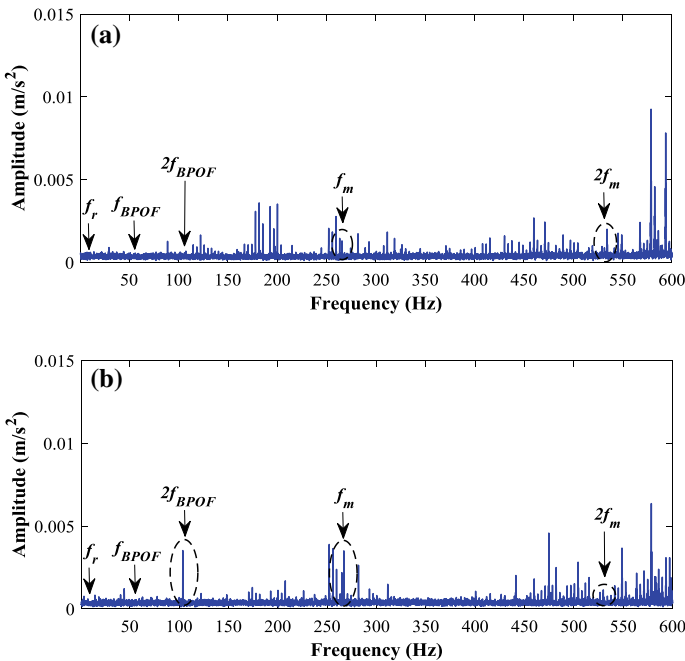


Fig. 8.8 Vibration spectra obtained by applying the FFT to the vibration signals acquired during the experimental test of the: **a** the damaged bearing and **b** the damaged bearing mixed with the gear with 75% of uniform wear when the IM is driven at 15 Hz

hand, when the gear with uniform wear of 75% and the damaged bearing are mixed and tested, an amplitude increase is presented in the frequency component related to the second harmonic of the damaged bearing ($2f_{BPOF} = 103.8$ Hz), as it can be seen in the spectrum of Fig. 8.8b. Moreover, an amplitude increase in the regions of the f_m and $2f_m$, and the addition of unexpected frequency components can be also appreciated in spectra of Fig. 8.8b.

Despite the accelerometer is mounted on the top of the gearbox, the vibrations produced by the damaged bearing are transmitted along the whole electromechanical system and acquired by the sensor. In this sense, it can be assert that the characteristic fault frequencies related to the damaged bearing may be detected by installing an accelerometer sensor in the nearest place to the damaged bearing. Moreover, in all the spectra appear unexpected frequency components that are not directly associated to a specific fault-frequency. These components appear due to working condition of the complex elements that are linked in the electromechanical system; therefore, elements such as bearings and gearboxes lead to produce nonlinear vibration responses. Thus, after performing all the experiments, the vibration spectra are also analyzed by comparing the amplitude increase in the fault-related frequencies; the results are numerically summarized in Tables 8.2, 8.3, 8.4, 8.5.

Table 8.2 Amplitudes of the characteristic fault-related frequencies for the different gear conditions without damaged bearing and the IM driven at 15 Hz

Condition (%)	Amplitude ($\times 10^{-3}$ m/s 2)					
	f_m	$2f_m$	$3f_m$	f_{BPOF}	$2f_{BPOF}$	$3f_{BPOF}$
Healthy	0.75	2.86	0.52	1.24	0.41	0.26
25	1.45	3.13	0.62	0.59	0.39	0.47
50	4.95	13.74	1.51	0.89	0.57	0.35
75	1.17	12.12	4.19	0.51	1.39	0.28

Table 8.3 Amplitudes of the characteristic fault-related frequencies for the different gear conditions with damaged bearing and the IM driven at 15 Hz

Condition (%)	Amplitude ($\times 10^{-3}$ m/s 2)					
	f_m	$2f_m$	$3f_m$	f_{BPOF}	$2f_{BPOF}$	$3f_{BPOF}$
Healthy	0.42	2.00	1.23	0.32	0.26	0.77
25	2.68	2.44	4.15	0.24	1.40	0.54
50	7.92	4.02	1.91	0.53	1.26	0.50
75	3.50	0.77	3.047	0.44	3.52	0.52

Table 8.4 Amplitudes of the characteristic fault-related frequencies for the different gear conditions without damaged bearing and the IM driven at 50 Hz

Condition (%)	Amplitude ($\times 10^{-3}$ m/s 2)			
	f_m	f_{BPOF}	$2f_{BPOF}$	$3f_{BPOF}$
Healthy	1.11	0.19	0.49	2.88
25	14.7	0.32	0.35	7.16
50	27.4	0.46	0.33	31.6
75	4.00	0.75	0.32	9.83

Table 8.5 Amplitudes of the characteristic fault-related frequencies for the different gear conditions with damaged bearing and the IM driven at 50 Hz

Condition (%)	Amplitude ($\times 10^{-3}$ m/s 2)			
	f_m	f_{BPOF}	$2f_{BPOF}$	$3f_{BPOF}$
Healthy	26.0	3.55	2.75	5.31
25	8.22	0.50	0.58	3.30
50	58.1	0.79	0.64	15.5
75	23.0	0.50	0.65	2.86

Accordingly, by means of performing different experiments at different operating frequencies and in regard to the obtained results; the lower operating frequency of 15 Hz allows to assess the gearbox condition through the comparison of the amplitude increase in the f_m , $2f_m$ and $3f_m$ frequency components when the damaged bearing is not taken into account. In this sense, the most significant results are related to the monotonical increase of the amplitude of the $2f_m$ component. Indeed, the monotonical increase is due to the nonlinear effects produced by the uniform wear in gears. On the other hand, when the different worn gears are tested in combination with the damaged bearing, the amplitude of the f_m , $2f_m$ and $3f_m$ components also increase and appear in an irregular way. In this regard, this effect is produced by the combination of complex mechanical elements such as bearings and gears in the electromechanical system. Moreover, a low amplitude increase is detected in the harmonics of the bearing fault-related components $2f_{BPOF}$ and $3f_{BPOF}$. From the combination of bearing defects with the worn gears, it must be highlighted that the vibrations produced by the damaged bearing tend to modify the vibration response; thus, the fault assessment in the gearbox result in a more complex task.

The spectral analysis performed when the IM is driven at 15 Hz allows to perform the identification of different conditions of uniform wear in gears since the amplitude increase in the fault-related frequencies respond to a monotonical behavior. Thereby, this monotonical increase grants the diagnosis and identification of four different conditions of wear in the gearbox under test. In Fig. 8.9a, b are shown the obtained vibration spectra for all levels of uniform wear, these spectra are focused on the first and second harmonic of the meshing frequency component (f_m and $2f_m$) when the IM is driven at 15 Hz and the damaged bearing is not considered in the test. From these spectra it is important to highlight that the sideband frequency components appear separated at a distance that is equal to the rotating frequency (f_r) from the f_m and $2f_m$ components; thus, as aforementioned, these sidebands components are mainly related to gear with wear.

On the other hand, the spectral analysis performed at the operating frequency of 50 Hz has some limitations during the assessment of the worn gears. Specifically, the main disadvantage is that the frequency value of the f_m component increase considerably as the operating frequency increases; thus, the bandwidth of the accelerometer sensor is not enough to acquire the vibration response of the gearbox if the corresponding harmonics of the f_m component are intended to be analyzed. Another disadvantage of this higher operating frequency is that the addition of unexpected frequency components is inherent to the working condition of the electromechanical system; indeed, the overlapping of important fault-related components may occur by the appearance of these unexpected components. From the obtained results at this operating frequency, it should be mentioned that there exist some problems in detecting the different levels of uniform wear in gears. In this sense, in Fig. 8.10 is shown the vibration spectrum in the region of the f_m component, and it is seen that the amplitude increase is not presented in a monotonical way as the level of wear increases. Moreover, the modification in the sidebands that appear around the f_m component are related to the worn gear conditions. In regard to the damaged bearing, it is perfectly detected by comparing the amplitude increasing of the fault-

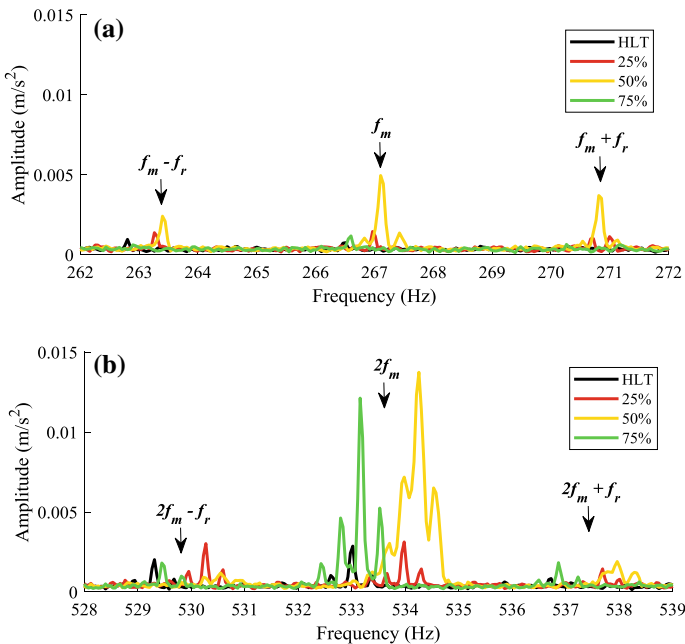


Fig. 8.9 Vibration spectra obtained through the application of the FFT to the vibration signals acquired during the experimental test of all considered conditions of worn gears: **a** at the region of the f_m component and **b** at the region of its corresponding harmonic $2f_m$, when the IM is driven at 15 Hz

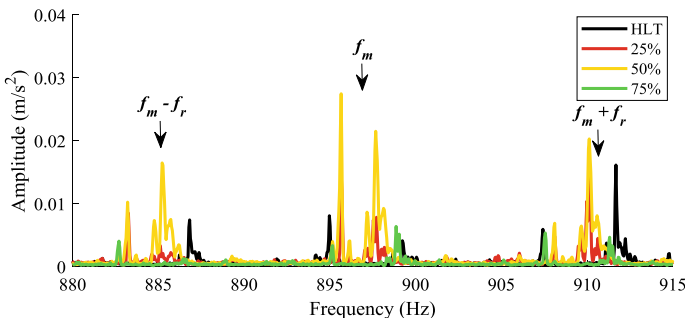


Fig. 8.10 Vibration spectra performed by means of applying the FFT to the vibration signals acquired during the experimental test of all worn gears when the IM is driven at 50 Hz

related frequencies f_{BPOF} , $2f_{BPOF}$ and $3f_{BPOF}$. However, the influence of wear in the gearbox tend to complicate the detection of the damaged bearing due to the inclusion on noise which results in unexpected frequency components.

The proposed study includes also the spectral analysis of the stator current signature through the PSD, this analysis is performed aiming to analyze the effects that

the occurrence of vibration produce in the stator current consumption. Thereby, the analysis is based on the estimation of the PSD from the stator current signals acquired during the experimental test for each considered condition. In this sense, classically, most of the analysis are focused on the modification and the appearance of sidebands frequency components around the supply frequency (f_s) [17]. Regarding the considered faults, worn gears and damaged bearing, the vibration response produced by any fault in a bearing element has a direct influence over the stator current consumption. Indeed, this influence may be associated to those fault-related frequencies estimated from the acquired vibration signals, as in Sect. 8.2 has been mentioned. Thus, for the considered bearing defect, there exist a specific fault-related frequency component that may be analyzed in the stator current spectrum.

On the other side, the vibration response produced by faults in gearboxes does not have a direct influence over the stator current consumption; that is, does not exist a specific theoretical approximation that allows to analyze the stator current consumption during the assessment of faults in gearboxes. However, according to [3], the appearance of incipient faults in gearbox transmission systems may not directly modify the amplitude of the rotating and mesh frequency in the electrical response; but, may generate harmonics around the f_s component, where such components will appear separated from the f_s at the distance that the gear with damage rotates.

Thereby, significant results have been obtained from the stator current spectral analysis; indeed, when the stator current is analyzed, better results are performed when the IM is driven at the operating frequency of 50 Hz. In Fig. 8.11 is shown the PSD estimated from the stator current signals acquired when the healthy condition and all the levels of uniform wear are tested in the gearbox and when the IM is feed at a supply frequency of 50 Hz. From this figure it is possible to notice the appearance of sidebands frequency components on the right and left side of the central frequency f_s ; thus, the behavior and modification of these sidebands are produced due to the influence of the considered conditions, uniform wear in gears and damaged bearing. From Fig. 8.11, there are five principal component frequencies that appears (a, b, c, d and e). Yet, although, the condition of wear in gears does not have a mathematical approximation to observe its effects in the stator current spectrum, by comparing its amplitude increasing it is possible to prove that different conditions of uniform wear in gears led to modify the behavior of such frequency components.

In this regard, aiming to facilitate the understanding of the results, the numerical location of the principal frequency components are summarized in Table 8.6 for the different operating frequencies (50 and 15 Hz) used in the VFD to feed the IM. As aforementioned, better results are obtained by analyzing the stator current signature acquired when the IM is driven at 50 Hz. However, in the stator current signature spectrum estimated when the IM is driven at 15 Hz there are also five significant frequency components that appear as a sidebands around the f_s frequency component. In this sense, in Table 8.6 are summarized the location of those sideband frequency components that appear in the stator current spectrum when the IM is driven at 15 Hz. Additionally, in Table 8.6 is also summarized the location of the specific fault frequency related to the damaged bearing f_{BE} .

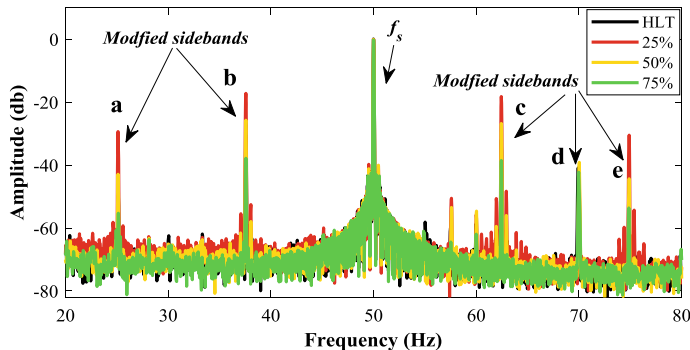


Fig. 8.11 Stator current spectra performed by means of estimating the PSD from the acquired stator current signature during the experimental test of all worn gears when the IM is driven at 50 Hz

Table 8.6 Principal frequency components to be analyzed in the stator current spectra when the considered conditions are experimentally tested at operating frequencies of 15 and 50 Hz

Operating frequency (Hz)	Amplitude ($\times 10^{-3}$ m/s 2)						
	f _s	a	b	c	d	e	f _{BE}
15	14.98	7.59	11.29	18.71	22.4	26.09	67.57
50	49.99	25.12	37.57	62.44	70.01	74.89	225.1

Aiming to observe the modification of such sidebands frequency components, in Fig. 8.12a, b is shown a zoom of the regions that correspond to the sidebands *b* and *c* of the spectrum of Fig. 8.11. From these zoom it is possible to notice that in both frequency components is presented a different amplitude level for each one of the conditions tested in the gearbox. Moreover, the behavior in the amplitude response of these sidebands indicate that there not exists a linear pattern that describe the amplitude increase in function of the level of uniform wear. However, the frequency amplitude produced by the healthy condition is considered as the reference, and any other value different to this reference describe improper malfunctions in the working condition of the gearbox. In order to summarize the results and to provide a better understanding, in Tables 8.7 and 8.8 are summarized the amplitudes of such sidebands frequency components (f_s , *a*, *b*, *c*, *d*, *e* and f_{BE}). These tables summarize the results for all the considered conditions of uniform wear when the IM is driven at 15 Hz and the bearing is in the healthy condition and damaged condition, respectively. On the other side, in Tables 8.9 and 8.10 are summarized the amplitudes of the same sideband frequency components when the IM is driven at 50 Hz and the condition of the bearing element is healthy and damaged, respectively.

Through this analysis, it is proved that mechanical vibrations produced by the appearance of incipient faults, such as wear in gears, tend to produce modification in the stator current consumption. Indeed, according to these results, it is possible to perform the identification of different conditions of wear in gears by comparing the amplitude increase or modification of the lateral sidebands that appear around

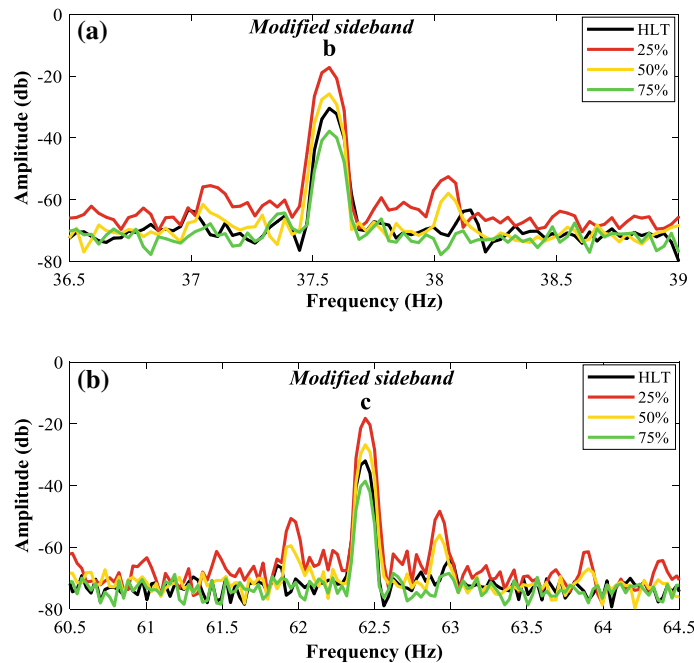


Fig. 8.12 Zoom of the stator current spectra at specific sidebands frequency components: **a** the modified sideband “*b*” and at **b** modified sideband “*b*”

Table 8.7 Amplitude of the frequency components for the stator current spectrum analysis for all the considered conditions of uniform wear when the IM is driven at 15 Hz and the damaged bearing is not considered

Condition (%)	Amplitude (db)						
	f_s	a	b	c	d	e	f_{BE}
HLT	0.680	-33.84	-51.25	-55.31	-37.61	-6056	-50.04
25	0.604	-31.32	-34.30	-38.19	-35.07	-41.86	-48.29
50	0.604	-33.76	-43.03	-47.28	-37.85	-45.59	-50.74
75	0.542	-37.57	-54.20	-56.96	-39.32	-55.4	-53.94

Table 8.8 Amplitude of the frequency components for the stator current spectrum analysis for all the considered conditions of uniform wear when the IM is driven at 15 Hz and considering the damaged bearing

Condition (%)	Amplitude (db)						
	f_s	a	b	c	d	e	f_{BE}
HLT	0.573	-41.90	-47.59	-51.68	-45.64	-50.50	-58.04
25	0.575	-32.79	-34.42	-41.19	-36.69	-45.34	-49.73
50	0.547	-31.54	-37.65	-37.77	-36.06	-39.88	-48.70
75	0.751	-35.78	-48.29	-51.19	-38.05	-49.90	-52.66

Table 8.9 Amplitude of the frequency components for the stator current spectrum analysis for all the considered conditions of uniform wear when the IM is driven at 50 Hz and the damaged bearing is not considered

Condition (%)	Amplitude (db)						
	f_s	a	b	c	d	e	f_{BE}
HLT	0.065	-49.19	-37.85	-38.55	-40.93	-53.63	-49.73
25	-0.587	-29.35	-17.21	-18.22	-44.35	-30.49	-50.04
50	-0.587	-42.92	-30.43	-32.01	-39.13	-46.73	-59.90
75	-0.269	-55.31	-37.85	-38.55	-42.27	-53.63	-70.11

Table 8.10 Amplitude of the frequency components for the stator current spectrum analysis for all the considered conditions of uniform wear when the IM is driven at 50 Hz and considering the damaged bearing

Condition (%)	Amplitude (db)						
	f_s	a	b	c	d	e	f_{BE}
HLT	-0.113	-45.28	-29.73	-30.57	-44.76	-45.86	-63.06
25	-0.903	-28.95	-17.40	-18.29	-47.49	-29.93	-51.27
50	-0.168	-35.31	-22.66	-23.56	-45.92	-36.20	-54.5
75	-0.84	-60.42	-30.26	-29.54	-41.02	-69.61	-68.9

the f_s component frequency. In regard to the bearing condition, its identification is also performed by comparing the amplitude increase of the specific fault-related frequency component f_{BE} .

Subsequently, an analysis through a time-frequency domain technique is performed in order to highlight that rotating machinery composed by gears and bearing elements produce nonlinear responses which result in nonlinear vibrations. In this regard, the Morlet-Wavelet transform is used to compute and to analyze the time-frequency maps obtained from the acquired vibration signals. Thus, for all the considered conditions a time-frequency map is obtained, however, more representative results are obtained during the analysis of the vibrations signals acquired when the IM is driven at 50 Hz. Indeed, the consideration of this operating frequency provide better results during the analysis, this is due to the dynamic forces that are inherent to the working condition of the electromechanical system are highlighted.

In this sense, in Fig. 8.13a, b are shown two time-frequency maps obtained through the application of the Morlet-Wavelet transform to the acquired vibrations signals when IM is driven at 50 Hz; the assessed conditions in the gearbox are healthy and 75% of uniform wear mixed with damaged bearing, respectively. From both figures it is possible to appreciate that there exist dominant frequencies that appear constantly. Yet, although most of these frequencies belong to a specific frequency component produced by a specific mechanical element, the presence of nonlinear frequency components is inevitable in the vibration response of the electromechanical system. In fact, there exit several differences between both

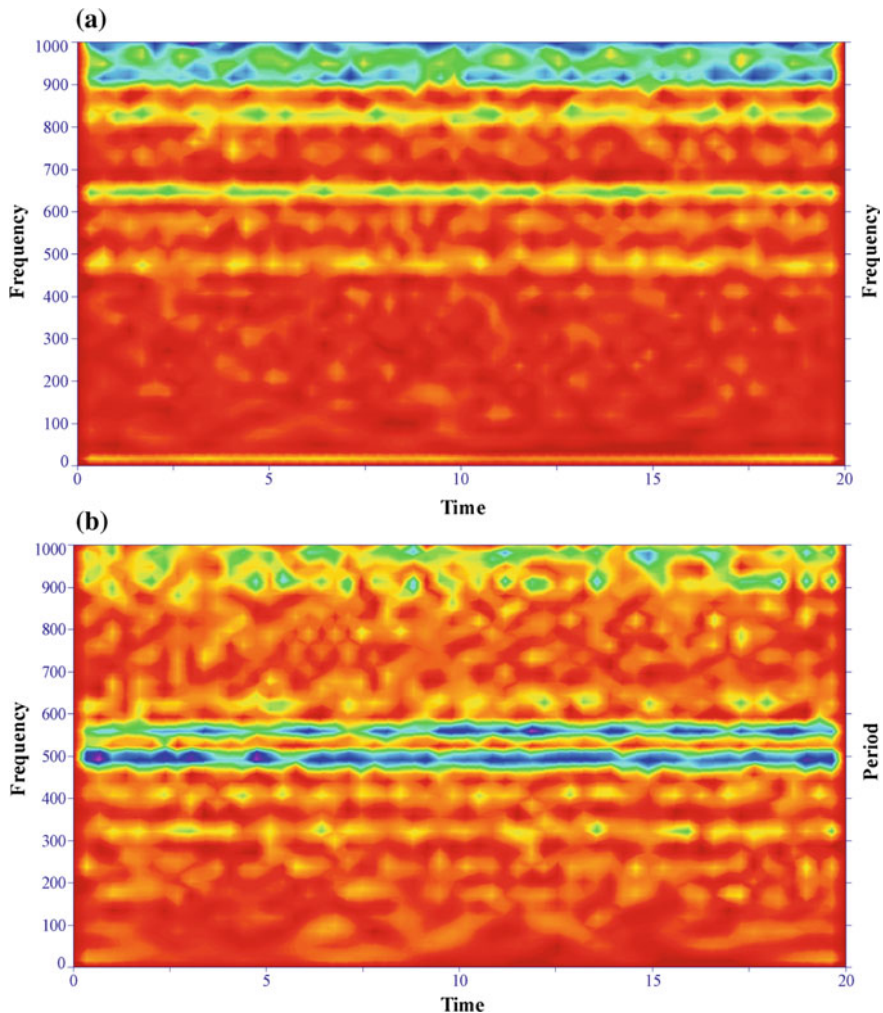


Fig. 8.13 Time-frequency spectrogram obtained by means of applying the Morlet Wavelet Transform to the acquired vibration signals when the IM is driven at 50 Hz for the experimental test of: **a** the healthy condition of the gearbox and **b** the gear with 75% of uniform wear mixed with the damaged bearing

time-frequency maps of Fig. 8.13a, b; that is, if the time-frequency map of Fig. 8.13a is used as the reference, the appearance of additional and unexpected frequency components may lead to provide the diagnosis assessment of the electromechanical system. Specifically, there is a strong modification in the vibration pattern around the band frequencies of 300, 400, 500, 650, 800 and 900 Hz. Thus, the modification of the time-frequency maps in the band frequency of 900 Hz is directly related to the appearance of wear in the gearbox; whereas, the modification of the time-frequency

maps in the band frequency between 300 and 400 Hz is due to the second harmonic of the fault-related frequency component of the damaged bearing. Furthermore, in both time-frequency maps there are regions where appear some vertical strips that are considered as a transitory frequency components produced by nonlinear behaviors.

8.6 Conclusions

In this work is performed a spectral analysis of the nonlinear vibration effects produced by worn gears and damaged bearings during the condition monitoring and fault assessment in an electromechanical system. The analysis is performed by means of acquiring the available vibrations signals from the perpendicular plane of the IM rotating shaft, and by acquiring its stator current consumption. Subsequently, the diagnosis outcome is performed by carrying out a proper signal processing through the FFT and PSD in order to obtain a frequency spectrum for the acquired vibration and stator current signals, respectively.

There exist important aspects that must be highlighted about the obtained results by the proposed analysis. First, the spectral vibration analysis shown that an amplitude increase, in the mesh frequency component (f_m) and their corresponding harmonics, allows to assess the gearbox condition; that is, the influence of uniform wear tend to increase the amplitude of the f_m component in a monotonical way. Second, the monotonical increase of such frequency components is due to the nonlinear vibration response produced by the worn gears; in this regard, the analysis performed at low operating frequencies (15 Hz) is suitable to assess and to detect the different levels of uniform wear. Otherwise, the non-monotonical increase of the f_m component produced at high operating frequencies (50 Hz) do not allow to identify the presence of the different levels of uniform wear; however, this amplitude modifications may be considered as an indicator produced by the malfunction operating condition in the electromechanical system. Third, through this analysis, it has been proved that the occurrence of nonlinear vibrations produced by the appearance of unexpected faults, such as wear in gears and damage in bearings, tend to modify the normal operating condition of the whole electromechanical system. This assumption has been affirmed by analyzing the stator current consumption that present modifications in the sidebands component frequencies that appear around the supply component frequency in presence of the abnormal operating conditions that have been addressed.

Finally, by means of the time-frequency maps it is also proved that the appearance of faults in rotating machinery may produce nonlinear vibration responses that affect its proper operating condition. Specifically, the nonlinear behavior produced by the appearance of uniform wear in gears may be perfectly analyzed through time-frequency domain techniques; this analysis is suitable for a better understanding of the electromechanical system operating condition. Indeed, through this techniques it is also possible to detect external frequency components that are not related to those mechanical elements with damage.

Therefore, from an industrial point of view, the proposed analysis is a suitable approach to assess the operating condition of rotating machinery used in industrial applications. Despite frequency and time-frequency domain are classical signal processing, its proper application may be a useful assessing tool for being applied in the condition monitoring and fault identification in industrial sites; moreover, theoretical models are also advantageous to understand how will be the response produced by the appearance of unexpected faults in rotating electromechanical systems.

Acknowledgements This proposed research has been partially supported by CONACyT under the Doctoral scholarship number 278033 and by FOFIUAQ-2018.

References

1. Yin, S., Ding, S.X., Xie, X., Luo, H.: Review on basic data-driven approaches for industrial process monitoring. *IEEE Trans. Ind. Electron.* **62**(11), 6418–6428 (2014)
2. Antonino-Daviu, J., Riera-Guasp, M., Pons-Llinares, J., Park, J., Lee, S.B., Yoo, J., Kral, C.: Detection of broken outer-cage bars for double-cage induction motors under the startup transient. *IEEE Trans. Ind. Appl.* **48**(5), 1539–1548 (2012)
3. Kia, S.H., Henao, H., Capolino, G.-A.: Trends in gear fault detection using electrical signature analysis in induction machine-based systems. In: Proceedings of the IEEE Workshop on Electrical Machines Design, Control and Diagnosis (WEMDCD 2015), pp. 297–303, Torino (March 2015)
4. Cheng, G., Li, H., Hu, X., Chen, X., Liu, H.: Fault diagnosis of gearbox based on local mean decomposition and discrete hidden Markov models. *Proc. Inst. Mech. Eng. Part C J. Mech. Eng. Sci.* **0**, 1–12 (2016)
5. Frosini, L., Harlisca, C., Szabó, L.: Induction machine bearing fault detection by means of statistical processing of the stray flux measurement. *IEEE Trans. Ind. Electron.* **62**(3), 1846–1854 (2015)
6. Lei, Y., Lin, J., Zuo, M.J., He, Z.: Condition monitoring and fault diagnosis of planetary gearboxes: a review. *Measurement* **48**, 292–305 (2014)
7. Antonino-Daviu, J., Riera-Guasp, M., Pons-Llinares, J., Park, J., Lee, S.B., Yoo, J., Kral, C.: Detection of broken outer-cage bars for double-cage induction motors under the startup transient. *IEEE Trans. Ind. Appl.* **48**(5), 1539–1548 (2012)
8. Bellini, A., Immovilli, F., Rubini, R., Tasson, C.: Diagnosis of bearing faults in induction machines by vibration or current signals: a critical comparison. In Proceedings of Industry Applications Society Annual Meeting (IAS), pp. 1–8, Edmonton, Alta (Oct 2008)
9. Chaari, R., Khabou, M.T., Barkallah, M., Chaari, F., Hadda, M.: Dynamic analysis of gearbox behavior in milling process-non-stationary operations. *Proc. Inst. Mech. Eng. Part C J. Mech. Eng. Sci.* **0**, 1–17 (2015)
10. Li, C., Sanchez, R.V., Zurita, G., Cerrada, M., Cabrera, D., Vasquez, R.E.: Gearbox fault diagnosis base on deep random forest fusion of acoustic and vibratory signals. *Mech. Syst. Signal Process.* **66–67**, 283–293 (2016)
11. Henríquez, P., Alonso, J.B., Ferrer, M.A., Travieso, C.M.: Review of automatic fault diagnosis systems using audio and vibration signals. *IEEE Trans. Syst. Man Cybern. Syst.* **44**(5), 642–652 (2014)
12. Kia, S.H., Henao, H., Capolino, G.A.: Gear tooth surface damage fault detection using induction machine stator current space vector analysis. *IEEE Trans. Ind. Electron.* **62**(3), 1866–1878 (2015)

13. Guoji, S., McLaughlin, S., Yongcheng, X., White, P.: Theoretical and experimental analysis of bispectrum of vibration signals for fault diagnosis of gears. *Mech. Syst. Signal Process.* **43**(1–2), 76–89 (2014)
14. Jauregui-Correa, J.C.: The effect of nonlinear traveling waves on rotating machinery. *Mech. Syst. Signal Process.* **39**(1–2), 129–142 (2013)
15. Leite, V.C.M.N., da Silva, J.G.B., Veloso, G.F.C., da Silva, L.E.B., Lambert-Torres, G., Bonaldi, E.L., de Oliveira, L.E.D.L.: Detection of localized bearing faults in induction machines by spectral kurtosis and envelope analysis of stator current. *IEEE Trans. Ind. Electron.* **62**(3), 1855–1865 (2015)
16. Uddin, J., Kang, M., Nguyen, D.V., Kim, J.M.: Reliable fault classification of induction motors using texture feature extraction and a multiclass support vector machine. *Math. Probl. Eng.* **2014** Article ID 814593, 9 pp. (2014)
17. Trajin, B., Regnier, J., Faucher, J.: Comparison between vibration and stator current analysis for the detection of bearing faults in asynchronous drives. *IET Electr. Power Appl.* **4**(2), 90–100 (2010)
18. Cerrada, M., Sanchez, R.V., Cabrera, D., Zurita, G., Li, C.: Multi-stage feature selection by using genetic algorithms for fault diagnosis in gearboxes based on vibration signal. *Sensors* **15**(9), 23903–23926 (2015)
19. Goyal, D., Pabla, B.S.: The vibration monitoring methods and signal processing techniques for structural health monitoring: a review. *Arch. Comput. Methods Eng.* **23**(4), 585–594 (2016)
20. Geramitcioski, T., Trajcevski, L., Vilos, I., Mitrevski, V.: Early gear tooth damage diagnostic from the vibration signatures. In: Proceedings of the 3rd International Conference Power Transmissions '09, Thessaloniki, Greece (2009)
21. Li, W., Zhu, Z., Jiang, F., Zhou, G., Chen, G.: Fault diagnosis of rotating machinery with a novel statistical feature extraction and evaluation method. *Mech. Syst. Signal Process.* **50–51**, 414–426 (2015)
22. Chen, J., Zhang, C., Zhang, X., Zi, Y., He, S., Yang, Z.: Planetary gearbox condition monitoring of ship-based satellite communication antennas using ensemble multi wavelet analysis method. *Mech. Syst. Signal Process.* **54–55**, 277–292 (2015)
23. Mark, W.D.: Time-synchronous-averaging of gear-meshing-vibration transducer responses for elimination of harmonic contributions from the mating gear and the gear pair. *Mech. Syst. Signal Process.* **62–63**, 21–29 (2015)
24. Liu, Z., Zuo, M.J., Xu, H.: Fault diagnosis for planetary gearboxes using multi-criterion fusion feature selection framework. *Proc. Inst. Mech. Eng. Part C J. Mech. Eng. Sci.* **227**(9), 2064–2076 (2015)
25. Ayad, M., Chikouche, D., Boukazzoula, N., Rezki, M.: Search of a robust defect signature in gear systems across adaptive Morlet wavelet of vibration signals. *IET Signal Process.* **8**(9), 918–926 (2014)
26. Bangalore, P., Tjernberg, L.B.: An artificial neural network approach for early fault detection of gearbox bearings. *IEEE Trans. Smart Grid* **6**(2) (2015)
27. Igba, J., Alemzadeh, K., Durugbo, C., Eriksson, E.T.: Analyzing RMS and peak values of vibration signals for condition monitoring of wind turbine gearboxes. *Renew. Energy* **91**, 90–106 (2016)